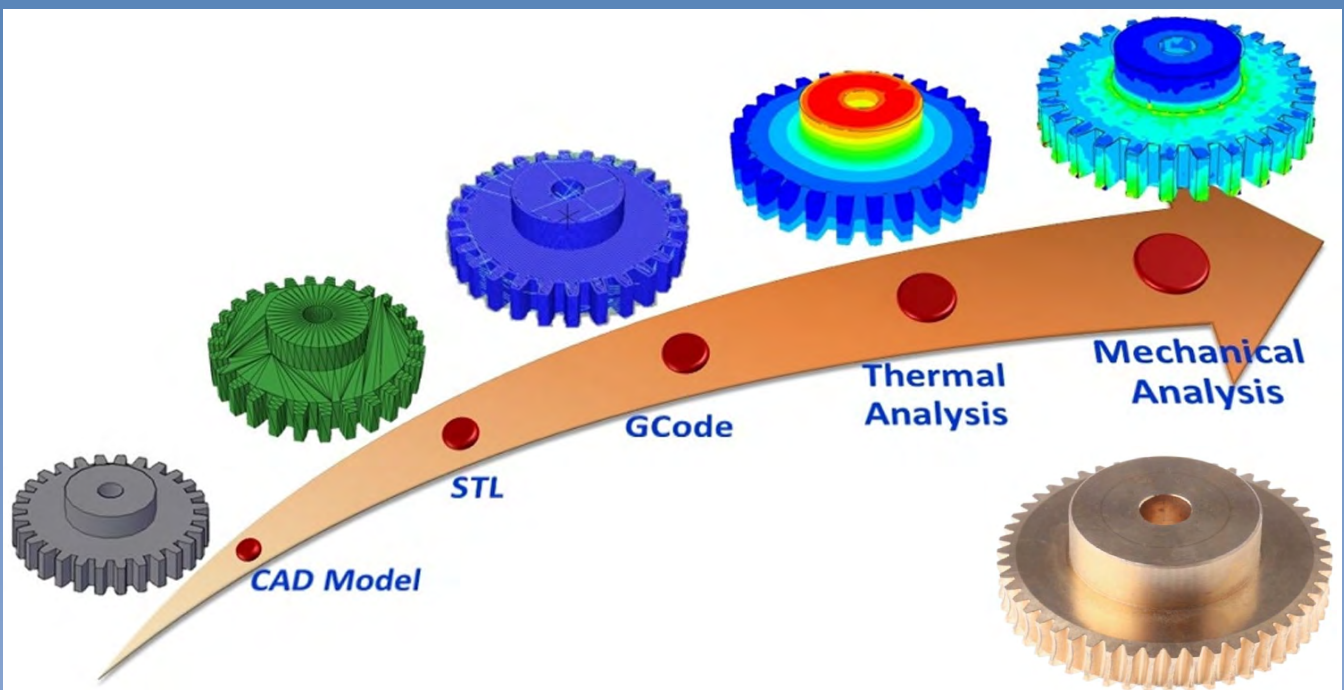
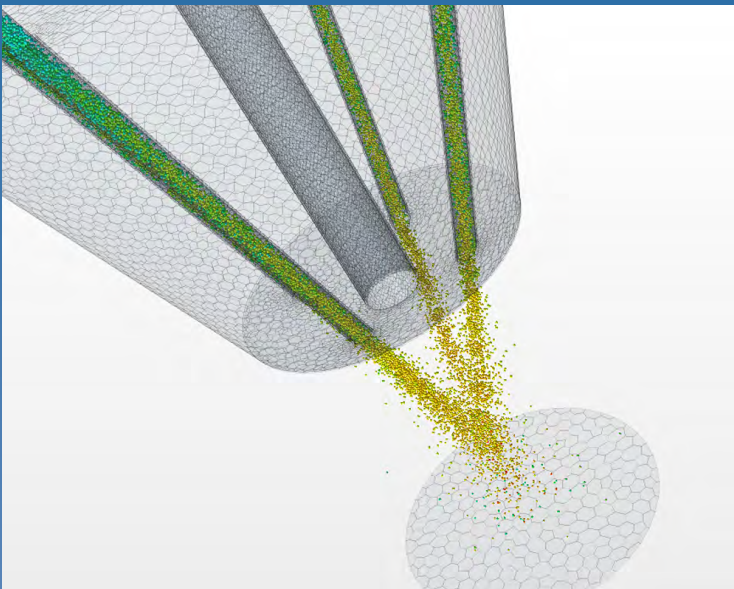


II International Conference on Simulation for Additive Manufacturing

Sim-AM 2019

11-13 September, 2019
Pavia, Italy

F. Auricchio, E. Rank, P. Steinmann, S. Kollmannsberger and S. Morganti (Eds.)



**II International Conference on
Simulation for Additive Manufacturing**

Sim-AM 2019

**Pavia, Italy
September 11 - 13, 2019**

A publication of:

**International Centre for Numerical
Methods in Engineering (CIMNE)**

Barcelona, Spain



First Edition: September 2019

© The Authors

ISBN: 978-84-949194-8-0

Printed by: Artes Gráficas Torres S.L., Huelva 9, 08940 Cornellà de Llobregat,
Spain

TABLE OF CONTENTS

Preface	7
Acknowledgements	9
Summary	11
Contents	13
Lectures	18
Authors Index	467

PREFACE

This E-book contains 44 full-length papers of the contributions presented at SIM-AM 2019, the second *International Conference on Simulation for Additive Manufacturing*, held in Pavia, Italy, hosted by the University of Pavia, from 11 to 13 September 2019.

In 2003, ECCOMAS initiated the successful experience of creating a series of Thematic Conferences, to be held in the odd years, on state-of-the-art topics in computational science and engineering. They are organized with the support of ECCOMAS and they attract overall about 3,000 participants.

In 2017, following the disruptive success of additive manufacturing as a new, very promising, production technology for creating solid structures of virtually any shape, the first thematic conference on *Simulation for Additive Manufacturing* was organized at TUM in Munich, Germany.

Additive Manufacturing (AM) products and processes are often much more complex than those obtained through classical manufacturing techniques, raising new questions for numerical simulations. Applications for AM products range across many fields in engineering, from design models to lightweight components for the automotive or aerospace industry, or to medical applications. Moreover, AM processes involve multi-physics and multi-scale phenomena: whereas relevant spatial scales range over many orders of magnitude, important time scales start at microseconds for physical processes and reach to hours or even days. Physics involved include mechanical, thermal, radiation and phase change problems. And most essential for simulation of AM is validation and verification. Last but not least a lack of appropriate manufacturing technologies hindered for a long time the realization of designs as obtained, e.g., by shape and/or topology optimization.

All these reasons together with the recorded great success of the 2017 event in Munich represent the strong motivations for the promotion and continuation of a dedicated ECCOMAS Thematic Conference on *Simulation for Additive Manufacturing*, covering topics that range from CAD-to-part chain to innovative applications, from material modeling to multi-physics and multi-scale simulation, from shape and topology optimization to validation and verification.

Our sincere appreciation goes to plenary lecturers, invited session organizers and all the authors who have contributed to the outstanding scientific quality of the conference. Finally, we wish to thank Mr. Alessio Bazzanella from CIMNE, Barcelona, Spain, and Mrs. Laura Mazzocchi from the University of Pavia, Italy, for their excellent work in the support of the conference organization and for the publication of this volume.

Ferdinando Auricchio

Department of Civil Engineering
and Architecture
University of Pavia
Italy

Simone Morganti

Department of Electrical, Computer,
and Biomedical Engineering
University of Pavia
Italy

ACKNOWLEDGEMENTS

The conference organizers acknowledge the support of the following organizations and sponsors:



UNIVERSITÀ
DI PAVIA

University of Pavia, Italy



SPP 1748



International Center for Computational Methods in Engineering, Spain



European Community on Computational Methods in Applied Sciences (ECCOMAS)



International Association for Computational Mechanics (IACM)



Associazione Italiana per l'Analisi delle Sollecitazioni (AIAS)



Institute of High Performance Computing (IHPC)



Società Italiana di Scienza delle Costruzioni (SISCO)



Associazione Italiana di Meccanica Teorica e Applicata



AITA-ITALIAN ASSOCIATION FOR ADDITIVE TECHNOLOGIES



Gold Sponsor



Silver Sponsor



Bronze Sponsor



SUMMARY

INVITED SESSIONS

IS - Additive Manufacturing for Biomedical Applications	19
IS - Advanced Simulation Technologies in Additive Manufacturing	40
IS - Efficient approaches for simulating additive manufacturing.....	51
IS - Mathematical Modelling and Analysis for advanced structural Design, Simulation and Optimization	60
IS - Modeling and Simulation of Advanced Manufacturing of Functional Materials	72
IS - Simulation and Fatigue in Metal Additive Manufacturing	83
IS - Simulation in the Design of AM Devices	99
IS - Topology and Shape Optimization for AM-ready Design.....	130

GENERAL SESSIONS

GS - AM Material Modeling	246
GS - AM Multi-Physics and Multi-Scale Problems	274
GS - AM Process Simulation.....	340
GS - AM Product Simulation and Innovative Applications	361

CONTENTS

INVITED SESSIONS

IS - Additive Manufacturing for Biomedical Applications

A combined approach of numerical simulation and additive manufacturing technique for in-silico and in-vitro testing of a 3D printing-based aortic polymeric heart valve	19
<i>E. Gasparotti, U. Cella, E. Vignali, E. Costa, G. Soldani, A. Cavallo, P. Losi, M. E. Biancolini and S. Celi</i>	

A numerical and 3D printing framework for the in vivo mechanical assessment of patient-specific cardiovascular structures	31
<i>B.M. Fanni, E. Sauvage, C. Capelli, E. Gasparotti, E. Vignali, S. Schievano, L. Landini, V. Positano and S. Celi</i>	

IS - Advanced Simulation Technologies in Additive Manufacturing

An efficient approach based on geometrical analysis to optimize AM process	40
<i>F. Valente and S. Papadopoli</i>	

IS - Efficient approaches for simulating additive manufacturing

Boundary conditions for simulation of powder bed fusion for metallic glass formation: measurements and calibrations	51
<i>J Lindwall, J J Marattukalam and C-J Hassila</i>	

IS - Mathematical Modelling and Analysis for advanced structural Design, Simulation and Optimization

Fast macroscopic thermal analysis for Laser Metal Deposition. Application to multiphase steels.	60
<i>D Weisz-Patrault</i>	

IS - Modeling and Simulation of Advanced Manufacturing of Functional Materials

Microstructure and Martensitic Transformation of Selective Laser Melted NiTi Shape Memory Alloy Parts	72
<i>C. A. Biffi, J. Fiocchi, P. Bassani and A. Tuissi</i>	

IS - Simulation and Fatigue in Metal Additive Manufacturing

Influence of as-built surface topography on the fatigue behavior of SLM Inconel 718: experiments and modeling	83
<i>G. Nicoletto, G. Tinelli, A. Lutey and L. Romoli</i>	

Simulation of residual stresses due to SLM fabrication and correlation with directional fatigue behavior of AlSi10Mg	91
<i>G. Nicoletto, D. Daviddi and A. Fornaci</i>	

IS - Simulation in the Design of AM Devices

Mechatronic approach to the design of AM machines	99
<i>P. Righettini and R. Strada</i>	
Modeling and simulation of a linear motor in a liquid-frozen deposition system for additive manufacturing.	111
<i>M. Silvestri and H. Giberti</i>	
Simulation of a robotic arm for multi-directional 3D printing	120
<i>K. Castelli and H. Giberti</i>	

IS - Topology and Shape Optimization for AM-ready Design

A Generative Design Optimization Approach for Additive Manufacturing	130
<i>N. Strömberg</i>	
Additive Manufacturing of a topology optimized lightweight part of a humanoid robot	142
<i>S. Junk, B. Klerch and U. Hochberg</i>	
Functional Lightweight Design for Additive Manufactured Vehicle Liftgate Door Hinge	154
<i>İ. Aydın, E. Akarçay, Ö. F. Gümüş, Ş. Özcan, H. Yelek and C.B. Engin</i>	
Functionally Graded Material Design for Plane Stress Structures using Phase Field Method	162
<i>G. Alaimo, M. Carraturo, E. Rocca, A. Reali and F. Auricchio</i>	
Guidelines for a post processing oriented design of additive manufactured parts for use in topology optimization	174
<i>S. Lammers, J. Tominski and D. Zimmer</i>	
Lattice topology optimization and 3D printing of a 316L control arm	186
<i>C. López and J. Stroobants</i>	
Mixed Integer Optimization for Truss Topology Design Problems as a Design Tool for AM Components	193
<i>C. Reintjes and U. Lorenz</i>	
Optimal Design of Lattice Structure Considering Constraints through Additive Manufacturing Process	205
<i>Y. Koike, K. Ushijima and J. Kato</i>	
Stress-based non intrusive shape optimization for additive manufacturing parts	215
<i>K. El Rai, C. Ghnatios and F. Chinesta</i>	

Topology Optimization of 3d Printed Prototypes	225
<i>I. Ntintakis, G. E. Stavroulakis, N. Lyroni and N. Plakia</i>	

Towards compliant and structural optimization of a Compliant Rotation Reducer Mechanism (Sim-AM 2019)	237
<i>L. Komini, J. Kruis, G. Perruchoud, F. Cosandier, L. Kiener and H. Saudan</i>	

GENERAL SESSIONS

GS - AM Material Modeling

In-situ thermographic monitoring of the laser metal deposition process ..	246
<i>N. Scheuschner, A. StraÙe, S. J. Altenburg, A. Gumenyuk and C. Maierhofer</i>	

Material modelling of UV curing polymers for additive manufacturing processes	256
<i>T. Rehbein, A. Lion and M. Johlitz</i>	

Simulation-based investigation of statistical fatigue strength of selective laser melted lightweight alloys	262
<i>M. Awd and F. Walther</i>	

GS - AM Multi-Physics and Multi-Scale Problems

A Mesoscopic Approach for Modelling Laser Beam Melting (LBM)	274
<i>Y.A. Mayi, M. Dal, P. Peyre, M. Bellet, C. Metton, C. Moriconi and R. Fabbro</i>	

A numerical model for the simulation of shallow laser surface melting	286
<i>A. Caboussat, J. Hess, A. Masserey and M. Picasso</i>	

Finding Optimal Parameter Ranges for Laser Powder Bed Fusion with Predictive Modeling at Mesoscale	297
<i>D. Nakapkin, A. Zakirov, S. Belousov, M. Bogdanova, B. Korneev, A. Stepanov, A. Perepelkina, V. Levchenko, B. Potapkin and A. Meshkov</i>	

Particle Scale Numerical Modelling of Heat Transfer and Melt Pool Dynamics in Selective Laser Melting	309
<i>E.L. Li, R.P. Zou, A.B. Yu and Z.Y. Zhou</i>	

Particle-based simulations and dimensional analysis of selective laser sintering of PA12 powder	316
<i>C. Bierwisch, S. Mohseni-Mofidi, B. Dietemann, J. Rudloff, S. Baumann, K. Popp and M. Lang</i>	

Simulation of heat transfer and metal flow in wire-based electron beam additive manufacturing	328
<i>A. Shcherbakov, D. Gaponova, R. Rodyakina, A. Gudenko, A. Sliva, V. Rubtsov and V. Dragunov</i>	

GS - AM Process Simulation

Forecasting the residual stresses in a polymer layer manufactured additively by the technology of centrifugal material application.	340
<i>D.A. Parshin</i>	

Numerical Analysis of Support Structures' Removal from Additively Manufactured Components	349
<i>L. Papadakis</i>	
GS - AM Product Simulation and Innovative Applications	
3D Finite Element Simulation of Polymer Extrudate in FDM 3D Printers ...	361
<i>O. Hira and A. Altinkaynak</i>	
Computational and Experimental Investigation of Vibration Characteristics of Variable Unit-Cell Gyroid Structures	369
<i>U. Simsek, C. Gayir, B. Kavas and P. Sendur</i>	
Designing additively manufactured parts via topology optimization - a space industry case study	381
<i>B. Barroqueiro, A. Andrade-Campos and R.A.F. Valente</i>	
DUOADD: a software to detect and export damages of 3D scanned objects	391
<i>M Perini and P Bosetti</i>	
Early Student Engagement in the Development of Process Monitoring Tools for Additive Manufacturing	403
<i>M. Moeckel</i>	
Numerical and Experimental Crushing Behaviour Investigation of EBM Printed Auxetic Chiral Lattices - KEYNOTE LECTURE	408
<i>K. Gunaydin, F. G. Gallina, A. A. Airoidi, G. Sala and A. M. Grande</i>	
Parametric Study in Co-Extrusion-Based Additive Manufacturing of Continuous Fiber-Reinforced Plastic Composites	417
<i>H. Albrecht, C. Savandaiah, A. Lepschi, B. Loew-Baselli and A. Haider</i>	
Particle Finite Element Simulation of Extrusion Processes of Fresh Concrete during Additive Manufacturing	428
<i>J. Reinold, G. Meschke, V.N. Nerella and V. Mechtcherine</i>	
POEAM, a method for the Part Orientation Evaluation for Additive Manufacturing	440
<i>S. Jung, S. Peetz and M. Koch</i>	
Probabilistic Finite Element Analysis of a Bespoke Titanium Implant Fabricated using Additive Manufacturing Technology	444
<i>A. Gupta, H Millward and A Lewis</i>	
Variation of optimal gas-supply condition along with deposition height in directed energy deposition	456
<i>S. Takemura, R. Koike, Y. Kakinuma and Y. Oda</i>	

LECTURES

A COMBINED APPROACH OF NUMERICAL SIMULATION AND ADDITIVE MANUFACTURING TECHNIQUE FOR IN-SILICO AND IN-VITRO TESTING OF A 3D PRINTING-BASED AORTIC POLYMERIC HEART VALVE

E. Gasparotti^{*†}, U. Cella[‡], E. Vignali^{*†}, E. Costa^{††}, G. Soldani^{}, A. Cavallo^{**}, P. Losi^{**}, M.E. Biancolini[‡] and S. Celi^{*}**

^{*} BioCardioLab, Fondazione Toscana "G. Monasterio",
Heart Hospital, Via Aurelia Sud, 54100 Massa
e-mail: gasparotti@ftgm.it, evignali@ftgm.it, s.celi@ftgm.it web page: bcl.ftgm.it

[†] Department of Information Engineering, University of Pisa, Italy
Via G. Caruso 16 - 56122 - Pisa

^{**} Biomaterials and regenerative medicine, Clinical Physiology Institute CNR
Heart Hospital, Via Aurelia Sud, 54100 Massa
aida.cavallo@ifc.cnr.it, giorgio.soldani@ifc.cnr.it, losi@ifc.cnr.it

^{††} RINA Consulting S.p.A.
Viale Cesare Pavese, 305 - 00144, Roma, Italy
emiliano.costa@rina.org

[‡] Department of Enterprise Engineering Mario Lucertini, University of Rome Tor Vergata
Via del Politecnico 1, Rome 00133, Italy
ubaldo.cella@uniroma2.it, biancolini@ing.uniroma2.it

Key words: Polymeric Heart valve, 3D printing, Computational Methods, RBF, Mock Loop

Abstract. Heart valve diseases are among the leading causes of cardiac failure around the globe. Current advances in imaging technology, in numerical simulation and in additive manufacturing are opening new frontiers in the field of development of new personalised prosthetic devices. The 3D printing technique could allow the realisation of personalised models for each patient undergoing valve replacement surgery. A CAD model of an aortic valve prosthesis was designed on the basis of elliptic-hyperboloid formulation. The resulting CAD model was used both to perform numerical in-silico simulation and to design a modular mould for AV fabrication. Simulations were performed through a novel hybrid approach based on RBF mesh morphing technique and CFD simulations. The polymeric aortic valve was manufactured by 3D printed process and spray deposition technique. To assess the in-vitro valve properties, the prototype was inserted in a custom mock circulatory loop to reproduce the aortic flow conditions. The manufacturing process of both the mould and the valve was successful and the in-vitro testing showed an effective orifice area (2.5 mm²) and regurgitation fraction (5%) in accordance with the ISO-5840-2. The novel simulation strategies have revealed to be a promising approach to test both structural and functional device performances.

1 INTRODUCTION

The heart valves play a crucial role in regulating the blood flow by continuous cyclic opening and closing under an extremely demanding mechanical environment. In case of valve pathologies, prosthetic heart valves have been commonly used to address the increasing prevalence of valvular heart disease. The ideal prosthetic heart valve replacement should closely mimic the characteristics of a normal native heart valve. Currently, available options for heart valve replacement include mechanical (MHV) and bio-prosthetic (BHV) valves, both of which have severe limitations [1]. The long-term durability is the main advantage of MHVs, but their use is limited by substantial risks of thrombogenicity. Involving the use of 3D printed mechanical valves exhibited a thrombogenicity potential index comparable with the BHVs score and, consequently, much lower if compared with other MHVs [2]. BHVs do not show thrombogenicity complications and circumvent the problem of anti-coagulation medications. Moreover, they have significantly improved hemodynamic results, lower gradients and larger AV/orifice areas [3]. To date, pericardium xenografts are the only leaflet material for flexible prosthetic AV to gain FDA and CE approval. However, many of the persistent limitations associated with bioprosthetic valves are inherently related to the tissue material (i.e. calcific degeneration, crimping and deployment damage, durability). Polymers provide better design freedom to overcome many of the aforementioned limitations as they offer the possibility to specifically design and optimize a valve from the bottom up, and can be potentially produced with high reproducibility and lower costs [4]. Despite the numerous advantages of BHVs, they are not as mechanically robust if compared to MHVs and they exhibit limited durability in younger patients (particularly those younger than 60 years), which is a current obstacle hindering the progress of bioprostheses. Polymers provide better design freedom to overcome many of the aforementioned limitations. In recent years, significant advances have been made in the world of polymeric materials and subsequently novel polymeric AV have been developed, showing very promising in-vitro results [5,6]. In-silico characterization plays a key role within the context of development of new AV designs. The in-silico evaluation of prosthetic heart valves can be divided in structural simulations, where the fluid flow across the prosthetic valve is neglected and only the pressures is considered as a condition of the structure domain [7,8], and fluid-structure interaction (FSI) simulations, where the interaction between two different physics phenomena, mechanical and fluid dynamic, computed in separate analyses, are taken into account [9,10]. The structural simulation of the valve opening presents the major drawback of overestimating the deformations as the pressures are applied uniformly on the leaflet during the whole opening phase, while in the FSI simulation the load conditions depend directly on the leaflets opening position [11,12]. A negative aspect of FSI simulation concerns a significant increase in computing time.

In the current study, we present a complete design of a novel polymeric AV for surgical application, from numerical hemodynamic evaluation to valve manufacturing based on 3D printing technique and hydrodynamic in-vitro test. In particular a novel combined approach of structural simulations, morphing techniques and CFD simulations is presented to simulate the opening phase of the valve. Regarding the mesh morphing techniques, the theoretical basis of RBF was

established [13–16] to manage problems of multidimensional interpolation. These approaches has been demonstrated to be useful for the study of hemodynamic CFD problems [17, 18].

2 MATERIALS AND METHODS

Our study consists of four main blocks: valve design (i), numerical simulation (ii), valve manufacturing (iii) and experimental tests (iv). The entire scheme of the study is reported in Figure 1.

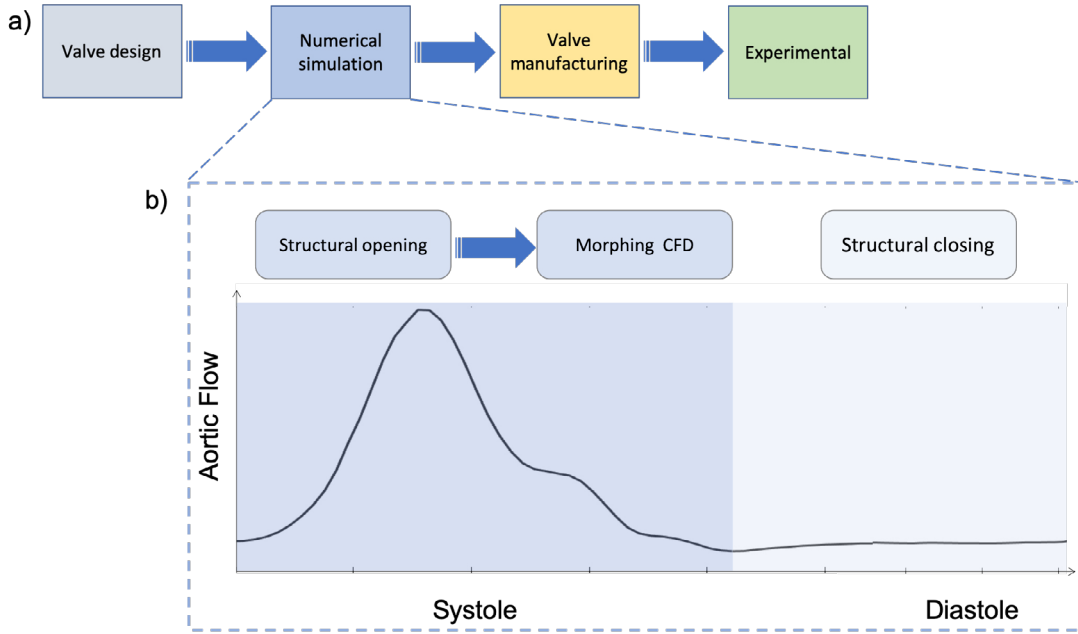


Figure 1: Overall workflow of the study (a) and schematic workflow of the numeral approach.

Valve design - The polymeric AV prosthesis is composed of three leaflet attached to a polymeric crown shape ring. The ring has the function to support the leaflets during their opening and closing phases and to constrain the valve on the aortic root. A tri-leaflet geometry permits to reproduce the kinematic of the replaced native AV. In this study the leaflet shape in the close position was defined by the elliptic hyperbolic surface [19] as described in the following equation:

$$\frac{x^2}{a^2} + \frac{y^2}{b^2} - \frac{z^2}{c^2} = -1 \quad (1)$$

where x, y, z are the spatial coordinates of the surface and a, b, c are the surface shape parameters. In particular the fraction c/a represents the slope of hyperbola curve asymptotes; its value was assumed equal to $\pm\sqrt{3}/3$ in order to realize two hyperbola asymptotes with an angle of 120° [20]. In this condition two adjacent leaflet approach the common asymptote at the commissure zone of the valve, leaving theoretically no gap between them. A small gap was left

at the commissure level in order to avoid cuspid zones. The complete 3D geometry of the valve was designed using Solidworks ® software (Dassault Systemes, Waltham, MA).

Numerical simulations - The finite element analyses of the AV behavior during the cardiac cycle were conducted by simulating the systolic (valve opening) and the diastolic phases (valve closing) separately. In the systole phase the system is influenced by both static and dynamic pressures. On the contrary, in the diastolic phase, the velocities of the fluid flow became negligible so the system is influenced only by the static physiological transvalvular pressure.

Regarding the systolic phase a FSI simulation was performed. In particular a "1-way" FSI approach was implemented, according to the following phases: firstly a transient structural analysis was performed applying a systolic physiological pressure on the valve leaflets in the FEM model, (i); selected deformed valve shapes resulting from the FEM analysis were used to define the mesh morphing system (ii), and finally a FSI simulation was done by imposing the adaptation of the fluid domain on the basis of the leaflets position (iii), (Figure 1.b).

In the structural analysis of the AV, the model was meshed with tetrahedral elements (727000 SOLID187). The AV ring material was assumed as linear elastic isotropic with Young's modulus equal to 4.6 MPa and Poisson ratio of 0.4 [21]. Regarding the leaflet, the material properties were assumed linear elastic isotropic with Young's modulus equal to 6.5 MPa and Poisson ratio of 0.4. The AV was constrained at the lower face of its ring in order to avoid translation and rotation in all directions. The pressure load was applied on the leaflets and it was set equal to systolic physiological transvalvular pressure. The load was applied by a step time of 0.5 s, instead the solution was found by using a substep time equal to 10^{-5} s.

Three different deformed configurations were exported from the FEM simulation and used as inputs for the mesh morphing technique (Figure 2). Due to the capability of the *RBF Morph* tool, the deformed shapes were exported in stereolithographic format (.STL) and used as target for the morphing action without any additional file conversion.

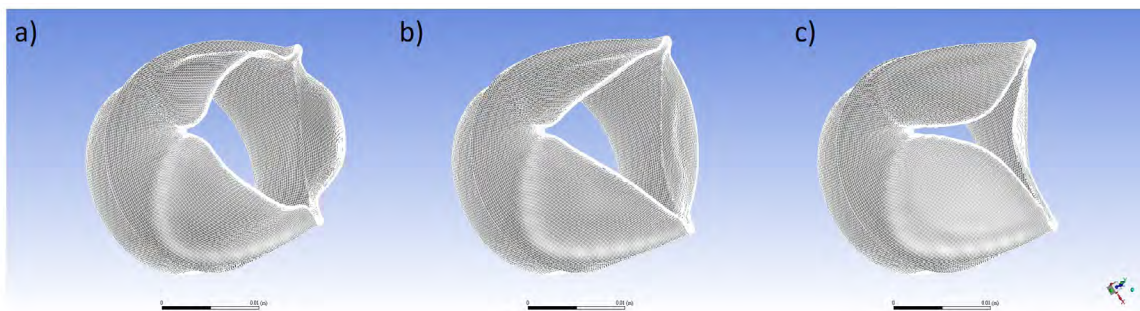


Figure 2: Example of morphing process at three different opening levels: maximum opening (a), mid opening (b), minimum opening (c).

The definition of the source points was performed interactively using a GUI and subsequently batch commands were adopted to combine the shape modifications in a non-linear fashion. The displacement of the prescribed set of source points and the combination of RBF solutions are then amplified according to the parameters that constitute the parametric space of the model

shape. The mid opening position was used as the starting baseline shape from which the mesh morphing process is performed (Figure 2.b). In our case two reference geometries were adopted to implement the RBF solution: one at a maximum opening (Figure 2.a) and one at the minimum opening (Figure 2.c). Two separated RBF solutions were setup according to the two reference target geometries. The setup split gave the possibility to cope the leaflet shape during the displacements in all positions between the two extreme configurations. The two solutions were made available to the solver to adapt the fluid domain for the subsequent CFD computation. Figure 3 displays the source points involved in the RBF setup and the visualization of the STL surface of the valve in the maximum opening position used as target for the morphing action. The RBF solution was configured to map the complete mesh morphing through an amplification parameter ranging from 0 to 1, where the value 1 corresponds to the target geometry.

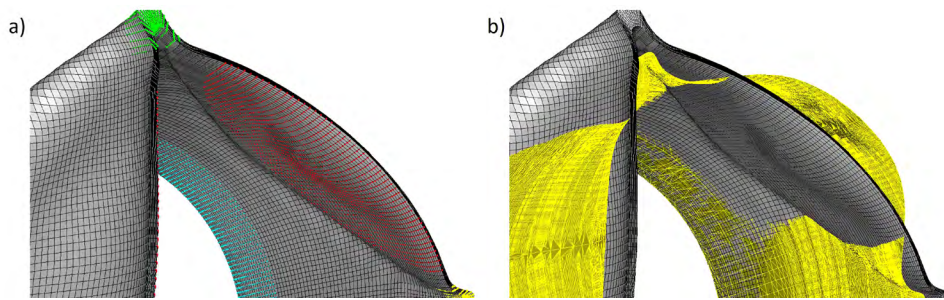


Figure 3: Setup of the RBF problem valve opening: source (a) and target points (b).

The CFD consisted in a pressure based transient run, in which the Realizable $k - \epsilon$ turbulence model was adopted. The boundary layer was solved by using standard wall functions. The fluid was considered as incompressible and non-Newtonian, the viscosity was modeled through the Carreau formulation. The analysis for the systolic phase was extended up to 0.5 seconds with a time step of 0.005 seconds. To correctly control the fluid domain modification through the morphing action on the mesh, a custom *Scheme* script was continuously recalled at every time step. The implemented procedure was in charge of loading the opportune RBF solution (depending on the target position with respect to the mid shape of the valve) and of amplifying it by a value given by a sinusoidal law with the computation time. The minimum opening position occurred at the beginning and at the end of the computation while the maximum opening occurred at 0.25 seconds. A custom UDF (User Defined Function), written in *C* language, was used to define the velocity inlet and pressure outlet time history profiles to be imposed as boundaries condition.

Concerning the diastolic phase, the valve closing was simulated through a structural transient analysis. The diastolic simulation was ran with the same FEM model described in the previous structural systolic simulation. leaflets surface was loaded with a pressure equal to diastolic physiological transvalvular pressure.

The structural transient analyses were performed with software *ANSYS Mechanical*; the fluid dynamic analysis was obtained by the *ANSYS Fluent* CFD solver and the *RBF Morph* tool [15] was used for mesh morphing techniques, which is recognized to constitute one of the most efficient mathematical frameworks to face the morphing problem [22].

Valve manufacturing - The valve leaflets were fabricated using spray technology and a custom 3D printed mould-modular outer mould system. The thermoplastic silicone polycarbonate urethane (Carbosil) was supplied by DSM Biomedical (Geleen, The Netherlands) for valve leaflets manufacturing. The valve ring was made by fused deposition technique, using a CarboSil extruded filament, according to [21]. The fabricated valve ring was positioned onto a tubular mould and dipped in a CarboSil 10% - tetrahydrofuran/dioxane 1:1 solution for 10 times. A 2% CarboSil solution containing 30% of silicone (polydimethylsiloxane, PDMS) was sprayed onto the mould by a custom spray-machine apparatus (Figure 4 (a)), allowing the polymer deposition in microfibrillar structure on the basis of the phase-inversion principle [23]. The spray process fabrication parameters were the following: 400 cycles, flow rate of 2 ml/min and rotation speed of 88 RPM. The mould with the sprayed polymer was dipped again in CarboSil solution for 10 times. Finally, the 3-layered tubular valve was housed in a valve mould, pressed by a modular outer mould (Figure 4 (b)) and incubated in distilled water at 40°C o.n. to allow the valve consolidation. The material excess on the leaflets was removed by a welder at 110°C. The polymeric valve was stored in distilled water up to hydrodynamic characterization (Figure 4 (c)).

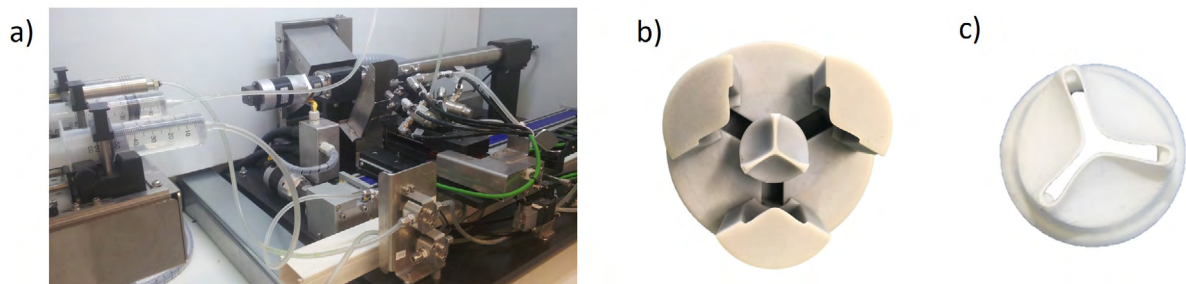


Figure 4: Spray machine (a); custom mould/modular outer mould system (b) and final valve (c).

In vitro tests - The hydrodynamic performances of the polymeric HV were evaluated by following the directives of ISO-5840 standard. In particular the manufactured valve was positioned inside a custom mock circulatory loop (Figure 5) able to reproduce the left ventricle flow and pressure conditions. The setup consists in an custom alternative piston pump, able to apply mitral and aortic pulsatile flows on the mock system. To guarantee physiological pressure conditions on the aortic outlet, a pinch valve resistance and a compliant cylindrical air chamber were adopted. The atrial physiological pressure was obtained by the insertion of another pinch valve resistance and a compliant cylindrical air chamber in addition to a centrifugal pump at the piston pump inlet pipe. The HV was placed into a 3D printed seat. The valve seat was designed with two orifices to measure the transvalvular pressure during the hydrodynamic tests. The transvalvular and the ventricular pressures were measured using clinical TruWave transducers (Edwards, Irvine, California, USA) A clamp-on ultrasound flow sensor was placed at the piston pump outlet to evaluate the resulting aortic flow. The device hydrodynamic testing was per-

formed with heart-rate of 70 bpm, cardiac output of 5 L/min (with flow systolic peak equal to 35 l/min), mean aortic pressure of 100 mmHg and aortic peak systolic pressure 120 mmHg. To define the valve performances minimum tele-diastolic, maximum systolic, the transvalvular drop pressures were evaluated to calculate the Effective Orifice Area (EOA) and the total regurgitation fraction (RF) parameters.

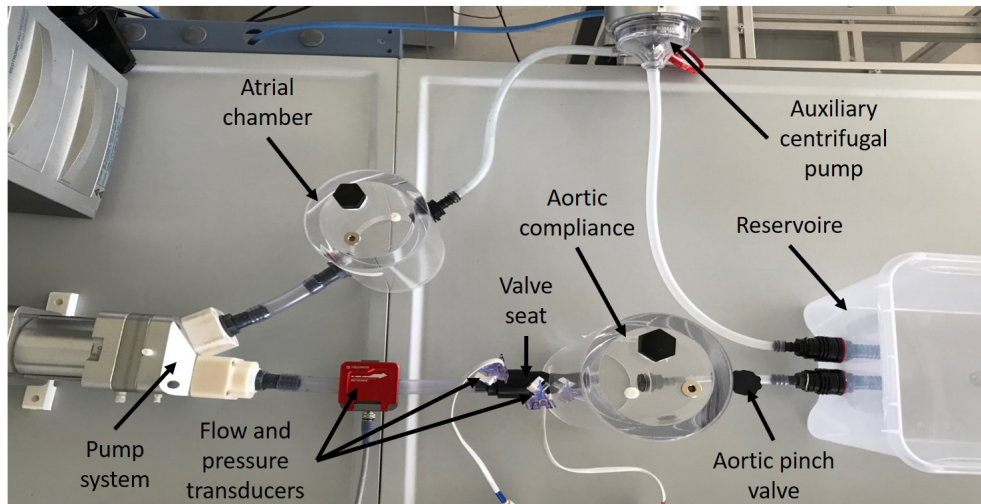


Figure 5: Mock circulatory loop

3 RESULTS

Numerical simulations - The structural simulation of the valve opening and closing phases are reported in Figure 6. During the opening phase the maximum radial displacement of the leaflet was equal to 8.4 mm (Figure 6.a) and the maximum equivalent Von-Mises strain value was equal to 0.6 mm/mm (Figure 6.b). Regarding the closing phase, the maximum radial contraction of the leaflet was equal to 3.8 mm (Figure 6.a) and the maximum equivalent Von-Mises strain value was equal to 0.20 mm/mm (Figure 6.b).

From the CFD simulations the pressure and velocity fields during the valve opening and closing can be observed in Figure 7 and Figure 8, respectively. In the acceleration phase, it was possible to observe a uniform pressure distribution on both the external and internal leaflet surfaces (Figure 7.a). On the contrary, a pressure gradient was visible on the internal surface of the leaflet during the peak systolic phase (Figure 7.b).

In vitro tests - Figure 9 shows a representative example of the pressure and flow trends measured during the in-vitro test. The reported values were consistent with typical systemic in-vivo waveforms. In particular, the aortic pressure was in the 125/80 mmHg range, ventricular pressure was in the 130/0 mmHg range, while the aortic output was 5 l/min with a peak equal to 35 l/min. The corresponding EOA and RF values were 2.5 cm^2 and 5%.

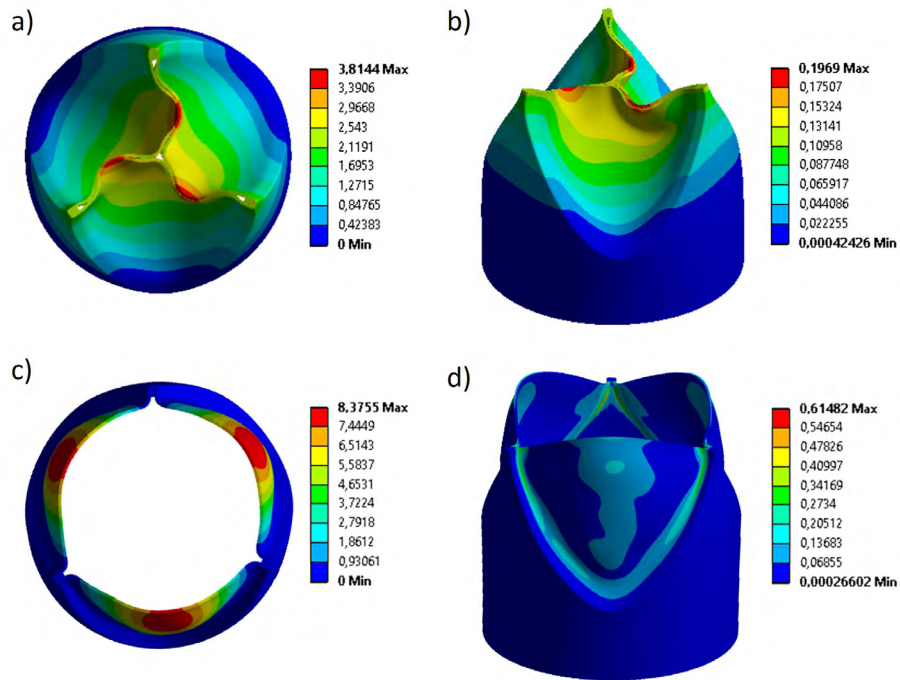


Figure 6: Systole results a) radial displacement (mm) and b) equivalent strain (mm/mm); diastole results c) radial displacement (mm) and d) equivalent strain (mm/mm)

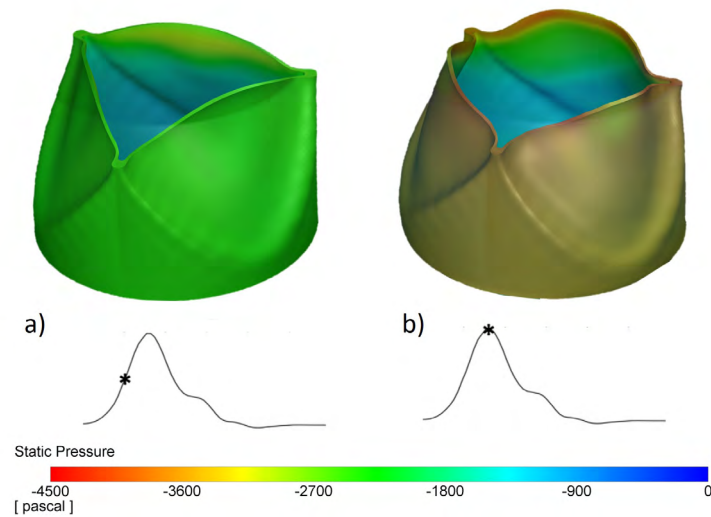


Figure 7: Pressure fields at two instances throughout the cardiac cycle corresponds to the acceleration phase (a) and to peak systole (b).

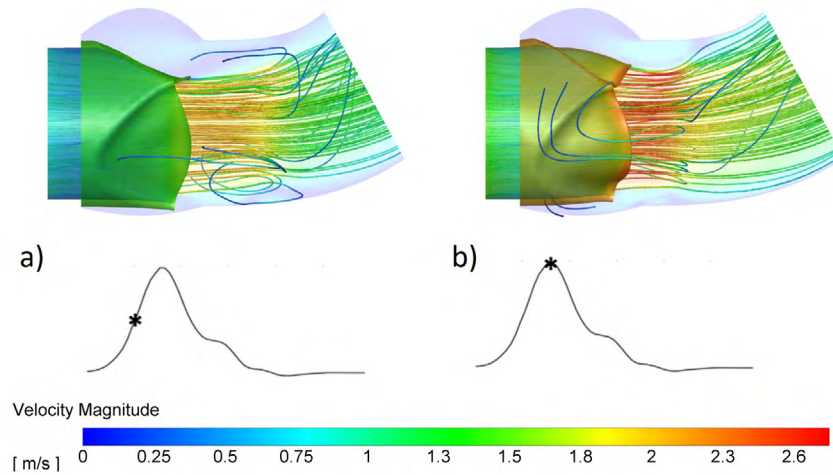


Figure 8: Flow velocity streamlines at two instances throughout the cardiac cycle corresponds to the acceleration phase (a) and to peak systole (b).

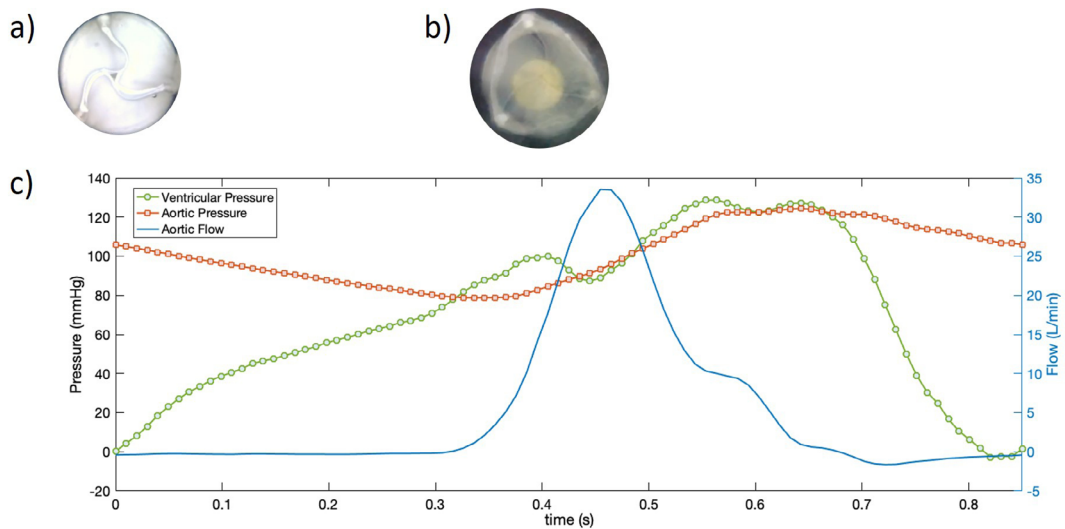


Figure 9: Example of valve closure (a); valve opening (b) and circuit transvalvular pressures and aortic flow (c).

4 DISCUSSION AND CONCLUSIONS

In this paper, the feasibility of a custom polymeric surgical AV prosthesis was demonstrated. The structural simulation of the AV opening/closure process was successful. The reported maximum strain was lower than the corresponding ultimate strain value of the material (4.73 mm/mm according to the value reported by DSM material datasheet for Carbosil). The simulations of the valve during the cardiac cycle presented in this paper exhibited an overestimation of the

leaflets displacement as a consequence of the uniform pressure load conditions. Nevertheless, the proposed approach correctly reproduced the AV opening kinematics that were successfully transferred to the CFD analysis through the morphing technique. A given advantage of adopting the morphing technique is constituted by the possibility to obtain a CFD evaluation of the AV without the computational burden of classic FSI analysis. The developed workflow represents a preparatory step that allowed to lay the basis of the development of a complete 2-way FSI setup based on mesh morphing method.

The manufacturing process based on 3D printing and spray technologies made possible the realization of a full functional valve. These manufacturing approaches represent a valid alternative to the traditional fabrication valve process, based on injection moulding [20] and dip coating [24] techniques. Moreover, it is important to underline the possibility to open new pathways in the world of personalized medicine. In particular, versatility of 3D printing technique allows an high customization of the valve prosthesis in terms of patient specific dimensions and sizes.

Concerning the in-vitro results, a complete hydrodynamic setup for the prosthesis validation has been correctly developed. The performance of the manufactured device were confirmed on the basis of the ISO5840-2. In particular, the EOA and the RF indexes showed values within the reported standard ranges ($EOA > 1.95 \text{ cm}^2$ and $RF < 20\%$). To obtain a further characterization of the device, future works will include a full fatigue fluid-dynamic validation test for both the Carbosil and the AV prosthesis. Different studies concerning the development of AV prostheses reported thrombogenicity evaluation [25], this aspect represents another possible point of improvement of the current work. Nevertheless, it is worth to affirm that the preliminary fluid dynamic parameters reported are promising and remarkable.

ACKNOWLEDGEMENTS

This work was supported by the VIVIR (PE-2013-02357974) grant from the Minister of Health and by 3D VIRTUAL BABY HEART project (GR-2016-02365072).

REFERENCES

- [1] Deon Bezuidenhout et al. Polymeric heart valves for surgical implantation, catheter-based technologies and heart assist devices. *Biomaterials*, 36:6 – 25, 2015.
- [2] Lawrence Scotten. Are anticoagulant independent mechanical valves within reach-fast prototype fabrication and in vitro testing of innovative bi-leaflet valve models. *Ann Transl Med*, 3(14):197–197, August 2015.
- [3] Marie-Annick Clavel et al. Comparison of the hemodynamic performance of percutaneous and surgical bioprostheses for the treatment of severe aortic stenosis. *Journal of the American College of Cardiology*, 53(20):1883–1891, 2009.
- [4] Kan Yan Chloe Li. Bioprosthetic heart valves: Upgrading a 50-year old technology. *Front.Card. Medicine*, 6, 2019.

- [5] Oren Rotman, Brandon Kovarovic, et al. Novel polymeric valve for transcatheter aortic valve replacement applications: In vitro hemodynamic study. *Annals of Biomedical Engineering*, 47, 09 2018.
- [6] Benyamin Rahmani, S Tzamtzis, et al. In vitro hydrodynamic assessment of a new transcatheter heart valve concept (the triskele). *Journal of cardiovascular translational research*, 10, 12 2016.
- [7] Qing Wang and Shiwen Chen. A general class of linearly extrapolated variance estimators. *Statistics Probability Letters*, 98:29 – 38, 2015.
- [8] Simone Morganti, Michele Conti, et al. Simulation of transcatheter aortic valve implantation through patient-specific finite element analysis: Two clinical cases. *Journal of Biomechanics*, 47(11):2547 – 2555, 2014.
- [9] Ram Ghosh, Gil Marom, et al. Comparative fluid-structure interaction analysis of polymeric transcatheter and surgical aortic valves' hemodynamics and structural mechanics. *J. Biomech. Eng.*, 140, 06 2018.
- [10] Giulia Luraghi, Wei Wu, Francesco De Gaetano, et al. Evaluation of an aortic valve prosthesis: Fluid-structure interaction or structural simulation? *Journal of Biomechanics*, 58:45 – 51, 2017.
- [11] Giulia Luraghi and Francesco others Migliavacca. Study on the accuracy of structural and fsi heart valves simulations. *Cardiovascular Engineering and Technology*, 9, 08 2018.
- [12] Finja Borowski, Michael Smann, and othersl. Fluid-structure interaction of heart valve dynamics in comparison to finite-element analysis. *Current Directions in Biomedical Engineering*, 4:259–262, 09 2018.
- [13] Yong Duan. Duan, y.: A note on the meshless method using radial basis functions. *comput. math. appl.* 55(1), 66-75. *Computers Mathematics with Applications*, 55:66–75, 01 2008.
- [14] Ubaldo Cella, Corrado Groth, et al. Geometric parameterization strategies for shape optimization using rbf mesh morphing. *Lecture Notes in Mechanical Engineering*, pages 537–545, 01 2017.
- [15] M.E. Biancolini, C. Biancolini, E. Costa, D. Gattamelata, and P.P. Valentini. Industrial application of the meshless morpher RBF morph to a motorbike windshield optimisation. In *4th Eu. Aut. Sim. Conf.*, Munich, Germany, 2009.
- [16] Marco Evangelos Biancolini. *Fast radial basis functions for engineering applications*. 2018.
- [17] K. Capellini et al. Computational fluid dynamic study for ataa hemodynamics: An integrated image-based and radial basis functions mesh morphing approach. *J Biomech Eng*, 140(140):111007–111017, 2017.

- [18] K. Capellini et al. A coupled cfd and rbf mesh morphing technique as surrogate for one-way fsi study. 2019.
- [19] M.E.Leat and J.Fisher. A synthetic leaflet heart valve with improved opening characteristics. *Medical Eng Physics*, 16(6):470 – 476, 1994.
- [20] Hongjun Jiang, Gord Campbell, et al. Design and manufacture of a polyvinyl alcohol (pva) cryogel tri-leaflet heart valve prosthesis. *Medical Engineering Physics*, 26(4):269 – 277, 2004.
- [21] Emanuele Gasparotti et al. A 3d printed melt-compounded antibiotic loaded thermoplastic polyurethane heart valve ring design: an integrated framework of experimental material tests and numerical simulations. *Int. J. Poly. Mat.Polymeric Biomat.*, 68(1-3):1–10, 2019.
- [22] Stefan Jakobsson and Olivier Amoignon. Mesh deformation using radial basis functions for gradient-based aerodynamic shape optimization. *Computers & Fluids*, 36(6):1119–1136, 2007.
- [23] E Briganti, Paola Losi, et al. Silicone based polyurethane materials: A promising biocompatible elastomeric formulation for cardiovascular applications. *Journal of materials science. Materials in medicine*, 17:259–66, 2006.
- [24] New polyurethane heart valve prosthesis: design, manufacture and evaluation. *Biomaterials*, 17(19):1857 – 1863, 1996.
- [25] Hemodynamic and thrombogenic analysis of a trileaflet polymeric valve using a fluid-structure interaction approach. *Journal of Biomechanics*, 48(13):3641 – 3649, 2015.

A NUMERICAL AND 3D PRINTING FRAMEWORK FOR THE IN VIVO MECHANICAL ASSESSMENT OF PATIENT-SPECIFIC CARDIOVASCULAR STRUCTURES

**BENIGNO M. FANNI^{*†}, EMILIE SAUVAGE[‡], CLAUDIO CAPELLI[‡], EMANUELE
GASPAROTTI^{*†}, EMANUELE VIGNALI^{*†}, SILVIA SCHIEVANO[‡], LUIGI
LANDINI[†], VINCENZO POSITANO^{*} AND SIMONA CELI^{*}**

^{*} BioCardioLab, Fondazione Toscana Gabriele Monasterio
Ospedale del Cuore, Via Aurelia Sud, 54100 Massa, Italy
e-mail: bmfanni@ftgm.it, egasparotti@ftgm.it, evignali@ftgm.it, positano@ftgm.it, s.celi@ftgm.it
Web page: bcl.ftgm.it

[†] DII, Department of Information Engineering, University of Pisa
Via G. Caruso 16, 56122 Pisa, Italy
e-mail: luigi.landini@iet.unipi.it
Web page: www.dii.unipi.it

[‡] UCL Institute of Cardiovascular Science, University College London
62 Huntley Street, WC1N 1EH London, United Kingdom
e-mail: e.sauvage@ucl.ac.uk, c.capelli@ucl.ac.uk, s.schievano@ucl.ac.uk
Web page: www.ucl.ac.uk/cardiovascular

Key words: 3D Printing, Fluid-Structure Interaction, Material Properties, Mock Loop, Magnetic Resonance Imaging

Abstract. Computational simulations represent a powerful tool for the pre-procedural clinical assessment of minimally invasive cardiovascular interventions. Patient-specific simulations rely on the accurate numerical implementation of both geometrical and mechanical features. While current imaging techniques are able to depict accurately patient-specific anatomies, at date, a similar image-based tool capable to retrieve subject-specific material properties is missing. The scope of this study is to present a framework, involving *in silico* tools and 3D printing, for the refinement of an image-based technique capable to retrieve *in vivo* patient-specific mechanical information from functional and morphological magnetic resonance imaging (MRI) data. The workflow consists in different steps: (i) selection and mechanical testing of 3D commercially available deformable 3D printed materials; (ii) fluid-structure interaction (FSI) simulation of a vessel model under pulsatile regime; (iii) elaboration of *in silico* results and calibration of the image-based method; (iv) 3D printing of the model and experimental replica in MRI environment; (v) finally, the image-based technique is applied to MRI data (iv) to retrieve material information to compare to reference (i). The described workflow strategy was successfully implemented by our group. The deformable material TangBlackPlus FLX980 (TangoPlus) was selected and mechanically tested, resulting in an elastic module (E) of 0.50 ± 0.02 MPa ($n = 5$). FSI simulations of a simplified vessel were carried out with different E values (from 0.5 to 32 MPa). *In silico*, the indirect material evaluation resulted, after the calibration, in a good

matching between inputted E values and estimated ones, leading to a percentage difference of $7.8 \pm 4.1\%$ ($n = 12$). The simulated vessel was 3D printed with TangoPlus and acquired in terms of MRI data. The application of the proposed image-based method resulted in a E value of the phantom of $E = 0.54$ MPa, very close to the one directly assessed via tensile tests (0.5 MPa). Although very good results were achieved in this study, other deformable materials and shapes will be investigated by using the described framework. With further refinements, this strategy would lead to an indirect and image-based tool for the *in vivo* assessment of patient-specific material properties, thus enhancing the confidence of patient-specific computational models.

1 INTRODUCTION

Patient-specific computational modeling represent a powerful and promising tool for the simulation of minimally invasive cardiovascular procedures in a clinical pre-planning scenario [1]. However, the use of computational methods in clinics is still scarce and limited [2]. The challenges consist in a faithful adaptation of computational models into the patient-specific clinical conditions [3].

Simulation of such interventions requires specific information on both the patient's implantation site and the device. While this latter is fully known, both for geometrical and mechanical features, accurate data of patient are available only for the anatomy, easily retrievable from current imaging techniques. In fact, actual limitation of cardiovascular computational modeling is represented by the patient-specific material properties which are lacking. This lack of information introduce approximations of the mechanical modelling [4] of patients cardiovascular structures. Enhanced material information, which include patient-specific information, would certainly improve the accuracy of the numerical results, thus favoring the use of computational tools in the daily clinical practice.

In this study we tested a framework involving 3D printing facilities and *in silico* tests for the calibration of a novel technique for the image-based extraction of mechanical information of compliant materials. The feasibility of the presented framework was proven on one material, showing excellent agreement between direct and indirect mechanical assessment. With further refinement, including the testing on different materials and more complex geometries, the proposed method could be applied on *in vivo* imaging data for the assessment of patient-specific material information.

2 MATERIAL AND METHODS

The framework we described in this section aims to predict the elastic modulus of materials based on an indirect and non-invasive method.

The entire workflow of this research consists in the following steps:

1. Selection of a compliant material available on the market of additive manufacturing and its mechanical testing.
2. Fluid-structure interaction (FSI) simulations of a vessel-shaped model subjected to pul-

satile conditions. A wide range of elastic moduli was used as input (E_{INP}) for the mechanical description of the vessel's wall.

3. Post-processing results of the simulations are used to calibrate the QA-based formulation for inferring the E values used in the simulations (E_{OUT}).
4. 3D printing of the vessel model with the selected material and an *in vitro* replica of the simulation; this step includes a phase contrast magnetic resonance imaging (PC MRI) acquisition of the phantom.
5. Segmentation of the PC MRI dataset and application of the proposed image-based method to infer the E value of the material, which is compared to the one directly assessed in step (1) with mechanical tests.

In this work we demonstrated the feasibility of the described framework for one material and shape. A scheme of the described workflow is shown in Fig. 1.

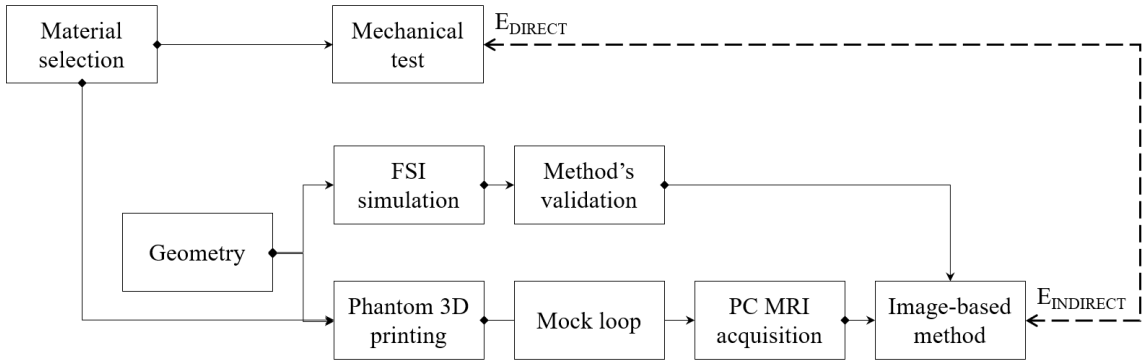


Figure 1: Representative scheme of the described workflow.

2.1 QA-based method

The formulation we propose in this work is based on the flow-area (QA) method and on equations available in literature. The QA method is an image-based technique, first used on MRI data [5] and then on ultrasound images [6], for the assessment of the pulse wave velocity (PWV), which is considered a good surrogate of the arterial stiffness [7, 8]. According to this method, the relationship during the early systolic period between the cross-sectional area of a blood vessel and the passing flow can be approximated as a first-order linear equation. The PWV can be defined as the slope of such linear portion:

$$PWV = \frac{dQ}{dA} \quad (1)$$

where dQ is the incremental variation of the passing flow and dA is the incremental variation of the cross-sectional area of the vessel.

Laurent et al. [9] proposed a formulation for the estimation of the E value of the vessel's wall based on the distensibility compliance (DC) and some geometrical parameters:

$$E_{DC} = \frac{3 \left(1 + \frac{A_0}{WCSA}\right)}{DC} \quad (2)$$

where A_0 is the cross-sectional area of the vessel, $WCSA$ is the wall cross-sectional area, both evaluated at diastole. Usually the DC value is evaluated by coupling area and pressure information at diastole and systole.

To overcome the use of pressure, which is an invasive measure and moreover not available for all the patients, we considered the inverted Bramwell-Hill equation [10] for the definition of the DC value:

$$DC = \frac{1}{\rho PWV^2} \quad (3)$$

where the density of the fluid flowing through the section is ρ .

In our study we defined the following PWV -based equation for the estimation of E value (E_{OUT}):

$$E_{OUT} = k \left(3 \rho PWV^2 \left(1 + \frac{A_0}{WCSA} \right) \right) \quad (4)$$

Eq. 4 derives by combining Eq. 2 and 3 and it allows the estimation of the E value of a vessel's wall based on the PWV , which can be easily calculated by means of the QA method. The k parameter is a correction factor introduced for a more reliable estimation of the E values.

2.2 Material selection and mechanical testing

For this feasibility study, we selected one deformable material available in the market of additive manufacturing. The chosen material was TangoBlackPlus FLX980 (TangoPlus) which was tested via uniaxial tensile tests. Five dogbone-shaped specimens were 3D printed with an Object500 Connex machine (Stratasys, Minnesota, USA). The samples were mechanically tested with a custom-made tensile machine [11] to retrieve the E value of the 3D printed TangoPlus material. The E value obtained from tensile tests (E_{tt}) was considered as ground of truth and compared to the E value estimated from the MRI experiment (E_{MRI}).

2.3 *In silico* campaign

A vessel model under cardiac-like pulsatile conditions was implemented by using the software LS-DYNA R.10 (LSTC, Livermore, USA). For this study of feasibility, the geometry of the vessel was drawn as cylindrical, with a length of 150 mm, an internal diameter of 12.7 mm and a thickness of 2 mm. The wall was modelled as isotropic and linear elastic. A total of twelve simulations were carried out with different E_{INP} values for the vessel's wall, ranging from 0.50 MPa to 32 MPa, with an oversampling in the region close to 1 MPa (Fig. 2). The fluid domain was modelled as an incompressible and non-Newtonian fluid with a density of 998

kg/m^3 and a dynamic viscosity of $0.001 \text{ kg m}^{-1} \text{ s}^{-1}$. Periodic boundary conditions were set up to impose velocity at the inlet and pressure at the outlet. Four cardiac cycles were simulated. A time step of 0.01 s was used.

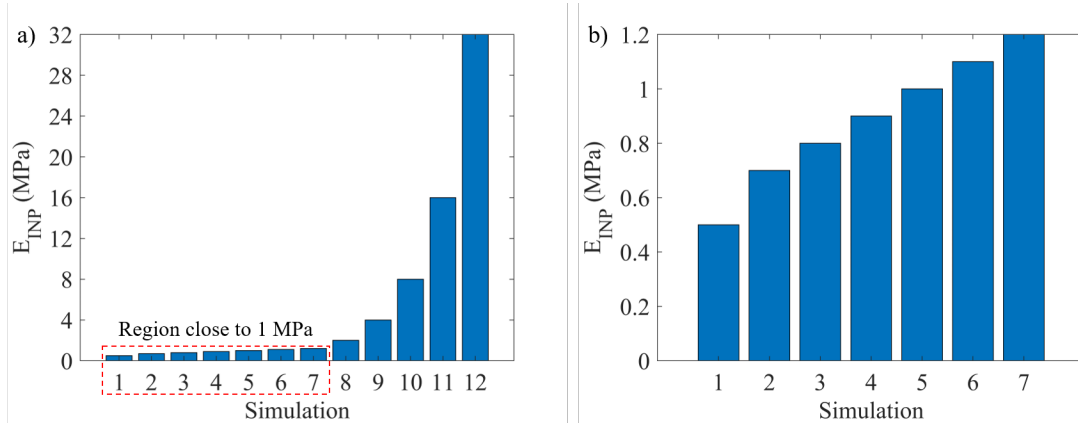


Figure 2: (a) E_{INP} values used in the simulations; (b) zoom of the E_{INP} in the region of 1 MPa.

The twelve simulations were elaborated with the proposed QA-based technique. The last cardiac cycle was considered for analysis. Flow and area information along time were extracted in the middle cross-section of the numerical models using ParaView (<https://www.paraview.org/>). At this stage, the k parameter was determined with an iterative process until (E_{OUT}) matched (E_{INP}).

2.4 MRI experiment

The simulation was replicated *in vitro*. The vessel model was 3D printed with TangoPlus and inserted in an ad-hoc mock circulation circuit providing a pulsatile regime (Fig. 3). Cardiac-like conditions were provided by a Harvard apparatus pulsatile blood pump (Harvard apparatus, Massachusetts, USA). Similar flow and pressure conditions were imposed by tuning the action of the pump and adjusting the passive elements of the system in terms of compliance (C) and resistance (R).

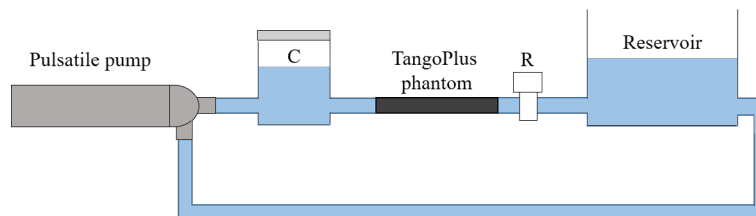


Figure 3: Scheme of the mock loop built for the MRI experiment.

Finally, the circuit was positioned in MRI environment to acquire PC images of the phantom in the middle cross-section. The acquisition resulted in 40 frames along the cardiac cycle.

Images were segmented using Segment v2.0 (<http://segment.heiberg.se>) [12] to obtain area and flow values for all the frames. The proposed QA-based method was applied and the E_{MRI} value of the phantom was calculated by using Eq. (5) with the k value obtained from the *in silico* analysis.

3 RESULTS

3.1 Tensile tests

Uniaxial tensile tests were successful for all the specimens. The mechanical tests were conducted until the rupture of the sample. The stress-strain curves obtained from the tests were linearly fitted (Fig. 4) to get the E_{tt} value, which resulted to be 0.50 ± 0.02 MPa ($n = 5$).

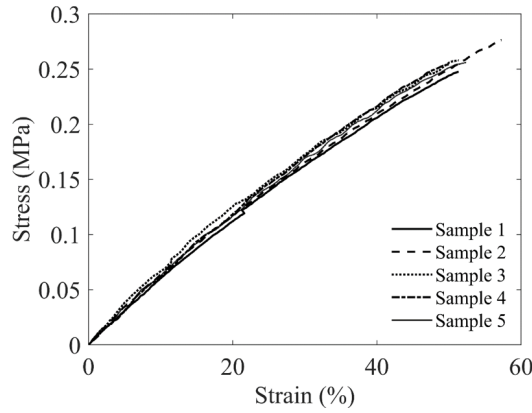


Figure 4: Stress-strain curves from uniaxial tensile tests of the five 3D printed TangoPlus specimens.

3.2 *In silico* outcomes

The twelve FSI simulations with different E_{INP} values reached successfully the convergence. The iterative tuning of the k parameter led to the following definition:

$$k = c RAC \quad (5)$$

where RAC is the relative area change expressed as:

$$RAC = \frac{A_{max} - A_0}{A_0} \quad (6)$$

and c is a constant parameter which was defined for each simulation as:

$$c = \frac{E_{INP}}{RAC E_{PWV}} \quad (7)$$

The c value, as obtained from Eq. 7 resulted equal to 12.6949 ± 1.1210 ($n = 12$). The mean value of c ($\bar{c} = 12.6949$) was used in Eq. 4 to obtain the estimation (E_{OUT}) of the E_{INP} values used in the simulations. The E_{OUT} values well replicated the E_{INP} values, with a mean error of $7.8 \pm 4.1\%$ ($n = 12$). Fig. 5 shows how the inclusion of the $\bar{c} RAC$ factor hugely reduces the non-linearity between E_{OUT} and the E_{INP} values in respect to using $k = 1$.

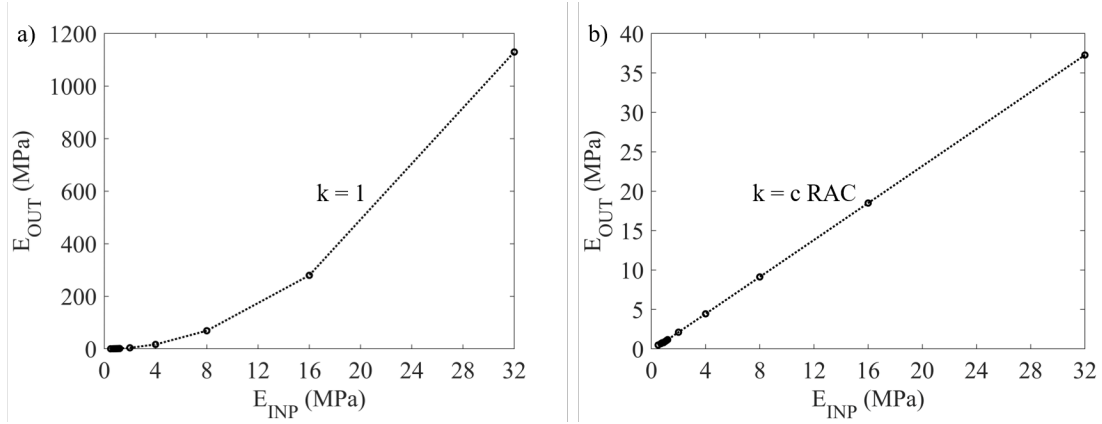


Figure 5: Relationship between E_{OUT} and E_{INP} with $k = 1$ (a) and $k = c \text{ RAC}$ (b).

3.3 Experimental results

The application of the presented QA-based method was feasible on the acquired PC images. The PWV , calculated as stated in Eq. 1, was found to be 5.57 m s^{-1} . Calculation of the E_{OUT} with $k = 1$ resulted in 0.21 MPa , which, accordingly to the equivalent *in silico* case, underestimates the real E value of the material ($E_{tt} = 0.50 \text{ MPa}$). While the application of the found k factor (Eq. 5) led to an E_{MRI} value of 0.54 MPa , with a percentage difference of 8% in respect to the direct estimation.

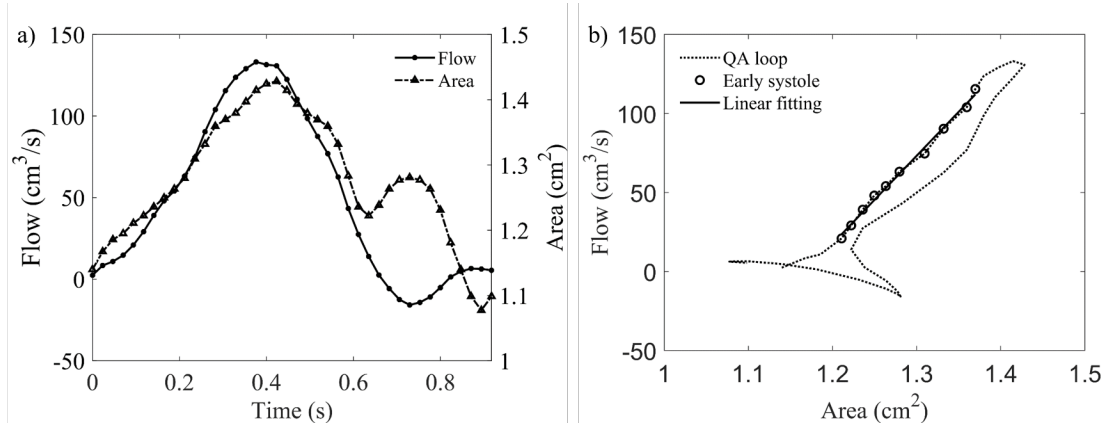


Figure 6: Segmentation results of PC MRI dataset (left) and resulted QA loop (right).

4 DISCUSSION

In this work we presented a proof of concept of a framework able to infer the E value of materials based on PC MRI data. The framework relies on an empirically modified equation based on the QA method. We first tested the proposed formulation in a controlled *in silico* environment taking advantage of the knowing of the E values implemented in the simulations.

This allowed the determination of the c value present in the definition of the k factor (Eq. 5). In fact, while the RAC parameter seems to have the role of adjusting the linearity between the inferred E and the reference (Fig. 5), a constant value (i.e. the c value), which may be considered the same for all the stiffnesses, is necessary for a correct matching of the E values. However, the predictive capability of the presented technique was confirmed *in vitro*, where a very good matching between the real E value of the 3D printed material and the image-based one was found (8%).

Although very promising results were achieved, this work represents a study of feasibility of a framework which was experimentally tested just for one material and one geometry. Future works will surely include the analysis of other 3D printed materials, such as Agilus30 (Stratasys, Minnesota, USA) and Elastic and Flexible resins (Formlabs, Massachusetts, USA), as well as different and more complex geometries, starting from different sized pipes to patient-specific anatomies. In fact, with further refinements, this technique would be able to assess an estimation of the patient-specific implantation site material properties, useful for a more reliable implementation of the mechanical response of the vessel's wall against the expansion of a device.

5 CONCLUSIONS

In this study, we demonstrated the feasibility of a framework involving additive manufacturing and *in silico* simulations for the non-invasive assessment of the E value of deformable materials. While computational modeling allowed us to refine the methodology in a controlled space, with 3D printing we were able to test the developed formulation with a ad-hoc MRI experiment and to compare the outcomes against the results from tensile tests, which are for obvious reasons impracticable for *in vivo* tissues. The proposed image-based method showed promising results. Future works will focus on the exploration of other *in silico* and *in vitro* scenarios with the main aim to apply this technique on *in vivo* patient-specific imaging data. This would reduce the gap between numerical and clinical world, thus enhancing the efficacy of the intervention procedures and the healthcare of patients.

REFERENCES

- [1] Capelli, C., E. Sauvage, G. Giusti and al. Patient-specific simulations for planning treatment in congenital heart disease. *Interface Focus*, 2018, 8:20170021.
- [2] Biglino, G., C. Capelli, J. Bruse, G. M. Bosi, A. M. Taylor, and S. Schievano. Computational modelling for congenital heart disease: how far are we from clinical translation? *Heart* 103:98103, 2017.
- [3] Huberts, W., S. G. H. Heinen, N. Zonnebeld, D. A. F. van den Heuvel, J.-P. P. M. de Vries, J. H. M. Tordoir, D. R. Hose, T. Delhaas, and F. N. van de Vosse. What is needed to make cardiovascular models suitable for clinical decision support? A viewpoint paper. *Journal of Computational Science* 24:6884, 2018.

-
- [4] Celi, S., and S. Berti. Biomechanics and FE Modelling of Aneurysm: Review and Advances in Computational Models. *Aneurysm*, 2012.doi:10.5772/46030.
- [5] Vulliemoz, S., N. Stergiopoulos, and R. Meuli. Estimation of local aortic elastic properties with MRI. *Magnetic Resonance in Medicine* 47:649654, 2002.
- [6] Rabben, S. I., N. Stergiopoulos, L. R. Hellevik, O. A. Smiseth, S. Slrdahl, S. Urheim, and B. Angelsen. An ultrasound-based method for determining pulse wave velocity in superficial arteries. *J Biomech* 37:16151622, 2004.
- [7] Boonyasirinant, T., P. Rajiah, and S. D. Flamm. Abnormal aortic stiffness in patients with bicuspid aortic valve: phenotypic variation determined by magnetic resonance imaging. *Int J Cardiovasc Imaging* 35:133141, 2019.
- [8] Wentland, A. L., T. M. Grist, and O. Wieben. Review of MRI-based measurements of pulse wave velocity: a biomarker of arterial stiffness. *Cardiovasc Diagn Ther* 4:193206, 2014.
- [9] Laurent, S., J. Cockcroft, L. Van Bortel, P. Boutouyrie, C. Giannattasio, D. Hayoz, B. Pannier, C. Vlachopoulos, I. Wilkinson, and H. Struijker-Boudier. Expert consensus document on arterial stiffness: methodological issues and clinical applications. *Eur Heart J* 27:25882605, 2006.
- [10] Bramwell, J. C., and A. V. Hill. The velocity of pulse wave in man. *Proc. R. Soc. Lond. B* 93:298306, 1922.
- [11] Gasparotti, E., E. Vignali, P. Losi, M. Scatto, B. M. Fanni, G. Soldani, L. Landini, V. Positano, and S. Celi. A 3D printed melt-compounded antibiotic loaded thermoplastic polyurethane heart valve ring design: an integrated framework of experimental material tests and numerical simulations. *International Journal of Polymeric Materials and Polymeric Biomaterials* 0:110, 2018.
- [12] Bidhult, S. L., M. Carlsson, K. Steding-Ehrenborg, H. Arheden, and E. Heiberg. A new method for vessel segmentation based on a priori input from medical expertise in cine phase-contrast Magnetic Resonance Imaging. *Journal of Cardiovascular Magnetic Resonance* 16:P355, 2014.

An efficient approach based on geometrical analysis to optimize AM process

Federico Valente* & Salvatore Papadopoli*

* ITACAe S.r.l.

Corso Moncalieri 223 – 10133, Turin, Italy e-mail: info@itacae.com, web page:

<http://www.itacae.com>

Key words: Geometric Analysis, Build Orientation, Distortions, Simulation

1. Introduction

New methodologies of Design for Additive Manufacturing (DFAM) and relative CAX tools are the key enabling technologies allowing to get the major benefits from AM. It is evident that an increased integration of all CAX phases would lead to a more efficient design and engineering workflow. One of the major bottlenecks of such a holistic approach, which affects AM product time-to-market and restricts its commercial exploitation, is the need of a high amount of time and human resources for simulation, modelling and postprocessing of all the engineering activities. That is not always manageable, especially during a preliminary stage of concept design or feasibility analysis.

Modern mathematical approaches are facing, with the ambition to contribute to some of the most challenging engineering tasks to fulfil strict requirements of structural resistance, lightness, noise, static and dynamic stiffness. The effectiveness of analytical and geometrical tools and methods for the study and the optimization of shapes were already demonstrated. As an example, it is well known that small fillet radius are stress concentrators and must be avoided for a robust design of structural parts. In the same way, we can demonstrate that poorly uniform temperature distribution of the material during additive layer manufacturing can be correlated with geometrical section areas and variations along the growing axis, as well as with supports shape configurations.

In this paper, a novel approach is presented which identifies optimal orientation and support configurations, uniquely based on geometrical criteria. The benefits are avoiding long structures to minimise the amount of waste material, accounting for the distribution of the piece weight, effectively draining the thermal field from all the areas of the piece to the build platform. With FE based macroscale process simulations, it is possible to evidence improved thermal strain distributions of the optimised configuration.

As part of the R&D activity within the “STAMP” project financed by Regione Piemonte, an innovative function was developed and successfully applied to minimize distortions and residual stresses of SLM parts. Within the same project, a software interface was developed for setting user parameters and individual jobs. The interface provides detailed information of the laser path and physical variables, which can be used for off-line or in-line monitoring and control and provides a model for process simulation. It is also possible to view the entire laser path and the detail of each individual trait, and to generate a file containing

structured data as a FEM model, for setting boundary conditions and process parameters.

The algorithms are included in the integrated platform for AM developed by ITACAe, named AMTOP[®]. Starting from geometrical, functional and structural product specifications, the platform includes a topological optimization phase, new geometry construction, FEM discretization, FEA validation, optimal orientation and supports creation, so representing a fully integrated product & process engineering workflow.

2 AN APPROACH BASED ON GEOMETRICAL ANALYSIS

Among the most challenging tasks, which a process engineer must face during the phase of design of the additive manufacturing process, there are the definition of the most suitable build orientation of the piece, a proper choice of process parameters and the configuration of supports. An already vast literature is furtherly growing, trying to standardize fundamental design-process-material correlations by design rules within additive manufacturing processes, not forgetting extensive normative activity by the working groups belonging to ISO TC 261. The aim is suggesting best choices to the process engineer before launching a job.

All the stakeholders from both academic and industrial value chain are committed in this task that is afforded with different complementary ways and methods, of which the most rigorous one is a multi-scale modelling of the complex thermal-structural phenomenon with material phase change. This is currently tremendously expensive. However, we are still far from the definition of a rigorous methodology of optimization of build orientation to minimize the thermal distortion in AM build process. This is probably due to lack of efficient part-scale AM modelling tools which can accurately predict thermal distortions.

The “trial & error” approach often appears to more efficient and is therefore mostly adopted by manufacturers, who employ a relevant portion of their resources to capitalise their own expertise and to develop process databases. In this scenario, the use of machine learning or artificial intelligence methods might be envisaged against competitive traditional numerical simulation methodologies. Engineering software vendors are reacting with proposing simplified methods, based on rough but effective methods based on geometrical analyses, often disregarding assumptions about physical boundary conditions and material properties.

3.1 A brief state-of-the-art

One update that stands out is ANSYS[®] Additive Prep. This tool sits inside ANSYS SpaceClaim and produces heat maps that help engineers predict how additive manufacturing build orientations impact support structures, build times, distortions and overall print performance. Heat maps are combined into an overall performance heat map, which is made using a weighing function that is controlled by a triangular input graph.

The product Amphyon by Additive Works, who joined ALTAIR Partner Alliance uses data to consider all possible orientations and determines which is optimal for the part. The software analyses the accessibility, support volume, build time, post-processing effort, functional faces, distortion tendencies and the build chamber for each orientation.

MSC Software[®]'s Simufact[™] Additive version 4 comes with a workflow-oriented user interface, which guides the user through the simulation process workflow and supports him

with new automation and assistant functionalities among which are notable automated support optimization and build orientation assistant.

FE Software vendors' proposals have great appeal with user-friendliness built-in functions. In order to fit requirements due to rapidly evolving technologies and consider all machine process parameters, many more software interfaces are being developed by the other stakeholders that is machine manufacturers, engineering service providers and users from universities and industry.

3.1 The geometrical analysis method

The proposed method is based on the assumptions that a high level of distortion and defects may be correlated to not uniform distribution of temperatures during the part building. The loading condition is a heat source applied to a very small region of material, which transfers it through radiation, conduction and convection. It is also assumed that in most situations, radiation and convection contributions are negligible. Limiting to the case of SLM PB processes, we encounter the following simplified situation: three materials with different mechanical and thermal properties are in contact to each other. The three materials are air, metal powder and metal solid. This can be assimilated to a composite with the three materials having different thermal conductivities α_a , α_p and α_s , respectively.

We implicitly say that the most robust manufacturing process would be ideally the one associated with the maximum effectiveness of the thermal drain from the source at the level of the current layer to the surrounding air in the domain Ω_a and the base through the underlying solid layers and supports and the metal powder in the domains Ω_s , Ω_p , respectively. The conductivity α of the whole domain Ω ($\Omega_a \cup \Omega_s \cup \Omega_p$) is:

$$\alpha(x) = \alpha_a \chi_a(x) + \alpha_s \chi_s(x) + \alpha_p \chi_p(x) \quad (1)$$

Where $\chi_a(x)$, $\chi_s(x)$, $\chi_m(x)$ are the characteristic functions of $x \in \Omega_a$, Ω_s , Ω_p , respectively. To compute the inner temperature u with a heat source q , we consider the Fourier's law and the condition of static thermal equilibrium:

$$\begin{cases} -div(\alpha(x)\nabla u) = q & \text{in } \Omega \\ u = 0 & \text{on } \delta\Omega \end{cases} \quad (2)$$

The problem can be simplified with the assumption that a thermal exchange far from the heat source can be neglected for the evaluation of local deformations, so that to minimise the domain size to $\Omega' \subset \Omega$. If we assume to neglect the contribution of thermal exchange with air and powder, the domain will be furtherly restricted to Ω'_s . A functional to be minimised must be identified, which can relate to the distribution of temperatures inside the restricted domain. Considering a normal distribution inside the restricted domain, we decide to assume the functional defined as the variance of the function $f(x, u(x))$ within the restricted domain Ω'_s .

$$J(\Omega'_s) := \int_{\Omega'_s} (f(x, u(x)) - m)^2 f(x, u(x)) dx \quad (3)$$

This problem has no classical solution, and a relaxed form and homogenization techniques can be used to get a well-posed problem, which is not discussed here. Once solved the optimization problem, the optimal orientation is identified, which minimises the functional.

3 DESCRIPTION OF THE SOFTWARE INTERFACE

ITACAe in agreement with 3D-NT within the Piemonte project “STAMP” has set the requirements for the realization of a software able to manage the user-machine interface, which allows the setting of the parameters and the communication with a non-relational database (DB) in order to define the settings of the "job", that is, of the script containing the implementation process procedure. The DB for the application is a source of numerical data deriving from sensors in the working chamber, spectral images in the visible and near-infrared fields. With the communication with the DB and the predisposition to the insertion of "Machine Learning" functions, it is possible to certify or reject new non-labelled data and make real-time corrections to the "job file" and delayed to the component during manufacturing.

An application developed by ITACAe interfaces with Application Program Interface (API) created by 3D-NT. The application was developed in C# and contains subroutines developed in Fortran. In particular, the reading of the CLI files takes place through a code developed in Fortran while the call to the API and the management of the laser path was developed in the .Netframework environment using the C# language.

The code has also the function to write FE files, in the Nastran, Abaqus and Ls-Dyna formats to allow viewing of the laser path with any pre-processor and setting process simulations. Some steps lead from the triangulation of the input geometry (file in STL format) to the voxelization (**Figure 1**), for the process simulation.

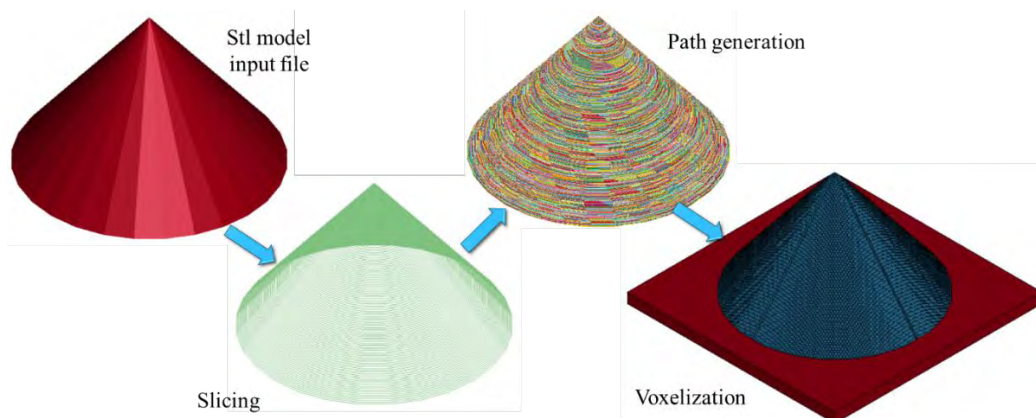


Figure 1: Steps from geometrical model to voxelization

Starting from the STL model, the CLI (Common Layer Interface) file is obtained by means of the API created by 3D-NT. The CLI file constitutes the input of the software interface created by ITACAe.

3.1 Common Layer Interface

The CLI format is a universal format for the input of geometry data to model fabrication systems based on layer manufacturing technologies (LMT). The CLI is based on a 2.5D representation. The geometric information of the intersection of a 3D model with a plane is called a slice. The volume between two parallel sections is called a layer.

3.2 Input file

The application requires the following input information.

1. CLI geometry file (FILENAME.cli)
2. Optional parameter file (FILENAME_par.txt). The parameters that can be supplied are the following:
 - Beam diameter;
 - Layer thickness;
 - Distance between the hatches;
 - Base length;
 - Width of the base;
 - Base height;
 - Laser source power;
 - Recoating time;
 - Releasing time;
 - Beam speed.

If the file containing the parameters is not supplied as input, the code deduces the data necessary for calculating the performance of the machine.

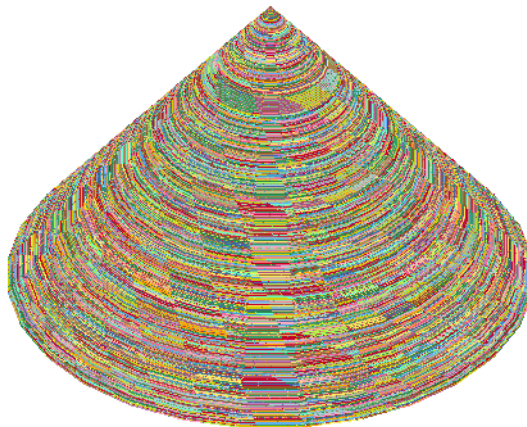


Figure 2: Representation of each treats of the laser path through coloured segments

3.3 Output results file

The code outputs three text files: FILENAME.txt, FILENAME_res.txt and FILENAME_lay.txt.

The FILENAME.txt file contains the following information:

1. ID of the points and respective coordinates x, y, z: Point id, x, y, z coordinates
2. ID of the line, ID of the property and identification of the points of departure and arrival of the individual sections of the laser path.

The quantities shown in the output file are:

1. ID_LAY, Layer identifier. The layers are numbered in progressive order starting from the first layer;

2. ZLAY, dimension in Z of the layer in mm;
3. PATH, path length expressed in mm;
4. TIME, time expressed in s necessary to walk the path;
5. SPEED, beam speed in mm/s;
6. ENERGY, energy spent to make the layer, expressed in mJ.

Considering the layer 2 positioned at $Z = 1$ mm, the length of the complete path is about 56 m, the time taken to complete it is equal to about 130 seconds, at an average speed of 430 mm/s and with an amount of energy absorbed equal to 5.9 J. The output file FILENAME_lay.txt supplies the process information layer by layer.

The FILENAME_vec.txt file provides more detailed process information. In this case, in the FILENAME_vec.txt file, in addition to the data already present in the FILENAME_lay.txt file, it is possible to read the following additional data:

1. M / J, which identifies the action Move (M) or Jump (J) of the laser. In the case of jumps, as shown on line 1 of, the dissipated power is zero. On the contrary, in the case of Move, the dissipated power is different from zero and is expressed in mW;
2. (Xi, Yi), pair of coordinates in the X and Y plane of the starting point (1) and arrival (2) of the vector, expressed in mm;
3. DIAMETER, beam diameter;
4. Cumulative quantities, sum of the contribution of the generic quantity from the first vector to the current vector.

3.4 Optimization of orientation and generation of supports

The software allows to set the following geometric parameters for the generation of supports:

- Overhang Angle, the angle above which it is no longer necessary to insert supports,
- Baseplate Offset, the minimum distance of the component from the plate,
- Contact Edge Size, the length of the contact side between the supports and the part surface,
- Max Unsupported Size, a value that depends on the material and is the maximum length such that the sintered powder is self-sustaining,
- Thickness of the supports,
- Filling factor of the support grid (relationship between these two lengths).

Different types of supports can be chosen: solid, hollow and cross. The orientation of the part is based on different criteria of minimization: supports volume, supports height, process cost or part distortion. A combination of all of them with weighing factors is also implemented. The tool allows a full customization of both support configuration generation and orientation optimization objective function.

The algorithm was applied to an automotive gear bracket in the frame of the “STAMP” project (**Figure 3**). The part was previously topologically optimised by ITACAe for maximum mechanical strength, starting from technical specifications provided by FCA. Two configurations are analysed: not optimised orientation and orientation for minimum distortion.



Figure 3: Model of an automotive gear bracket obtained from a previous phase of topological optimisation for maximum mechanical strength



Figure 4: Part oriented for minimum distortion

Table 1: Results of the optimization of build orientation

Crit. #	Target	Part/support data	Density	Volum e mm ³	Mass AlSi10Mg g	Dx mm	Dy mm	Dz mm	Area mm ²
	Part	Part	99%	251783	673				
0	No optimisation	Support	70%	467061	883	190	150	102	28500
2	Min variance	Support	70%	625955	1183	102	162	184	16524

4 NUMERICAL SIMULATION

4.1 Part orientation

In order to demonstrate the effectiveness of the described approach about the definition of the optimal orientation, numerical simulation results of a selected case study are presented in this paragraph. Two different kinds of orientation are assumed for the component characterized respectively by not optimised orientation and orientation for minimum distortion.

For each orientation of the component, an Additive Manufacturing Simulation was carried out by means of the software Simufact™ Additive by MSC® Software. In the frame of the powder bed fusion (PBF) methods, the additive manufacturing process optimization faces two main issues affecting the metal-based manufacturing processes: the distortion of the geometry and the residual stresses. The first undesired effect could cause deviations from the optimal shape and require the use of outside tolerances. The second issue, instead, could be reason for cracking, failure of supports and reduction in the strength and fatigue life of the component.

The macro scale approach followed by Simufact™ Additive makes use of a voxel technique that discretizes the entire volume in millions of finite elements and adopts a layer-based additive manufacturing process. The distortion effect is a direct consequence of the heat distribution on the component that causes a not homogeneous thermal expansion depending on the local temperature of the metal. This phenomenon in Simufact™ Additive is predicted by the “inherent strain method”. This method is beneficial due to the faster computation time in comparison with coupled thermo-mechanical simulations. The inherent strain method assumes that the laser spot size is negligible compared to the built components. The inherent strains must be determined preliminarily and are then used to calculate the residual stress and distortions by imposing them on linear elastic purely mechanical FE models.

4.2 Simulation parameters and results

In this paragraph, a series of simulation parameters set before running the simulation are reported. The machine type adopted for the layer-based process is M400 manufactured by EOS. The part to produce, whose model has been implemented by means of a STL file, is made of AlSi10Mg, has a relative material density equal to 99%, a surface of 79.369 mm² and a volume of 319.543 mm³. The supports, automatically created in Additive Simufact™ environment, have relative material density equal to 80%, isotropic elastic properties and isotropic thermal conductivity. A base plate is defined with the same material of the part and the supports and with dimensions: 400x400x10 mm³.

As a result of the simulations, it was possible to demonstrate a reduction of deviations from nominal geometry, with the orientation suggested by AMTOP® for minimum distortion compared to not optimised configuration, from $-4.01 \div 3.88$ mm to $-2.14 \div 2.90$ mm (**Figure 5 & Figure 6**).

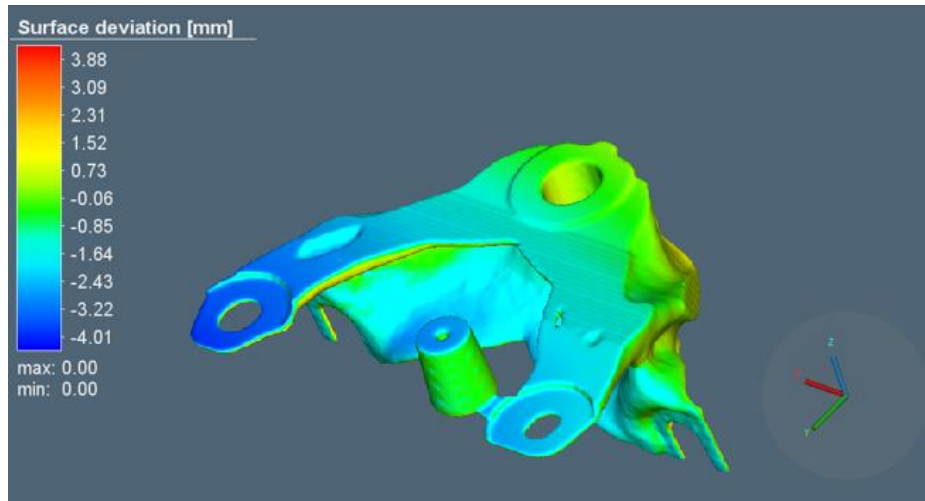


Figure 5: Surface deviation [mm] for the component with not optimised orientation (case A)

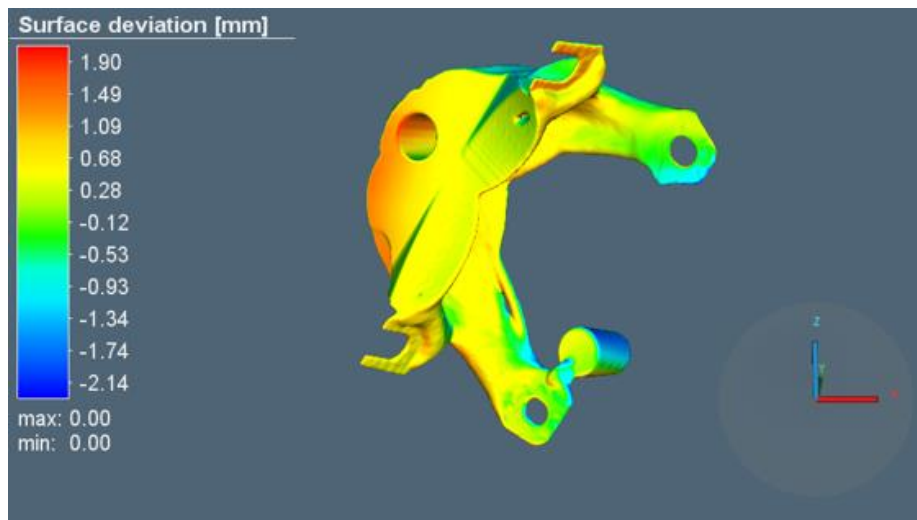


Figure 6: Surface deviation [mm] for the component oriented with minimum distortion (case B)

5 CONCLUSIONS

The described activity relates to the programming of a software interface for setting user parameters and individual jobs. The software provides detailed information on the laser path and physical variables, which can be used for off-line or in-line monitoring and control. It is also possible to view the entire laser path and the detail of each individual trait, and to generate a file containing structured data as a FEM model, for setting boundary conditions and process parameters for the definition of a process simulation model.

One of the possible part orientations provided by AMTOP[®] (for minimum distortion) and the configuration with not optimised orientation were analysed with FE macro-scale simulation. The numerical results of each calculation were compared in terms of surface deviation of the original shape computed after the supports removal and cooling.

As expected, the orientation of the component for minimum distortion allows to reduce the final part surface deviation range. This effect is assumed to be related to a more homogeneous distribution of the temperature on the volume that determines a more regular thermal expansion of the material.

ACKNOWLEDGEMENTS

The work has been partially funded through the participation to the innovation project “STAMP” (Sviluppo Tecnologico dell'Additive Manufacturing in Piemonte), within the program agreement MIUR - Piemonte Region, action 3 of "Smart Factory". The authors are grateful to all the partners who were committed in the task: 3D-NT, Prima Electro, FCA, GE AVIO, ELLENA, APR and to the project leader Prima Industrie.

REFERENCES

- [1] A. Henrot and M. Pierre, Shape Variation and Optimization: A Geometrical Analysis, *European Mathematical Society*, (April 25, 2018).
- [2] J. W. Booth, J. Alperovich, T. N. Reid, K. Ramani, The Design for Additive Manufacturing Worksheet., Proceedings of the ASME 2016 International Design Engineering Technical Conferences & Computers and Information in Engineering Conference IDETC/CIE 2016, August 21-24, 2016, Charlotte, North Carolina, USA.
- [3] Zeng, Kai, Optimization of support structures for selective laser melting. (2015). Electronic Theses and Dissertations. Paper 2221. <http://dx.doi.org/10.18297/etd/2221>
- [4] Cherkaev, Andrej & Cherkaev, Elena. (2002). Structural Optimization and Biological “Designs”. 10.1007/0-306-46939-1_22.
- [5] Feppon, Florian & Michailidis, Georgios & Sidebottom, Mark & Allaire, Grégoire & Krick, Brandon & Vermaak, Natasha. (2016). Introducing a level-set based shape and topology optimization method for the wear of composite materials with geometric constraints. Structural and Multidisciplinary Optimization. 10.1007/s00158-016-1512-4.
- [6] Pinar Mert Cuce, Erdem Cuce, Optimization of configurations to enhance heat transfer from a longitudinal fin exposed to natural convection and radiation, International Journal of Low-Carbon Technologies, Volume 9, Issue 4, December 2014, Pages 305–310, <https://doi.org/10.1093/ijlct/ctt005>.
- [7] Malekipour, Ehsan & Tovar, Andres & El-Mounayri, Hazim. (2018). Heat Conduction and Geometry Topology Optimization of Support Structure in Laser-Based Additive Manufacturing. 10.1007/978-3-319-62834-9_4.
- [8] Wang, Cunfu & Qian, Xiaoping & Gerstler, William & Shubrooks, Jeff. (2019). Boundary Slope Control in Topology Optimization for Additive Manufacturing: for Self-support and Surface Roughness *. Journal of Manufacturing Science and Engineering. 10.1115/1.4043978.
- [9] Taufik, Mohammad & Jain, Prashant. (2014). Role of build orientation in layered manufacturing: A review. International Journal of Manufacturing Technology and Management. 27. pp.47 - 73. 10.1504/IJMTM.2013.058637.
- [10] Peng, H.; Ghasri-Khouzani, M.; Gong, S.; Attardo, R.; Ostiguy, P; Aboud Gatrell, B.; Budzinski,

- J.; Tomonto, C.; Neidig, J; Shankar, M.R.; Billo, R.; Go, D.B.; Hoelzle, D.: Optimization of build orientation for minimum thermal distortion in DMLS metallic Additive Manufacturing, Solid Freeform Fabrication: Proceedings of the 28th Annual International Solid Freeform Fabrication Symposium, 2017.
- [11] E. Ulu, E. Korkmaz, K. Yay, O. Burak Ozdoganlar, L. Burak Kara, Enhancing the Structural Performance of Additively Manufactured Objects Through Build Orientation Optimization, *J. Mech. Des.* 137 (2015) 111713. doi:10.1115/1.4030998.
- [12] C. Thompson, David & Crawford, Richard. (1998). *Optimizing Part Quality with Orientation*.
- [13] Das, Paramita & Chandran, Ramya & Samant, Rutuja & Anand, Sam. (2015). Optimum Part Build Orientation in Additive Manufacturing for Minimizing Part Errors and Support Structures. *Procedia Manufacturing*. 1. 343-354. 10.1016/j.promfg.2015.09.041.
- [14] Ninshu Ma, Keiji Nakacho, Takahiko Ohta, Naoki Ogawa, Akira Maekawa, Hui Huang, and Hidekazu Murakawa. Inherent strain method for residual stress measurement and welding distortion prediction. In *ASME 2016 35th International Conference on Ocean, Offshore and Arctic Engineering*, pages V009T13A001–V009T13A001. American Society of Mechanical Engineers, 2016.
- [15]] MSC Simufact. Simufact additive tutorial, April 2018.
- [16] ISO/ASTM 52915:2016, Specification for additive manufacturing file format (amf) version 1.2
- [17] "ISO/IEC 23271, Common Language Infrastructure". ISO. Retrieved September 27, 2006.

BOUNDARY CONDITIONS FOR SIMULATION OF POWDER BED FUSION FOR METALLIC GLASS FORMATION: MEASUREMENTS AND CALIBRATIONS

J. Lindwall*, C.-J. Hassila[†], J. J. Marattukalam⁺ AND A. Lundbäck*

*Department of Engineering Science and Mathematics
Luleå University of Technology, 971 87 Luleå, Sweden
e-mail: johan.lindwall@ltu.se

⁺ Department of Engineering Science - Ångström Laboratory
Uppsala University, Box 534, 75121, Uppsala, Sweden

[†] Department of Physics and Astronomy - Ångström Laboratory
Uppsala University, Box 516, 751 20 Uppsala, Sweden

Key words: Computational Methods, Additive Manufacturing, Thermal Simulation, Bulk Metallic Glass

Abstract. A finite element model for prediction of the temperature field in the powder bed fusion process is presented and compared to measurements. Accurate temperature predictions at the base plate are essential to accurately predict the formation of crystals in a metallic glass forming material. The temperature measurements were performed by equipping the base plate with thermocouples during manufacturing of a cylinder with the glass forming alloy AMZ4. Boundary conditions for heat losses through the base plate/machine contact interfaces was calibrated to fit the measurements. Additional heat losses was used to account for radiation at the top surface and conduction through the powder bed. An interface boundary condition based on conservation of heat flux was examined to match the heat flow to the machine structure and the temperature predictions was satisfying. Still, temperature predictions with a constant heat transfer coefficient matched the measurements within 1.5°C during the entire building process of about 9 hours.

1 INTRODUCTION

Additive manufacturing with the powder bed fusion (PBF) process enables rapid solidification which is essential for formation of metallic glass. Metallic glass possesses desirable properties for a variety of applications [1]. Unfortunately, they can be difficult to produce in practical dimensions by traditional manufacturing techniques, such as suction casting, melt pinning etc, where the cooling rate might be too low in the bulk. The amorphous structure can only be achieved when crystallization is bypassed and maintained only if not subjected to temperatures above a critical temperature of crystallization. Thus, the temperature history in the material during the PBF process dictates the amount of amorphous phase and formation of crystalline phases.

During simulation of the PBF process, it becomes critical to accurately predict the temperature field close to the melt pool and also in the surrounding material. The base plate/substrate acts as a heat sink that accumulates heat by conduction. During the melting of each layer, heat is conducted through the built material and the base plate. After a few layers, the overall temperature will rise and affect the temperature gradients and hence the cooling rates of the melt pool. The temperature of the base plate can rise to close to the glass transformation temperature if heat is not transported away. Thus, heat losses by radiation, convection and conduction through contact interfaces to the machine plays an important role in the manufacturing of bulk metallic glasses (BMG) with low crystalline fraction. Chiumenti et al. [2] presented a model to account for the heat losses to the powder bed, but without modelling the powder bed domain. Other studies have applied constant convection coefficients to the solid/powder interface [3, 4].

Many researchers have printed BMGs using a laser heat source in PBF [5]. However, crystals can still be found in the manufactured material, even though it looks amorphous in X-ray diffraction measurements. The crystalline phases have been argued to form as a result of thermal cycling in the heat affected zone [6–11]. When the material is remelted, nuclei will dissolve; otherwise, they become trapped in the amorphous matrix and may grow due to diffusion. Simulations of the process can help us understand the thermal events in critical regions where crystals may form and persist. These types of simulations will offer new insights into the process, and in the long term aid the process development, possibly reducing the crystalline fraction in BMG manufactured via PBF.

This study aims to contribute to thermal simulations of the PBF process for accurate predictions of the temperature field that drives crystallization and devitrification. The work is limited to thermal modelling on the overall process with heat losses to the environment. Contact interfaces are replaced with boundary conditions that are estimated by the temperature measurements.

2 EXPERIMENTAL SETUP

A cylinder with a diameter of 10 mm was built on a cylindrical base plate with an EOS M100 system. The layer thickness was 20 μm and the total build height was 60 mm, resulting in a total of 3000 layers. The cylinder was centred on the build plate to ensure rotational symmetry. The diameter and thickness of the base plate was 100 and 21.4 mm respectively. Furthermore, the build plate was prepared with three holes on the bottom side of the plate into which type-K thermocouples were inserted. The holes were drilled to a depth of 16.4 mm, leaving 5mm of material to the surface of the plate. One hole was placed in the central position of the plate, i.e., right below where the BMG cylinder was to be built. The other two holes were placed 17.5 mm and 35.0 mm from the central position respectively, as shown in Figure 1. The laser power was 80 W with a scanning speed of 2000 mm/s and a hatch distance of 100 μm . Each layer was scanned twice with an angular rotation of 67°. The process parameters are summarized in Table 1.

The temperature response was measured during the entire building process (about 9 hours)

¹Estimated value used in simulations

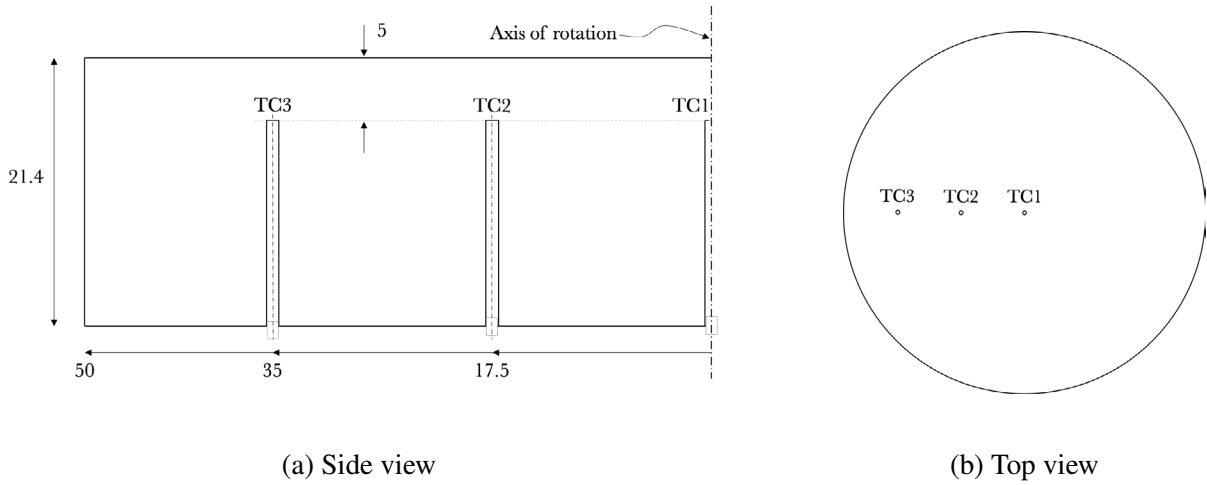


Figure 1: Measurements of base plate (unit mm) and locations of thermocouples (TC).

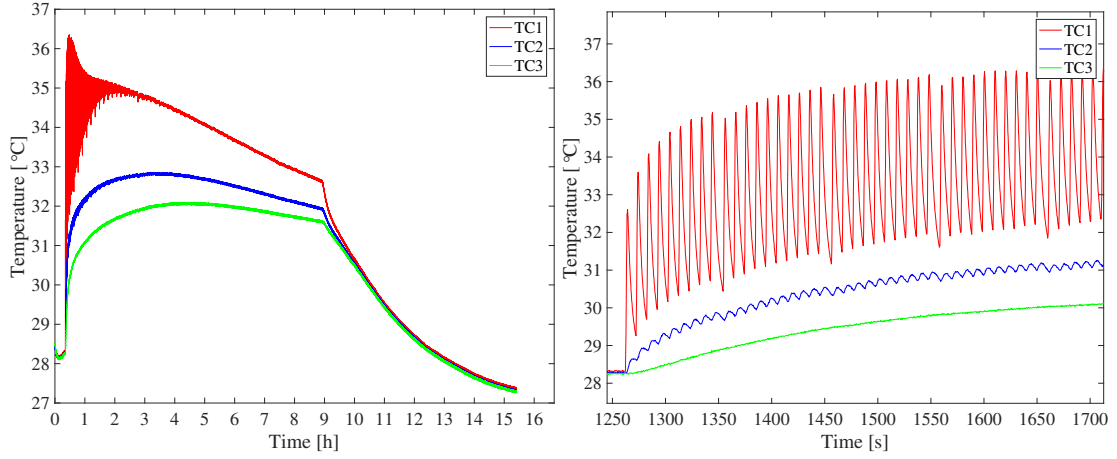
Table 1: Process parameters

Laser power	80	W
Scan speed	2000	mm/s
Layer thickness	20	μm
Laser efficiency ¹	40	%
Hatch distance	100	μm
Penetration depth	80	μm

as well as during the time it took for the machine to reach ambient temperatures, a total of 15 hours, as presented in Figure 2. From the beginning of the build, Figure 2b, it was possible to determine the time between each successive layer to 10 seconds. It was also found that every 10th layer used an additional pause time of 2.65 seconds, possibly for referencing of the laser. During this extra pause, the base plate is given additional time to dissipate heat and results in lowering of the temperature of the whole system.

3 MODELLING APPROACH

The manufacturing process was reduced to a two dimensional axisymmetric modelling domain, including the base plate and the cylinder of the printed material, Figure 3. All elements that represent the build material were first subdivided in three levels and then deactivated during the initiation of the simulation. Each sub-element then reached the thickness of one layer, i.e., 20 μm . These sub-elements were then activated in a layer-by-layer fashion and later on unrefined to restore the parent elements.



(a) Whole range with gas flooding, printing and cooling

(b) Beginning of printing

Figure 2: Temperature response at the three thermocouples in the base plate during printing with 80 W.

3.1 Heat input

The heat input was modelled by a volumetric heat flux acting on the entire layer simultaneously. The heat was distributed using a Gaussian expression according to Equation (1), as presented previously by [11],

$$q(z) = \frac{2\sqrt{3}\eta Q}{\sqrt{\pi}ch^2} e^{-\frac{3z^2}{c^2}} \quad (1)$$

where Q is the laser powder, η the efficiency/absorption fraction of the laser, c the penetration depth and h the hatch spacing. The heat input acted during a characteristic time of $t_{heat} = h/v$ where v is the scanning speed. The heating procedure in the simulation used two heating sequences for each layer and was modelled with two heating load cases with a dwell time in between. The dwell time corresponds to the scanning time of an entire layer in the PBF experiment.

3.2 Heat losses

Heat dissipate from the heated area and conducts through the built material and base plate and further on to the powder bed and to the machine. Described in this section are the boundary conditions for heat losses into the powder bed, the atmosphere and to the printer.

3.2.1 Powder bed

The interaction between the cylinder and the powder bed was represented by a face film boundary condition with a coefficient, h_{powder} , acting on all surfaces facing the powder bed,

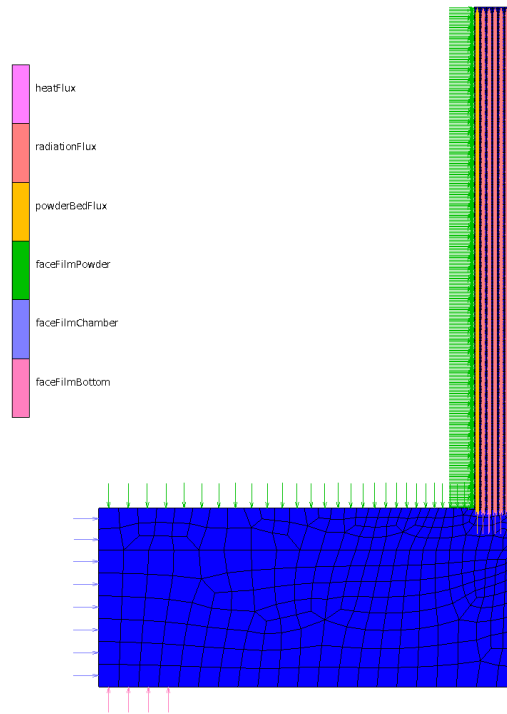


Figure 3: Two dimensional axisymmetric modelling domain.

as shown by the boundary condition `faceFilmPowder` in Figure 3. During the course of the simulation/build, as the height of the cylinder increased, the active face film area continuously increased as more layers were activated. In the beginning of the printing process, the cross-sectional area of the printed component is much larger than the circumferential area. This combined with a much larger conductivity in the solid material compared to the powder bed results in a heat flux that is dominated by thermal conductivity towards the base plate. On the other hand, as the build progresses, the circumferential area becomes much larger than the cross sectional area (which stays constant) and heat flux towards the powder bed can instead be the dominating heat loss, provided that the powder bed conducts heat and continues to lose heat to the environment. These arguments can explain why the temperature curves in Figure 2 have a peak temperature and then starts to decline, i.e., after the peak temperature, the heat flux towards the thermocouples in the base plate is continuously reduced.

3.2.2 Free surface

The top surface of the scanned area was subjected to heat losses by radiation. This boundary condition was updated every time a new layer was activated to only act on the top surface of the cylinder. Heat loss by convection from the free surface was neglected as the protective argon gas is a very poor heat conductor and the gas was circulated.

3.2.3 Machine

During the printing process, the base plate is held in place by a vacuum. This attachment results in a contact pressure in the outer rim of the base plate and offers a possibility for heat transport towards the machine. This contact was modelled using a face film with a film coefficient, h_{bottom} acting on the edges indicated by `faceFilmBottom` in Figure 3.

The radial contact to the machine is non or very low as there is a small gap between the base plate and the chamber wall such that the build plate can move freely in the vertical direction. Thus, heat transport through this interface was assumed to be very low and a face film coefficient on `faceFilmChamber` was set to zero.

4 CALIBRATION TO EXPERIMENTS

The temperature was predicted at the locations that corresponds to the positions of the thermocouples. The boundary conditions in the FE-model was calibrated to fit the temperature measurements on the base plate.

4.1 Bottom face film

The face film coefficient at the bottom of the base plate was estimated by conservation of heat flux through the base plate and the interface to the machine. The rate of heat flow between TC2 and TC3, J , can be estimated by the thermal conductivity of the material, a cross-sectional area, S and the temperature gradient.

$$J = -kS \frac{\Delta T}{x} \quad (2)$$

In this expression, k is the thermal conductivity of Titanium, hence a fixed value of 21.8 W/mK was used, corresponding to the conductivity at 32°C. The area was selected as indicated in Figure 4a located at the mean radius between TC2 and TC3. The temperature gradient was computed by the measured temperature difference between TC2 and TC3 and the fixed distance of $x = 17.5$ mm. The rate of heat transfer was then assumed to equal the heat transfer through the contact interface, S_I , that covers the outer 10 mm of the base plate as indicated by the highlighted area in Figure 4b.

$$J = h\Delta T_I S_I \quad (3)$$

Here, h is the film coefficient (W/m²K), ΔT_I the temperature difference between the base plate and the machine over the interface. Thus, equating Equations (2) and (3) gives:

$$h = \frac{kS\Delta T}{x\Delta T_I S_I}. \quad (4)$$

The resulting film coefficient was then computed by letting ΔT_I be the difference between an estimated temperature at the base plate, extrapolated by TC2 and TC3, and the surrounding temperature of 27°C. The computed film coefficient and an estimated function is presented in Figure 5.

$$h = a \cdot t^b + c \quad (5)$$

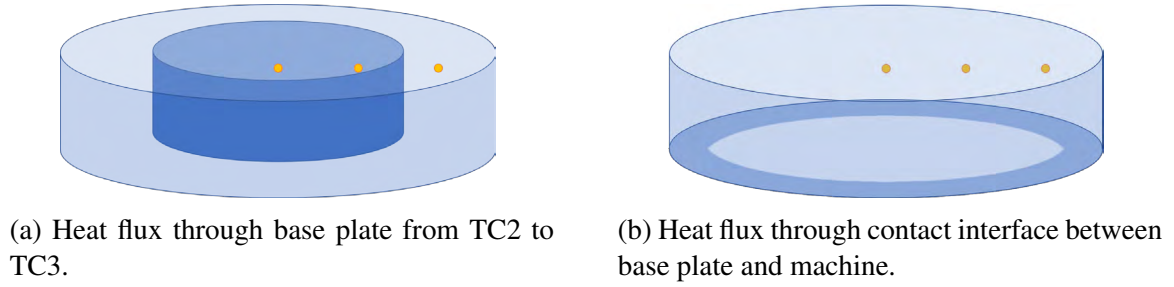


Figure 4: Conservation of heat flux through the highlighted areas in the base plate is used to estimate the film coefficient. Dots indicates the locations of thermocouples.

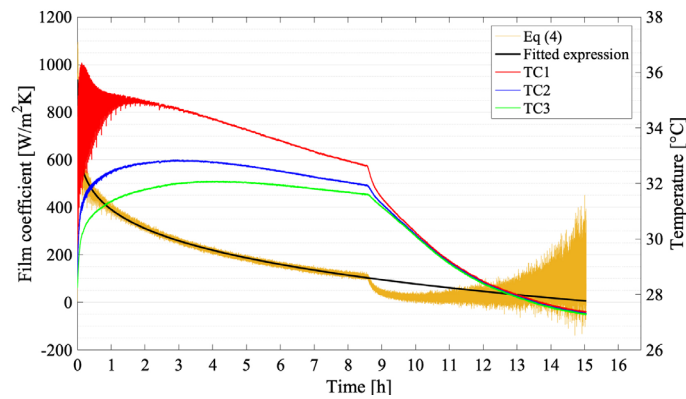


Figure 5: Estimated film coefficient by temperature difference at TC2 and TC3 and fitted with a simple power law equation $h = a \times t^b + c$ with $a = -109.6$, $b = 0.1964$ and $c = 938.2$.

5 RESULTS & DISCUSSION

The temperature history at the locations that corresponds to the positions of the thermocouples was computed during the full time of the experiment. The result with a varying film coefficient over time is shown in Figure 6a. The predicted temperature is a few degrees lower than the measured during the first half of the built. During the end on the other hand, the predicted temperature have continued to increase above the measured temperatures. The continuously decreasing heat transfer coefficient allowed the thermal energy to be stored in the base plate.

The results were compared to a model with a fixed heat transfer coefficient of $150 \text{ W/m}^2\text{K}$ at the bottom of the base plate. Then, the predicted temperatures became comparable to the measured, as shown in Figure 6b. A lower heat transfer in the beginning of the simulation resulted in higher temperatures in the base plate compared to the PBF measurements and previous simulation. The predicted temperature then decreased and became 1-1.5 degrees lower than the measured temperature at the end of the 9 hours built time.

During the cooling sequence, when the cylinder is completed, the computed temperature dropped more quickly compared to the PBF measurements. The slow cooling indicates that the surrounding environment and machine have been heated and stores most of the transferred heat.

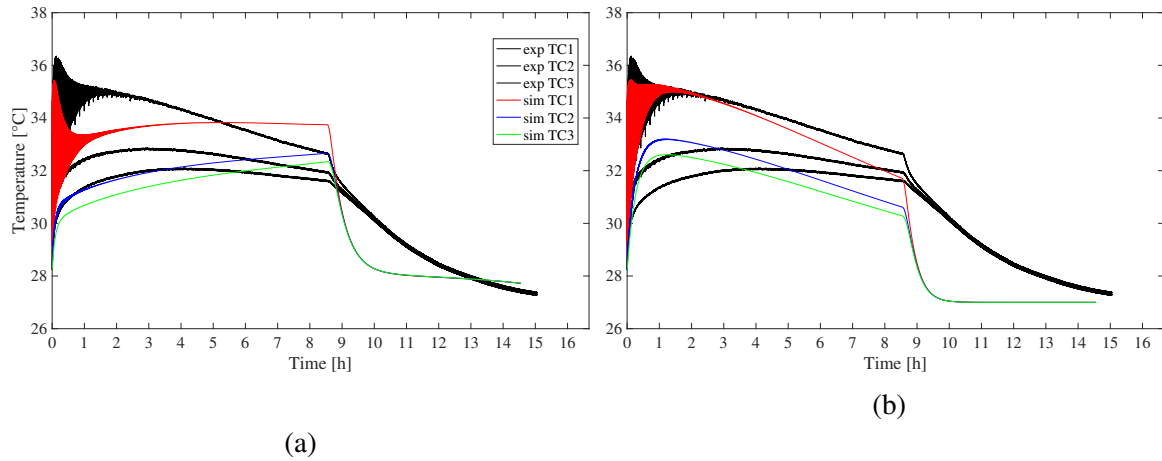


Figure 6: Temperature prediction with a film coefficient that is; (a), time dependent according to fitted exponential function and (b) a constant value.

Thus, accurate predictions of the temperature after build completion should be done with an extended model, including the mass of the machine.

6 CONCLUSION

This study elaborates on the boundary conditions for heat losses in the PBF process for accurate predictions of the temperature field in the base plate while printing a bulk metallic glass. Accurate predictions of the temperature field in the base plate becomes necessary when predicting the microstructure in the manufactured component. Lack of boundary conditions for heat losses would lead to increasing temperatures in the base plate. Increasing temperatures would favor crystallization and result in in-accurate phase predictions.

This work uses measured temperatures in the base plate for calibration of boundary conditions when manufacturing a 60 mm high cylinder. A time varying heat transfer coefficient based on the temperature measurements was proposed to define the heat losses at the machine/base plate contact interface. At the beginning of the build, the heat transfer coefficient is high due to the temperature difference at TC2 and TC3 together with a small temperature difference between the base plate and machine material. As the build progresses, the temperature difference between the thermocouples reduces and the temperature of the base plate increases, which results in a reduced heat transfer coefficient. Satisfying predictions was achieved using this boundary condition together with a fixed heat transfer coefficient in the powder interface. Yet, the time varying heat transfer provided to much cooling at the beginning of the build that indicated an overestimation of the heat transfer coefficient through the interface. Instead, good predictions within 1.5°C was achieved during the roughly 9 hours built by choosing a constant heat transfer coefficient at the contact interface.

ACKNOWLEDGEMENT

This research was supported by the Swedish Foundation for Strategic Research, SSF, project "Development of Process and Material in Additive Manufacturing", Reference number GMT14-0048.

References

- [1] M. M. Khan, A. Nemati, Z. U. Rahman, U. H. Shah, H. Asgar, and W. Haider. "Recent Advancements in Bulk Metallic Glasses and Their Applications: A Review". *Critical Reviews in Solid State and Materials Sciences* 43.3 (2018), pp. 233–268.
- [2] M. Chiumenti, E. Neiva, E. Salsi, M. Cervera, S. Badia, J. Moya, Z. Chen, C. Lee, and C. Davies. "Numerical modelling and experimental validation in Selective Laser Melting". *Additive Manufacturing* 18 (Dec. 2017), pp. 171–185.
- [3] Y. Z. B and G. Guillemot. "Macroscopic Finite Element Thermal Modelling of Selective Laser Melting for IN718 Real Part Geometries". *Industrializing Additive Manufacturing - Proceedings of Additive Manufacturing in Products and Applications - AMPA2017* September (2017).
- [4] E. R. Denlinger, M. Gouge, J. Irwin, and P. Michaleris. "Thermomechanical model development and in situ experimental validation of the Laser Powder-Bed Fusion Process". *Additive Manufacturing* 16 (2017), pp. 73–80.
- [5] E. Williams and N. Lavery. "Laser processing of bulk metallic glass: A review". *Journal of Materials Processing Technology* 247.March (2017), pp. 73–91.
- [6] G. Yang, X. Lin, F. Liu, Q. Hu, L. Ma, J. Li, and W. Huang. "Laser solid forming Zr-based bulk metallic glass". *Intermetallics* 22 (2012), pp. 110–115.
- [7] B. Chen, T. Shi, M. Li, C. Wen, and G. Liao. "Crystallization of Zr₅₅Cu₃₀Al₁₀Ni₅ Bulk metallic glass in laser welding: Simulation and experiment". *Advanced Engineering Materials* 17.4 (2015), pp. 483–490.
- [8] Y. Zhang, X. Lin, L. Wang, L. Wei, F. Liu, and W. Huang. "Microstructural analysis of Zr₅₅Cu₃₀Al₁₀Ni₅ bulk metallic glasses by laser surface remelting and laser solid forming". *Intermetallics* 66 (2015), pp. 22–30.
- [9] Y. Lu, H. Zhang, H. Li, H. Xu, G. Huang, Z. Qin, and X. Lu. "Crystallization prediction on laser three-dimensional printing of Zr-based bulk metallic glass". *Journal of Non-Crystalline Solids* 461 (2017), pp. 12–17.
- [10] Y. Shen, Y. Li, and H.-L. Tsai. "Evolution of crystalline phase during laser processing of Zr-based metallic glass". *Journal of Non-Crystalline Solids* 481 (Feb. 2018), pp. 299–305.
- [11] J. Lindwall, V. Pacheco, M. Sahlberg, A. Lundbäck, and L. E. Lindgren. "Thermal simulation and phase modeling of bulk metallic glass in the powder bed fusion process". *Additive Manufacturing* 27.October 2018 (2019), pp. 345–352.

FAST MACROSCOPIC THERMAL ANALYSIS FOR LASER METAL DEPOSITION. APPLICATION TO MULTIPHASE STEELS.

Daniel WEISZ-PATRAULT*

*LMS, CNRS, École Polytechnique, Institut Polytechnique de Paris, F-91128 Palaiseau, France

Key words: Additive manufacturing, Phase transitions, Heat conduction, Semi-analytical solution

Abstract. Recently, a simplified macroscopic and semi-analytical thermal analysis of Laser Metal Deposition (LMD) has been submitted to publication. The model is fast enough to simulate the entire process. The proposed approach enables to compute: temperature, solidification and solid-state phase transitions kinetics. Process parameters, substrate characteristics and heat sources due to the enthalpy change during phase transitions are taken into account as well as convection due to the carrying and shielding gas. The present work exploits the proposed model to investigate the influence of some process parameters in order to determine whether complex multiphase steels (such as high strength steels) could be controllably obtained by LMD. Indeed, material properties of such steels are not only a matter of chemical composition but also and mostly a matter of phase proportions in a multiphase mixture (austenite, ferrite, pearlite, bainite and martensite). Within this framework, temperature control strategies during the process are numerically tested for a simple cylindrical geometry.

1 INTRODUCTION

Laser Metal Deposition (LMD) consists in injecting a stream of metallic powder that is molten by a laser beam in order to deposit material layer-by-layer on a substrate [1, 2]. The LMD process induces very specific temperature history including very high temperature gradients (near the molten pool) and thermal cycling. Both the microstructure formation/evolution (solidification, solid state phase transitions, grain mobility etc.) and the formation of residual stresses are driven by thermal conditions during the process. Therefore, significant efforts have been made to simulate accurately, at the macroscopic scale, both temperature evolutions and solidification kinetics. However, macroscopic modeling of such processes is computationally costly [3–12]. The order of magnitude of computation cost for relatively small parts is several tens of hours. This hinders the development of efficient numerical optimization of process parameters in order to reach microstructure and material properties requirements.

Recently, a simplified macroscopic and semi-analytical thermal analysis of LMD has been submitted to publication [13]. The approach relies on a semi-analytical solution of the transient heat conduction problem in a two-dimensional multilayer composite (r, z radial and vertical coordinates). The solution derivation extends previous analytical thermal analysis on composites (e.g., [14, 15]). The model enables us to efficiently compute temperature, solidification and

solid-state phase transitions kinetics in the whole part. Powder melting is not simulated, as molten metal is directly deposited on top of the already existing layers. However, several other aspects have been taken into account such as some process parameters (e.g., laser speed and power etc.), substrate characteristics (e.g., thickness and material properties), heat sources due to the enthalpy changes during phase transitions and forced convection due to the gas flow (used for carrying the powder and for shielding). In addition, the laser power is partly transmitted to the top layer of the already existing part.

In this contribution, the recently proposed model [13] is exploited to investigate the influence of some process parameters in order to determine whether complex multiphase steels (such as high strength steels) could be controllably obtained by LMD. Indeed, material properties of such steels are not only a matter of chemical composition but also and mostly a matter of phase proportions in a multiphase mixture (austenite, ferrite, pearlite, bainite and martensite). Within this framework, temperature control strategies during the process are numerically tested for a simple cylindrical geometry (even though the simulation strategy applies to arbitrary shapes in the horizontal plane and to arbitrary laser paths: continuous, back and forth etc.).

2 MODEL STRATEGY AND ASSUMPTIONS

The model developed in [13] relies on a semi-analytic solution of the unsteady and nonlinear heat equation. The general strategy is summarized in this section. In addition, the proposed solution is obtained by introducing some assumptions that are also recalled for sake of clarity. Further details and all mathematical developments are given in [13].

Volumetric heat sources due to the enthalpy changes during phase transitions arise as a right side term in the unsteady heat equation. As these heat sources strongly depends on the temperature field, the heat equation is non linear. This issue is overcome by an alternating scheme. Indeed, the heat equation becomes linear and easier to solve if the right side term is imposed (fixed to a known evolution). Thus, a first estimation of the temperature field is performed with a right side term arbitrarily set to zero. Then, the obtained estimated temperature field is used as inputs of a simple phase transition model detailed in section 3 and based on Johnson-Mehl-Avrami-Kolmogorov (JMAK) equation. Phase proportion rates are then used to compute the right side term of the heat equation and a new estimation of the temperature field is computed on this basis. This procedure is repeated until convergence.

Despite the fact that a nonlinear problem is solved as a succession of linear problems, the unsteady linear heat equation remains difficult to solve analytically mostly because of geometrical complexity and time dependency of the domain. Indeed, as new mass is regularly added to the part during the process, the support domain of the heat equation is strongly time dependent. To overcome these geometrical difficulties, the main assumption is to neglect heat fluxes along the tangent direction of the laser path (denoted by χ). That is to say that successive points on χ can be considered as independent. The validity of this assumption is questionable in the vicinity of the molten pool where temperature gradients are very significant in all directions. However, at the scale of the part, as molten metal is deposited at very high temperature on top of a relatively cold multilayer structure, heat fluxes along the vertical direction prevail.

This assumption leads to consider several independent computations at different positions

on the path χ . Each of these computation points consists in multilayer 2D structure in the (r, z) plane, where r is the radial coordinate (thickness direction) and z the vertical coordinate. The number of layers gradually increases as metal deposition goes on. Each computation point is characterized by (i) the radius of curvature of the path χ at the corresponding position and (ii) the different times of metal deposition on top of the multilayer structure denoted by (t_1, \dots, t_{N+1}) (where N is the final number of layers). The simulation strategy consists in solving analytically the heat equation for each computation point on each time interval $[t_n, t_{n+1}]$ ($1 \leq n \leq N$). Thus, each computation point requires N sub-computations that are simply connected to each other by setting the initial condition on the time interval $[t_n, t_{n+1}]$ as the final condition on the previous time interval $[t_{n-1}, t_n]$. It should be noted that for the same geometry different laser paths and dwell times can be simulated through different (t_1, \dots, t_{N+1}) . The layer thickness $h_r = 0.75$ mm and height $h_z = 0.2$ mm are fixed parameters that can be measured.

For sake of simplicity, the power per unit area brought to the system by the radiative term and by the laser is modeled as a power per unit volume. In addition, the gas flow increases significantly the heat transfer coefficient for all layers under the flow. However, the mathematical solution is based on constant heat transfer coefficient (denoted by H). Thus, temperature losses due to the gas flow are also modeled through the introduction of an additional negative volumetric heat source. On this basis, the unsteady heat conduction equation reads:

$$\frac{\partial^2 T^{(i)}}{\partial r^2} + \frac{1}{r} \frac{\partial T^{(i)}}{\partial r} + \frac{\partial^2 T^{(i)}}{\partial z^2} - \frac{1}{D} \frac{\partial T^{(i)}}{\partial t} = \frac{Q^{(i)}(t)}{\lambda} \quad (1)$$

where $T^{(i)}$ is the temperature in the layer (i) , D ($\text{m}^2 \cdot \text{s}^{-1}$) is the thermal diffusivity. In this contribution, material parameters (D diffusivity and λ thermal conductivity) are assumed to be temperature independent for sake of simplicity. However, temperature dependent properties are considered in [13]. The volumetric heat source $Q^{(i)}$ contains four contributions: the radiative term, the heat source due to the enthalpy change during phase transition, the volumetric heat source Q_{beam} in the top layer of the already existing part due to the laser and the volumetric negative heat source $Q_{\text{gas}}^{(i)}$ associated to the local increase of the heat transfer coefficient due to the gas flow. A Gaussian model adapted from [7] is used for the layer $i = n - 1$:

$$Q_{\text{beam}}(t) = -\frac{2\eta_{\text{beam}}P_{\text{beam}}}{\pi h_z R_{\text{beam}}^2} \exp\left(-2V_{\text{beam}}^2 \frac{(t-t_n)^2}{R_{\text{beam}}^2}\right) \quad (2)$$

where η_{beam} is the absorption coefficient, P_{beam} is the laser power, R_{beam} is the laser radius and V_{beam} is the laser speed. A Gaussian approximation similar to (2) is introduced for $Q_{\text{gas}}^{(i)}$:

$$Q_{\text{gas}}^{(i)}(t) = \tilde{Q}_{\text{gas}} \exp\left(-2V_{\text{beam}}^2 \frac{(t-t_n)^2}{R_{\text{gas}}^2}\right) \quad (3)$$

where \tilde{Q}_{gas} is a power per unit volume and R_{beam} is a characteristic length controlling the affected area by the gas flow.

The substrate is modeled in a simplified way. It is assumed that the substrate temperature T_{sub} is constant on each time interval $[t_n, t_{n+1}]$. The substrate temperature T_{sub} is updated at the end of the n -th sub-computation according to the total energy received during the time interval $[t_n, t_{n+1}]$. Thus, boundary conditions read:

$$\begin{aligned}
 (a) : & \begin{cases} \lambda \frac{\partial T^{(i)}}{\partial r} = H(T^{(i)} - T_{\text{ext}}) & r = R_{\text{inf}} \quad (1 \leq i \leq n) \\ \lambda \frac{\partial T^{(i)}}{\partial r} = -H(T^{(i)} - T_{\text{ext}}) & r = R_{\text{sup}} \quad (1 \leq i \leq n) \end{cases} \\
 (b) : & \begin{cases} \lambda \frac{\partial T^{(1)}}{\partial z} = H_{\text{sub}}(T^{(1)} - T_{\text{sub}}) & z = Z^{(0)} \\ \lambda \frac{\partial T^{(n)}}{\partial z} = -H(T^{(n)} - T_{\text{ext}}) & z = Z^{(n)} \end{cases} \\
 (c) : & \begin{cases} T^{(i)} = T^{(i+1)} & z = Z^{(i)} \quad (1 \leq i \leq n-1) \\ \frac{\partial T^{(i)}}{\partial z} = \frac{\partial T^{(i+1)}}{\partial z} & z = Z^{(i)} \quad (1 \leq i \leq n-1) \end{cases}
 \end{aligned} \tag{4}$$

where $Z^{(i)}$ denotes the interfaces in the multilayer structure, R_{inf} and R_{sup} denote the inner and outer radius respectively. In addition, H_{sub} denotes the heat transfer coefficient between the part and the substrate.

Mathematical developments to solve analytically the heat equation (1) with boundary conditions (4) are not detailed in this paper. Interested readers are therefore referred to [13].

3 PHASE TRANSITIONS

The phase transition model simply consists in JMAK equation or Koistinen-Marburger equation. Multiphase steel is considered. Each phase transition is characterized by a temperature range. Phase proportions are denoted by X_{liq} , X_{aus} , X_{fer} , X_{per} , X_{bai} and X_{mar} (liquid, austenite, ferrite, pearlite, bainite and martensite respectively). Solidification and fusion are approximated by a temperature dependent exponential model, for $T \in [T_{\text{sol}}, T_{\text{liq}}]$:

$$X_{\text{aus}} = 1 - \exp(-k_{\text{liq}}(T_{\text{sol}} - T)^{n_{\text{liq}}}) \tag{5}$$

where T_{sol} is the solidus temperature and T_{liq} the liquidus temperature. The identification based on the data given in [7] leads to $k_{\text{liq}} = 0.02$ and $n_{\text{liq}} = 1.22$. For austenite to ferrite, pearlite and bainite phase transitions, the classic JMAK equation is used. Phase proportions X_{fer} , X_{per} and X_{bai} are initially set to zero and are updated by computing the increase of phase proportion denoted by ΔX_{ϕ} :

$$\Delta X_{\phi} = X_{\text{aus}} [1 - \exp(-k_{\phi}(t - t_{\phi})^{n_{\phi}})] \tag{6}$$

where ϕ stands for ferrite, pearlite or bainite and k_{ϕ} and n_{ϕ} are the Avrami coefficients assumed to be independent on temperature and t_{ϕ} is the time when the phase transition starts. Furthermore, for the martensitic phase transition the classic Koistinen-Marburger equation is used. Consider ΔX_{mar} the phase proportion increase of martensite during cooling, for $T \leq \text{MS}$:

$$\Delta X_{\text{mar}} = X_{\text{aus}} [1 - \exp(\alpha_{\text{MS}}(T - \text{MS}))] \tag{7}$$

where M_S is the temperature start of martensite phase transition and α_{MS} a coefficient. With intense thermal cycling, the material is significantly reheated after cooling and may reach the temperature of austenitization. As heating rates are very high during the LMD process it seems sufficient to use an exponential interpolation similar to (5). Consider ΔX_{aus} the phase proportion increase of austenite during reheating, for $T \in [AE_3, T_{\text{aus}}]$:

$$\begin{cases} \Delta X_{\text{aus}} = X [1 - \exp(-k_{\text{aus}} (T_{\text{aus}}^{\text{start}} - T)^{n_{\text{aus}}})] \\ X = X_{\text{fer}} + X_{\text{per}} + X_{\text{bai}} + X_{\text{mar}} \end{cases} \quad (8)$$

where T_{aus} is the temperature end of austenitization and AE_3 is the temperature start of austenite to ferrite phase transition (we consider in this paper that it is also the temperature start of austenitization).

4 RESULTS

In this section the model developed in [13] is used to analyze different fabrication strategies with respect to the formation of multiphase microstructures. Would it be possible to control the formation of predefined multiphase arrangements during the LMD process? Material parameters and process parameters (excepted those tested in this paper) are extracted from [13]. Phase transition parameters are also extracted from [13] and do not correspond to a specific steel, but are coherent with multiphase steels. Following computations explore the idea of tailoring phase proportions by controlling substrate temperature and other process parameters. Thus, the substrate temperature is assumed to be controllable. The development of a real physical system enabling to adjust in real time the substrate temperature is not broached in this contribution. The main difficulty to favor austenite to ferrite, pearlite or bainite phase transformations is that those transitions are driven by carbon diffusion, hence slow evolutions of the corresponding phase proportions. Thus, the challenge is to maintain the part in the temperature range corresponding to these diffusive phase transitions during a sufficient amount of time. Three parameters are tested to achieve this objective: substrate temperature, laser speed and dwell time. All simulations consist in a 100 layers cylinder with 20 mm inner radius. Computations parameters are listed in table 1. The first computation is used as a reference to compare to other strategies. For each computation listed in table 1, the temperature at different fixed locations

Table 1: Computations

Computation	Substrate temperature (K)	Laser speed (mm.s ⁻¹)	Dwell time (s)
1	700	30	0
2	700	30	40
3	700	3	0

is given in figures 1, 4 and 7. The whole temperature field is also given at different times in figures 2, 5 and 8. Finally, the most significant phase proportion fields are given at different times in figures 3, 6 and 9. The last phase proportion field is the final phase mixture of the part. Further evolutions may be obtained with heat treatments.

The reference computation presented in [13] shows that without substrate temperature control, cooling rates are very fast and mostly martensite can be formed. (Of course for austenitic steels such as the widely used stainless steel 316L, mostly austenite is formed). The first computation listed in table 1 only consists in controlling the substrate temperature fixed at 700 K (with the same process parameters). Cooling rates are very similar as the those obtained for the reference computation. The part is globally in the austenite temperature range during the fabrication. Then, pearlite slowly starts to form during cooling to 700 K (around 1 min), then bainite is produced as the temperature is maintained at 700 K. The part is finally mostly composed of bainite.

More complex multiphase mixtures are obtained for the second computation, by introducing a dwell time. The main effect of combining the substrate temperature control and a long dwell time is that the part is in the pearlite or bainite temperature range for a sufficient amount of time during the fabrication. Similar phase proportions of pearlite and bainite are obtained. However, it is clear from figure 6 that the phase proportion field is not homogenous in the part. The third computation strategy consists in maintaining the substrate temperature at 700 K and decreasing the laser speed by a factor 10. This idea is similar as the second computation: lengthen the duration of the build so that slow diffusive phase transitions have time to occur. The difference is that the gas flow has been assumed to stop during dwell time although it is continuous with a low speed build. Thus, the cooling effect of the gas flow is very significant as shown in figures 7 and 8. This leads to a different multiphase mixture mostly composed of bainite and martensite as shown in figure 9. However, as for the second computation, the phase proportion fields are not homogenous in the part.

5 CONCLUSION

In this paper, a fast macroscopic model analyzing thermal evolution coupled with phase transitions during laser metal deposition process has been used to determine whether multiphase steel could be processed without further thermal treatment. Indeed, overall material properties do not only depend on the chemical composition but also on the multiphase mixture that is obtained during the process. Three sets of process parameters have been tested, assuming a hypothetical control of the substrate temperature. Very distinct multiphase mixtures have been obtained, which indicates that the proposed fast numerical strategy could be used to optimize process parameters in order to reach the targeted microstructure. However, a difficulty remains as the phase proportion fields are inhomogeneous in the part.

References

- [1] William E Frazier. Metal additive manufacturing: a review. *Journal of Materials Engineering and Performance*, 23(6):1917–1928, 2014.
- [2] Tarasankar DebRoy, HL Wei, JS Zuback, T Mukherjee, JW Elmer, JO Milewski, Allison Michelle Beese, A Wilson-Heid, A De, and W Zhang. Additive manufacturing of metallic components—process, structure and properties. *Progress in Materials Science*, 92:112–224, 2018.

- [3] Liang Wang, Sergio D Felicelli, and James E Craig. Thermal modeling and experimental validation in the lens tm process. In *18th Solid Freeform Fabrication Symposium. Austin, TX*, pages 100–111, 2007.
- [4] Heng Liu. *Numerical analysis of thermal stress and deformation in multi-layer laser metal deposition process*. PhD thesis, Missouri University of Science and Technology, 2014.
- [5] Guillaume Marion, Georges Cailletaud, Christophe Colin, and Matthieu Mazière. A finite element model for the simulation of direct metal deposition. In *International Congress on Applications of Lasers & Electro-Optics*, volume 1, pages 834–841. LIA, 2014.
- [6] Erik R Denlinger and Pan Michaleris. Effect of stress relaxation on distortion in additive manufacturing process modeling. *Additive Manufacturing*, 12:51–59, 2016.
- [7] Jacob Smith, Wei Xiong, Jian Cao, and Wing Kam Liu. Thermodynamically consistent microstructure prediction of additively manufactured materials. *Computational mechanics*, 57(3):359–370, 2016.
- [8] Trevor Keller, Greta Lindwall, Supriyo Ghosh, Li Ma, Brandon M Lane, Fan Zhang, Ursula R Kattner, Eric A Lass, Jarred C Heigel, Yaakov Idell, et al. Application of finite element, phase-field, and calphad-based methods to additive manufacturing of ni-based superalloys. *Acta materialia*, 139:244–253, 2017.
- [9] Qiang Chen, Gildas Guillemot, Charles-André Gandin, and Michel Bellet. Three-dimensional finite element thermomechanical modeling of additive manufacturing by selective laser melting for ceramic materials. *Additive Manufacturing*, 16:124–137, 2017.
- [10] DongYun Zhang, Zhe Feng, ChengJie Wang, Zhen Liu, DongDong Dong, Yan Zhou, and Rui Wu. Modeling of temperature field evolution during multilayered direct laser metal deposition. *Journal of Thermal Spray Technology*, 26(5):831–845, 2017.
- [11] Cengiz Baykasoglu, Oncu Akyildiz, Duygu Candemir, Qingcheng Yang, and Albert C To. Predicting microstructure evolution during directed energy deposition additive manufacturing of ti-6al-4v. *Journal of Manufacturing Science and Engineering*, 140(5):051003, 2018.
- [12] M Biegler, B Graf, and Michael Rethmeier. In-situ distortions in lmd additive manufacturing walls can be measured with digital image correlation and predicted using numerical simulations. *Additive Manufacturing*, 20:101–110, 2018.
- [13] Daniel Weisz-Patrault. Fast macroscopic simulation of laser metal deposition process. thermal analysis coupled with phase transitions. *Submission*, 2019.
- [14] F De Monte. Unsteady heat conduction in two-dimensional two slab-shaped regions. exact closed-form solution and results. *International Journal of Heat and Mass Transfer*, 46(8):1455–1469, 2003.

- [15] Daniel Weisz-Patrault. Coupled heat conduction and multiphase change problem accounting for thermal contact resistance. *International Journal of Heat and Mass Transfer*, 104:595–606, 2017.

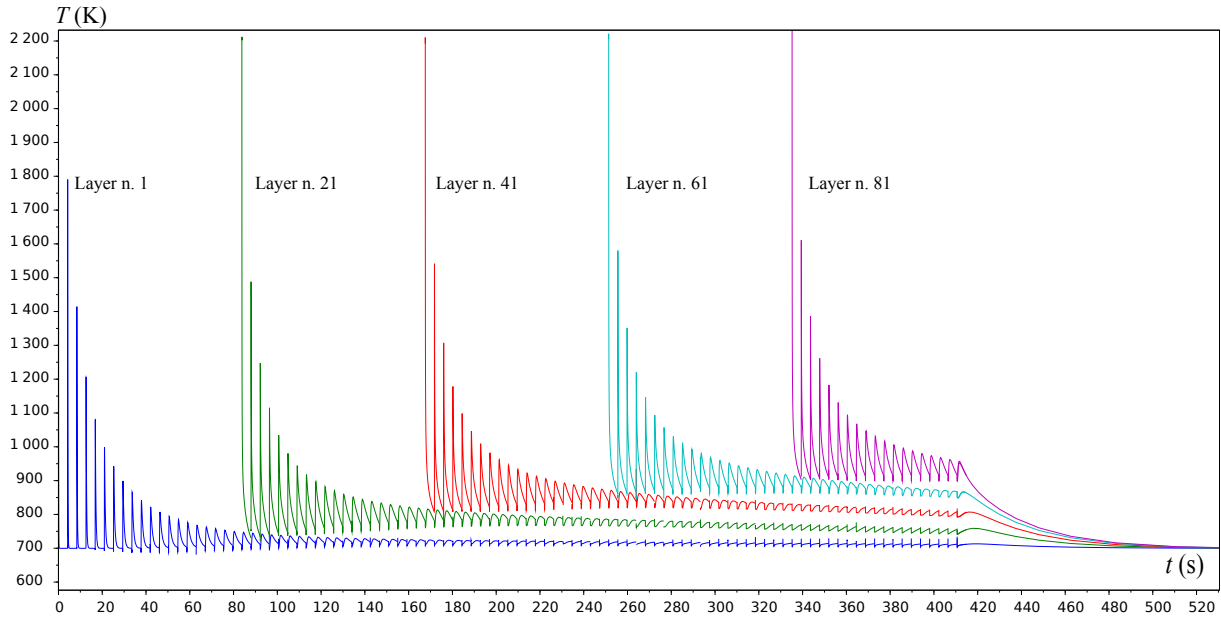


Figure 1: Temperature evolution of some layers, computation 1

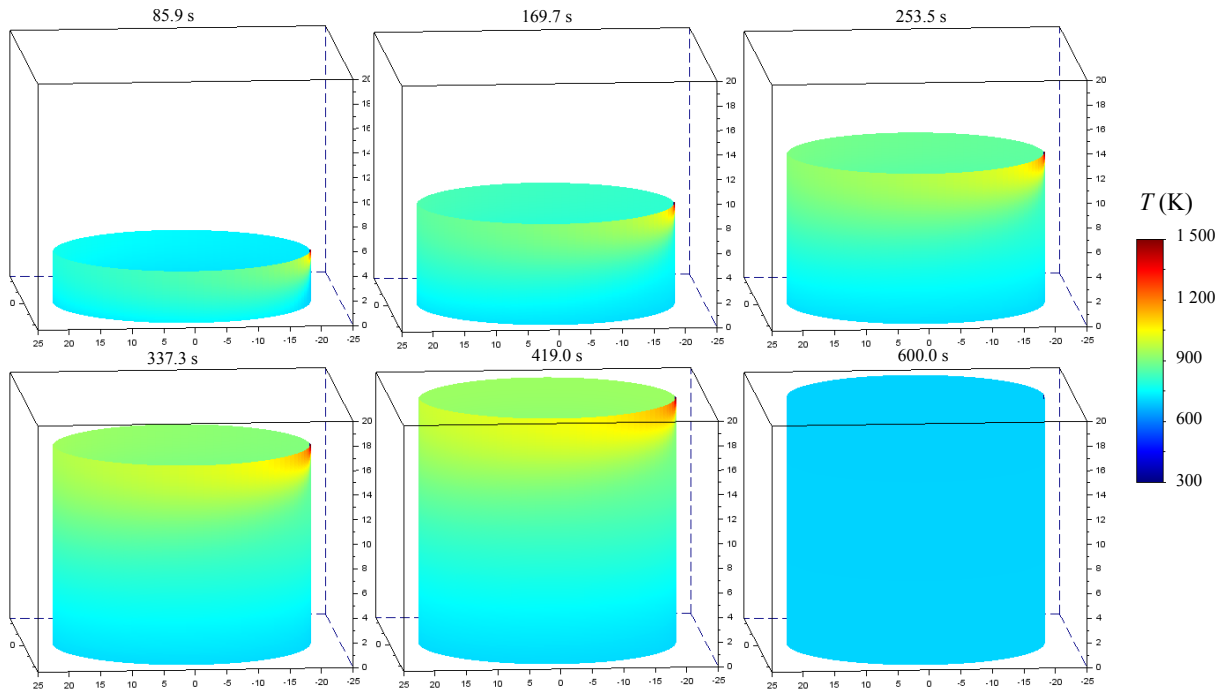


Figure 2: Temperature field, computation 1

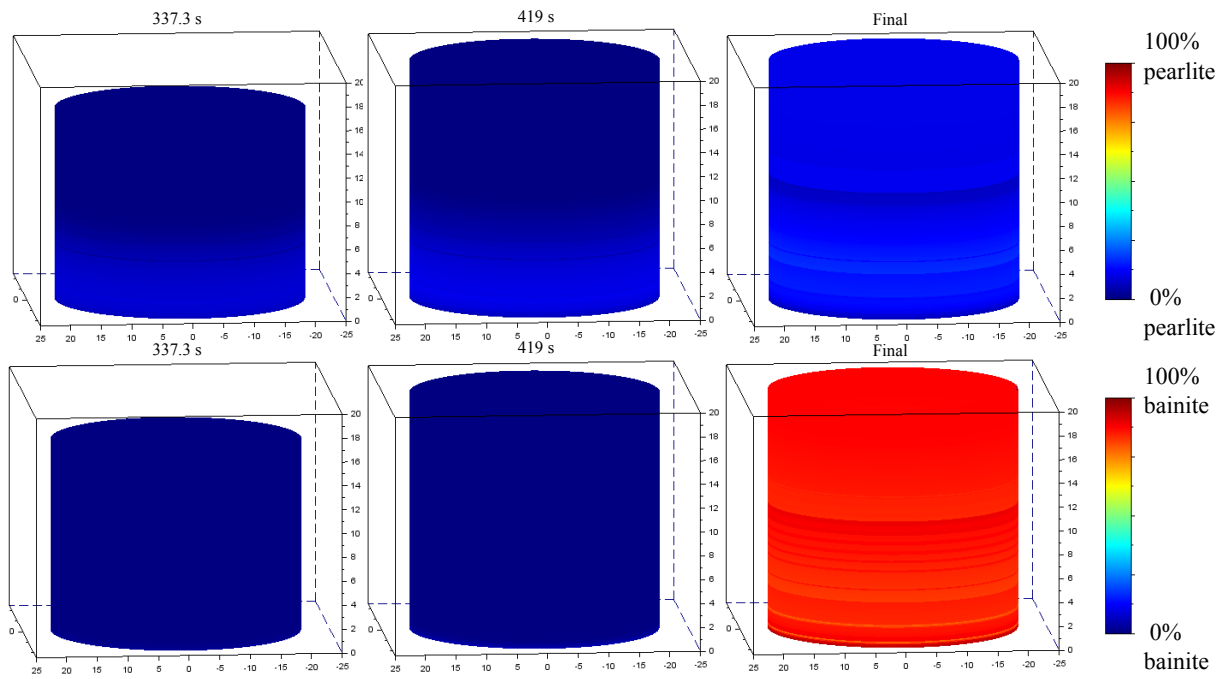


Figure 3: Phase proportion field, computation 1

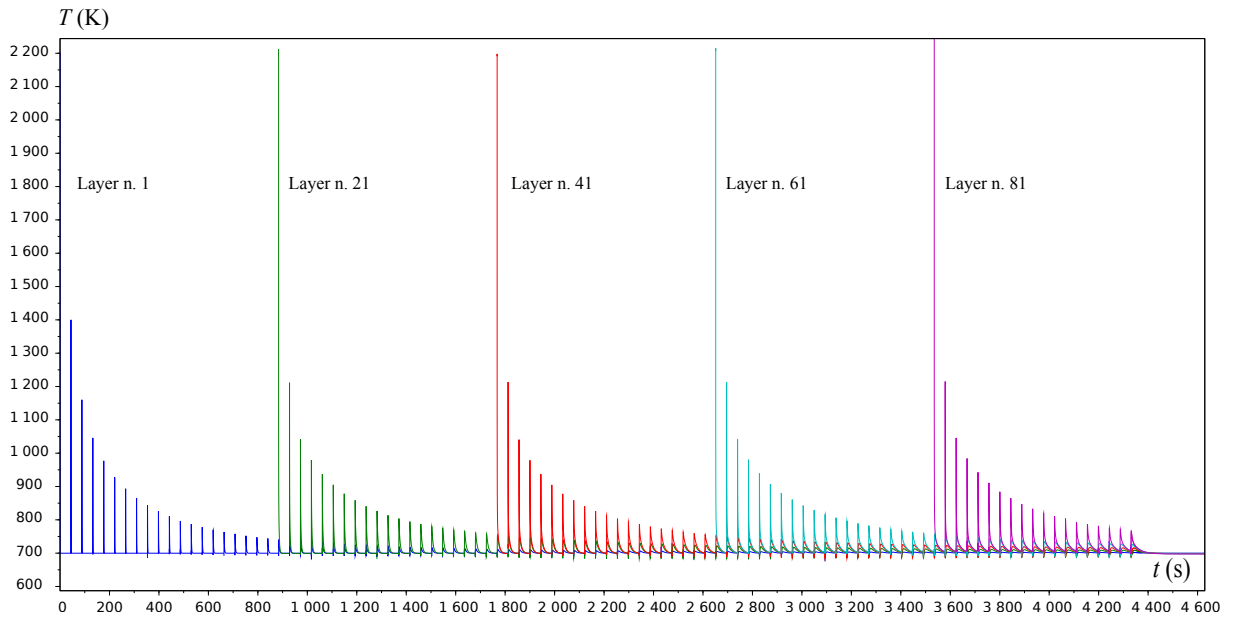


Figure 4: Temperature evolution of some layers, computation 2

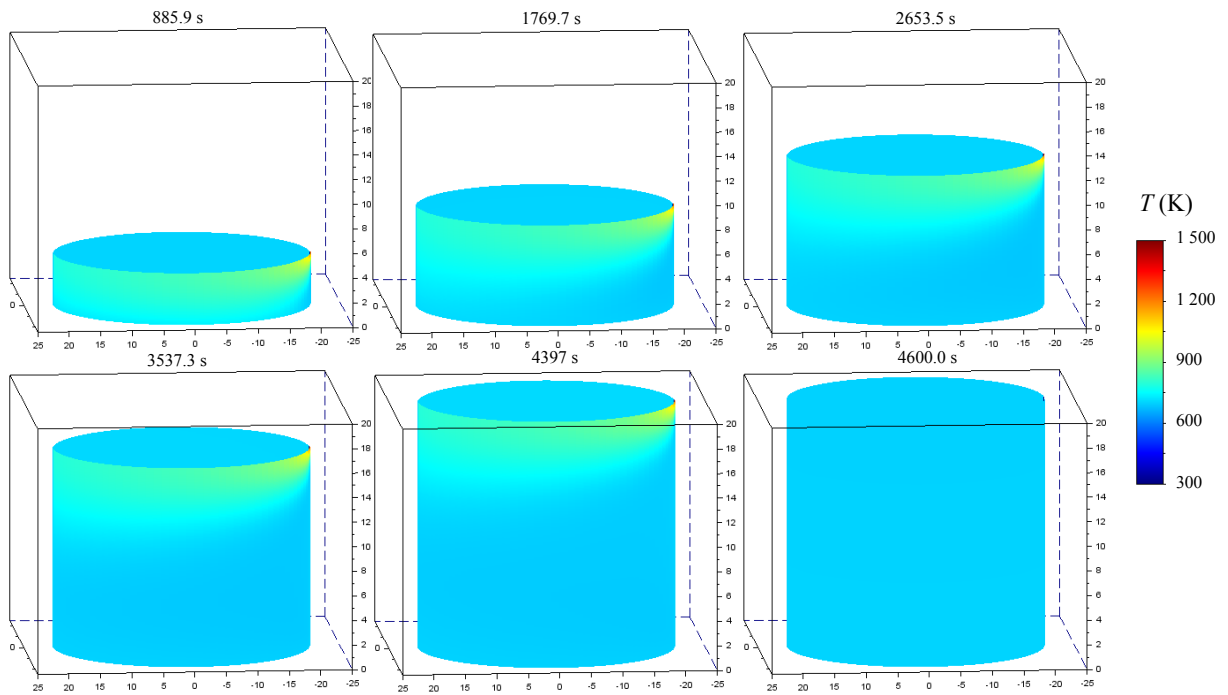


Figure 5: Temperature field, computation 2

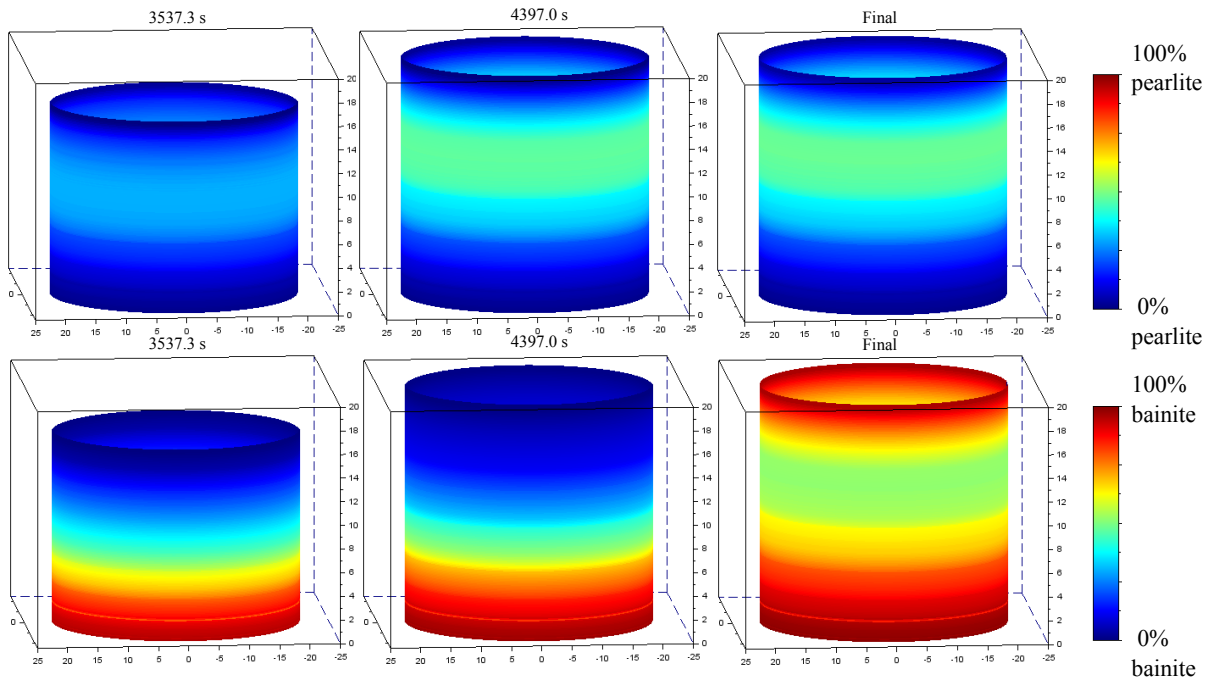


Figure 6: Phase proportion field, computation 2

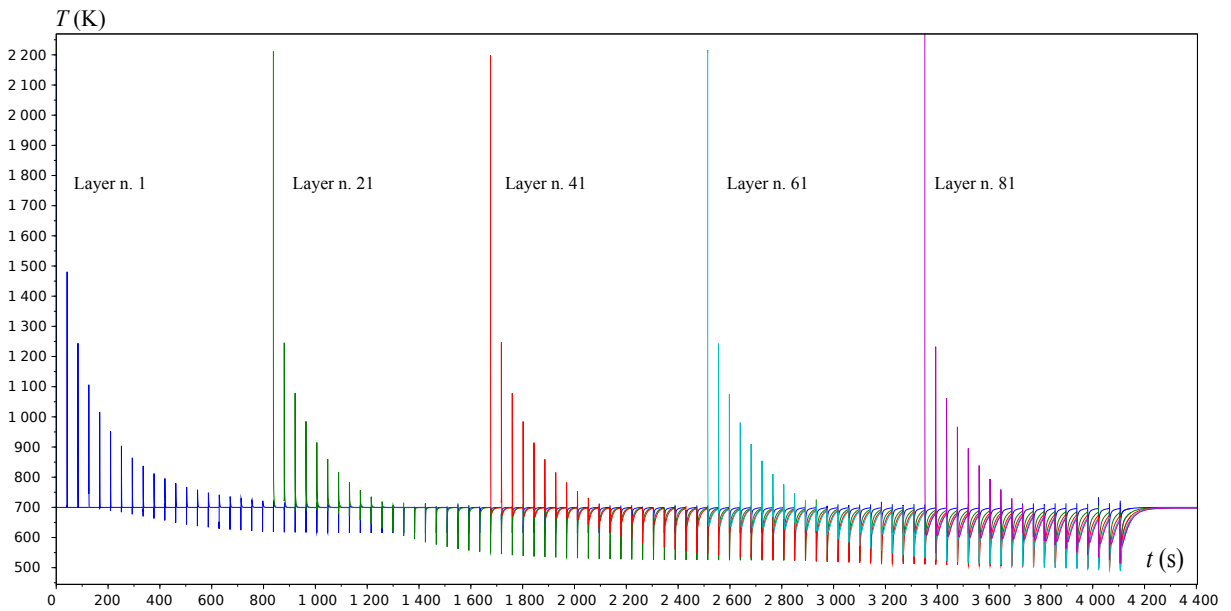


Figure 7: Temperature evolution of some layers, computation 3

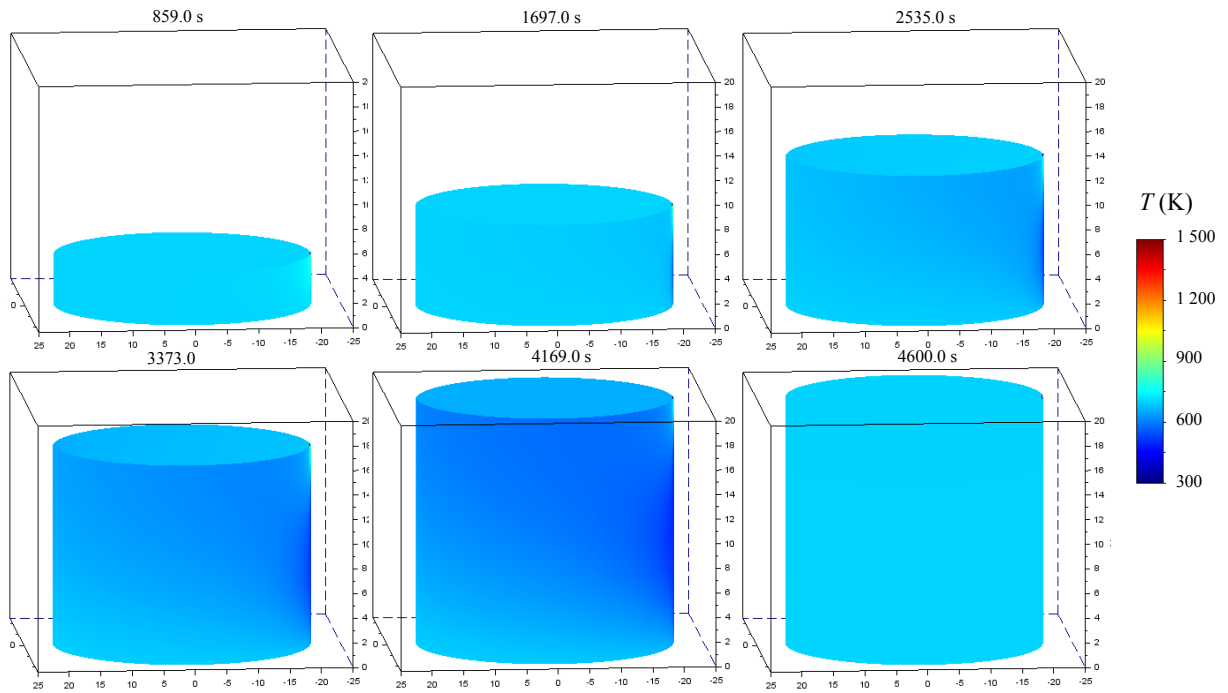


Figure 8: Temperature field, computation 3

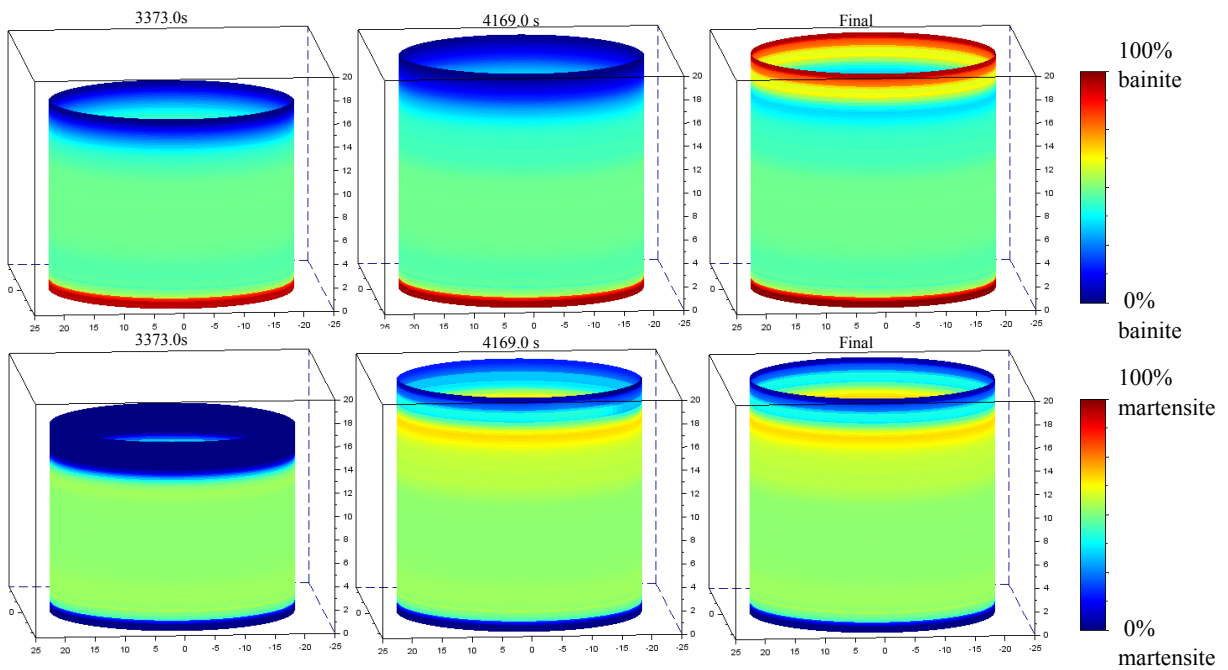


Figure 9: Phase proportion field, computation 3

MICROSTRUCTURE AND MARTENSITIC TRANSFORMATION OF SELECTIVE LASER MELTED NiTi SHAPE MEMORY ALLOY PARTS

CARLO A. BIFFI^{*}, JACOPO FIOCCHI[†], PAOLA BASSANI[‡] AND AUSONIO
TUISSI^Ψ

^{*} National Research Council Institute of Condensed Matter Chemistry and Technologies for Energy,
Unit of Lecco, CNR ICMATE; Via Previati 1/E, 23900 Lecco, Italy.
e-mail: carloalberto.biffi@cnr.it

[†] National Research Council Institute of Condensed Matter Chemistry and Technologies for Energy,
Unit of Lecco, CNR ICMATE; Via Previati 1/E, 23900 Lecco, Italy.
e-mail: jacopo.fiocchi@icmate.cnr.it

[‡] National Research Council Institute of Condensed Matter Chemistry and Technologies for Energy,
Unit of Lecco, CNR ICMATE; Via Previati 1/E, 23900 Lecco, Italy.
e-mail: paola.bassani@cnr.it

^Ψ National Research Council Institute of Condensed Matter Chemistry and Technologies for Energy,
Unit of Lecco, CNR ICMATE; Via Previati 1/E, 23900 Lecco, Italy.
e-mail: ausonio.tuissi@cnr.it

Key words: Niti, Shape Memory Alloy, Additive Manufacturing, Selective Laser Melting, Microstructure, Martensitic Transformation.

Abstract.

Additive Manufacturing allows to design and realize 3D parts, integrating additional functionalities offered by the interaction between complex shapes and the material properties. Results can be even more appealing when functional materials, like Shape Memory Alloys, are printed: new opportunities for smart devices can be opened.

In the present bulk and lattice structures of Nitinol were additively manufactured with a Selective Laser Melting. A pulsed laser, which is more suitable for manufacturing thin parts, was selected to process the initial powder. The selection of the process parameters, like laser power and exposure time, was performed for maximizing the relative density. Furthermore, the microstructure and the martensitic transformation temperatures were analyzed through X-rays diffraction and differential scanning calorimetry, respectively. A comparison between the initial powder and SLMed parts was also considered. Finally, the mechanical properties of Niti builds under compression were tested for both bulk and lattice structures.

1 INTRODUCTION

Among smart and functional materials, Shape Memory Alloys (SMAs) are well known, thanks to their unique properties, namely shape memory effect (SME) and pseudoelasticity (PE) [1]. Quasi-equiatomic NiTi compound is the most diffused SMAs for their stable and optimal functional properties. These properties depend on a solid to solid phase transformation, indicated as martensitic transformation (MT), which can be found in Ti rich-NiTi and Ni rich-NiTi alloys above or below room temperature, respectively. This permits to determine the use of these materials as actuators or for biomedical devices, according with the implementation of the SME or PE, respectively.

The operating temperatures of the MT is of relevant importance for the specific application. Anyways, these are affected strongly by Ni/Ti ratio, the manufacturing of the NiTi SMAs is very challenging for getting stable functional characteristics [2].

In the recent years, the use of Additive Manufacturing (AM) techniques for realizing 3D parts in Nitinol is becoming an attractive solution for advanced devices [3-5]. The manufacturing of Nitinol using different AM technologies, like selective laser melting (SLM), electron beam melting (EBM) and direct energy deposition (DED), has been studied in several experimental works [6-8]. Anyways, among the AM methods the SLM process is the most diffused one and nowadays it can offer the best performances and compositional control, which is fundamental for this system. In fact, the MT and the related functional properties of SLM built Nitinol parts have been shown to be almost comparable to those of the wrought alloy [9-11]. The compositional issue remains an aspect to be controlled during the laser process in order to allow the Ni/Ti ratio [12-13]. Moreover, the SLMed microstructure can be strongly textured, depending of the process conditions, and this can be optimized for enhancing the functional response of NiTi parts [14].

It is demonstrated that the heat transfer during SLM, particularly the laser emission mode, can affected the microstructure and the corresponding mechanical properties [15] in AlSi based alloys. Moreover, it was even found that the relative density and the geometric features can be affected by the laser emission modes: continuous wave (CW) or pulsed wave (PW) [16]. In fact, it is reported that a CW laser is preferable for producing fully dense large parts, while PW is more suitable for thin and precise structures. These results can be supported by previous works regarding some experiments using CW and PW lasers in welding, too [17].

As in literature the SLM process has been studied for printing Nitinol samples only by means of CW lasers, in the present work the feasibility of SLM with a PW laser was investigated in the view of realizing thin parts in Nitinol, in which more gentle energies are deposited on the powder bed for the local melting.

2 EXPERIMENTAL

Bulk and lattice samples were produced from quasi equiatomic NiTi powder (see Figure 1a) by means of a SLM system (mod. AM400 from Renishaw), equipped with a pulsed wave laser. The process parameters, listed in Table 1, were used for manufacturing cylinders (5 mm

in height and 3 mm in diameter) printed on a Ti6Al4V platform. Full factorial design was performed for fixing the optimal set of process parameters able to maximize the relative density. Moreover, selected process parameters, reported in Table 2, were used for printing lattice structures (10 mm x 100 mm x 30 mm), whose schematic is depicted in Figure 1b. The schematics of the scanning strategies, used for printing the cylinders and lattice parts, are shown in Figure 2, respectively.

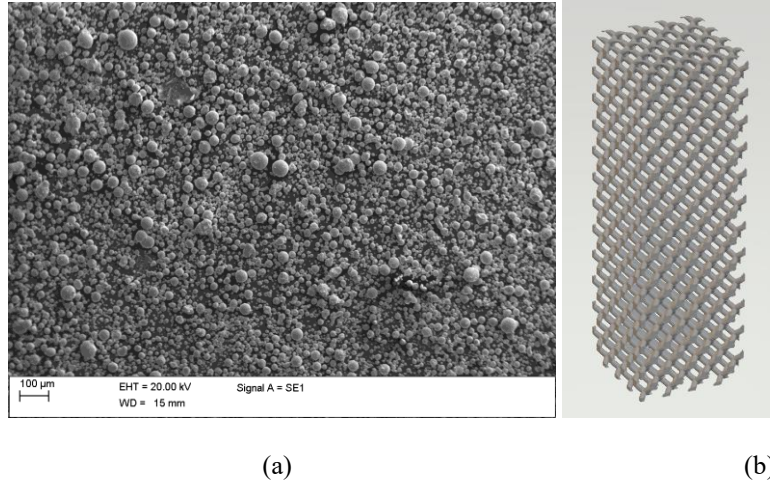


Figure 1: Nitinol powder used for the SLM printing (a) and schematic of the lattice structure (b).

Table 1: List of variable and fixed process parameters used for printing NiTi cylinders

Parameters	Values
Power	50-75-100-125-150 W
Exposition time	25-50-75-100 µs
Scanning strategy	Meander
Atmosphere	Argon
Layer thickness	30 µm
Hatch distance	50 µm
Point distance	50 µm
Laser spot size	65 µm

Table 2: List of process parameters used for printing NiTi lattice structure

Parameters	Values
Power	75 W
Exposition time	75 µs
Scanning strategy	Contour
Atmosphere	Argon
Layer thickness	30 µm
Hatch distance	50 µm
Point distance	50 µm
Laser spot size	65 µm

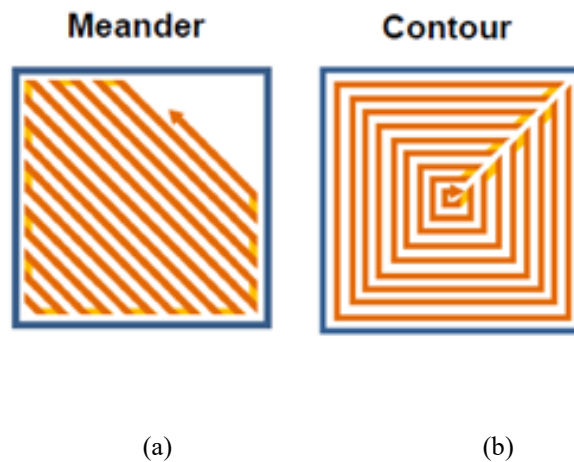


Figure 2: Schematic of the scanning strategies, used for printing the cylinders and lattice parts, respectively: meander (a) and contour (b).

The cylinders, in as built condition, were characterized according to the following features : (i) relative density with the Archimede's method; (ii) martensitic transformation via differential scanning calorimetry (DSC) ; (iii) microstructure via X-rays diffraction (XRD); and (iv) superelasticity via compression testing. As term of comparison, the characteristic features of the initial powder were studied and compared to the ones of the as built samples. Moreover, the lattice, in as built condition, were studied according to DSC and compression testing.

In details, relative density measurements were performed with a Gibertini E 50 S/2 balance as set up for implementing the Archimedes method. Calorimetric properties of the SLMed Niti samples were investigated through a differential scanning calorimeter (DSC, mod. SSC 5200 by Seiko Instruments), in the $[-100^{\circ}\text{C}; 150^{\circ}\text{C}]$ range with heating/cooling rate of 10°C min . Characteristic temperatures and corresponding transformation enthalpies were evaluated for both direct/reverse transformations upon cooling/heating scans respectively. XRD spectra were collected by a diffractometer (Panalytical X'Pert Pro) using $\text{Cu K}\alpha$ radiation operating at 40 kV and 30 mA on the samples' xy surfaces in the $20\text{-}70^{\circ}$ 2θ range; the measurements were performed using a spinner at 30°C . Compressive tests were conducted at room temperature by means of an MTS 2/M machine, equipped with extensometer, at strain rate of 0.01 min^{-1} . 8 complete loading and unloading cycles, up to 10% in strain, were carried out on cylindrical and lattice samples.

3 ANALYSIS OF RESULTS AND DISCUSSION

3.1 Evaluation of the feasibility window

According with the PW emission mode in SLM process, the energy density per unit of volume, F , namely fluence, was calculated as follows:

$$F = \frac{P \cdot t_{exp}}{d_p \cdot d_h \cdot s} \quad (1)$$

where P , t_{exp} , d_p , d_h and s indicate laser power, exposition time, point distance, hatch distance and layer thickness, respectively. The schematic of the temporal and spatial distribution of the laser pulses is shown in Figure 3.

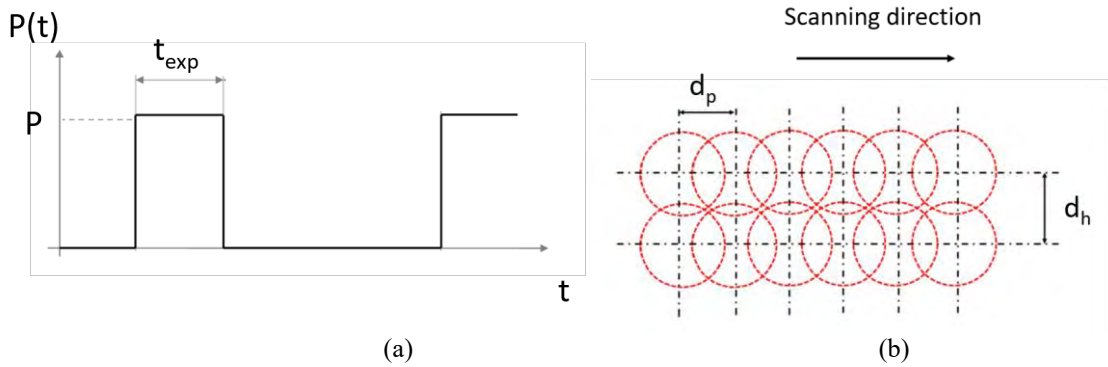


Figure 3: Schematic of the temporal power profile and spatial pulses path (b) in SLM performed with PW emission mode [17].

The identification of the feasibility window has been performed considering the main process parameters (power and exposition time), representative of the PW emission mode, aimed at the maximization of the relative density. Figure 4 shows the correlation between the relative density, measured with the Archimede's method, and the energy density.

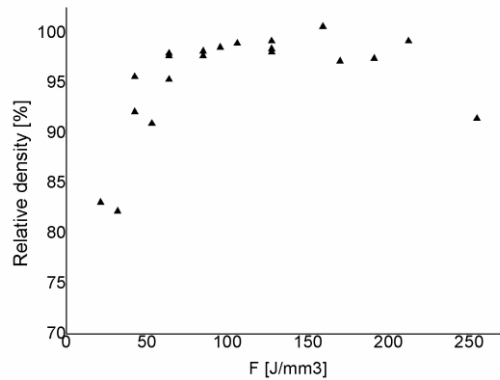


Figure 4: Evolution of the relative density as function of the energy density F .

The evolution of relative density as function of the energy density is coherent with what is reported in literature: density first steeply increases up to a peak, and then decreases more gradually. It is noteworthy that the peak of density for the different exposure time values occurs for higher energy densities with increasing exposure time. The highest relative density value, is achieved with laser power of 125 W and exposure time of 75 μ s.

3.2 Martensitic transformation, microstructure and mechanical behaviour of massive Nitinol samples

In Figure 5 the DSC scans of the sample, obtained with the process condition previously selected for maximizing the relative density, and the initial powder, are shown. A unique peak can be detected upon heating, while two peaks, characteristics of the transformation from austenite to R phase, and from R phase to martensite, are visible upon cooling. The SLMed sample, in as built condition, shows the peaks of the MT upon heating and cooling at temperatures, which are pretty lower to the ones of the Nitinol powder, probably due to the presence of internal stresses. The transformation enthalpies are almost constant, indicating that the amount of material involved in the MT is maintained after the SLM process: about 7 J/g and 9 J/g are the heats exchanged during the direct and reverse MT for both the SLMed sample and initial powder.

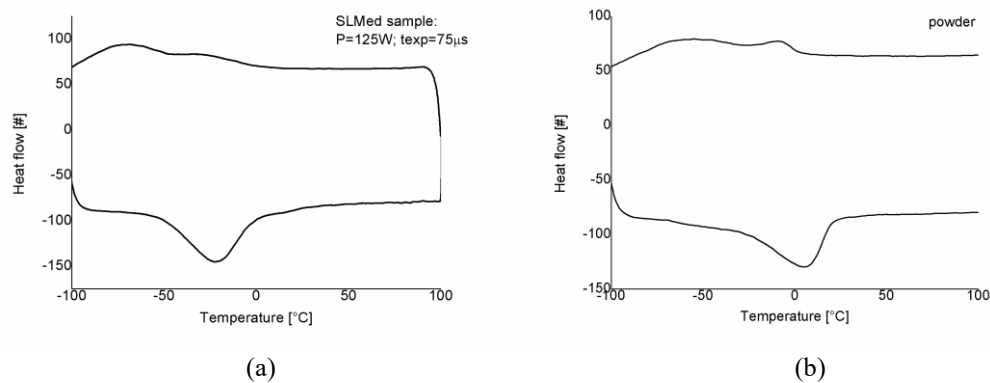


Figure 5: DSC scans of the NiTiNol cylindrical sample, realized in the process condition: P=125W; texp=75 μ s (a); Nitinol powder (b).

In Figure 6 the XRD patterns, acquired at room temperature, of the SLMed sample and the initial powder, are shown. XRD spectrum of the SLMed sample indicates that the principal phase is austenite (B2). This is in good agreement with the DSC scan shown in Figure 5a. However, other peaks, related to residual martensite (B19'), could be found, too. On the contrary, the initial powder is fully characterized by austenite (see Figure 6b). Moreover, the shape of the peaks is quite different: as in the SLMed sample, broader peaks with lower intensity are present, if compared to the Nitinol powder. The broadening effect of the peaks and the presence of martensite can be due to different microstructures, associated to cooling rates faster in SLM than in the powder production, and to residual stresses, respectively.

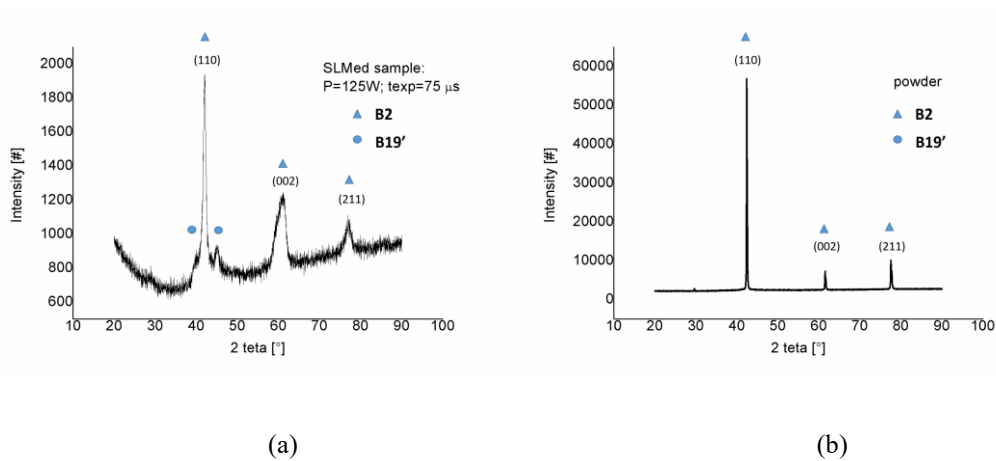


Figure 6: XRD patterns of the NiTiInol cylindrical sample, realized in the process condition: $P=125W$; $t_{exp}=75\mu s$ (a); Nitinol powder (b).

In Figure 7 the stress-strain behavior of the SLMed sample, obtained by mechanical testing at room temperature in compression configuration, is shown. Here, some loading/unloading cycles, characterized by increasing the applied strain, were performed in order to analyze the PE. The sample does not exhibit a complete recovery of the applied strain at room temperature. An evident PE behavior is visible, according to the majority of recoverable strain up to 6% in correspondence of the last cycle, with a residual strain of 1%. Anyways, a flag like behavior was not observed.

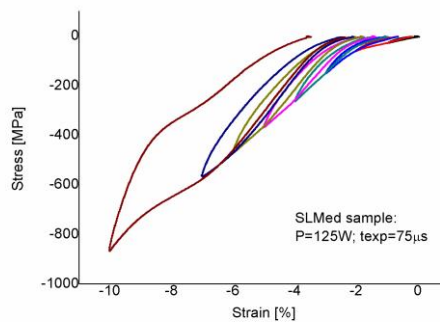


Figure 7: Mechanical cycling under compression of the NiTiInol cylindrical sample.

3.3 Martensitic transformation and mechanical behavior of Nitinol lattice structures

In this paragraph the characterization of the Nitinol lattice structures is reported. In Figure 8 some lattice structures are shown. The process parameters were slightly varied with respect to the ones used for the massive samples because generally lower energy density is required for building thinner structures. The martensitic transformation of the lattice part is

depicted in the DSC scan, reported in Figure 9. The main difference among the lattice part and the other samples, characterized in Figure 5, is the one step MT upon heating and cooling. Table 3 summarizes the transformation temperatures and enthalpies of the SLMed samples in both massive and lattice configurations, and the powder. The variability of the enthalpies of the direct (indicated as ΔH_{dir}) and reverse (indicated as ΔH_{rev}) processes is quite limited: 6-7 J/g and 8-10 J/g, respectively. This indicates that the amount of material involved in the MT remains almost unvaried by the SLM process. On the contrary, the transformation temperatures are more affected by the process. Particularly, the lattice structure shows a broadening of the MT peaks. Due to the energy density being lower in the lattice structure than in the massive samples, it appears reasonable that Ni evaporation, usually present during laser processing, is not the reason of the temperatures shift. On the contrary, residual stresses can be more probably the cause of the modification of the peaks of the MT. In fact, the geometry of the lattice structure printed in this work (see Figure 1b and Figure 8) is characterized by thin struts, linked each other in several points of joining at limited distances: this may provoke the formation of intense values of residual stresses, which could be relaxed after proper heat treatments. This aspect will be analyzed in future works.



Figure 8: Picture of the NiTiInol lattice structures, realized in the process condition: $P=75W$; $t_{exp}=75\mu s$.

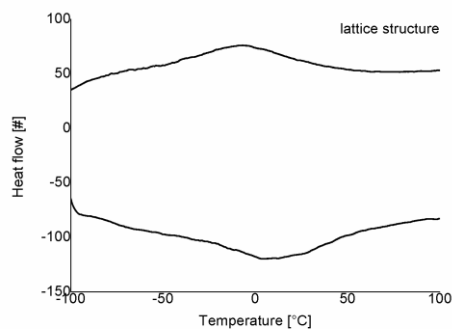
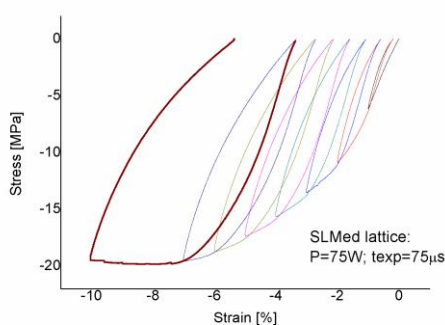


Figure 9: DSC scans of the NiTiInol lattice structure, realized in the process condition: $P=75W$; $t_{exp}=75\mu s$.

Table 3: Characteristic temperatures and transformation enthalpies of massive sample, lattice structure and initial Nitinol powder.

Samples	ΔH_{dir}	R_s	M_f	ΔH_{rev}	A_s	A_f
	[J/g]	[°C]	[°C]	[J/g]	[°C]	[°C]
Massive sample	6.3	7	-97	9.8	-53	1
Lattice structure	7.5	44	-52	10.5	-47	76
Powder	7.0	3	-94	8.1	-34	19

According with the measurement of the A_f temperature from the DSC scan of Figure 9, the mechanical response of the lattice structure can be affected by the presence of both austenite and martensite, due to the uncomplete reverse MT at room temperature. Figure 10 shows the mechanical cycling behavior under compression of the lattice sample, evaluated at room temperature. After an initial elastic part, the curves are characterized by a flat plateau, which shall be ascribed to the densification process typical of trabecular structures. A limited pseudoelastic behavior is evident, presumably because of the presence of martensite in the sample, as evidenced by DSC analyses. Measured stresses, computed considering the nominal section of the whole structure, are sensibly lower than the ones typical of bulk samples because of the large void areas that characterize the lattice part. Moreover, it shall be considered that the deformation mechanism involves bending of the struts, thus further reducing the apparent strength. The large area subtended by the loading-unloading curves, higher than the one displayed by bulk parts, confirms the ability of the lattice structure of absorbing high energy during deformation.

**Figure 10:** Mechanical cycling under compression of the NiTiNol lattice structure.

4 CONCLUSIONS

In the present work the feasibility of Selective Laser Melting process of Nitinol samples, using a pulsed wave emission mode for emitting the laser power, was studied.

According to the selection of the best combination between laser power and exposition time, almost full dense samples can be obtained. Further characterizations were performed on the as built sample produced in this optimized process condition. The martensitic transformation is exhibited in the as built condition, without any post heat treatment, with enthalpies comparable to the powder and transformation temperatures just decreased. The microstructure of the printed sample, analyzed at room temperature via XRD measurements, indicates the presence of martensite, probably induced by residual stresses. Mechanical testing under compression indicates a PE behaviour at room temperature, showing a recoverable strain up to 6% in correspondence of a residual strain of 1%.

Additionally to the manufacturing and characterization of massive samples, lattice structures, representative of thin elements, were successfully printed with selected process parameters. For the lattice samples the martensitic transformation varied significantly from the initial powder and the SLMed massive samples, probably more due to residual stresses than to potential compositional modifications. The mechanical properties are also very interesting, as both PE and energy absorption contributes are present, thanks to the integration of functional performances of Nitinol and deformability and ductility of lattice structures within the same part.

ACKNOWLEDGEMENTS

The authors would like to acknowledge Nicola Bennato from CNR ICMATE for assisting during the experiments.

REFERENCES

- [1] H. Funakubo, *Shape Memory Alloys*, Gordon and Breach Science Publishers, Amsterdam, (1987).
- [2] M. Nishida, C. Wayman, T. Honma, Precipitation processes in near-equiatomic TiNi shape memory alloys, *Metallurgical Transactions A* (1986) **17**:1505-1515.
- [3] Elahinia, M., Shayesteh Moghaddam, N., Taheri Andani, M., Amerinatanzi, A., Bimber, B. A., & Hamilton, R. F. Fabrication of NiTi through additive manufacturing: A review. *Progress in Materials Science* (2016) **83**:630-663.
- [4] Van Humbeeck J. Additive Manufacturing of Shape Memory Alloys, *Shape Memory and Superelasticity*, (2018) **4-2**:309-312.
- [5] S. Dadbakhsh, M. Speirs, J. Van Humbeck, J.-P. Kruth, Laser additive manufacturing of bulk and porous shape memory NiTi alloys: from processes to potential biomedical applications, *MRS Bulletin* (2016) 765-7774.
- [6] C. Wang, X.P. Tan, Z. Du, S. Chandra, Z. Sun, C.W.J. Lim, S.B. Tor, C.S. Lim, C.H. Wong, Additive manufacturing of NiTi shape memory alloys using pre-mixed powders, *Journal of Materials Processing Technology* (2019) **271**:152-161.
- [7] Quan Zhou, Muhammad Dilawer Hayat, Gang Chen, Song Cai, Xuanhui Qu, Huiping Tang, Peng Cao, Selective electron beam melting of NiTi: Microstructure, phase transformation and mechanical properties, *Materials Science and Engineering A* (2019) **744**:290-298.
- [8] Reginald F. Hamilton, Beth A. Bimber, Todd A. Palmer, Correlating microstructure and

- superelasticity of directed energy deposition additive manufactured Ni-rich NiTi alloys, *Journal of Alloys and Compounds* (2018) **739**:712-722.
- [9] S. Saedi, N. S. Moghaddam, A. Amerinatanzi, M. Elahinia, H.E. Karaca, On the effects of selective laser melting process parameters on microstructure and thermomechanical response of Ni-rich NiTi, *Acta Materialia* (2018) **14**:552-560.
- [10] M. Speirs, X. Wang, S. Van Baelen, A. Ahadi, S. Dadbakhsh, J.P. Kruth, J. Van Humbeck, On the Transformation Behavior of NiTi Shape-Memory Alloy Produced by SLM, *Shape Memory and Superelasticity* (2016) **2-4**:310.
- [11] S. Saedi, A.S. Turabi, M.T. Andani, C. Haberland, H.Karaca, M. Elahinia, The influence of heat treatment on the thermomechanical response of Ni-rich NiTi alloys manufactured by selective laser melting, *Journal of Alloys and Compounds* (2016) **677**:204-210.
- [12] S. Shiva, I.A. Palani, S.K. Mishra, C.P. Paul, L.M. Kukreja, Investigation on the influence of composition in the development of Ni-Ti shape memory alloy using laser based additive manufacturing, *Optics and Laser Technology* (2015) **69**:44-51.
- [13] M. Mahmoudi, G. Tapia, B. Franco, J. Ma, R. Arroyave, I. Karaman, A. Elwany, On the printability and transformation behavior of nickel-titanium shape memory alloys fabricated using laser powder-bed fusion additive manufacturing, *Journal of Manufacturing Processes* (2018) **35**:672-680.
- [14] T. Bormann, B. Muller, M. Schinhammer, A. Kessler, P. Thalmann, M. de Wild, Microstructure of selective laser melted nickel-titanium, *Materials Characterization* (2014) **94**:189-202.
- [15] C.A. Biffi, J. Fiocchi, P. Bassani, A. Tuissi, Continuous wave vs pulsed wave laser emission in selective laser melting of AlSi10Mg parts with industrial optimized process parameters: Microstructure and mechanical behaviour, *Additive Manufacturing* (2018) **24**:639-646.
- [16] A.G. Demir, P. Colombo, B. Previtali, From pulsed to continuous wave emission in SLM with contemporary fiber laser sources: effect of temporal and spatial pulse overlap in part quality, *Int. J. Adv. Manuf. Technol.* (2017) 1–14.
- [17] E. Assuncao, V. Williams, Comparison of continuous wave and pulsed wave laser welding effects, *Opt. Lasers Eng.* (2013) **51**:674–680.
- [18] M.T. Andani, S. Saedi, A. S. Turabi, M.R. Karamooz, C. Haberland, H.E. Karaca, M. Elahinia, Mechanical and Shape Memory properties of porous Ni50.1Ti49.9 alloys manufactured by selective laser melting, *Journal of the mechanical behavior of biomedical materials* (2017) **68**:224–231.

INFLUENCE OF AS-BUILT SURFACE TOPOGRAPHY ON THE FATIGUE BEHAVIOR OF SLM INCONEL 718: EXPERIMENTS AND MODELING

Sim-AM 2019

G. NICOLETTO*, G. TINELLI, A. LUTEY* AND L. ROMOLI*

* Department of Engineering and Architecture
University of Parma
Viale Parco Area delle Scienze 181/A, 43124 Parma, Italy
e-mail: gianni.nicoletto@unipr.it

Key words: Fatigue, Inconel 718, Selective Laser Melting, Surface Topography, Roughness

Abstract. The fatigue behavior of ABS SLM Inconel 718 obtained by testing directionally-fabricated specimens is presented and discussed together with characterization of surface topography of the specimens using green light interferometry.

1 INTRODUCTION

One of the most important qualification challenges of structural parts produced by selective laser melting (SLM) is their fatigue strength. Metal SLM specimens with machined surfaces typically achieve comparable fatigue strength to their conventionally-produced counterparts [1]. On the other hand, SLM parts with as-built surfaces (ABS) are characterized by drastically lower fatigue strength due to the relatively high roughness of the produced surfaces. While external, accessible surfaces have the potential to be machined and made smoother, inaccessible internal surfaces are difficult or impossible to post-process. Fatigue design and qualification of SLM parts should take into account the effective surface quality.

Several material and processing factors can influence SLM surface quality, including the powder characteristics, process parameters and surface orientation, amongst others. The surface roughness is controlled by the contouring parameters such as laser power and laser speed, [2]. Laser power and laser focal height have been studied in [3], where it was found that while it was difficult to isolate desired laser settings, laser power and focal height in a combination with other process variables have significant influence on the quality and material properties of components.

The relationship between surface roughness and fatigue life has been studied in several works, where it has been found that surface roughness typically dominates high cycle fatigue properties. More specifically, Greitmeier et al. concluded that high cycle fatigue life of L-PBF specimens was correlated with surface roughness based on the total height of a line measurement (R_t), [4]. Surface topography is either reported from a line measurement, designated with R, or a surface measurement of an area, designated with S. The PSPP relationship relating the contour process parameters to surface roughness and fatigue for AM alloy 718 was examined in [5]. Multiple surface roughness measurement techniques and parameters were employed. When comparing the surface roughness metrics to the fatigue life,

the maximum pit height S_v inversely correlated to the fatigue life.

This study comprises experimental activities linking fatigue strength to topography parameters followed by development of a modelling approach aimed at providing insight into the observed outcomes. The fatigue behavior of ABS SLM Inconel 718, obtained by testing directionally-fabricated specimens, is initially presented together with characterization of surface topography of the specimens using a green light interferometry microscope.

The measured surface topography is used as input for the development of a 3D finite element (FE) model of the surface layer under tensile loading in order to quantify its effect in terms of the stress concentration distribution responsible for fatigue crack initiation.

2 EXPERIMENTS

2.1 Specimen fabrication

This study adopts a recent testing method based on the use of a miniature prismatic specimens with geometry presented in Fig. 1 (22 mm in length, $5 \times 5 \text{ mm}^2$ minimum cross section and 2 mm radius lateral semi-circular notch) subjected to plane cyclic bending loading with load ratio $R=0$, [6]. Previous studies of DMLS Ti6Al4V have demonstrated that this specimen geometry and loading condition result in fatigue data that are coherent with standard rotating bending specimen data and even standard cyclic tensile specimen data.

Four sets of miniature specimens for a total of about 50 specimens were manufactured with an SLM® 280HL system (SLM Solution Group AG, Germany) equipped with two 400 W fiber lasers. Gas atomized Inconel 718 alloy powder with an average particle size of μm was processed using a layer thickness of $50 \mu\text{m}$ and an energy density of $F = 54.82 \text{ J/mm}^3$. After fabrication, the specimens were heat treated with a solution treatment plus a two-step aging treatment, [7].

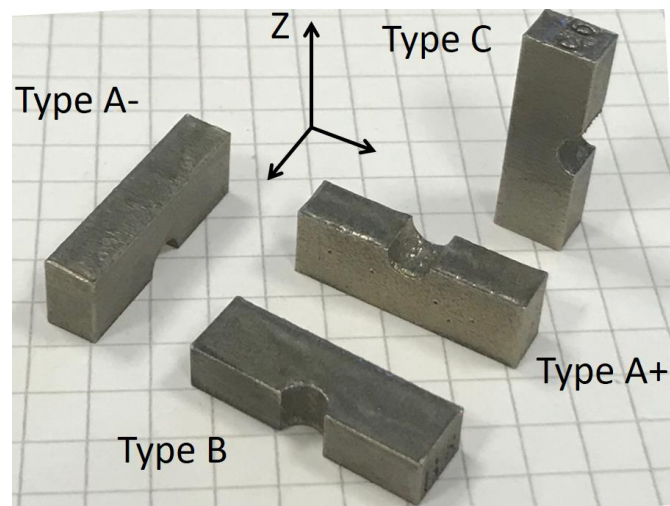


Figure 1: Specimen lay-out on the build plate

2.2 Fatigue test results

The fatigue data of the four types of miniature specimens tested in an unnotched configuration (see Fig. 1 for denomination) are presented in Fig. 2 using the maximum nominal cyclic stress in the plot. The significant degree of directionality of the fatigue behavior of as-built SLM Inconel 718 after heat treatment is apparent. The trends for each of the four fabrication directions are similar but are clearly shifted towards different absolute values depending on the build direction. Material scattering appears limited in all cases.

Fig. 2 shows that the fatigue performance of Type C specimens is the best, followed by that of the Type B specimens. Type A+ and Type A- specimens perform similarly but clearly represent the worst orientations in terms of fatigue strength. The S/N trends define fatigue strength (i.e. the maximum nominal stress σ_{\max} at $R = 0$ with 2×10^6 cycles) ranging from approximately $\sigma_{\max} = 500$ MPa for Type C specimens, to $\sigma_{\max} = 400$ MPa for Type B specimens and $\sigma_{\max} = 340$ MPa for Type A+ and Type A- specimens.

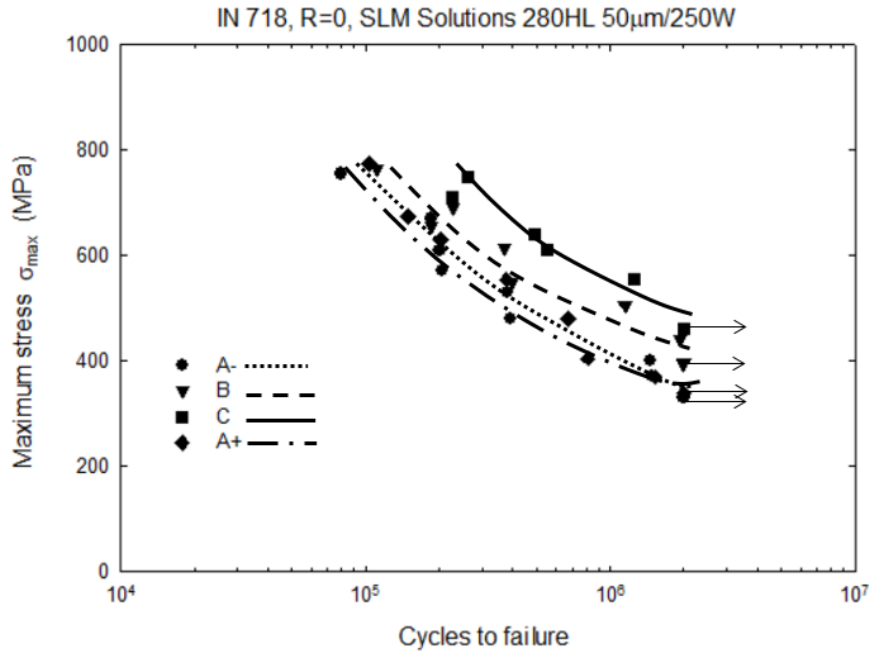


Figure 2: Directional fatigue behavior of SLM Inconel 718 with as-built surfaces

2.3 Surface topography

The surface topography of all specimen types was measured with a Taylor Hobson Talysurf CCI optical profiler with $50\times$ objective. In the employed configuration, the profiler was capable of scanning a $336 \mu\text{m} \times 336 \mu\text{m}$ area with a horizontal resolution of $1.3 \mu\text{m}$ and a vertical resolution of 1 nm . To acquire data over larger areas, several measurements were performed and joined via data stitching with dedicated software. Areal roughness parameters were calculated in line with ISO 25178 [8], including the area surface roughness (S_a), skewness (S_{sk}), kurtosis (S_{ku}), maximum peak height (S_p), maximum valley depth (S_v) and

total roughness (S_z). Within the software, it was also possible to extract sections of the measured surface and calculate the equivalent one-dimensional roughness parameters (R) in line with ISO 13565-1 [9].

Representative surface profiles obtained through data stitching of 9 measurements in a 3×3 configuration are presented in Fig. 3 for Type A- and Type C specimens. The influence of the laser scanning strategy is evident for the Type A- specimen, where the surface topography is dictated by the geometry of the final melted layer. The influence of layer height is instead somewhat evident for the Type C specimen, together with residual un-melted powder protruding from the surface.

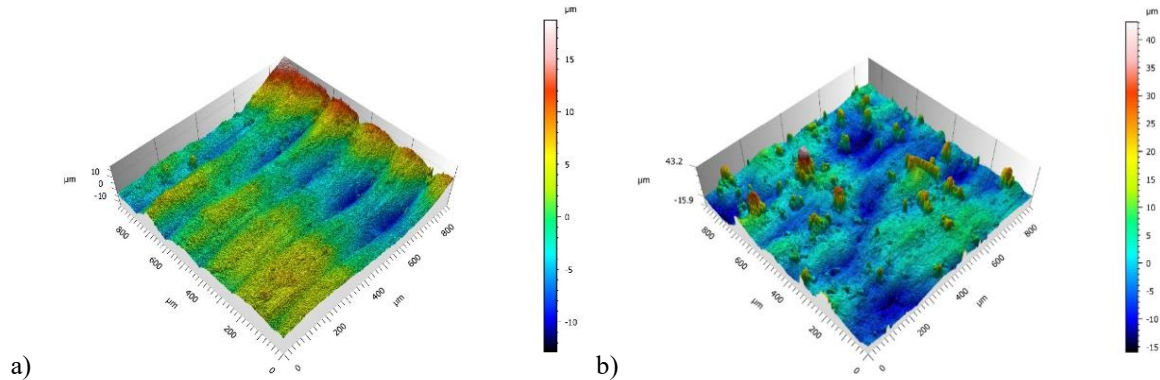


Figure 3: Typical as-built surface topography a) Type A- ; b) Type C

2.4 Surface roughness and correlations with fatigue strength

The fatigue strength and areal surface roughness S_a of all samples are presented in Tab. 1

Table 1: Fatigue strength vs areal surface roughness of different specimen types

	Type C	Type B	Type A+	Type A-
Fatigue strength (MPa)	500	400	340	340
S_a (μm)	3.87	5.05	7.40	2.31

A comparison of the values reveals that the average arithmetic areal roughness is not always inversely related to fatigue strength as might be expected. While this is indeed the case for Type A+, B and C specimens, where the fatigue strength decreases as the surface roughness increases, the Type A- specimens represent an important exception as they are characterized by both the lowest surface roughness and fatigue strength. It is clear that, in this case, the onset of crack formation during cyclic loading is influenced by the geometry of the surface and not simply the average surface roughness.

A more accurate correlation between the surface roughness and fatigue strength can be seen in Tab. 2, where it is possible to observe a direct relationship between the fatigue strength and the areal skewness (S_{sk}). Higher values of skewness are clearly associated with higher fatigue strength, while lower values were observed for both Type A+ and A- specimens, which were characterized by the lowest fatigue strength.

Table 2: Fatigue strength vs areal surface skewness of different specimen types

	Type C	Type B	Type A+	Type A-
Fatigue strength (MPa)	500	400	340	340
S_{sk}	1.61	0.90	0.09	0.07

The correlation between skewness and fatigue strength has important implications relating to the geometry of surface defects and their influence on crack formation and growth. This areal roughness factor expresses the symmetry of the height distribution; a positive value implies a surface characterized predominately by peaks, while a negative value implies a surface characterized predominately by valleys. In the context of crack initiation and growth during cyclic loading, valleys or incisions are expected to be of greater influence due to their larger contribution to stress concentration than are peaks. As a result, negative or lower skewness values imply a greater presence of surface features contributing to stress concentration for a given average surface roughness.

Though S_{sk} is positive for all of the tested samples, higher values for Type C and B specimens imply that a larger proportion of peak-type surface features contribute to the average surface roughness, which likely to be of more limited impact on fatigue strength. In contrast, Type A+ and A- specimens both have lower skewness, implying more balanced presence of peaks and valleys and therefore more relevant contribution of the latter. Within the tested parameter range, leading to relatively limited differences in average surface roughness, it is clear that skewness has an important impact on the fatigue life of components produced via SLM.

3 MODELING APPROACH

Numerical simulations using FEM using the surface scans obtained by profilometry and tomography were recently reported in [10]. Based on extreme values statistics of a non-local fatigue indicator parameter (FIP), a methodology was proposed to take into account the effect of the surface roughness on the HCF life. Here a similar modeling approach based on transformation of the measured surface topography into a 3D finite element (FE) model of a thin surface layer is developed to quantify the effect of surface roughness on the resulting stress distribution. The approach is preliminarily applied to the specimen achieving the highest fatigue strength amongst those that were tested (i.e. Type C).

3.1 FE model generation

Tetrahedral elements were used within the FE model, with material behavior assumed to be linear elastic. The FE mesh, see the example of Fig. 4 was defined on the surface with nodes corresponding to data obtained from the optical profiler on the surface. The mesh size was therefore approximately 1.3 μm on the surface, increasing gradually towards the bulk to limit calculation times. A fixed constrain was applied to one of the two smaller faces orthogonal to the measured surface, while a constant axial load was applied to the other parallel face.

This configuration led to a nominal tensile stress state in the same direction as was induced during fatigue testing. Following calculation of the resulting stress state, the local stress concentration factor (K_t) was calculated by dividing the local elastic surface principal stress by the nominal stress calculated as the applied axis load divided by the nominal cross-section

of the modelled object.

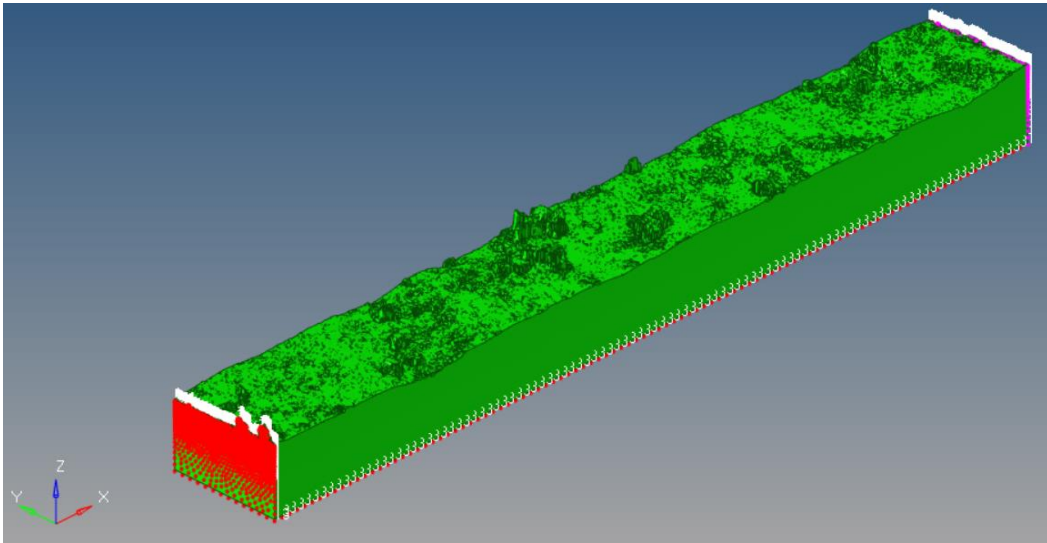


Figure 4: Finite element model of the surface layer (Type C specimen)

3.2 FEM results

The stress concentration factor distribution on the as-built surface of the selected Type C sample is shown in Figure 5. The maximum value of K_t is 3.81, implying that the surface roughness has a significant influence on the resulting localized stress state.

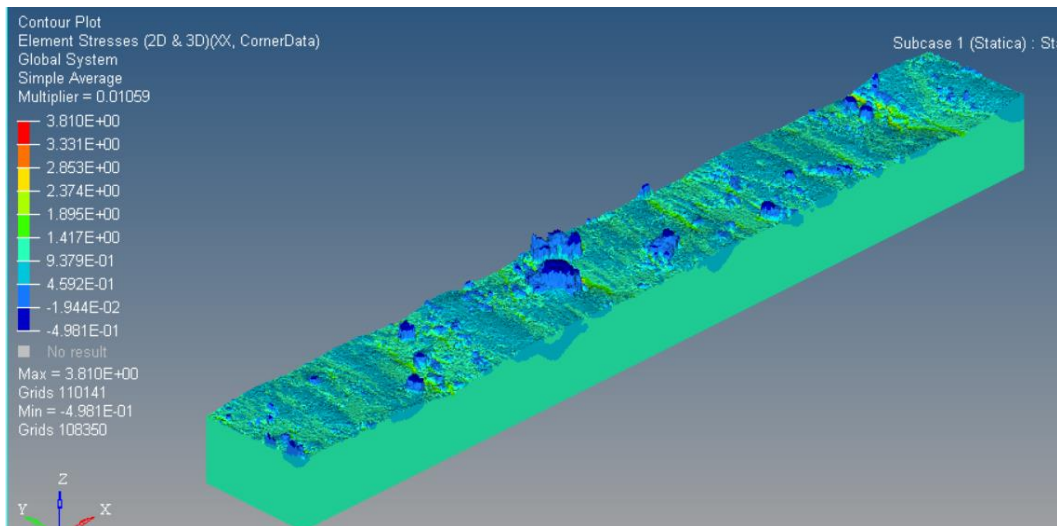


Figure 5: Stress concentration factor (K_t) distribution on the as-built surface

Values of K_t for each node were imported into MATLAB to determine the stress concentration factor distribution over the entire surface. Values are presented in Fig. 6, where it can be seen that most of the surface has a value of $K_t < 1.5$, corresponding to limited or no

stress concentration. A small but significant proportion of nodes has values of $1.5 < K_t < 2.5$. A negligible fraction of the surface reaches even higher K_t values possibly due to discretization effects. These are only preliminary observations, while the on-going activity involves the FE modeling of the surface layers of the other specimen types to address the role of surface orientation (i.e. specimen fabrication direction).

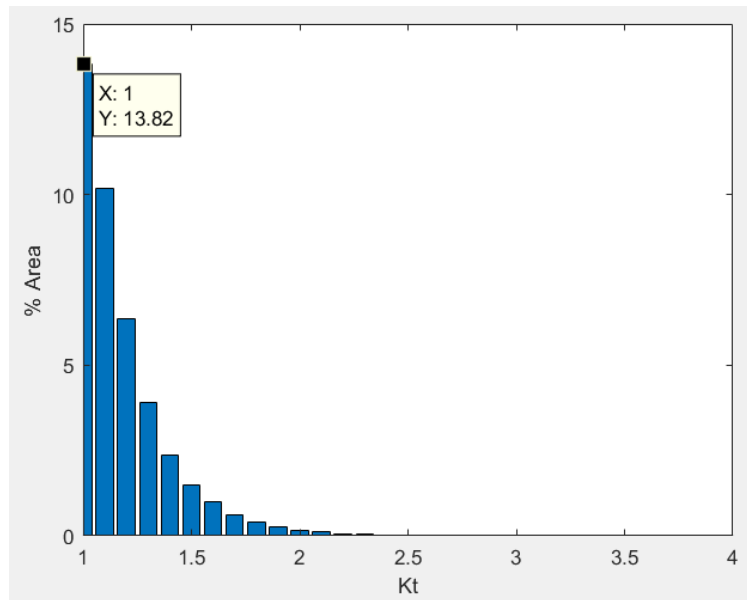


Figure 6: K_t distribution vs percentage of surface area (Specimen Type C).

5 CONCLUSIONS

Two approaches have been presented correlating the surface topography of metallic specimens produced by SLM and the fatigue strength.

The first involved acquisition of the surface topography of SLM specimens built in different orientations with an optical profiler and correlation of the experimental fatigue strength with the average areal surface roughness and skewness. In most cases, an inverse correlation was found between the surface roughness and fatigue strength; however, this was not the case for all samples. By also considering skewness, the fatigue behavior could more accurately be accounted for as lower skewness factors were strongly correlated with lower fatigue strength due to the greater influence of surface valleys or incisions on crack formation and propagation.

The second approach, still at the preliminary stage, involved modelling a thin layer of the acquired surface with a FEM software and considering the ratio of the local elastic surface principal stress to the nominal stress for calculation of the local stress concentration factor (K_t). The distribution of K_t with respect to the surface area fraction shows that fatigue crack initiation occurs at localized areas of high stress. Here only Type C specimen surface was modeled. On-going work is directed in the FE modeling of the as-built surfaces of the other three specimen orientations.

REFERENCES

- [1] Fatemi A, Molaei R, Sharifimehr S, Phan N, Shamsaei N. Multiaxial fatigue behavior of wrought and additive manufactured Ti-6Al-4V including surface finish effect. *Int J Fatigue* (2017) 347–66.
- [2] B. Whip, L. Sheridan, J. Gockel, The effect of primary processing parameters on surface roughness in laser powder bed additive manufacturing, *International Journal of Advanced Manufacturing Technology*, (2019) <https://doi.org/10.1007/s00170-019-03716-z>
- [3] Fox JC, Moylan SP, Lane BM. Effect of process parameters on the surface roughness of overhanging structures in laser powder bed fusion additive manufacturing. *3rd CIRP conference on surface integrity* (2016).
- [4] D. Greitemeier C. Dalle Donne, F. Syassen, J. Eufinger, T. Melz. Effect of surface roughness on fatigue performance of additive manufactured Ti-6Al-4V. *Mater Sci Technol* 32 (2016) 629–34.
- [5] J. Gockel, L. Sheridan, B. Koerper, B. Whip, The influence of additive manufacturing processing parameters on surface roughness and fatigue life. *Int J Fatigue* 124 (2019) 380–388
- [6] G. Nicoletto, Anisotropic High Cycle Fatigue Behavior of Ti-6Al-4V obtained by Powder Bed Laser Fusion. *International Journal of Fatigue*, 94 (2017) 255-262.
- [7] ASTM. Standard specification for additive manufacturing nickel alloy (UNS N07718) with powder bed fusion. ASTM Book of Standards. (2014).
- [8] ISO 25178-2,2012 Geometrical product specifications (GPS)- surface texture: areal- part 2: terms, definitions and surface texture parameters
- [9] ISO 13565-1:1996 Geometrical Product Specifications (GPS) -- Surface texture: Profile method; Surfaces having stratified functional properties -- Part 1: Filtering and general measurement conditions
- [10] B. Vayssette, N. Saintier et al., Numerical modelling of surface roughness effect on the fatigue behavior of Ti-6Al-4V obtained by additive manufacturing, *International Journal of Fatigue*, 123 (2019) 180-195

SIMULATION OF RESIDUAL STRESSES DUE TO SLM FABRICATION AND CORRELATION WITH DIRECTIONAL FATIGUE BEHAVIOR OF AlSi10Mg

Sim-AM 2019

G. NICOLETTO*, D. DAVIDDI AND A. FORNACI §

* Department of Engineering and Architecture
University of Parma
Viale Parco Area delle Scienze 181/A, 43124 Parma, Italy
e-mail: gianni.nicoletto@unipr.it

§ BEAM-IT
Strada Prinzera, 43124 Fornovo Taro (PR), Italy

Key words: Fatigue, AlSi10Mg, Selective laser melting, Residual stress, Process simulation

Abstract. The selective laser melting process causes high thermal-induced residual stresses that may result in unwanted part distortion and may affect fatigue strength of the part. This study initially presents the fatigue behavior obtained by testing directional specimens of SLM AlSi10Mg in the as-built condition (i.e. no heat treatment after fabrication). Then, the SLM process of specimen fabrication is simulated using the inherent strain approach to determine residual stresses at the location and in the direction of fatigue crack initiation. A direct correlation of the computed residual stresses and the actual fatigue behavior provides qualitative insight into the simulation accuracy.

1 INTRODUCTION

Selective laser melting (SLM) is a layer-by-layer manufacturing process that allows the building of complex, lightweight and customized parts by consolidating successive layers of metal powder via localized melting by a laser. During the SLM process, the material experiences large localized temperature fluctuations in a short time. This causes high thermal-induced residual stresses that may result in unwanted part distortion or material cracking and consequently waste of time and resources, [1]. Complex physical interactions cause an inconsistent quality of the produced parts. Even experienced technologists may not be able to identify the most suitable fabrication strategies for parts of complex geometry. Therefore, computer-based process simulation tools are proving valuable for the successful implementation of SLM in industry, [2].

Thermo-mechanical FEM simulations show that distortion of SLM parts tends to be a macroscopic phenomenon, which is mostly dependent on the hatching strategy and the geometry of the manufactured part, [3-5]. Since stress and temperature in a layer are affected only by a few neighboring layers, a computationally-efficient multiscale method for the prediction of residual stresses and deformation of SLM parts has been developed in [3]. The strains determined in the mesoscopic hatching model are applied as inherent strain in the

macroscopic layer model via the inherent strain vector.

Along with part deformation, residual stresses are predicted by SLM process simulation, [5]. Residual stresses due to SLM process may affect the fatigue strength of parts in the absence of post fabrication heat treatments, [6]. Generally, residual stresses are expected to be either detrimental on fatigue strength when tensile or positive when compressive.

Since the complex link between the SLM process, residual stresses and fatigue response would gain irreplaceable insight by experiments, this contribution integrates SLM process simulation for residual stresses with fatigue testing of AISi10Mg specimens in the as-manufactured state (i.e. without post fabrication heat treatment). A direct correlation of the computed residual stresses and the actual fatigue behavior provides qualitative insight into the simulation accuracy.

2 FATIGUE OF AS-BUILT SLM AISi10Mg

This study initially presents the directional fatigue behavior obtained by testing specimens of SLM AISi10Mg in the as-built condition (i.e. no heat treatment after fabrication) so that residual stresses are expected.

2.1 Experimental details

A fatigue testing method based on a miniature specimen geometry recently developed is adopted, [7]. Previous studies of DMLS Ti6Al4V demonstrated that this specimen geometry and loading condition result in fatigue data that are coherent with standard rotating bending specimen data and even standard cyclic tension specimen data. and possibly show their effects in fatigue. The specimen geometry is quite small, hence “miniature”, and prismatic (22 mm in length, 5 x 5 mm² minimum cross section, 5x7 mm² gross section and lateral semi-circular notch 2 mm in radius).

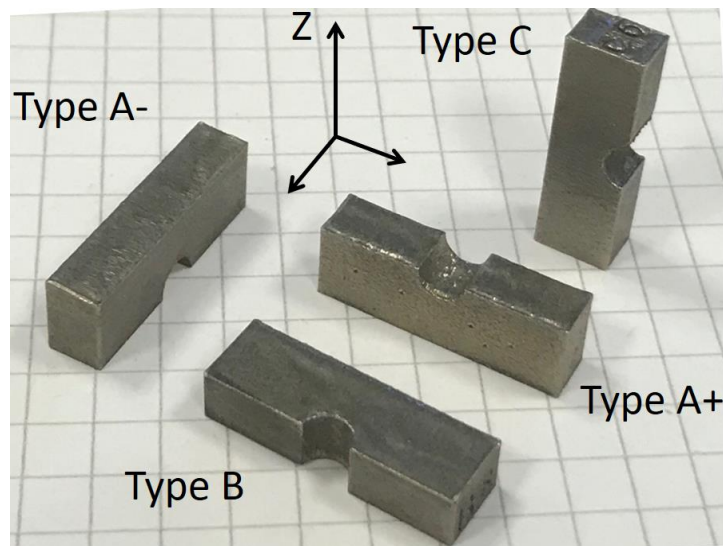


Figure 1: Specimen lay-out on the build plate

For its small size and type of loading, the specimen is readily adapted for investigating directional effects on the fatigue behavior, [7]. Fig. 1 shows four different orientations of the miniature specimen with respect to build direction and their respective denominations.

Four sets of such miniature specimens for a total of about 50 specimens were manufactured using a SLM® 280HL system (SLM Solution Group AG, Germany) equipped with 2x400W lasers. Gas atomized AlSi10Mg alloy powder was processed using a layer thickness of 50 μm and a fluence $F = 54.82 \text{ J/mm}^3$. After fabrication, the specimens were removed from the build plate without any additional processing or heat treatment. Therefore, the surfaces were relatively rough and the SLM-processing-induced residual stresses were not affected.

The four different sets of miniature specimens were then tested under cyclic plane bending with a load ratio $R = 0$ using a table-top electromechanical testing machine working at 25 Hz with continuous load monitoring. The flat surface opposite to the circular notch was subjected to the pulsating tensile stress (i.e. the notch was in compression) to localize fatigue crack initiation under unnotched condition, [7]. The cyclic displacement-controlled test ended either when the applied bending decreased of 10% below the initial level or when the specimen reached $2 \cdot 10^6$ cycles without an appreciable load change.

2.2 Directional fatigue behavior

The fatigue data of the four types of miniature specimens tested in the unnotched configuration, (see Fig. 1), are presented in Fig. 2 using the maximum nominal cyclic stress vs. number of cycles to crack initiation. in the plot.

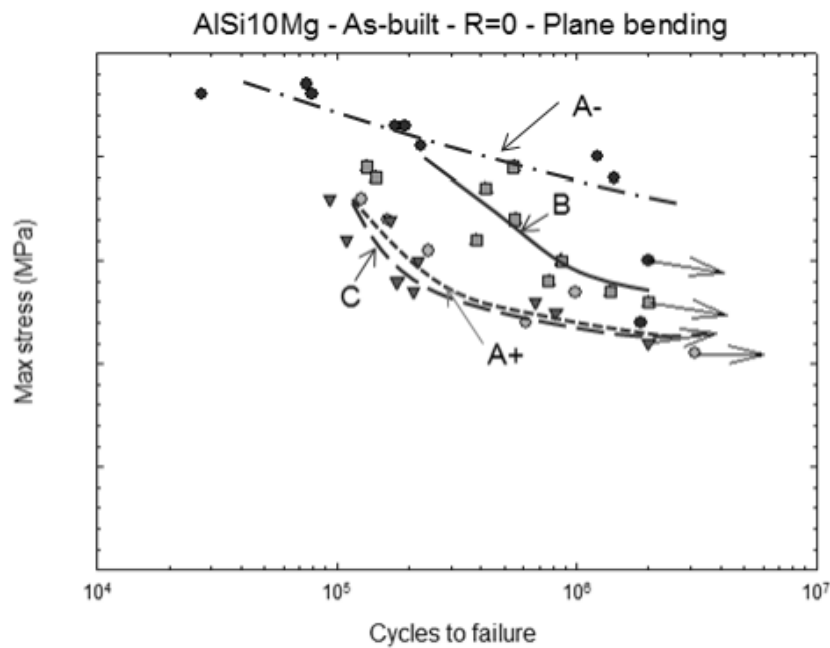


Figure 2 - Directional fatigue behavior of SLM AlSi10Mg with as-built surfaces

The significant degree of directionality of the fatigue behavior of the present as-built SLM AlSi10Mg without heat treatment is apparent. Two specimen orientations (Type A+ and C)

have similar trends and a lower fatigue strength than the Type B orientation. On the other hand, the fatigue behavior of Type A- oriented specimens is significantly different. Material scatter appears limited in all cases and the trend curves are well defined. If Type C orientation (i.e. long axis parallel to build) is considered the reference, Type A+ orientation (i.e. long axis perpendicular to build) shows the same behavior, Type B orientation (also perpendicular to build) is about 25% stronger than Type C and the Type A- orientation is 80% stronger than the reference.

Since the specimens are in the as-built surface condition, the surface quality to the fatigue directionality could contribute to the observed response of Fig. 2. However, previous studies of stress relieved SLM Ti 64 and SLM In718 showed only a slight degree of directionality in the fatigue response [8, 9]. Unpublished studies on T6-heat-treated SLM AlSi10Mg with the same specimen geometry and as-built surfaces showed also limited directional behavior.

Therefore, this novel evidence of strong directional fatigue behavior is attributed to SLM-generated residual stresses affecting to a different degree the fatigue crack initiation phase.

2 SLM PROCESS SIMULATION

The thermo-mechanical FEM simulation is a common and validated tool for the prediction of residual stress in conventional thermal processes like welding. However, since SLM parts are much larger than the size of the micro-weld and each weld seam experiences an identical or comparable thermo-mechanical history, a fast solution of the mechanical problem on the basis of the method of inherent strain has been proposed to reduce the time consuming transient thermo-mechanical problem, [3]. The complete method involves the use of three sub-models: i) heat source model (Goldak's model); ii) hatching model (elasto-plastic thermo-mechanical modeling of the laser trajectory); iii) layer model (mechanical equivalent due to layer-by-layer updating). Such an approach is implemented in the commercial SIMUFACT software (MSC Software, Germany), which has been used here to determine the residual stresses in the directional specimens of AlSi10Mg shown in Fig. 1 due to the SLM fabrication

The SLM process simulation approach consisted of two-steps: i) a calibration phase that accounts for the material powder, process parameters and the scan strategy is performed on cantilever specimens of prescribed geometry, ii) simulation of the SLM fabrication of the directional specimens to determine the macroscopic residual stresses that may affect the fatigue behavior. Distortion of AM parts tends to be a macroscopic phenomenon, which is mostly dependent on the hatching strategy and the geometry of the manufactured part [8].

2.1 Calibration

A preliminary calibration phase of the scan strategy parameters was performed on cantilever specimens of the recommended geometry shown in Fig. 3a. The same SLM 280HL system and process parameters (Table 1) used to fabricate the miniature specimens of Fig. 1 was used to print cantilever beams of AlSi10Mg shown in Fig. 3a.

Table 1 - SLM process parameters of AlSi10Mg.

Laser power	Scan Speed	Layer thickness
W	mm/s	μm
350	1250	50

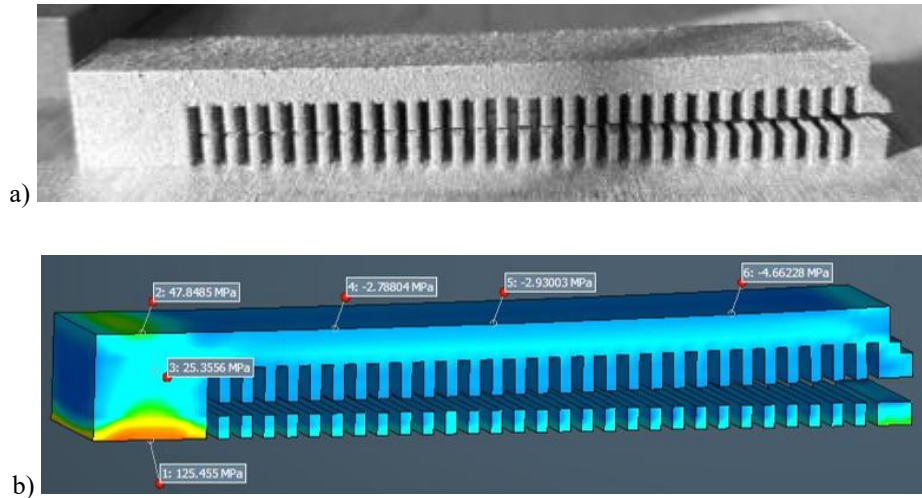


Figure 3: Physical (top) and simulated (bottom) deflected cantilever beam used for SLM process calibration

Dimensions were: length = 72 mm, height = 9 mm (including 3-mm-thick solid section) and width = 12 mm. A comb-shaped structure supports more than 80% of the solid beam length, Fig. 3a. Cutting of the support structure results in beam deformation due to residual stress redistribution. The resulting maximum deflection is measured at the tip of the beam to calibrate the specific inherent strains simulation parameters.

A sensitivity campaign was preliminarily conducted with the simulation code to determine the optimal size of the Voxel mesh (from 3 mm to 0.5mm) used to model the cantilever specimen, Fig. 3b, because it links the inherent strains and the simulated component. The optimal Voxel size was experimentally determined to be 1 mm. Considering the beam height of 9 mm and SLM layer thickness of 50 μm , the beam was made of 180 layers. Each Voxel layer of Fig. 3b represented 20 physical metal layers.

2.2 Simulated residual stresses in the directional specimens

The residual stresses due to SLM fabrication were computed in each directional specimen of Fig. 1. While the state of stress is typically triaxial in the body interior and biaxial on the surface, the residual stress component of specific interest is here the longitudinal stress acting on the flat surface shown in Fig. 4a because the bending loading during fatigue testing applies a cyclic longitudinal principal stress in the same direction. Therefore, the residual stress can be superposed on the pulsating bending stress similarly to a mean stress of a stress cycle.

The computed longitudinal residual stresses across the specimen width due to SLM fabrication for each oriented specimen is shown in Fig. 4b. The Type C specimen is characterized by a relatively high tensile stress with a maximum value of 140 MPa, while the other specimens show stresses below 30 MPa. Type B specimens show a trend in residual stress from positive to negative. Type A+ a gradient from compressive on the outer surfaces and traction in the middle and Type A- a rather uniform and low tensile stress.

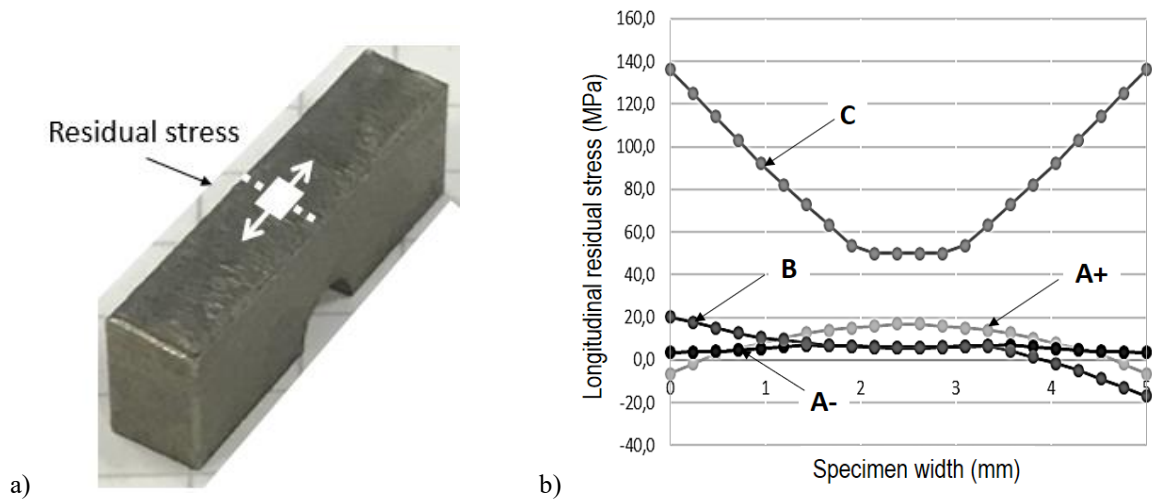


Figure 4: a) Residual stress of interest in a mini specimen b) computed residual stresses of the four directional specimens

Average values of the longitudinal stress distribution are given in Fig. 5. Significantly, residual stresses acting parallel to layer (i.e Type A+, A- and B) are low while residual stress perpendicular to layer are high (i.e Type C). Further, for the present SLM process modeling there is no significant difference in residual stresses between Type A- specimens where under test is the top and final layer and Type A+ specimens where under fatigue test is the first layer connected to the build plate, which undergoes cyclic thermal cycles of the subsequent layers.

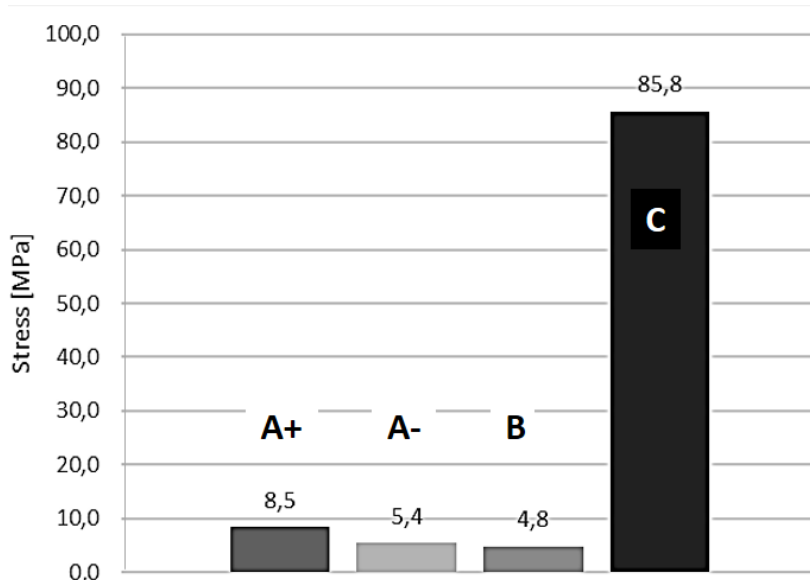


Figure 5: Average longitudinal residual stresses in fatigue specimens

3 CORRELATION OF EXPERIMENTS AND SIMULATION

The originality of this study is in the direct correlation of results of fatigue experiments and simulation of the SLM residual stresses. It is an accepted fact that residual stresses are detrimental in fatigue when tensile and, conversely, beneficial when compressive.

The fatigue experiments show a very significant increase in fatigue strength of Type A- specimens compared to the Type C and A+ specimens. On the other hand, the simulated residual stresses are high and tensile for Type C specimens while are negligible for the other directions. Type C shows the lowest fatigue strength, coherently with the residual stress levels. However, the other three specimen directions show practically negligible tensile residual stresses.

Type A+ and Type A- specimens show very different fatigue strengths but the simulated residual stresses are quite similar. Here the simulation may be inaccurate as it predicts similar residual stresses while in practice in first case the layer under test is the last and in the second case is the first. The very high fatigue strength of Type A- specimens could be attributed to high compressive residual stresses that however are not identified by simulation. Only Type B specimens shows a slight computed compressive stress on part of the specimen.

At this stage of still limited experience with the process simulation tool, the adoption of the recommended procedures (Voxel size determination by calibration) was inevitable. Further, deformation of actual parts was successfully predicted and corrected by Beam-It company resulting in compliant SLM parts for the customer. However, it is believed that the multilayer Voxel may be inappropriate for modeling the type A- specimen orientation because the top layer under tensile fatigue stress is also the last melted layer where severe stress gradients are expected.

4 CONCLUSIONS

This study originally presented a direct correlation of the fatigue behavior obtained by testing directional specimens of SLM AlSi10Mg without heat treatment after fabrication and residual stresses in the specimens associated to the simulation of the SLM process. The SLM process simulation tool based on the inherent strains approach was experimentally calibrated. The fabrication of directional fatigue specimens was simulated determining longitudinal residual stresses on the surfaces under cyclic stress. The main conclusions are as follows:

- The fatigue behavior of the as-built SLM AlSi10Mg is strongly directional.
- The lowest fatigue strength was determined for Type C specimens where the applied stress is perpendicular to the layers and the simulation predicts strong tensile residual stresses.
- The fatigue behavior of Type A+ and Type A- specimens is very different with a very high strength achieved by Type A-. This may be attributed to strong compressive residual stress.
- The computed residual stresses of Type A+ and Type A- specimens are similar. It is believed that the homogenization of the multiple layers into a single Voxel element may not be appropriate here.
- The experimental methodology and evidence originally presented here may help in fine tuning SLM process simulation tools.

REFERENCES

- [1] M.F. Zaeh, G. Branner, Investigations on residual stresses and deformations in selective laser melting, *Prod. Eng.* 4 (1) (2010) 35–45.
- [2] J. Kruth, J. Deckers, E. Yasa, R. Wauthlé, Assessing and comparing influencing factors of residual stresses in selective laser melting using a novel analysis method, *Proc. Inst. Mech. Eng. Pt. B: J. Eng. Manuf.* 226 (2012) 980–991.
- [3] N. Keller, F. Neugebauer, H. Xu, V. Ploshikhin, Thermo-mechanical Simulation of Additive Layer Manufacturing of Titanium Aerospace structures, *LightMAT Conference* (2013).
- [4] C. Li, C.H. Fu, Y.B. Guo, F.Z. Fang, A multiscale modeling approach for fast prediction of part distortion in selective laser melting, *J. Mater. Process. Tech.* 229 (2016) 703–712.
- [5] C. Li, J.F. Liu, X.Y. Fang, Y.B. Guo, Efficient predictive model of part distortion and residual stress in selective laser melting, *Additive Manufacturing*, 17 (2017) 157–168
- [6] N. Shamsaei, J. Simsiriwong, Fatigue behaviour of additively-manufactured metallic parts, *Procedia Structural Integrity*, Vol. 7 (2017) 3-10
- [7] G. Nicoletto, Anisotropic High Cycle Fatigue Behavior of Ti-6Al-4V obtained by Powder Bed Laser Fusion. *International Journal of Fatigue*, 94 (2017) 255-262.
- [8] G. Nicoletto, Directional and notch effects on the fatigue behavior of as-built DMLS Ti6Al4V, *International Journal of Fatigue* 106, (2018) 124-131
- [9] R Konečná, G Nicoletto, L Kunz, A Bača, Microstructure and directional fatigue behavior of Inconel 718 produced by selective laser melting, *Procedia Structural Integrity* 2 (2016) 2381-2388

MECHATRONIC APPROACH TO THE DESIGN OF AM MACHINES

Paolo Righettini*, **Roberto Strada***

*Department of Engineering and Applied Sciences
University of Bergamo

Viale Marconi 5, 24044 Dalmine (BG) Italy

e-mail: paolo.righettini@unibg.it, roberto.strada@unibg.it, web page: <http://www.unibg.it>

Key words: Additive manufacturing, Selective Laser Sintering/Melting, Mechatronic design

Abstract. Any manufacturing process which allows to create a product in its finished form without the need for other machining operations belongs to Net Shape Forming family. Additive Manufacturing (AM) is a part of NSF family; it allows to build 3D objects by adding layer-upon-layer of material (polymers, metals, ceramics) and includes different manufacturing techniques as stated by ISO/ASTM Standard.

In order to get good results by the application of these techniques, some technological problems has to be faced and solved. They mainly concern: temperature control of the material to be processed, characteristics of the energy source for material transition, control of the power transferred to the material, scanning system's head control, 3D model's layer definition, generation of the laser point's trajectories. The quality of the product strongly depends on all these aspects, that are sinergically linked each other, as well as on the technical solutions to realize them. In other words, the machine implementing the AM technological process is crucial for the product's manufacturing. From the early stages of machine's concept, a multidisciplinary and synergic approach which allows to take into account all the different aspects involved in the process must be followed. This is the typical approach followed by Mechatronics which deals with the synergistic application of mechanics, electronics, controls and computer engineering in the development of product and systems through an integrated design approach.

In this paper, the fundamental aspects that must be taken into account in the design process of an AM machine are highlighted, and the design approach is discussed.

1 INTRODUCTION

Net Shape Forming (NSF) refers to any manufacturing process which allows to create a product in its finished form without the need for other machining operations. Additive Manufacturing (AM) technology belongs to NSF manufacturing processes' family and it was born in the early 80s thanks to several inventors who worked on different 3D Printing techniques; by means of AM technology, 3D objects are built by adding layer-upon-layer of material (plastics, metals, ceramics) [1] [2].

The family of Additive Manufacturing technologies is quite wide and it is characterized by several different kinds of processes, according to the specific technology used. As an example we can talk about selective laser sintering (SLS), selective laser melting (SLM), electron

beam melting (EBM), Direct Metal Deposition (DMD), Fused Deposition Modelling (FDM), Stereolithography(SLA), etc. In order to clearly categorize the AM processes, ISO/ASTM 52900:2015 standard has defined seven different kinds of process [3].

The application and implementation of each kind of process lead to several and peculiar technological problems that, in order to get good results in terms of product's quality and productivity, have to be tackled and solved. In general they concern: temperature control of the material to be processed, characteristics of the energy source for material transition, control of the power transferred to the material, scanning system's head control, 3D model's layer definition, generation of the laser point's trajectories (when a laser is used as energy source). All of these aspects have the same importance to guarantee the quality of the product and they are synergically linked each other. As an example, the power of the energy source and the temperature of the material are strongly related; the power transferred to the material is related to the trajectories running speed; the 3D model's layer definition influences the resolution of the positioning system; on the performances and control of the scanning head, the accuracy of the trajectories depends.

The analysis of the influence of these process characteristics on the product has been, and still is, strongly investigated by researchers, along with the way to control the process parameters [4]. Just as an example, investigations concerning heat transfer by means of thermography [5] [6], and analysis of the effect of laser's power on temperature and material defects were made [7]. Moreover, in the last years the effort of researchers seems to be focused on investigations concerning new methods to control the quality of the product in-situ [8] [9] [10].

The quality of the product strongly depends on all the aforementioned aspects as well as on the technical solution to realize them. In other words, the machine implementing the specific AM technological process is crucial for the product's manufacturing. From the early stages of machine's concept, a multidisciplinary and synergistic approach which allows to take into account all the different aspects involved in the process must be followed. This is the typical approach followed by Mechatronics; as a matter of fact, Mechatronics concerns the synergistic application of mechanics, electronics, control and computer engineering in the development of products and systems through an integrated design approach.

This paper mainly focuses on the AM technology known as Powder Bed Fusion, in which thermal energy selectively fuses regions of a powder bed as stated by [3]; more in detail the Selective Laser Melting(SLM) and Selective Laser Sintering (SLS) are addressed. The fundamental aspects that must be taken into account in the design process of an AM machine are highlighted, and the used design approach is discussed.

2 GENERAL MACHINE'S CONFIGURATION

As explained in [2], the production process of an AM machine can be summarized as follows: 3D CAD model preparation and STL conversion, slicing of the STL file, machine set-up, building of the product, removing from the machine, possible post-processing operations.

With particular reference to a Selective Laser Melting (SLM) or Selective Laser Sintering (SLS) machines, the product's building consists of heating a portion of the powder bed by means of a laser moving the scanning head according to the "sliced" 3D CAD model, lowering

the platform of the building volume, dispensing another layer of powder and recoating with another powder's layer. Then the working cycle restarts.

Figure 1a and figure 1b show a conceptual sketch of a machine. In particular figure 1a focuses on the laser source, the scanning head and the layer heated by the laser; figure 1b highlights the building powder container and the relevant lowering platform, the dispensing container and the recoating device.

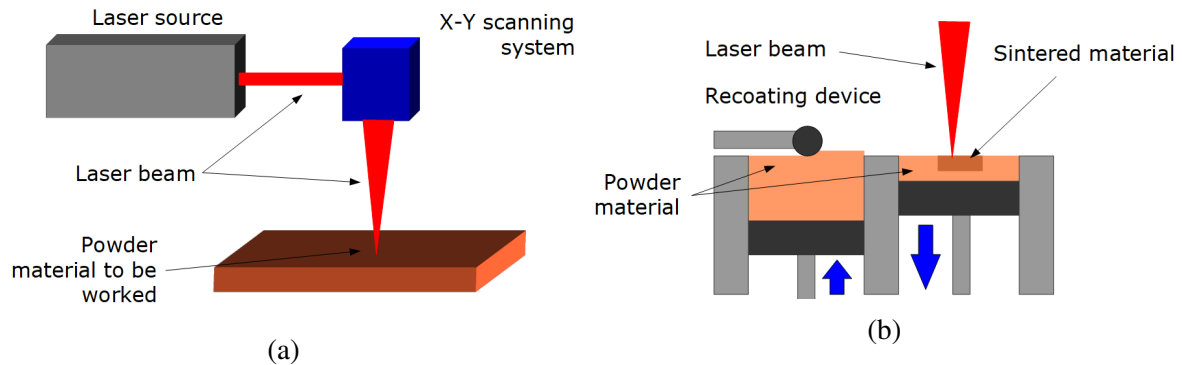


Figure 1: Conceptual scheme of a machine

From a simply conceptual point of view, a machine for Additive Manufacturing doesn't seem to be strongly complex; a specific sequence of motions and operations allow to realize the building process. Actually there are some technological aspects that are very crucial to have a successful production process.

Again with reference to a Powder Bed Fusion machine, one of those crucial aspects is related to SLS/SLM technology: it is based on the use of a laser source, whose power depends on the powder material processed [11], for sintering portions of a surface of pre-heated powder material. Figure 2 schematically shows the conceptual scheme of sintering process. Hence the thermal energy control along with the laser energy control are very important issues of a machine.

Besides the thermal energy control, another important issue concerns the control of the laser beam, that is the control of the laser scanning head and the choice of the path to be sintered.

Moreover, the slicing operation of the STL 3D model is very important for the quality of the product, in particular the choice of the slicing step and the algorithm to extract layers from the STL model.

3 THERMAL ENERGY CONTROL

A Powder Bed Fusion process needs thermal energy to bring the material powder within a specific range of temperature in order to make sintering or melting occur. As a matter of fact, the melting temperature must be reached for SLM, while the mechanism of sintering is the fusion of powder particles in their solid state at high temperature, between one half of the melting temperature and the melting temperature, which depends on the powder material.

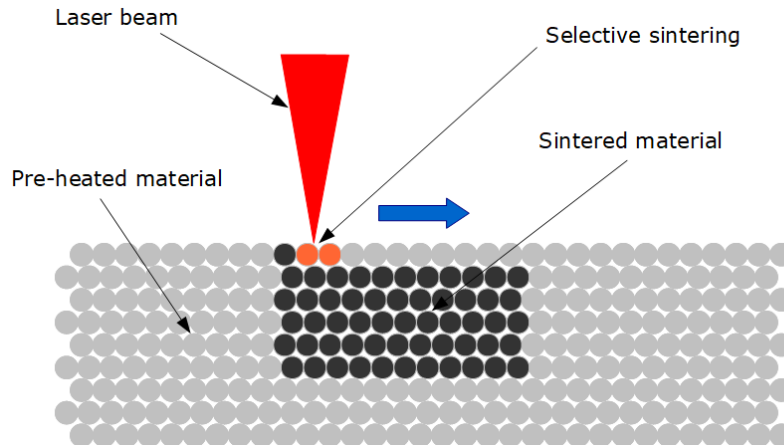


Figure 2: Conceptual scheme of the sintering process

Depending on the powder temperature and on the time at which the temperature is maintained, the sintering process gives different results, mainly concerning the porosity, that is the density of the product. In order to have products with high density, high sintering temperatures and high sintering times are needed; on the contrary, fusion by melting is quicker. That's why sintering is rarely used as the primary fusion mechanism [2].

However, it is still an important mechanism in most Powder Bed Fusion processes, and the design of a machine implementing this technology, must properly take into account some important effects that sintering has on the product building: also the loose powder within the building container, and not only the one that has to be sintered, begins sintering. This means that the dimensional characteristics change leading to a change of the behaviour when used as recycled powder for another production process. Another important aspect is related to the growth of a "skin" around the built part; when the desired cross-section is fused, the loose surrounding powder increases its temperature and, mainly when melting is the primary fusion mechanism, it remains at high temperature for long time; it results in part growth. Moreover, since the lower layers (i.e. the first fused) are maintained to high temperature for a time longer than the upper ones, the product part has higher density in lower regions rather than in the upper ones.

Powder bed temperature has a great influence also on the geometry of the single fused layer; as a matter of fact, the fused cross section could be subjected to curling effects due to the temperature difference between the loose powder and fused cross section [12].

All these typical aspects highlighted, it's clear that temperature and thermal energy needed to get it are important issues of a PBF process [4]. Hence, from a design point of view, the choice of the thermal source to guarantee the proper temperature of the powder bed is crucial as well as the methods to control its distribution on the powder bed. The issue of temperature monitoring have been dealt with in literature by several authors as [5][6][7][8][10]. Infrared thermal cameras and pyrometers are commonly used. As far as thermal source is concerned, infrared lamps are generally used for polymers, sometimes in conjunction with resistors in order to prevent border effects around the building volume.

4 LASER ENERGY CONTROL

In Powder Bed Fusion process in which melting is the primary fusion mechanism the powder bed is maintained at a specific temperature, lower than melting point, and a laser, or an electron beam in case of EBM (Electron Beam Melting), is used to give the powder the energy increment needed for melting. Hence the control of laser energy is a very important issue to guarantee the proper powder melting. Laser energy needed depends on powder characteristics like thermal conductivity, absorptivity and reflectivity; as an example a powder with high thermal conductivity requires a laser with higher power because heat dissipates very fast [12].

Moreover, the total amount of energy that is absorbed by the powder depends on laser beam speed, on beam spot size and on scan spacing [2][12]. Hence, rather than the absolute laser energy or power, the most important parameter is the laser energy density. A simplified model for the energy density on the surface of the powder bed can be written as [2][12]:

$$E_S = \frac{W_L}{v_s \delta} \quad (1)$$

where $E_S [J/m^2]$ is the surface energy density, $W_L [W]$ is the laser power, $v_s [m/s]$ is the scan speed and $\delta [m]$ is the spacing between adjacent scan lines.

A similar equation can be written for the energy density across the thickness:

$$E_T = \frac{W_L}{v_s \delta \sigma} \quad (2)$$

where $E_T [J/m^3]$ is the energy density across thickness and $\sigma [m]$ is the layer thickness.

The laser effect depends also on the spot size, which must be strictly related to the distance between adjacent scan lines. As a matter of fact, if the spot size is smaller than scan spacing, it results in inappropriate fusing and porosity of the product. A bigger spot size requires more power from the laser in order to have the same energy density.

Moreover, the spot size is related to resolution and to production time; the smaller the spot size, the higher the resolution, but the longer the production time. Hence a proper balance between these different aspects must be sought after and reached.

All things considered, the proper choice of laser parameters has a very high influence on the results obtained on the product.

5 LASER BEAM CONTROL

For a proper implementation of Powder Bed Fusion technology, and in particular Selective Laser Sintering/Melting, besides the control of the laser energy and parameters, also the control of the path followed by the laser beam is very important; it is still a research issue [13].

As a matter of fact, in order to properly fuse the powder within the desired cross section, the laser beam has to move along a path, filling the cross-section itself. According to the kind of path, different scanning strategies can be defined. The main differences concern the kind of path (linear, spiral, etc.), the distance between adjacent lines, possible division of the cross section area into sub-sections. [2][12].

One of the process characteristics influenced by the chosen scanning strategy is the productivity; as a matter of fact, a longer path leads to a longer time to fill the cross section area. Besides the length of the path, also its shape is very important; as an example, if the cross section is filled just with linear parallel paths, it results in shrinkage stress and anisotropic strength, leading to warp and distortion. Moreover, linear paths aren't the best choice in case of presence of cavities inside the cross section; as a matter of fact, as it's schematically shown in figure 3, the laser beam should travel along the empty area with the laser switched off. This results in wasting of time while, frequently switching on and off, the laser reduces its lifetime.

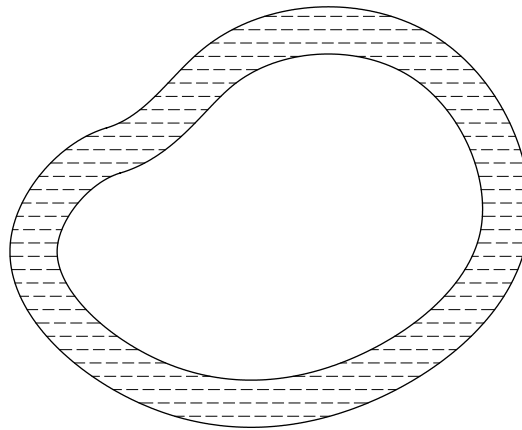


Figure 3: Example of cross section with cavity (linear paths in dotted lines)

Another parameter already mentioned in the previous section is the distance between adjacent scan lines, that is how dense the path is. The density of the path, being related to the path's length, influences the building time of the product, i.e. the productivity. A less dense path increases the productivity but, depending on the spot size, it could lead to an inappropriate powder fusion and hence to a product with high porosity and inadequate mechanical characteristics. In order to find a good balance between these different aspects, a scanning strategy could include variable distance between adjacent lines, according to the position inside the area. An example is shown in figure 4, where paths near to the border have a distance lower than the ones in the inner part of the area. The choice to lower the distance near to the borders allows to have good finishing of the external surface of the product.

However, the results obtained with a specific path could be different depending on its position inside the building volume. As a matter of fact, heat transmission is strongly affected by the position and so the effect on the resulting product.

The design process of a machine cannot disregard all these important issues concerning scanning strategies, mostly when a mechatronic approach is followed.

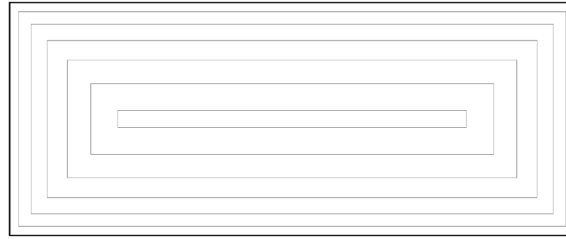


Figure 4: Path with variable distances between lines

6 3D MODEL SLICING

In previous sections, important issues concerning Power Bed Fusion technology and the process design of the relevant machines have been highlighted. One of these aspects is the layer thickness; as explained in the laser section, it is related to the volume energy density.

In general, the choice of the layer thickness is done in a pre-processing phase of the product building, precisely during the STL file manipulation phase. On the STL file, the machine's control software has to perform a slicing operation in order to get the cross section areas to be sintered (figure 5). Obviously, the layer thickness influences also the pre-processing time needed.

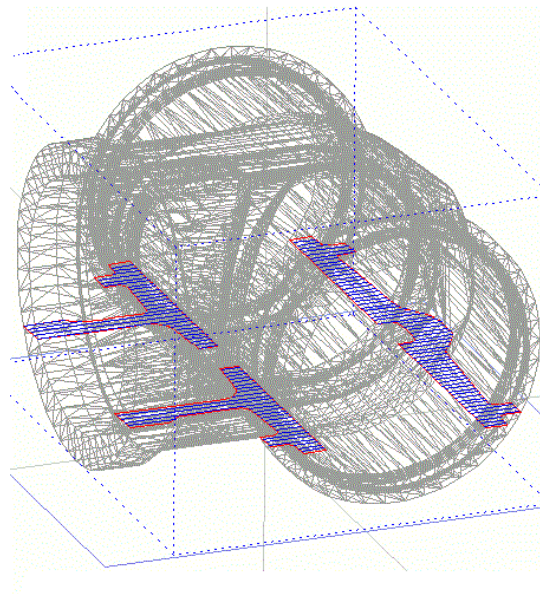


Figure 5: Slicing of a STL file

As well known, in a STL file, surfaces are approximated by a mesh of triangles. The slicing software must recognize intersection between the cutting plane and the triangles giving as output the shape of the cross section to be sintered.

From the choice of layer thickness, the productivity and the resolution of the outer surface of the product depend. As a matter of fact, the higher the thickness, the shorter the product building time, but with high layer thickness the well known staircase effect becomes more evident. Figure 6 schematically shows a vertical plane section where the solid line represents the ideal profile while dotted line is the actual one. The staircase effect is clearly showed: the higher the layer thickness, the larger the gaps between ideal and actual profile.

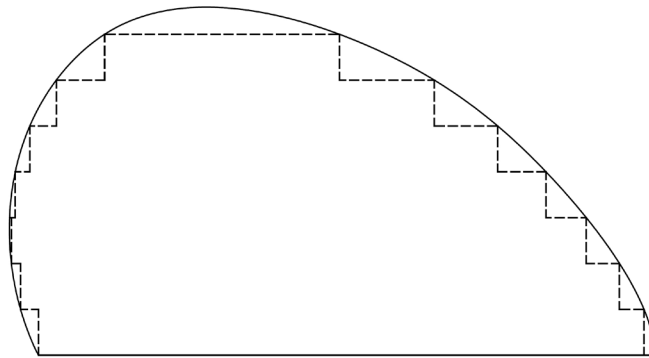


Figure 6: Staircase effect

The choice of the thickness depends on the building strategy used, that is for example the growth direction of the product, which influences the staircase effect. As shown in figure 7, the same product positioned in a different way can lead to dramatically different results in terms of geometric quality.

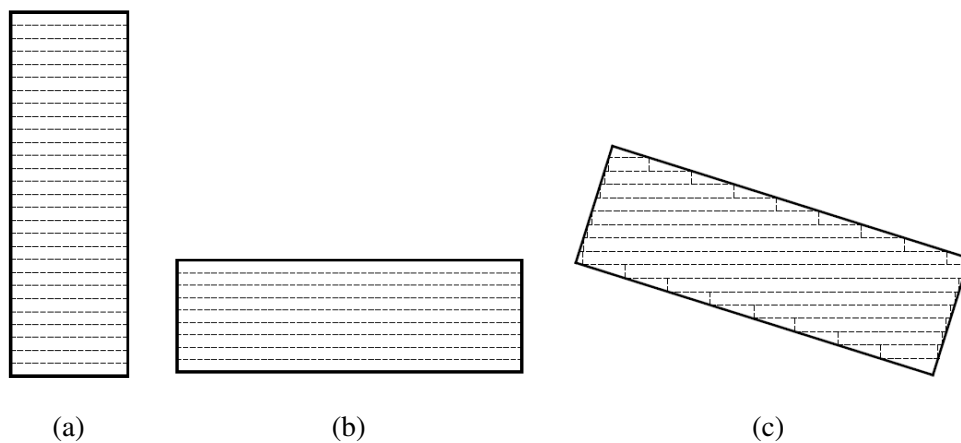


Figure 7: Positioning into build chamber

In particular, figure 7c shows, for the same product shape, how much the orientation influences the staircase effect. Moreover, between figure 7a and 7b, it is also clear that the best

orientation is (7b), allowing to have a very low number of layers. It should be also noticed that orientation (7a) and (7b), not having problems related to staircase effect, could allow to use layers with higher thickness than orientation (7c). So, the building strategy has a big influence on the production time because, according to the orientation of the product the number of layers could be definitely different.

7 MECHATRONIC APPROACH

From the technological point of view, the problems related to Additive Manufacturing and, in particular to Powder Bed Fusion, are clear. As seen in the previous sections there are issues concerning thermal control, laser energy and relevant parameters, laser beam control, scanning path definition and so on.

In order to design and develop a machine that implements PBF technology, it is necessary to set-up proper and efficient technical solutions to transform technological needs in an industrial machine as schematically represented in figure 8.

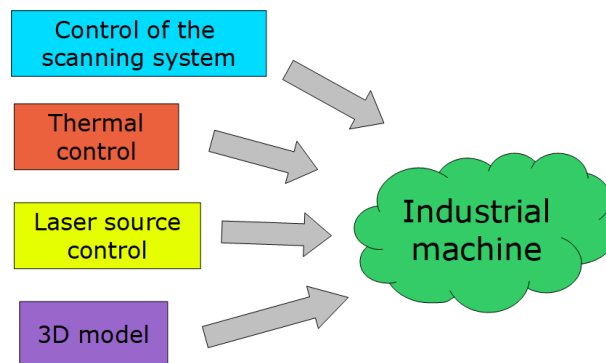


Figure 8: From technological issues to industrialization

In literature, papers concerning the design of industrial machines aren't so widespread, probably for confidentiality reasons, while it is possible to find some works concerning development of prototypes even characterized by new solutions at the aim to improve the production process [14][15][16][17][18].

All the aspects involved in the design of an Additive Manufacturing machine cannot be dealt with separately, but they are linked each other and not independent. A synergistic approach is needed, which is typical of Mechatronics; even from the concept phase of the machine the technological issues and the relevant technical solutions must be tackled as a whole. One of the main aspects concerns the optimal choice of the motor-transmission system [19].

As an example, concerning the displacement of the building platform, it depends on layer thickness which generally varies between $100\mu\text{m}$ and $300\mu\text{m}$. Hence a very accurate transmission system is needed; as an example a recirculating balls screw coupled with a brushless servomotor, which is a system characterized by high stiffness, could be used.

Another important motion is the one devoted to powder recoating; in this case, the axis should be as fast as possible in order to reduce the time of this process step, that isn't a product

building step. Also in this case, a solution with high performances should be used; again, a brushless servomotor with a stiff transmission like a recirculating balls screw would be a good solution.

For powder distribution, instead of having a container with a moving piston near the building container, the best solution would be to leave the powder fall down from a hopper in front of the recoating mechanism; a simpler solution without the need for another axis, the one to move the piston. In order to reduce the waste of time, two hoppers could be used, one on the left and one on the right of the building volume; in this way, the recoating axis lays the powder in each direction without having a working stroke and a return stroke.

According to the mechatronic approach [20], simulation can be carried on to predict the behaviour of the system. Besides simulations concerning the axis motion and the production cycle of the machine, also thermal simulation should be carried on to define the position and the power of the heating elements like infrared lamps and resistors that guarantee the proper temperature distribution on the powder bed.

Then the control software must manage all the functionalities required; it has to perform the pre-processing activities like STL slicing, to allow parameters setting, temperature control, laser control, scanning path control, axes motion control and it has to coordinate the different steps of the productin process. Hence, since the early stage of the design process, the concept of the software must take into consideration all the functionalities that must be guaranteed to the system.

8 CONCLUSIONS

In this paper, the main technological issues related to Powder Bed Fusion process have been highlighted. All these issues are equally important in order to guarantee the quality of the product and they are synergistically linked each other.

The design of an industrial machine for Additive Manufacturing, and in particular Powder Bed Fusion, needs to transform the technological issues in technical solutions which allow their implementation with reference not to a prototypical environment, but to an industrial one.

The mechatronic approach, thanks to its typical synergistic characteristic, has a fundamental role in the design of such machines; since the early stage of concept design, all technological aspect, which synergistically interacts each other, must be taken into account as a whole, along with the relevant technical solution. That's the way to make an optimal design and to develop an efficient machine with high performances.

REFERENCES

- [1] M. Molitch-Hou, Overview of additive manufacturing process, *Additive Manufacturing-Materials, Processes, Quantifications and Application*, pp. 1–38, 2018
- [2] I. Gibson, D. Rosen, B. Stucker, *Additive Manufacturing Technologies - 3D Printing, Rapid Prototyping and Digital Manufacturing*, Springer, 2015.

- [3] Standard ISO/ASTM 52900:2015 *Additive manufacturing – General principles – Terminology*, 2015.
- [4] Jinliang Zhang, Bo Song, Qingsong Wei, Dave Bourell, Yusheng Shi, A review of selective laser melting of aluminum alloys: Processing, microstructure, property and developing trends, *Journal of Materials Science & Technology* 35 (2019) 270–284
- [5] H. Krauss, C. Eschey, M. F. Zaeh, Thermography for Monitoring the Selective Laser Melting Process, *Proceedings of the 23rd Annual International Solid Freeform Fabrication (SFF) Symposium – An Additive Manufacturing Conference, Austin, Texas, USA, August 6-8, 2012*
- [6] Kai Zeng, Deepankar Pal, Brent Stucker, A review of thermal analysis methods in Laser Sintering and Selective Laser Melting, *Proceedings of the 23rd Annual International Solid Freeform Fabrication (SFF) Symposium – An Additive Manufacturing Conference, Austin, Texas, USA, August 6-8, 2012*
- [7] M. Islama , T. Purtonena, H. Piilia, A. Salminenena, O. Nyrhil, Temperature profile and imaging analysis of laser additive manufacturing of stainless steel *Physics Procedia* 41, pp. 835-842, 2013.
- [8] Sarah K. Everton, Matthias Hirscha, Petros Stravroulakis, Richard K. Leach, Adam T. Clare, Review of in-situ process monitoring and in-situ metrology for metal additive manufacturing, *Materials and Design* 95 (2016) 431–445.
- [9] Giulia Repossini, Vittorio Laguzza, Marco Grasso, Bianca Maria Colosimo, On the use of spatter signature for in-situ monitoring of Laser PowderBed Fusion, *Additive Manufacturing* 16 (2017) 35–48
- [10] M. Grasso, A.G. Demir, B. Previtali, B.M. Colosimo, In situ monitoring of selective laser melting of zinc powder via infrared imaging of the process plume, *Robotics and Computer-Integrated Manufacturing* 49 (2018) 229–239.
- [11] Andrew J. Pinkerton, Lasers in additive manufacturing, *Optics & Laser Technology* 78 (2016) 25–32
- [12] Kumar, S., Selective Laser Sintering/Melting, *Comprehensive Materials Processing*, vol. 10, 2014
- [13] Ben Ezair, Saul Fuhrmann, Gershon Elber, Volumetric covering print-paths for additive manufacturing of 3D models, *Computer-Aided Design* 100 (2018) 1–13
- [14] Scott Fisha, John C. Bootha, Steven T. Kubiaka, William W. Wroea, Adam D. Bryantb, Daniel R. Mosera, Joseph J. Beamana, Design and subsystem development of a high temperature selective lasersintering machine for enhanced process monitoring and control, *Additive Manufacturing* 5 (2015) 60–67

- [15] Frederik Wullea, Daniel Coupek, Florian Schäffner, Alexander Verl, Felix Oberhofer, Thomas Maier, Workpiece and Machine Design in Additive Manufacturing for Multi-Axis Fused Deposition Modeling, *Procedia CIRP* 60 (2017) 229 – 234
- [16] Taku Yamazaki, Development of A Hybrid Multi-tasking Machine Tool: Integration of Additive Manufacturing Technology with CNC Machining, *Procedia CIRP* 42 (2016) 81 – 86
- [17] Jyoti Mazumder, Design for Metallic Additive Manufacturing Machine with Capability for “Certify as You build”, *Procedia CIRP* 36 (2015) 187 – 192
- [18] Tim Phillips, Scott Fish, Joseph Beaman, Development of an automated laser control system for improving temperature uniformity and controlling component strength in selective laser sintering, *Additive Manufacturing* 24 (2018) 316–322.
- [19] H. J. F. Roos and J. Wikander, Optimal selection of motor and gearhead in mechatronic application, *Mechatronics*, vol. 16, pp. 63–72, 2006
- [20] C. W. De Silva *Mechatronics – an integrated approach*, CRC Press - Taylor & Francis Group, 2005

MODELING AND SIMULATION OF A LINEAR MOTOR IN A LIQUID-FROZEN DEPOSITION SYSTEM FOR ADDITIVE MANUFACTURING

M. SILVESTRI^{*,†} AND H. GIBERTI[✳]

^{*} Department of Engineering and Architecture
University of Parma
Parco Area delle Scienze 181/A, 43124 Parma, Italy
e-mail: marco.silvestri2@unipr.it, web page: <http://silvestri.rocks>

[†] Department of Innovative Technologies
University of Applied Sciences and Arts of Southern Switzerland (SUPSI)
Via Cantonale 2C, 6928 Manno, Switzerland
Email: marco.silvestri@supsi.ch

[✳] Department of Electrical, Computer and Biomedical Engineering
University of Pavia
Via A. Ferrata 5, 27100 Pavia, Italy
Email: hermes.giberti@unipv.it

Key words: liquid frozen deposition, linear motor, multiphysics model, 3D printing

Abstract. The present work is related to the fabrication of a scaffold with a customized shape through a variant of an additive manufacturing process often called liquid frozen deposition manufacturing, which consists in depositing layer by layer a polymer solution in a low temperature platform or chamber with an x-y-z motion platform. In this specific application, the x-y stage is actuated by high precision linear motors, located into a thermal chamber and must work at the temperature of -15° C, facing control problems related to variations of the electromagnetic interactions. Hence a multi-physics simulation has been developed in Open Modelica environment to understand the motor behavior and to allow the development of an amended control system.

1 INTRODUCTION

Additive manufacturing technologies are expanding their field of application in an ever-increasing number of industrial sectors through the development of new processes [1], the use of new materials [2] and, by consequence, the design of new machines [3,4]. In the medical devices industry, the augmented demand for devices devoted to tissue regeneration based on a controlled micro-architecture in recent years led the interest for industrial scale-up in the production of hydrogel-based mass-customized artefacts. The present work is related to the fabrication of a scaffold with a customized shape through a variant of an additive manufacturing process that in the literature has been proposed by different names such as low temperature manufacturing (LTM), liquid frozen deposition manufacturing, cryogenic prototyping and rapid freeze prototyping [5]. This process can be successfully carried out by controlling a set of parameters that includes the role of the viscosity of the starting hydrogel solution and the effect of temperature and speed on the success of frozen deposition [6].

The LTM system here discussed constitutes the evolution of a first prototype presented in the past and allows improved features and performances (precision, print speed, work envelope) through two fundamental design choices: firstly, the adoption of a thermal chamber to control humidity and temperature of the work envelope; secondly, the use of a XY-stage actuated by high precision linear motors of reduced dimensions. As a consequence, linear motors operation at low temperature (-15°C) constitutes a technological challenge because of the temperature influence on the electromagnetic phenomena underlying linear motor working principle. In fact, such temperature makes the behaviour of the system substantially different from what occurs at environmental conditions and requires a complete overhaul of the control system.

2 LINEAR ELECTROMAGNETIC MOTOR MODEL

2.1 Stator permanent magnet

Inside the several existing kinds of permanent magnets, rare earth magnets which are the strongest ones produced from alloys of rare earth elements. Two principal types, samarium-cobalt and neodymium magnets, found the largest number of industrial applications and the latter has been used for the model here illustrated, as Neodymium magnets (NdFeB, NIB or Neo) which are made from an alloy of neodymium, iron and boron are the most widely used. The model is, in particular, composed by two lines of 15 blocks ($15 \times 8 \times 20\text{mm}$). To calculate the value of the B field on the symmetry axis of an axially magnetized block magnet the approach proposed by [7] has been followed:

$$B = \frac{B_r}{\pi} \left[\tan^{-1} \left(\frac{LW}{2z \sqrt{4z^2 + L^2 + W^2}} \right) - \tan^{-1} \left(\frac{LW}{2(D+z) \sqrt{4(D+z)^2 + L^2 + W^2}} \right) \right] \quad (1)$$

where B_r is the remanence field, independent from the magnet geometry, z is the distance from a pole face on the symmetry axis, L , W , and D are the length, the width and the height of the block, as shown in figure 1.

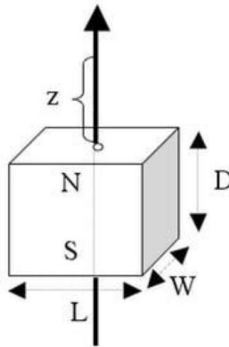


Figure 1: Permanent magnet block

2.2 Slider

The motor slider is composed by 3 solenoids. Each solenoid is independent from the others and they are represented by the same circuit but with a different way of voltage source. In order to calculate the force necessary to move the slider, it is necessary to calculate the magnetic field

created by each solenoid. As a first approximation, this can be done using the Biot-Savart law and assuming that this value does not change moving far to the axis and near to the coil [8]:

$$B(r) = \frac{\mu_0 i}{4\pi} \int \frac{d\vec{l} \wedge \vec{r}'}{|\vec{r}'|^3} \quad (2)$$

In the equation above, \vec{l} and \vec{r}' are the line segment and distance vector from the viewpoint of the source charge as shown in figure 2 and μ_0 represents the permeability of the vacuum.

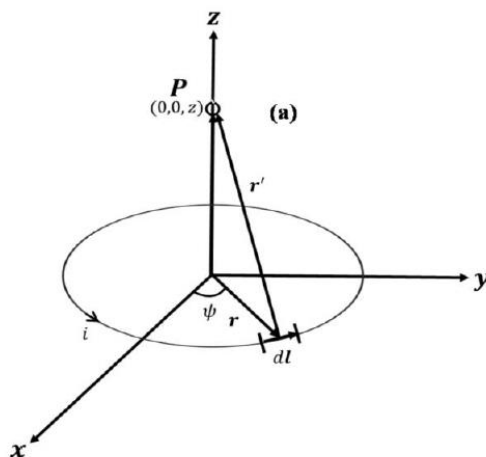


Figure 2: Solenoid magnetic field representation [8]

2.3 Operation and power supply

The motor operational mode has been treated according to the model proposed in [7], which uses unipolar rectangular impulse of direct current to power supply the system.

The change of the amplitude is evaluated by the current factor:

$$y = \frac{I}{I_m} \quad (3)$$

The duration of the current impulse is characterized by the power supply current impulse duration factor:

$$\beta = \frac{t_{imp}}{T} = t_{imp} \cdot f_{imp} \quad (4)$$

Among the various possible control approaches, as a first step to simulate the effect of the temperature on the motor operation, the well-known six-step commutation has been adopted, following the implementation presented in [9].

Such an approach, beside its relative simplicity, has the inherent advantage of being based on a current control loop, so that the effect of the temperature in the copper can be directly evaluated in terms of current variation. The solution is based on powering the motor three-phases with three current square waves with a phase displacement of 120 degrees among each other, as illustrated in figure 3. Each phase can be set at three different states, *fully positive*, *fully negative* and *zero*.

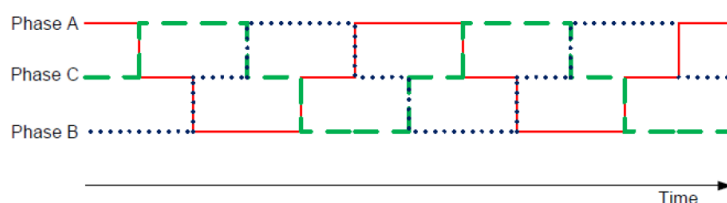


Figure 3: Six-step commutation concept

3 OPEN MODELICA MODEL

3.1 Stator

The stator of the motor is built up by permanent magnets alternated between each tooth, so in OpenModelica is inserted the value of the magnetic field created by the magnets along the axis x , positive or negative, depending on the teeth, that appears as a constant in the model of the translational emf. To introduce the positive value and the negative value of the permanent magnet, the circuit has been duplicated: the positive value of the magnet is set as the constant of the electromechanical force of the positive pulse current while the negative value is set on the other side. Then, when each pulse works, it produces an acceleration on the same direction directly related to the value of the pulse, and it results easy to be controlled.

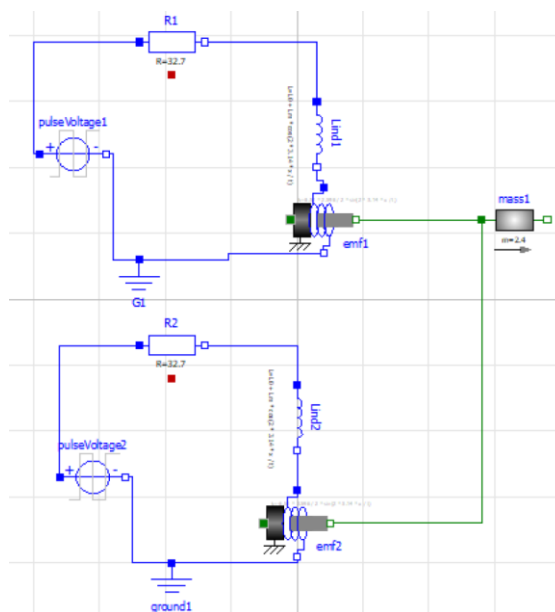


Figure 4: Stator with pulse divided

3.2 Slider

The representation of the slider is obtained by combining three solenoids, represented by 3 equal R-L circuits isolated. Each solenoid produces a force and the three forces are joined and applied to the mass. Along the time, the inductor force is not constant, as it depends on the displacement of the motor following a sinusoidal law, then, with the objective to improve the accuracy of our model a variable inductor has been introduced.

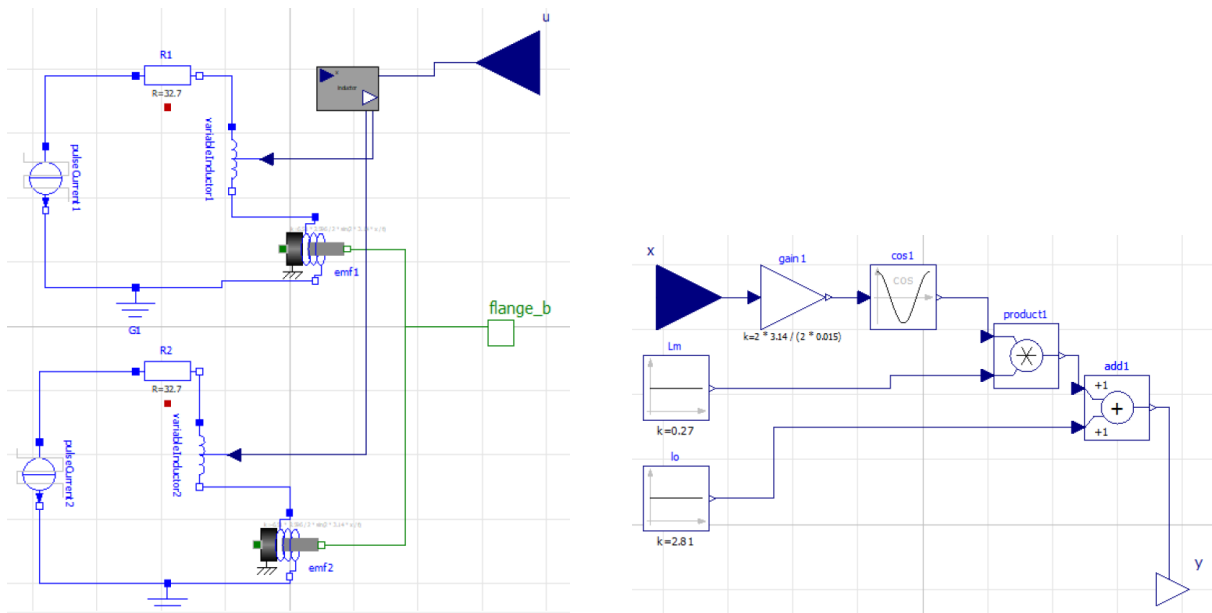


Figure 5: Solenoid with variable inductor (left) and the model of variable inductor (right)

3.3 Friction

The friction model proposed in [10] consists of two components which take account of two different physical phenomena: the friction force under microscopic motion and the frictional effects related to velocity. The first one has been modeled as a non-linear spring whose behavior has been obtained from the results of low frequency harmonic motion tests, while the second one has been implemented through the non-linear relationship represented by the classical Stribeck curve experimentally measured at different speed.

The overall frictional effect is then approximated by the following relationship:

$$f_v(v) = \left\{ f_s(x) + C_{t1} v^\alpha \exp\left(-\left(\frac{v}{v_a}\right)^\beta\right) \right\} \text{sgn}(v) + C_{t2} v^r \quad (5)$$

where $f_s(x)$ is friction force for the non-linear spring characteristics which is a function only of displacement. When, as in the present case, movements are in the order of millimeters, $f_s(x)$ is of the same order of magnitude of the Coloumb friction force. The Open Modelica model of $f_v(v)$ is illustrated in figure 6.

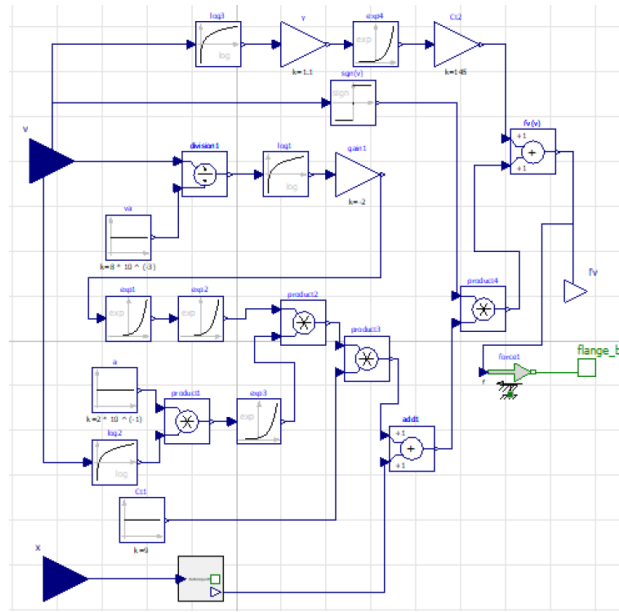


Figure 6: Model of $f_v(v)$

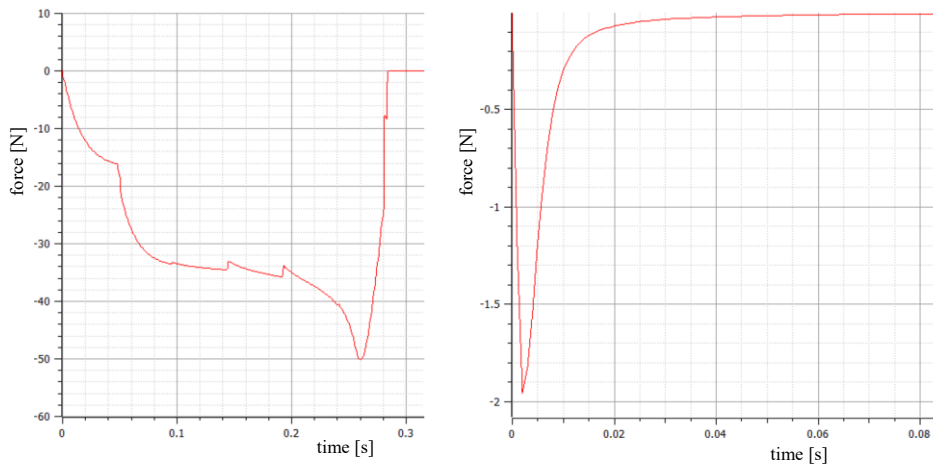


Figure 7: Friction forces depending on position (left) and velocity (right)

3.4 Controller

The controller created to implement the six-step commutation described above at the higher level uses two input signals (one designated to the reference position of the motor and the other coming from the position sensor) and one output, which define the current to power supply motor windings. At a lower level, this has been implemented through two separate blocks: the first calculate the feedback as the difference between the position reference and the position measured by sensor, and the second uses this value in a purely proportional control.

A further complication is given by the need to stop the functioning of the motor before it arrives to the target, taking in account that, when the current stops, the inductor introduces a certain delay, because the residual generates a not negligible amount of force. This current will depend on the reference position setpoint, so this has been considered in advance by creating a

model that depending on the reference position produce a signal that represents the distance to the position setpoint where the motor must stop.

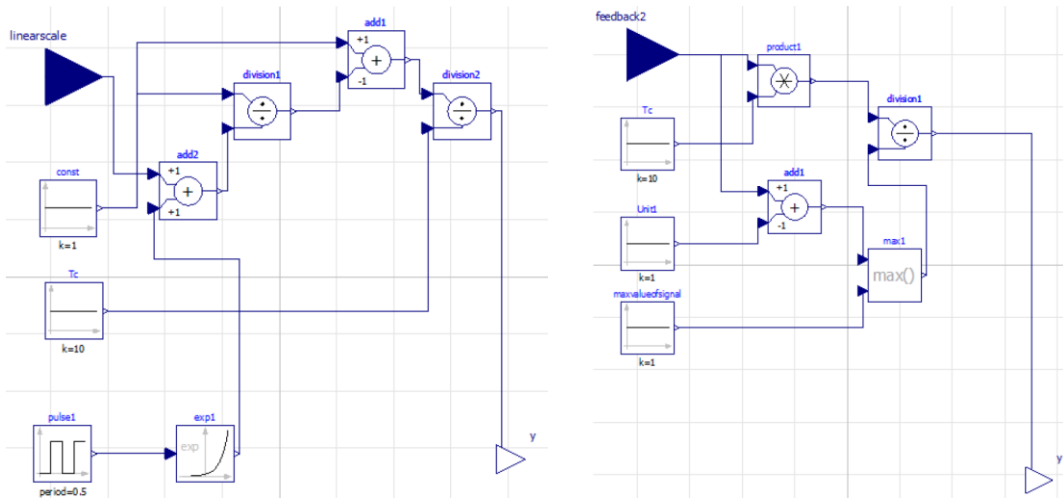


Figure 8: Model of the first (left) and second (right) blocks of control

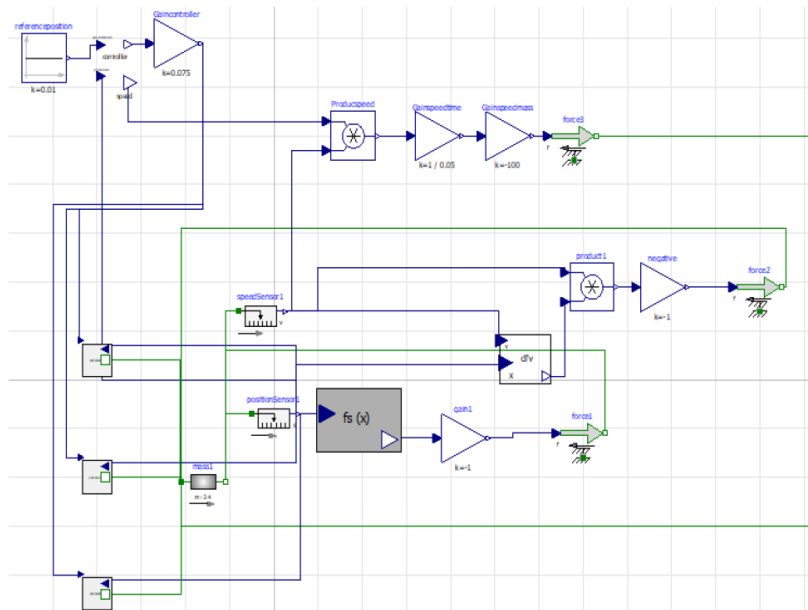


Figure 9: Controller implementation in the complete system

4 SIMULATIONS ON VARYING THE TEMPERATURE

4.1 Temperature effects

Finally, simulations are executed to test the motor behavior at different temperatures. The results illustrated in the next paragraphs show the differences between the two main reference scenarios of standard environmental temperature (20° C) and the printer operating temperature

(-15°C). The effect of the temperature on the system dynamic depends on two main phenomena: a reduction of electrical resistance in the copper, which is in the order of -14% , and an increasing of the residual flux density and intrinsic coercive field intensity generated by the motor permanent magnet. Both the effects contribute to increase the magnetic fields and hence the force exchanged between stator and slider.

4.2 Position

In the reference scenario adopted, it is possible to observe that the positioning is affected by an error of 0.5 mm . The absolute value of this error, at this stage of development of the simulator, should not be considered significant. It is instead relevant its percentage value, close to 5% of the position set point.

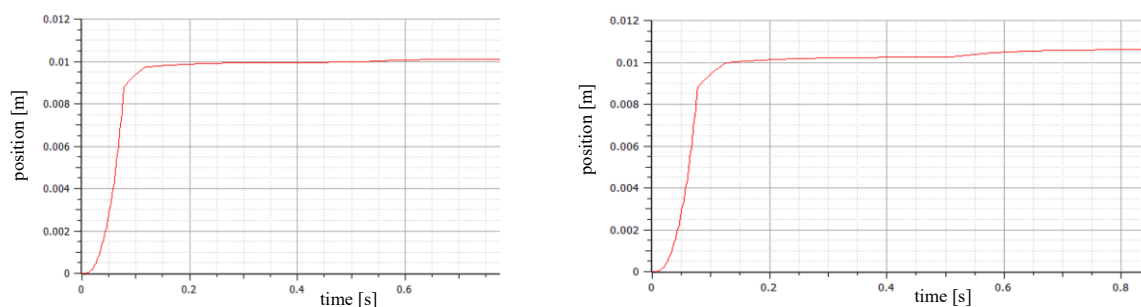


Figure 10: Position transient at 20°C (left) and -15°C (right)

4.3 Speed

On decreasing the temperature, it is possible to observe that the speed increases of about 3% , as well as the speed produced by the current pulse when the motor stops.

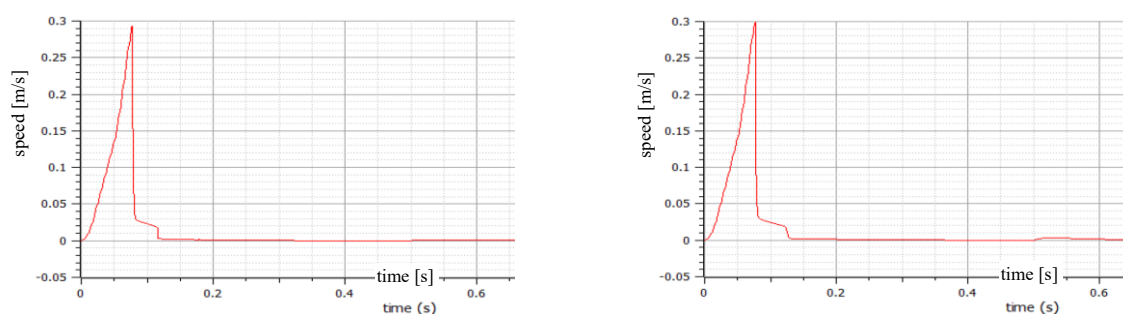


Figure 11: Speed transient at 20°C (left) and -15°C (right)

5 CONCLUSIONS

A model of a linear motor that represents the functioning at low temperature has been implemented in Open Modelica environment. Such a model has been used to a positioning task at the operating temperature of -15°C . It reproduces with great accuracy the functioning of the stage subsystem and the consequent behavior of the machine, taking into account the influence of the temperature on the solenoid intensity, the voltage, the exerted forces, the velocity and the

position, which shows an error related to the low temperature effect in the order of 5%. The results obtained confirm that, at the temperatures considered, the motor positioning error is significant and undermines the correct operation of the controller. On the basis of the values found, the correct control system is currently under development.

ACKNOWLEDGEMENTS

This work was made possible thanks to the contribution provided by Eng. Adrián Vieco Jiménez in implementing and executing the Open Modelica model.

REFERENCES

- [1] Silvestri, M. and Pedrazzoli, P. and Boër, C. and Rovere, D. *Compensating High Precision Positioning Machine Tools by a Self Learning Capable Controller*, Proceedings of the 11th International Conference of EUSPEN, Como, 23-27 Maggio 2011, pp. 121-124.
- [2] Silvestri, M. and Confalonieri, M. and Ferrario, A. and Bettoni, A. and Floris, M. and Banfi, M. *Use of Laser Scanners in Machine Tools to Implement Freeform Parts Machining and Quality Control*, in Advances in Neural Networks, Chapter 52, Ed. Springer Publishing International
- [3] Silvestri, M. and Confalonieri, M. and Ferrario, A. *Piezoelectric Actuators for Micro Positioning Stages in Automated Machines: Experimental Characterization of Open Loop Implementations*, FME Transactions (2017) 45, 331-338, doi:10.5937/fmet1703331S
- [4] Avventuroso, G. and Silvestri, M. and Pedrazzoli, P. *A Networked Production System to Implement Virtual Enterprise and Product Lifecycle Information Loops*, IFAC-PapersOnLine, Volume 50, Issue 1, July 2017, pp. 7964-7969, doi: 10.1016/j.ifacol.2017.08.902
- [5] Elviri, L. and Foresti, R. and Bergonzi, C. and Zimetti, F. and Marchi, C. and Bianchera, A. and Bernini, F. and Silvestri, M. and Bettini, R. *Highly defined 3D printed chitosan scaffolds featuring improved cell growth*, Biomed. Mater. Vol. 12, N. 4. DOI: 10.1088/1748-605X/aa7692
- [6] Bergonzi, C. and Di Natale, A. and Zimetti, F. and Marchi, C. and Bianchera, A. and Bernini, F. and Silvestri, M. and Bettini, R. and Elviri, L. *Study of 3D-printed chitosan scaffold features after different post-printing gelation processes*, Scientific Reports volume 9, Article number: 362 (2019) <https://doi.org/10.1038/s41598-018-36613-8>
- [7] Molis, M. and Matkevicius, E. and Radzevicius, L. *Calculation of the Mathematical Model of the Linear Motor* – Electronics and Electrical Engineering. - Kaunas: Technologija, 2009. - No. 7(95). - P. 91-94
- [8] Song, C-W and Lee, S-Yop *Design of a Solenoid Actuator with a Magnetic Plunger for Miniaturized Segment Robots*, Appl. Sci. 2015, 5(3), 595-607
- [9] Xie, Q. *Modeling and Control of Linear Motor feed drives for grinding machines* – Georgia Institute of Technology, PhD dissertation, May 2008.
- [10] Kaneko, S. and Sato, R. and Tsutsumi, M. *Mathematical Model of Linear Motor Stage with Non-Linear Friction Characteristics*, Journal of Advanced Mechanical Design, Systems, and Manufacturing, 2008 Volume 2 Issue 4 Pages 675-684, DOI <https://doi.org/10.1299/jamdsm.2.675>

SIMULATION OF A ROBOTIC ARM FOR MULTI-DIRECTIONAL 3D PRINTING

Kevin Castelli*, **Hermes Giberti** †

* Dipartimento di Ingegneria Industriale e dell'Informazione
Università di Pavia
via Ferrata 5, 27100, Pavia, Italy
email: kevin.castelli@unipv.it

† Dipartimento di Ingegneria Industriale e dell'Informazione
Università di Pavia
via Ferrata 5, 27100, Pavia, Italy
email: hermes.giberti@unipv.it

Key words: Serial Manipulator, Simulation, Multi-Direction 3D Printing, FDM

Abstract. The need to investigate new solutions and novel 3D building strategies not only requires the development of new slicing algorithms and the exploitation of machines with more than 3 Dofs, but also a safe and reliable test-bench to optimize all the phases of the process. The following article describes the assessment by simulation of suitable control architectures for the realization of a Fused Deposition Modeling printer based on a 6 Dofs serial manipulator. The focus is put on the obtained position and speed profiles for unidirectional and multi-directional 3D printing to determine the weak points associated with each control strategy.

1 Introduction

Additive Manufacturing (AM), in the last decades, has aroused great interest among people and researchers thanks to its flexibility and versatility, making it the most widespread solution for prototyping and one-off production. One of the advantages of AM is that it can build complex shapes that with Subtractive Manufacturing would not have been feasible. AM technologies, on the other hand, are a direct evolution of subtractive ones and this can be seen from the exploitation of the same machines, but also of the same machining strategy (layer based approach). This represents a constraint to the potentiality of AM to build 3D object in three dimensional space (multi-directional printing) and not just an approximation by 2D features (unidirectional printing). Therefore, new solutions and novel building strategies are being researched (examples can be found in [1],[2],[3]). Industrial robots have been used to this end. Integration is required to perform 3D printing task, from the outline of the working cell to the definition of the control strategy. The flexibility given by systems with more than 3 Degrees of Freedom (Dofs) increases the complexity of the design of the working cell, of the tool and of the trajectories that prevent the collision with the piece ([4] shows this by adopting service robots instead). Simulation is a safe and indispensable tool to carry out this task.

In [5], the authors report their experience with an analogous machine focusing on a visual feedback of the material deposition in the off-line environment. [6] highlights issues arising when the printing process does not reflect the one prescribed, especially related to the machine itself. The authors of [7], [8] and [9] describe their involvement with conventional and multi-directional printing with industrial robots. [10] is an example of three dimensional tool-path generation.

In this context, the following article describes the assessment of suitable control architectures for the realization of a Fused Deposition Modeling (FDM) printer based on a 6 Dofs industrial serial manipulator. Off-line programming (using the software released by the manufacturer for better compliance with the physical robot system) is preferred to validate the robot behavior in order to avoid wastes and damage to the machine. One additional advantage of the simulation is the possibility to easily exchange virtual subsystem with the real ones to assess them individually.

For each identified control strategy, that easily integrate the extruder with the robotic system, the results obtained are shown for paths generated for conventional as well as for multi-directional printing. The focus is put on the obtained position and speed profiles, two of the several aspects that yield a minimization of the error between designed and manufactured object, but strictly concern the robotic system in itself. Simulation results are then compared to the acquisitions on the physical system.

The following article recalls in Section 2 a core aspect of the AM technology here addressed, that is extrusion flow rate; in Section 3, path planning is deepened to highlight the robotic system requirements and constraints; the extrusion subsystems and robot are then briefly introduced as well as its virtual counterpart (Section 4). In the following section, the different control strategies are discussed and simulated (Section 5-6). In Section 7, the results are summarized.

2 Extrusion flow rate

FDM technology can be described as the controlled deposition of molten material on a substrate. In order to determine how much filament needs to be forward through the nozzle, it's important to understand how the extruded material will be added to the existing substrate. The nozzle will be spaced of a quantity h from the interested surface and some material will be squirted out taking on a certain shape, usually approximated by a rounded rectangle (see Fig.1 where the convention used to determine the transferred section are indicated). This shape can be deterministically obtained (under the assumption that w is smaller than the surface curvature) by solving equation (1) that represents the relationship among the volumetric flow rates at the filament, nozzle and substrate.

$$A_{wire}V_{robot} = \frac{\pi d_n^2}{4}V_{extrusion} = \frac{\pi d_f^2}{4}V_{feed} \quad (1)$$

The extruded material could be not only constrained frontally, but also on one or both sides. The distance between two adjacent wires is a parameter used moreover to control the density of the build.

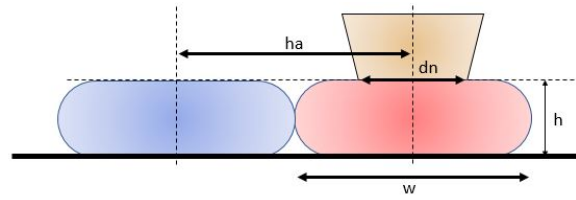


Figure 1: Material deposition. Nomenclature: nozzle diameter (dn), layer height (h), width (w) and hatch distance (ha)

Thus, a FDM system has to guarantee the designed robot-filament speed ratio as well as the relative positioning.

3 Path planning

In the previous section, some tool path constrains have been derived related to the process itself. An additional requirement, self-explanatory but not trivial, is that the resulting trajectory reconstructs the 3D CAD model the operator needs to build, not only under a geometrical, but also mechanical point of view. The trace that the TCP (Tool Center Point) has to follow can be determined in several ways.

Conventional 3D printing strategies only require to evaluate the position of the nozzle outlet, approximated as a point, in \mathbb{R}^3 . Available software return the intersection (contours) of the mesh (stored in the STL file) with planes parallel to the printing bed (transformation to \mathbb{R}^2) accounting for the infill or the need for support material.

In the case of multi-direction building strategy, this approach undergoes some modification to compute the generic plane-plane intersection or the recognition of unidirectional blocks to recycle the standard algorithms. Fig.2 shows a robot arm during the building process of a circular rib on a cylindrical surface.

A third approach takes advantage of functions that map a complete 3D problem (thus including



Figure 2: Circular rib

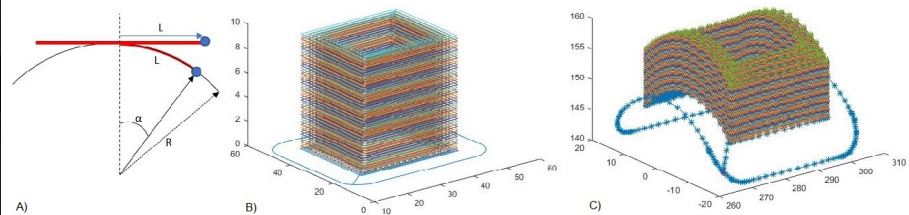


Figure 3: Multi-direction printing by slicing after a $\mathbb{R}^3 \rightarrow \mathbb{R}^2$ map

the orientation) to a mono-directional one in order to use commercial slicing software before reverting to the initial space ([11]). In Fig.3 an example is reported where geometrical consideration (A) are used to determine the dimension of the CAD model that later undergoes slicing (B). The tool path is mapped in the required domain and without loss of information (C).

4 Physical and offline systems

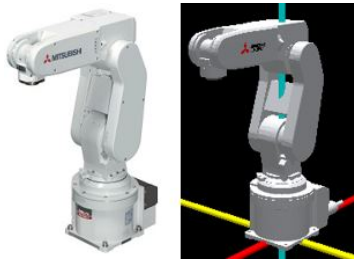


Figure 4: Real system vs virtual twin (*RT ToolBox3*)



Figure 5: Extrusion system

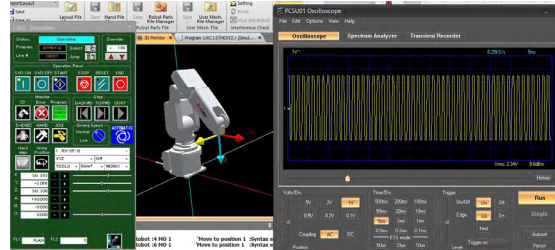


Figure 6: *Virtual robot - Real Extruder*: the PWM is read by means of an oscilloscope

The overall machine is constituted by two subsystems, an industrial 6 DoFs robot (Mitsubishi RV-2F-Q, Fig.4) with its control unit and a commercial FDM extruder controlled by means of an Arduino Mega with Ethernet connection and custom made firmware (Fig.5). The robot moves and orients the nozzle to comply with the requirements introduced heretofore.

The extruder accepts instructions to set the heat block temperature and the motor/fan speeds and to inquire the current temperature. The firmware is coded to be able to comply any new instruction as soon as it is read and processed.

The robot is replicated in the manufacturer software (*RT Tool-Box3*) that offers offline all the functionalities that the real system posses (the one that are going to be extensively used are TCP/IP communication, motion planner and oscillograph) because when recreating the digital twin it is not only important to match the mechanical aspects, but especially those concerning movements and communication.

Here the possible combination between physical and simulated systems are listed pointing out some remarks. The dissertation will afterwards vert solely on the robot.

- *Virtual robot - Virtual Extruder*: Consider each system on its own. Used solely during the early stage of the assessment of the robotic system. The offline extruder requires a code capable of reproducing the reading and the generation of the output signals (pulse-width modulation, PWM, of the stepper motor driver and of the MOSFET).
- *Real robot - Virtual Extruder*: This case could be used when the robot is reading the G-code and mastering the extruder. It's advised during the first robot tests to avoid that the heated element fortuitously collides with any object present in the cell.
- *Virtual robot - Real Extruder*: This combination can be used to validate the extrusion system during the print while keeping it still (see Fig.6).
- *Real robot - Real Extruder*: the system is printing.

5 Control architectures

Industrial robots offer several means to communicate with the external world: I/O modules, serial and Ethernet ports. It has been decided for the two subsystems to talk via Ethernet to simplify future addition of devices in the network. Thus, a LAN is designed with the robot as server and the extruder as client (with the possibility to be converted into a server).

Two possible scenarios therefore arise. The first (*DL, Data Link*) sees the robotic system as any CNC machine, to which is feed a series of target positions leaving the motion law assignment to the built-in functions. The second (*RT, Real Time*) relies on real-time protocols to master the actual motion profile, therefore it should make sure that the synchronization of the extruder to the TCP speed is obtained as designed.

Both solutions requires an extra device (although the *DL* case might be adjusted to read a G-code file on the hard disk of the controller) able to guarantee the time interval between two instructions (down to milliseconds) and to process the trajectory. Therefore, a PC is set up to belong to the LAN. On the computer side all the planning is performed ahead (using *MATLAB*) and, once checked and post-processed, the data is send to the robot controller where the control loops are closed.

In order to mimic these configurations offline, the only alterations required concern the LAN setup. The IP addresses identifying the robot ad the computer become one, that is, since all the talking has to happen internally to the PC, *127.0.0.1* (i.e. localhost). The communication is finally established by indicating the port, in both software, according to the scenario selected. This resolves into the following cases.

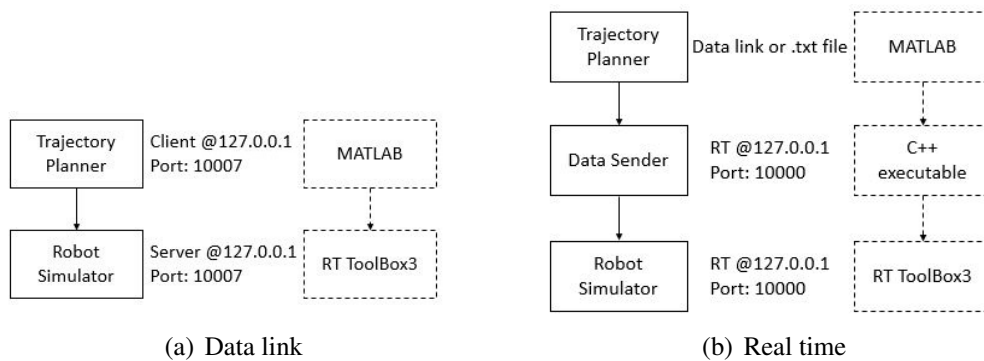


Figure 7: Off-line control scenario: data link and real time

5.1 Data Link

The data returned by the slicer (G-code) is post-processed and send over Ethernet with TCP/IP protocol. The data packet is constituted by the X-Y-Z coordinates followed by the A-B-C to impose the orientation of the tool and the commanded velocity (feed).

In *MATLAB* the communication is opened using the function `tcpip(IP,port)` (`tcpip('127.0.0.1', 10007);`) and by setting the terminator and the timeout. Analogously, the extruder could be

included in the simulation.

In *RT ToolBox3*, the *IP*, *Mode*, *Protocol* and *Packet type* parameters need to be customized to match the ones demanded by the network.

5.2 Real Time

The robot controller can retrieve the reference position at real-time (in cycle units of 7.11 [ms]) and execute it. To operate in this mode, it is required the adoption of a specific UDP packet, determined by manufacturer. The size of the data package is fixed to 196 byte, either for monitoring or instructing and ordering method is little-endian.

In this configuration an executable (.exe, written in c++) is used to generate the data packet according to the prescribed structure and to deal with the transmission and reception of the information. The trajectory, sampled every 7.11[ms] and stored in a text file (although it could be streamed via localhost as well), is read one line at a time at every cycle.

In *RT ToolBox3*, the default port for real time is the 10000, so only the network IP has to be set.

6 Simulation

In this section, the simulation conducted are going to be deepened for both a unidirectional case as well for a multi-direction build. The *DL* is configured to transit from one instruction to the other using a 1[mm] radius circumference.

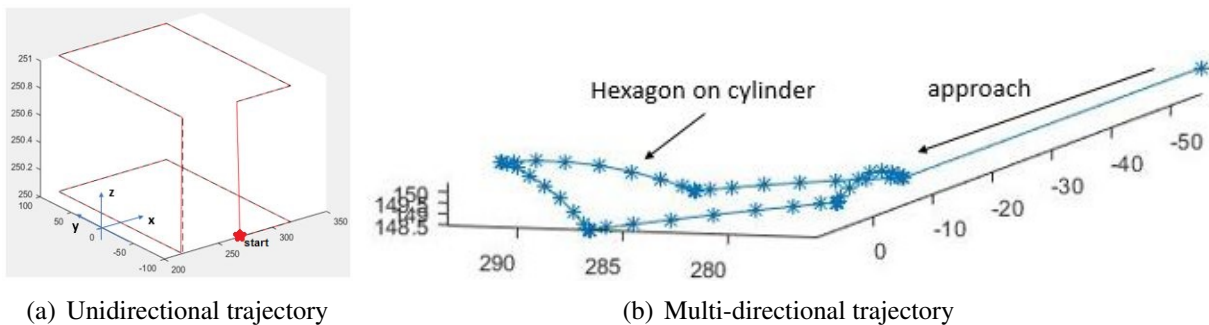


Figure 8: Representation of the test cases trajectories

6.1 Unidirectional printing (in \mathbb{R}^2)

To simulate the behavior of the AM machine with this particular built philosophy, a simple two layer square is chosen (see Fig.8(a)) with 35.16 [mm/s] feed.

In Fig.9(a), it's possible to see a corner using the *DL* approach; in Fig.9(b), the same feature, but with the *RT* strategy. What can be noticed is that even *RT* give rise to a smooth corner despite the fact that was not instructed, thus a motion planner is still applied to the data via UDP. In both cases a positioning error is present.

In Fig.9(c) and 9(d), the respective speed module profiles (evaluated along the path), obtained by numerical derivation can be seen. The *DL* shows less bounded fluctuation (± 1 [mm/s]) around

the feed then the *RT*, although it tends to approach zero speed during the path more markedly.

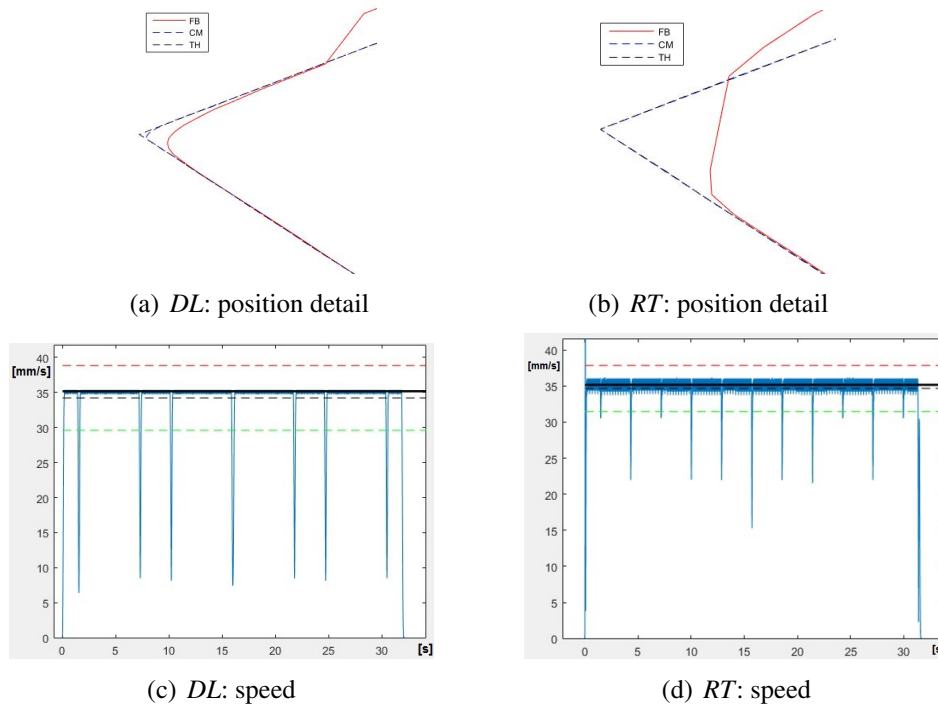


Figure 9: Unidirectional printing simulation: *DL* vs *RT*

6.2 Multi-directional printing (in \mathbb{R}^3)

The trajectory, that can be seen in Fig.8(b), has to be followed at 15 [mm/s]. The path is obtained by slicing a hexagon by a cylindrical surface (2nd approach of the section on path planning).

6.2.1 Real Time case

For the *RT* case, the motion law is designed offline by means of a look-ahead algorithm and discretized with a 7.11 [ms] interval. The robot is moved imposing the reference at the TCP. In Fig.10(a) the position is depicted while in Fig.10(b) the positioning errors (only the rotation around the X-axis (*A*) are shown since the cylindrical surface is oriented in that direction, therefore any normal vector on the surface will intersect the X-axis). In Fig.10(c)-10(d), the speed profile simulated is superimposed to the theoretical one and the error profiles are shown, as previously the robot controller performed a smoothing operation on the commanded points. Running the *RT* example on the real system, outputted similar results to the one simulated, but with the introduction of terms unmanageable by the simulator, strictly related to the physical system considered (Fig.11).

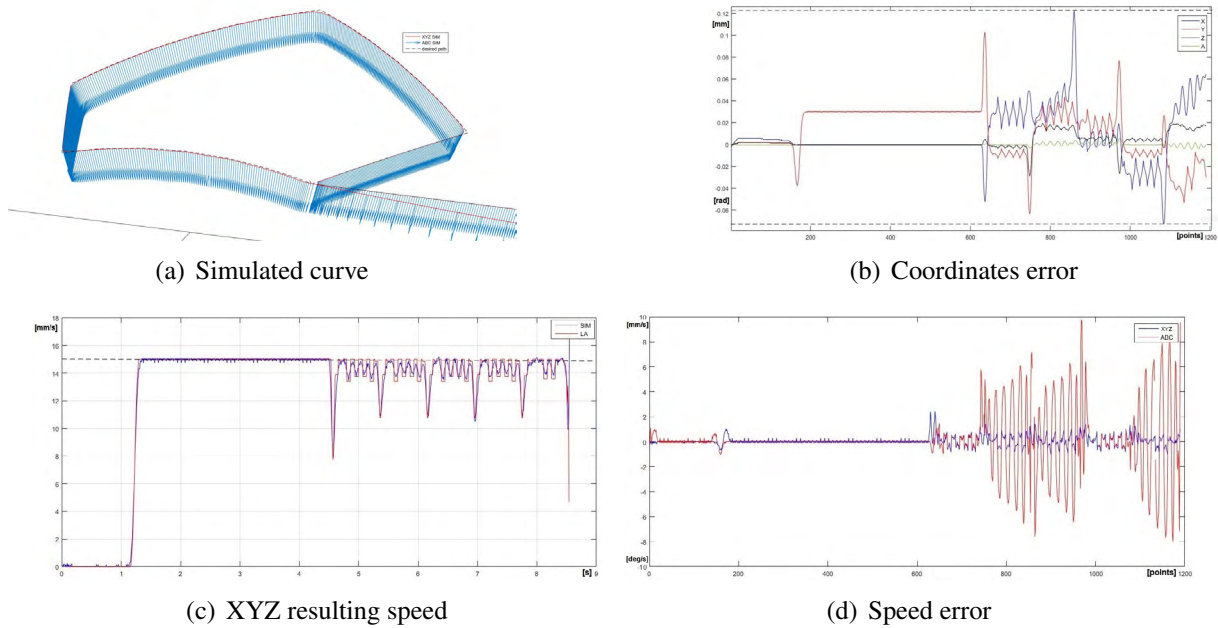


Figure 10: RT: simulation

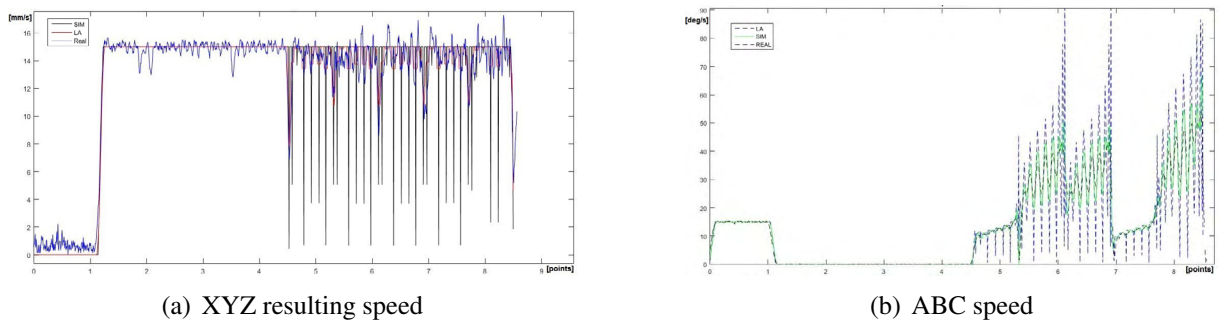


Figure 11: RT: real

6.2.2 Data Link case

Fig.12(a)-12(b) report the speed for the simulation of this typology. What can be inferred is that the system is not capable of guaranteeing the feed speed during the build on the cylinder giving the sampling distance chosen. One possible solution could be to let the system know more than one point at a time, therefore developing a more sophisticated mean to synchronize the speeds. An other possible fix could be to use the simulation itself to predict the correct extrusion speed. At the end in Fig.12(c), it possible to inspect the deviation from the one desired.

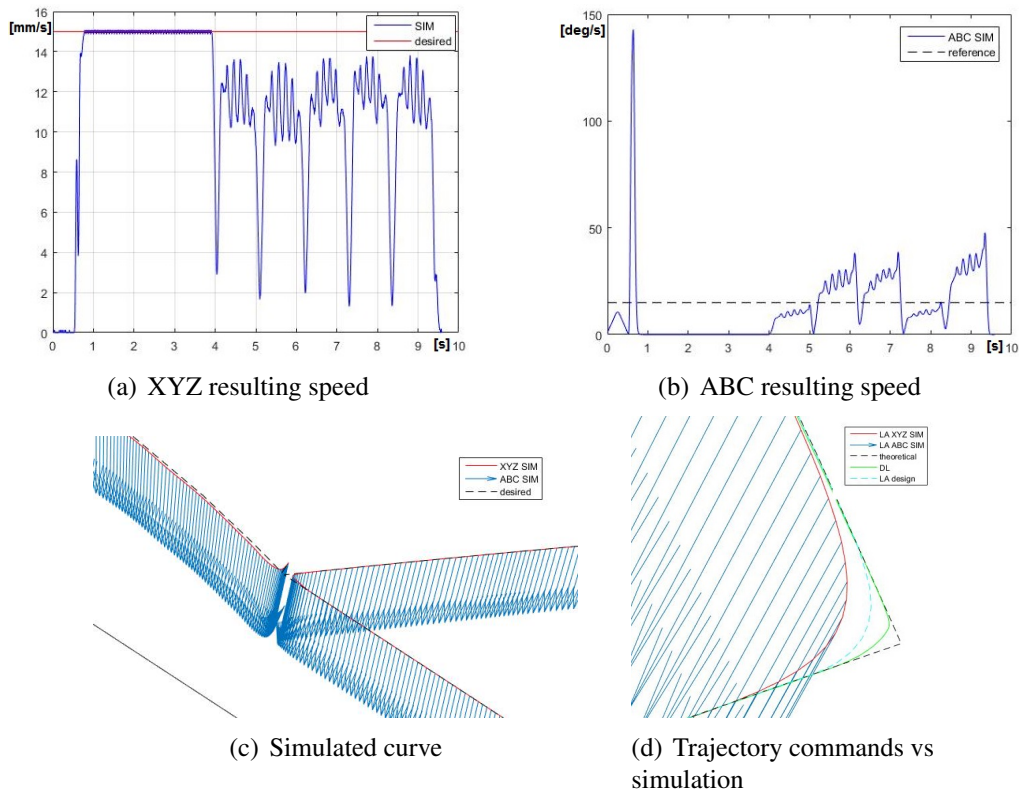


Figure 12: DL: simulation

6.2.3 Comparison

In Fig.12(d), the difference among the theoretical curve, the one evaluated with the look ahead algorithm and the results of the simulations is portrayed. A corner is enlarged because it's the most delicate situation since it has to be assured that the robot arm moves smoothly without under or over extrusion. The *DL* method is less affected by speed fluctuations when performing unidirectional printing. The *RT* is able to follow more closely the speed profile designed along the path while reorienting the tool.

7 Conclusions

This paper describes the assessment of two control strategy for a 6 Dofs robotic arm equipped to become a FDM printer. A LAN is created to connect the robot, the extruder and in case a PC that enables to master the system using real time control or via Ethernet communication. Off-line programming is chosen to inquire the robot behavior in order to avoid wastes or damage to the machine. The simulation accounts for the dynamic behavior of the robot as well as for the communication with the external world. Obtained position and speed profiles are used to spot strengths and weaknesses of each method, having identified them as principle factors, on the robot side, that affect the final result. From the results reported, it's possible to comprehend how spacial and time discretization affects the

speed profile and how the *DL* method could be preferred over the *RT* in the case of unidirectional print and vice versa.

The implementation of an hybrid solution might lead to an optimal result and moreover it will require to instruct less points during the execution of straight lines, that fall into the *DL* category, than a pure *Real Time* control strategy.

REFERENCES

- [1] Stavropoulos, P., Foteinopoulos, P., Papacharalampopoulos, A. Bikas, H., *Addressing the challenges for the industrial application of additive manufacturing: Towards a hybrid solution*. International Journal of Lightweight Materials and Manufacture (2018).
- [2] Castelli, K., Giberti, H., *A Preliminary 6 Dofs Robot Based Setup for Fused Deposition Modeling*. Advances in Italian Mechanism Science. IFToMM ITALY 2018. (2019).
- [3] Giberti, H., Sbaglia, L., Silvestri, M., *Mechatronic design for an extrusion-based additive manufacturing machine*. Machines 5(4), art. no. 29. (2017).
- [4] McPherson, J., and Zhou, W., *A chunk-based slicer for cooperative 3D printing*. Rapid Prototyping Journal, Vol. 24 Issue: 9. (2018)
- [5] Zhang, G.Q., Spaak, A., Martinez, C., Lasko, D.T., Zhang, B., Fuhlbrigge, T.A., *Robotic Additive Manufacturing Process Simulation towards Design and Analysis with Building Parameter in Consideration*. IEEE International Conference on Automation Science and Engineering (CASE). (2016).
- [6] Evjemo, L.D. et al., *Additive manufacturing by robot manipulator: An overview of the state-of-the-art and proof-of-concept results*. 22nd IEEE International Conference on Emerging Technologies and Factory Automation (2017).
- [7] Pollák, M., Török, J., Zajac, J., Kočiško, M. and Telišková, M., *The structural design of 3D print head and execution of printing via the robotic arm ABB IRB 140*. 5th International Conference on Industrial Engineering and Applications (ICIEA). (2018).
- [8] Kubalak, J.R., Wicks, A.L., Williams, C.B., *Exploring multi-axis material extrusion additive manufacturing for improving mechanical properties of printed parts*. Rapid Prototyping Journal (2018).
- [9] Dine, A., Vosniakos, G.-C., *On the development of a robot-operated 3D-printer*. Procedia Manufacturing, Volume 17. (2018).
- [10] Isa, M.A., Lazoglu, I., *Five-axis additive manufacturing of freeform models through buildup of transition layers*. Journal of Manufacturing Systems, Volume 50. (2019).
- [11] Zhao, G., Ma, G., Feng, J. et al., *Nonplanar slicing and path generation methods for robotic additive manufacturing*. Int. J. Adv. Manuf. Technol. (2018) 96: 3149.

A GENERATIVE DESIGN OPTIMIZATION APPROACH FOR ADDITIVE MANUFACTURING

N. STRÖMBERG

Department of Mechanical Engineering
Örebro University
SE-701 82 Örebro, Sweden
e-mail: niclas.stromberg@oru.se, web page: <http://www.fema.se/>

Key words: Topology optimization, Support vector machines, Lattice Structures, Metamodels

Abstract. In this paper, we present a generative design optimization (GDO) approach for additive manufacturing (AM) by using topology optimization, support vector machines, cellular lattice structures (CLS), design of experiments, morphing and metamodel-based design optimization. By starting from appropriate design domains, a trade-off curve of design concepts is generated by SIMP-based topology optimization (TO). Then, a smooth implicit representation of the TO-solution is established by classifying the discrete density values using soft non-linear support vector machines (SVM). Instead of using the standard soft non-linear SVM of Cortez and Vapnik, we classify the TO solutions by using the 1-norm SVM of Mangasarian. In such manner, the classification is obtained by linear programming instead of quadratic programming. The implicit SVM-model is further modified by incorporating cellular lattice structures, such as e.g. Gyroid lattice structures, by applying boolean operators. Design of experiments using finite element analysis are then set up by morphing the CLS-modified SVM models for different volume fractions. Finally, metamodel-based design optimization is performed by using optimal ensembles of polynomial regression models, Kriging, radial basis function networks, polynomial chaos expansion and support vector regression. The steps presented above constitute our proposed generative design optimization approach for additive manufacturing and are presented in more detail in the paper.

1 INTRODUCTION

Today, topology optimization is a standard tool in product development [1]. In particular, the problem of minimization of compliance for a prescribed volume fraction is most established. But still the transfer of the optimal solution of element densities to a CAD geometry might be time consuming. In this work, we propose an automatic postprocessing approach of topology optimization solutions by letting support vector machines classify the TO solutions of elements with no density and density of ones. In Figure 1, the workflow of the proposed approach is demonstrated by automatically generating a stl-file of graded Schwarz-D lattice structure starting from a SIMP-based TO solution of a design domain subjected to prescribed boundary conditions. The topic of this paper is to present the key ideas of the proposed 1-norm SVM-based TO

postprocessing approach and discuss how this can be used to set up metamodel-based design optimization of TO-based concepts.

The soft non-linear support vector machine introduced by Cortes and Vapnik [2] defines a paradigm shift in machine learning and the paper has been cited more than 15000 times. By adopting the kernel trick and the soft penalization, we are able to classify non-linear separable data including misclassified data points. In this paper, we classify three-dimensional TO solutions by applying the 1-norm SVM suggested by Mangasarian [5, 6]. In such manner, the support vectors defining the separating boundary of material (element densities with values of ones) and no material (element densities with values of zeros) are obtained by linear programming (LP). The main difference of the two SVM approaches is that the Euclidean norm used to measure the distance to the support vectors in the original formulation is switched to the taxicab norm in Mangasarian’s formulation. In such manner, the SVM-based boundary is obtained by solving a LP-problem instead of a QP-problem.

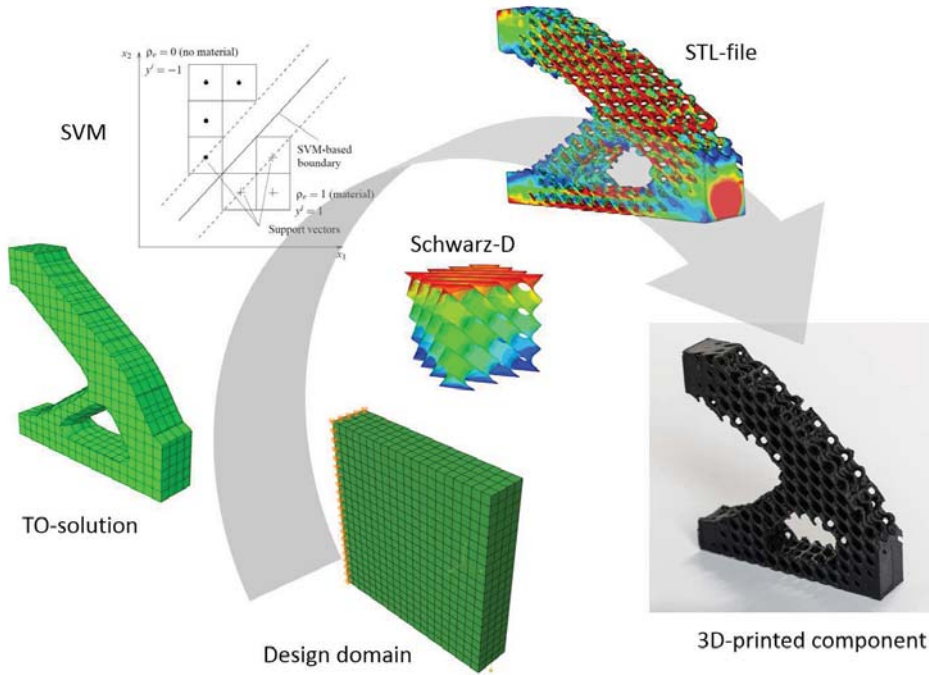


Figure 1: A 3D-printed component from a stl-file of graded Schwarz-D lattice structures generated automatically by the proposed SVM-based postprocessing approach.

In this paper, the TO solutions are obtained by solving the hyperoptimal formulation suggested in Strömberg [7]. Instead of minimizing the compliance c subjected to a constraint on the material volume V , the product cV^η is minimized for $\eta > 0$. This new compliance-volume product is minimized for linear elastic structures by using the established SIMP (Solid Isotropic Material with Penalization) model suggested by Bendsøe [9], see also Zhou and Rozvany [10]

who independently developed and implemented the SIMP model. The concept of hyperoptimality was introduced by Rozvany et al. [11]. The approach has also been explored in the field of evolutionary structural optimization (ESO). For instance, Tanskanen [12] performed a theoretical study on this topic and Edwards et al. [13] compared ESO and SIMP by using this objective. For readers not familiar with topology optimization we suggest the well-known textbook by Bendsøe and Sigmund [14].

The outline of the paper is the following: in the next section the SIMP-based hyperoptimality TO formulation is reviewed, in section 3 the 1-norm SVM-based TO postprocessing approach is presented, then the proposed postprocessing approach is demonstrated by generating stl-files of three-dimensional benchmarks and, finally, some concluding remarks are given.

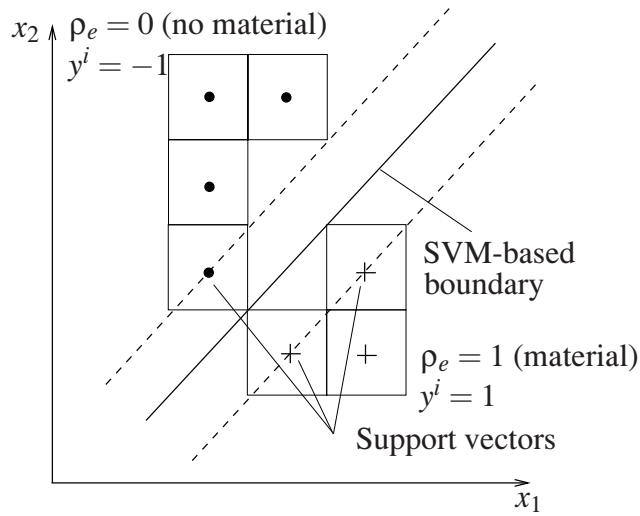


Figure 2: The basic idea of the proposed SVM-based postprocessing approach.

2 The HYPEROPTIMALITY FORMULATION

Let us consider a linear elastic design domain which is parameterized by using the SIMP technique, i.e. each finite element is provided with a density variable ρ_e and the global stiffness of the design domain is given by

$$\mathbf{K} = \mathbf{K}(\rho) = \prod_e \rho_e^n \mathbf{k}_e, \quad (1)$$

where \prod is an assembly operator and the vector ρ contains density variables $\varepsilon \leq \rho_e \leq 1$, where ε is a small positive number representing zero density in order to avoid difficulties with singular stiffness matrices. The value $\rho_e = 1$ represents of course a completely filled element with material and $\rho_e = \varepsilon$ represents no material.

The total volume of the design $V = V(\rho)$ is obtained as

$$V = \sum_e \rho_e V_e, \quad (2)$$

where V_e represents the volume of element e . The compliance is defined by

$$c = \mathbf{F}^T \mathbf{d}, \quad (3)$$

where \mathbf{F} represents the external forces and \mathbf{d} is the displacement vector. For a given density distribution $\hat{\rho}$, the state of the system $\mathbf{d} = \{\mathbf{d}^A\}$ is obtained by solving $\mathbf{K}(\hat{\rho})\mathbf{d} = \mathbf{F}$.

For the state problem presented above, we consider now the following optimization problem:

$$\begin{cases} \min_{(\rho, \mathbf{x})} cV^\eta \\ \text{s.t.} \begin{cases} \mathbf{K}\mathbf{d} = \mathbf{F}, \\ \boldsymbol{\varepsilon} \leq \rho \leq \mathbf{1}, \end{cases} \end{cases} \quad (4)$$

where $\boldsymbol{\varepsilon} = \{\varepsilon, \dots, \varepsilon\}^T$, $\mathbf{1} = \{1, \dots, 1\}^T$ and $\eta > 0$ is a new design parameter introduced to be able to define different products of the compliance and the volume. In Strömberg [7], trade-off curves between compliance and volume were generated by changing the value of this design parameter.

The optimization problem in (4) is solved by sequential LP by using a nested approach such that problem is solved in the density variables only, i.e. $\mathbf{d} = \mathbf{d}(\rho) = \mathbf{K}^{-1}\mathbf{F}$. Thus, we consider

$$\begin{cases} \min_{\rho} f = f(\rho) = \mathbf{F}^T \mathbf{d}(\rho)V(\rho)^\eta \\ \text{s.t.} \boldsymbol{\varepsilon} \leq \rho \leq \mathbf{1}. \end{cases} \quad (5)$$

By using

$$\xi_e = \frac{\partial c}{\partial \rho_e} = -\mathbf{d}^T \frac{\partial \mathbf{K}}{\partial \rho_e} \mathbf{d}, \quad (6)$$

where

$$\frac{\partial \mathbf{K}}{\partial \rho_e} = n\rho_e^{n-1} \mathbf{k}_e, \quad (7)$$

the sensitivity of the objective in (5) becomes

$$s_e = \frac{\partial f}{\partial \rho_e} = \xi_e V^\eta + \mathbf{F}^T \mathbf{d} \eta V^{(\eta-1)} V_e. \quad (8)$$

Sigmund's filter [15] is also applied when the sensitivities are calculated in order to avoid well-known difficulties of mesh-sensitivity and checkerboards. Instead of applying this filter on the ultimate sensitivities s_e , we have found it more efficient to only filter ξ_e . This done by applying the following formula:

$$\hat{\xi}_e = \frac{\sum_{f=1}^{n_{el}} \delta_f \rho_f \xi_f}{\rho_e \sum_{f=1}^{n_{el}} \delta_f}, \quad (9)$$

where

$$\delta_f = (r_{\min} - \text{dist}(e, f))_+. \quad (10)$$

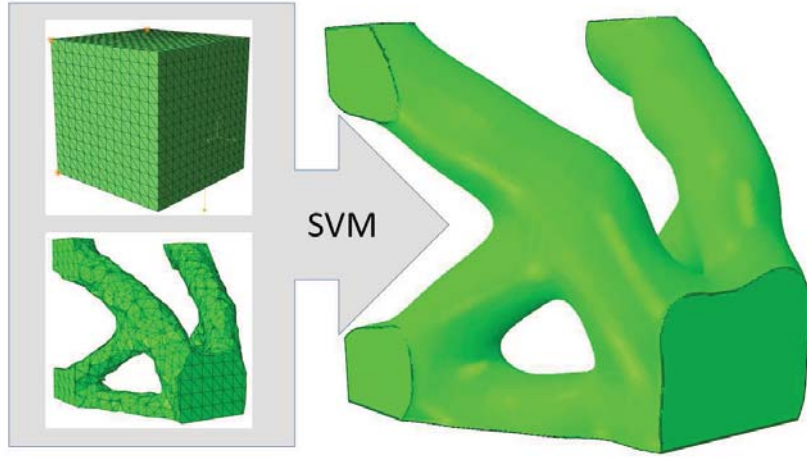


Figure 3: The cubic benchmark. The shaded geometry to the right is the optimal SVM-boundary in (22) of the SIMP-based TO solution shown at the lower left. The design domain with boundary conditions is shown at the upper left.

In this latter relationship, $\text{dist}(e, f)$ denotes the distance between the centers of element e and f , and r_{\min} is the filter radius. Thus, the sensitivity in (8) is modified to read

$$\hat{s}_e = \hat{\xi}_e V^\eta + \mathbf{F}^T \mathbf{d} \eta V^{(\eta-1)} V_e. \quad (11)$$

All \hat{s}_e are collected in the column vector $\hat{\mathbf{s}}$.

Finally, by using $\hat{\mathbf{s}}$ to linearize (5) according to the procedure discussed above, we obtain the following LP-problem at an iteration point $\rho = \hat{\rho}$:

$$\begin{cases} \min_{\rho} \hat{\mathbf{s}}^T \rho \\ \text{s.t. } \hat{\rho} + \rho^l \leq \rho \leq \hat{\rho} + \rho^u, \end{cases} \quad (12)$$

where ρ^l and ρ^u define lower and upper move limits, respectively.

The separable constraints in (12) imply that the objective can be minimized separately for each element density. Thus, the problem in (12) is solved easily by the following scheme:

$$\rho_e = \begin{cases} \hat{\rho}_e + \rho_e^l & \text{if } \hat{s}_e > 0, \\ \hat{\rho}_e + \rho_e^u & \text{if } \hat{s}_e < 0, \\ \hat{\rho}_e & \text{otherwise.} \end{cases} \quad (13)$$

This scheme was suggested and utilized in Strömberg [7] to solve three-dimensional TO problems with contact conditions and manufacturing constraints. In a recent paper [8], topology optimization of orthotropic elastic bodies in unilateral contact with mortar conditions was studied.

3 THE SUPPORT VECTOR MACHINE APPROACH

For a SIMP-based topology optimization formulation as presented in the previous section, each element e is equipped with a center point \mathbf{x}^e and a density value ρ_e , where $\rho_e = 0$ (or a

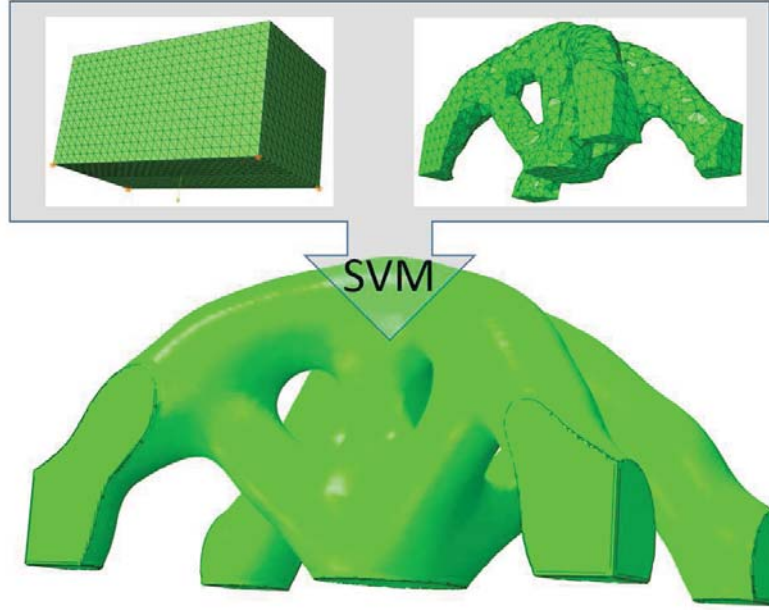


Figure 4: Michell's benchmark. The shaded geometry at the bottom is the optimal SVM-boundary in (22) of the SIMP-based TO solution shown at the upper right. The design domain with boundary conditions is shown at the upper left.

small number ε in order to avoid singularities) means no material in the element and $\rho_e = 1$ corresponds to a filled element. Thus, for an optimal solution we can identify one set of points \mathbf{x}^e with density values $\rho_e = 0$ and another set with density values $\rho_e = 1$. By adopting the idea of support vector machines we can classify the data (\mathbf{x}^e, ρ_e) for all elements e of the design domain into these two sets by finding a separating hypersurface that maximizes the distance from this boundary to the closest point of each set, see Figure 2. These points are called the support vectors and will uniquely define the separating boundary between no material and filled regions. By utilizing the kernel trick we can do this for non-linear separable sets and by adding a penalty term to the objective function we can also handle misclassified points efficiently.

Thus, let us consider N sampling points \mathbf{x}^i , which take values $y^i = 1$ or $y^i = -1$. In this work, we let the sampling points be the center points of the elements $\mathbf{x}^i = \mathbf{x}^e$ as discussed above, $y^i = 1$ corresponds to $\rho_e = 1$ and we set $y^i = -1$ for $\rho_e = \varepsilon$. Furthermore, we assume that it exists a hyperplane

$$\mathbf{w} \cdot \mathbf{x} + b = 0, \quad (14)$$

which separate these sampling points into two subsets; one that only takes values $y^i = 1$ (material) and the other one with values $y^i = -1$ (no material). This is shown in Figure 2.

The hyperplane in (14) can be established by the soft SVM suggested by Cortez and Vap-

nik [2] reading

$$\left\{ \begin{array}{l} \min_{(\mathbf{w}, b, \mathbf{v})} \frac{1}{2} \|\mathbf{w}\|^2 + C \sum_{i=1}^N v_i \\ \text{s.t.} \left\{ \begin{array}{l} 1 - v_i - y^i (\mathbf{w} \cdot \mathbf{x}^i + b) \leq 0, \quad i = 1, \dots, N, \\ v_i \geq 0, \quad i = 1, \dots, N. \end{array} \right. \end{array} \right. \quad (15)$$

By applying the kernel trick using an appropriate kernel $k(x, y)$ like e.g. the Gaussian kernel, which is used in this paper, we can derive the following dual formulation of the soft non-linear SVM from the Karush-Kuhn-Tucker (KKT) conditions:

$$\left\{ \begin{array}{l} \min_{\lambda} \frac{1}{2} \sum_{i=1}^N \sum_{j=1}^N \lambda_i \lambda_j y^i y^j k(\mathbf{x}^i, \mathbf{x}^j) - \sum_{i=1}^N \lambda_i \\ \text{s.t.} \left\{ \begin{array}{l} \sum_{i=1}^N \lambda_i y^i = 0, \\ 0 \leq \lambda_i \leq C, \quad i = 1, \dots, N. \end{array} \right. \end{array} \right. \quad (16)$$

This QP problem was derived from the KKT-conditions and solved in Strömberg [3] by using sequential minimal optimization [4] for two-dimensional SIMP-based TO solutions. By applying the kernel trick, the hyperplane in (14) was of course modified to the following corresponding hypersurface:

$$\sum_{i=1}^N \lambda_i y^i k(\mathbf{x}, \mathbf{x}^i) + b = 0. \quad (17)$$

Thus, (17) was the representation of the SVM-based boundaries presented in Strömberg [3]. However, in this paper, we adopt instead the 1-norm SVM suggested by Mangasarian [5, 6] as presented below in order to postprocess three-dimensional TO solutions.

Instead of using the Euclidean norm in (15), we can use the taxicab norm (1-norm), i.e.

$$\left\{ \begin{array}{l} \min_{(\mathbf{w}, b, \mathbf{v})} \sum_{i=1}^N |w_i| + C \sum_{i=1}^N v_i \\ \text{s.t.} \left\{ \begin{array}{l} 1 - v_i - y^i (\mathbf{w} \cdot \boldsymbol{\xi}(\mathbf{x}^i) + b) \leq 0, \quad i = 1, \dots, N, \\ v_i \geq 0, \quad i = 1, \dots, N. \end{array} \right. \end{array} \right. \quad (18)$$

Here, we have also introduced the mapping $\boldsymbol{\xi} = \boldsymbol{\xi}(\mathbf{x})$ from the original space to the feature space, which we assume is given by

$$\xi_i(\mathbf{x}) = k(\mathbf{x}, \mathbf{x}^i). \quad (19)$$

By introducing $u_i = w_i/y^i$ and using (19), (18) can be written as

$$\left\{ \begin{array}{l} \min_{(\mathbf{u}, b, \mathbf{v})} \sum_{i=1}^N |u_i| + C \sum_{i=1}^N v_i \\ \text{s.t.} \left\{ \begin{array}{l} 1 - v_i - y^i \left(\sum_{j=1}^N y^j u_j k(\mathbf{x}^i, \mathbf{x}^j) + b \right) \leq 0, \quad i = 1, \dots, N, \\ v_i \geq 0, \quad i = 1, \dots, N. \end{array} \right. \end{array} \right. \quad (20)$$



Figure 5: *Stl-files of grade lattice structures generated by the proposed SVM-based postprocessing approach. 3D-printed components of these stl-files are presented in the next figure.*

Furthermore, if we also introduce $u_i = q_i - p_i$, where $q_i \geq 0$ and $p_i \geq 0$, then we obtain the following LP-problem:

$$\left\{ \begin{array}{l} \min_{(q,p,b,v)} \sum_{i=1}^N q_i + \sum_{i=1}^N p_i + C \sum_{i=1}^N v_i \\ \text{s.t.} \left\{ \begin{array}{l} 1 - v_i - y^i \left(\sum_{j=1}^N k(\mathbf{x}^i, \mathbf{x}^j) y^j (q_j - p_j) + b \right) \leq 0, \quad i = 1, \dots, N, \\ q_i \geq 0, p_i \geq 0, v_i \geq 0, \quad i = 1, \dots, N. \end{array} \right. \end{array} \right. \quad (21)$$

This is the 1-norm SVM which is used in the next section to establish SVM-based boundaries of three-dimensional SIMP-based TO solutions, given by

$$\sum_{j=1}^N y^j u_j k(\mathbf{x}^i, \mathbf{x}^j) + b = 0, \quad (22)$$

and corresponding stl-files by applying marching cubes on these implicit surfaces.

4 NUMERICAL EXAMPLES

The proposed SVM-based postprocessing approach of SIMP-based TO solutions is demonstrated in this section by considering two three-dimensional benchmarks in different settings. The approach is implemented in our in-house toolbox TopoBox¹ using Matlab and Fortran (mex-files). All stl-files presented in this work are generated using this implementation with TopoBox following the workflow presented in Figure 1.

The first example is a cubic design domain, where four corner of one of the square faces are fixed and one of the opposite edge is subjected to a vertical force at the middle according to

¹www.fema.se

Figure 3. The discretization of the design domain is performed using 18350 linear tetrahedral elements of equal size. A TO solution is generated after 50 iterations using the algorithm presented in Section 2, see Figure 3, and this solution is the input to the 1-norm SVM by letting elements with zero density having category $y^i = -1$ and elements with density one having $y^i = 1$. The 1-norm SVM problem in (21) is solved using *linprog* of Matlab and the optimal solution consists of 282 support vectors. The corresponding optimal SVM-based boundary in (22) is shown in Figure 3. The volume of the corresponding stl-model is 25.1 percent of the design volume.



Figure 6: 3D-printing of the two benchmarks with and without graded lattice structures.

The next example is one of Michell's benchmarks [16]. The design domain is taken to be a rectangular cuboid using 15565 linear tetrahedral elements. The bottom rectangle is fixed at the corners and a force is applied at the center of this rectangle, see Figure 4. The optimal TO solution shown in Figure 4 is obtained after 50 iterations. This solution is again categorized according to the principle shown in Figure 2. The 1-norm SVM problem in (21) is solved and the solution contains of 130 support vectors. The corresponding SVM-based boundary in (22) is shown in Figure 4. The volume of the corresponding stl-model is 23.7 percent of the design volume.

In conclusion, our discrete optimal SIMP-based TO solutions are now represented by smooth support vector machines. Notice that our SVM-based postprocessing approach applied on

coarse discrete TO solutions generates continuous smooth representations of the optimal geometries automatically. This is of course most preferable from a computational point of view. In addition, the SVM in (22) is extremely fast since it is completely defined by the support vectors (summation in (22) is only needed for the support vectors, i.e. over index i satisfying $u_i \neq 0$) and one additional bias. Thus, we can now start to operate quickly on these surfaces in different manners. Our specific goal is to have a powerful tool that automatically generates stl-files for additive manufacturing. In Figure 5, this is demonstrated by using our two SVMs established above to generate stl-files with graded Schwarz-D lattice structures automatically. Here, the grading is performed at the supports and the loads, see Figure 5. Thus, the volume of the two optimal design are reduced even further. The volume of the optimal design of the block with graded lattice is now 13.4 percent of the original design domain, and the volume of the Michell structure with graded lattice structure is 14.4 percent of the design domain. Figure 6 shows the corresponding 3D-printed components of the generated stl-files for these two benchmarks with and without graded lattice structures². A recent paper on graded lattice structures was presented by Panesar et al. [17].

Next, we can set up design of experiments by morphing the SVM-based representation of the TO-concepts. In such manner, detailed design optimization of the TO-concepts by using metamodels can be applied. This is illustrated in Figure 7. More details concerning the morphing and metamodeling of the TO-based concepts can be found in [18]. Some other recent papers on metamodel-based design optimization are given by Strömberg in [19, 20].

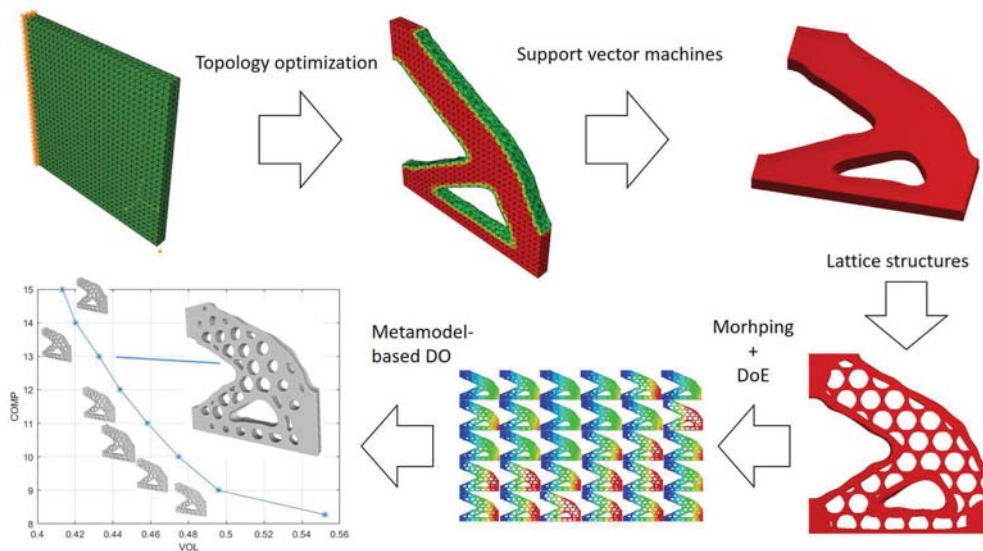


Figure 7: The generative design approach for additive manufacturing.

²A link to these stl-files can be obtained by sending an e-mail to the author.

5 CONCLUSIONS

In this paper a new SVM-based approach for automatic postprocessing of SIMP-based TO solutions is presented. By using the SVM-based representation, the TO-based concepts can be modified by morphing and adding lattice structures. Furthermore, design of experiments of these modifications can easily be set up and detailed design optimization by using metamodel can be applied. These steps constitute our proposed generative design optimization approach, see Figure 7.

REFERENCES

- [1] J.-H. Zhu, W.-H. Zhang & L. Xia, Topology Optimization in Aircraft and Aerospace Structures Design, *Archives of Computational Methods in Engineering*, **23**, 595–622, 2016.
- [2] C. Cortes & V. Vapnik, Support-Vector Networks, *Machine Learning*, **20**, 273–297, 1995.
- [3] N. Strömberg, Automatic Postprocessing of Topology Optimization Solutions by using Support Vector Machines, in the proceedings of *the ASME 2018 International Design Engineering Technical Conferences & Computers and Information in Engineering Conference IDETC/CIE*, August 26–29, Quebec City, Canada, 2018.
- [4] J. Platt, Fast training of SVMs using Sequential Minimal Optimization. *Advances in Kernel Methods Support Vector Machine*, Hoboken, MIT Press, Cambridge, 185–208, 1999.
- [5] O. L. Mangasarian. Generalized Support Vector Machines. in *Advances in Large Margin Classifiers*, 135–146, Cambridge, MA, 2000.
- [6] O. L. Mangasarian. Exact 1-norm Support Vector Machines via Unconstrained Convex Differentiate Minimization, *Journal of Machine Learning Research*, 1517–1530, 2006.
- [7] N. Strömberg, Topology Optimization of Structures with Manufacturing and Unilateral Contact Constraints by Minimizing an Adjustable Compliance-Volume Product, *Structural and Multidisciplinary Optimization*, **42**, 341–350, 2010.
- [8] N. Strömberg, Topology Optimization of Orthotropic Elastic Design Domains with Mortar Contact Conditions, in the proceedings of *the 12th World Congress on Structural and Multidisciplinary Optimization*, Braunschweig, Germany, June 5–9, 2017.
- [9] M.P. Bendsøe, Optimal Shape Design as a Material Distribution Problem, *Structural Optimization*, **1**, 193–202, 1989.
- [10] M. Zhou & G.I.N. Rozvany, The COC Algorithm, Part II: Topological, Geometrical and Generalized Shape Optimization, *Computer Methods in Applied Mechanics and Engineering*, **89**, 309–336, 1991.

- [11] G.I.N. Rozvany, O.M. Querin, Z. Gaspar & V. Pomezanski, Extended Optimality in Topology Design, *Structural and Multidisciplinary Optimization*, **24**, 257–261, 2002.
- [12] P. Tanskanen, The Evolutionary Optimization Method: Theoretical Aspects, *Computer Methods in Applied Mechanics and Engineering*, **191**, 5485–5498, 2002.
- [13] C.S. Edwards, H.A. Kim & C.J. Budd, An Evaluative Study on ESO and SIMP for Optimising a Cantilever Tie-Beam, *Structural and Multidisciplinary Optimization*, **34**, 403–414, 2007.
- [14] M.P. Bendsøe. & O. Sigmund, *Topology Optimization: Theory, Methods, and Applications*, Berlin: Springer, 2003.
- [15] O. Sigmund, Morphology-based Black and White Filters for Topology Optimization, *Structural and Multidisciplinary Optimization*, **33**, 401–424, 2007.
- [16] A. Michell, The Limits of Economy of Material in Frame Structures, *Philosophical Magazine*, **8**, 589–597, 1904.
- [17] A. Panesara, M. Abdia,, D. Hickmana & Ian Ashcrofta, Strategies for Functionally Graded Lattice Structures Derived using Topology Optimisation for Additive Manufacturing, *Additive Manufacturing*, **19**, 81–94, 2018.
- [18] N. Strömberg, Efficient Detailed Design Optimization of Topology Optimization Concepts by using Support Vector Machines and Metamodels, in review, 2019.
- [19] N. Strömberg, Reliability Based Design Optimization by using Metamodels, in the proceedings of *the 6th International Conference on Engineering Optimization*, September 17–19, Lisboa, Portugal, 2018.
- [20] N. Strömberg, Reliability Based Design Optimization by using Ensembles of Metamodels, in the proceedings of *3rd ECCOMAS Thematic Conference on Uncertainty Quantification in Computational Sciences and Engineering*, 24—26 June, Crete, Greece, 2019.

ADDITIVE MANUFACTURING OF A TOPOLOGY OPTIMIZED LIGHTWEIGHT PART OF A HUMANOID ROBOT

Sim-AM 2019

STEFAN JUNK^{*A}, BENJAMIN KLERCH^{*} AND ULRICH HOCHBERG[†]

^{*}Offenburg University of Applied Sciences
Department of Business and Engineering
Laboratory of Additive Manufacturing
77723 Gengenbach, Germany

[†] University of Applied Sciences Offenburg
Department of Mechanical and Process Engineering
77652 Offenburg, Germany

^A Corresponding author. Tel.: +49 7803 9698 4421; fax: +49 7803 9698 4449.
E-mail address: stefan.junk@hs-offenburg.de

Key words: Additive Manufacturing, Topology Optimization, Lightweight Design, Humanoid Robot

Abstract. Due to its high design freedom and flexibility, Additive Manufacturing is often used as an alternative to the conventional manufacturing. In order to be competitive, as many advantages of additive manufacturing as possible should be used. Lightweight construction is one of the biggest advantages of Additive Manufacturing. However, implementing lightweight design for AM requires different product design approaches compared to conventional development.

To achieve the lowest possible part volume combined with a high strength, it is possible to optimize the topology. At first, stresses in the part are localized by means of a numerical simulation. Subsequently, by comparing them with a reference, high and low-loaded regions can be separated. Thus, a targeted volume reduction can be implemented. In order to be able to respond to the restrictions of the manufacturing processes, these must be considered before the optimization.

This paper presents a procedure for a production-oriented simulation and topology optimization for the SLM process (Selective Laser Melting). An approach to optimizing the topology is presented with regard to technical as well as economic aspects. In doing so, methods for the quantitative assessment of success factors are used.

Since various procedural restrictions exist for the SLM process, such as anisotropy or thermal distortion, these must be considered before the topology optimization. This is done by adjusting the simulation and optimization parameters. Through this adaptation, it is also possible to take into account the previous assembly concept and to improve it by an integrated design. In order to comply with required tolerances, both a thermal and mechanical post-

processing is necessary. This in turn must already be considered in the optimization task.

This approach is illustrated by the optimization of the topology of the pelvis of "Sweaty", the humanoid robot. This robot was developed by students and is able to play football. It is a participant in the annual RoboCup, where he is currently Vice World Champion. In a previous study, three different materials were already evaluated. Among these is a novel high-tech material called Scalmalloy, which is used in this case study. It has been developed for the aircraft industry and has excellent properties in terms of density and strength.

Two design variants were developed using topology optimization and iteratively optimized by adjusting the parameters. These each have different mounting concepts. Finally, the design variants were compared in terms of weight, stiffness and cost to find the best technical and economical solution. For this purpose, an economic analysis was carried out to evaluate the costs and benefits. This design solution was subsequently validated and manufactured using the SLM process.

1 INTRODUCTION

Additive manufacturing is widely used as an alternative to conventional production, especially in single piece and small batch production [2]. It offers many design freedom benefits and lightweight options [3]. Precisely because of the lack of complexity costs in additive manufacturing, comparatively favorable lightweight structures can be realized. To develop such lightweight designs, however, a completely different approach is needed than the conventional product design. In doing so, it must be ensured that a quantified decision on the meaningfulness of an additive lightweight concept is made by means of industry and potential assessments that are as accurate as possible. There are special considerations of cost sensitivity and the accepted additional costs for lightweight design [4].

The above-mentioned additional costs arise in the design of a lightweight component for additive manufacturing in that a numerical simulation with a subsequent topology optimization should be carried out in order to make optimal use of the potentials.

In the simulation, this requires accurate data on the corresponding load case as well as material properties in order to achieve usable results. Due to the fact that many additive processes are still relatively young, little reliable data is available on the processable materials. Furthermore, due to the layered material application, additive manufacturing is characterized by anisotropic material properties [5]. These must be taken into account both in the material data selection and in the implementation in the simulation model.

In addition, already in the simulation and the topology optimization some restrictions of the subsequent manufacturing process must be considered, as they can lead to significant additional effort if not observed.

For this reason, a procedure for a simulation and topology optimization considering additive manufacturing was developed (Figure 1) . In addition, a case study will be carried out using the example of the humanoid robot "Sweaty" of the University of Applied Sciences Offenburg to optimize the component in a high-tech aluminum alloy.

2 PROCEDURE

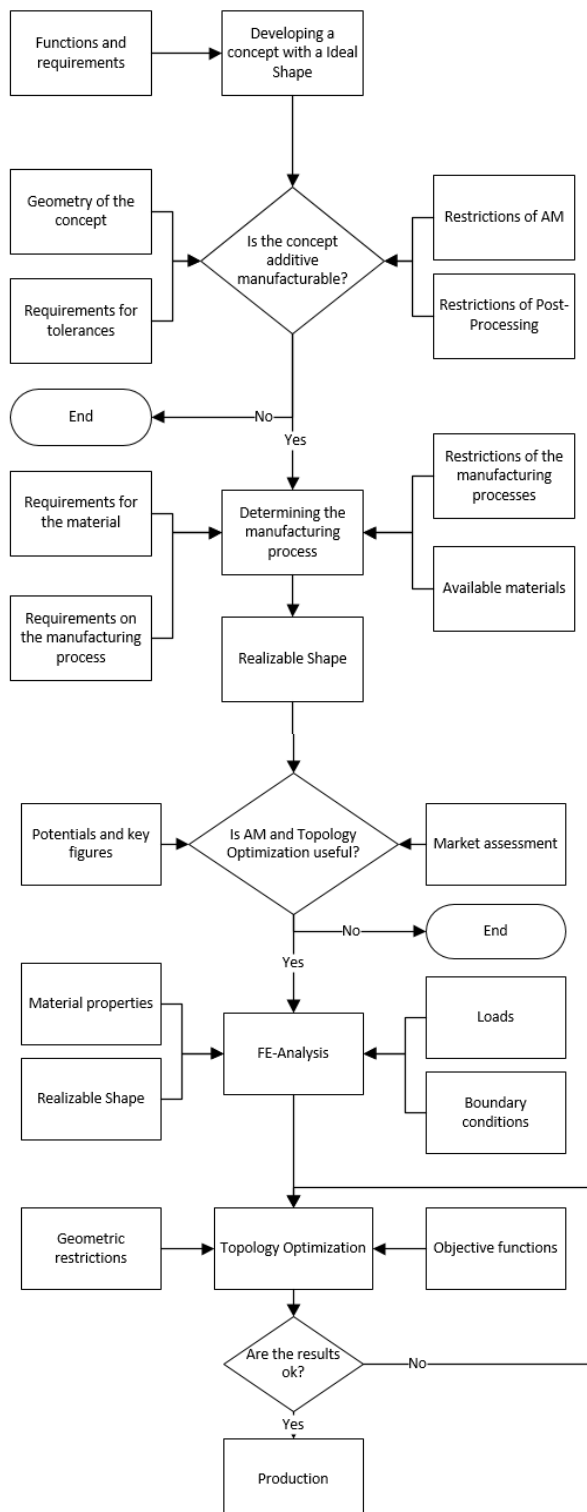


Figure 1: Flow Chart Optimization [7]

To start the process, an ideal shape should be designed first [6]. Here it is possible to consider individual components, as well as assemblies. With the help of additive manufacturing, an integral design can be realized. This results in advantages in terms of installation effort and mountability. However, a subsequent dismantling and replacement is usually no longer possible.

The individual components of an assembly are subdivided into functions, and then a shape is created that makes it possible to fulfill these functions.

The next step is to check whether this concept is generally additively manufacturable. For this purpose, both the geometry of the concept and the requirements of the tolerances are compared to the restrictions of additive manufacturing, as well as the post-processing. In many cases, tolerance is an exclusion criterion for additive manufacturing. However, it is possible both by a mechanical and thermal post-processing to comply with very tight position and dimensional tolerances. Especially with joining or bearings, this option is often used.

Then the manufacturing process is selected based on material and process requirements and their restrictions. It should be noted that in most cases in additive manufacturing a process-material combination is selected [7]. This happens because of many processes on a particular material, or one Material group are specialized or limited. By defining the manufacturing process, the Realizable Shape can be generated. This reflects the actual realizable geometry and serves as a basis for later simulation

and optimization.

Once this initial geometry has been determined, economic and sector-specific success factors can be used to evaluate different variants. These variants may differ, for example, in terms of their installation concept, integral design. In order to make a decision, it is necessary to constantly compare these variants with a conventional design. Assessment criteria can be cost, weight, rigidity, assembly concept, etc. The weighting of the individual criteria always takes place with regard to the respective industry and according to the respective product.

After the multi-criteria decision analysis, a statement can be made about the advantages of an additive lightweight design. This means that such is potentially beneficial and this strategy should be pursued. This inspection represents an important function, since the optimization of lightweight design can sometimes result in very high additional costs whose use must be justified.

The next step is the FEM simulation. Care must be taken here to pay attention to material- and process-specific characteristics such as anisotropy or minimum wall thicknesses [8]. The geometry should be chosen as large as possible, as the topology optimization algorithm can achieve better results. Nevertheless, care should be taken when dimensioning the geometry that the function of the component is not restricted and the necessary accessibility is given in certain regions.

In order to achieve reliable results, it is important to know the exact load case and to generate the meshing fine enough. When considering the geometry, it must be ensured that the position of the later component in the building space of the 3D printer is already known. The layer structure gives rise to the anisotropic properties along the z-axis. Thus, these can only be considered in the simulation with the exact position.

After the FEM simulation a topology optimization has to be carried out. Using the optimization algorithm, it is possible to adjust the local modulus of elasticity depending on the occurring stresses. As a result, a sharp separation can be achieved after a few iterations, through which volume reductions can be made.

Both objective functions and geometric restrictions are to be chosen for the optimization. After the optimization run, the results must always be checked. In order to obtain the best possible results, it is often necessary to repeat the process of topology optimization several times. In this case, the respective starting situation is influenced by changing, for example, the design space or the volume reduction factor.

In order to validate the results, the simulation plots as well as the respective success factors such as weight and deformation energy (representing stiffness) are considered. Then the geometry can be exported and prepared for production.

3 CASE STUDY PELVIS MODULE HUMANOID ROBOT “SWEATY”

To illustrate the procedure, a case study was conducted on the pelvis module of the humanoid robot "Sweaty".

3.1 Humanoid Robot “Sweaty”

The humanoid robot "Sweaty" (Figure 2) is a joint project of professors and students of the University of Applied Sciences Offenburg. Among other things, this robot is able to play football autonomously. In addition, he competes in the annual RoboCup against other humanoid

robots from around the world. In this competition, he was able to occupy second place in the last two years and is therefore the reigning Vice World Champion [9].

Since the individual components must be driven electrically, lightweight design is the main focus for the robot. That is why the robot consists largely of aluminum and CFRP.

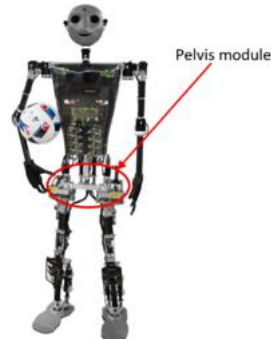


Figure 2: Robot "Sweaty"

3.2 Pelvis Module

The component to be optimized represents the human pelvis. As can be seen in Figure 3, the original component consists of four individual parts, which are connected to each other with screw connections. Due to the sometimes high dynamic loads, it has already happened in the past that screw connections have been untied. For this reason, an at least partially executed integral design in addition to lightweight design in the foreground of the redesign. The individual parts were all made of a high-strength aluminum conventionally by milling.

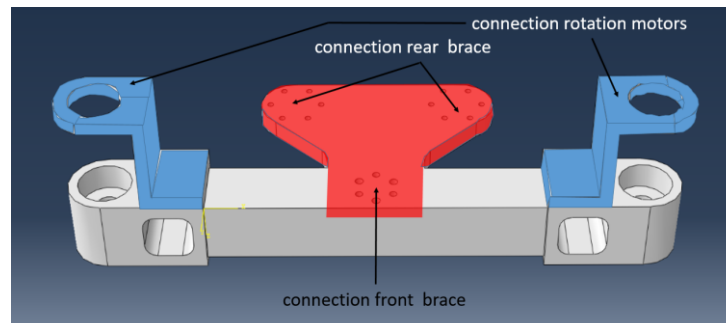


Figure 3: Pelvis Module

3.3 Developing a Concept

For the development of the concept, first of all all functions which the assembly "Pelvis module" has to meet have been discussed. Subsequently, the maximum permissible design space for the component and areas for joining or bearing surfaces was determined.

3.4 Feasibility of AM

In order to check whether the concept is additively manufacturable, a check must first be made. In the process, the generally expected tolerances of additive manufacturing and post-processing are compared with the requirements of the component. This is not about the planning in detail, but rather an estimation of whether AM is an option or not. When manufacturing the

"Sweaty" pelvis, it is important that the joining surfaces in particular can achieve a sufficient tolerance. Due to the relatively rough tolerances in the AM, therefore, a suitable post-processing is necessary. Due to the thermal and mechanical reworking by means of annealing and machining, it is possible to comply with both the required dimensional and positional tolerances. In this review, the machinability and accessibility for post-processing must be guaranteed. This concerns above all the clamping of the workpiece as well as the tool accessibility. For example, Figure 4 shows a version of the pelvis that could be implemented in an integral design. However, the upper bearing seats can not be milled because the overhang is too large. Because of this, the plates were removed.

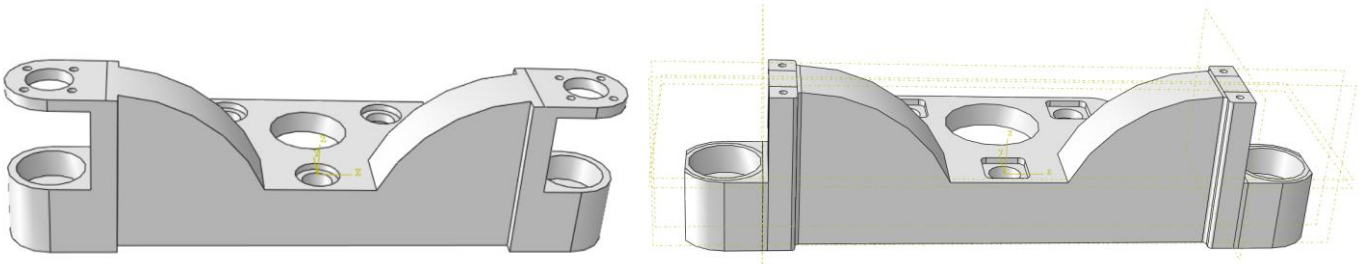


Figure 4: Accessibility for post-processing (left: not manufacturable, right:manufacturable)

3.5 Determination of the AM process

In general, a material-process combination is usually chosen because it is often related in additive manufacturing. After a previous selection of materials, in which three different materials (aluminum, stainless steel and titanium) were evaluated for their use, the aluminum alloy Scalmalloy was selected [10]. This has the advantage that it can have a very low density and a comparatively high strength [11]. Since this material can only be processed by the SLM process (Selectiv Laser Melting), the process was already determined after the material selection. In this step, the position of the component should already be determined in the later building space of the machine. This has an influence on the subsequent simulation as well as the achievable tolerances and costs. Both the costs and the tolerances are factors that influence the decision for or against a lightweight design for additive manufacturing in the next step.

3.6 Decision Making

In order to be able to make an evidence-based decision, economic and technical success factors should be weighted sector-specifically and then evaluated. In the Sweaty pelvis module, as shown in Table 1, the weight and cost criteria were the most important. Other criteria such as integral design, rigidity and the assembly concept also have a great influence. It can be seen that the additive manufactured variant could achieve more points than the conventional variant. For this reason, it should be noted that the costs for the topology optimization and the additional costs for additive manufacturing in this case are justified and the potential that is likely to arise from this can be used.

Criteria	Weighting	AM		Conventional Manufacturing	
		Rating	Value	Rating	Value
Costs	25	3	75	9	225
Integrated Design	15	10	150	3	45
Stiffness	15	9	135		60
Weight	30	8	240	5	150
Assembly	15	7	105	8	120
			705		600

Table 1: Multi Criteria Decision Making

3.7 FEM-Simulation

For the simulation, the starting geometry is the Realizable Shape. For the simulation of the pelvis module the software Abaqus from Dassault Systemes was used. Tosca also from Dassault Systemes was used for the subsequent topology optimization. Since Tosca is not able to simulate a dynamic load case, this must already be taken into account during the simulation in Abaqus. As can be seen in Figure 5, two individual forces are introduced at the bearing seats. These arise when the robot takes a step as the legs are mounted underneath. This force is 250 N. In order to simulate a dynamic load case, one-sidedly ten times this single force was assumed and also introduced from below. On each of the two upper brackets a rotary motor is screwed on. This allows twisting of the legs and causes a torque of 15 Nm. This torque is therefore to be considered equally in both brackets.

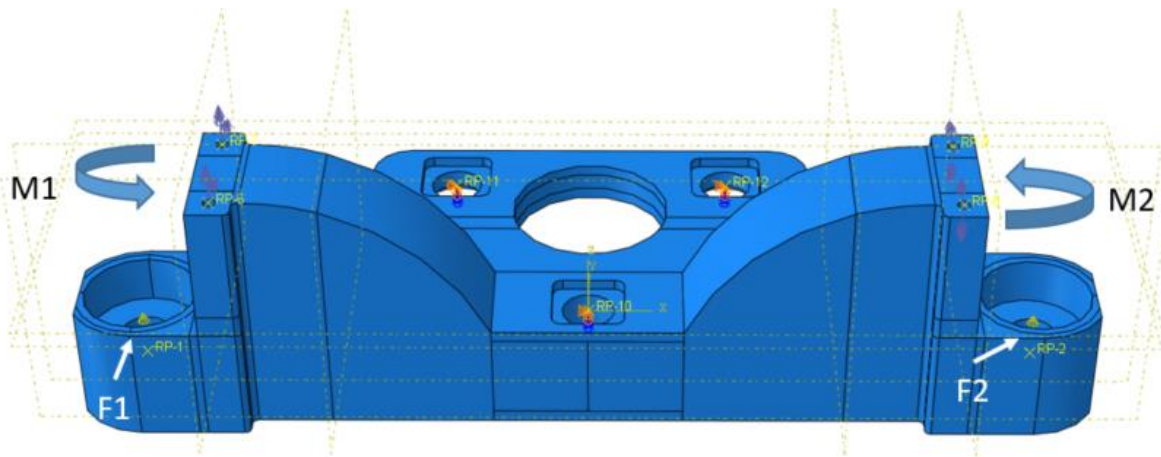


Figure 5 Loads (F) and Moments (M)

As seen in Figure 6, there are a total of three bearings. These are each designed as cardan joints and absorb forces in the xy and z directions and prevent rotation around the z axis.

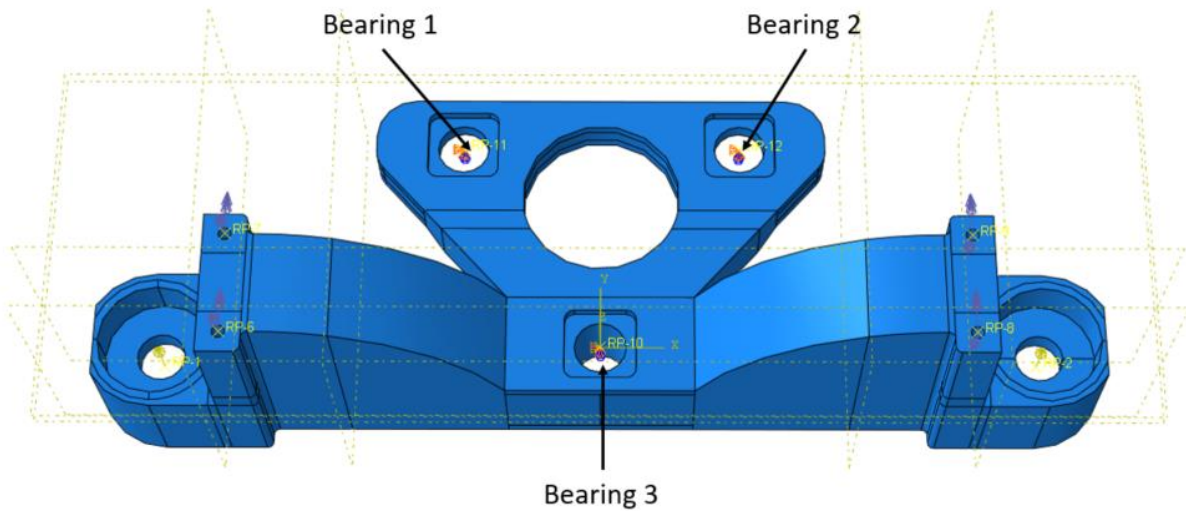


Figure 6: Bearings

The material properties were deposited taking into account the anisotropy. The values for the anisotropy were calculated by a percentage adjustment to the values from VDI Guideline 3405 [12]. Due to the position of the component in the building space, the building axis could be correctly considered. The anisotropy was deposited by means of the respective engineering constant for the three spatial axes in the plastic area and aligned by means of local orientation in the solid.

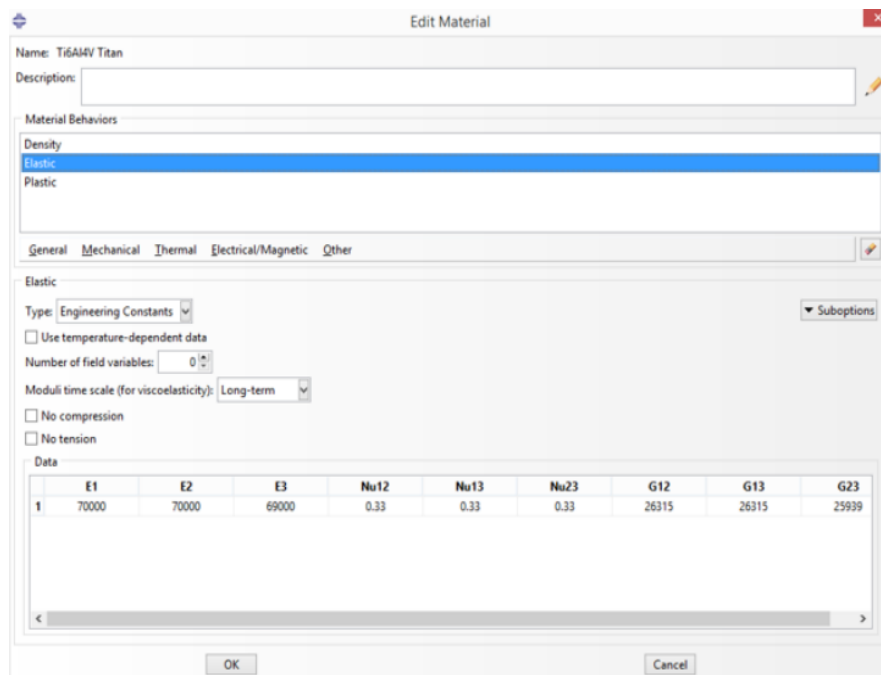


Figure 7: Material Properties in Abaqus

To start the calculation you have to do the meshing first. It should be noted that this is done as wide as possible and as fine as necessary. If indicators for unrealistic results can be detected

after the simulation, a refinement of the mesh is often expedient.

Subsequently, the FEM simulation can be started. After this, a plausibility check must always be carried out, in which the stresses (see Figure 8) are examined.

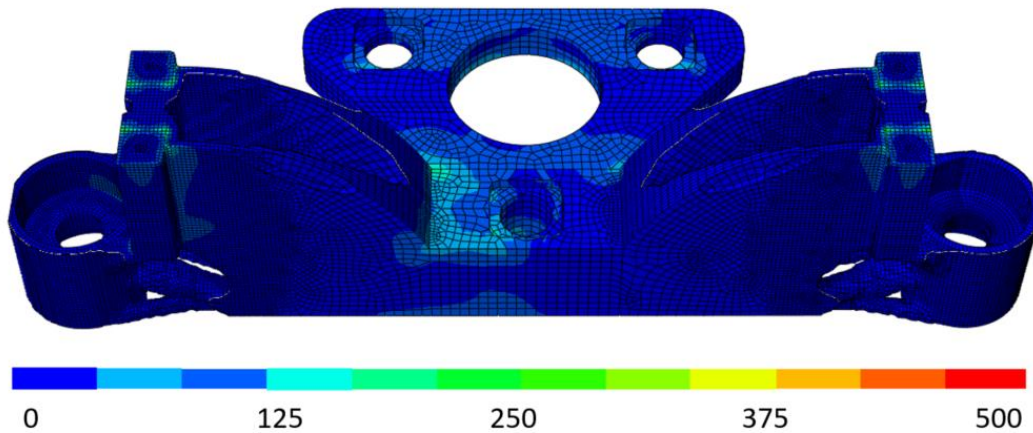


Figure 8: Mises Stresses in MPa

3.8 Topology Optimization

In order to achieve a lightweight construction, it is possible after the FEM simulation by an algorithm to eliminate lightly loaded areas. This creates bionic, light and stiff geometries.

To create the optimization task, objective functions must be set. The case study used a reduction in strain energy to increase stiffness as well as a reduction in volume.

So that the optimization can be influenced accordingly, there is the possibility to deposit geometrical restrictions. Frozen areas (see Figure 9) have been set up in the bearing and load initiation areas to exclude them from optimization. Thus, their subsequent function is still guaranteed. Furthermore, planar symmetries were implemented to avoid asymmetric optimization due to the asymmetric load distribution. In addition, minimum wall thicknesses were implemented to avoid an overdone material reduction in certain areas.

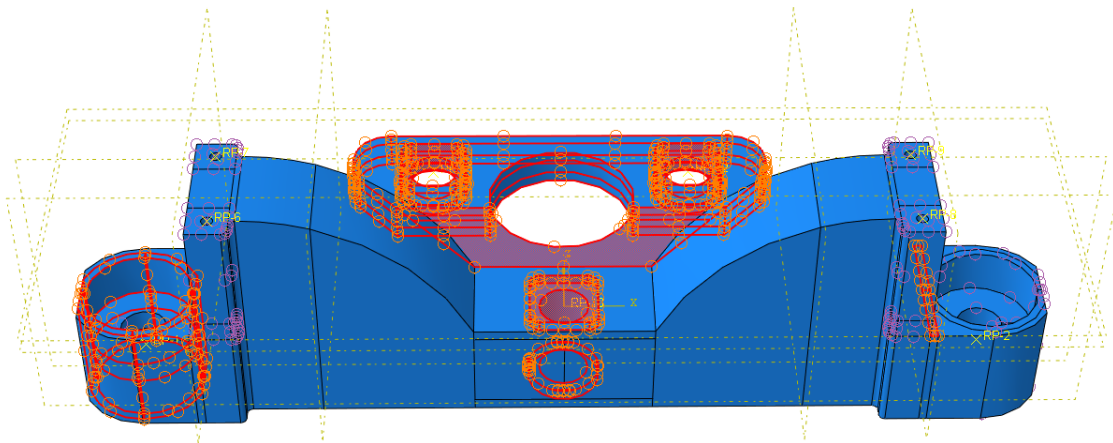


Figure 9 Frozen Areas (in orange)

After optimization, the geometry must be checked for plastic deformation (see Figure 10). For this purpose, different design proposals are issued. For each optimization loop, a design proposal is generated which differs by a specified factor of volume reduction.

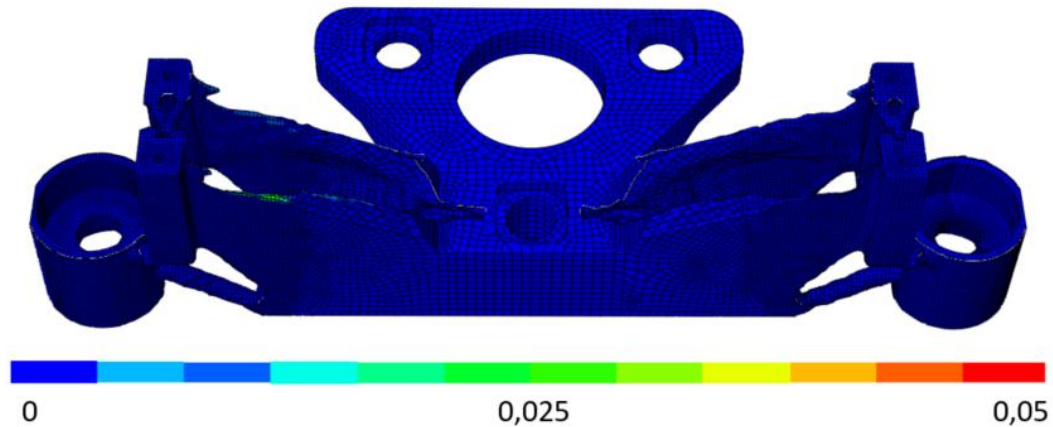


Figure 10: Verification of plastic deformation (in %)

In order to obtain the best possible results, some adjustments were made to the parameters after which the component was re-simulated and optimized. These parameters are particularly the design space, the geometric restrictions and the factor for volume reduction. After selecting the most advantageous solution, the geometry was smoothed using Tosca.smooth and then exported.

3.9 Results

The results for the final geometry of the pelvis module from “Sweaty” (Figure 11) has achieved a weight reduction of 29.2 g (-4.7 %) and a reduction of deformation energy of 2.6 J as seen in Table 2.

Manufacturing Process	Material	Yield Strength [MPa]	Weight [g]	Strain energy [mJ]	Costs [%]
Milling	AlZnMgCu1.5	450	617,2	4,3	100
AM	AlMgSc	470	588 (-4,7%)	1,7 (-60,5%)	377

Table 2: Results

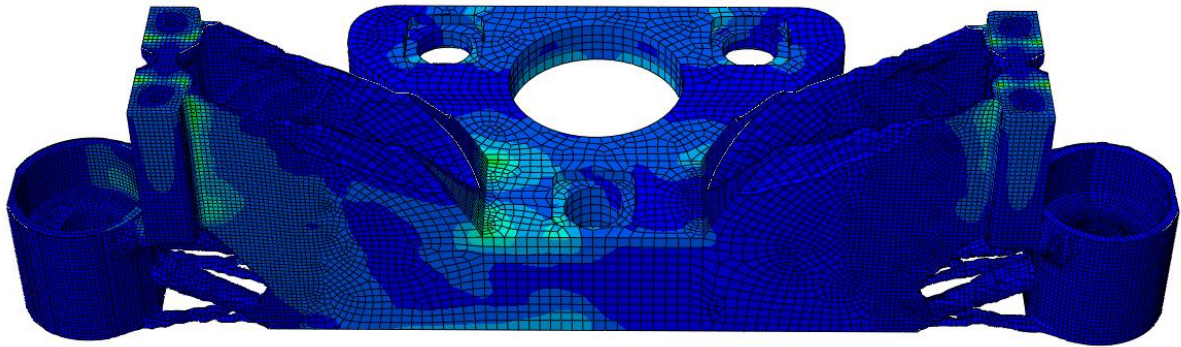


Figure 11: Final Result

4 CONCLUSION

In order to carry out a process-oriented topology optimization for the SLM process, a few points should be considered. Procedural restrictions such as tolerances and the like are just as important as the anisotropic material properties. For this reason, some questions should be clarified before a topology optimization. In this case study, it was first of all examined with the aid of an ideal shape and the requirements of the tolerances whether the component can principally be manufactured additively. It could be stated that the position of the component has a tremendous influence already in the very early conception phase. On the one hand, production-related restrictions such as the achievable quality change and, on the other, factors relevant to the decision, such as costs and output.

After the restrictions of production and post-processing met the requirements, the additive process could be selected. The process was selected based on the material restrictions. In this way one can conclude that attention should always be paid to the material-process combination and its restrictions.

It has been shown that a design change was necessary because the post processing would otherwise not be possible.

In order to make a decision on topology optimization for additive manufacturing, a quantitative analysis should be carried out. In this case, the potentials of topology optimization and additive manufacturing such as weight and rigidity as well as other factors such as costs have to be assessed sector-specifically. Special attention should be paid to the integral design in particular, since this would be a major encroachment on the overall assembly concept and a holistic functional integration can also have disadvantages. The analysis has shown that the specific potentials of the topology optimization of the pelvic module justify extra effort for the optimization.

In the FE analysis, it has been shown that the component orientation in the building space has a very decisive role in taking into account the anisotropy in the design space.

REFERENCES

- [1] Associates, W.: Wohlers report 2017. 3D printing and additive manufacturing state of the industry : annual worldwide progress report. Fort Collins (Colo.): Wohlers Associates 2017
- [2] Bikas, H., Stavropoulos, P. a. Chryssolouris, G.: Additive manufacturing methods and modelling approaches: a critical review. *The International Journal of Advanced Manufacturing Technology* 83 (2016) 1-4, S. 389–405
- [3] Sauer, A.: Bionik in der Strukturoptimierung. Praxishandbuch für ressourceneffizienten Leichtbau. *Konstruktionspraxis*. Würzburg: Vogel Communications Group 2018
- [4] Yang, L., Hsu, K., Baughman, B., Godfrey, D., Medina, F., Menon, M. a. Wiener, S.: *Additive Manufacturing of Metals: The Technology, Materials, Design and Production*. Springer Series in Advanced Manufacturing. Cham, s.l.: Springer International Publishing 2017
- [5] Klahn, C., Meboldt, M. a. Fontana, F.: *Entwicklung und Konstruktion für die Additive Fertigung. Grundlagen und Methoden für den Einsatz in industriellen Endkundenprodukten*. Würzburg: Vogel Business Media 2018
- [6] Zaman, U. K. a., Rivette, M., Siadat, A. u. Mousavi, S. M.: Integrated product-process design: Material and manufacturing process selection for additive manufacturing using multi-criteria decision making. *Robotics and Computer-Integrated Manufacturing* 51 (2018), S. 169–180
- [7] Stefan Junk, Benjamin Klerch a. Ulrich Hochberg: *Structural Optimization in Lightweight Design for Additive Manufacturing*. (submitted). *Procedia CIRP* (2019)
- [8] Zhang, P., Liu, J. a. To, A. C.: Role of anisotropic properties on topology optimization of additive manufactured load bearing structures. *Scripta Materialia* 135 (2017), S. 148–152
- [9] Hochschule Offenburg Sweaty. <https://sweaty.hs-offenburg.de/projekt/>, abgerufen am: 04.01.2019
- [10] Junk, S., Klerch, B., Nasdala, L. a. Hochberg, U.: Topology optimization for additive manufacturing using a component of a humanoid robot. *Procedia CIRP* 70 (2018), S. 102–107
- [11] Scalmalloy. <https://apworks.de/de/scalmalloy/>, abgerufen am: 07.01.2019
- [12] VDI-Richtlinie 3405 Blatt 3 Additive Fertigungsverfahren Konstruktionsempfehlungen für die Bauteilfertigung mit Laser-Sintern und Laser-Strahlschmelzen (2015)

Functional Lightweight Design for Additive Manufactured Vehicle Liftgate Door Hinge

Ismet Aydin*, Erhan Akarcay, Omer Faruk Gumus, Can Baran Engin, Humeyra Yelek and Sevket Ozcan

*Rollmech Automotive San. ve Tic. A.Ş.
BTSO Organize Sanayi Bölgesi Yeşil Cd. No.15, 16140 Nilüfer, Bursa / Turkey
e-mail: ismet.aydin@rollmech.com*

ABSTRACT

Additive manufacturing technology provides extraordinary handling of producing mechanical parts regardless of their geometric complexity which traditional way are not sufficient. Furthermore, in the global automotive industry, replacing body components with lightweight designs is an important advantage which distinguishes from competitors. In recent years, topology optimization used as a tool for optimum solutions throughout the product development phase. However, automotive manufacturers must think the global technical regulations. In this study, mechanical properties of different build directional (0°, 45°, and 90°) tensile specimens fabricated from aluminium alloy (AlSi10Mg) using direct metal sintering (DMLS) have been investigated. Specimens are analysed by the mechanical tensile test and the Vickers hardness test. As a case study the development of the vehicle liftgate door hinge will be presented, which has been topological optimized. Complex geometry hinges component designs are manufactured in EOS M290 additive manufacturing system using aluminium alloy (AlSi10Mg) powder. This paper presents, numerical and experimental solutions for behaviour of liftgate door hinge under the regulatory conditions. Referring to the results obtained, an interpretation was made to increase the use of potential of additive manufacturing technology in the automotive industry.

Keywords: Additive Manufacturing, Finite element analysis, Mechanical properties, Topology optimization, Vehicle door hinge

INTRODUCTION

The additive manufacturing enables innovative thinking of design perspective in opposition to traditional manufacturing methods which consist of removing redundancy of material. Although traditional manufacturing tools are being improved, but it is still challenging or even infeasible to produce parts with geometric complexity. Furthermore, increasing of demanding for lightweight designs naturally make topology optimization substantial. The use of numerical simulation to structural optimize the parts has become required to obtain minimum mass without process restriction. Since the additive manufacturing enables to fabricate parts regardless of their complicatedness, topology optimization has become substantial technique for convenient design [1].

Although, several materials are used for additive manufacturing, aluminium alloys are increasingly becoming desirable due to their density-strength ratio [2]. AlSi10Mg using by EOS for their Direct Metal Laser Sintering (DMLS) systems is one of the materials for use of additive manufacturing. Materials fabricated by additive manufacturing need further development for requirement of isotropy, mechanical properties, fatigue resistance, porosity and surface roughness [3, 4, 5, 6]. Therefore, it is considerable to optimize process parameters in order to obtain optimum properties and consistency [7]. This study aims to investigated influence of different build directional on the mechanical properties of DMLS produced AlSi10Mg alloy. In this direction, tensile specimens were built in three orientation of horizontal, 45° diagonal and vertical using with fixed laser processing parameters. Additionally, hardness, mechanical properties and microstructure was examined in order to use in industrial applications.

The obtained results were used in Optistruct® software to optimize vehicle tailgate door hinge mechanism. To determine the boundary conditions, global technical regulations (ECE-11) were used [8]. Optimized vehicle tailgate hinge system is numerical and experimental analysed.

MATERIAL AND METHODS

1. Fabrication on Specimens

AlSi10Mg tensile specimens were produced in three different orientation (0° horizontal, 45° angle inclined and 90° vertical) on EOS M290 additive manufacturing machine (Fig. 1a). A set of four specimen per orientation was fabricated for tensile test in process working area. This represents influence of different build orientation on anisotropy level of additive manufactured parts. The testing procedure was based on ASTM E8 standard. The fabricated specimens were machined and surface-grinded to standard geometry and tolerance which is shown in Fig. 1b. EOS Additive manufacturing system default process parameters were used while specimens' fabrications procedure. The building parameters of samples were stable for all production phase.

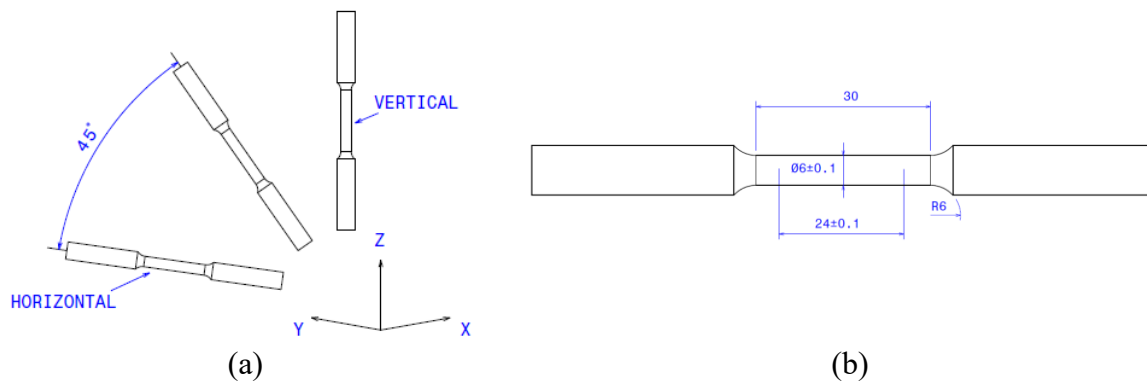


Figure 1. (a) built orientation (b) geometry and dimension of test specimens according to standard ASTM E8 (all dimensions in mm).

Chemical composition of AlSi10Mg alloy was shown in Table 1. Measured particle size distribution of AlSi10Mg alloy powder was mainly range of 25-35 μm . Recommended 30 μm layer thickness was applied for tensile specimens, hardness specimen and vehicle liftgate door hinge. Nonetheless, heat treatment for age-hardening didn't implement to samples.

Table 1. Chemical composition (wt%) of AlSi10Mg powder.

Alloying Element	Ti	Al	Fe	Mn	Ni	Si	Cu	Mg	Zn	Pb	Sn
wt (%)	≤ 0.15	Balance	≤ 0.55	≤ 0.45	≤ 0.05	$\leq 9-11$	≤ 0.05	$\leq 0.2-0.45$	≤ 0.1	≤ 0.05	≤ 0.05

2. Characterization

For the evaluation of mechanical properties, specimens were tested tensile and hardness test, moreover printed hinge parts were investigated for United Nations Agreement of Uniform Provisions Concerning the Approval of Vehicles with Regard to Door Latches and Door Retention Components (ECE-11). Tensile measurement was carried out on 3 samples of each build orientation and average of this results was received for consideration. Tests were performed using of the * Tensile tester (ASTM E8).

Hardness measurement of AlSi10Mg were conducted using of *Vickers Hardness tester. The specimens were built and polished at $6\text{mm} \times \text{Ø}12\text{mm}$ dimensions. The specimens were built directly on the base plate with a support structure. Measurement was performed on two surfaces at four different locations. Average of this these results was taken into consideration.

ECE-11 Regulation applies to vehicle door retention components such as hinges and other supporting parts. According to regulation each door hinge system shall not separate when a longitudinal load of 11 000 N is applied, and a transverse load of 9 000 N is applied.

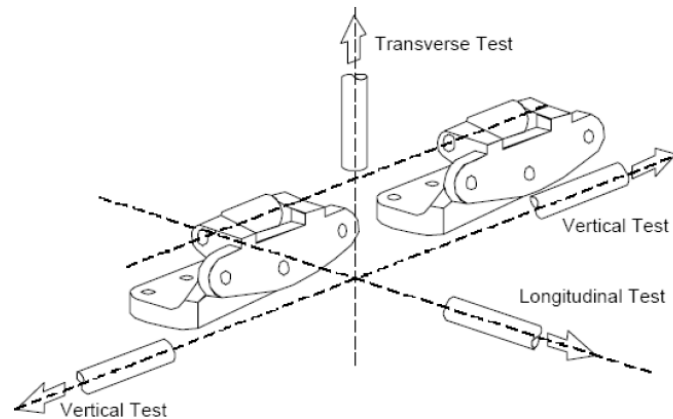


Figure 2. Static load test directions for doors [8]

3. Topology Optimization

Topology optimization process is basically mathematical method of removing material in design space where it is not necessary, under specific loads and boundary conditions. In this worked, topology optimization was conducted on a vehicle liftgate door hinge mechanism with Altair OptiStruct software (Fig. 3). Interface surface (connection between hinges and door or body), pin holes, bearing hole, and a flat surface for hard stop were considered as non-design space. The basic idea of this approach, fixed hinges where door must connect to the body and correspond to attachment will remain as it is, and mobile hinges geometry will be optimized. For simplicity of design, loading orientation on the hinge system was designated based on the regulatory conditions. Also, washers were design and utilized for each side of the hinges to functionality of rotational movement. Material properties of AlSi10Mg produced by DMLS were adapted from the experimental data from tensile tests. Furthermore, anisotropy level of AM materials was ignored at these phases. Results of the topology optimization are discussed in the results and discussion section.

4. Finite Element Analysis

The analysis of hinge strength under regulatory condition was performed with Altair's Radioss as a solver. The critical loads and boundary conditions were considerate similar as optimization procedure. However, FEA assumed mechanical behavior is isotropic, even though AM materials show build direction dependent anisotropy. Experimental results of mechanical properties of AlSi10Mg which is assumed nonlinear plastic material, were employed in structural analysis. Similar procedures were repeated to the topology optimized hinge system for the different directions of failure loads.

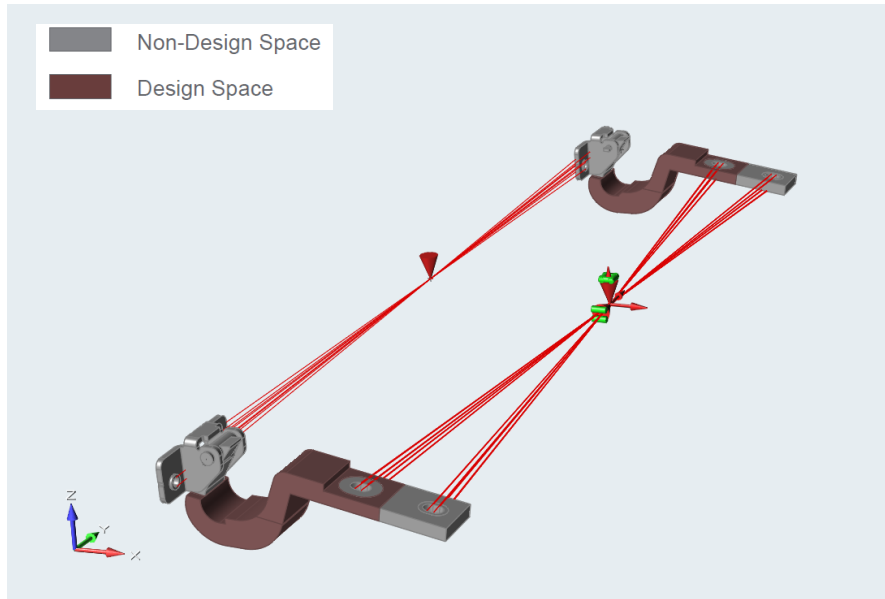


Figure 3. Loading directions for baseline geometry made with AlSi10Mg alloy.

RESULT AND DISCUSSION

1. Mechanical Properties

Tensile stress (σ)-strain (ϵ) curves and measured values of produced by DMLS with different build directions is illustrated in Fig. 4 and Table 2. Curves of tensile diagrams show that slightly anisotropy has been confirmed. As a result, yield strength and ultimate tensile strength significantly similar for specimens' curves. Nonetheless, elongation at break decreased when the inclined build angle scales up. Oriented specimens' measured values are nearly identical to referenced reports.

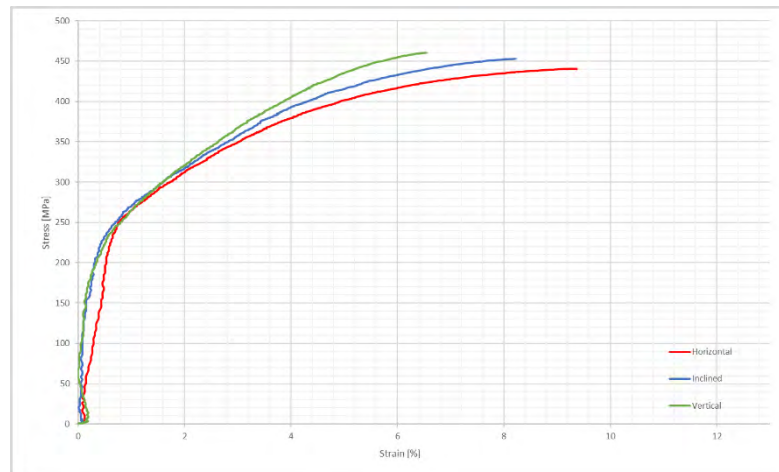


Figure 4. Stress (σ)-strain (ϵ) curves of AlSi10Mg test-specimens

Table 2. Mechanical properties data retrieved from MS1 produced by DMLS

Orientation	E [GPa]	R _{p0.2} [MPa]	R _{UTS} [MPa]	A _t [%]
<i>EOS Horizontal</i>	75±10	270±10	460±20	9±2
<i>EOS Vertical</i>	70±10	240±10	460±20	6±2
Horizontal	55	240	440	9.3
45° Angle Inclined	65	240	453	8.2
Vertical	65	238	460	6.5

The hardness measurements of AlSi10Mg alloy made by DMLS are shown in Fig. 5. The graph comparing Vickers Hardness value of supported surface and non-supported surface shows notable discrepancy between variables. Non-supported surface shows much lower hardness values. Moreover, to determine actual sample hardness, surface of the sample less hardness than the center of the sample.

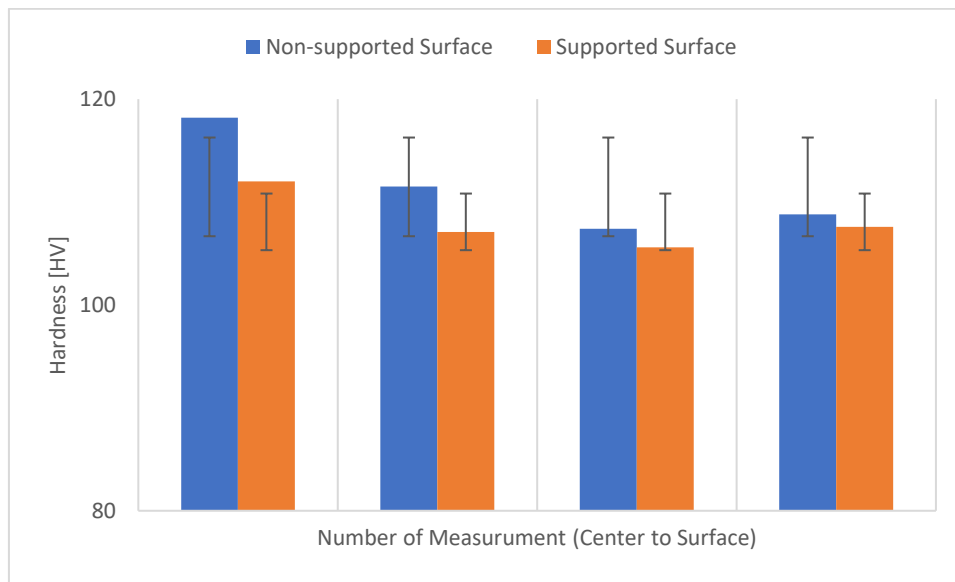


Figure 5. Ratio of hardness (HV)

2. Optimization Result

Topology optimization was performed on the baseline geometry at regulations norms. Under the optimization phase, vertical oriented AlSi10Mg data was used to modelling of material behavior of baseline geometry. Left and right hinge components were considered as symmetrical, and Fig. 6 shows the structures that were obtained. For optimized components, %60 weight was significantly alleviate from baseline geometry. Due to definition of materials in Inspire optimization software considered as linear isometric, some unrealistic geometries were eliminated. Additionally, undercut and overhang angle was adjusted for DMLS process support parameters.



Figure 6. The topology optimized component.

3. Finite Element Analysis

Based on the ECE-11 regulation, failure loads were applied separately all hinge system and under these loads separation must not be observed. As a result of this, plastic deformation will be considered as acceptable unless it is not surpassing the plastic deformation limits of materials which include fix hinges and central pins. Their mechanical behaviors were analyzed and compared all directions. For the rest of the data collecting from analysis, Von Mises stress are shown in Fig. 7. For this set of tests, it is worth noting that failure is defines as above the elongation at break strain levels. That means, it is important to excerpt the fix hinge and central pin materials suitable for the tests.

Based on the maximum Von Mises stress under longitudinal test, 390 MPa was observed on optimized mobile also fix hinge part which meet safety criteria. Fig. 7 (a, b) shows longitudinal analysis results with maximum Von Mises stress on mobile hinge below the elongation at break values of AlSi10Mg materials. For the vertical test results, Fig. 7 (c) shows maximum Von Mises stress which is observed in the fixed hinge. Although, for hinge material this value is also higher than the yield point, but it is acceptable for regulation norms. Also, on the optimized mobile hinge, observed plastic deformation considered as in safety regions. For the transverse loading scenario, Fig. 7 (e, f) shows maximum Von Mises stress under 9 kN load is measured 353 MPa on the fix hinges. Although, 325 MPa Von Mises stress observed on the optimized Alsi10Mg hinge parts, it is also considered as reasonable. All these results emphasize that, plastic deformation on the hinge system is inevitable, but separation of hinge system is improbable.

Moreover, experimental results show that all the three load simulations met the specifications defined in regulation norm. The experimental data obtained confirm the validity of the three numerical models tested. No separation was observed.

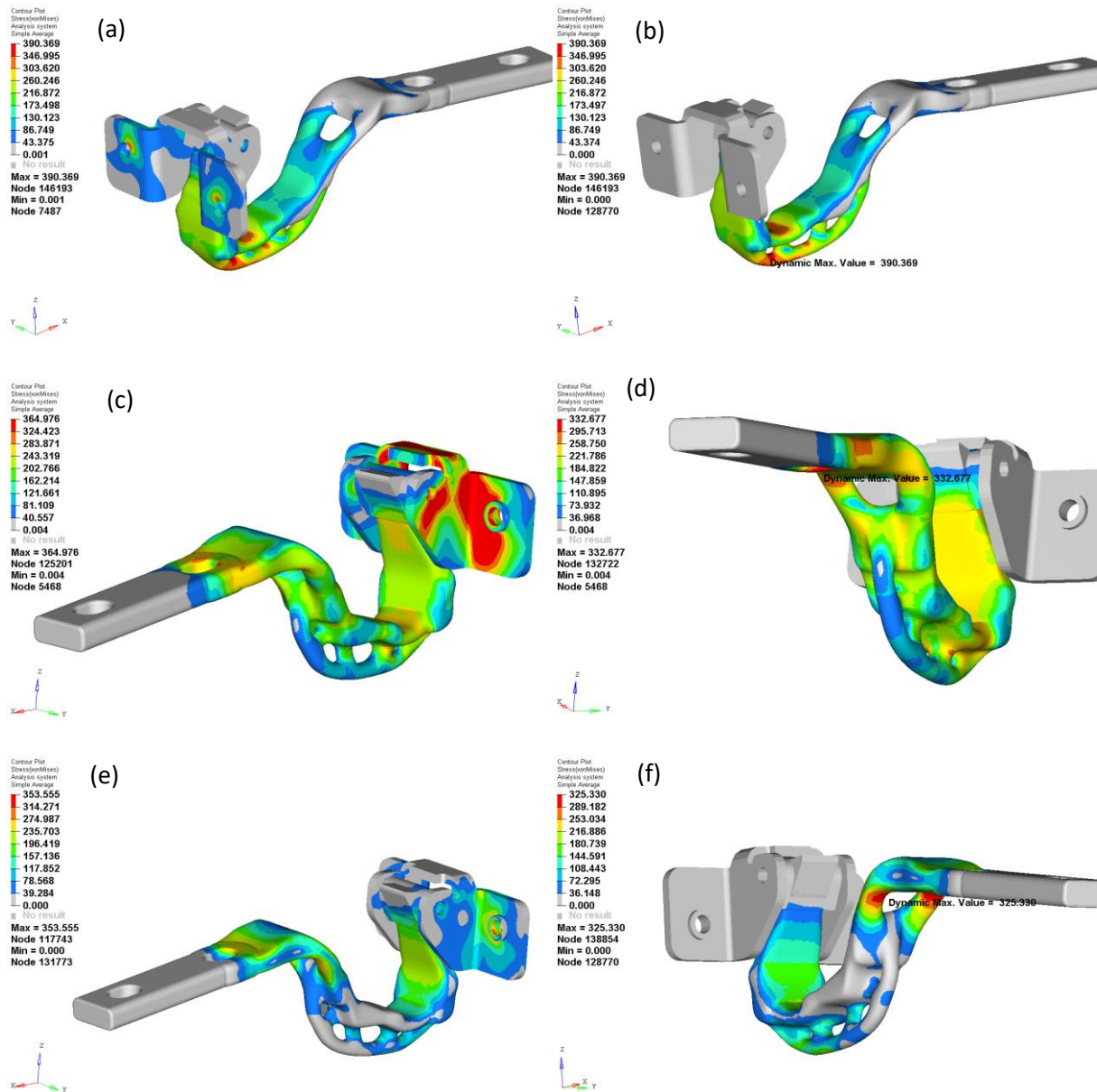


Figure 7. Optimized structure solutions resulting from the model (a) longitudinal test (b) vertical test (c) transverse test

CONCLUSION

For adaptation of additive manufacturing into the automotive industry, a case study has been demonstrated to be successful under safety regulations by using topology optimization which reduce reduces weight of functional hinge system. The following conclusions can be made based on the above research.

- (1) There are some challenges associated with anisotropy level of AM materials. Characterization of AM AlSi10Mg alloy hinge components using DMLS is still a merging area, but standardization of process is noticeably.

- (2) Topology optimization simulation leads to multiple solution, especially under failure loads above the yield point of material stress-strain curve. It needs intervention of designer to determine right solutions.
- (3) While optimized parts met the mass target, it is also meet the safety criteria. Potential of using AM technology in automotive industry is inevitable, we foresee rapid progress in the near future.
- (4) The aim of this study was to demonstrate value of topology optimization combine with the simulation of AM materials parts. It was found that significant weight reduction is feasibly due to simulation approach.

REFERENCES

- [1] S. Yoder, S. Morgan, C. Kinzy, E. Barnesa, M. Kirkab, V. Paquitb, P. Nandwanab, A. Plotkowskib, R. Dehoffb and S. Babua, "Characterization of Topology Optimized Ti-6Al-4V Components Using Electron Beam Powder Bed Fusion," *Additive Manufacturing*, vol. 19, pp. 184-196, 2018.
- [2] B. Mfusi, L. Tshabalala, A. Popoola and N. Mathe, "The Effect of Selective Laser Melting Build Orientation on the Mechanical Properties of AlSi10Mg Parts," in *Conference of the South African Advanced Materials Initiative*, Vanderbijlpark, 2018.
- [3] B. Mooney, K. I. Kourousis, R. Raghavendra and D. Agius, "Process Phenomena Influencing the Tensile and Anisotropic Characteristics of Additively Manufactured Maraging Steel," *Materials Science & Engineering A*, vol. 745, pp. 115-125, 2019.
- [4] A. Maamoun, M. Elbestawi, G. Dosbaeva and S. Veldhuis, "Thermal post-processing of AlSi10Mg parts Produced by Selective Laser," *Additive Manufacturing*, vol. 21, pp. 234-247, 2018.
- [5] C. Marinelli, "Mechanical Characterization and Post-Process Heat Treatment of Selectively Laser Melted AlSi10Mg," Master of Science Thesis, , Politecnico di Torino, 2018.
- [6] A. Brandão, J. Gumpinger, M. Gschweidl, C. Seyfert, P. Hofbauer and T. Ghidini, "Fatigue Properties Of Additively Manufactured AlSi10Mg – Surface Treatment Effect," *Procedia Structural Integrity*, vol. 7, pp. 58-66, 2017.
- [7] B. Palumbo, F. Re, M. Martorelli, A. Lanzotti and P. Corrado, "Tensile Properties Characterization of AlSi10Mg Parts Produced by Direct Metal Laser Sintering via Nested Effects Modeling," *Materials*, vol. 10, pp. 144-160, 2017.
- [8] *Vehicles with Regard to Door Latches and Door Retention Components*. [Art]. Status of United Nations Regulation, 2010.

FUNCTIONALLY GRADED MATERIAL DESIGN FOR PLANE STRESS STRUCTURES USING PHASE FIELD METHOD

Gianluca Alaimo*, Massimo Carraturo*, Elisabetta Rocca[†], Alessandro Reali* and Ferdinando Auricchio*

*Department of Civil Engineering and Architecture (DICAr)

[†]Department of Mathematics
University of Pavia
Via Ferrata 3, 27100, Pavia, Italy

Key words: Topology optimization, additive manufacturing, phase-field, homogenization, functionally graded materials

Abstract. We present a functionally graded material design (FGMD) approach relying on a topology optimization procedure based on asymptotic homogenization and phase-field method. We also introduce a complete framework from which numerical results lead to 3D printed structures. We firstly present numerical experiments to verify the proposed methodology and, subsequently, we discuss experimental measurements comparing optimized FGMD with a constant density structure having the same weight. Experimental evidence shows the effectiveness of the proposed methodology in improving the overall stiffness of optimized structures.

1 INTRODUCTION

Additive Manufacturing (AM) technologies introduce a change in design and manufacturing paradigms, shifting the focus from a manufacturing oriented design, also known as *design for manufacturing*, to the so called *functional design*, that mainly focuses on the functionality of the product almost without manufacturability limitations. In this work, we focus on a special type of functional design, the so called *functionally graded material design* (FGMD).

FGMD aims at obtaining structures with mechanical properties similar to fully dense material structures but employing less material, exploiting the possibility to produce local voids and/or lattice microstructures by means of AM processes. Such a result can be achieved by means of a topology optimization [1, 2] which is able to optimally distribute the material within the structure (see, e.g, [4]).

Starting from the seminal work of Bourdin and Chambolle [5], phase-field methods are nowadays well established in the topology optimization field [11, 10, 3]. In [6] it has been developed a phase-field topology optimization procedure suitable for FGMD. There are other methods in the literature which allow to obtain similar structures, for example, we mention the landmark contribution of Cheng *et al.* [7], where the method of moving asymptotes (MMA) is used to minimize the mass of the structure under stress constraints using an homogenized material definition. Contrary to the method proposed in [7], which can only distribute the material within a given domain, the phase-field approach proposed in [6] allows to obtain structures

where also regions of voids can be accounted for, substantially introducing an additional degree of freedom within the design process.

Accordingly, the present work, we introduce a complete pipeline from numerical results to 3D printed component. Employing an *in-house* developed *Mathematica*® code we are able to convert a continuous density map obtained from the phase-field based topology optimization into a 3D virtual model suitable for AM technologies.

The paper is organized as follows: in section 2 an asymptotic homogenization suitable for FGMD is presented, in section 3 we recall the phase-field topology optimization for graded materials first introduced in [6]. In section 4 we verify the implementation of the asymptotic homogenized material tensor by means of a numerical example and subsequently we show the results of a graded material phase-field topology optimization for the classical, well established MBB-beam benchmark problem; moreover we introduce a complete pipeline to convert numerical results into 3D printed structures, and finally we discuss experimental measurements showing the effectiveness of topology optimization in improving stiffness of FGMD. In section 5 we draw our main conclusions and discuss some possible further outlook for this research.

2 ASYMPTOTIC HOMOGENIZATION

FGM may be obtained creating a microstructure into the solid part of the component to form a cellular medium. One way of creating such microstructures is the introduction of regularly spaced holes. More in details, square cells with centrally-placed squared holes are considered in this work (see Figure 1).

We assume that the solid part of the microstructure is an isotropic material of elastic modulus E and Poisson ratio ν . We also introduce a field variable $\chi \in [0, 1]$ that is a measure of the dimension of the squared hole a with respect to the dimension of the side l of the cell, as shown in Figure 1:

$$\chi = 1 - \frac{a}{l}. \quad (1)$$

Because of the squared holes, the cellular medium can be considered an orthotropic material, for which the (homogenized) elastic tensor $\mathbb{C}^H(\chi)$ at the macroscale is expressed, under the hypothesis of plane stress state, as follows:

$$\mathbb{C}^H(\chi) = \begin{bmatrix} C_{11}^H(\chi) & C_{12}^H(\chi) & 0 \\ C_{12}^H(\chi) & C_{22}^H(\chi) & 0 \\ 0 & 0 & C_{66}^H(\chi) \end{bmatrix}. \quad (2)$$

Given a value of χ , we evaluate the components of $\mathbb{C}^H(\chi)$ considering an asymptotic homogenization procedure for which the Representative Volume Element (RVE) is the square cell with the squared hole. The RVE is denoted in the following by Π_χ and its area by Y_χ . A Cartesian coordinate coordinate system $\{y_1, y_2, y_3\}$ is introduced in Π_χ , with the origin in the center of the RVE.

According to relation (2), only three components of $\mathbb{C}^H(\chi)$ have to be evaluated, namely $C_{11}^H(\chi)$, $C_{12}^H(\chi)$ and $C_{66}^H(\chi)$, since from symmetry considerations it results that $C_{11}^H(\chi) = C_{22}^H(\chi)$.

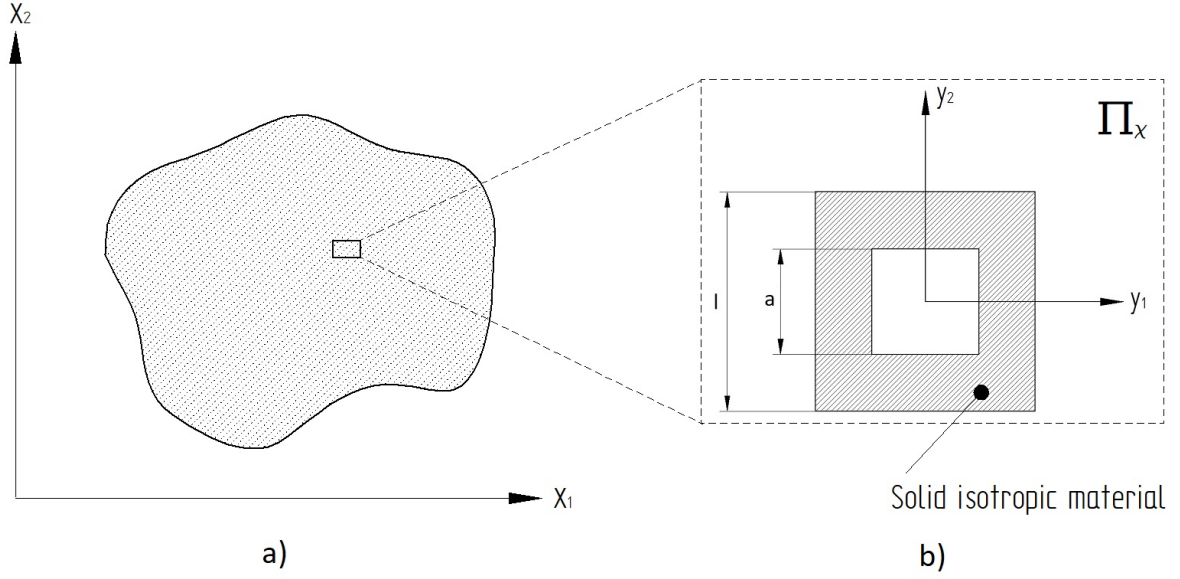


Figure 1: a) Schematic representation of the FGM; b) microstructure consisting of square cells with centrally-placed squared holes (RVE).

The equations that allow to obtain the homogenized material tensor components, under the hypotheses of linear elastic behavior and small strain approximation used for the RVE are:

$$C_{11}^H = C_{22}^H = \frac{1}{Y_\chi} \frac{E}{1-\nu^2} \int_{\Pi_\chi} [1 - \tilde{\epsilon}_{11}(\mathbf{y}) - \nu \tilde{\epsilon}_{22}(\mathbf{y})] d\mathbf{y} \quad (3a)$$

$$C_{12}^H = \frac{1}{Y_\chi} \frac{E}{1-\nu^2} \int_{\Pi_\chi} [\nu - \tilde{\epsilon}_{11}(\mathbf{y}) - \nu \tilde{\epsilon}_{22}(\mathbf{y})] d\mathbf{y} \quad (3b)$$

$$C_{66}^H = \frac{1}{Y_\chi} \frac{E}{2(1+\nu)} \int_{\Pi_\chi} [1 - \tilde{\gamma}_{12}(\mathbf{y})] d\mathbf{y} \quad (3c)$$

In equations (3) $\tilde{\epsilon}_{11}(\mathbf{y})$, $\tilde{\epsilon}_{22}(\mathbf{y})$ and $\tilde{\gamma}_{12}$, are the microscopic strain fields occurring in the RVE, with applied periodicity boundary conditions, and resulting from the application of specific macroscopic strain histories $\bar{\epsilon}_{ij}$. More in detail, the strain histories $\bar{\epsilon}_{11}$, $\bar{\epsilon}_{22}$ and $\tilde{\gamma}_{12}$ applied for equations (3a), (3b) and (3c) respectively, are shown in figure 2. Equations (3) have been numerically solved by Finite Element Analyses (FEA) in [8].

In FGM the value of the density field variable χ is allowed to continuously vary on the whole structure. In order to perform topology optimization using the model involving a material with square micro cells, we need to determine the functional relationship between the constitutive matrix C^H components and the field variable χ , i.e. to construct $C^H(\chi)$. To this aim, a table of 11 equally spaced sampling points representing 11 values of χ was extracted from [8]. Finally, we use a least squares approximation polynomial fitting to find the elements of the homogenized elasticity matrix $C^H(\chi)$ in a continuous form, relying on the discrete values obtained at the sampling points.

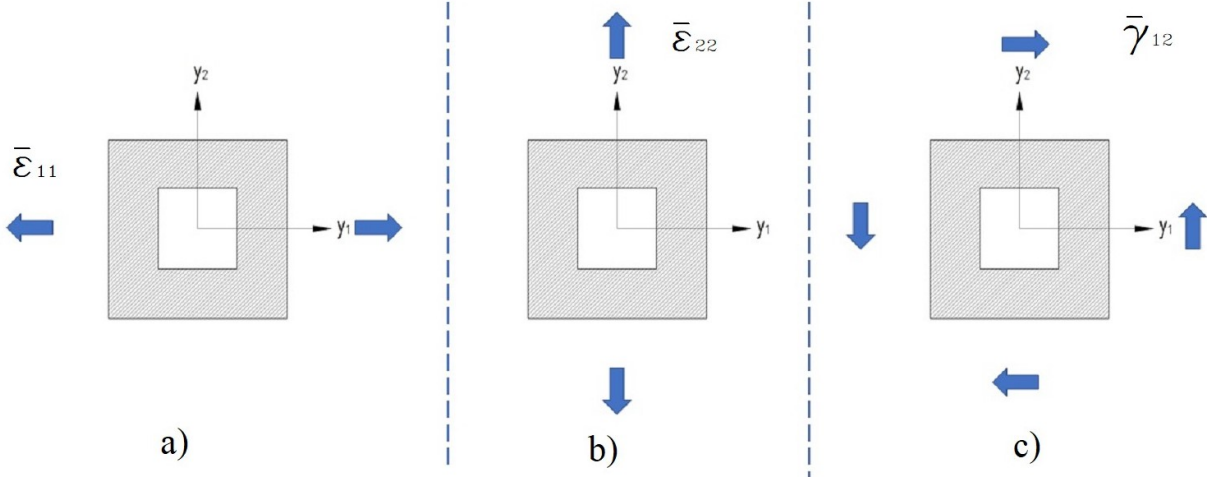


Figure 2: Macroscopic strain histories applied to the RVE for the evaluation of the components of the homogenized material tensor $\mathbb{C}^H(\chi)$. a) $\bar{\varepsilon}_{11}$, b) $\bar{\varepsilon}_{22}$, c) $\bar{\gamma}_{12}$

3 PHASE-FIELD TOPOLOGY OPTIMIZATION FOR FUNCTIONALLY GRADED MATERIALS

We now consider a domain $\Omega \subset \mathbb{R}^d$, where a material is distributed by means of two phase field variables: $\varphi \in [0, 1]$ and $\chi \in [0, \varphi]$, where $\varphi \equiv 0$ corresponds to voids and $\varphi \equiv 1$ indicates bulk material, while χ varies continuously, such that it can be considered as a measure of the material density in the domain regions ($\varphi \neq 0$).

We aim at solving a linear elastic problem formulated as follows:

$$\operatorname{div}(\boldsymbol{\sigma}(\varphi, \chi)) = \mathbf{0} \quad \text{in } \Omega \quad (4a)$$

$$\mathbf{u} = \mathbf{0} \quad \text{on } \Gamma_D \quad (4b)$$

$$\boldsymbol{\sigma}(\varphi, \chi) \cdot \mathbf{n} = \mathbf{g} \quad \text{on } \Gamma_N \quad (4c)$$

$$\boldsymbol{\varepsilon}(\mathbf{u}) = \operatorname{sym}(\nabla \mathbf{u}) \quad \text{in } \Omega \quad (4d)$$

$$\boldsymbol{\sigma}(\varphi, \chi) = \mathbb{C}(\varphi, \chi) : \boldsymbol{\varepsilon}(\mathbf{u}) \quad \text{in } \Omega \quad (4e)$$

with \mathbf{g} external load vector, \mathbf{n} the unit normal vector, and with the material tensor $\mathbb{C}(\varphi, \chi)$ defined as follows:

$$\mathbb{C}(\varphi, \chi) = \mathbb{C}^H(\chi)\varphi^3 + \gamma_\varphi^2 \mathbb{C}^H(\chi)(1 - \varphi)^3 \quad (5)$$

with $\gamma_\varphi > 0$.

In this work we aim at minimizing the compliance of the structure defined as the inverse of the stiffness:

$$\mathcal{C}(\mathbf{u}) = \int_{\Gamma_N} \mathbf{g} \cdot \mathbf{u} \, dx$$

under a volume constraint and such that the linear elastic problem (4) is satisfied.

To this end, following [6], we introduce the Ginzburg-Landau functional, which defines the free energy of the system as follows:

$$\mathcal{E}(\varphi, \chi) = \int_{\Omega} \frac{\gamma_{\varphi}}{2} |\nabla \varphi|^2 + \frac{1}{\gamma_{\varphi}} \psi_0(\varphi) dx + \int_{\Omega} \frac{\gamma_{\chi}}{2} |\nabla \chi|^2 dx \quad (6)$$

where $\gamma_{\chi} > 0$ and $\psi_0(\varphi) = (\varphi - \varphi^2)^2$ is the double-well potential.

In order to minimize the compliance together with the free-energy functional, we construct a cost functional of the form:

$$\mathcal{J}(\varphi, \chi, \mathbf{u}) = C(\mathbf{u}) + \kappa \mathcal{E}(\varphi, \chi) \quad (7)$$

with $\kappa > 0$.

We now define the set of admissible phase-field variable φ and χ , Φ_{ad} and Ξ_{ad} respectively:

$$\Phi_{ad} := \{\varphi \in H^1(\Omega) : 0 \leq \varphi \leq 1 \text{ a.e. in } \Omega\} \quad (8)$$

and

$$\Xi_{ad} := \{\chi \in H^1(\Omega) : 0 \leq \chi \leq \chi \text{ a.e. in } \Omega\}, \quad (9)$$

where $H^1(\Omega)$ indicates the first order Sobolev space on Ω .

The optimization problem can be then formulated as follows:

$$\min_{\varphi \in \Phi_{ad}, \chi \in \Xi_{ad}} \mathcal{J}(\varphi, \chi, \mathbf{u}), \quad (10)$$

verifying the conditions:

$$\int_{\Omega} \varphi dx = m_{\varphi} |\Omega|, \quad (11)$$

$$\int_{\Omega} \chi dx = m_{\chi} |\Omega|, \quad (12)$$

and such that the linear elastic problem (4) is satisfied.

The volume constraints of equations (11) and (12) are imposed introducing the Lagrange multipliers λ and μ for the functional $\mathcal{M}^{\varphi} = \int_{\Omega} (\varphi - m_{\varphi}) dx$ and $\mathcal{M}^{\chi} = \int_{\Omega} (\chi - m_{\chi}) dx$, whereas the state equation is inserted into the problem by means of the adjoint operator \mathcal{S} :

$$\mathcal{S} = - \int_{\Omega} \boldsymbol{\sigma} : \boldsymbol{\varepsilon}(\mathbf{p}) dx + \int_{\Gamma_N} \mathbf{g} \cdot \mathbf{p} dx, \quad (13)$$

where \mathbf{p} is the so-called adjoint variable.

A Lagrangian functional \mathcal{L} can now be defined as follows:

$$\mathcal{L} = \mathcal{J} + \lambda \mathcal{M}^{\varphi} + \mu \mathcal{M}^{\chi} + \mathcal{S}. \quad (14)$$

Since the compliance minimization problem in equation (10) is self-adjoint we have $\mathbf{p} = \mathbf{u}$. We want that our optimal control solutions satisfy the first order optimality conditions defined as

$$D_{\varphi} \mathcal{L} v_{\varphi} \geq 0 \quad \forall \varphi \in \Phi_{ad}, \quad (15)$$

and

$$D_{\chi} \mathcal{L} v_{\chi} \geq 0 \quad \forall \chi \in \Xi_{ad}. \quad (16)$$

To solve the optimality inequalities of equations (15) and (16), we employ Allen-Cahn gradient flow. Introducing a pseudo-time step τ , the Allen-Cahn equation can be written as:

$$\begin{aligned} \frac{\gamma_{\phi}}{\tau} \int_{\Omega} (\phi - \phi_n) v_{\phi} d\mathbf{x} + \frac{\gamma_{\chi}}{\tau} \int_{\Omega} (\chi - \chi_n) v_{\chi} d\mathbf{x} + \gamma_{\phi} \kappa \int_{\Omega} \nabla \phi \cdot \nabla v_{\phi} d\mathbf{x} + \gamma_{\chi} \kappa \int_{\Omega} \nabla \chi \cdot \nabla v_{\chi} d\mathbf{x} + \\ \int_{\Omega} (\phi - m_{\phi}) v_{\lambda} d\mathbf{x} + \int_{\Omega} (\chi - m_{\chi}) v_{\mu} d\mathbf{x} + \int_{\Omega} v_{\phi} \lambda d\mathbf{x} + \int_{\Omega} v_{\chi} \mu d\mathbf{x} - \\ \int_{\Omega} \boldsymbol{\varepsilon}(\mathbf{u}) : \frac{\partial \mathbb{C}}{\partial \phi} v_{\phi} \boldsymbol{\varepsilon}(\mathbf{u}) d\mathbf{x} - \int_{\Omega} \boldsymbol{\varepsilon}(\mathbf{u}) : \frac{\partial \mathbb{C}}{\partial \chi} v_{\chi} \boldsymbol{\varepsilon}(\mathbf{u}) d\mathbf{x} + \frac{\gamma}{\varepsilon} \int_{\Omega} \frac{\partial \psi_0}{\partial \phi} (\phi_n) v_{\phi} d\mathbf{x} = 0, \end{aligned} \quad (17)$$

which we solve using the finite element method. For a more detailed explanation of the method and the implemented algorithm we refer to [6].

4 RESULTS

In this section we discuss numerical and experimental results showing the effectiveness of the proposed methodology. The finite elements and the phase-field topology optimization results are obtained using a FEniCS [9] environment, whereas the procedure to generate 3D virtual models from numerical results is implemented in *Mathematica*®. A *Stratasys Object 260 Connex 3*® is used to print the specimens.

Verification of asymptotic homogenization procedure To estimate the modeling error introduced by asymptotic homogenization we study the simple numerical benchmark described in Figure 3, namely a quarter of traction test sample. We apply a load $g = 100[N/mm]$ and we evaluate the compliance and the maximum displacement in x -direction $u_{x,max}$ of the specimen. We consider domains with microstructure having different cell size and the corresponding homogenized structure. Table 1 reports the results obtained for three different macroscopic density fraction $\rho_f = \rho_{str}/\rho_{bulk} = 0.25, 0.5$ and 0.75 , where $\rho_{bulk} = 7850[N/m^3]$ is the density of the bulk material and ρ_{str} the actual density of the perforated structures (e.g, see Figure 4). It can be observed that for lower density fraction the error of the homogenized model increases. This effect is due to both boundary effects and an intrinsic modeling error which we introduced with the asymptotic homogenization assumptions. Nevertheless, due to the extremely high computational costs of simulations resolving a time evolving microstructure domain, we can consider the homogenized model a sufficiently good trade-off between accuracy and computational efforts.

Topology optimization of an MBB-beam We apply the phase-field topology optimization procedure described in section 3 to the *Messerschmitt-Bölkow-Blohm* (MMB) beam problem described in Figure 5. We set $g = 25$ N and we consider the RGD851 rigid polymer from Stratasys, having elastic modulus $E = 2300$ MPa and a Poisson ratio $\nu = 0.3$. The volume filling ratios are $m_{\phi} = 0.7$ and $m_{\chi} = 0.4$. In order to satisfy the machine manufacturing constraints,

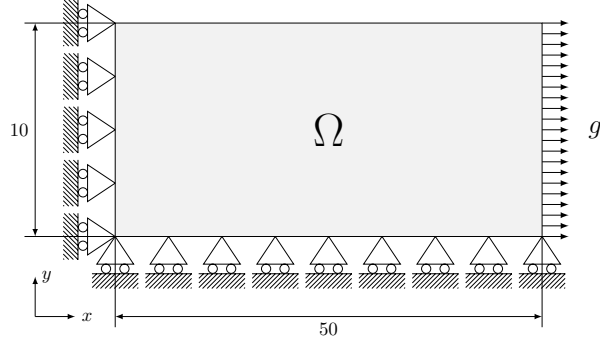


Figure 3: One-quarter traction test. All units are in mm.

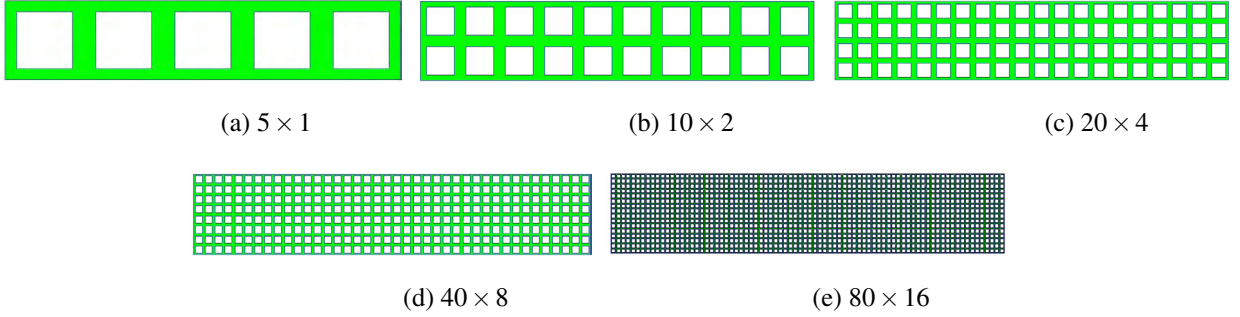
Figure 4: Microstructure domains with different cell sizes and fixed density fraction $\rho_f = 0.5$.

Table 1: Compliance and max. displacement value of different microstructures and corresponding homogenized material.

ρ_f	0.25			0.75			0.5		
	#cells	#DOFs	\mathcal{C}	$u_{x,max}$	#DOFs	\mathcal{C}	$u_{x,max}$	#DOFs	\mathcal{C}
5x1	30346	496.0	0.78	26288	48.1	5.31E-02	59564	103.0	1.29E-01
10x2	30788	295.5	0.45	82262	46.5	4.91E-02	58482	89.0	1.04E-01
20x4	36376	203.4	0.24	252262	45.8	4.71E-02	60544	82.9	8.99E-02
40x8	144558	188.44	0.21	333984	45.3	4.60E-02	66082	79.2	8.21E-02
80x16	819714	185.4	0.20	339608	44.5	4.48E-02	111350	76.6	7.86E-02
hom	402402	169.0	0.17	402402	44.8	4.47E-02	402402	79.7	7.97E-02

which do not allow to print infinitely small thicknesses, we set a minimum value for the density parameter $\chi_{min} = 0.29$, such that $\chi \in [\chi_{min}, \varphi]$ where $\varphi \neq 0$ and $\chi = 0$ otherwise. The evolution of the density phase-field variable χ at different time steps is shown in Figure 6.

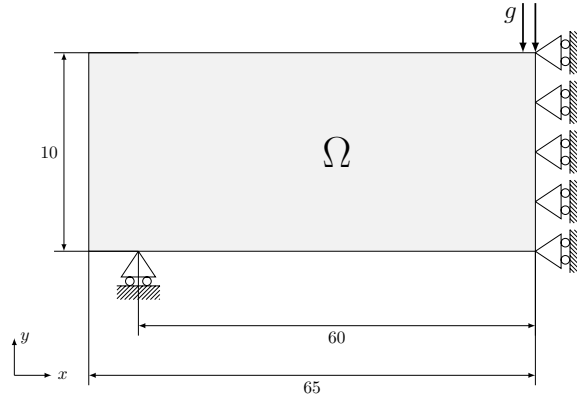


Figure 5: MBB-beam half-domain setup

From analysis to 3D printing In order to convert the result of Figure 6f into printable data we implemented the following procedure:

1. Choose the shape and the size of the microstructure cells. In this work we choose squared cells with dimensions fulfilling technological requirements such as the minimum printable thickness and hole dimension. The dimension of the cell $l = 1\text{ mm}$ is determined according to the resolution capability of the Connex 3 3D-printer.
2. Generate a Cartesian grid Λ_χ over the domain Ω with a constant size equal to the cell dimension;
3. Evaluate the average value $\bar{\chi}$ within each cell of Λ_χ ;
4. Generate a cuboid for each cell of Λ_χ ; each cuboid results from the extrusion of a square of side equal to a , evaluated through equation (1). Each cuboid represents the void that has to be introduced to create the microstructure.
5. Generate an high resolution Cartesian grid Λ_φ over the domain Ω with a constant size equal to the finite element mesh dimension; for each cell of Λ_φ the corresponding value of the field variable φ is assigned. For each cell, if the value of $\varphi > \xi$ a cuboid is generated, being ξ a threshold value.
6. By means of a boolean operation subtract the solid obtained at step 4 from the solid obtained at step 5.

This procedure is implemented in *Mathematica* such that we have obtained a complete conversion pipeline within a single numerical framework.

The complete process, from analysis to 3D printing is described in Figure 7 where the main steps of this method are highlighted. Finally, we print the final structure using the *260 Connex 3®* available at the laboratories of the University of Pavia.

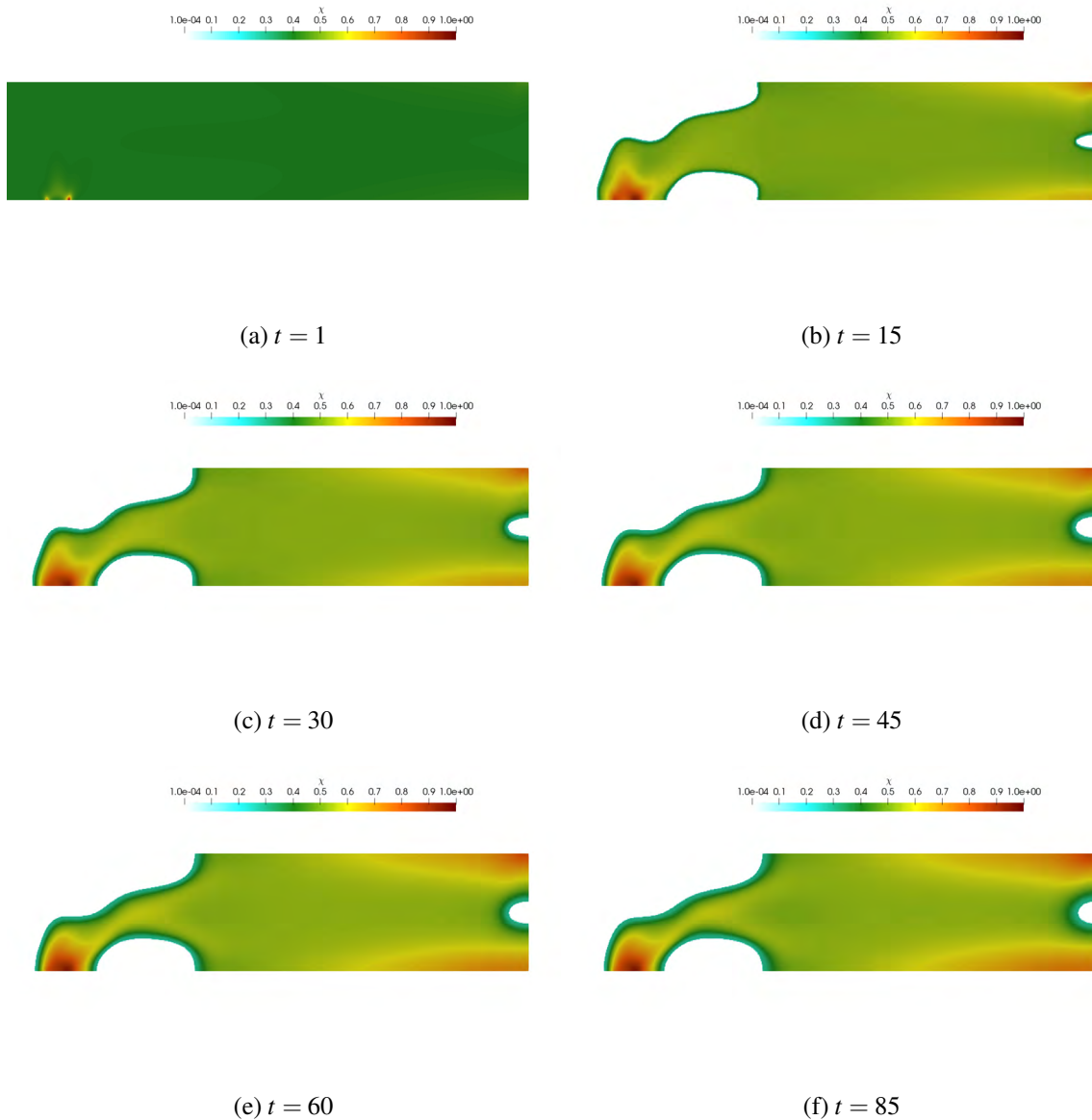


Figure 6: Evolution of the density variable χ at different time steps t .

Experimental results We now aim at assessing the higher mechanical properties (e.g., stiffness) which topologically optimized structures can achieve compared to lattice structures having the same weight but constant density. We printed five different specimens: 3 using the optimized model and 2 constant density beams. One of the optimized specimen was used to calibrate the machine, thus we report results only of 4 measurements. Figure 8 shows the two different kind of specimens (constant density and FGM) in the testing machine. We perform a 3-point bending test and measure the maximum displacement along the axis of symmetry of the structure. The experimental results are reported in Figure 9. They clearly show the benefits of performing

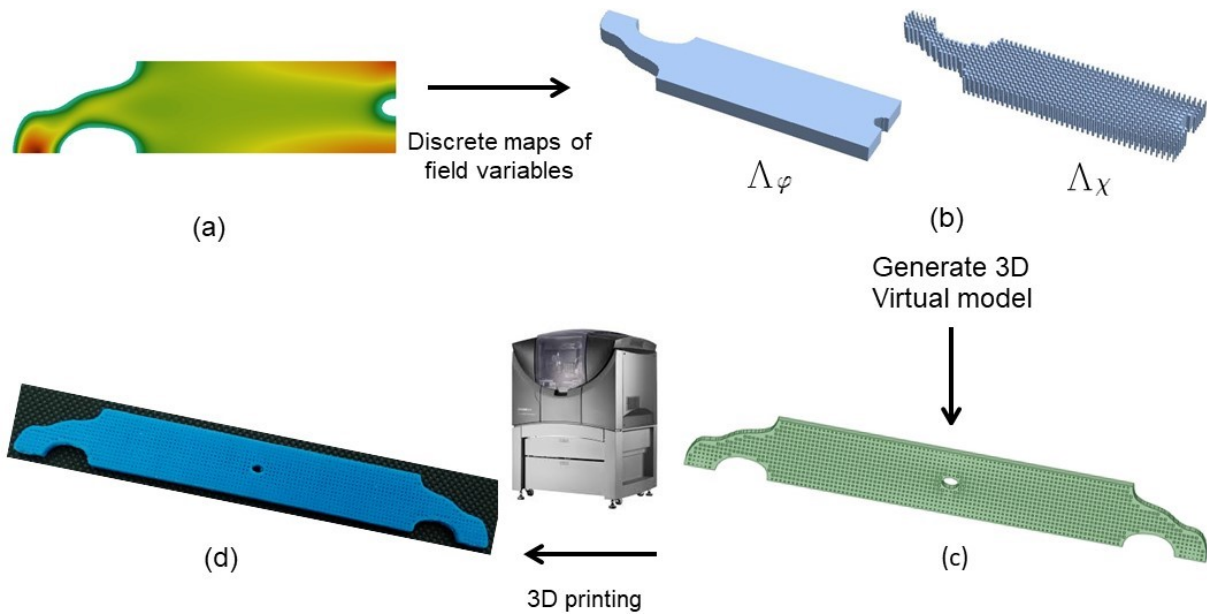


Figure 7: From analysis to 3Dprinting: A complete pipeline from a continuously graded numerical solution to a 3D printed FGM structure; a) phase-field based topology optimization, b) generation of 3D virtual model from the discrete maps of the field variables, c) finished 3D virtual model, d) 3D-printed part

topology optimization on the mechanical response of the structure: for the same load (50 N) we have more than two times less maximum displacements in the optimized specimen than in the constant density one.

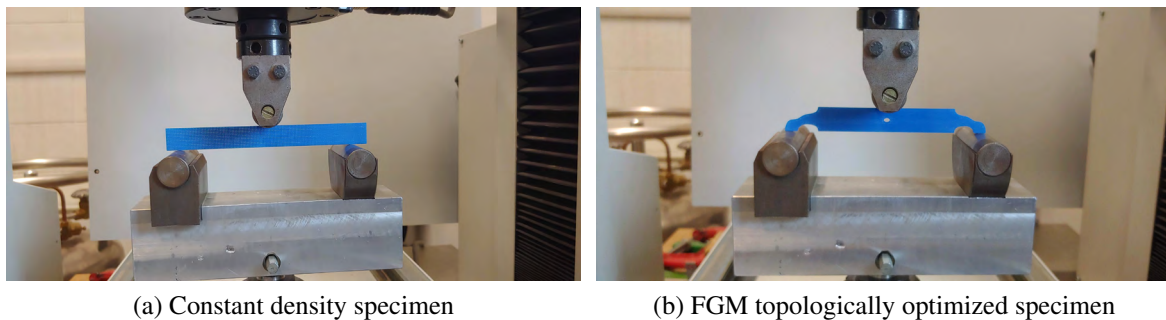


Figure 8: Specimens used in the experiment.

5 CONCLUSIONS

In this work we develop a complete pipeline to obtain 3D printed FGM structures. In particular, we employ the phase-field method together with asymptotic homogenization for the analysis and the topological optimization of the structure, whereas an *in-house* developed code

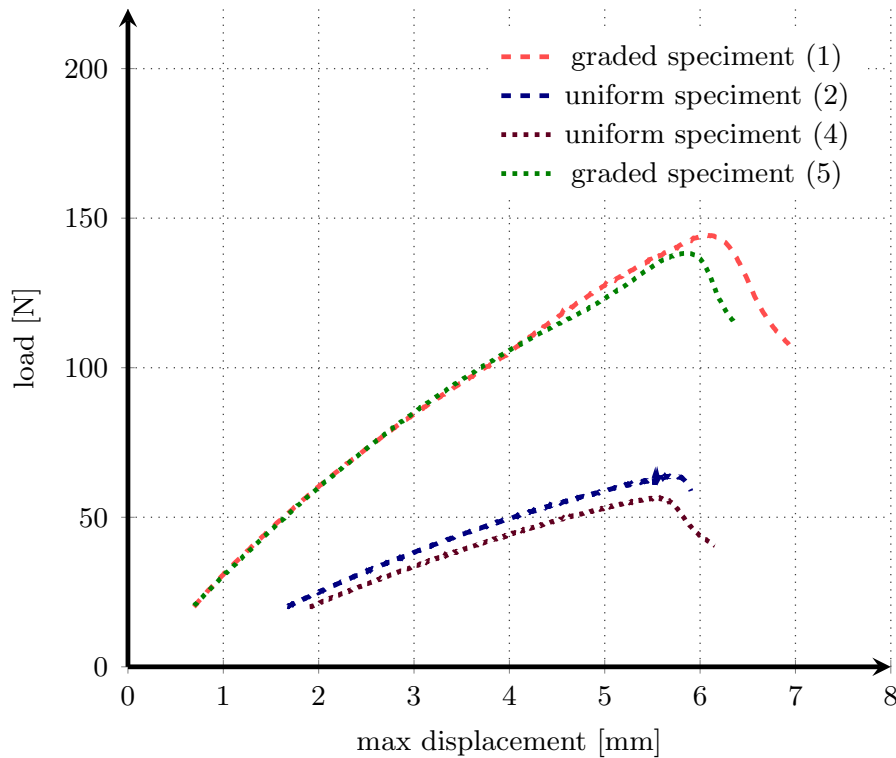


Figure 9: Load vs displacements plot.

is used to convert the density map into a 3D virtual model suitable for 3D printing.

As a validation benchmark we investigate an MBB-beam problem under the hypothesis of plane stress state. The resulting optimized structure is printed and experimentally tested. Measurements data are also obtained for a similar beam structure having constant density and equal weight. Experimental evidence shows that for a fixed weight of the structure, FGM structures obtained by means of the proposed methodology are more effective in terms of stiffness with respect to an analogous lattice structure with constant density.

This experimental results show that the phase-field approach can be useful in case of FGMD optimization. In fact, contrary to similar methods available in literature, the proposed phase-field based topology optimization allows to not only redistribute the material within a given domain but also to indicate void regions, by means of an additional degrees of freedom into the problem.

As further outlooks for the present research we aim at extending the presented method to 3D problems and to mass minimization under both functional (e.g., maximum stress constraint) and technological constraints related to AM processes (e.g., overhang building angles, feature resolution of the specific AM process).

Acknowledgements This work was partially supported by Regione Lombardia through the project "TPro.SL - Tech Profiles for Smart Living" (No. 379384) within the Smart Living program, and through the project "MADE4LO - Metal ADditivE for LOmbardy" (No. 240963) within the POR FESR 2014-2020 program. MC

and AR have been partially supported by Fondazione Cariplo - Regione Lombardia through the project “Verso nuovi strumenti di simulazione super veloci ed accurati basati sull’analisi isogeometrica”, within the program RST - rafforzamento. This research has been performed in the framework of the project Fondazione Cariplo-Regione Lombardia MEGAsTAR “Matematica d’Eccellenza in biologia ed ingegneria come acceleratore di una nuova strategia per l’AtRattività dell’ateneo pavese”. The present paper also benefits from the support of the GNAMPA (Gruppo Nazionale per l’Analisi Matematica, la Probabilità e le loro Applicazioni) of INdAM (Istituto Nazionale di Alta Matematica) for ER.

REFERENCES

- [1] Bendsøe, M. P., On obtaining a solution to optimization problems for solid, elastic plates by restriction of the design space, *J. Struct. Mech.*, vol. 11 (1983), 501–521.
- [2] Bendsøe, Martin P. and Ole Sigmund, *Topology Optimization - Theory, Methods, and Applications*, ed. Springer Verlag (2003).
- [3] L. Blank, H. Garcke, M.H. Farshbaf-Shaker, V. Styles, Relating phase field and sharp interface approaches to structural topology optimization. *ESAIM Control Optim. Calc. Var.* **20** (2014), 1025–1058.
- [4] D. Brackett, I. Ashcroft, R. Hague, Topology Optimization for Additive Manufacturing, *Solid Freeform Fabrication Symposium (SFF)*, Austin (2014).
- [5] B. Bourdin, A. Chambolle, Design-dependent loads in topology optimization. *ESAIM Control Optim. Calc. Var.* **9** (2003), 19–48.
- [6] Carraturo M., Rocca E., Bonetti E., Hoemberg D., Reali A., Auricchio A., Graded-material Design based on Phase-field and Topology Optimization, *Computational Mechanics* (2019), DOI: 10.1007/s00466-019-01736-w.
- [7] Cheng L., Bai J. and To A.C., Functionally graded lattice structure topology optimization for the design of additive manufactured components with stress constraints, *Computer Methods in Applied Mechanics and Engineering*, 344 (2019) 334–359.
- [8] Hassani B. and Hinton E., *Homogenization and structural topology optimization : theory, practice and software*, Springer (1998).
- [9] A. Logg and K.-A. Mardal and G. N. Wells, *Automated Solution of Differential Equations by the Finite Element Method*, Springer (2012).
- [10] P. Penzler, M. Rumpf, B. Wirth, A phase-field model for compliance shape optimization in nonlinear elasticity. *ESAIM Control Optim. Calc. Var.* **18** (2012), 229–258.
- [11] A. Takezawa, S. Nishiwaki, M. Kitamura, Shape and topology optimization based on the phase field method and sensitivity analysis. *J. Comput. Phys.* **229** (2010), 2697–2718
- [12] M. Zhou and O. Sigmund, On fully stressed design and p-norm measures in structural optimization, *Struct Multidisc. Optim* 56 (2017) 731–736.

GUIDELINES FOR A POST PROCESSING ORIENTED DESIGN OF ADDITIVE MANUFACTURED PARTS FOR USE IN TOPOLOGY OPTIMIZATION

Sim-AM 2019

STEFAN LAMMERS^{*,†}, JOHANNES TOMINSKI[†] AND DETMAR ZIMMER^{*,†}

^{*} Direct Manufacturing Research Center (DMRC)
Paderborn University
Mersinweg 3, 33098 Paderborn, Germany
e-mail: stefan.lammers@dmrc.de, www.dmrc.uni-paderborn.de

[†] Chair of Design and Drive Technology (KAt)
Paderborn University
Warburger Str. 100, 33098 Paderborn, Germany
email: stefan.lammers@upb.de, www.mb.upb.de/kat/

Key words: Additive Manufacturing, Design for Additive Manufacturing (DFAM), Topology optimization

Summary: *This document provides a method to derive guidelines for a post processing oriented design of additive manufactured parts based on experimental investigations.*

1 INTRODUCTION

According to ISO / ASTM 52900, additive manufacturing (AM) is defined as "the process of joining materials to make parts from 3D model data, usually layer upon layer, as opposed to conventional manufacturing including subtractive manufacturing technologies and formative manufacturing methodologies" [1]. This results in significant advantages over conventional manufacturing methodologies, such as the production of topologically optimized, complex structures, lower material consumption or shorter product development cycles. In order to be able to use these advantages, the possibilities and restrictions of the processes must be known. In particular, selective laser beam melting (SLM), in which a powdery metallic starting material is melted by means of a laser, requires a sound understanding of the process. For this purpose, design guidelines have been presented in various scientific papers. These design guidelines help to design a component in such a way that it can be manufactured successfully using additive manufacturing. These so-called "AM-suitable design guidelines" can be found among others at Adam, Kranz and Thomas [2,3,4,5]. In contrast to established manufacturing processes, the post-processing of additive components is divided into two steps. First, the AM immanent post processing, such as the removing of the component from the building platform or the removing of the remaining powder. These post-processing steps are in the following referred to "post-processing". Secondly, the subsequent post-processing steps to improve the component properties, such as milling and turning or a stress-relief annealing. These are referred to as "finishing" and form the focus of this paper. With regard to a successful finishing of additively manufactured

components, design guidelines must be taken into account that consider the finishing inherent restrictions and possibilities. In the following, these design guidelines are referred to “finishing suitable”. They can deviate significantly from those of conventionally manufactured components in the case of additively manufactured components. Although there are some investigations that deal with the post-processing of additively manufactured components [6,7], there are hardly any design guidelines that are suitable for finishing [8]. Therefore, knowledge about the finishing of additively manufactured components is based on experimental experience rather than on scientific knowledge. For this reason, design guidelines for a finishing suitable design must be methodically determined and quantified. These quantified design guidelines can be used for an automated design check on complex components like topology optimized geometries.

2 EXPERIMENTAL PROCEDURE

On the way to an automated, software-supported and finishing suitable design check of components built with AM, a method is developed that enables the development of design guidelines for a finishing suitable design. For this purpose, suitable finishing processes are identified, their influence on the component properties is mapped and quality criteria for a quality assessment are established. Test specimens are developed and produced for experimental investigation and quantification of the quality criteria. The results of the experimental investigations on the test specimens are prepared graphically and textually in design guidelines and provided in tabular form for a design checking software.

2.1 Identification of suitable finishing processes

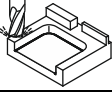
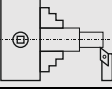
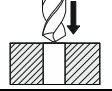
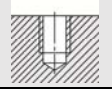
In order to identify suitable finishing processes for additively manufactured components, it is advisable to take inspiration from the finishing procedures for conventionally manufactured components. Through extensive research, finishing methods were compiled for casted, formative and subtractive generated components. For SLM parts the in Table 1 listed processes could be identified as suitable. The advantages of these processes are their wide availability and the comprehensive understanding of the process that has been built up over decades of use in conventionally manufactured components. These processes also showed good suitability for additive manufactured components and had positive effects on the component properties [9,10]. The different finishing processes have different influences on additive manufactured components. The six defined types of influence are briefly explained in the following:

- Surface quality: The finishing process improves the surface quality of additive manufactured components.
- Functional area: The finishing process enables the realization of functional areas such as fits or threads.
- Deburring: The process enables deburring and removal of support residues on the component surface.
- Corrosion protection: The finishing process enables the additive manufactured component to be coated to counteract corrosion.
- Optics: The finishing process improves the appearance of the additive manufactured component

- Material properties: The finishing process enables the improvement of the material properties, such as improved tensile strength or the reduction of residual stresses.

The finishing processes are underlined in Table 1 and marked with a pictogram were classified as relevant. They are available in the most companies and show good results in the finishing of additively manufactured components.

Table 1: Finishing processes and their influence on additive manufactured components

Finishing groups	Finishing process	Pictogram	Influence on additive manufactured component	Examples	
Machining	Geometric defined cutting edge	<u>Milling</u>		<ul style="list-style-type: none"> • Surface quality • Functional area • Deburring 	<ul style="list-style-type: none"> • Face milling • Circumferential milling
		<u>Turning</u>		<ul style="list-style-type: none"> • Surface quality • Functional area 	<ul style="list-style-type: none"> • Face turning • Longitudinal turning
		<u>Drilling</u>		<ul style="list-style-type: none"> • Surface quality • Functional area • Deburring 	<ul style="list-style-type: none"> • Round drilling • Screw drilling • Profile drilling
		<u>Thread cutting</u>		<ul style="list-style-type: none"> • Functional area 	<ul style="list-style-type: none"> • Thread whirling • Manual thread cutting
	Geometric undefined cutting	<u>Sanding</u>		<ul style="list-style-type: none"> • Surface quality • Functional area • Deburring 	<ul style="list-style-type: none"> • Vibratory finishing • Belt sanding
		Polishing		<ul style="list-style-type: none"> • Surface quality • Optics 	<ul style="list-style-type: none"> • Electro polishing • Manual polishing
		Blasting		<ul style="list-style-type: none"> • Surface quality • Material properties 	<ul style="list-style-type: none"> • Sandblasting • Vacuum suction blasting
		Lapping		<ul style="list-style-type: none"> • Surface quality • Functional area 	<ul style="list-style-type: none"> • Flat lapping • External lapping
	Erode	Thermic		<ul style="list-style-type: none"> • Surface quality • Deburring 	<ul style="list-style-type: none"> • Wire eroding • Die sinking
		Electrochemically		<ul style="list-style-type: none"> • Surface quality • Deburring 	<ul style="list-style-type: none"> • Elysing
Heat treatment	Tempering		<ul style="list-style-type: none"> • Material properties 	<ul style="list-style-type: none"> • Nitrate • Carburize 	
	<u>Annealing</u>		<ul style="list-style-type: none"> • Material properties 	<ul style="list-style-type: none"> • Stress-relief annealing • Solution annealing 	
Surface treatment	Coating		<ul style="list-style-type: none"> • Corrosion protection • Optics 	<ul style="list-style-type: none"> • Galvanize • Chromate 	
	Painting		<ul style="list-style-type: none"> • Corrosion protection • Optics 	<ul style="list-style-type: none"> • Dip coating • Spray painting 	

The method for the development of design guidelines for a finishing suitable design is derived from the relevant finishing procedures carried out with a geometric defined cutting edge. In the following, the pictograms are used to clarify which kind of finishing is considered.

2.2 Additive manufacturing of specimens

The specimens which are defined for the experimental investigations are listed in chapter 2.3. All specimens were manufactured additively with the material AlSi10Mg. This material has good casting properties and is optimized for the SLM process on corresponding machines. AlSi10Mg is suitable for thin-walled components and has a good dynamic load capacity. The material is suitable for highly stressed components and for applications requiring a combination of low weight and good thermal properties at the same time. Before processing in the SLM process, the material is available in powder form with a distribution of 15 μm to 45 μm . In the horizontal direction, a tensile strength R_m of 460 ± 20 MPa and a yield strength $R_{p0.2}$ of 270 ± 10 MPa can be achieved. The machines used for the investigations and the main manufacturing parameters are listed in table 2. The test specimens were manufactured in triplicate in order to obtain meaningful results taking into account a resource-efficient number of test specimens.

Table 2: Manufacturing boundary conditions.

Machinery			
Machine	SLM Solutions SLM 250HL	SLM Solutions SLM 280 HL	
Building chamber size	250x250x250mm	280x280x350mm	
Max. laser power	400W	1000W	
Manufacturing Parameters for core hatching			
Parameter set name	PS1	PS2	PS3
Layer thickness [μm]	50	30	50
Laser Power [W]	350	100	400
Scan Speed [mm/s]	930	100	950

2.3 Definition and finishing of test specimens

In order to be able to evaluate the finishing processes and parameters, examination areas and quality criteria were defined which show restrictions or positive effects of the finishing. On the basis of these defined examination areas and quality criteria, suitable test specimens were designed on which the experimental examination can be carried out. The design of the test specimens was carried out with the 3D CAD software SolidWorks.

In the following, the test specimens developed for the investigation of each relevant finishing process are listed in a structured form in tables 3, 5, 7 and 8. For each test specimen, the associated examination areas, quality criteria and variants are listed in tabular form. The performed investigations and their results are discussed.

2.3.1 Test specimens for milling investigation

Before finishing the test specimen 1.1 (Table 3), photos of the examination area ① "run-out surface" were taken with a macroscope. The supporting structures of the specimens were removed with a milling head with carbide inserts. The different run-out surfaces in the

examination area ① were measured using a Keyence VR 3200 macroscope and the formation of the run-out surfaces was investigated. It can be seen that even the smallest run out surface V1 is sufficient to allow safe milling of the adjacent surfaces. The surface roughness was measured using the macroscope before the examination areas ② and ④ were finished. The examination areas were machined with a 10 mm diameter end mill. In order to ensure a defined clamping of the test specimens on the milling table, they were fixed with a clamping device and mill parallel supports.

Table 3: Specimen data sheet for milling.

Finishing process	Specimen	① Examination areas · Quality criterion 1 · Quality criterion ...	Test specimen variants / test specimen parameters				
	1.1 	① Run-out surface · Sufficient run-out surface	Run-out surface geometry:				
			Variant	V1	V2	V3	
			b [mm]	1	2	3	
		h [mm]	0,3	0,45	0,6		
		② Face milling surface · Required machining allowance MA · Surface quality	Machining allowance (MA):				
			Variant	V1	V2	V3	
			MA[mm]	0,1	0,3	0,5	
		③ Wall thickness (t_w) · Min. t_w at MA = 0,15 mm	Wall thickness:				
			Variant	V1	V2	V3	
			t_w [mm]	1,5	3	4,5	
		④ Circumferential milling surface · Required machining allowance · Surface quality	Machining allowance (MA):				
			Variant	V1	V2	V3	
MA[mm]	0,1		0,3	0,5			

After the milling process, the surface roughness R_z and the average roughness value R_a were determined for the specimens with the macroscope. Table 4 shows the measurement results for face and circumferential milling before and after finishing for different machining allowances (MA).

Table 4: Measured surface roughness before and after milling.

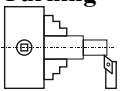
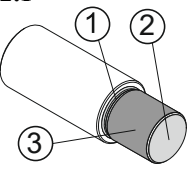
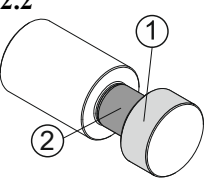
		MA=0,1mm		MA=0,3mm		MA=0,5mm	
		R_z	R_a	R_z	R_a	R_z	R_a
Face milling	Before Finishing	78,7	9,4	85,5	10,0	74,8	9,8
	After Finishing	17,5	2,8	12,2	1,8	12,6	1,9
Circumferential milling	Before Finishing	180,1	29,8	168,3	25,9	163,6	24,9
	After Finishing	10,8	1,4	10,8	1,5	12,8	1,8

The measurements show that AlSi10Mg delivers good results for face and circumferential milling by a machining allowance of 0.3 mm. So a complete finishing of the surface is ensured. Furthermore, it can be seen in the examination areas ③ that a wall thickness of 1.5 mm, independent of the parameter set, is not sufficient to allow complete finishing of the surface. This can be explained by an oscillation of the wall, which leads to an inhomogeneous milling of the wall surface. With a wall thickness of 3 mm acceptable results could be achieved.

2.3.2 Test specimens for turning investigation

Before the test specimens 2.1 (Table 5) were finished on a flatbed lathe, the surface roughness of the examination areas was determined with the macroscope and the undercut formation in the examination area was recorded photographically. In addition, the remaining support structures were removed from the test specimens using indexable turning inserts KC5410 from Kennametal.

Table 5: Specimen data sheet for turning.

Finishing process	Specimen	Ⓝ Examination areas · Quality criterion 1 · Quality criterion ...	Test specimen variants / test specimen parameters				
	2.1 	① Undercuts DIN 509, form E · Sufficient undercut	Undercut geometry DIN 509:				
			Variant	V1	V2	V3	
			f [mm]	2,5	3	3,5	
		t [mm]	0,3	0,45	0,6		
		② Face turning surface · Required machining allowance · Surface quality	Machining allowance:				
			Variante	V1	V2	V3	
	MA[mm]		0,1	0,3	0,5		
	③ Longitudinal turning surface · Required machining allowance · Surface quality	Machining allowance:					
		Variante	V1	V2	V3		
		MA[mm]	0,1	0,3	0,5		
2.2 	① Inner lattice structure · Damage to the structures due to the turning process · Possibility of parting off	-					
	② Outer lattice structures · Possibility of plan and longitudinal turning of supporting structures						

During finishing it was found in examination area ① that the smallest undercut with a width of 2.5 mm and a height of 0.3 mm (according to DIN 509, Form E) allows a sufficient tool run-out. The post-processing was carried out at 1200 rpm with a feed rate of 0.039 1/mm for facing and 0.053 1/mm for longitudinal turning. A feed rate of 0.1 mm was set until an optically homogeneous surface was achieved. Subsequently, the examination areas ② und ③ were subjected to a surface roughness measurement. Table 6 shows the measurement results for face and longitudinal turning with different machining allowances before and after finishing.

Table 6: Measured surface roughness before and after turning.

R_z, R_a [μm]		(MA=0,1mm)		(MA=0,3mm)		(MA=0,5mm)	
		R_z	R_a	R_z	R_a	R_z	R_a
Longitudinal turning	Before Finishing	64,0	8,1	57,0	7,6	62,1	8,2
	After Finishing	19,0	2,6	14,2	2,0	18,8	2,7
Face turning	Before Finishing	63,1	10,1	63,1	9,8	73,2	11,4
	After Finishing	18,5	2,6	18,8	2,7	20,8	2,9

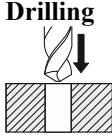
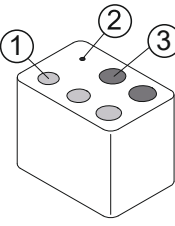
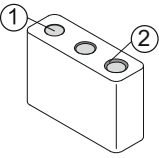
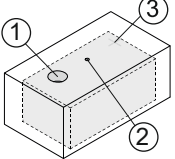
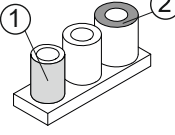
The optical inspection of the test specimens showed that a machining allowance of 0.1 mm

effects no homogeneous surface during face and longitudinal turning. A variation of the cutting speed showed that better surface qualities are possible with a faster cutting speed. The test specimen 2.2 allowed conclusions to be drawn about the lathe-turnability of support and lattice structures. For this purpose, the shoulder with the inner lattice structure in the examination area ① was tapped off with a parting of tool. The outer support structure in the examination area ② was machined with a carbide indexable turning insert. Basically it could be determined that a rotating machining of support structures is possible. Attention has to be paid to fragments and powder residues which contaminate the environment. It is therefore recommended to remove the supporting structures with other means (e.g. pliers) before turning.

2.3.3 Test specimens for drilling investigation

The test specimens 3.1 to 3.4 (Tabel 7) were drilled with a pillar drill machine and an HSS drill with a diameter of 5 mm.

Table 7: Specimen data sheet for drilling

Finishing process	Specimen	Ⓝ Examination areas · Quality criterion 1 · Quality criterion ...	Test specimen variants / test specimen parameters			
	3.1 	① Positive machining allowance · Surface quality · Ridge at outlet	Machining allowance:			
			Variant	V1	V2	V3
			MA ⁺ [mm]	0,1	0,3	0,5
		② Pilot hole (Ø1mm) · Surface quality · Ridge at outlet	-			
		③ Negative machining allowance · Surface quality · Ridge at outlet	Machining allowance:			
			Variant	V1	V2	V3
		MA ⁻ [mm]	0	-0,1	-0,3	
	3.2 	① Cutting speed · Surface quality	Cutting speed			
			Variant	V1	V2	V3
			v [m/min]	28,3	26,7	25,1
		② Chamfer formation	Chamfer geometry			
			Variant	V1	V2	V3
		b [mm]	0,15	0,3	0,45	
	α [°]	45	45	45		
3.3 	① Internal structure drilling with core hole	Core hole geometry Ø = 4,7 mm, t = 3mm				
	② Internal structures drilling with small pilot hole	Pilot hole geometry Ø = 1 mm, t = 3mm				
	③ Internal structure drilling without pilot hole	-				
3.4 	① Drillable hole length for thin-walled structures	Cylinder height				
		Variant	V1	V2	V3	
		h [mm]	10	20	30	
	② Drillable wall thickness for thin-walled structures	Wall thickness				
		Variant	V1	V2	V3	
		t [mm]	1	1,5	2	
	MA [mm]	0,3	0,3	0,3		

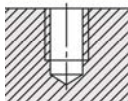
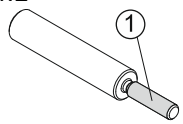
In order to be able to drill at the defined points, the test specimens were fixed to the drilling machine table with a clamping device. The drilling speed of 1700 rpm and a feed rate of 0.1 mm/1 could be set on the drilling machine, resulting in a cutting speed of 26.7 m/min. The test specimens 3.1 to 3.3 were milled in the middle after the drilling process. The optical inspection of the test specimens 3.1 showed that there is no significant difference between drilling a pilot hole and a hole with positive machining allowance (examination area ① and ②). A machining allowance of +0.3 mm is recommended to compensate any dimensional inaccuracies for the investigated size ratios. Negative machining allowances (examination area ③) lead to insufficient surface quality and are not recommended. In order to be able to assess possible influences of the drilling parameters on the result, the three holes of test specimen 3.2 in the examination area ① were reworked at different cutting speeds (Table 7). The inspection of the holes after drilling showed that different cutting speeds do not lead to optically perceptible differences. The formation of additive chamfers was evaluated in the examination area ②. These could no longer be clearly identified after the drilling process, so that subsequent machining of the chamfers is recommended. Test specimen 3.3 shows that internal lattice structures are partially destroyed during the drilling process. The essential structure of the lattice structures is retained, so that positive effects of internal structures, e.g. damping [11], are retained to a limited extent. However, parts of the lattice structure are destroyed by drilling and remain inside the component. For this reason, the drilling of lattice structures should be avoided. Test specimen 3.4 enables the determination of the minimum wall thickness required for drilling additively manufactured parts (examination area ②) and the determination of the relationship between the bore length and the bore quality (examination area ①). It was found that only a minimal wall thickness of 0.7 mm was safely drillable without annealing or deforming the cylinders. A connection between the bore length and the bore quality could not be established.

2.3.4 Test specimens for thread cutting investigation

Before thread cutting, the machining allowances for half of the test specimens 4.1 (Table 8) were removed by drilling. The other half of the specimens were left in as-built condition with machining allowance. The individual cylinders were separated from their base plate and clamped in a flat bed lathe with an HSS tap for thread cutting and the thread was cut at a speed of 65 rpm in addition of cutting oil. After machining, the test specimens were milled crosssectionalwise and visually inspected under the microscope in order to identify the respective thread characteristics. It could be observed that pre-machining of the shaft shoulder by drilling ensures good thread formation. If the machining allowance is negative, the thread is not fully formed. It is possible to cut a thread without drilling the additive manufactured hole. However, it is not advisable to do so as there may be differences in the thread characteristics. With a machining allowance of 0.3 mm and pre-machining by drilling, the thread is fully formed. Half of the test specimens 4.2 were prepared with a turning process to remove the machining allowances and to obtain the nominal core diameter according to the standard DIN 13. The other half was not subjected to a preparatory turning process, so that the thread could be applied directly to the additive manufactured surface provided with a machining allowances. To apply the threads, the test specimens and an M5 HSS die were clamped in the lathe. The thread was applied to the test specimen at a speed of 65 rpm. In

order to facilitate thread cutting, cutting oil was added during the process. The threads were visually inspected using a macroscope. It could be seen that pre-processing of the shaft shoulder by turning ensures fully developed thread flanks characteristics. However, it is possible to cut a thread without pre-machining with a positive machining allowance. With a negative machining allowance, the thread is not fully formed. A machining allowance of 0.3 and an upstream turning process are recommended in order to obtain the best possible external thread geometry.

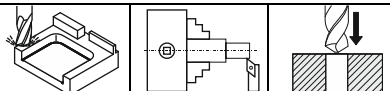
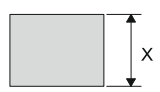
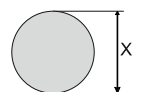
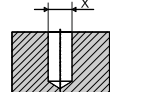
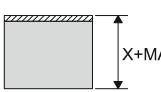
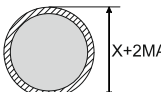
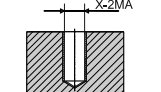
Table 8: Specimen data sheet for thread cutting.

Finishing process	Specimen	Ⓝ Examination areas · Quality criterion 1 · Quality criterion ...	Test specimen variants / test specimen parameters			
Thread cutting 	4.1 	① Internal thread · Machining allowance with and without additive manufactured core hole	Thread geometry			
	Variant		V1	V2	V3	
	Thread		M5 M10	M5 M10	M5 M10	
	MA ⁺ [mm]		0	0,15	0,3	
	MA ⁻ [mm]		0	-0,15	-0,3	
	4.2 	② External thread · Machining allowance with and without turning of surface	Thread geometry			
	Variant		V1	V2	V3	
	Thread		M5	M5	M5	
MA ⁺ [mm]			0	0,15	0,3	
MA ⁻ [mm]		0	-0,15	-0,3		

3 Design guidelines for a finishing suitable design

The carried out investigations and the results obtained on the various test specimens and examination areas allow to derive quantifiable design guidelines for a finishing suitable design for different material, machine and parameter combinations.

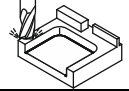
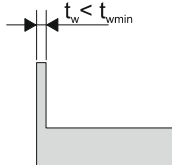
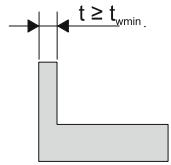
Table 9: Design guideline to specify the required machining allowance for milling, turning and drilling

Machining allowance milling /turning /drilling: Surfaces that have a dimensional requirement after machining must be provided with a machining allowance (MA).					
Unfavourable			Finishing suitable		
					
Material	Machine	Parameter set	MA face milling [mm]	MA circumf. milling [mm]	
AlSi10Mg	SLM 250HL	PS1	0,3	0,3	
	SLM 280HL	PS2	0,3	0,3	
		PS3	0,3	0,3	

Some of the quantifiable design guidelines which can be applied in a software-based shape optimization are shown in Table 9 and 10. For this purpose, the technical implementation of the design guidelines in software tool is given. A machining allowance must be provided to ensure sufficient surface quality and finishing by milling. The calculated machining allowances for the material AlSi10Mg can be applied as an offset to the component surfaces

to be reworked by means of an automated shape optimization software and thus taken into account before additive manufacturing. When turning and drilling, it must be ensured that the machining allowance is applied to the radius.

Table 10: Design guideline to specify the required minimal wall thickness for milling in the investigated size ratios

Min. wall thickness milling: A minimum wall thickness must be maintained in order to enable machining by circumferential milling.			
Unfavourable		Finishing suitable	
			
Material	Machine	Parameter set	Min. wall thickness t_{wmin} at circumf. milling [mm]
AlSi10Mg	SLM 250HL	PS1	3,0
	SLM 280HL	PS2	4,5
		PS3	3,0

Wall thicknesses must be sufficiently stable to mill without wall oscillation. A minimum wall thickness must be maintained depending on the material, machine and parameter combination used. This wall thickness can be checked using numerical methods such as the extraction of centre line points and the calculation of diameters of maximum circles or spheres as described in [12]. This method has already been used in order to numerically check AM suitable design guidelines on topologically optimized components [13]. If necessary, the wall thickness can be automatically adjusted by adding a surface offset before additive manufacturing.

Further design guidelines were drawn up on the basis of the investigation results, which provide the designer with assistance in the finishing suitable design of components. These qualitative design guidelines provide information on the achievable surface quality of milled or turned, additive-manufactured components [Table 4, 6]. They show feasible undercut and tool run-out geometries. Undercuts according to DIN 509 Form E with a width of 2.5 mm and a height of 0.3 mm are sufficient for a successful turning process and run-out surfaces with a width of 1 mm and a height of 0.3 mm for a successful milling process.

The investigations into the turning finishing of support structures induced a guideline that recommends the manual removal of support structures with regard to occupational safety and tool life.

For drilling, it was possible to derive qualitative design guidelines that exclude the influence of pilot drilling on the post-processing result. An influence of the cutting speed was not observable on the drill hole quality. Here, an extended scope of investigations with varying drilling parameters could provide new insights. Drilling in support structures has also been described by a qualitative design guideline, which prohibits the drilling of support structures, since support structures are drillable but no defined drill hole shape can be guaranteed. The finishing by means of thread cutting led to further qualitative design guidelines, which recommend a machining allowance of 0.3 mm and a cutting preparation of

the threads. Only in this way the threads can be generated in accordance with the standards. The qualitative design guidelines are not suitable for automated, software-based design checking and optimization, but offer the design engineer extensive knowledge on how to design components suitable for finishing and thus save costs.

4 Conclusion and perspectives

In the present study, a method was presented which enables the generation of design guidelines for different combinations of materials, machines and parameters for a finishing suitable design for additive manufacturing. For this purpose, suitable finishing processes were identified, test specimens were developed and, with regard to suitable finishing of common AM parts, experimental investigations were carried out on the test specimens. The investigations were carried out using the material AlSi10Mg which was processed with machines of the type SLM 250 HL and SLM 280 HL and different parameter sets. For these material, machine and parameter combinations, design guidelines could be drawn up. The design guideline generation is multiple applicable and enables that further material, machine and parameter combinations or different size ratios can be added to create an extensive knowledge database. Depending on the used finishing process, it was possible to determine necessary machining allowances, minimum wall thicknesses and finishing specific restrictions that had to be taken into account in the design process prior to additive manufacturing. These values are available in quantitative form and can be used for software-supported automated design checking of parts.

It is recommended to produce further test specimens by varying the process parameters of the SLM process, the machine type or the material in order to gain more in-depth knowledge. Furthermore, the process parameters of the finishing processes can be varied and the test specimen geometry can be scaled to extend the scope of the design guidelines.

In addition, the test specimens can be manufactured with different orientations in the building chamber in order to establish a possible relationship between the orientation and the required machining allowance. Further post-processing methods can be used which could not be considered in the context of this paper in order to gain further insights into the post-processing of additively manufactured components.

12 ACKNOWLEDGEMENTS

The research leading to these results has received funding from the BMBF project OptiAMix – “Multi-target-optimized and continuously automated product development for additive manufacturing in the product development process”. This research and development project is funded by the German Federal Ministry of Education and Research (BMBF) within the program “Innovations for Tomorrow’s Production, Services and Work” (funding number 02P158131) and managed by the Project Management Agency Karlsruhe (PTKA). Furthermore, the authors would like to thank the industrial partners of the DMRC and the joint project "OptiAMix" for their financial and operational support. The authors are responsible for the contents of this publication.

REFERENCES

- [1] ISO / ASTM 52900:(2015) *Standard terminology for additive manufacturing – general*

- principles–terminology*, Annual Book of ASTM Standards, ASTM International, West Conshohocken, PA, USA (2017)
- [2] Adam, G.O. *Systematische Erarbeitung von Konstruktionsregeln für die additiven Fertigungsverfahren Lasersintern, Laserschmelzen und Fused Deposition Modeling*. Shaker Verlag GmbH, ISBN: 978-3-8440-3474-5, Paderborn, (2015)
- [3] Kranz, J., Herzog, D. and Emmelmann, C. *Design guidelines for laser additive manufacturing of lightweight structures in TiAl6V4*. Journal of Laser Applications, Vol 27 S14001, (2015)
- [4] Thomas D. *The Development of Design Rules for Selective Laser Melting*. University of Wales Institute, (2009)
- [5] Lammers, S.; Tominski, J.; Magerkohl, S. et al. „*Design Guidelines for a Software-Supported Adaptation of Additively Manufactured Components with Regard to a Robust Production*”. 29th Annual International Solid Freeform Fabrication (SFF) Symposium – An Additive Manufacturing Conference, pp. 527-540, Austin, TX, USA, (2018)
- [6] Shahzad, K.; Deckers, J.; Kruth, J.P. et al. *Additive manufacturing of alumina parts by indirect selective laser sintering and post processing*. Journal of Materials Processing Technology, Volume 213, Issue 9, pp. 1484-1494, (2013)
- [7] Löber, L.; Flache, C. Petters, R. et al. *Comparison of different post processing technologies for SLM generated 316l steel parts*. Rapid Prototyping Journal, Volume 19, Issue 3, pp 173-179, (2013)
- [8] VDI 3405-3 *Additive fertigungsverfahren Konstruktionsempfehlungen – für die Bauteilfertigung mit Laser-Sintern und Laser-Strahlschmelzen*, Beuth Verlag GmbH, Düsseldorf, (2015)
- [9] Karunakaran, K.P.; Suryakumar, S.; Pushpa, V. *Low cost integration of additive and subtractive processes for hybrid layered manufacturing*. Robotics and Computer-Integrated Manufacturing, Volume 26, Issue 5, pp. 490-499, (2010)
- [10] Newman, S.T.; Zhu, Z.; Dhokia, V.; *Process planning for additive and subtractive manufacturing technologies* CIRP Annals, Volume 64, Issue 1 pp. 467-470, (2015)
- [11] Künneke, T; Zimmer, D. *Funktionsintegration additiv gefertigter Dämpfungsstrukturen bei Biegeschwingungen*. Additive Fertigung von Bauteilen und Strukturen, pp. 61-74, Wiesbaden, Germany, (2017)
- [12] Ma, J.; Bae, S.W.; Choi, S. *3D medial axis point approximation using nearest neighbors and the normal field*. In: The Visual Computer, Vol. 28(1), pp. 7-19, (2012)
- [13] Tominski, J.; Lammers, S.; Wulf, C. and Zimmer, D. *Method for a Software-Based Design Check of Additively Manufactured Components*. 29th Annual International Solid Freeform Fabrication (SFF) Symposium – An Additive Manufacturing Conference. S. 69-79, Austin, TX, USA, (2018)

LATTICE TOPOLOGY OPTIMIZATION AND ADDITIVE MANUFACTURING OF A 316L CONTROL ARM

Carlos Lopez *, Jan Stroobants *

* Core lab CodesignS, Flanders Make vzw.
Gaston Geenslaan 8, B-3001 Leuven, Belgium
e-mail: carlos.lopez@flandersmake.be, web page: <https://www.flandersmake.be/en>

Key words: Lattice structures, topology optimization, software engineering, additive manufacturing

Abstract. This paper presents a methodology to design optimum lattice-like engineering components that can be easily created using additive manufacturing. The optimal performance of the design is assured through a topology optimization, whereas the manufacturability is ensured thanks to the lattice nature of the designs. The paper discusses some advantages of lattice topology optimization compared to a traditional topology optimization approach, both in terms of performance and manufacturability of the final designs. The methodology combines different commercial software tools in order to effectively create such designs, that can be used in a wide range of sectors such as automotive, aerospace or medical.

1 INTRODUCTION

Topology optimization (TO) and Additive manufacturing (AM) techniques are nowadays mature enough disciplines to be used in industry [1]. The combination of both opens the door to produce novel and disruptive designs, such as the ones presented in [2, 3], that are not possible to create with traditional manufacturing processes. However, there are still some practical limitations for combining TO and AM effectively, mostly related to the fact that the TO results generally require a post-processing step in order to fine-tune the design and make it apt for AM. This fine-tuning process is usually done by a CAD engineer and includes, among others, avoiding overhanging structural members or limiting massive members that may lead to stress concentrations in the material (caused by overheating). As a consequence, several interactions between the design and manufacturing experts are required, and different alternatives might come up for the same optimal results. Figure 1 shows an example of the TO results of baffle supports in a satellite (left), several design interpretations of the results (middle) and the final design created using AM (right). This iterative design process also involves that the final design that is manufactured usually deviates from the optimum in terms of mass and stiffness.

In order to overcome some of these difficulties, novel optimization strategies, such as Lattice Topology Optimization (LTO) are increasingly being used. Lattice structures consist of a pattern repetition of small cell shapes or types, trying to simulate the internal micro-structure of the material. As a consequence of being built-up by small "bars" that are connected to each other,

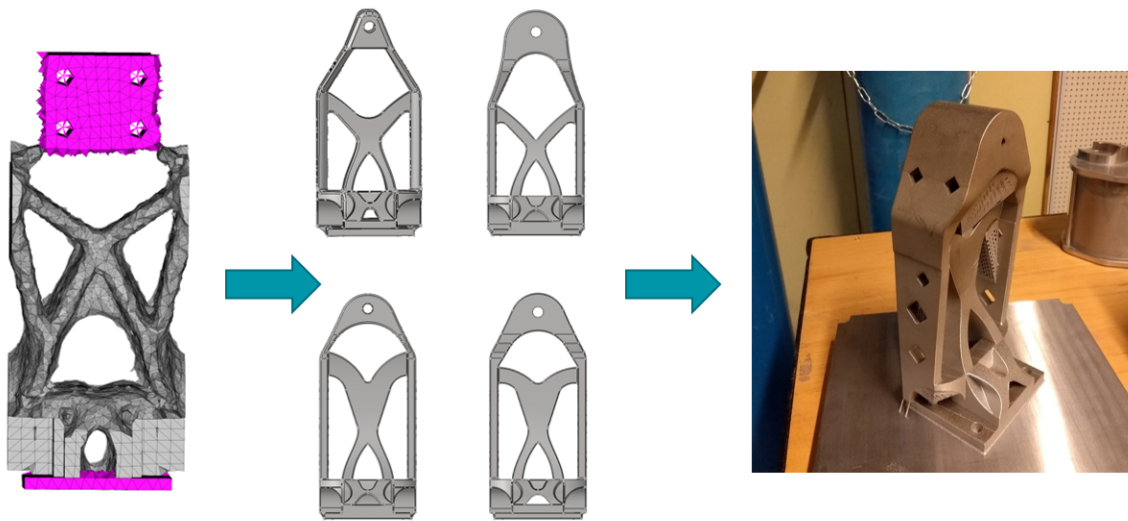


Figure 1: TO results of baffle supports in a satellite, several design interpretations and final design using AM

most of the AM problems described in the above paragraph do not apply to them. In particular, overhanging is avoided since the dense network of small bars is self-supporting (when talking about printability) and the small size of the bars avoids any stress concentration problem due to material overheating.

As stated in [4], the development of AM technology has relaxed the limitations when fabricating lattice structures (although there still exist some manufacturing constraints, they are way less than in a design coming from a traditional TO). In other words, LTO enables a faster process from design towards manufacturing, mainly because the LTO output relates directly to the shape to be manufactured, meaning that it does not require (or very limited) design interpretation of the optimum results.

Another advantage of lattice structures is that they possess some desirable characteristics from a design perspective, such as lower weight, better performance and stability (due to the large network of structural members), good energy absorption and high thermal and acoustic insulation compared to its solid counterpart [5]. This increased performance of LTO designs over traditional TO designs supports the choice of LTO for this study.

2 METHODOLOGY

This paper proposes a methodology that covers all the steps in the design of a new lattice optimized component that is intended to be produced using additive manufacturing (Figure 2). It starts with a LTO that is performed in Altair Optistruct [6], and afterwards the results are converted into "lattice printable information" (generally a geometry file such as .STL) using the dedicated software 3matic-STL from Materialise [7]. The final step is to prepare the geometry files so they can be properly processed by the 3D printer in order to achieve the best manufacturing quality (i.e. create supports, check printability, etc.). This is done using the dedicated

software 3DXpert [8]. In order to perform a LTO in Altair Optistruct, the optimization problem is split into two phases:

- PHASE I: consists of a conventional topology optimization applied to the design space, followed by a lattice generation (replacing solid elements with intermediate densities by lattices) that depends on the parameters defined by the user.
- PHASE II: consists of a sizing optimization of the lattice structure obtained in PHASE I, where the design variables are the cross-section of the small bars. The size optimization phase is aimed at incorporating some anisotropy to the lattice structure, thereby making the structure more efficient.

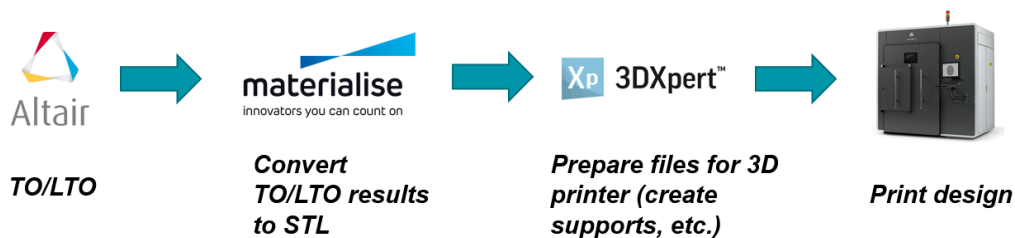


Figure 2: Flowchart of steps for the design and additive manufacture of a lattice metal component

In PHASE I, the optimization problem is defined, including the lattice settings such as the "Lattice type" (internal structure or cell shape of the lattice), "Porosity" (similar to the penalization factor in a traditional TO using the SIMP approach, which leads to a lower or higher number of elements with intermediate densities, that correspond to a lower or higher percentage of lattice structures), and "Lattice fill" (defines the upper and lower bound of the element densities in order to replace solid elements by lattices). From the designer perspective, one of the hardest decisions in this phase is the selection of the lattice cell type, which must be done up-front without knowing the potential effects that it will have in the structural behaviour of the optimal design. Probably it will not have a major effect due to the optimization process afterwards, but it is possible that the stiffness properties of the lattice cell have their influence on the final structure. In general, there are a few parameters that the designer needs to tune in this phase in order to perform the LTO.

In PHASE II, the definition of the optimization problem stays the same, however the user needs to perform two operations: define the upper bounds (UB) and lower bounds (LB) of the new design variables (cross-section of lattice beams), and ensure that all the solid elements in the model (i.e. in the non-design space) are tetrahedrons, since this is necessary to export the geometry in an .STL format. Altair Optistruct provides an option to convert all the solid non-tetrahedral elements into tetrahedrons within the software.

3 APPLICATION EXAMPLE

The methodology described in Section 2 is tested with a case example of an automotive control arm (see Figure 3), taken from the Altair Optistruct documentation [6].

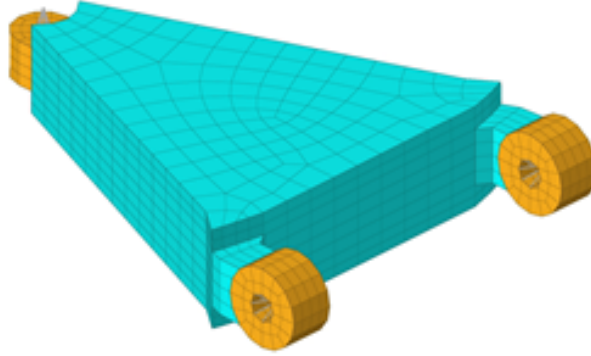


Figure 3: Automotive control arm

The dimensions have been modified (102x133x21 mm) in order to make it fit in the printing area (maximum of 275x275x420 mm). The material is defined as 316L stainless steel, with mechanical properties of $E = 210000$ MPa and $\rho = 7.85e - 9$ T/mm³. The goal of the optimization is to reduce the mass of the control arm, while fulfilling a number of displacement constraints in three different load cases.

$$\min_x Mass \quad (1)$$

subject to:

$$disp(LC1) = 0.05 \text{ mm} \quad (2)$$

$$disp(LC2) = 0.02 \text{ mm} \quad (3)$$

$$disp(LC3) = 0.04 \text{ mm} \quad (4)$$

Several optimization have been performed in order to evaluate the influence of the UB and LB of the parameter "Lattice fill" in the performance of the designs. In this study, the rest of parameters were not modified since the focus of this study was to obtain a simple-cell lattice structure that could be easy to manufacture. In that sense, the "Lattice type" is always a tetrahedron, and the "Porosity" is set as "HIGH" (generating a structure with a higher number of lattice elements, which is beneficial for buckling considerations). The optimal designs obtained from the LTO have been compared against traditional TO with and without manufacturing constraints (see Figure 4), in terms of mass and stiffness. An artificial metric "Performance" has been defined in order to compare in an easy way all the designs (y-axis of Figure 4). The x-axis of the figure shows the different cases that are studied (i.e. "LTO 001-06" states that the case is a LTO design where the bounds of the "Lattice fill" parameter are LB = 0.01 and UB = 0.6).

$$Performance = 1/(Mass * Compliance) \quad (5)$$

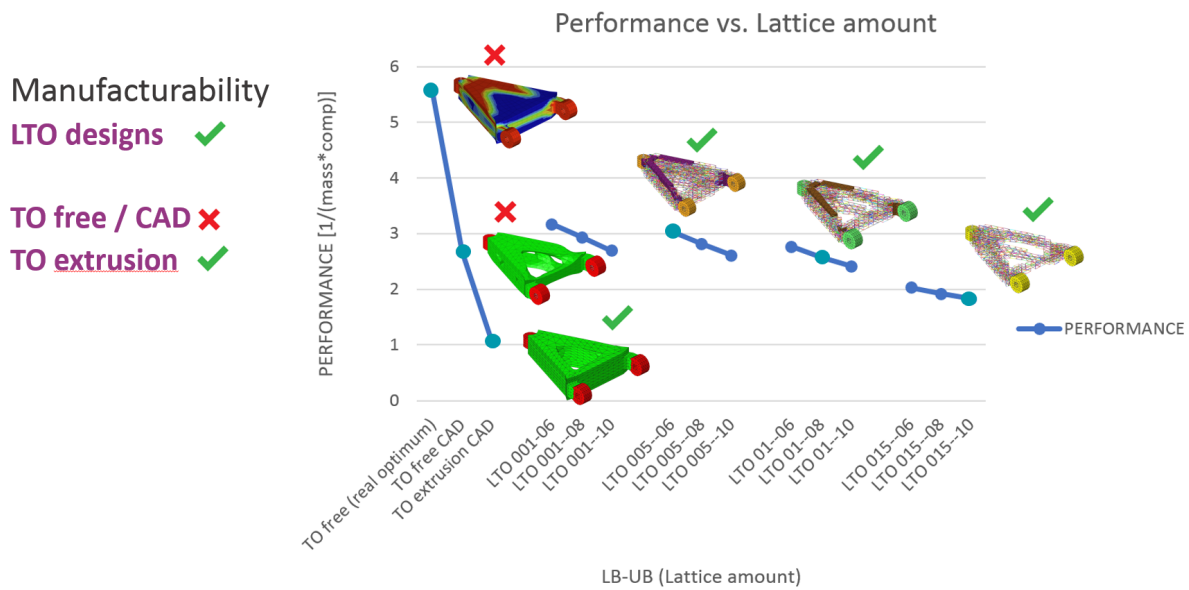


Figure 4: Summary results of TO and LTO

The results prove that the performance of all the LTO designs is higher than the TO designs when manufacturing constraints are considered. On the other hand, the performance of the LTO can be worse if it is compared to a free TO where manufacturing constraints are not taken into account. However, in this scenario the LTO designs offer the extra advantage of being always manufacturable, as explained in Section 1.

The results show that, if the LB of the "Lattice fill" parameter is constant, an increase of the UB implies a decrease in the performance of the design (this is expected since more intermediate elements that were solid are replaced with lattices, which are less stiff). A similar conclusion can be drawn from the LB of the "Lattice fill": if such parameter increases and UB stays constant, the performance tends to decrease, since lattice elements are replaced by void elements. The mass improvement in the model if such elements are removed is not enough to compensate the loss of stiffness. Table 1 shows a more detailed view of some of the results of Figure 4.

Table 1: Comparison of TO designs (with and without manufacturing constraints) vs. LTO

Case (LB-UB)	TO (free)	TO (extrusion)	LTO (0.05-0.6)	LTO (0.1-0.8)	LTO (0.15-1.0)
Mass [kg]	0.68	0.97	0.638	0.767	1.127
Comp [mm/N]	55	97	51.44	51.9	48.58
Performance	2.67	1.06	3.04	2.51	1.82

After the LTO study, one of the LTO designs (LB = 0.05, UB = 0.6) has been transformed

to an .STL file in order to be sent to the metal 3D printer. Figure 5 shows the FE model of the design (left) and the .STL geometry generated in 3DXpert (right). The selection of the design among all the ones studied is arbitrary, the only requirements are that it should be a mixed solid-lattice design with a high enough number of lattices, in order to see if the 3D printer runs into problems. The 3D printer is a ProX DMP 320 from 3D Systems, which allows to print components up to 275x275x420 mm, in different metal and ceramic options. The printing layer thickness is set to 5 μ m, although other thicknesses are also possible. The intention is to finalize this research by 3D printing the prototype shown in Figure 5, verify its manufacturability and perform a test in order to validate its stiffness.

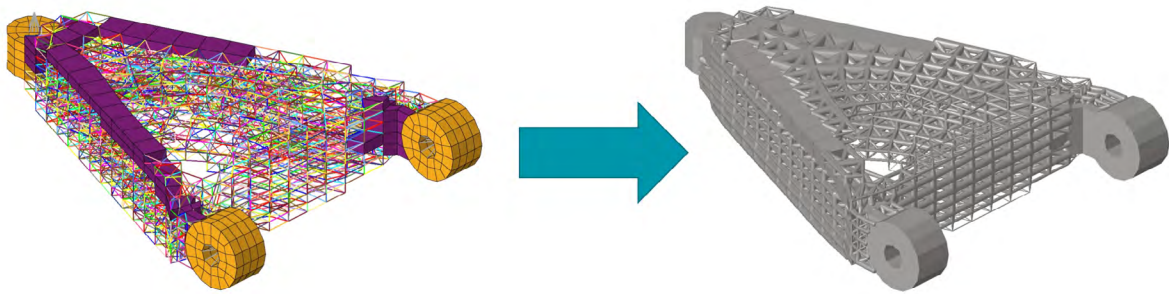


Figure 5: Example of lattice design (left) and STL file for sending to the 3D printer (right)

4 CONCLUSIONS

This study proposes a general methodology to design lattice topology optimized engineering components, that can be fabricated through additive manufacturing (AM) techniques. Topology optimization (TO) is a discipline that is heavily related to AM, however the manufacturability of TO designs is not trivial or straightforward. It always requires the explicit definition of manufacturing constraints in the optimization problem, and usually even extra iterations between the design and manufacturing experts. Lattice topology optimization (LTO) is introduced in this paper as an alternative to traditional TO in order to ease the manufacturability of designs, avoiding the classical problems of TO. The results show that the performance of LTO designs is consistently higher than in TO designs where manufacturing constraints are set. Moreover, LTO assures the manufacturability of the designs even if manufacturing constraints are not explicitly defined in the optimization. On the other hand, the main drawback of LTO is that it requires an extensive knowledge from the designer, in order to tune some specific key parameters of the LTO such as the lattice type, the porosity or the upper and lower bounds of the lattice fill.

REFERENCES

- [1] Gebisa, A.W. and Lemu, H.G. A case study on topology optimized design for additive manufacturing. *IOP Conf. Series: Materials Science and Engineering* (2017) **276**:012026.

- [2] Orme, M., Madera, I., Gschweidl, M. and Ferrari, M. Topology Optimization for Additive Manufacturing as an Enabler for Light Weight Flight Hardware. *Designs* (2018) **2(4)**:51.
- [3] Zegard, T. and Paulino, G.H. Bridging topology optimization and additive manufacturing. *Structural and Multidisciplinary Optimization* (2016) **53**:175-192.
- [4] Tang, Y., Dong, G., Zhou, Q., and Zhao, Y.F., Lattice Structure Design and Optimization With Additive Manufacturing Constraints. *IEEE Transactions on Automation Science and Engineering* (2018) **15(4)**:1546-1562
- [5] Liu J., Gaynor A.T., Chen, S., Kang, Z., Suresh, K., Takezawa, A., Li, L., Kato, J., Tang, J., Wang, C.C.L., Cheng, L., Liang, X., To, A.C., Current and future trends in topology optimization for additive manufacturing. *Structural and Multidisciplinary Optimization* (2018) **57**:2457-2483
- [6] Altair Hyperworks. Altair Optistruct 2017.1 documentation (2018)
- [7] Materialise. 3matic-STL documentation (2018)
- [8] 3D Systems. 3DXpert documentation (2018)

MIXED INTEGER OPTIMIZATION FOR TRUSS TOPOLOGY DESIGN PROBLEMS AS A DESIGN TOOL FOR AM COMPONENTS

Christian Reintjes*, Ulf Lorenz

University of Siegen
Institute of Technology Management
Unteres Schloß 3, 57072 Siegen, Germany
e-mail: {christian.reintjes, ulf.lorenz}@uni-siegen.de, web page:
<https://www.wiwi.uni-siegen.de/technologiemanagement/>

Key words: Truss Topology Design, Mixed Integer Optimization, Additive Manufacturing, Unstructured Lattices, Technical Operations Research

1 INTRODUCTION

One important advantage of Additive Manufacturing (AM) in relation to optimization for lightweight construction is that there is a reduction in manufacturing constraints compared to classical manufacturing methods [5]. To make full use of these advantages and to exploit the resulting potential, the components previously have to be designed using optimization (see [5]). Against this backdrop, a Mixed Integer Program (MIP) is developed in order to be able to use the methods of Technical Operations Research (TOR) in the context of Topology Optimization (TO) on the basis of a fitted Ground Structure Method (GSM) for lattice and truss structures. In addition, an optimization-oriented construction workflow (see figure 3) is developed in order to fully exploit the advantages in design freedom of AM. As shown in figure 3, this work addresses three interdisciplinary sub-areas; Operations Research (OR), AM as the manufacturing method and a link between this sub-areas in the form of a Computer Aided Design (CAD) solution, resulting in a TOR application.

Thematically, the problem concentrates on the application of OR methods to engineering issues and thus contributes to the generation of interdisciplinary expertise between the OR and the engineering sciences. TOR is a bridge discipline combining elements from mechanical engineering, computer science, mathematics and business administration.

2 MODEL

Section 2 is divided into three subsections. In subsection 2.1, the geometric structural conditions of the planned lattice structure are initiated, whereupon the mechanical relationships in a lattice structure are introduced in subsection 2.2. Building on the previous two subchapters, a MIP model is presented in subsection 2.3.

2.1 STRUCTURE

The geometric structural conditions of the three-dimensional lattice structure (see figure 1, left) are based on the definitions for a two-dimensional lattice structure as in [9]. In this subsection, as a continuation of [9, 10], all definitions of the Ground Structure (GS) are described for a three-dimensional lattice structure, see figure 1, right.

Let \mathbb{A} be the assembly space of an additive manufacturing machine, represented by a polyhedron as an open subset of \mathbb{R}^3 . Let $\mathbb{V} \subset \mathbb{A}$ be the reference volume to be replaced by a lattice structure and $\neg \mathbb{V} = \mathbb{A} \setminus \mathbb{V}$ the difference between the assembly space \mathbb{A} and the reference volume \mathbb{V} (3-orthotope or hyperrectangle). Let $\mathbb{L} \subset \mathbb{V}$ be the convex shell \mathbb{C} of the lattice structure created by optimization, hence the convex shell can be regarded as the volume of the actual required installation space for the optimized lattice structure, including the difference between the convex shell and the actual volume defined as \mathbb{L}' . Analogous to the previous definitions, $\neg \mathbb{L} = \mathbb{V} \setminus \mathbb{L}$ is the difference between the reference volume \mathbb{V} and the convex shell \mathbb{L} , leading to $\mathbb{L} \subset \mathbb{V} \subset \mathbb{A}$. \mathbb{L} and \mathbb{V} , as by defining \mathbb{A} , are represented by a polyhedron, which consists of the lattice structure (or free space). The differentiation of the installation space is done for minimization of \mathbb{V} in order to save computing effort.

Alternatively, a minimum bounding 3-orthotope (bounding box) \mathbb{B} can be set as the volume of the actually required installation space to build the optimized lattice structure including the difference $\bar{\mathbb{L}}$ between the 3-orthotope and the actual volume. In this case the difference is defined as $\bar{\mathbb{L}}'$. Assuming $\underline{\mathbb{L}}'$ is the actually required installation space, it applies $\underline{\mathbb{L}}' \subset \mathbb{L}' \subset \bar{\mathbb{L}}'$.

The GS is shown in figure 1 with a set of connecting nodes $V = \{1, \dots, 64\}$ with the polyhedron being equal to a hyperrectangle. It follows that - for the sake of a simple GS example - $\mathbb{C} \equiv \mathbb{B}$ and $\mathbb{L}' \equiv \bar{\mathbb{L}}'$. $B_{t,i,j}$ is a binary variable indicating whether a bar of type $t \in T$ is present between $i \in V$ and $j \in V$. The angle range of a bar (see figure 2) is set to 45° in relation to a local coordinate system centred on one node $v \in V$ so that $r_{i,j,x}, r_{i,j,y}, r_{i,j,z} \in \{0, \frac{\sqrt{2}}{2}, 1\}$ applies. By setting the angles to 45° and using Selective Laser Sintering (SLS) as the manufacturing method, only restrictions in terms of boundary conditions for bar thickness and length have to be modelled. For other manufacturing methods additional constraints have to be implemented and/or the GSM has to be adapted, see figure 3.

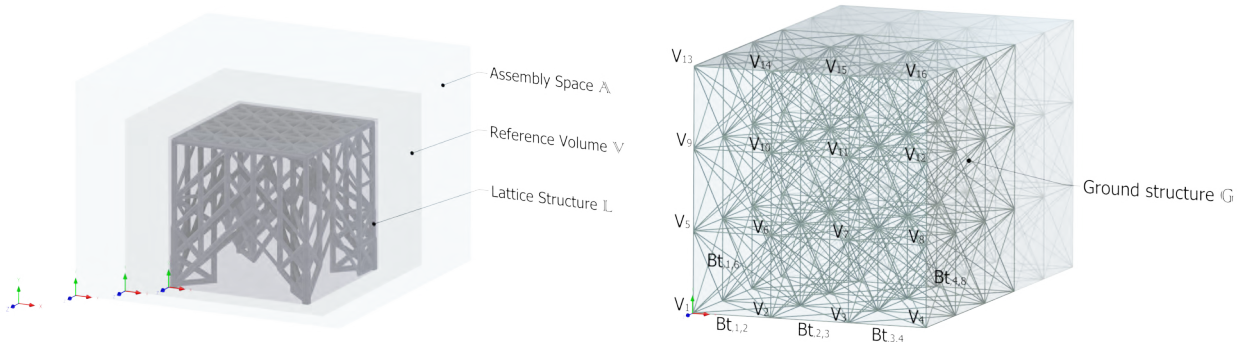


Figure 1: (Left) Illustration of the system boundaries. (Right) Illustration of the ground structure method

2.2 STATIC TRUSS TOPOLOGY DESIGN

The MIP model TTD_L uses beam theory for structural mechanics and constant cross sections, see [3] and figure 2. We assume a beam to be a structure which has one of its dimensions much larger than the other two so the kinematic assumptions of the beam theory (cf. [3]) apply. It follows that the cross sections of a beam do not deform in a significant manner under the influence of transverse or axial loads and therefore the beam is assumed to be rigid. If deformation is allowed, the cross sections of the beam are assumed to remain planar and normal to the deformed axis of the beam. Besides allowing no transverse shearing forces and bending moments, the displacement functions depend on the coordinates along the axis of the beam $\bar{u}_1(z_i) \in \mathbb{R}, \bar{u}_2(z_i), \bar{u}_3(z_i) = 0$ [3]. The normal force is defined by $N_{i,j}(x_1) = F_{i,j} = \int_A Q_{11}(x_1, x_2, x_3) dA$, where x_1, x_2, x_3 are the spatial coordinates of the cross sections and $F_{i,j}$ is the variable of the MIP, with corresponding parameter $c_t \in \mathbb{R}_+$, see table 1. Following the previous statement transverse shearing forces and bending moments have been simplified. The only external loads allowed are concentrated forces acting on nodes. Line and area loads are simplified by concentrated forces. We claim a linear-elastic isotropic material, with the given deformation restrictions causing no transverse stresses to occur $Q_{22}, Q_{33} \approx 0$. By Hooke's law, the axial stress Q_{11} is given by $Q_{11}(x_1, x_2, x_3) = E\bar{u}'_1(x_1)$, allowing only uni-axial stress.

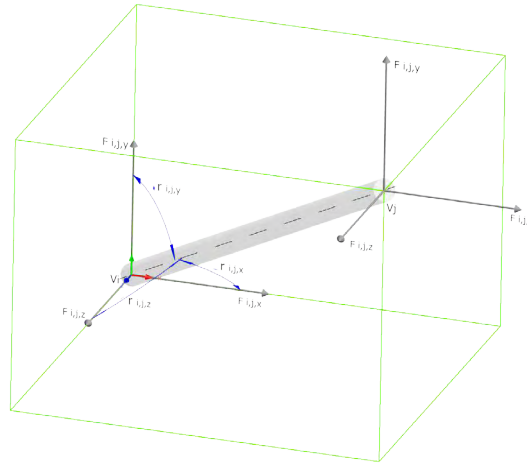


Figure 2: Reference truss $B_{\bar{i},i,j}$ and related local coordinate systems $F_{WP_{\hat{x},\hat{y},\hat{z}}}$, $F_{WP_{\hat{x},\hat{y},\hat{z}}}$

2.3 MIP MODEL TTD_L

The model and descriptions in this subsection are based on a previous work [10]. The objective function is to determine a statically determined lattice structure, which is minimal in terms of costs, volume and material consumption under the influence of external forces. Possible bar positions in space are determined by the introduced GSM, cf. subsection 2.1. The GS is influenced by external forces exerted perpendicular, depending on the given load case. The input

Table 1: Decision variables, parameters and sets

Symbol	Definition
$B_{t,i,j} \in \{0, 1\}$	Binary variable indicating whether bar of type $t \in T$ is present between $i \in V$ and $j \in V$
$F_{i,j} \in \mathbb{R}$	Flow of forces between nodes $i \in V$ and $j \in V$
$x_{i,j} \in \{0, 1\}$	Binary variable indicating whether a bar is present between nodes $i \in V$ and $j \in V$
$L_{i,x}, L_{i,y}$	Level number measured from the reference node $i = 1$ in the direction of space x or y
$R_{i,z}$	Bearing reaction force in z direction
$X, Y, Z \in \mathbb{N}$	Length, width and height of the assembly space stated as the number of connection nodes
$r_{i,j,x}, r_{i,j,y}, r_{i,j,z} \in \{0, \frac{\sqrt{2}}{2}, 1\}$	Force component at node i relative to the reference plane x, y, z , caused by beam structure between $i \in V$ and $j \in V$
$V = \{1, \dots, XYZ\}$	Set of connecting nodes (possible truss joints)
$T = \{0, 1, \dots, s\}$	Set of different beam types
$c_t \in \mathbb{R}_+$	Capacity of beam type t or allowable normal stress $\sigma_N = \sigma_{allow}$ of a certain beam type t
$M \in \mathbb{R}$	Big M - maximum capacity of the most robust beam type
$cost_t \in \mathbb{R}$	Cost of beam type t
$Q_{i,x}, Q_{i,y}, Q_{i,z} \in \mathbb{R}_+$	Force component in x, y or z direction of the applied concentrated load at node $i \in V$
$NB(i) \subseteq V$	Set of neighbouring nodes of i
$NB_x(i), NB_y(i), NB_z(i) \subseteq NB(i)$	Set of neighbouring nodes of i which have a force component in x, y or z direction in space
$B \subseteq V$	Set of nodes acting as bearings

parameters of the MIP are the load case and the sizing of the reference volume \mathbb{V} . The sizing (assembly space of the AM machine) is determined by the variables $x, y, z \in \mathbb{N}$.

The variables represent the number of nodes in the respective spatial direction in space. Taking into account the length of a beam element $B_{t,i,j}$ the dimensions of the assembly space are given. Furthermore a set of bearings NB is assigned. Each bearing NB_i is assigned to position $BLoc_i$ and a maximum permissible load in the respective spatial direction in space $BCap_i$. The position of bearing NB_i in space corresponds to the indexing of the node at the

position, and the maximum permissible load $BCap_i$ to the maximum permissible load of the bearing for a static load case.

The minimization of costs in the target function represents a minimization of the required construction volume and material, since these sizes are decisive for the costs. Specifying the equilibrium of forces as hard constraints and the cost per bar type as a soft constraint - resulting from bar volume and material specification - seems reasonable, since a linear formulation is necessary due to the MIP and the objective function can thus be kept simple. Ancillary, no cost differences need to be taken into account in the assembly effort per bar type in AM, as it is the case in classic construction applications (e.g. bridge construction) due to standard fasteners and time differences during assembly. The very important phenomena of AM "*complexity for free*" is to be fully exploited by the objective function, to achieve a holistic design approach and overcome conventional manufacturing constraints, see [6]. If the model is formulated for classical construction applications, the influence of standard fasteners and time differences during assembly can be considered by penalty parameters related to the parameter $cost_t$. A formulation of the equilibrium of forces as a soft constraint and cost per bar type as a hard constraint is not practicable, since then the assumptions (see subsection 2.2) do not apply and a formulation of the potential energy stored in all bars, given by the compliance, is necessary as soft constraint and the description of the equilibrium of forces as a function of compliance as a hard constraint. This leads to a nonlinear problem TTD_{NL} , which is equivalent to the semidefinite problem TTD_{SD} [7]. The result of the optimization (assembly) is corrected in the CAD tool called *constructOR* by an overlay check of the solid and surface objects. Sphere surfaces are added and overlapping material dispensed at the intersection points, see section 4.

Conditions (1) to (3) determine a force equilibrium at every node of the GS for the external forces Q_i and active forces $F_{i,j}$ of the beam elements in all spatial directions in space. Each node i considers its direct neighbouring nodes $NB_{x,y,z}(i)$ for the whole GS, so that $NB_{x,y,z}(i) \subseteq V$ applies and three equations ((1) to (3)) are necessary. The external forces are considered as force components $Q_{i,x,y,z}$ depending on the global spatial direction in space, see subsection 2.2. The decomposition of the forces in direction x, y and z is obtained by applying the appropriate trigonometric function to the angle of revolution in relation to the principal axis (see e.g. $r_{i,j,x}$).

Constraints (4) and (5) define the statical area moment which results from the external forces and the bearing reaction forces $R_{k,z}$. Analogous to restrictions (1) to (3) all three spatial directions in space are considered, whereat one is obsolete since only pure vertical forces are exerted. Thus, only two moment equilibrium conditions are given. Constraints (3) (see $R_{z,i}$), (4) and (5) unify the external and internal statical determinacy. Constraints (6) and (7) are of use for the necessary lever arms and define the specific positions $L_{i,x}$, $L_{i,y}$ of a node i in the assembly space: $L_{i,x}$, $L_{i,y}$ are defined as numbers of levels - with regard to the respective direction - measured from the origin of the coordinate system ($L_{1,x} = L_{1,y} = 1$).

Constraint (8) ensures that only applied beams can transfer forces. Constraint (9) represents Newton's third law and constraint (10) limits the force in a beam with regard to the permissible force of the used beam type, whereas constraint (11) guarantees that a specific beam type is selected if a beam is used. The two last constraints demand a used beam to go both ways (13) and finally constraint (14) sets the bearing reaction forces of non-bearing nodes to zero.

A MIP is chosen as the starting point for modelling the real-world problem Truss Topology Design (TTD), as there are multiple options for which soft- and hard constraints to choose besides a variety of available solvers (e.g IBM Ilog Cplex). Based on this, other optimization approaches can be developed. With regard to the MIP it is important to include external heuristics especially starting solutions in the solution strategy and to develop lower and upper bounds.

$$\begin{aligned}
 & \min \sum_{i \in V} \sum_{j \in V} \sum_{t \in T} B_{t,i,j} \cdot cost_t \\
 \text{s.t. } & \sum_{j \in NB_x(i)} F_{i,j} \cdot r_{i,j,x} + Q_{i,x} = 0 \quad \forall i \in V & (1) \\
 & \sum_{j \in NB_y(i)} F_{i,j} \cdot r_{i,j,y} + Q_{i,y} = 0 \quad \forall i \in V & (2) \\
 & \sum_{j \in NB_z(i)} F_{i,j} \cdot r_{i,j,z} + Q_{i,z} + R_{i,z} = 0 \quad \forall i \in V & (3) \\
 & \sum_{\substack{i \in V \\ Q_{i,z} \neq 0}} Q_{i,z} \cdot (L_{i,y} - L_{j,y}) + \sum_{k \in B} R_{k,z} \cdot (L_{k,y} - L_{j,y}) = 0 \quad \forall j \in B & (4) \\
 & \sum_{\substack{i \in V \\ Q_{i,z} \neq 0}} Q_{i,z} \cdot (L_{i,x} - L_{j,x}) + \sum_{k \in B} R_{k,z} \cdot (L_{k,x} - L_{j,x}) = 0 \quad \forall j \in B & (5) \\
 & L_{i,x} = (i \bmod (xz - 1)) \bmod x \quad \forall i \in V & (6) \\
 & L_{i,y} = \left\lfloor \frac{i-1}{xz} \right\rfloor \quad \forall i \in V & (7) \\
 & F_{i,j} \leq M \cdot x_{i,j} \quad \forall i, j \in V & (8) \\
 & F_{i,j} = -F_{j,i} \quad \forall i, j \in V & (9) \\
 & F_{i,j} \leq \sum_{t \in T} c_t \cdot B_{t,i,j} \quad \forall i, j \in V & (10) \\
 & B_{t,i,j} = B_{t,j,i} \quad \forall i, j \in V, t \in T & (11) \\
 & \sum_{t \in T} B_{t,i,j} = x_{i,j} \quad \forall i, j \in V & (12) \\
 & x_{i,j} = x_{j,i} \quad \forall i, j \in V & (13) \\
 & R_{i,z} = 0 \quad \forall i \in V \setminus B & (14) \\
 & x_{i,j}, B_{t,i,j} \in \{0, 1\} \quad \forall i, j \in V, t \in T & (15)
 \end{aligned}$$

3 WORKFLOW - TOR TO PART CHAIN

As shown in figure 3, the process is twice iterative. The AM method (see lower left) influences the restrictions of the TTD model and vice versa, which is necessary as the manufacturing constraints of the various AM processes must be taken into account (e.g. min. layer thickness, max. overhangs). Furthermore, the designer should be able to control the results of the optimization (.sol) through the assembly (.iam) automatically generated by the CAD tool and by the implementation of numerical methods (Finite Element Analysis (FEA)). Either the design

results are not sufficient, so that the boundary conditions of the TTD have to be adapted, or the assembly can be manufactured straightforward with AM. The processing step TTD encompasses all optimization methods available or planned to TOR.

In relation to the TTD model (in this case TTD_L), instance variables such as the load case, material specifications and the installation space are specified. The instance variables represent the specifications that are necessary to describe the respective loading case. The aim is to use a TOR at the first chronological level of the design process implemented by a MIP and an adapted GS. Subsequently, the optimization results of the MIP are converted into an assembly (.iam) by a CAD tool. The design results can afterwards be subjected to a FEA. Finally, the AM can be used to produce the lattice structure. As can be seen in figure 3 (overlapping of the areas TOR, CAD and AM), the CAD tool is the data interface from TOR to AM and from optimization software (e.g. IBM Ilog Cplex) to model analysis and Finite Element Method (FEM) software. An automated process chain has been implemented. This work puts the workflow into practice using the processing steps marked in red (TTD_L , CAD tool, FEA, SLS). The TTD is implemented by a MIP, following the workflow the CAD tool is used and a FEA takes place (see figure 5). Last a functional prototype is manufactured with SLS, in detail plastic laser-sintering and the AM machine EOSINT P 760.

A fundamental idea of TOR is to build tools such that engineers can formulate a problem without the necessity to interact directly with various sorts of optimization types and algorithms and solve them supported by tools, e.g. a CAD tool in cooperation with a MIP solving problems of the field solid mechanics [10] or an algorithmic system design of thermofluid systems [11]. This necessitates the development of tailored modelling languages for describing problem instances as well as interfaces to navigate and explore the solution space in a user-friendly manner.

With regard to the TTD, various optimization types appear to respectively offer value for engineering. Beside the problem of optimum TTD with subject to equilibrium of forces and stress constraints based on the GSM (see [1]), a mixed integer linear model, a model with quadratic formulation and a semidefinite model have their own advantages [4]. These models can be partly extended for discrete bar thicknesses, vibrations, active elements, multiple load cases, time-invariant systems and an uncertainty set implemented by an ellipsoid containing nominal loads (cf. [4, 7]). The control of uncertainties in load-bearing lattice structures with the use of mathematical models and methods and the optimal combination of passive and active structural elements within lattice structures appear to be of particular importance for mechanical engineering [7]. For this reason, the aim is to extend the workflow, and thus to offer greater added value for engineers.

4 CAD TOOL

Current design methods and CAD tools are not tailored for the shape of additive manufactured lightweight lattice structures and are not yet optimized to achieve the great potential offered by AM. The innovation in manufacturing technology is not yet followed by an adaption in design and CAD software and tools [2]. It is necessary to develop tools (Add-In) for CAD standard software tailored for AM. For the comparison of CAD programs and their differences

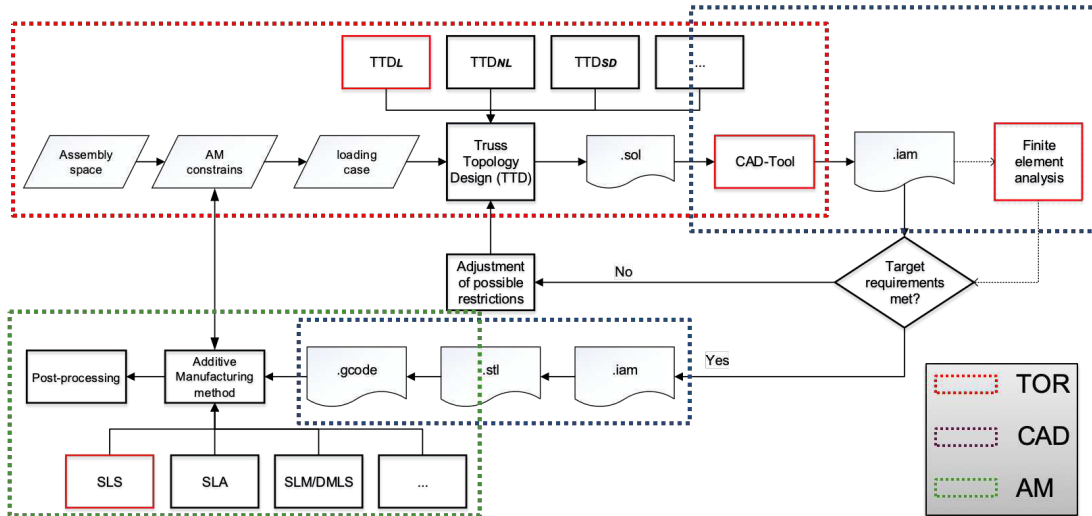


Figure 3: Iterative workflow using the methodologies of TOR for construction for AM

regarding design methodology and file formats to increase performance, reference is made to [2]. In this paper our design methodology to realise a TOR to CAD workflow is described, using existing file formats and a bottom-up construction with part and assembly modelling using our own ANSYS SpaceClaim extension.

The following variables are stored in table 1. The construcTOR routine iterates over the hyperrectangle \mathbb{V} represented by the number of connection nodes (MIP)/working points (CAD) ($WP_{x,y,z}$) to reproduce the assembly space. Afterwards an iteration over the set of connection nodes takes place, evaluating whether a beam is to be constructed to one of the neighbouring working points. The DrawBar function constructs a bar using two working points and the material \mathbb{M} arguments. Two local coordinate systems ($F_{WP_{x,y,z}}$) are needed at the respective working points, with the relative and absolute relation to the global coordinate system. On the line segment ($L_{WP_{x,y,z}}$), a plane ($P_{WP_{x,y,z}}$) is orthogonally created with a circle ($C_{WP_{x,y,z}}$) as base and a working point as center. The base is extruded along the line segment to get the volume body $B_{WP_{x,y,z}}$. The Material \mathbb{M} with corresponding modulus of elasticity is selected identical to the MIP.

As can be seen in figure 4 right, material overlaps (red) and unwanted free spaces (green) can inevitably occur due to the connection of beam elements with variable diameters at the intersection points. In accordance with [8] in the case of round bars, it is necessary to correct the intersection points between the bars, see figure 4 left. A sphere solid needs to be added at the intersection points to fill the missing space. The radius of added sphere surface should be at least equal to the radius of bars [8]. The overlapping objects are segregated through splitting the overlapping object at their overlap limits. Only one of the previously overlapping objects is retained, so that the topology including material distribution is merged ($\bar{B}_{WP_{x,y,z}}$). The sphere surfaces $\mathbb{S}_{i,k,d}$ are created as a function of working point i , the maximum bar diameter d_{max} and a scaling factor k , so that $\mathbb{S}_{i,k,d} = k \cdot d_{max}$ applies. This makes the assembly ready for additive manufacturing, but local stress concentrations caused by the crossover of the sphere

Function 1: construcTOR routine, sketched

```

Function construcTOR(MIP solution,  $\mathbb{M}$ )
  input : solution and instance data of the MIP (.sol), material  $\mathbb{M}$ ; IBM Ilog Cplex
  output : a lattice structure as assembly (.step); Ansys SpaceClaim
  /* create reference volume  $\mathbb{V}$  existing of  $V$  points */
1  foreach  $x \in \{1, \dots, X\}$  do
2    foreach  $y \in \{1, \dots, Y\}$  do
3      foreach  $z \in \{1, \dots, Z\}$  do
4         $WP_{x,y,z} := WorkingPoint.Create(x, y, z);$ 
        end
      end
    end
  end
  /* create all bars */
5  foreach  $v \in V$  do
6    foreach  $j \in NB_v$  do
7      if  $x_{v,j} == 1 \ \&\& \ v < j$  then
8         $DrawBar(v, j, \mathbb{P}_{t,i,j}, B_{t,i,j}, \mathbb{M});$ 
        end
      end
    end
  end
end

```

Function 2: function DrawBar, sketched

```

/* create a bar with circular profile; merge the topology; add sphere
   surface at intersection point */
Function DrawBar( $WP_{\hat{x},\hat{y},\hat{z}}$ ,  $WP_{\hat{x},\hat{y},\hat{z}}$ ,  $\mathbb{P}_{t,i,j}$ ,  $B_{t,i,j}$ ,  $\mathbb{M}$ ,  $S_{i,k,d}$ ):
1   $F_{WP_{\hat{x},\hat{y},\hat{z}}} \leftarrow Frame.Create(WP_{\hat{x},\hat{y},\hat{z}});$ 
2   $F_{WP_{\hat{x},\hat{y},\hat{z}}} \leftarrow Frame.Create(WP_{\hat{x},\hat{y},\hat{z}});$ 
3   $L_{WP_{x,y,z}} \leftarrow Line.CreateThroughPoints(WP_{\hat{x},\hat{y},\hat{z}}, WP_{\hat{x},\hat{y},\hat{z}});$ 
4   $P_{WP_{x,y,z}} \leftarrow Plane.Create(WP_{\hat{x},\hat{y},\hat{z}}, L_{WP_{x,y,z}});$ 
5   $C_{WP_{\hat{x},\hat{y},\hat{z}}} \leftarrow Profile.Create(F_{WP_{\hat{x},\hat{y},\hat{z}}}, P_{WP_{x,y,z}}, L_{WP_{x,y,z}}, \mathbb{P}_{t,i,j}, B_{t,i,j});$ 
6   $B_{WP_{\hat{x},\hat{y},\hat{z}} \leftrightarrow \hat{x},\hat{y},\hat{z}}} \leftarrow Body.ExtrudeProfile(C_{WP_{\hat{x},\hat{y},\hat{z}}}, L_{WP_{x,y,z}});$ 
7   $B_{WP_{\hat{x},\hat{y},\hat{z}} \leftrightarrow \hat{x},\hat{y},\hat{z}}} \leftarrow MaterialProperty.ElasticModulus(B_{WP_{x,y,z}}, \mathbb{M});$ 
8   $\overline{B}_{WP_{\hat{x},\hat{y},\hat{z}} \leftrightarrow \hat{x},\hat{y},\hat{z}}} \leftarrow Body.MergeTopology(B_{WP_{x,y,z}});$ 
9   $\overline{\overline{B}}_{WP_{\hat{x},\hat{y},\hat{z}} \leftrightarrow \hat{x},\hat{y},\hat{z}}} \leftarrow Body.Surface.IntersectCurve(B_{WP_{x,y,z}}, S_{i,k,d});$ 
return  $\overline{\overline{B}}_{WP_{\hat{x},\hat{y},\hat{z}} \leftrightarrow \hat{x},\hat{y},\hat{z}}}$ 

```

surface are expected for the FEA. The postprocessing of the intersection points is segregated considered in CAD. On one hand, the problem appears to be inconvenient to solve with the framework conditions of a MIP; on other hand, it contradicts the basic idea of TOR to offer global optimization tools that detach themselves from a differentiated optimization idea (cf. [11]).

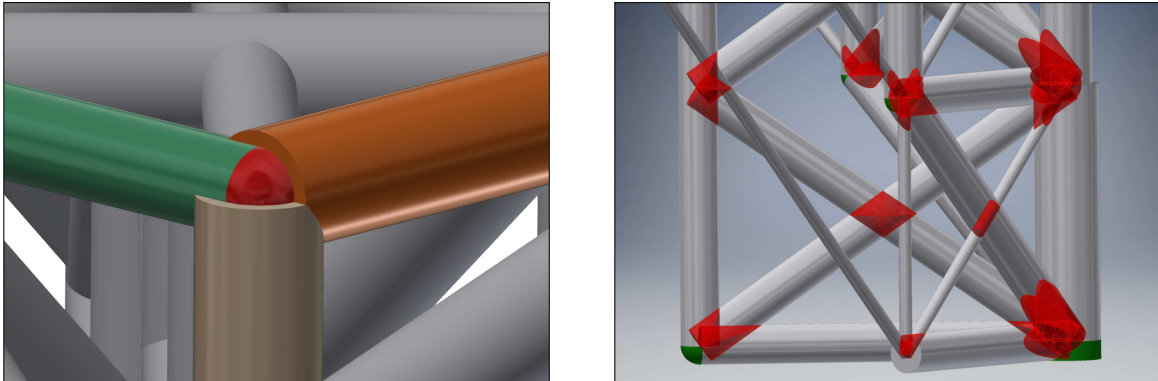


Figure 4: (Left) Necessary postprocessing intersection. (Right) Preparing interference for numerical analysis

5 RESULTS AND CONCLUSIONS

The results show the basic idea of TOR and that a MIP can be used to design additive manufactured lattice structures for lightweight construction. The possibility of a GS with a practically relevant number of bars and a true to scale modelling of common assembly spaces of additive manufacturing machines is shown. Using the provided approach assemblies with up to 2000 bars can be generated within a maximum of 12 hours. The example instance, see figure 5, is a positioning of a static area load.¹ The computation time (manually interrupted) was 10 hours 51 *min* and 12 permissible solutions were determined, whereby the duality gap was 55.73 %. The assembly space \mathbb{A} of the additive manufacturing machine Eos Int P 760 was represented as a polyhedron consisting of $V = \{1, \dots, 1928\}$ connecting nodes, resulting from the dimensions $700 \times 380 \times 580 \text{ mm}$ and a bar length of 20 mm for a non-angled bar. The reference volume \mathbb{V} was set to the dimensions $120 \times 120 \times 120 \text{ mm}$. Hence, there are 216 connection nodes in \mathbb{V} . The four corner points of the first plane in z -direction are defined as bearings. It is predetermined that the top level in z -direction is fully developed with beam elements. The beam element diameters 2, 4, 6 and 8 *mm* together with the associated $c_t \in \mathbb{R}_+$ and $cost_t \in \mathbb{R}$ are passed as parameters. Furthermore, the nonlinear material behaviour of the construction proposal was investigated by means of a FEA analysis. Figure 5 (left) shows the boundary conditions and

¹The calculation were executed on a workstation with an Intel Xeon E5-2637 v3 (3,5 GHz) and 128 GB RAM using CPLEX Version 12.6.1. The CAD construction (Inventor 2017 Pro) as well as the FEM simulation (Ansys 18.2) was performed on a workstation with an Intel Core i7-4710HQ (2,5 GHz), NVIDIA GeForce GTX 860M (4096 MB) and 16 GB RAM.

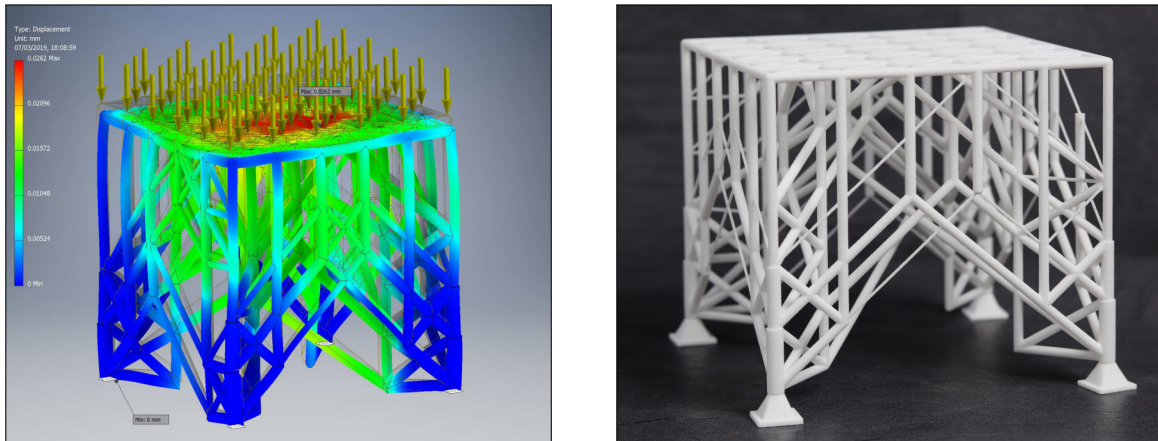


Figure 5: (Left) FEA of the example instance. (Right) Additive manufactured part including bearings, SLS; EOSINT P 760.

the deformation behaviour (total deformation) as a fringe plot. The number of bars could be reduced from 3336 (entire GS) to 665, which is a reduction of 80.07 %.

Furthermore, the developed CAD tool `constructOR` implemented in the developed workflow from TOR to part can contribute to solve the problem that current design methods and CAD tools are not tailored for the shape of additive manufactured lightweight structures and are not yet optimized to achieve the great potential offered by the technology AM [2]. The automated post-processing of the connection nodes, as demonstrated in section 4, leads to ready-to-manufacture lattice structures.

6 OUTLOOK

The applied MIP in combination with the presented CAD tool is the first attempt to use the methods of the TOR in the field of construction for AM. Based on this, other optimization approaches can be developed. With regard to the MIP it is important to include external heuristics especially starting solutions in the solution strategy and to develop lower and upper bounds. Typical process-specific geometrical limitations of AM technologies like delamination of layers, curling or stair-step effects should be minimized by formulating boundary conditions, so that the part quality gets maximized. It should also be possible to minimize the material of the support structure by minimizing the sum of the angles between the orientation of a particular part and the direction of build.

We manufactured a prototype with SLS but in future a real part and practical loading case shall be optimized with TOR and manufactured with direct metal laser sintering. A use case including tree like support structures is of particular interest. For the CAD tool parallelism is inescapable to increase the performance. Furthermore it should be possible to directly generate stereolithography files out of the MIP solution to bypass the CAD performance issues and produce ready-to-manufacture lattice structures.

REFERENCES

- [1] W. Achtziger. Truss topology optimization including bar properties different for tension and compression. *Structural optimization*, 12(1):63–74, Aug 1996.
- [2] A. H. Azman, F. Vignat, and F. Villeneuve. Evaluating current cad tools performances in the context of design for additive manufacturing. 06 2014.
- [3] O. A. Bauchau and J. I. Craig. *Euler-Bernoulli beam theory*, pages 173–221. Springer Netherlands, Dordrecht, 2009.
- [4] T. Gally, C. M. Gehb, P. Kolvenbach, A. Kuttich, M. E. Pfetsch, and S. Ulbrich. Robust truss topology design with beam elements via mixed integer nonlinear semidefinite programming. *Applied Mechanics and Materials*, 807:229–238, November 2015.
- [5] I. Gibson, D. W. Rosen, B. Stucker, et al. *Additive manufacturing technologies*, volume 17. Springer, 2014.
- [6] B. H. Jared, M. A. Aguilo, L. L. Beghini, B. L. Boyce, B. W. Clark, A. Cook, B. J. Kaehr, and J. Robbins. Additive manufacturing: Toward holistic design. *Scripta Materialia*, 135:141–147, 2017.
- [7] A. Kuttich. *Robust Topology Optimization and Optimal Feedback Controller Design for Linear Time-Invariant Systems Via Nonlinear Semidefinite Programming*. Sierke Verlag, 2018.
- [8] D. S. Nguyen and F. Vignat. A method to generate lattice structure for additive manufacturing. In *2016 IEEE International Conference on Industrial Engineering and Engineering Management (IEEM)*, pages 966–970, Dec 2016.
- [9] C. Reintjes, M. Hartisch, and U. Lorenz. Lattice structure design with linear optimization for additive manufacturing as an initial design in the field of generative design. In N. Kliewer, J. F. Ehmke, and R. Borndörfer, editors, *Operations Research Proceedings 2017*, pages 451–457, Cham, 2018. Springer International Publishing.
- [10] C. Reintjes, M. Hartisch, and U. Lorenz. Design and optimization for additive manufacturing of cellular structures using linear optimization. In B. Fortz and M. Labbé, editors, *Operations Research Proceedings 2018*, Cham, 2019. Springer International Publishing. (in press).
- [11] J. B. Weber and U. Lorenz. Algorithmic system design of thermofluid systems. In H. Rodrigues, J. Herskovits, C. Mota Soares, A. Araújo, J. Guedes, J. Folgado, F. Moleiro, and J. F. A. Madeira, editors, *EngOpt 2018 Proceedings of the 6th International Conference on Engineering Optimization*, pages 132–143, Cham, 2019. Springer International Publishing.

OPTIMAL DESIGN OF LATTICE STRUCTURE CONSIDERING CONSTRAINTS THROUGH ADDITIVE MANUFACTURING PROCESS

Yusuke Koike^{1*}, Kuniharu Ushijima² and Junji Kato³

¹Graduate School of Engineering, Tokyo University of Science
6-3-1 Niijyuku, Katushika-ku, Tokyo 125-8585, Japan
e-mail : 4518523@ed.tus.ac.jp

²Faculty of Engineering, Tokyo University of Science
6-3-1 Niijyuku, Katushika-ku, Tokyo 125-8585, Japan
e-mail : kuniharu@rs.tus.ac.jp

³Graduate School of Engineering, Nagoya University
Furo-cho, Chikusa-ku, Nagoya, Aichi 464-8603, Japan
e-mail : junjikato@nagoya-u.jp

Key words: Topology optimization, Additive manufacturing, 3D printing, Lattice structure, Cellular structure, Robust design

Abstract. In this research, an optimization design of the lattice structure is investigated, which is based on the ground structure method. In recent years, as a result of rapid development of additional manufacturing technology, it has become possible to manufacture complicated shapes including periodic lattice structure. However, in real metal lattice samples, geometric imperfections may exist in every unit because of the stochastic influence of feasible processing path. In this study, a new ground structure method which does not leave elements with small cross sectional area was proposed. In particular, the effect of geometric constraints caused by additive manufacturing techniques on optimized results are discussed based on the robust topology optimization combining perturbation methods for quantifying uncertainty. In the end, a robust topology optimization was also discussed as a problem to minimize expected value and standard deviation of compliance.

1 INTRODUCTION

Recently, due to the dramatic advance of additive manufacturing technology for metals using laser beams, more precise and complicated structures can be produced easily. For example, the micro-lattice structure which contains slender beams with a dimension of micrometre can be fabricated by using a metal 3D printer based on Selective Laser Melting (henceforth, depict as SLM) technology. As a result, many researches on topology optimization for lightweight structure produced by 3D printers have been published in many journals. However, the metal 3D printer cannot produce any shapes, and there are some geometrical constraints for producible shapes. If some constraints cannot be satisfied, large amount of geometrical imperfections that cannot meet the requirements and lack of mechanical response would be observed. Besides,

since the lattice structures are composed of slender beams, the optimized results obtained by ground structure method can be applied directly as a final product. Also, in the ground structure method, the numerical model is composed of 2D beams and trusses, the numerical algorithm becomes more simple than the conventional optimization methods for continuous model.

In our study, an optimization design of the lattice structure is investigated, which is based on the ground structure method, and the effects of structural robustness on the optimized results were discussed as a problem to minimize expected value and standard deviation of compliance.

2 ANALYTICAL METHOD

2.1 Conventional ground structure method

The ground structure method is one of the optimization method that finds the optimum structure excluding unnecessary elements in the frame structure in which each node is connected by a large number of beam elements. The conventional ground structure method sets the cross-sectional area of each member by using the following equation;

$$A_e = \alpha_e A_{\max}, 0 \leq \alpha_e \leq 1 (e = 1, 2, \dots, N_e) \quad (1)$$

In Eq.(1), A_e is the cross-sectional area of each beam element, A_{\max} is the maximum cross-sectional area, α_e is the design variable of each element of element number e changing between 0 and 1, and N_e is the number for all elements. In our optimization algorithm, the cross-sectional area of each element was optimized by changing the design variable $\alpha = \{\alpha_1, \alpha_2, \dots, \alpha_{N_e}\}$.

The optimization problem dealt with in this research is formulated as the following problem which minimizes the compliance C of the whole structure under a volume constraint \bar{W} ;

$$\begin{aligned} & \text{minimize} \quad C(\alpha) = \mathbf{d}^T \mathbf{K} \mathbf{d} \\ & \text{subject to} \quad W(\alpha) = \sum_{e=1}^{N_e} W(\alpha_e) \leq \bar{W} \\ & \quad \quad \quad 0 \leq \alpha_e \leq 1 (e = 1, 2, \dots, N_e) \end{aligned} \quad (2)$$

In Eq.(2), \mathbf{K} is the overall stiffness matrix and \mathbf{d} is the nodal displacement vector. $W(\alpha)$ is the total volume of the member, and \bar{W} is the constraint value of the total volume.

2.2 Ground structure method applying three-phase material model

As described in Section 2.1, the ground structure calculation is a method for finding the optimum structure by regarding the cross-sectional area of each member as a design object. However, this method does not necessarily provide a simple shape consisting of thick elements only, and some thin elements would remain. Therefore, in order to eliminate such thin whose design variable α_e has a value between 0 and 1 effectively, Eq.(3) is generally used to calculate the cross section as;

$$A_e = \alpha_e^p A_{\max}, 0 \leq \alpha_e \leq 1 (e = 1, 2, \dots, N_e) \quad (3)$$

As compared with Eq.(1), Eq.(3) has an exponent p for α_e . Equation (3) is simple and easy to be programmed, but there is an unavoidable problem for fabricating the optimized shape, since there are no restriction of the minimum size for A_e .

On the other hand, as for the cross-sectional area A_e for struts in a lattice fabricated by SLM, it can be designed freely within the range $A_{\min} \leq A_e \leq A_{\max}$. However, in the method for calculating the cross-sectional area of each beam element by using Eq.(3), the cross-sectional area would converge to 0 or A_{\max} . Based on this fact, a new formula for controlling the cross-sectional area is used as follows;

$$A_e = \beta_e^p \{(1 - \alpha_e)A_{\min} + \alpha_e A_{\max}\} \quad (4)$$

This equation is based on the theory of three-phase material model proposed by Kato et al.[1] Since it is not restricted that the cross-sectional area of the beam element is between A_{\min} and A_{\max} , no penalties is set for the design variable α_e . On the other hand, since the design variable β_e has a penalty, it is unlikely that there is an element whose cross-sectional area is less than A_{\min} .

In this paper, the minimum producible diameter is set to 0.2 mm, so the minimum cross-sectional area can be calculated as $A_{\min} = 0.031416 \text{ mm}^2$. In addition, the maximum productable diameter is 0.4 mm, and the maximum cross-sectional area is set to $A_{\max} = 0.125665 \text{ mm}^2$.

2.3 Robust optimization method

In a real metal lattice specimen, it contains some geometric uncertainty and does not always have the rigidity as designed. So, in this research, we performed robust optimization, assuming that Young's modulus E of each beam element contains uncertainty. The Young's modulus E of the beam element is modeled by an uncorrelated normal distribution such that the standard deviation σ is 10 % of the averaged Young's modulus.

In our robust optimization, Eq.(5) is used instead of the objective function in Eq.(2) as;

$$\text{minimize } \hat{C} = \frac{w_E}{\mu^*} E[C] + \frac{1 - w_E}{\sigma^*} \text{Std}[C] \quad (5)$$

Here, $E[C]$ and $\text{Std}[C]$ represent the expected value of compliance and the standard deviation of compliance, respectively. Considering that the Young's modulus of each element is uncorrelated, $E[C]$ and $\text{Std}[C]$ are respectively obtained by Eq.(6) as;

$$\begin{aligned} E[C] &= \mathbf{f}^T \mathbf{d}_0 + \sigma^2 \sum_i \mathbf{d}_i^T \mathbf{K}_0 \mathbf{d}_i \\ \text{Std}[C] &= \sqrt{\mathbf{f}^T \left(\sigma^2 \sum_i \mathbf{d}_i \mathbf{d}_i^T \right) \mathbf{f}} \end{aligned} \quad (6)$$

Here, μ^* is the value of $E[C]$ for $(w_E/\mu^*, (1 - w_E)/\sigma^*) = (1, 0)$, and σ^* is the value of $\text{Std}[C]$ for $(w_E/\mu^*, (1 - w_E)/\sigma^*) = (0, 1)$. Also, the paramter w_E is a constant arbitrarily defined between 0 and 1 and adjusts the weight of the expected value and standard deviation of compliance in

the objective function. In this paper, w_E is varied between 0 and 1, and the influence of the difference in the objective function on the optimized result is examined.

The sensitivity to the design variable α_e in the objective function defined by Eq.(5) can be calculated from Eq.(7);

$$\begin{aligned} \frac{\partial \hat{C}}{\partial \alpha_e} = & -\frac{w_E}{\mu^*} \left\{ \mathbf{d}_{e0}^T \frac{\partial \mathbf{K}_{e0}}{\partial \alpha_e} \mathbf{d}_{e0} + \boldsymbol{\zeta}_e^T \frac{\partial \mathbf{K}_{e0}}{\partial \alpha_e} \mathbf{d}_{e0} + \sigma^2 \sum_i \left(\mathbf{d}_{ei}^T \frac{\partial \mathbf{K}_{e0}}{\partial \alpha_e} \mathbf{d}_{ei} + 2\mathbf{d}_{ei}^T \frac{\partial \mathbf{K}_{ei}}{\partial \alpha_e} \mathbf{d}_{e0} \right) \right\} \\ & - \frac{1-w_E}{\sigma^* \text{Std}[C]} \left\{ \sigma^2 \sum_i \mathbf{f}^T \mathbf{d}_i \left(\mathbf{d}_{e0}^T \frac{\partial \mathbf{K}_{ei}}{\partial \alpha_e} \mathbf{d}_{e0} + 2\mathbf{d}_{e0}^T \frac{\partial \mathbf{K}_{e0}}{\partial \alpha_e} \mathbf{d}_{ei} \right) \right\} \end{aligned} \quad (7)$$

Here, parameters \mathbf{d}_i , \mathbf{K}_i and $\boldsymbol{\zeta}$ in Eqs.(5) and (6) can be found in reference[2]. The sensitivity to the design variable β_e is also determined in the same method as α_e .

Robust optimization can be summarized in the form of the following algorithm:

1. Set initial model data (shape, material characteristics, boundary conditions). Determine the initial value of the element design variables in vectors $\boldsymbol{\alpha}$ and $\boldsymbol{\beta}$.
2. Assemble the stiffness matrix \mathbf{K}_0 without uncertainty.
3. Structural analysis is performed using \mathbf{K}_0 to solve the displacement vector \mathbf{d}_0 .
4. Assemble \mathbf{K}_i and solve for \mathbf{d}_i and $\boldsymbol{\zeta}$.
5. Evaluate the expected value and standard deviation of compliance using Eq.(6).
6. Compute the sensitivity of the objective function using Eq.(6).
7. Update the element design variables in vectors $\boldsymbol{\alpha}$ and $\boldsymbol{\beta}$ using OC method.
8. Check convergence; if not converged go to step 2.

2.4 Boundary conditions and physical property values

In this study, an optimization design is conducted on the core part (shown in pink) in a sandwich structure subjected to three-point bending load as shown in Fig. 1(a). As a boundary condition, a 1/4 model as shown in Fig. 1(b) was used by considering a geometrical symmetry. A sandwich structure with a core of BCC lattice structure as shown in Fig. 2 is used as the base model. In this study, the volume constraint is set to 208.96 mm^3 according to the volume of the core part when the diameter of all beam elements in the BCC lattice structure shown in Fig. 2 is 0.2 mm. In addition, the dimensions and physical properties of each part are shown in Table 1 below.

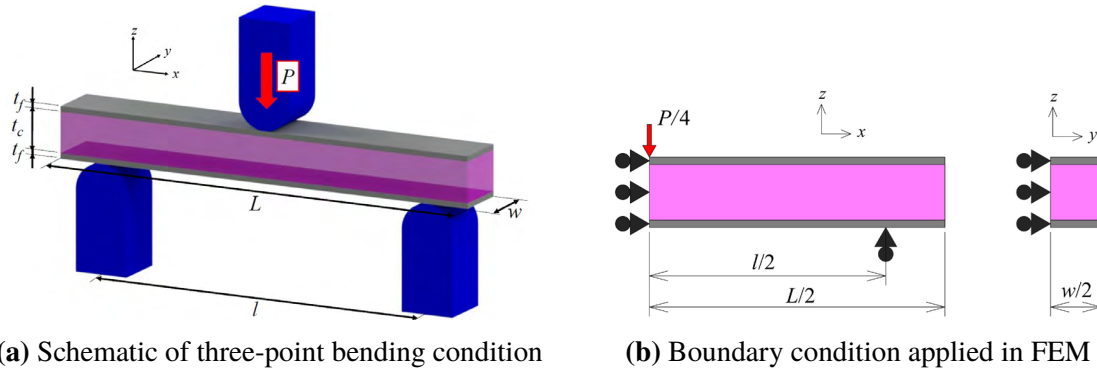


Figure 1: Analysis model



Figure 2: Layout of BCC lattice structure before optimization

Table 1: Values of geometrical and material parameters

The length of between indenters l	64 mm
The length of the sandwich beam L	80 mm
The width of the sandwich beam w	10 mm
The thickness of core t_c	7.5 mm
The thickness of facesheet t_f	1 mm
External force P	100 N
Young's modulus of the core and facesheet E	180 GPa
Poisson's ratio of the core and facesheet ν	0.3

3 ANALYSIS RESULTS

3.1 Effect of proposed equation on cross-sectional area range

Figure 3 shows the optimization results of the existing method by using Eq.(3) and the proposed method using Eq.(4). In addition, Fig. 4 shows a histogram of the number of beam elements in each section area.

The optimization discussed in this section does not use the robust optimization method according to Eq.(5), but uses the objective function shown in Eq.(2).

The optimized structure obtained by the conventional method with $p = 1$ has beam elements with small diameter. Some of the struts are not satisfied the minimum condition $A_{\min} \leq A_e$, so they cannot be fabricated by SLM. The optimized structure obtained by the existing method with $p = 2$ has a convergence in cross section of almost all elements to 0 or the maximum, and the

compliance C increase in comparison with the case of $p = 1$. On the other hand, the optimum structure obtained by the proposed method has elements with various cross-sectional areas, and there are no elements whose area is less than A_{\min} . In addition, the compliance C is almost the same as the conventional method with $p = 1$.

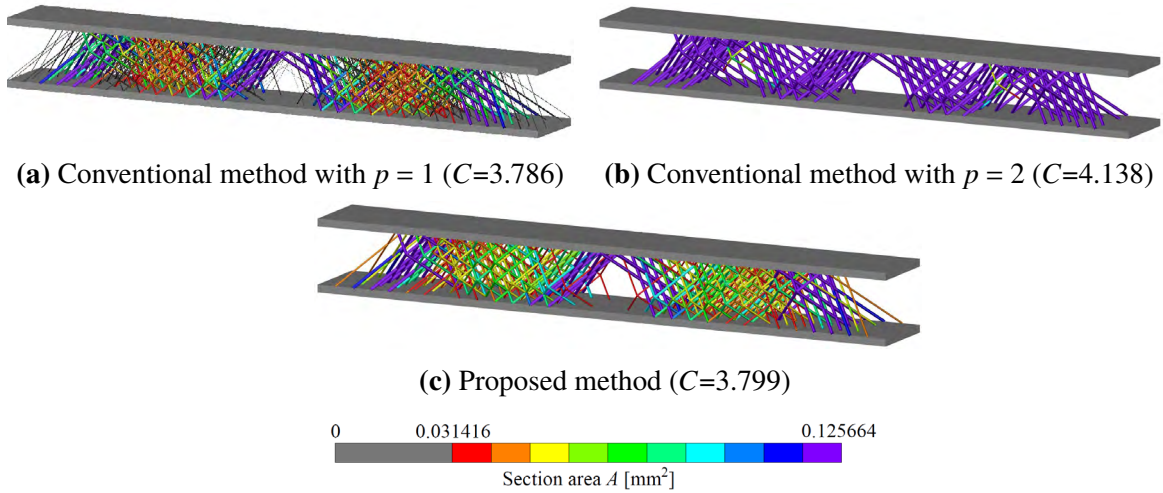


Figure 3: Comparison of results in each method

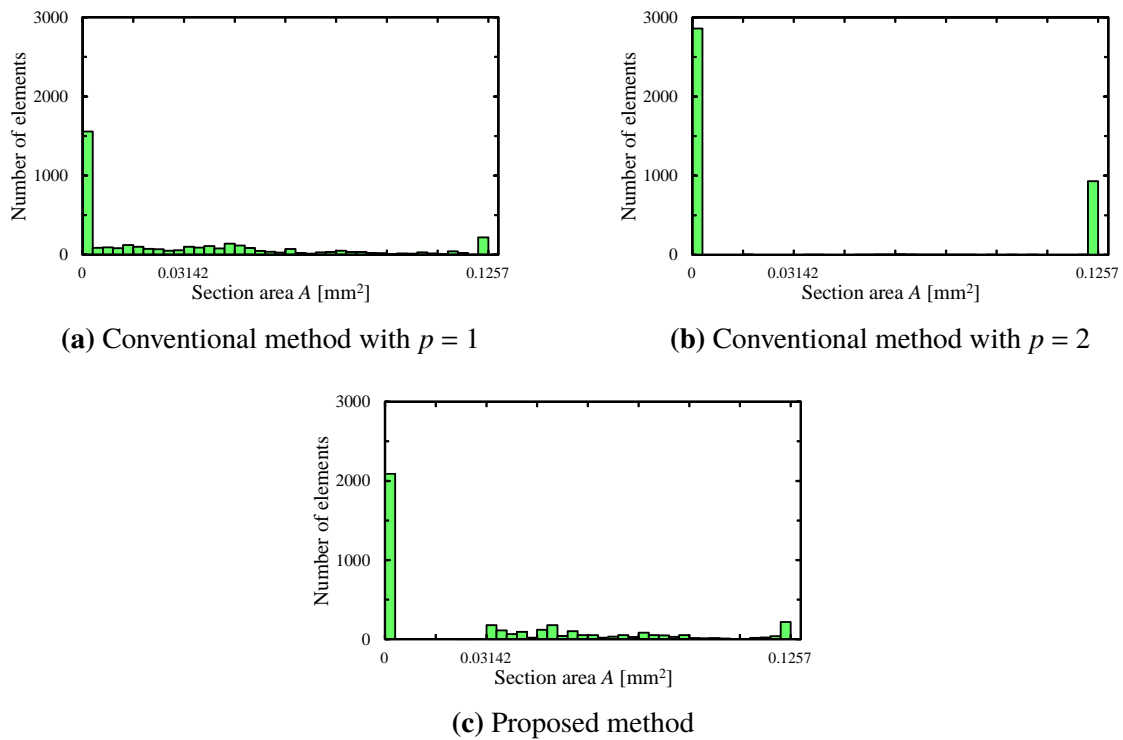


Figure 4: Histogram of the number of beam elements in each section area

3.2 Robust optimization results

The effects of the weights of the objective function on the optimal shape are compared in Fig. 5. Figure 5(b) shows the optimum structure obtained by $w_E = 1.0$, namely, the analysis that minimizes the expected value of compliance. It is almost the same as the optimal structure by deterministic optimization shown in Fig. 5(a). In addition, by comparing results shown in Figs. 5(b)–(d), it can be confirmed that as the value of w_E decreases, the number of beam elements with large cross-sectional area would decrease and the total number of beam elements increases.

Figure 6 shows the effect of the weighting factor w_E on the objective function. As shown in Fig. 6, the expected value of the compliance decreases and the standard deviation of compliance increased as w_E increases. Therefore, the expected value of the compliance and the standard deviation are in a trade-off relationship, and the balance can be arbitrarily determined by designers by changing the factor w_E .

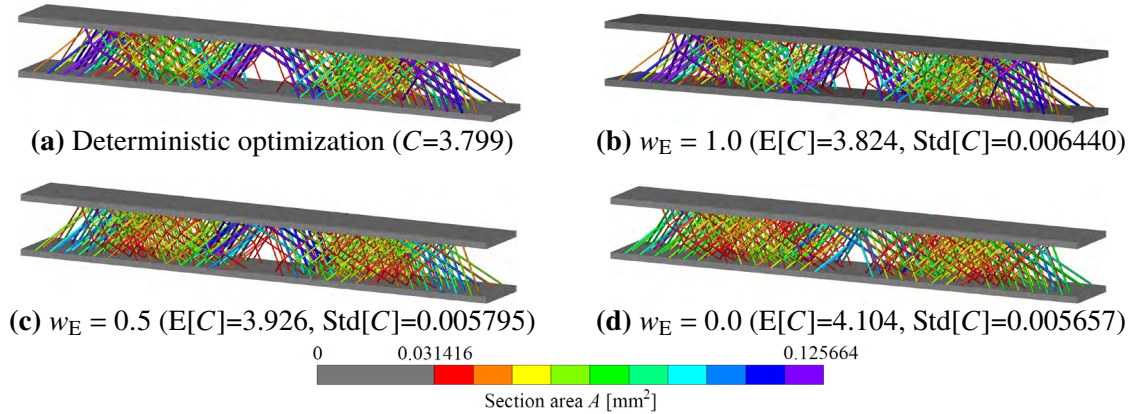


Figure 5: Examination of the influence on the result by weight coefficient w_E

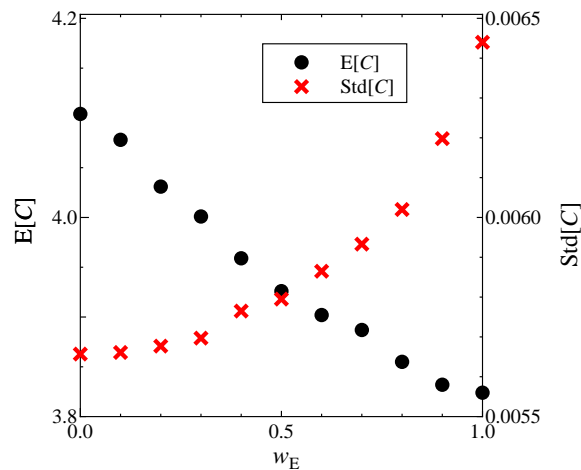
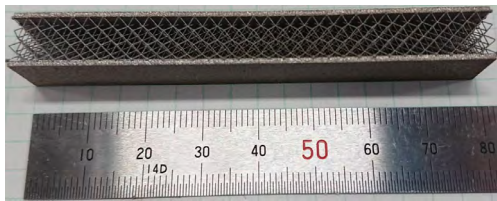


Figure 6: Relationship between weighting factor w_E and expected value and standard deviation of compliance

4 FABRICATION AND EXPERIMENT

4.1 Verification of molding accuracy

In our study, the initial and optimized shape of BCC structures are fabricated using the metal 3D printer (3D Systems, ProX 300) A photograph of the fabricated test piece is shown in Fig. 7. In order to measure the beam diameter of the fabricated product, a test piece was photographed using a scanning electron microscope (SEM) JCM-6000. One of the images taken is shown in Fig. 8.



(a) The shape before optimization (Fig. 2)



(b) Shape that minimizes the expected value of C (Fig. 5(b))



(c) Shape that minimizes standard deviation of C (Fig. 5(d))

Figure 7: Photograph of test pieces molded by metal 3D printer

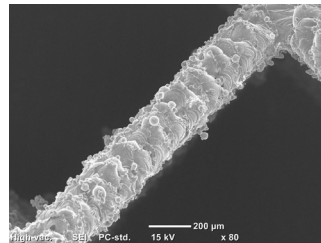
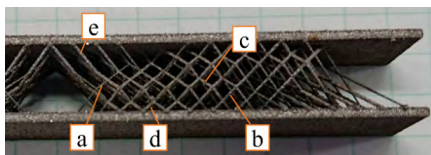
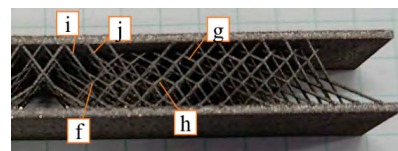


Figure 8: Picture of beam element taken by SEM

The diameter of ten beam elements a–j (see Fig. 9) was measured from the pictures. The design value of the diameter by optimization and the average value of the diameter obtained by measuring from the SEM image are compared in Tables 2 and 3 below.



(a) Test piece of Fig. 7(b)



(b) Test piece of Fig. 7(c)

Figure 9: Measurement point of each test pieces

Table 2: Measurement results for each test piece of beam elements shown in Fig. 9(a) (mm)

Measurement points	Design values	Measured values				Relative error [%]
		Specimen ①	Specimen ②	Specimen ③	Average	
a	0.200	0.186	0.200	0.190	0.192	3.87
b	0.258	0.248	0.270	0.260	0.259	0.56
c	0.311	0.339	0.349	0.316	0.335	7.60
d	0.367	0.375	0.384	0.371	0.376	2.56
e	0.400	0.415	0.396	0.392	0.401	0.20

Table 3: Measurement results for each test piece of beam elements shown in Fig. 9(b) (mm)

Measurement points	Design values	Measured values				Relative error [%]
		Specimen ①	Specimen ②	Specimen ③	Average	
f	0.200	0.178	0.199	0.206	0.194	2.96
g	0.234	0.227	0.244	0.233	0.234	0.20
h	0.275	0.261	0.285	0.269	0.272	1.21
i	0.311	0.308	0.313	0.305	0.308	0.83
j	0.362	0.363	0.371	0.362	0.366	1.01

According to Table 2 and 3, although there are some errors, the diameter of the designed beam element is almost equal to the measured value. Therefore, it is concluded that the lattice structure composed of struts with various area A_e can be fabricated appropriately, which is based on the optimized result derived from using our ground structure method.

4.2 Experimental result

A three-point bending test was conducted for the fabricated test pieces. The load-displacement diagram obtained by the experiment is shown in Fig. 10. In addition, Table 4 shows the results of calculating compliance from the graph.

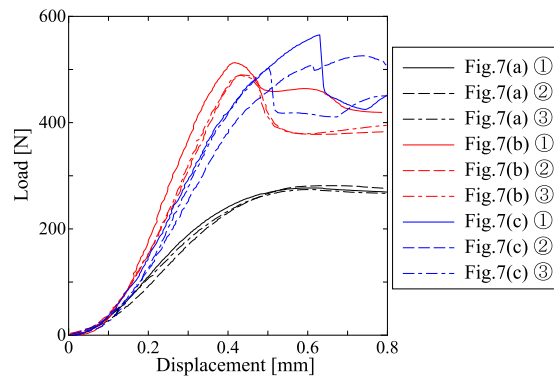
**Figure 10:** Load-displacement diagram obtained by experiment

Table 4: Comparison of theoretical and analysis compliance values

Constitution	Analysis values	Experimental values				Relative error [%]
		Specimen ①	Specimen ②	Specimen ③	Average	
Fig. 7(a)	5.376	11.690	12.812	13.351	12.617	134.69
Fig. 7(b)	3.824	5.335	6.392	6.098	5.907	54.49
Fig. 7(c)	4.104	6.850	7.500	6.476	6.917	68.55

According to Fig. 10, compared to the test piece before optimization, the test piece after optimization is higher in rigidity and the maximum load is also larger. On the other hand, there are still large errors between the analysis value and the experimental value of compliance, which is due to the inferior quality of metal additive manufacturing on molding. As shown in Fig. 8, the fabricated test pieces has a roughness in the strut surface, and the diameter contributing to the mechanical properties would be smaller than the diameter obtained by measurement.

5 CONCLUSION

In this study, optimization was carried out using the new ground structure method in consideration of restriction due to additive manufacturing, and the following findings were obtained by performing the fabrication and three-point bending experiment.

1. In our method, the cross-sectional area A_e is controlled between A_{\min} and A_{\max} , which is based in the three-phase material model proposed by Kato et al.[1]. The optimized shape can be fabricated by metal 3D printer.
2. In our calculation, the structural robustness is considered and the effect of designed performance (to minimize the expected value or the standard deviation for the compliance) on the optimized shape is discussed.
3. The optimum shape obtained in this research can be fabricated by using the metal 3D printer. The product quality is strongly dependent on the fabrication condition. In the next work, the structural optimal design in consideration with the appropriate fabrication condition and its robustness will be studied.

REFERENCES

- [1] J. Kato, A. Lipka, and E. Ramm. Multiphase material optimization for fiber reinforced composites with strain softening, *Structural and Multidisciplinary Optimization*, **39** – 1, 2008, pp. 63–81.
- [2] A. Asadpoure, M. Tootkaboni, and J. K. Guest. Robust topology optimization of structures with uncertainties in stiffness - application to truss structures, *Computers and Structures*, **89** – 11, 2011, pp. 1131 – 1141.

STRESS-BASED NON INTRUSIVE SHAPE OPTIMIZATION FOR ADDITIVE MANUFACTURING PARTS

KHALIL EL RAI*, CHADY GHNATIOS[†] AND FRANCISCO CHINESTA*

* PIMM Lab
Arts et Métiers ParisTech
155 Boulevard de l'Hopital, 75013 Paris, France
e-mail: khalil.el_rai@ensam.eu; francisco.chinesta@ensam.eu
web page: <https://artsetmetiers.fr/>

[†]Mechanical Engineering department
Notre-Dame University - Louaize
e-mail: cghnatios@ndu.edu.lb
web page: <https://ndu.edu.lb/>

Key words: Shape optimization, topological optimization, mesh smoothing, additive manufacturing.

Abstract. We live in a time where resources are scarce and tools are developed to control their use. One of the most powerful material-saving tools is shape optimization. This method produces complex shapes, difficult to manufacture using classical techniques. In such situations, additive manufacturing appears to be as an appealing approach. In this paper, a non intrusive average stress based shape optimization technique is presented. This technique is composed of a processing phase followed by a post processing smoothing phase. The processing phase aims at minimizing the deviation of the calculated Von Mises stress field using FEM, from the average stress in the part divided by a certain factor by element removal. In the next phase, the obtained non smooth surface of the part is smoothed using the weighted laplacian smoothing algorithm. This method is attractive since it doesn't need to re-mesh the domain at every iteration. In addition, it does not require a high processing power since the results were obtained during half an hour using a medium fine mesh on an i5 processor with a home made code. Furthermore, at the end of this algorithm the stress distribution in the part is quasi-homogeneous and it gives flexibility for the user to choose the desired stress criterion which is suitable for the studied application.

1 INTRODUCTION

The development of shape optimization techniques has gone hand in hand with the industrial development due to the feasibility of the complex optimized shapes resulting from these techniques. These latter are highly used nowadays due to their environmental advantages by reducing the material waste and use, as well as for increasing the efficiency of the desired part in a certain application. Seing their numerous advantages, shape optimization techniques are

widely used in many fields such as in the automotive industry [10] and in fluid mechanics [7].

Shape optimization consists of finding the optimum shape for a certain application and it contains three subfields which are: parametric, geometric and topological. In the parametric shape optimization, the shape is defined by a set of parameters that are changed in order to maximize or minimize a certain function [8] [6]. The parameters can be process related as time, velocity, etc..., or shape related as the length or thickness of a part [5], or structure related as the size of bars in a truss for example [12]. This type of optimization is limited to the chosen parameters a priori and thus it offers limited options of shape variations.

The geometric shape optimization consists of optimizing the shape of the part through modifying his boundary. The shape can be thus represented numerically through a finite element mesh for example [2], and the variable to optimize is the solution of a certain differential equation which is evaluated inside the domain; and at each iteration, changes are applied to the domain boundary. In order to implement parametric optimization to geometric optimization, Ammar et al. [3] chose the parameters as to define the problem geometry and get the optimal parameter choice (dimensions) using the proper generalized decomposition technique.

As for the topology shape optimization, it consists of finding the best material distribution to satisfy an optimization goal. It starts from any shape and redistributes the material in an optimum way that satisfies the optimization criterion. This latter can be performed using different methods. For example, the homogenization method [1], or the SIMP (Solid Isotropic Material with Penalization) method [4]. After using any of these two methods, the initial shape is lost since they consider materials with intermediate densities to give the final material distribution.

In this paper we will present a simple shape optimization technique which consists of two phases. In the processing phase the part is represented numerically using finite elements and solving the elasticity equation to get the Von Mises stresses in each element. Then setting the function to minimize as the difference between the stress in each element and the average stress in the part divided by a certain user chosen safety factor, at each iteration, the elements which have a stress lower than the set stress are removed and hence the stress difference function decreases with each iteration as the number of removed elements decreases until none is found. After the processing phase, the part will have a non smooth boundary making it difficult to print, thus the post processing phase consists of smoothing the boundary using the laplacian mesh smoothing technique.

In what follows, the processing phase is presented in section 2 followed by the post-processing phase presented in section 3. Furthermore, to show the effectiveness of this method, the algorithm was tested on two load configurations and the obtained results are shown in section 4.

2 PROCESSING PHASE

As discussed previously, this method is a geometric shape optimization approach with the following function Ψ to minimize:

$$\min_{\Omega} \Psi = \sigma(\Omega) - \frac{\sigma_{avg}}{n} \quad (1)$$

In which σ is the Von Mises stress element field, σ_{avg} is the average Von Mises stress in the studied part and n is a factor of safety specified by the user.

Therefore, the first phase consists of evaluating the Von Mises stresses at each element of a 3D mesh which will be presented in section 2.1. Later on the processing algorithm will be presented in section 2.2.

2.1 Stress evaluation

In order to find the stresses in each element, the elasticity equation shown in equation (2) must be solved:

$$\{K\}\{\varepsilon\} = \{\sigma\} \quad (2)$$

Where $\{K\}$ is the stiffness 3D tensor, $\{\sigma\}$ is the 3D stress vector and $\{\varepsilon\}$ is the 3D strain vector. Let $\{U\} = \{u, v, w\}$ be the displacement field at every node. Hence the strains can be expressed by:

$$\{\varepsilon\} = \{D\}\{U\} \quad (3)$$

Where D is the matrix differentiation operator expressed by:

$$D = \begin{pmatrix} \partial/\partial x & 0 & 0 \\ 0 & \partial/\partial y & 0 \\ 0 & 0 & \partial/\partial z \\ \frac{1}{2}\partial/\partial y & \frac{1}{2}\partial/\partial x & 0 \\ 0 & \frac{1}{2}\partial/\partial z & \frac{1}{2}\partial/\partial y \\ \frac{1}{2}\partial/\partial z & 0 & \frac{1}{2}\partial/\partial x \end{pmatrix} \quad (4)$$

The finite element solution of this problem is the displacement field that corresponds to the minimum elastic energy expressed by equation (5), assuming neither body forces nor thermal strains that could be added :

$$\Pi = \int_{\Omega} \{U\}^T \{P\} d\Omega \quad (5)$$

Where $\{P\}$ is a surface force vector with $\{P\} = \{P_x, P_y, P_z\}$.

To minimize Π , $\frac{\partial \Pi}{\partial U} = 0$ which yields the following form to solve using finite elements method.

$$\{K\}\{U\} = \{F\} \quad (6)$$

Where $\{K\}$, $\{U\}$ and $\{F\}$ are the global stiffness, displacement and load matrices respectively. For this purpose, linear interpolation shape functions were used in a tetrahedral mesh and the obtained results will be shown in section 4. Once the displacement field is obtained, the strain field $\{\varepsilon\}$ is obtained by:

$$\begin{Bmatrix} \varepsilon_{xx} \\ \varepsilon_{yy} \\ \varepsilon_{zz} \\ \varepsilon_{xy} \\ \varepsilon_{xz} \\ \varepsilon_{yz} \end{Bmatrix} = \begin{Bmatrix} u_x \\ v_y \\ w_z \\ 1/2(u_y + v_x) \\ 1/2(u_z + w_x) \\ 1/2(v_z + w_y) \end{Bmatrix} \quad (7)$$

With $u_x = \partial u / \partial x$, $u_y = \partial u / \partial y$, $u_z = \partial u / \partial z$ and the same notation for v and w . The obtained element strain field is used to calculate the element stress field using equation 2. Thus the Von Mises element stress field is obtained using $\tau_{ij} = 2\varepsilon_{ij}$ by:

$$\sigma = \sqrt{0.5[(\sigma_x - \sigma_y)^2 + (\sigma_y - \sigma_z)^2 + (\sigma_z - \sigma_x)^2] + 3(\tau_{xy}^2 + \tau_{yz}^2 + \tau_{zx}^2)} \quad (8)$$

Any solver can be used to obtain these stress fields, the loop of the optimization only acts outside of the solver core. Therefore, any solver can be used to optimize the shape using this algorithm which makes it a non intrusive method.

2.2 Processing algorithm

After calculating the Von Mises stress field, the average stress in the part σ_{avg} is calculated and divided by a factor n specified by the user. The elements in which $\sigma < \frac{\sigma_{avg}}{n}$, are removed from the mesh. A diagram explaining the algorithm is shown in fig. 1

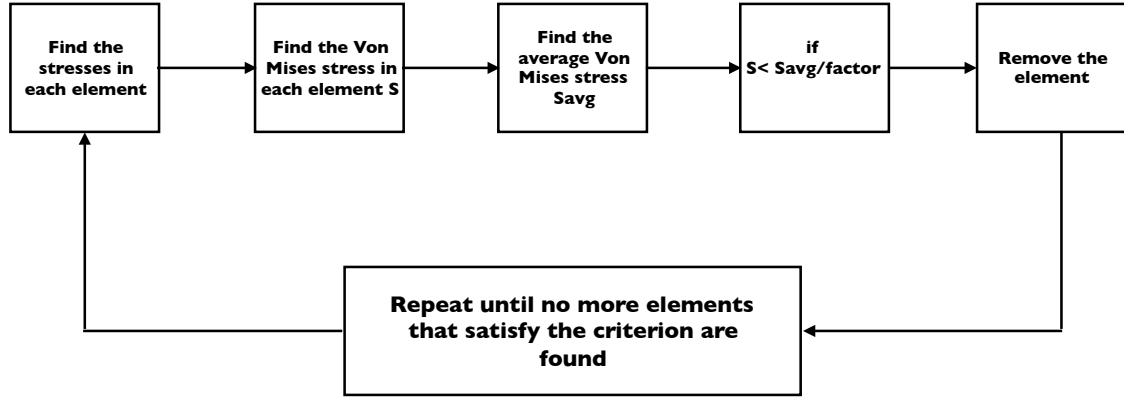


Figure 1: Processing algorithm diagram

After the first iteration a certain number of elements N_i will be removed. In the next iteration, no re-meshing is needed since the elements are only removed from the connectivity matrix and hence won't get involved in the calculations. The new Von Mises stress field is calculated and another number $N_{i+1} < N_i$ will be removed. The same procedure will be repeated until no element satisfying the set criterion is obtained indicating that the target function which is the difference between the element stress and the average stress is minimized and the stress distribution in the part is quasi-homogenous. After this iteration scheme, the obtained boundary is non-smooth and requires a boundary smoothing technique which will be discussed in the next section.

3 POST PROCESSING PHASE

In order to smoothen the boundary of the part, the weighted laplacian mesh smoothing technique [11] is used. This latter adjusts the position of each node with respect to its neighbors by compensating its concavity using the following:

$$P_j = P_j + \Delta P \quad (9)$$

$$\Delta P = \frac{1}{\sum_{i=1}^N [L_{ij}]} \sum_{i=1}^N L_{ij} P_j \quad (10)$$

Where $P_j = \{x_j, y_j, z_j\}$ is the node coordinate vector, ΔP is the numerical evaluation of the node concavity, N is the number of neighboring nodes on the boundary and L_{ij} is the distance between the selected node and the neighboring nodes as shown in fig. 2.

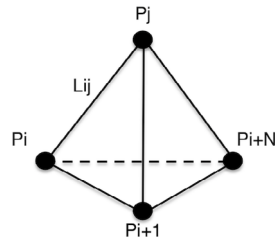


Figure 2: Schematic diagram of the selected node for the weighted laplacian smoothing

The same procedure is applied to all the nodes on the boundary and the iteration scheme can be applied on each node as much as needed depending on the desired quality of the final part. Fig. 3 shows the algorithm used in the post processing phase.

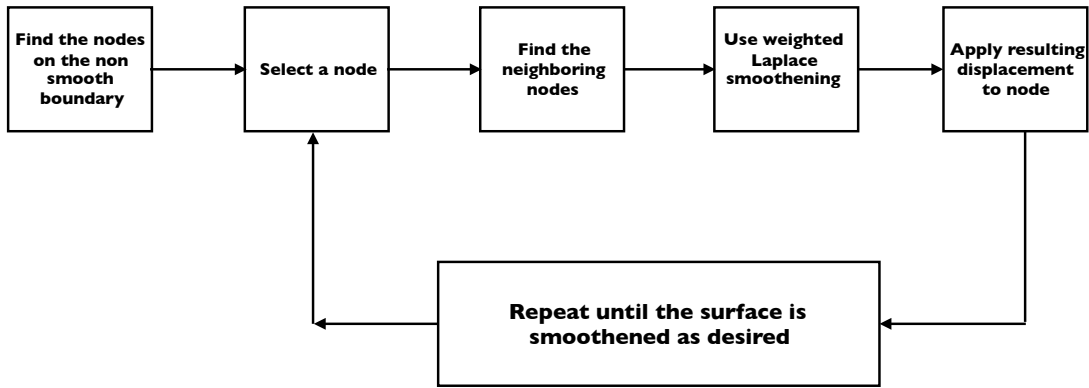


Figure 3: Schematic diagram of the post processing phase

To see the effectiveness of this method, two load configurations were tested and the obtained results are shown in the next section.

4 RESULTS AND DISCUSSION

4.1 Case 1

Fig. 4 shows the schematic representation of the load configuration of the first tested case. The load applied is compressive normal to the top surface with two fixed supports at the bottom corners.

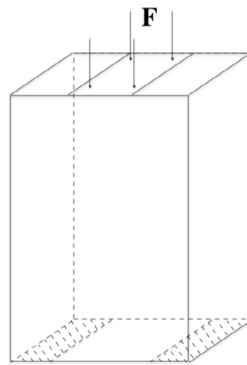


Figure 4: Schematic diagram of the load configuration of the first tested case

The obtained results are shown in fig. 5 with a safety factor of 2. As it can be seen, the boundary is modified in order to reach the optimal final shape based on the desired criterion.

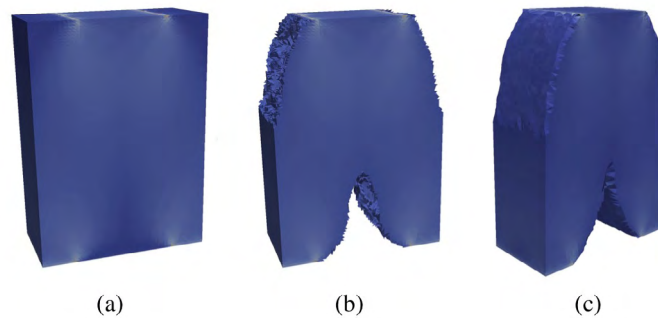


Figure 5: Obtained simulation results: a) The stress distribution, b) The part at the end of the processing phase and c) The part after boundary smoothing.

As a comparison, since we couldn't find a similar configuration in the literature, fig. 6 shows the results obtained using topological optimization in a cloud-based commercial software with targets 70% mass conservation and stiffness maximization. The obtained result is highly similar to the simulation using the software. In addition the processing time is about half an hour on an i5 processor using MATLAB with a fine mesh compared to 20 minutes using the software with online simulation and with restricted degrees of freedom. Note that the duration can be decreased without any problem with a coarser mesh similar to what the software uses and instead of the average stress criterion, the algorithm gives flexibility to the user in the sense that he can easily choose the yield stress or any other suitable criterion.

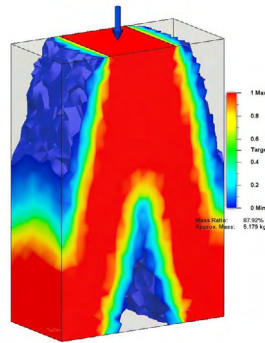


Figure 6: Optimized shape using topological optimization on a cloud-based commercial software

4.2 Case 2

In the second case, a force is applied at the end of a cantilevered part as shown in fig. 7. The obtained results are shown in fig. 8 with a factor of safety of 2.

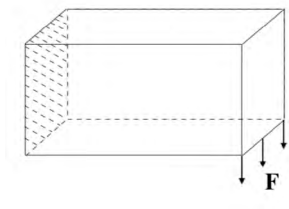


Figure 7: Schematic diagram of the load configuration of the second tested case

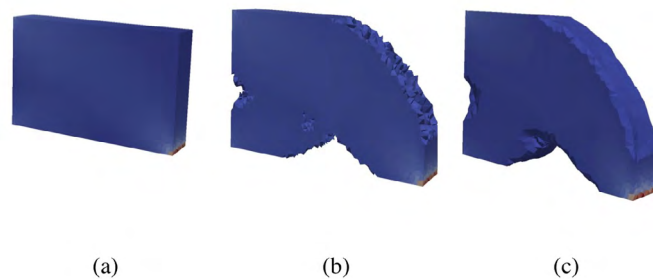


Figure 8: Obtained simulation results: a) The stress distribution, b) The part at the end of the processing phase and c) The part after boundary smoothing.

The same configuration is optimized using topological optimization [9] and its results are shown in fig. 9. It can be noticed that the two results have similar aspects but in the topological optimization case, the shape is lost and material is removed from inside the domain, whereas using our method, only the boundary is modified and the overall shape is maintained.

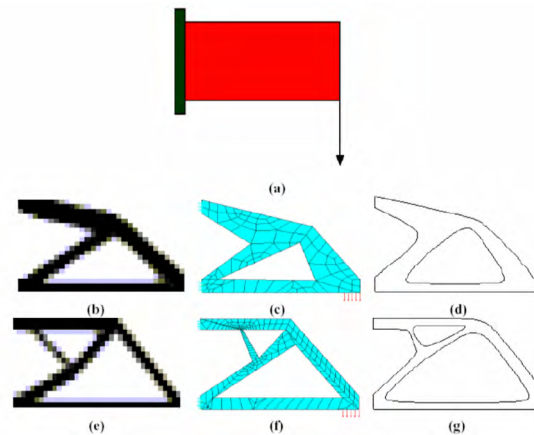


Figure 9: Optimized shape using topological optimization from the open literature

5 CONCLUSION

In this paper, we presented a simplified approach for average stress based geometric shape optimization. This method consists of a processing phase in which elements from the finite element mesh are removed based on a specified criterion which is in this case, the average stress divided by a certain safety factor; and a post processing phase in which the boundary is smoothed using the weighted laplacian mesh smoothing technique. This method offers flexibility to the user in the sense he can change the criterion (yield strength, ultimate stress, etc...) based on the load configuration, the factor of safety used, and the dimensional accuracy since this algorithm does not require a really fine mesh to converge. This method was tested for two load configurations and the obtained results were in agreement with optimized shapes from commercial softwares or from the open literature.

REFERENCES

- [1] G. Allaire. Shape optimization by the homogenization method. *Applied Mathematical Sciences*, 146, 2002.
- [2] G. Allaire and O. Pantz. Structural optimization with tt FreeFem++. *Structural and Multidisciplinary Optimization*, 32(3):173–181, 2006.
- [3] A. Ammar, A. Huerta, F. Chinesta, E. Cueto, and A. Leygue. Parametric solutions involving geometry: A step towards efficient shape optimization. *Computer Methods in Applied Mechanics and Engineering*, 268:178–193, 2014.
- [4] M.-P. Bendsøe and O. Sigmund. *Topology Optimization: Theory, Methods, and Applications*. Springer, 2003.
- [5] M.P. Bendsøe. Optimal shape design as a material distribution problem. *Structural and Multidisciplinary Optimization*, 1:193–202, 1989.

- [6] Ghnatios C., Ammar A., Cimetiere A., Hamdouni A., Leygue A., and Chinesta F. First steps in the space separated representation of models defined in complex domains. *ASME 2012 11th Biennial Conference on Engineering Systems Design and Analysis*, pages 37–42, 2012.
- [7] Charles Dapogny, Pascal Frey, Florian Omnès, Yannick Privat, and Florian Omnès. Geometrical shape optimization in fluid mechanics using freefem++. *Structural and Multidisciplinary Optimization*, 2018.
- [8] C. Ghnatios, Xu Guangtau, Michel Visonneau, Francisco Chinesta, and Alain Cimetiere. On the space separated representation when addressing the solution of pde in complex domains. *Discrete & Continuous Dynamical Systems-S*, 9(2):475–500, 2016.
- [9] Ghais Kharmanda, Nidal Kourdi, Ayman Daboul, Abdelkhalak ELHami, and Sylvein Lambert. Reliability-based topology optimization as efficient tool for structural designers. *2nd International Francophone Congress of Advanced Mechanics*, 2007.
- [10] Chao Li. Topology, size and shape optimization of an automotive cross car beam. *Journal of Automobile Engineering*, 2014.
- [11] Yatuaka Ohtake, Alexander Belyaev, and Ilia Bogaevski. Mesh regularization and adaptive smoothing. *Computer-Aided Design*, 33:789–800, 2001.
- [12] A.P. Seyranian, E. Lund, and N. Olhoff. Multiple eigenvalues in structural optimization problems. *Structural optimization*, 8:207–227, 1994.

THE PERSPECTIVE OF TOPOLOGY OPTIMIZATION ON 3D PRINTED FURNITURE PROTOTYPES

Sim-AM 2019

I. NTINTAKIS^{*}, G.E. STAVROULAKIS[†] N. PLAKIA[†]

^{*} School of Engineer, Department of Mechanical Engineering
Hellenic Mediterranean University, Estauromenos, 71004 Heraklion, Greece
e-mail: ntintakis@staff.teicrete.gr, web page: <https://www.hmu.gr>

[†] School of Production Engineering and Management
Computational Mechanics and Optimization Laboratory, Technical University of Crete
GR-73100 Chania, Greece
email: gestavr@dpem.tuc.gr, www.comeco.tuc.gr

University of Thessaly
V. Griva, 431 00 Karditsa, Greece
email: niki_plk@hotmail.com- Web page: <http://www.uth.gr>

Key words: Inject binder, additive manufacturing, topology optimization, compression test

Summary. A new design starts from an idea and become a final product, during design process the evaluation stage it's a necessity, the most useful evaluation tool is prototyping. Conceptual models are very important in product design. Improving product quality is always an important issue of manufacturing, even if a design study is well organized it is possible some errors may still escape from the review of engineers and designers. The touch of the physical objects can reveal unanticipated problems and sometimes spark a better design. With the traditional method, developing of prototypes to validate or optimize a design is often time consuming and costly. Inject Binder is one of the most well-developed rapid prototyping or additive manufacturing technology, actually is a Powder-based inkjet 3D printing method. Mainly is a powder-based RP system in which a binder solution spays onto pre-deposited powder layers. One of the main advantage of this method is the production of fullcolor models suitable for architecture maquets, prototypes of new products like furniture and other objects. In prototyping process, a restriction is production cost that basically depends from the amount of printed material. In current study furniture prototypes are printed in a inject binder printer, the printed models have common design like a chair and a table. The raw materials used in this study were a plaster-based powder (zp151) and an appropriate water based solution with 2-Pyrrolidone as a binder (zb63). Three different model of each model (three chairs and three tables) are printed, the main difference between them is wall thickness, the first model thickness is 5mm, the second 10mm and third is 20mm. The printed parts tested in a compression tester device to check models elasticity and compressive resistance. Then the lab results used to create a FEA (Finite Element Analysis) study in a popular CAE program. In the final stage, the perspective of an optimization study are presented to determine an optimized shell geometry and wall thickness. The paper discusses useful tools for designers and engineers in order to

decide the appropriate wall thickness and shell geometry (pattern) of furniture pieces, so to avoid model over dimension. And check functional and aesthetic aspects before massive production.

1 INTRODUCTION

1.1 Design Process and Methodology

Design process is a critical point for product development. From late of 19th and early 20th century established the principle that form follows function in architecture and industrial design, it means the shape of a building or object should primarily relate to its intended function or purpose. The American architect Louis Sullivan was the foremost exponent of this principle as it expressed in his article titled 'The Tall Office Building Artistically Considered', although he attributes its core idea to ancient roman architect Marcus Vitruvius Pollio (Sullivan, 1896). Before the second world war became a strong argument between the modernist architects for this phrase because of they believed that decorative elements, which architects call "ornament", were superfluous in modern buildings (Greenough, 1947). However, Sullivan did not contend with this view. Besides, the buildings he designed were characterized by art nouveau and celtic revival decoration elements. In the same periode the same argument took place in product design, between functional design and market demands. American auto industry halted attempts to introduce aerodynamics forms to mass production. The same time some car resellers thought that aerodynamic shape would lead to a specific form, very similar for all cars. That it would not be good for unit sales (Meikle's, 1939).

Although in early times after the second world war and until the Oxford conference on Design Methods in 1963 design was more considered as an intuitive work and less than a scientific process. The way in which designers follow in design process has been the subject of considerable investigation over the last six decades. In the beginning of design research, the contention was that designers have to follow specific design process through formalized procedures or 'design methods'. In the beginning the designers believes that following a specific process will eliminate the creativity and imagination. However, after the integration of brainstorming on design process this problem will overcome. A main point of this debate was the development of design methodology connected with computer science as requirement to understand and define exactly what we mean by design. Alan Colquhoun focused on topology centrality and in earlier knowledge in design thinking process (Colquhoun, 1967). Often a design problem did not processed by reference to a good past solution or through an analysis of the solution types that would be suitable for this specific problem. In seventies Bill Hillier developed a new design method (Hillier, Musgrove, et al., 1972; Hillier and Leaman, 1974), in which the knowledge from a local design problems could be useful for other design problems in global scale. During this period, many researchers were against of Design methods, even though in next years they change their opinion completely: Alexander: "I think I should be consistent here. I would say forget it, forget the whole thing." (Alexander, 1971), "in the seventies I reacted against design methods. I dislike the machine language, the behaviourism, the continual attempt to fix the whole of life into a logical framework." (Jones, 1977). This period the Design methods was developed rapidly through the recognition that following linear process, which characterized the early period of design methodology, was insufficient

(Checkland, 1981), *furthermore* the design problem was not specified clearly so on to adopt an optional solution through definition of possible solutions for a specific design problem.

The last decade's product development process follows a more specific process (fig.1). Designers have to make thinks that people wants so they must be sure that new products are well designed according to people needs. In the beginning of design process design team have to recognize the people needs from the initial research (market research, questionnaires, interviews etc), (Babalís et al. 2013). The second stage of product develop include concept design process, there design team have to select an appropriate idea which is capable to give solution in design problem. Next stage is model prototype, designers have to produce functional physical models in order to evaluate their ideas. Since 1984 when Charles Earls invent the first 3d printing machine until today great progress have been made in rapid prototyping. The ability to produce cheap and very accurate prototypes is a main advantage for designers so they can easily evaluate their ideas checking products ergonomic, functionality and stability. This stage is very critical in design process, prototypes are fully functional and end users can use these in real world life so to give back their feedback in design team. Now, design team is able to make all the appropriate changes so the new product to be closer to people needs.

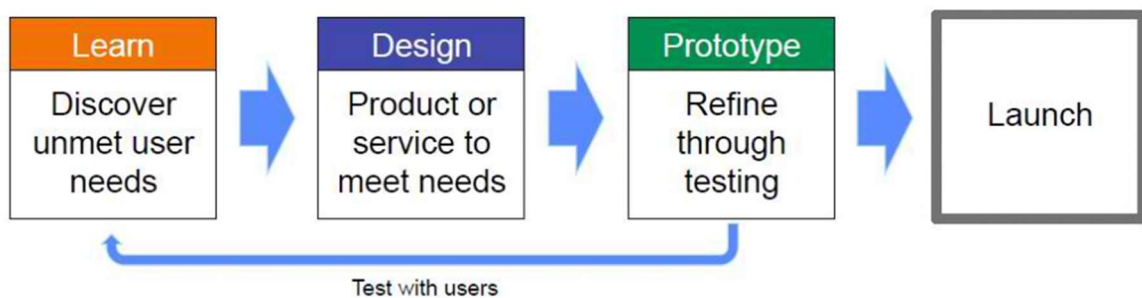


Figure 1: Product development process

1.2 Rapid Prototyping Technology

Rapid prototyping technologies adopted as a means of manufacturing physical prototypes and new product models that are in the design and development phase. These technologies have enabled designers to realize their ideas in natural prototypes that approach the final product in terms of geometry and function. One of the most well known technologies of rapid prototyping is 3d printing. In the last decades, more and more designers and engineers are using 3D print technology and adapted according to the new way of presenting complex structures, objects and services are created and at the same time realizing ideas and projects personalized, which a few years ago, looked utopian and the consumer becomes and producer (Wong & Hernandez, 2012). However, the most important contribution of 3D printing technology is based on a radical review of the core of scientific research, hence of knowledge (Giannatsis et al. 2015). 3D Printers allow designers to create tangible patterns of their designs quickly, compared to two-dimensional representations. In addition, "3D printers" allow designers to quickly create prototypes of objects they design which can touch so to evaluate and to improve them if is necessary.

With the evolution of technology various three-dimensional printing techniques have been well developed, each one has strengths and weaknesses. Differences are based on how the

individual layers have been spread to create the various components, such as material melting, melt deposition, or the use of liquid materials through different technological processes. Mainly, the discussion is related to the issues of speed, cost of prototype and 3D printers, choice and cost of materials and the ability for multicolor prototypes (Giannatsis, et al. 2015). According to the process parameters effects, concerning the dimensional accuracy of parts has been tried by (Kechagias et al. 2014)

One of the most well developed technologies is 'Inject Binder'. In this technique the main material is powder, the granules of the powder are homogeneous in size and shape, showing only limited variation with respect to their size. The smaller the particles they form, the better (Gibson et al. 2017). Modeling requires the use of powder (powder) as a feedstock and adhesive to achieve the agglomeration of powder grains to produce a solid physical prototype. In particular, the production of model is to be implemented in two distinct phases. In the first phase powder is going to be spread in each single layer of same thickness on the print table. Then, each powder layer be sprayed selectively with an adhesive. Selective spraying is determined by the structure of the digital model already created in CAD software. After the first layer has been sprayed, the second layer is deposited, the selective powder spray is repeated and the process continues until the entire model is printed / produced. In the second phase the produced model is removed from the container and using compressed air is cleaned from the excess powder (Figure 1.7). Then the model sprayed with cyanoacrylate or other substances to improve their strength and surface finish. The typical thickness of each cross section is 0.1mm. The technique is of high speed and produces objects with a relatively harsh finish (Papathanassis, 2005).

1.3 Inject Binder Printer Characteristics

Inject binder has some advantages over other 3D printing methods. Initially, in binder inject powder has two roles, the first is to be the main material for physical model, the second one is to support the structure as the model is being built so the need for supports is eliminated. Another advantage is the possibility of simultaneously producing multiple objects in the same manufacturing process (Gibson et al. 2017). Also is the only method that does not use heat in the production process. Other additive manufacturing techniques use a heat source that can create residual stresses in the parts. These stresses must be relieved in secondary operation after processing. Also has the ability to print large parts and is often more cost-effective than other additive methods. A particular advantage of Binder Jetting is that the adhesive can be sprayed from multi-nozzle print heads. Adhesives from different nozzles can differently allow changes in properties in the manufactured model, such as the change in color (Gibson et al., 2017). Despite the many advantages Binder Jetting has some drawbacks, such as the fact that only rough details can be printed with this printer, as the parts are very fragile, they may break during the post-processing. Also compared to other 3D printing processes, Binder Jetting offers a limited choice of material (Bournias, 2018). Finally, the surface quality and dimensional accuracy achieved by this method are in many cases lower than the corresponding 3D printing methods having raw materials in liquid form (Gibson et al. 2017).

1.4 Computational Mechanics

Computational mechanics is the scientific area that uses numerical methods to solve engineering problems. Traditionally, the problems of engineering were solved either

analytically or experimentally by making many measurements on a model of the problem that we are interested in. Computational mechanics is the third way, the development of computers over the last few decades has enabled engineers to approach problems that were impossible to solve in the past either because of the large size or the large amount of computing time required. Computational mechanics complements analytical solutions and significantly reduces the number of experiments required. In inject binder technique the printed models are consists from powder grain, because of the distinct grain structure of printed objects, the Finite Element Analysis (FEA) method can be implemented as a cost-effective computational engineering tool. Addressing the problem arises from developing specific tools based on examining the distinctive structure of the print material. Furthermore, the need for new products has increased rapidly. The same time products life cycle digressed. Manufacturers want to develop new robust products rapidly. Computational mechanics can play a significant role in this way. Shortening product development time can be achieved with method of structural optimization. Aims to improve the form of a construction, while satisfying various constraints. This method becomes significant in design because raw material stocks are limited, there is a need for light structures, economic construction with emphasis on efficiency and minimization of environmental impact. There are three different types in structural optimization: a) size optimization, b) shape optimization and c) topology optimization (Gebisa, 2017). In size optimization the values of the selected dimensions are defined, so on to satisfy the design constrains. In shape optimization the optimization of the shape within a given area is performed. In topology optimization size and shape are defined in same time (Fig.2). Topology optimization methods can be based on simplified Optimality Criteria iterative reanalysis methods, Heuristic and optimization techniques. (Zhou et al, 1993, Bendsoe, 2089).

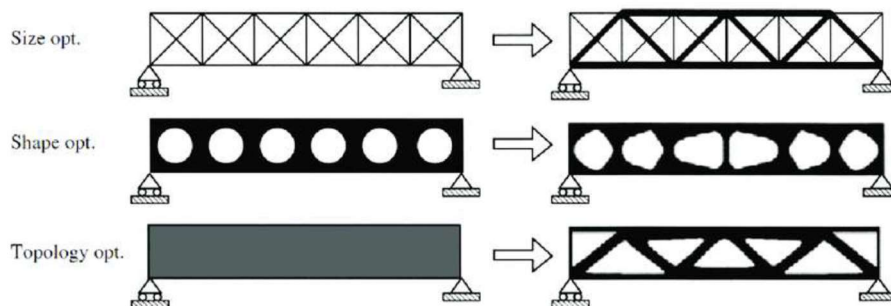


Figure 2: Optimization methods

2 MATERIALS AND METHODS

The main goal of current research is whether standard furniture designs can be reproduced on a 3D printer such as inject binder getting better mechanical strength minimized the used material. The study consists from two phases, initially two different furniture models are printed with different wall thickness and then tested in a compression tester device. In the second phase 3d models are redesigned in a CAE software using topology optimization tool to minimized the used raw material and improving the mechanical strength. Then, models are printed again and tested in compression tester.

2.2 Inject Binder Printer Z450

The selected printer is Z-450 from Z-Corp company, which is a fully automated and affordable color 3D printer. It delivers printing at a speed of up to 450 dpi, five to ten times faster than other printers and in half cost. In addition, it is ideal for applications such as design, education, architecture, medicine, geography and electronic art. Its automation simplifies printing and saves valuable time. Each model produced with ZPrinter® 450 and the excess powder after each printing is recycled in its entirety for re-use. In addition, this machine sets a new standard for office-to-office compatibility, office-safe materials, automated absorption systems, and no waste of material. It is also a great alternative to monochrome 3D printing and modeling costs less than half the cost of other three-dimensional printing technologies.

2.3 Compression test

The machine selected to control the mechanical strength of The 3d printed models are tested in Zwick / Roell Z020 Testing Device (Figure 3.2) The test engine is specifically designed for tensile, compression, curvature and bending tests, as well as shearing and turning tests that meet the highest requirements of the material and component testing industries. This device selected because of extremely low speeds can be set, coupled with excellent speed accuracy, also offers high head movement analysis. Additionally, test loads of up to 110% of the nominal machine load are allowed to compensate for heavy combinations of test pieces. The movement of the transverse head is guided with great precision through two steel columns, which allow accurate application of the force in the sample.

2.4 Topology Optimization (TO)

Topology Optimization of is a particularly powerful tool in the field of product design, in calculating mechanisms and elsewhere. Using topology optimization, engineers can find the best design plan that meets design requirements. The central idea in optimizing a structure is to use a smaller amount of material than it previously maintains the same or even better behavior under certain operating conditions. Often the resultant structure after topological optimization is extremely difficult or economically unprofitable to produce using abstract production methods.

Structural optimization, in general, has tremendous potential benefits in the process product development. Optimization of topology in particular has the following benefits in the design (Gebisa, 2017): a) creating light structures b) generation of a ready-to-build part/assembly c) minimize the amount of raw material d) energy saving e) less need for natural prototypes f) reduction of physical testing g) reduced entry time. Topology optimization has to main characteristics. The first is that elastic properties of a material compared with their density may vary in model area. The second is that the material can be permanently removed from model space (Querin, 2017). During the TO study models have to be applied all boundary conditions. Two methods have been developed for TO study. The first one is truss based and second is volume based (Wang et al. 2018).

2.4.1 Truss Based TO Method

The truss-based on elements relating to a grid of beams between a set of nodes that is in a

given volume. The method initially detects that supports are necessary for the structure and determine their size. Then removes the beams that not meet the study requirements. In the results, the necessary beams are represented with bold line and dark blue color. The less necessary beams with less dark blue colors and unnecessary beam without change in their thickness (Fig. 3), (Perez, 2007). Extension to multiobjective optimization has been tried by (Stavroulakis et al. 2008, 2009).

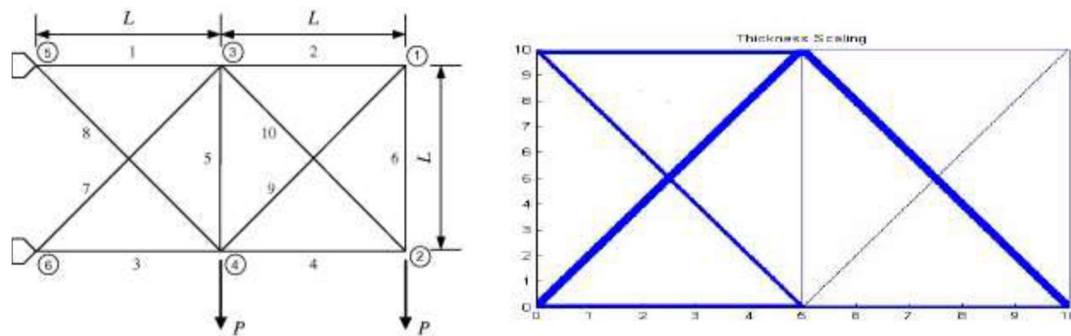


Figure 3: The initial design on the left side and the TO study results on the right

2.4.2 Volume Based TO Method

The Volume-based is known as SIMP - Solid Isotropic Material with Penalization- method and is widespread in CAE software. The process starts by defining a linear block of voxels. Density of each voxel is defining between zero to one. If value is equal to one then in this specific voxel the material is completely dense. If it is zero value then in this voxel there is no need for material. Any other value indicates that material in this voxel has not to be solid for the enforced loads. These value are very useful in FEA models for topology optimization analysis (Bendsoe, 2003). Voxel values are useful without restrictions in additive manufacturing rather than traditional manufacturing methods. In figure 4 is presented a typical topology optimization volume based problem (Bendsoe, 1989).

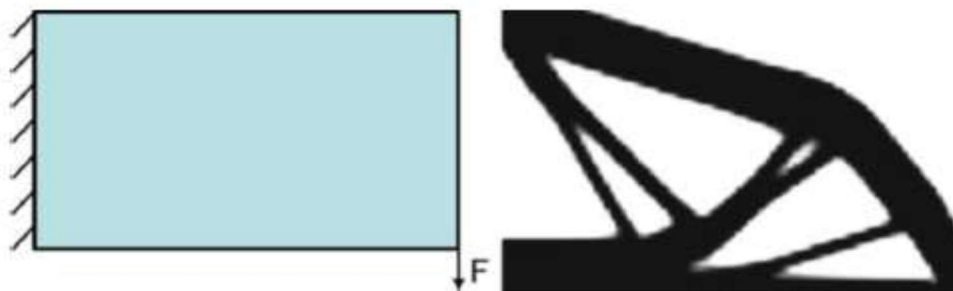


Figure 4: Typical optimization problem

3 RESULTS

3.1 3d Modeling and Printing

Initially two typical models of furniture created in CAD program (SolidWorks), the first

one was a chair (Fig.2) and the second was a table (Fig.3). Three different models for each type of furniture created. Chair 3d model basic dimensions are 450 mm length, 450 mm width and 950 mm height. Table 3d model basic dimensions are 550 mm length, 550 mm width and 450 mm height. Only wall thickness defers in each model, in the first model wall thickness is 10mm in the second 15mm and in the third 20mm. So three chair models and three models for table created. Each model has to export in .stl or .vrmf file, printing scale is 10% for chairs and 15% for tables, all models printed in same time (fig. 4), after printing process completed following the post process stage where moles must clean up from additional powder and smear them with the hardener.

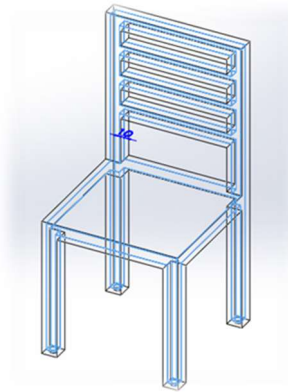


Figure 2: Chair 3d model



Figure 3: Table 3d model

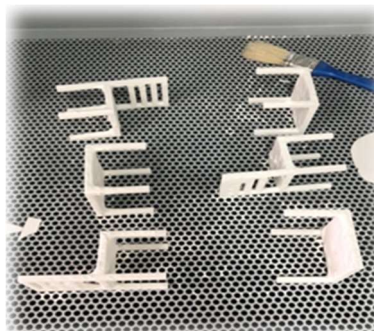
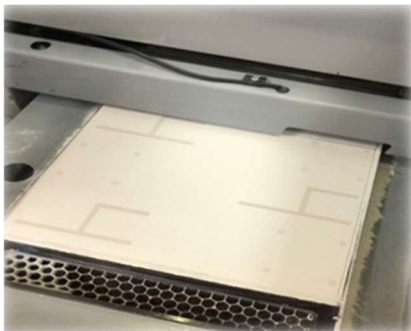


Figure 4: Printing Process

3.2 COMPRESSION TEST

Tests were performed with the Zwick / Roell Z020 test machine. In total, six tests performed for each model, designed to calculate their mechanical strength in compression. As previously mentioned, 3d models are three "hollow" chairs inside with a 10% scale and 10, 15 and 20 mm shells and three tables with a 15% print range, with 10, 15 and 20 mm shells respectively. The speed at which the test engine piston descended in all six tests was **2mm/min**. Specimens carefully on the compression pads of a universal testing machine. The specimens must be kept at the center of cross-head so that a uniform compressive loading can be assured on the specimens (Fig. 5).

The table below (Table 1), shows each sample the imposed force measured in Newton (N), the time taken to stop the piston at the surface of the model measured in seconds (s) and the distance that the plunger pulled to touch the surface of the model measured in millimeters (mm).



Figure 5: Compression Tests, chair and table specimens

Table 1: Experiment Results

Sample type	Force (N)	Time to stop (s)	Piston Distance (mm)
Chair 10mm	216	14	0,5
Chair 15mm	188	15	0,6
Chair 20mm	216	15	1,1
Table 10mm	84	38	1,3
Table 15mm	156	36	1,2
Table 20mm	244	25	1,5

3.3 TOPOLOGY OTIMIZATION FOR TABLE PROTOTYPE

Topology optimization study running in Siemens NX software. In the whole model used material like Z-450 printer origin use (Bibb et al. 2010, Pilipovi'c et al. 2009). The optimization scenario includes that table legs surface will remain the same and the main table surface will be optimized. As design space determined the whole model but only the upper surface was 'keep in'. The selected design constrains are a) Void Fill and b) Material Spreading in 35%. The load case is the same as in compression test results. At the center of the main surface forced with 244N. In fig. 6 & 7 are presented the results of optimization study.

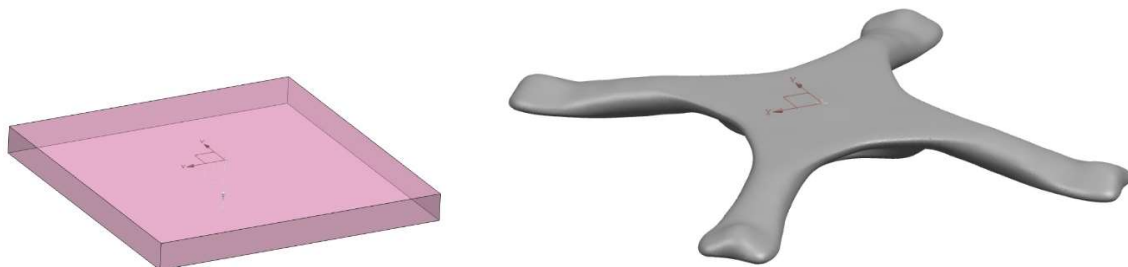


Figure 6: The 3d model before and after the optimization process



Figure 7: The bottom optimized surface and a perspective view of the whole model

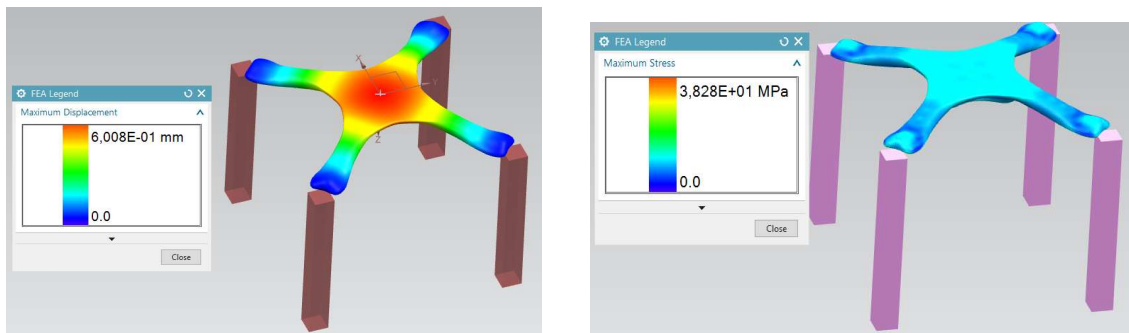


Figure 8 : Maximum Displacement and Maximum Stress

The total mass of the upper surface is reduced about 86 %. The same time the optimized model is stiffer than before as we can see in fig. 8.

4 CONCLUSIONS

Additive manufacturing – 3d printing are technologies that are convert a 3d model to physical prototype, through a fast and easy process. The 3d model is analyzed in a series of two-dimensional (2D) sections of a specific thickness, the feeding of which to AM machines are layer by layer until physical model to created. In current study 3d printing process has been carried out in an inject binder technology printer. The ability to print more than one model and different model designs simultaneously, thus leading us to save time. Additional savings time and the fact that the entire printing process followed was automated. Even all of the powder left over from the three-dimensional models was pulled back from the machine through its absorption system for future reuse, and therefore raw material savings were made. One further conclusion is that all models to be printed in 3D should be very well designed because of the sensitivity of the material there were cases of breakage of the printed tables when they were output from the print chamber but also during the printing process removing the excess powder in the respective chamber. In addition, the process of impregnation of physical models to increase their durability requires time and increases the cost of processes.

According to compression tests of initial chair prototypes we come to the following conclusions. The first 10mm thick shell chair withstand the largest load than the other two. The piston took less time to stop until specimen to break. During this time specimen had high

elasticity. The piston took less time to stop that means barely endured the pressure exerted on it, but it held the largest load compared to its thickness. The second chair with a 15mm shell thickness withstood the smallest load, it was less durable than the other two. The third 20mm shell thickness resisted the same power as the first and piston take the same time as the second. The piston moved almost twice the distance from the other two until to break the specimen. The third chair is more durable than the second one. Generally noticed that regardless of chairs shell thickness, there were not very large differences in the time required for the piston and the force exerted. According to the distance that piston passed, there is big difference that shows the third chair with a 20 mm shell thickness is more durable. However, it was also noticed that after the tests, there was not much damage to the chairs, which is attributed to their design structure.

About compression tests in table prototypes we come to following conclusions. The first 10mm wall thick table prototype withstand the smallest force in its mass. But it took more time and a very close distance to the other two tables until to break. It observed that it had the smallest strength but the greatest elasticity, while at the same time it had the smallest thickness than all. The second table prototype of 15mm shell thickness was approximately two times stronger than the first one, but it took less time and traveled a minimum length from the piston until to brake. So it is more durable than the first one. The third prototype of 20mm shell thickness withstand higher force about three times the first. But it destroyed in a much shorter period. The piston passed higher distance than the other two specimen.

Topology optimization combined with additive manufacturing can change the way that we design and produce products. Further research can be done in this interesting research area. There are so many possibilities and so many open means so lots of interesting research and development to be done.

REFERENCES

- [1] Alexander, C., (1971), "The State of the Art in Design Methodology", (replies to questions by M. Jacobson), DMG Newsletter, p. 3-7.
- [2] Babalis A., Ntintakis I., Chaidas D., Makris A.: Design and Development of Innovative Packaging for Agricultural Products. *Procedia Technology* 8 (2013) 575–579.
- [3] Bendsoe, M.P., Sigmund, O., (2003), *Topology Optimization: Theory, Methods, and Applications*, Springer-Verlag Berlin Heidelberg
- [4] Bendsoe, M.P., (1989), "Optimal shape design as a material distribution problem", *Structural Optimization* 1, Springer-Verlag, pp. 193-202
- [5] Richard Bibb, Darren Thompson, John Winder (2011) *Computed tomography characterisation of additive manufacturing materials*, *Medical engineering & physics*, ISSN: 1873-4030, Vol: 33, Issue: 5, Page: 590-6
- [6] Bournias Varotsis, A. (2018). *Introduction to Binder Jetting 3D printing*.
- [7] Checkland, P., 1981, *Systems Thinking, Systems Practice*, John Wiley and Sons, Chichester.
- [8] Colquhoun, A., 1967, "Typology and Design Method", *Arena*, 83, p.11-14.

- [9] Gebisa A.W, Lemu H.G, (2017), "A case study on topology optimized design for additive manufacturing", IOP Conference Series: Materials Science and Engineering, 276
- [10] Giannatsis G., Dedousis V. & Kanellidis V. (2015). Advanced Manufacturing Techniques with PC. Athens,2015
- [11] Hillier B., J. Musgrove, and P. O'Sullivan, 1972, "Knowledge and Design", Environmental
- [12] Hillier, B., and A. Leaman, 1974, "How is design possible?", Journal of Architectural Research, 3(1), p. 4-11.
- [13] Horatio Greenough, Form and Function: Remarks on Art, edited by Harold A. Small (Berkeley, Univ. of California Press, 1947)
- [14] Jones, C., 1977, "How My Thoughts about Design have Changed During the Years", Design Methods and Theories, 11(1), p.50-62.
- [15] J. Kechagias, P. Stavropoulos, A. Koutsomichalis, I. Ntintakis, and N. Vaxevanidis, "Dimensional Accuracy Recent Researches in Electrical and Computer Engineering ISBN: 978-1-61804-315-3 113 Optimization of Prototypes produced by PolyJet Direct 3D Printing Technology," in Proceedings of the 18th International Conference on Circuits, Systems, Communications and Computers, pp. 17-21.
- [16] Meikle's J. "Twentieth Century Limited: Industrial Design in America, 1925 – 1939"
- [17] Papathanasis H. (2005). 'The technology of 3d printing' Periscope of Science. Vol297,1-9
- [18] Perez, R.E and Behdinanb, K., (2007), "Particle swarm approach for structural design optimization", Computers & Structures, 85, Issues 19-20, pp. 1579-1588
- [19] Pilipovi'c A, Raos P, Šercer M. Experimental analysis of properties of materials for rapid prototyping. Int J Adv Manuf Technol 2009;40:105–15.
- [20] Querin, O., Victoria, M., Alonso, C., Ansola, R. and Marti, P., (2017), Topology Design Methods for Structural Optimization, Elsevier Academic Press
- [21] Stavroulakis, G.E., Kaminakis, N., Marinakis, Y., Marinaki, M., & Skaros, N. (2008). Optimal structural and mechanism design using topology optimization. Proc. MS'08 Jordan, International Conference on Modelling and Simulation, Petra (Jordan), 18-20 November, 2008.
- [22] Stavroulakis, G.E., Kaminakis, N., Marinakis, Y., & Marinaki, M. (2009). Multiobjective global topology optimization for structures and mechanisms. SEECM 2009, 2nd South-East European Conference on Computational Mechanics, M. Papadrakakis, M. Kojic, V. Papadopoulos (eds.), Rhodes, Greece, 22-24 June 2009.
- [23] Sullivan, Louis H. (1896). The tall office building artistically considered. Getty Research Institute.
- [24] Wong, V. & Hernandez, A. (2012). A Review of Additive Manufacturing. ISRN Mechanical Engineering. Vol 12, 10 pages
- [25] Zhou, M., Rozvany, G.I.N., (1993), "DCOC: An optimality criteria method for large systems.PartII:algorithm",Structural and Multidisciplinary Optimization,6,Issue4,p250262

TOWARD COMPLIANT AND STRUCTURAL OPTIMIZATION OF A COMPLIANT ROTATION REDUCER MECHANISM

Sim-AM 2019

L. KOMINI^{*}, J. KRUIS^{*}, G. PERRUCHOUD^{*}, F. COSANDIER^{*}, L. KIENER^{*},
H. SAUDAN^{*}

^{*} Centre Suisse d'Electronique et Microtechnique (CSEM)
Rue Jaquet-Droz 1, CH-2000 Neuchâtel, Switzerland
e-mail: ludian.komini@csem.ch, web page: www.csem.ch

Key words: structural topology optimization, flexural topology optimization, floating structure, modal objective function, flexure pivot synthesis, rotational center constraint.

Abstract.

This paper presents a Compliant Rotational Reducer Mechanism (CRRM), under development in the context of a space project. The CRRM is optimized using structural and flexural topology optimization for respectively, the structural and flexure problems. With respect to the structural optimization, a mass reduction of 20 % and a shift of the lowest undesirable eigenfrequency from 400 to 1000 Hz was obtained. For the flexural optimization, a Rotational Center Constraint (RCC) and a Floating Structure Modal Objective Function (FSMOF) are introduced. The FSMOF allows to impose a desired eigenmode of a mechanism. The RCC and FSMOF are applied to generate a flexure pivot with eigenmodes of a typical flexure pivot. Finally, these results are integrated into a novel version of the CRRM.

1. INTRODUCTION

Flexures use elasticity to realize precise displacements, this allows improved performance in terms of wear, backlash, and friction compared to mechanisms based on standard bearings. In the context of an ongoing space project, there was a need for a Compliant Rotational Reducer Mechanism (CRRM), with a reduction ratio of at least 10. The desired specifications of the CRRM are shown in Table 1.

Table 1: The CRRM specifications

Maximum mass	0.4 kg
Design volume	120 mm x 50 mm
Minimal reduction ratio	10
Minimal input angle	+/-10°
Minimal output angle	+/- 1°

This paper's goal is to use topology optimization to automate and optimize the design process of the CRRM depicted in Figure 1.

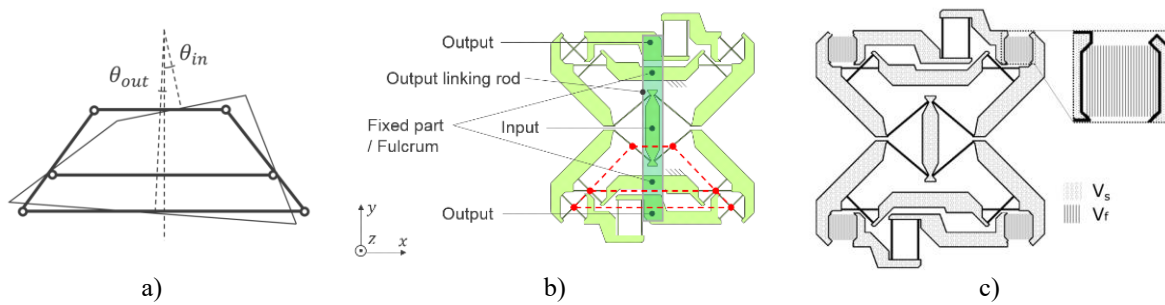


Figure 1: a) The reduction principle of the CRRM. b) the first pre-design of the CRRM. c) The definition of the structural optimization volume V_s , and the flexural optimization volume V_f .

The current approach consists of breaking down the design into structural and flexural sub-problems (Figure 1c). In the structural sub-problem a set of rigid bodies V_s , is optimized for minimal compliance. In the flexural sub-problem, the Floating Structure Modal Objective Function (FSMOF) is applied to 4 identical volumes V_f to generate a first pivot design.

Topology optimization is defined as a technique that distributes optimally the material in the design domain while satisfying an objective function and constraints [1]. This paper distinguishes two different types of topology optimization, namely structural and flexural.

Structural topology optimization its objective function is to minimize the compliance, i.e. the amount of elastic displacement as a function of an applied force. A good comparison of the various tools available commercially for structural topology optimization is offered by Frecker et al. 2016 [2]. Altair Optistruct[®] and Inspire[®] are used in this work for realizing the structural topology optimization.

Flexural topology optimization its objective function in this paper, is to minimize the required energy to perform the desired displacement combination at certain points, while at the same time maximizing the energy required to achieve any other displacement combination at the same points [1].

An overview of alternate formulations for flexural topology optimization is presented in detail by Deepak et al 2009 [3].

These alternate formulations rely on weighted multi-objective optimization and require multiple iterations for tuning their weighting factors. In addition, these alternate formulations require fixed points to avoid a singular stiffness matrix, i.e. to assure a positive definite stiffness matrix. Lastly, these formulations typically require more iteration to obtain symmetric designs. This paper presents a Floating Structure Modal Objective Function (FSMOF), based on the work by Hasse et al 2009[4], which was applied to fixed structures and enhanced in this paper by considering the design domain as a floating structure [5].

The FSMOF requires only the definition of the interfaces and the center of rotation for the implementation. The advantage of FSMOF is thus that it is easier to implement and doesn't require compensation loads for the fixation. In addition, symmetric designs can be more easily obtained with the FSMOF.

The results of the structural and flexural optimization are applied to a first novel version of the CRRM.

2. STRUCTURAL OPTIMIZATION.

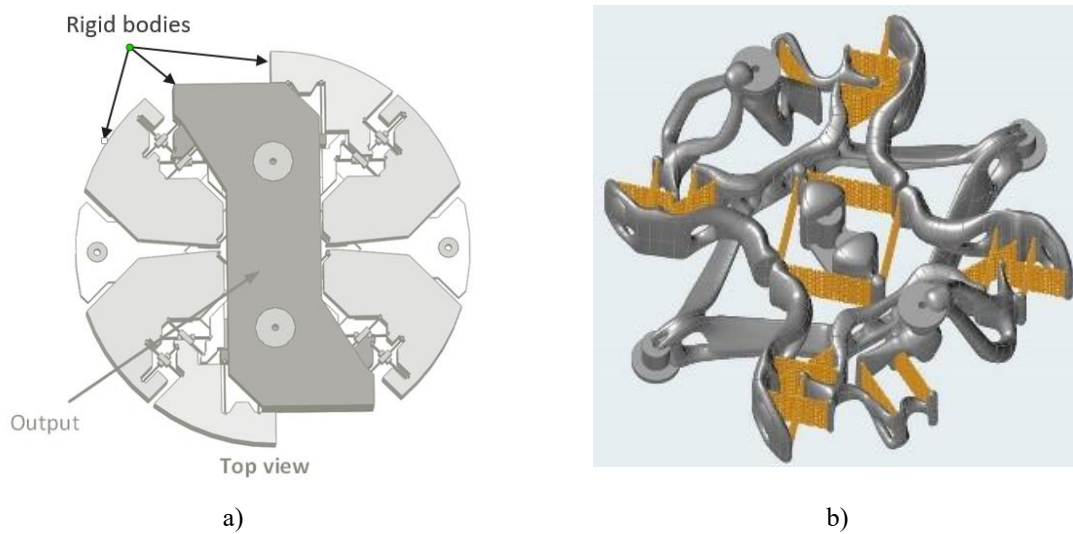


Figure 2: a) The rigid body design volumes for structural optimization V_s , of the CRRM. b) The optimized structural masses of the topology optimization.

The structural optimization steps are:

1. Design volume definition (Figure 2a).
2. Boundary condition and the load case definition.
3. Optimization objective and design constraint definitions (including increasing the lowest undesired eigenfrequency of the system)
4. Perform the topology optimization with the Altair Optistruct[®] default solver.
5. Smoothen the result with Altair Inspire[®] (Figure 2b)

The result of the structural topology optimization is a 20 % mass reduction compared to the original pre-design shown in figure 1b and an increase of the lowest desired eigenfrequency from 400 to 1000 Hz.

3. FLEXURE PIVOT TOPOLOGY OPTIMIZATION SYNTHESIS

In this chapter, the Floating Structure Modal Objective Function (FSMOF) and the Rotational Center Constraint (RCC) are represented and implanted on two pivot examples.

3.1 Floating Structure Modal Objective Function (FSMOF) for a flexure pivot

The modal objective function has been successfully applied by Hasse [4] for fixed compliant mechanisms, i.e. the rigid body modes are removed through fixing a part of the design domain. Here an adaptation of Hasse's methodology is presented. The novelty w.r.t. Hasse is step 3 where we remove the rigid body modes resulting in a floating structure.

The method thus is:

1. Static condensation of the master Degrees Of Freedom (DOFs), i.e. the DOFs which we

desire to displace in a certain way.

2. Original eigenvector and eigenvalue derivation of the condensed stiffness matrix
3. Remove the rigid body modes ϕ_r , i.e. those with zero eigenvalues.
4. Prescribed eigenvector substitution.
5. Gram-Schmidt Orthonormalization.
6. Rederive the eigenvalues of the new set of orthonormal eigenvectors.
7. Application of a summed eigenvalue ratio objective function.
8. Optimization with the Method of Moving Asymptotes (MMA) [6].

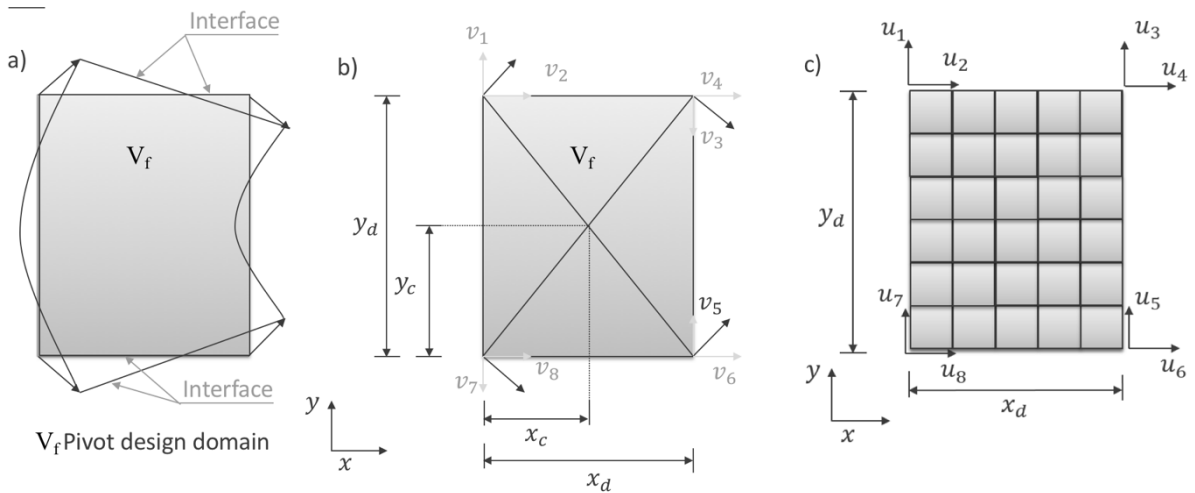


Figure 3: a) The eigenmode corresponding to the prescribed deformation, b) The displacement vectors of the master DOFs associated with the desired eigenmode. c) Discretization of the design domain V_f and the global displacements definition at the master DOFs.

The master DOFs of step 1 are u_1 to u_8 (Figure 3c). In order to allow for step 3, the forces f_i arising at the master DOFs need to be in self-equilibrium.

$$\sum_i^n f_i = 0 \quad (1)$$

The forces at the master DOFs are a result of the prescribed displacements ϕ_p acting on the condensed stiffness matrix K_c . The relation between the nodal displacements and the nodal forces is given in equation (2).

$$\phi_p K_c = f_i \quad (2)$$

3.2 Rotational Center Constraint (RCC)

In order to constrain the rotational center of the flexure pivot, its coordinates (x_c, y_c) are fixed by prescribing the eigenvector ϕ_p , as a function of (x_c, y_c) Figure 3b.

The vector of eigenvectors ϕ thus comprises the eigenvectors of the rigid body modes ϕ_r , the prescribed eigenvectors ϕ_p and the non-prescribed eigenvectors ϕ_{np} . This is shown in equation (3).

$$\phi = [\phi_r \quad \phi_p \quad \phi_{np}] \quad (3)$$

All the terms of ϕ_p are explicitly given in equation (4) as a function of the center of rotation (x_c, y_c) and the dimensions of the design domain (x_d, y_d) .

$$\begin{aligned} \phi_p &= \{v_i\} \quad i = 1 \dots 8 \\ v_1 &= \frac{x_c}{\sqrt{x_c^2 + (y_d - y_c)^2}} \\ v_2 &= \frac{y_d - y_c}{\sqrt{x_c^2 + (y_d - y_c)^2}} \\ v_3 &= -\frac{y_d - y_c}{\sqrt{(y_d - y_c)^2 + (x_d - x_c)^2}} \\ v_4 &= \frac{x_d - x_c}{\sqrt{(y_d - y_c)^2 + (x_d - x_c)^2}} \\ v_5 &= -\frac{y_c}{\sqrt{y_c^2 + (x_d - x_c)^2}} \\ v_6 &= \frac{x_d - x_c}{\sqrt{y_c^2 + (x_d - x_c)^2}} \\ v_7 &= \frac{x_c}{\sqrt{y_c^2 + x_c^2}} \\ v_8 &= \frac{y_c}{\sqrt{y_c^2 + x_c^2}} \end{aligned} \quad (4)$$

With the formulation of equation (4), the parasitic center shift of the rotational center is implicitly constrained. The magnitude of this implicit effect has not yet been quantified.

3.3 Implementation

The FSMOF is applied to the problems of the symmetrical pivot and a pivot with a shifted rotational center. For both problems, the objective function is defined in equation (5).

$$\begin{aligned} &\min \left(\sum_{i=2}^{i=n} \frac{\lambda_1}{\lambda_i} \right) \\ &\text{s.t.} \begin{cases} \sum_{j=1}^{j=nel} x_j v_j \leq 0.5V \\ 0.001 < x_j \leq 1 \end{cases} \end{aligned} \quad (5)$$

where:

- λ_i [J] the eigenvalue of the i^{th} mode, i.e. the energy required to actuate the mode.
- n [-] is the number the eigenvalues of the problem formulation.
- V [m³] is the total volume of the domain.
- nel [-] is the total number of elements.

v_j [m³] is the volume of one finite element.

The design domain given in (Figure 3b) is discretized in 20 elements in the x-direction and in 30 elements in the y-direction. With this design domain and the FSMOF two examples presented below were generated.

1 A symmetrical flexure pivot flexure pivot example

The optimization result of a symmetrical flexural pivot is illustrated in Figure 4.

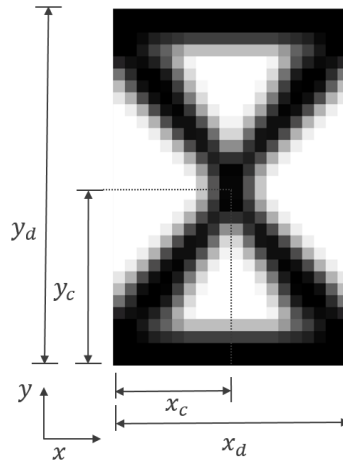


Figure 4: Synthesis of the flexure pivot when the center of rotation is placed at the center of the design domain.

The evolution of the objective function and the logarithmic scale of eigenvalues throughout the iterations are given in Figure 5 a and b. The objective function decays rapidly in the first iteration. This is due to the fact that a strong decrease of the first eigenvalue and an increase of all the other eigenvalues occurs in the first iterations, Figure 5b.

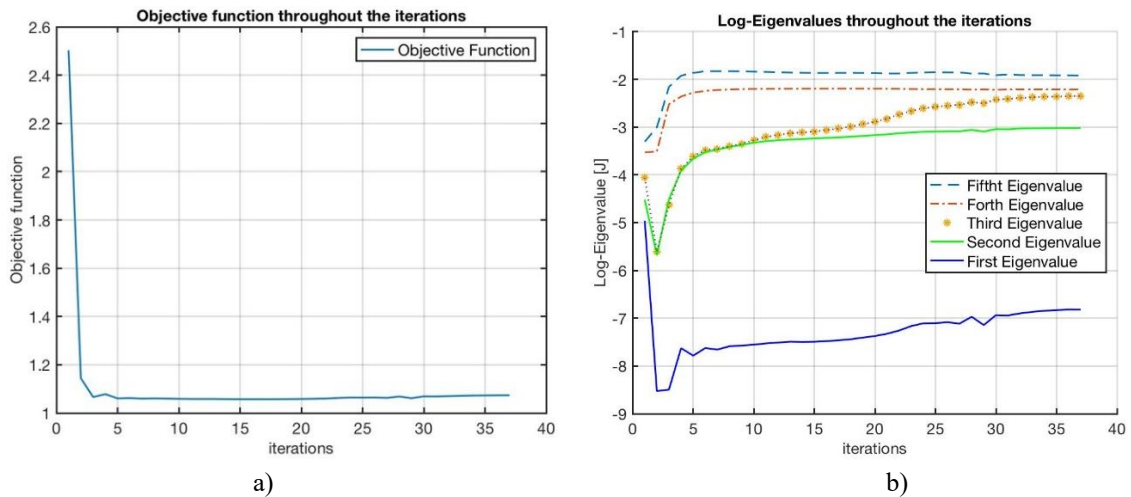


Figure 5: a) Evolution of the objective function throughout the iteration, b) Evolution of the logarithmic scale of the eigenvalues throughout the iteration.

2 An asymmetrical flexure pivot example

As a second demonstration, the optimization is performed, in this case, when the center of rotation is shifted at the $2/3^{\text{rd}}$ of the x_d dimension.

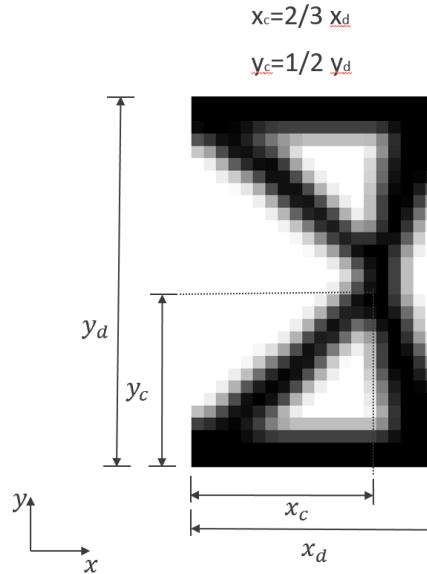


Figure 6: Synthesis of the flexure pivot when the center of rotation is placed at the $2/3^{\text{rd}}$ of the x_d dimension

The performance of the objective function and the eigenvalues don't deviate a lot compared to the first case. The only difference consists of a small oscillation of the second and third eigenvalue after the 50^{th} iteration.

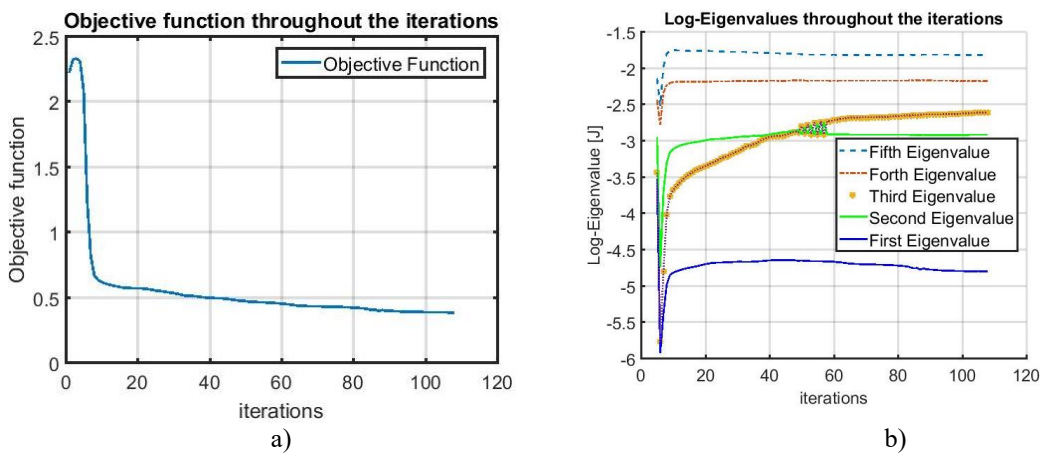


Figure 7: a) The objective function as a function of the iterations, b) evolution of the eigenvalues throughout the iteration.

4. THE OPTIMIZED CRRM

The results from the structural and flexural optimization are combined into the new updated CRRM as shown in Figure 8.

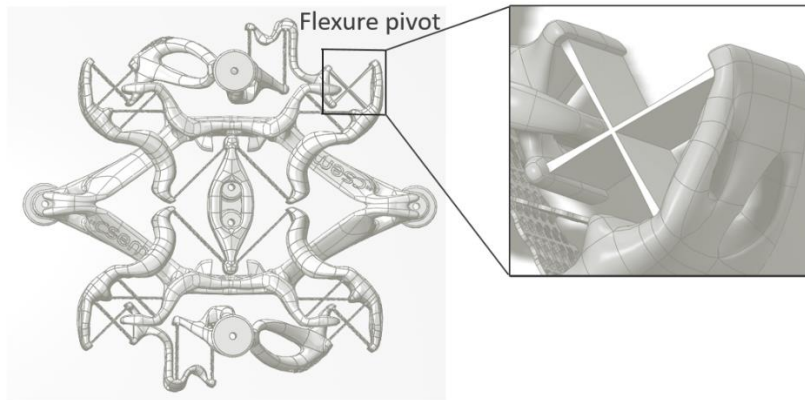


Figure 8: Final design layout

5. CONCLUSIONS AND RECOMMENDATIONS.

A mass reduction of 20 % and a shift of the lowest undesirable eigenfrequency from 400 to 1000 Hz was obtained using Altair Optistruct and Inspire.

The Rotational Center Constraint (RCC) and the Floating Structure Modal Objective Function (FSMOF) function are implemented for synthesizing flexure pivots through topology optimization. The principle difference with other modal formulations is that the rigid body modes are excluded during the analysis from the formulation. In order to apply FSMOF self-equilibrium of the forces at the master DOFs is required. These forces originate from the prescribed displacement.

For further development we recommend incorporating in the formulation the overhang constraint for additive manufacturing and stress constraint to avoid fatigue and improve the mechanism lifetime.

In addition, we want to determine how well the implicit parasitic rotational center shift is constrained by the RCC.

The long term ambition is to address problems similar to the CRRM directly with flexural optimization without splitting it into sub-problems.

6. ACKNOWLEDGMENT

We would like to acknowledge the funding from the European Space Agency through the ESA GSTP framework and the Swiss Space Office. In addition, we would like to thank Prof. Svanberg for providing his MMA code.

REFERENCES

- [1] Sigmund, O. *On the design of compliant mechanisms using topology optimization*. Mechanics of Structures and Machines, (1997) 25(4): 493-524.
- [2] Sai Nithin Reddy, K. Ferguson, I. Frecker, M. Simpson, W. T. and Dickman J. C. *Topology optimization software for additive manufacturing: A review of current capabilities and a*

- real-world example*. ASEM International Design Engineering Technical Conferences and Computers and Information in Engineering Conference IDETC/CIE 2016. Charlotte, North Carolina. 2016, DETC 2016-59718.
- [3] Deepak, R. S. Deepak K. S. Ananthasuresh, K. G. *A comparative study of the formulations and benchmark problems for the topology optimization of compliant mechanisms*. *Journal of Mechanisms and Robotics I* (1), 011003 2009 DOI:10.1115/1.2959094
- [4] Hasse, A, Campanile, L. F. Design of compliant mechanisms with selective compliance *Smart Material and Structures* 18 (2009) 115016(pp10).
- [5] Felippa, C.A. Park, K.C. A direct flexibility method. *Computer Methods in Applied Mechanics.*, vol. 149, issues 1-4, pp.3019-337. Oct. 1997.
- [6] K. Svanberg. *The method of moving asymptotes – a new method for structural optimization*, *International Journal for Numerical Methods in Engineering*, (1987) **24(2)**:359-373.
- [7] Pedersen, C. B. Buhl, T. and Sigmund, O. “Topology synthesis of large-displacement compliant mechanisms,” *Int. J. Numer. Methods Eng.*, vol. 50, no. 12, pp. 2683–2705, 2001.

IN-SITU THERMOGRAPHIC MONITORING OF THE LASER METAL DEPOSITION PROCESS

NILS SCHEUSCHNER*, ANNE STRASSE*, SIMON J. ALTENBURG*, ANDREY GUMENYUK* AND CHRISTIANE MAIERHOFER*

*Bundesanstalt für Materialforschung und –prüfung (BAM)
Unter den Eichen 87, 12205 Berlin, Germany
e-mail: nils.scheuschner@bam.de, web page: <http://www.bam.de/>

Key words: Infrared Thermography, In-situ Monitoring, Laser Metal Deposition, 316L, Additive Manufacturing

Abstract. In this paper shortwave infrared (SWIR) thermographic measurements of the manufacturing of thin single-line walls via laser metal deposition (LMD) are presented. As the thermographic camera is mounted fixed to the welding arm, an acceleration sensor was used to assist in reconstructing the spatial position from the predefined welding path. Hereby we could obtain data sets containing the size of the molten pool and the oxide covered areas as functions of the position in the workpiece. Furthermore, the influence of the acquisition wavelength onto the thermograms was investigated in a spectral range from 1250 nm to 1550 nm. All wavelengths turned out to be usable for the in-situ process monitoring of the LMD process. The longer wavelengths are shown to be beneficial for the lower temperature range, while shorter wavelengths show more details within the molten pool.

1 INTRODUCTION

By allowing economic on demand manufacturing of highly customized and complex workpieces, metal based additive manufacturing (AM) has the prospect to revolutionize many industrial areas [1]. Since AM is prone to the formation of defects during the building process, a fundamental requirement for AM to become applicable in most fields is the ability to guarantee the adherence to strict quality and safety standards. A possible solution for this problem lies in the deployment of various in-situ monitoring techniques. For most of these techniques, the application to AM is still poorly understood [2]. Therefore, the BAM in its mission to provide safety in technology has initiated the project “Process Monitoring of AM” (ProMoAM). In this project, a wide range of in-situ process monitoring techniques, including active and passive thermography, optical tomography, optical emission and absorption spectroscopy, eddy current testing, laminography, X-ray backscattering and photoacoustic methods, are applied to laser metal deposition (LMD), laser powder bed fusion (LPBF) and wire arc AM (WAAM). Since it is still unclear which measured quantities are relevant for the detection of defects, these measurements are performed very thoroughly. In successive steps, the data acquired by all these methods is fused and compared to the results of reference methods such as computed tomography and ultrasonic immersion testing. The goal is to find reliable methods or combinations

thereof to detect the formation of defects during the building process. The detailed acquired data sets may also be used for comparison with simulations. A requirement therefore is that all data sets use a common foundation such as the position in the workpiece. This position mapping is not always straightforward for all monitoring techniques without additional measures or processing steps.

In this paper we focus on the in-situ monitoring of the LMD process by a thermal camera. It is known from earlier experiments and simulations that thermal cameras can be used for in-situ monitoring the LMD process, however there are currently no integrated commercial solutions available, as a deeper understanding of the acquired data is still required [3, 4, 5, 6]. Furthermore, the cost of the camera system is a crucial factor for the usability in industrial applications. As fast thermal cameras tend to increase in cost the longer the detected wavelengths become, we decide to concentrate on the shortwave infrared (SWIR) range and investigate the influence of the acquisition wavelength on the thermographic data in this range in detail. Furthermore, we fixed the camera relatively to the molten pool in contrast to many earlier works, where the camera was mounted fixed relatively to the workpiece. This mounting setup has the advantage that the molten pool can permanently be kept in focus, regardless of the shape of the specimen. However, thermograms acquired in such a mounting setup, do not contain any information about the current spatial position during the building process. To overcome this problem, we show in this work how an acceleration sensor can be used to track the movement and synchronize the measured data with the predefined welding path. This allows us to reconstruct the geometry of the workpieces and generate in combination with the thermograms new datasets providing the size of the molten pool and the oxide covered area during manufacturing as a function of the position in the workpiece, as first examples. For the investigation of the influence of the acquisition wavelength on the thermographic data we used four different bandpass filters with 25 nm width of the transmission window in a spectral range from 1250 nm to 1550 nm. While all wavelengths showed comparable results and can be used for in-situ monitoring of the LMD process, there were subtle differences. While the use of longer wavelengths is beneficial for the observation down to lower temperatures, the use of lower wavelengths allows to resolve more details within the molten pool.

2 EXPERIMENTAL DETAILS

For our experiments we used a TruLaser Cell 3000, that is coupled with a 16 kW TruDisk 16002 disk laser with the wavelength of 1030 nm, see Fig.1(a). The welds were done with a three-jet LMD-nozzle with a working distance of 16 mm, see Fig. 1(b). The powder was supplied by a Flowmotions Twin powder feeder. Shielding and carrier gas was argon. The LMD process parameters are listed in Tab. 1. The camera and the acceleration sensor were mounted fixed onto the welding arm, as shown in Fig. 1(b), by employing two regularly unused machine threads. Hereby we were able to avoid any permanent modification to the LMD machine. The distance between the frontmost lens of the camera and the focal point of the laser was 9 cm, while the angle between surface normal of the base plate and the optical axis of the camera was approximately 40°.

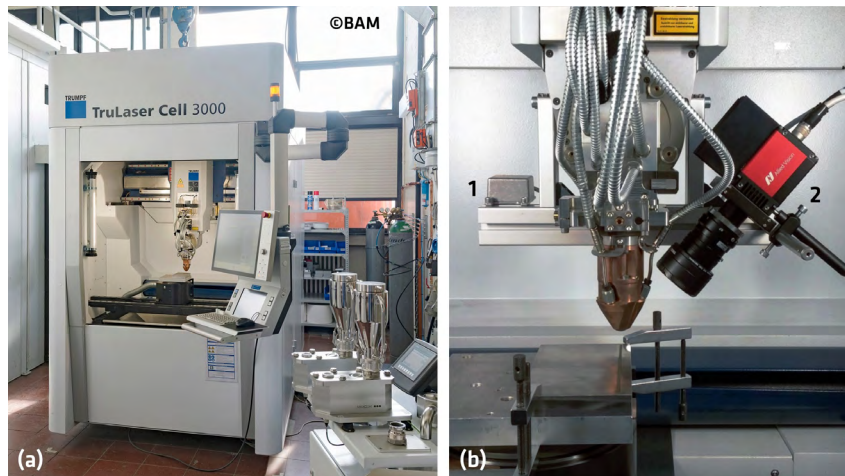


Figure 1: (a) TruLaser Cell 3000 (Trumpf) with Flowmotion Twin powder feeder (Medicoat). (b) Welding arm with three-jet nozzle (SO16) with mounted acceleration sensor (1) and SWIR camera (2).

Table 1: LMD process parameters.

Powder material	316L-Si
Powder grain size	53-106 μm
Powder mass flow	15 g/min
Laser power	800 W
Laser spot diameter	1.6 mm, Gaussian profile
Welding speed	0.8 m/min
Layer thickness	0.3 mm

2.1 Thermography

For the thermography measurements we used a Goldeye CL-033 TEC1 camera from Allied Vision with an 50 mm SWIR objective from Kowa. The camera is sensitive to IR radiation in a spectral range from 900 nm to 1700 nm with a quantum efficiency in the range of 70% to 80% between 1000 nm and 1640 nm. All presented measurements were acquired with the following settings, unless stated otherwise: The camera was operated in subframe mode (ROI: 640x210 pixel, 14-bit) with a framerate of 300 Hz, 200 μs exposure time, an aperture stop of $f/4.0$ and using the background subtraction and non-uniformity correction (NUC) functions of the camera. The thermograms were transferred to a computer by a Camera Link framegrabber card and recorded using Matlab. Since the distance of the camera to the molten pool was below the focusing range of the objective, a 2 cm extension tube was used. To suppress the laser radiation and to restrict the examined spectral region, four different 25 nm wide bandpass filters with a central wavelength in the range from 1250 nm to 1550 nm were employed. Additionally, a neutral density filter was used to avoid overexposure due to the high luminance of the molten pool.

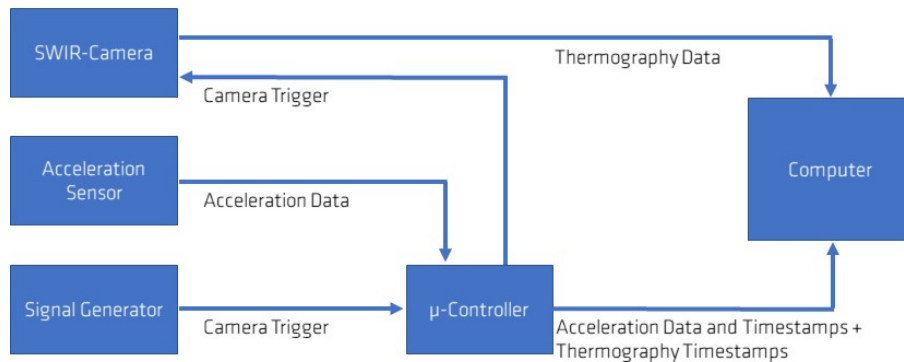


Figure 2: Schematic overview of the connections and data flow between the individual components of our measurement setup. The signal generator provides the camera trigger signal which is looped through the microcontroller. Simultaneously, the microcontroller receives the acceleration data from the sensor. Hereby time stamps for the camera and the acceleration sensor can be generated and forwarded to the computer together with the acceleration data. In contrast, the thermograms are transferred directly from the camera to the computer.

2.2 Acceleration sensor and data acquisition

The acceleration sensor was constructed using an ADXL345 chip from Analog Devices mounted on a breakout board from Adafruit. The sensor was mounted into a metal housing for electromagnetic shielding and operated with a sample rate of 800 Hz. To read out the acceleration data the sensor was connected via SPI bus to an Arduino Due microcontroller. The data was subsequently transferred via USB to the computer for recording. A challenge in designing the experimental setup was the requirement to have a common source for the time stamps for the camera and the acceleration sensor. We solved this problem by using a signal generator (Rohde & Schwarz HMF2525) to provide an external signal to trigger start of the acquisition for each frame for the camera. This trigger signal was looped through the microcontroller, which was thereby enabled to record the camera time stamps using the same clock as for the acceleration sensor. Fig. 2 schematically shows the connections and data flow between the components of our setup. The remaining offset between camera and acceleration sensor time stamps is thereby reduced to the characteristic uncertainties of both methods.

2.3 Radiometric Model

As the camera has no inbuilt calibration function to obtain temperature values from the measured intensities, we had to establish a radiometric model for our measurements. Due to the lack of reference measurements, we decided to use the knowledge of the solidification temperature of 316L (1660 K) as a reference point for calibration [7, 8]. As the area of solidification can be identified by optical inspection in the thermograms, the corresponding intensity value is determinable. Afterwards, we integrated numerically Plancks law in the spectral window of the bandpass filter and used the previously determined intensity value to scale the result linearly. This function was subsequently inverted to provide a look up table to map the intensity values to temperature values. A potential error source hereby is the neglect of the strong influence

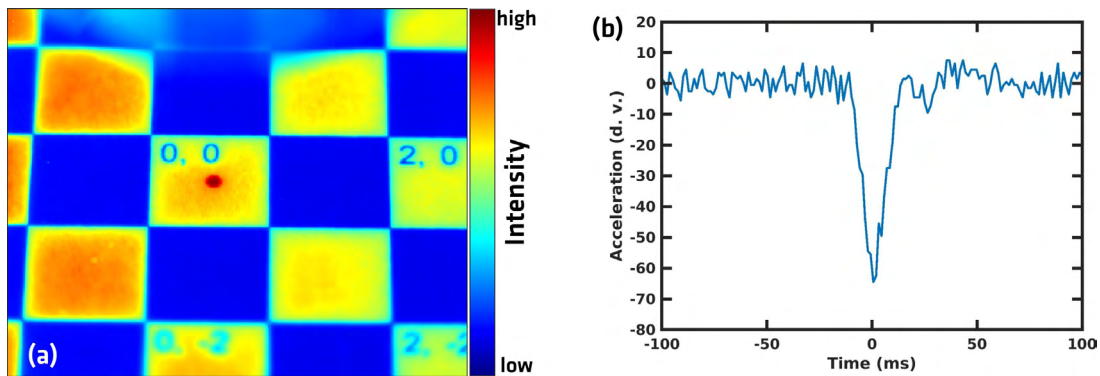


Figure 3: (a) Checkerboard pattern to determine the image ratio. The red dot on the 0,0 square is the stray light of the pilot laser indicating the position of the molten pool during manufacturing. The edge length of the squares is 5 mm. (b) Typical acceleration pattern of the welding arm at the end of a layer (constant offset subtracted).

of many external parameters on the emissivity such as the temperature itself, the observation angle, the aggregate state and the composition dependency that can be assumed to differ for each individual data point of the measurement [9]. As a result, all temperature values shown in this paper must be considered to be estimated values in the knowledge that the real temperature could differ strongly, especially for the liquid phase, the presence of oxides and progressively with increasing deviation towards lower temperatures from the solidification temperature.

2.4 Reconstruction of the spatial position

Figure 3(a) shows an image of a calibration card, with a checkerboard pattern, lying on the baseplate, acquired without filters. Due to the very long exposure time, features in the visible range such as the pilot laser become detectable. All machine coordinates show slightly different scales for each pixel of the detector due to the central projection. However, as we are primarily interested in the region the layers are built, we can focus our analysis to the middle row of the checkerboard pattern. For the horizontal direction of the camera, which is aligned parallel to the welding direction, we obtained a scaling factor of $30 \mu\text{m}/\text{pixel}$. The scaling factor of the vertical direction for structures oriented along the baseplate is $39 \mu\text{m}/\text{pixel}$. Using trigonometric functions we obtain a scaling factor of $47 \mu\text{m}/\text{pixel}$ for structures oriented along the normal of the baseplate. Figure 3(b) shows typical data from the acceleration sensor during the end of the welding process of a line. The welding arm is accelerated during the welding process only during very short ($\approx 25 \text{ ms}$) start and stop phases and moves with constant speed in between. By identifying the precise start and stop time from the acceleration data and the knowledge that the welding arm moves with constant speed in between, its position during image acquisition can easily be calculated for each thermogram from the time stamp and the length of the line.

3 EXPERIMENTAL RESULTS AND DISCUSSION

For the measurements, we built four identical single-line wall structures with a length of 155 mm and a height of 10 layers (approx. 3 mm) which were welded without additional delay between the layers other than the time the LMD machine required to move back to the starting

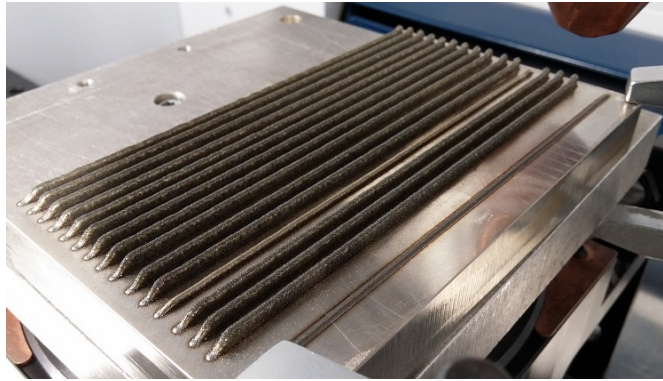


Figure 4: Photograph of the sample structures on the base plate after manufacturing (including additional test runs).

point. All layers were welded in the same direction. For each structure, a different bandpass filter was used. Fig. 4 shows a photograph of the samples after manufacturing.

3.1 Influence of the wavelength

Figure 5 shows thermograms of the molten pool of the welding process of the middle of the tenth layer acquired with the 1250 nm, 1350 nm, 1450 nm and 1550 nm bandpass filters, respectively. The temperature scale was adjusted to show primarily the solid phase. In all thermograms a reflection of the molten pool is visible on the baseplate. On first inspection, all thermograms show very comparable temperature distributions for the solid phase on a larger length scale. On a shorter length scale, more fluctuations can be seen in the thermograms acquired with a shorter wavelength. By analyzing the following frames, these fluctuations can be linked to actual surface features of the workpiece. Whether the visibility of this feature is useful for in-situ monitoring of the LMD process is yet unclear and will depend on the feasibility to link these features to quantities of interest, such as the presence of defects. Otherwise, the small scale fluctuations could turn out to be a disadvantage of using shorter wavelengths, as they might aggravate the data analysis compared to the smoother thermograms acquired with longer wavelengths. In all thermograms a thin ring shaped area of higher apparent temperatures around the laser spot can be identified. This effect is caused by the presence of oxides on the surface of the workpiece, which possess a higher emissivity than the surrounding area [7]. These oxides are probably created during the previous welds and are pushed to the periphery region of the molten pool during the remelting process. Although this might be unfavorable in terms of determining the temperature in these areas, it might be very useful for in-situ process monitoring, as the area covered by oxides can easily be extracted from the thermograms by using a threshold value.

For further analysis, cross sections of all thermograms from Fig. 5 along the middle line of the molten pool, as indicated by the dashed line in Fig. 5(c), are shown in Fig. 6. Between 4 mm and 6 mm, we observe the region of the solidification plateau, which we used to calibrate our radiometric model. The area between 0 mm to 2 mm is directly covered by the laser spot. The

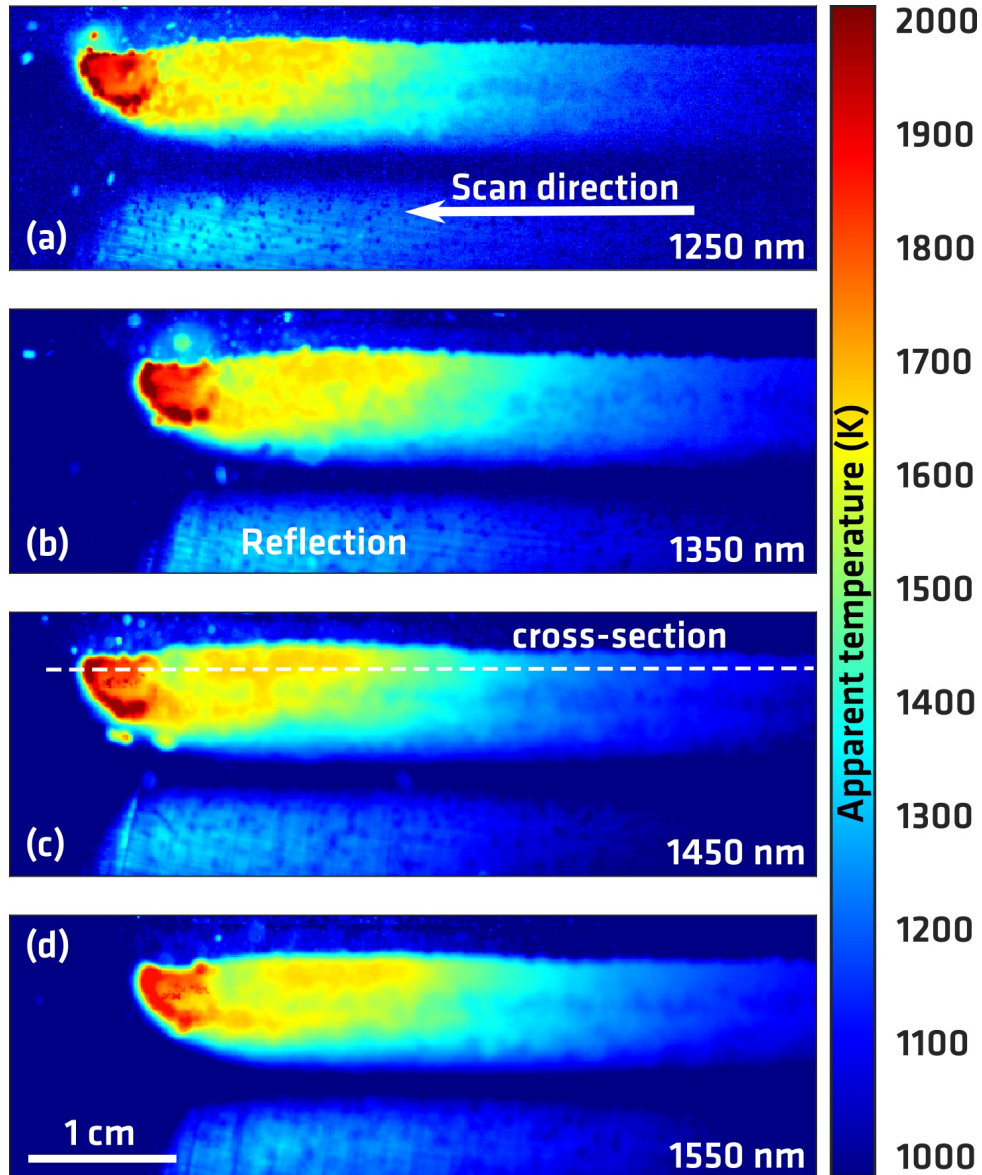


Figure 5: (a)-(d) Thermograms of the molten pool, during the welding process of the middle of the tenth layer acquired with bandpass filters in the range from 1250 nm to 1550 nm. The radiometric model used to determine the temperatures was adjusted to the emissivity of the solidification plateau. The dashed line in (c) indicates the cross section shown in Fig. 6. The offsets in the welding direction between the thermograms are caused by variances of the camera orientation.

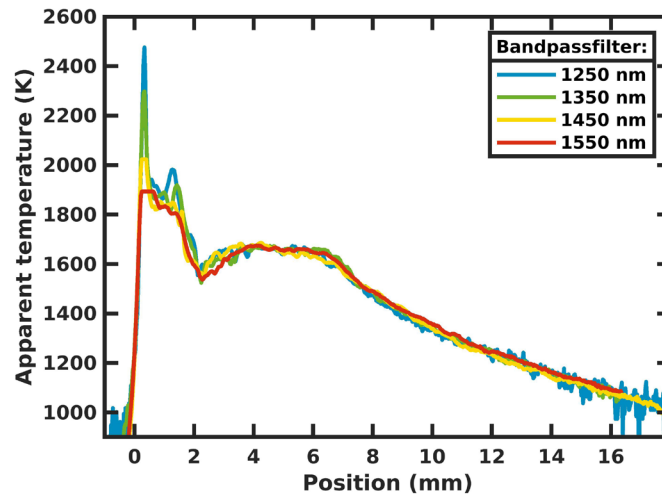


Figure 6: Cross section of the thermograms of the molten pool are shown in Fig. 5.

real temperature in this area will be clearly different from the real temperature, as the liquid phase which is found in this zone is expected to have a deviating emissivity. Furthermore, we see the emission from the oxides in this area [7]. Due to overexposure, it is not possible from these measurements to determine the trend of the ratio of the emission from the oxides to the emission of the solid phase as a function of the wavelength. The dip in temperature from 1.5 mm to 4 mm is probably caused by a change in emissivity with respect to the solidification plateau, since the liquid material within the molten pool is expected to be at temperatures above the solidification temperatures. Thus temperatures determined within the liquid part must be considered to be afflicted by a systematic error of unknown extent. For >6 mm, the cooling of the solid phase can be observed. For longer wavelengths the temperature data is less noisy, especially towards lower temperatures and therefore better suited for an analysis of the cooling process. This is consistent with the theory of thermal radiation. Thermal cameras with equal dynamic range will show a larger calibration range for longer wavelengths. This can easily be understood when considering that the Plancks law implies that the intensity contrast between two black bodies of different temperature increases with decreasing temperature.

3.2 Molten pool size and oxide covered area

By counting all pixels above a threshold value of 1550 K and using the scaling factors from section 2.4, we estimated the size of the molten pool area for each frame of the thermogram of the manufacturing process of a workpiece. Using the acceleration data we assigned each thermogram to a spatial position. Figure 7 shows the result for the measurement with the 1250 nm bandpass filter. For the first eighth layers, the average molten pool size increases with each subsequent layer and remains relatively constant for the following layers. From the fourth layer on, the molten pool shows a local maximum at the beginning of the welding process. This could be caused by a geometric effect, as the heat might accumulate at the edge. Figure 8 shows the area of the molten pool covered by oxides, extracted from the same measurement by using a

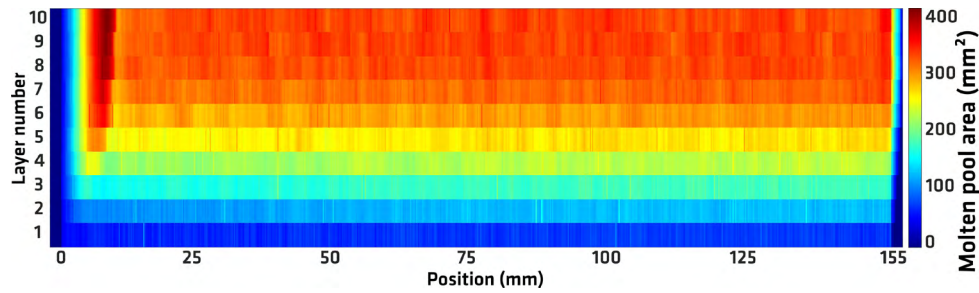


Figure 7: Area of the molten pool during the welding process, recorded with the 1250 nm bandpass filter, as a function of the layer number and the lateral position.

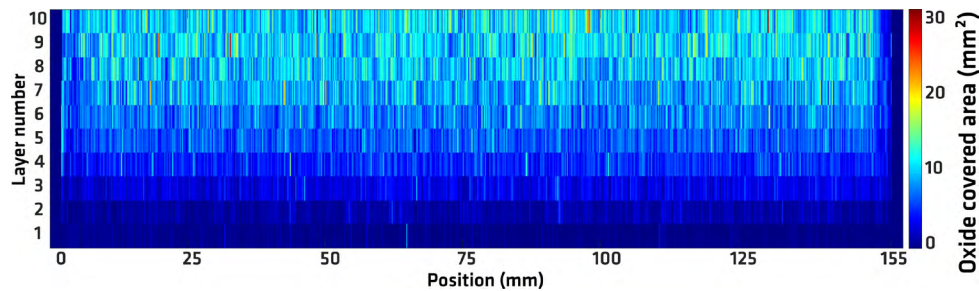


Figure 8: Oxide covered area of the molten pool during the welding process, recorded with the 1250 nm bandpass filter, as a function of the layer number and the lateral position.

threshold value of 2000 K. The area covered by oxides increases with increasing layer number. Furthermore, it can be observed, that the oxide covered area shows strong variations on a very small length scale (<1 mm).

4 CONCLUSIONS

We have successfully shown that an acceleration sensor can be used together with the pre-defined welding path to reconstruct the spatial position of the welding arm during the LMD process with sufficient temporal resolution to be usable in conjunction with a high speed SWIR camera system fixed to the welding arm. Hereby it becomes possible to assign quantities extractable from the thermograms to spatial information. As an example, we have presented the molten pool size and the area covered with oxides as a function of the position. Such data sets have the prospect to be more comparable to simulations and reference methods such as computed tomography than the raw thermographic data. Furthermore, we have investigated the influence of the wavelength on the thermograms in a range from 1250 nm to 1550 nm. For all wavelengths, the thermograms appear to be usable for in-situ monitoring purposes, whereby the used wavelength could result in subtle differences that might be advantageous or disadvantageous depending on the investigated quantity. While using longer wavelengths provides a larger range of temperatures that can be detected, which is beneficial when analyzing the cooling process, short wavelengths show more structure in the thermograms on a smaller length scale.

5 ACKNOWLEDGEMENT

This research was funded by BAM within the Focus Area Materials.

REFERENCES

- [1] DebRoy T., Wei H. L., Zuback J. S., Mukherjee T., Elmer J. W., Milewski J. O., Beese A. M., Wilson-Heid A., De A., Zhang W. "Additive Manufacturing of Metallic Components – Process, Structure and Properties" *Progress in Materials Science* Vol. **92** pp. 112–224 DOI:10.1016/j.pmatsci.2017.10.001 (2018).
- [2] Grasso M., Colosimo B. M. "Process Defects and in Situ Monitoring Methods in Metal Powder Bed Fusion: A Review" *Measurement Science and Technology* Vol. **28** no. 4 p. 044005 DOI:10.1088/1361-6501/aa5c4f (2017).
- [3] Everton S. K., Hirsch M., Stravroulakis P., Leach R. K., Clare A. T., "Review of in-situ process monitoring and in-situ metrology for metal additive manufacturing" *Materials & Design*, Vol. **95**, pp. 431-445, DOI:10.1016/j.matdes.2016.01.099 (2016).
- [4] Altenburg S.J., Maierhofer C., Straße A., Gumenyuk A., "Comparison of MWIR thermography and high-speed NIR thermography in a laser metal deposition (LMD) process" *14th Quantitative InfraRed Thermography Conference*, DOI:10.21611/qirt.2018.p35 (2018).
- [5] Stankevich S., Gumenyuk A., Strasse A., Rethmeier M., "Measurement of thermal cycle at multi-pass layer build-up with different travel path strategies during DLMD process" *Lasers in Manufacturing Conference 2019* (2019).
- [6] Hassler U., Gruber D., Hentschel O., Sukowskia F., Grulich T., Seifert L., "In-situ Monitoring and Defect Detection for Laser Metal Deposition by Using Infrared Thermograph" *Physics Procedia* Vol. **83** pp. 1244-1252, DOI:10.1016/J.PHPRO.2016.08.131 (2016).
- [7] Doubenskaia M., Pavlov M., Grigoriev S., Smurov I., "Definition of brightness temperature and restoration of true temperature in laser cladding using infrared camera" *Surface and Coatings Technology* Vol. **220** pp. 244–247, DOI:10.1016/j.surfcoat.2012.10.044 (2013).
- [8] Stichel W. *ASM speciality handbook: Stainless steels* ASM International, DOI: 10.1002/maco.19950460815 (1994).
- [9] Schöpp H., Sperl A., Kozakov R., Gött G., Uhrlandt D., Wilhelm G., "Temperature and Emissivity Determination of Liquid Steel S235", *Journal of Physics D: Applied Physics* Vol. **45** no. 23 p. 2352035 DOI:10.1088/0022-3727/45/23/235203 (2012).

MATERIAL MODELLING OF UV CURING POLYMERS FOR ADDITIVE MANUFACTURING PROCESSES

T. Rehbein*, A. Lion* and M. Johlitz*

*Institute of Mechanics
Faculty of Aerospace Engineering
Bundeswehr University Munich
Werner-Heisenberg-Weg 39, 85577 Neubiberg, Germany
e-mail: rehbein@unibw.de, web page: <https://www.unibw.de/lrt4>

Key words: UV curing, digital light processing, reaction kinetics, photopolymer, degree of cure

Abstract. This contribution focuses on the experimental investigation and material modelling of the crosslinking of UV curing polymers used in additive manufacturing processes such as digital light processing and stereolithography. First photocalorimetric measurements with varying temperature and light intensity are shown. From the exothermic specific heat flows measured during the crosslinking reaction, the degree of cure can be determined for each experimental scenario. It is shown that the test temperature and light intensity have a significant influence on the crosslinking reaction.

A first modelling approach for the mathematical description of the crosslinking reaction is presented. Moreover, parameter identification of the proposed model is conducted using the commercial optimisation program LS-OPT®.

1 INTRODUCTION

Additive manufacturing (AM) is an innovative technology to create three dimensional objects with complex geometry. Although the technology has been used in industrial applications for decades, reliable and experimentally validated models for the design of printed components are still missing. Especially the material modelling and finite element analysis of UV curing polymers (so-called photopolymers) used in processes like digital light processing and stereolithography are challenging tasks. For this purpose, the crosslinking reaction in the additive manufacturing process must be described correctly by a phenomenological model and adapted to experimental data.

The crosslinking of photopolymers is initiated by the absorption of a light source. Besides that, the process depends strongly on the ambient temperature: a higher ambient temperature leads to faster crosslinking whereby the same applies to an increasing light intensity. Calorimetric measurements with the aid of an additional light source have proved useful for the experimental investigation of the crosslinking reaction of photopolymers [1].

Since the degree of cure directly influences the mechanical, thermal and chemical properties of

photopolymers, a validated material model for the degree of cure is essential for finite element analysis of additive manufacturing processes.

2 EXPERIMENTAL INVESTIGATION

In order to understand and investigate the crosslinking process of commercial photopolymers used in additive manufacturing processes, differential photocalorimetry (DPC) measurements are conducted using the TA Instruments DSC Q2000 with an additional light source (OmniCure[®] S2000). The light source contains a high pressure 200 W mercury lamp with an spectral output of 320 to 500 nm.

To investigate the crosslinking reaction, the DSC measures the specific heat flow \dot{h} between a sample in a pan and an empty reference pan during the crosslinking reaction. The following relationship is used to convert the specific heat flow into the degree of cure:

$$q(t) = \frac{\int_0^t \dot{h}(\tilde{t}) d\tilde{t}}{h_{\text{tot}}} \quad (1)$$

Due to the normalisation to the maximum specific heat h_{tot} during the crosslinking reaction, the degree of cure assumes values between 0 and 1.

The commercial photopolymer LOCTITE[®] 3D 3830 was used for the photocalorimetric measurements. It is an acrylic compound for prototype development with low elongation at break, high tensile strength and low chemical shrinkage.

During the photocalorimetry measurement, following steps are performed subsequently for the determination of the specific heat flow $\dot{h}(\tilde{t})$ in eq. (1):

1. Equilibration of the measurement cell at a specific temperature ($-10^{\circ}\text{C} \dots 50^{\circ}\text{C}$).
2. Isothermal phase of 60 s.
3. Irradiation of the specimen for 300 s at constant light intensity (5 mW/cm^2 and 10 mW/cm^2).
4. Isothermal phase of 60 s.

After finishing step four, the whole procedure is repeated with the cured specimen generating the baseline. The baseline is subtracted from the heat flow signal of the first measurement to consider only the heat flow of the crosslinking reaction. Otherwise, the light energy input would be taken into account.

In order to determine the maximum specific heat h_{tot} during the crosslinking reaction, an additional measurement at non-isothermal temperature is performed. During 300 s irradiation, the temperature is increased from 20°C to 70°C at 5°C/min leading to a maximum specific heat of $h_{\text{tot}} = 319.73 \text{ J/g}$ which is taken as reference value for the conversion of the specific heat during crosslinking reaction into degree of cure for all measurements.

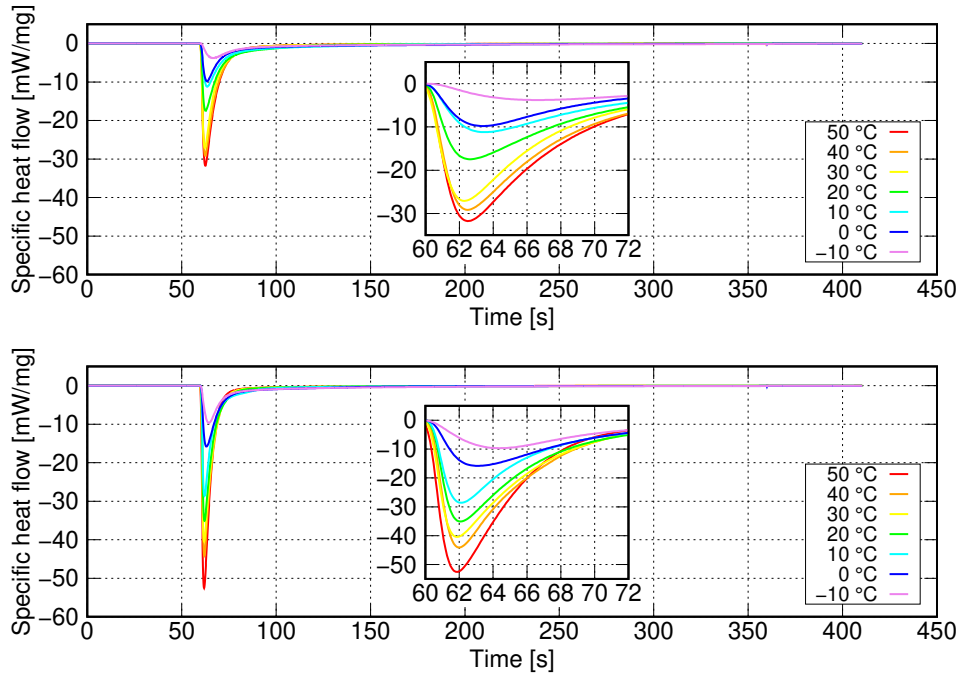


Figure 1: Measured specific heat flows after subtraction of the baseline. Top: light intensity $I = 5 \text{ mW/cm}^2$, bottom: light intensity $I = 10 \text{ mW/cm}^2$.

The specific heat flows after subtraction of the baseline of all measurements are shown in fig. 1. It can be clearly seen that the crosslinking reaction proceeds very quickly and that the specific heat flows have reached their maximum value after only a few seconds. Additionally, it is obvious that a higher light intensity leads to higher maximum values in the heat flows and that a higher temperature accelerates the reaction.

Moreover, complete curing is not achieved at low temperatures and light intensities and the crosslinking reaction is stopped prematurely, cf. fig. 2. The maximum attainable degrees of cure q_{\max} for all measurements are listed in table 1. It can be seen that an almost fully cured material is achieved at a temperature of $50 \text{ }^\circ\text{C}$, regardless of the light intensity. This result must definitely be taken into account when formulating the material model for the degree of cure.

Table 1: Maximum attainable degree of cure q_{\max} of all measurements

	$-10 \text{ }^\circ\text{C}$	$0 \text{ }^\circ\text{C}$	$10 \text{ }^\circ\text{C}$	$20 \text{ }^\circ\text{C}$	$30 \text{ }^\circ\text{C}$	$40 \text{ }^\circ\text{C}$	$50 \text{ }^\circ\text{C}$
5 mW/cm^2	0.469	0.619	0.675	0.775	0.851	0.904	0.947
10 mW/cm^2	0.593	0.685	0.775	0.845	0.907	0.949	0.997

3 MATERIAL MODELLING

The differential equation for the degree of cure q depends on time, light intensity $I(z(t), t)$ and temperature T . Following the work of Kamal [2], an autocatalytic model of $(m + n)$ th order

incorporating the maximum attainable degree of cure q_{\max} is applied for the degree of cure q :

$$\dot{q} = (k_1(I(z(t), t), T) + k_2(I(z(t), t), T)q^m)(q_{\max} - q)^n. \quad (2)$$

Here, $I(z(t), t)$ denotes the time- and location-dependent light intensity. The light intensity must depend on the vertical location $z(t)$ since it evolves during the printing process. The maximum attainable degree of cure acts as a limit value. The constants

$$k_i(I(z(t), t), T) = k_{0i}(T) I^b(z(t), t) \quad (3)$$

with the Arrhenius type equations

$$k_{0i}(T) = A_i \exp\left(-\frac{E_i}{RT}\right) \quad (4)$$

are based on the proposal by Maffezzoli and Terzi [3] depending on light intensity $I(z(t), t)$ and temperature T . If no light source is present, i.e. $I(z(t), t) = 0$, the crosslinking reaction is stopped. A_i and E_i are pre-exponential factors and activation energies, respectively. R denotes the universal gas constant. The additional parameter b is introduced for a better representation of experimental data.

4 PARAMETER IDENTIFICATION AND VALIDATION

The parameters in eq. (2) are identified using the commercial optimisation program LS-OPT[®] in combination with MATLAB[®]'s ode45 solver. LS-OPT[®] uses the sequential response surface method for optimisation. For further informations see [4].

The parameter identification depends strongly on the initial values. The parameters listed in table 2 represent the first result of the parameter identification which identified the equation for the degree of cure on the measurement results. For simplification, the particular maximum attainable degree of cure was specified as a parameter in order to achieve a better agreement with the measurement results.

Fig. 2 shows the simulations of the degree of cure compared to all measurements according to eqs. (1) and (2) with identified model parameters.

Table 2: Identified model parameters for the description of the crosslinking reaction

A_1	A_2	E_1	E_2	R	m	n	b
$(\text{cm}^2)^b / ((\text{mW})^b \text{s})$	$(\text{cm}^2)^b / ((\text{mW})^b \text{s})$	J/mol	J/mol	J/(mol K)	-	-	-
0.2	0.6	9744	6000	8.314	6	2.377	1.901

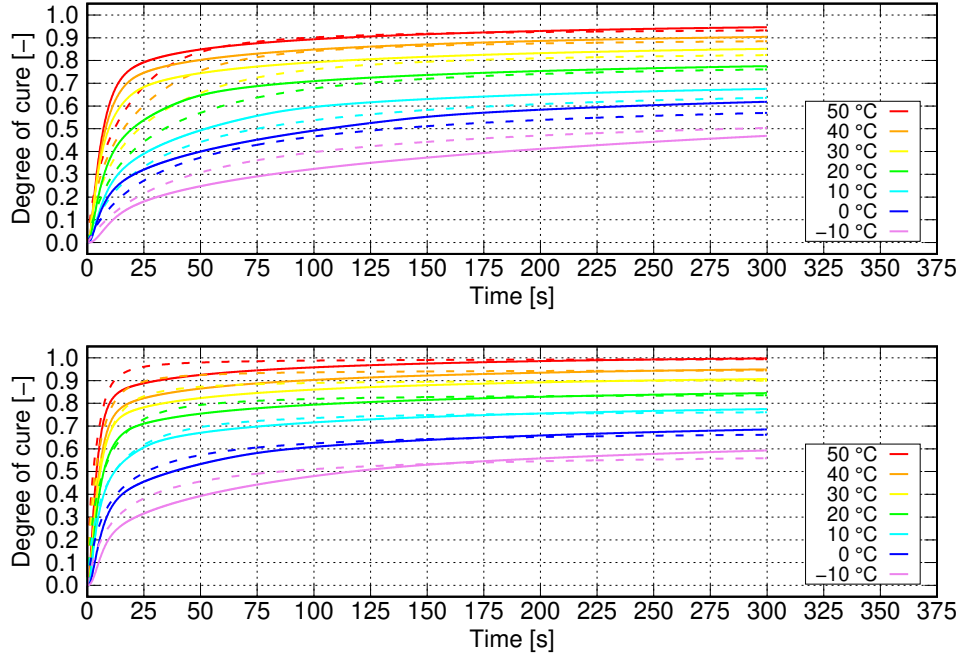


Figure 2: Measurement (—) and simulation (- -) of the degree of cure q according to eqs. (1) and (2) with identified model parameters. Top: light intensity $I = 5 \text{ mW/cm}^2$, bottom: light intensity $I = 10 \text{ mW/cm}^2$.

The simulations show a good agreement with the measurement results, although the maximum attainable degree of cure has been specified as a parameter. Especially the temperature dependence and the rapid increase of the degree of cure within the first seconds of irradiation are well represented.

5 SUMMARY AND OUTLOOK

First measurements for the experimental characterisation of the crosslinking reaction of photopolymers used in additive manufacturing processes are presented in this contribution. It is shown that temperature and light intensity have a significant influence on the crosslinking reaction.

A differential equation incorporating the maximum attainable degree of cure q_{\max} is proposed for the phenomenological description of the degree of cure. Parameter identification using commercial optimisation tools is carried out. The validation shows a good agreement between measurements and simulations.

Forthcoming considerations include the correct description of the maximum attainable degree of cure as a function of temperature and light intensity:

$$q_{\max} = f(T, I) \quad (5)$$

Kolmeder et al., for example, have already carried out work for this purpose [5].

6 ACKNOWLEDGEMENT

The authors would like to thank the German Research Foundation (DFG) and Agence nationale de la recherche (ANR) for the financial support of the project "Constitutive modeling of UV-curing printed polymer composites".

REFERENCES

- [1] Höhne, G.W.H., Hemminger, W.F. and Flammersheim, H.-J. *Differential scanning calorimetry*. Springer-Verlag Berlin Heidelberg, (2003).
- [2] Kamal, M.R. Thermoset Characterization for Moldability Analysis. *Polymer Engineering and Science* (1974) **14**:231–239.
- [3] Maffezzoli, A. and Terzi, R. Effect of irradiation intensity on the isothermal photopolymerization kinetics of acrylic resins for stereolithography. *Thermochimica Acta* (1998) **321**:111–121.
- [4] Stander, N., Roux, W., Basudhar, A., Eggleston, T., Goel, T. and Craig, K. *LS-OPT[®] User's Manual*. Livermore Software Technology Corporation, (2015).
- [5] Kolmeder, S., Lion, A., Landgrad, R. and Ihlemann, J. Thermophysical properties and material modelling of acrylic bone cements used in vertebroplasty. *J Therm Anal Calorim* (2011) **105**:705–718.

Simulation-based investigation of statistical fatigue strength of selective laser melted lightweight alloys

M. AWD, M. MERGHANY, S. SIDDIQUE, AND F. WALTHER

TU Dortmund University, Department of Materials Test Engineering (WPT)
Baroper Str. 303, D-44227 Dortmund, Germany
E-mail: mustafa.awd@tu-dortmund.de, www.wpt-info.de

Keywords: Weibull distribution, fatigue strength, porosity, variance, standard deviation

Abstract. Selective laser melting (SLM) process is based on the powder-bed fusion principle, which is using high-energy laser beams. SLM process is characterized by producing very finely grained cellular and columnar dendritic microstructure in aluminum alloy AlSi12. Melt pool instabilities are a key factor in the formation of the pores and increasing of the porosity within the produced parts. Through this study, structural characteristics were investigated using two approaches crack propagation-based and plastic damage-based to isolate influences of microstructure and defects on the fatigue lifetime. The influence of platform heating during deposition on fatigue strength was studied. Platform heating was concluded to reduce the remnant porosity, and consequently, fatigue strength scatter. Fatigue lifetime calculation, which utilized crack propagation curves and weakest-link theory, was consistent at low-cycle fatigue experiments. However, damage monitoring in a load increase test led to a prediction of lifetimes, which is more relevant, as a Monte-Carlo simulation was applied for post-processing of local stress distribution. The difference was the consideration of damage in the pre-crack initiation phase in the plasticity-based approach of the load increase test.

1 INTRODUCTION

Fatigue resistance and damage tolerance are from the dominant factors in designing of the industrial parts, especially additively manufactured parts that should meet demanding fatigue resistance standards to be able to withstand service loading. Therefore, the fatigue phenomena, including crack nucleation and propagation mechanisms, is the main subject of the study.

Fatigue lifetime prediction modeling approaches can be classified into two groups. The first one based on cumulative fatigue damage theory. This approach received more attention than earlier after works of Palmgren [1] and Miner [2] who were concerned with damage accumulation concepts and linear damage rules (LDR) [3, 4, 5]. Various cumulative fatigue damage equations can be derived based on different macroscopic quantities while the most widely used approaches are stress-based approaches which relate the number of cycles until failure (N_f) with the true stress based on Basquin equation [6]. Gough and Pollard used empirical equivalent stress, which was not able to address non-proportional damage [7, 8]. By adding an empirical criterion related to non-proportional loading, Lee was able to improve this aspect of the model [9]. A further LDR theory proposed by Coffin is based on plastic strain and plastic damage accumulation rather than stress [10, 11]. In this approach, the Coffin-Manson equation is used to define the fatigue resistance to cyclic deformation [12, 13].

The second main group is the fracture mechanics-based models for predicting the crack growth rate and the final fracture mode. The main difference concerning cumulative fatigue damage theory is the presence of cracks or process-induced defects as in the case of additively manufactured components. Paris et al. introduced the linear-elastic fracture mechanics (LEFM) method for estimation of the crack growth rate [14]. The model treats macrocracks and correlates the rate of growth with the range of stress intensity factor (ΔK) at the tip of the crack. In this method, the material behavior during the fatigue process is assumed to be linear [3].

The introduction of additive manufacturing processes like selective laser melting (SLM) and electron beam melting (EBM) for metallic parts led to a revolution in the mechanical design standards. Fatigue loading, damage mechanisms in additively manufactured titanium (Ti) and aluminum (Al) components can be profoundly influenced by process-induced microstructure, porosity as well as post-process treatments [15, 16, 17].

In this study, defect-based and damage-based fatigue lifetime prediction approaches were studied for two batches of SLM AlSi12. Through the study, damage and failure mechanisms are related to microstructure and remnant porosity. Internal structures reconstructed from μ -CT scans are used to calculate stress concentration factors and build finite-element (FE) models. Crack propagation curves are employed to calculate possible fatigue lifetimes which are calibrated by a Weibull probability density function. Plastic strain reaction from cyclic experiments is applied to simulate cyclic damage, which will give input to a Monte-Carlo simulation for final fatigue lifetime calculation. The reliability and accuracy of both techniques will be compared by using experimental data points of fatigue lifetimes in low-cycle- (LCF) to very-high-cycle fatigue (VHCF).

2 MATERIALS AND METHODS

2.1 Experimental setup

The specimens were manufactured using SLM 250 HL system with a fiber laser source with a maximum power of 400 W. Argon was used as a shielding gas during the process to prevent the contamination of the melt pools. Chessboard-like scanning strategy was used to decrease the residual stress as much as possible [18]. The factorial study is presented in Table 1. The experiments aim to the investigation of the effect of platform heating (PH) at 200 °C on the microstructure and the fatigue properties of AlSi12, while stress relief (SR) was applied to remove the effect of the residual stresses on reducing the fatigue lifetime. The cooling rates of melt pools in the SLM process can be as high as 10^4 - 10^6 K·s⁻¹, which results in a very fine cellular eutectic microstructure with a strong texture in the cooling direction [19]. This leads to increase the quasi-static strength up to ~3 times the strength of cast AlSi12. Moreover, the melt pool instability leads to the formation of pores, which affects negatively on the fatigue strength from the point of view of scatter, as wide scatter of fatigue strength is unreliable for dynamic applications. While PH heating is leading to reduce the cooling rate of the melt pools. Therefore, leads to more stability, enhanced degassing mechanisms, and reduced remnant porosity [18].

Table 1: Experimental design of the study.

Batch	Alloy	Process	Heat treatment	Build
A	AlSi12	SLM	SR	90°
B	AlSi12	SLM + PH	SR	90°

Scanning electron microscope (SEM) was used to investigate the effect of PH on the microstructure of SLM AlSi12. Metallographic specimens were prepared from cut sections along the build direction and embedded in a mixture of resin and epoxy with a ratio of 1:6, respectively. Grinding of the surface followed using standard grade 300 grit papers down to 1,200 according to DIN 50602. Etching of specimens was carried out using a solution of NaOH with 4% concentration.

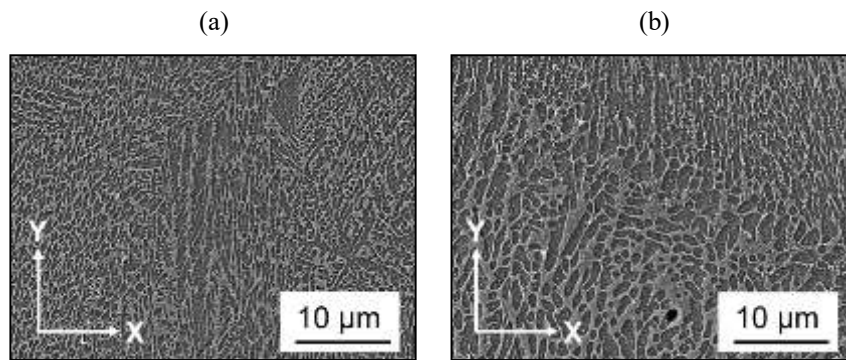
**Figure 1:** SEM micrographs of batches: (a) A (SR); (b) B (SR + PH).

Figure 1 shows a comparison between the microstructures of batch A and batch B (PH). It is observed in both micrographs, a very fine cellular dendritic microstructure with strong texture in the building direction (Y-axis) from bottom to top. It is also found that dendritic columns did not exactly follow a 90° orientation concerning X-axis. However, a rather along cooling direction due to the weld-bead-like shape of the melt pool; the dendrites converge along its radius. The highlight difference of both microstructures is that the microstructure of batch B is coarser than that of batch A as PH with reduced cooling rate allowed segregation of Si particles to the grain boundary. Accumulation of Si at grain boundaries resulted in the formation of thicker dendrites with rich Si content. The migration process changes the strengthening mechanism from matrix hardening in batch A to grain boundary strengthening in batch B. Such transformation is yet to develop a significant effect on the relationship between quasi-static and cyclic properties from LCF to VHCF.

X-ray micro-computed tomography (μ -CT) was used to investigate the PH effect on the remnant porosity. The setup in Nikon X TH 160 system is shown in Figure 2. A mechanical testing shape specimen is fixed on the holder in front of the X-ray gun, as shown in Figure 2. While the X-rays pass through the specimen and projected on the detector panel. The projection carries information about voids or inclusions. The specimen is rotated 360° such that an image is obtained every 0.227°. The images are then processed to build a volume including the grey value footprint, which is later analyzed by VG Studio Max 2.2 for quantitative evaluation of remnant porosity.

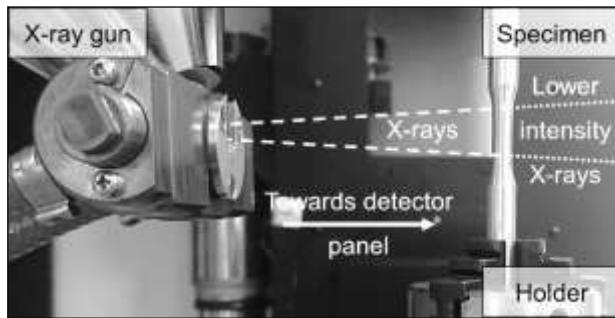


Figure 2: Experimental setup of micro-computed tomography (μ -CT).

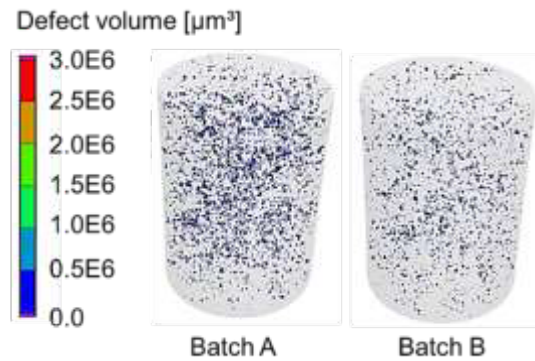


Figure 3: 3D-volume distribution of defects for batches: A (SR); B (SR + PH).

Figure 3 shows the 3D volumes of batch A and batch B, and it can be observed clearly that the remnant porosity of batch A is more than batch B. While the relative density of batch A was 99.51% and for batch, B was 99.67%. The reason for more efficient melt pool degassing if PH is applied was dependent on the Marangoni convection and the accompanying torque. The torque intensity is dependent on the intensity of the thermal gradient in the vicinity of the melt pool.

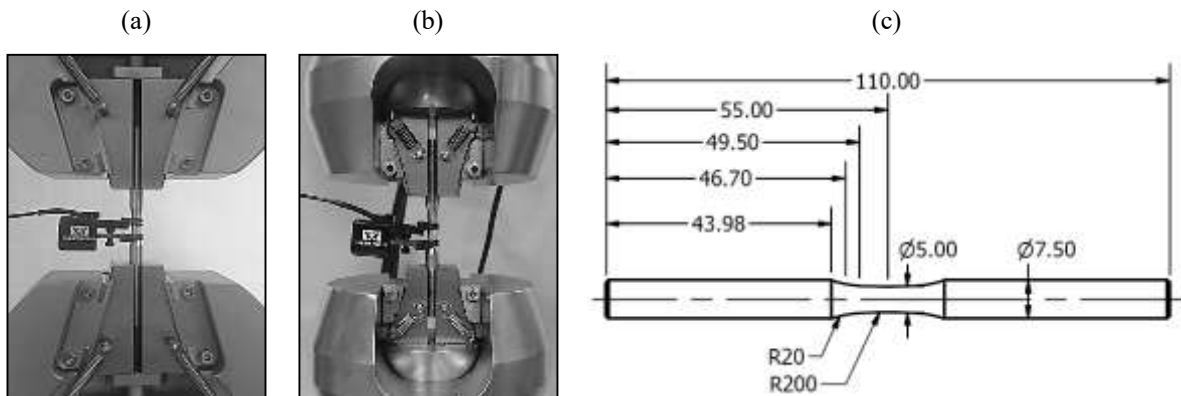


Figure 4: Experimental setup of mechanical testing: (a) tensile test; (b) fatigue test; (c) specimen geometry.

High-intensity torques transfer low-viscosity melt to the periphery by an act of centrifugal inertia which results in a void formation in the middle of the melt pool. When the applied energy density is not sufficient, fusion in the bead is not complete and sound solid track cannot be obtained. This results in the formation of keyhole defects with sharp corners and high-stress concentration factors, which is more detrimental to mechanical properties in general and fatigue damage in particular. As far as this study is concerned, no keyhole porosity is observed in batches A and B.

The experimental mechanical testing was classified into three main divisions. The first one is quasi-static tensile testing using machine Instron 3369 with 50 kN load cell and stroke rate

1 mm/min, while the experimental setup is shown in Figure 4a. The second part is servohydraulic fatigue testing using a system of Instron 8872 with a load cell of 10 kN with a fixed frequency $f = 20$ Hz and stress ratio $R = -1$ (fully reversed loading). The test setup is shown in Figure 4b. While both tests are sharing the same specimen geometry that is shown in Figure 4c. Within servohydraulic testing two types of testing are applied according to test control. First one is stress-controlled load increase test (LIT), it allows monitoring of material reaction as a function of applied stress in the wide range of fatigue regimes from LCF to VHCF. One of the advantages of this concept test is replacing the more traditional and time-consuming stress-wise lifetime determination using Woehler curve. The second fatigue testing type is stress-controlled constant amplitude testing (CAT), which is used as an experimental validation of the presented modeling procedures.

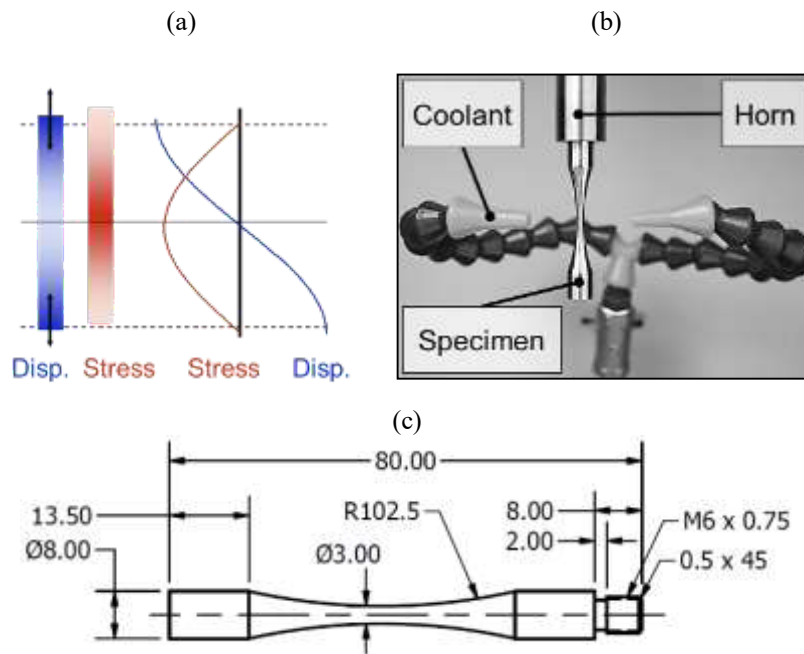


Figure 5: Experimental setup of ultrasonic VHCF testing: (a) stress and displacement distribution along with the specimen; (b) specimen setup against cooling media; (c) specimen geometry.

While the third type of testing, which is ultrasonic fatigue testing was used to experimental validation for VHCF and was carried out on USF-2000A system of Shimadzu at $f = 20 \pm 0.5$ kHz. Its principle is to transform an electric signal into mechanical resonance using a piezoelectric actuator fixed to a booster and a horn. It can oscillate at an ultrasonic eigenfrequency of 20 kHz. The oscillatory displacement at the end of the horn induces a displacement-dependent stress distribution, as shown in Figure 5a. While the experimental setup against the horn is shown in Figure 5, where dry cooling air is used to ensures temperature stability during the test. Figure 5c presents the analytical design of specimen geometry; the geometry ensures that maximum stress occurs only in the middle.

A high-intensity temperature is expected to develop during the test due to the cyclic speed deformation at the middle of the specimen. So, to counter this, first high-pressure, dry-air coolant is applied to ensure no moisture contamination on the specimen surface. Secondly, the

application of intermittent driving; such pulse:pause ratio of 50:50 allows coolant-assisted dissipation of the generated temperature, avoiding a temperature/burn effect on the specimen. This reduces the effective frequency of the system to 10 kHz but still much higher than mechanical mass spring-based resonance systems.

2.2 Theory and calculations

Modeling of crack propagation behavior was based on da/dN curves obtained according to ASTM E-647 standard. Further details can be found in [20]. A parametric equation for curve fitting is given as utilized

$$\frac{da}{dN} = A (\Delta K - B)^c, \quad (1)$$

where da/dN is the crack propagation rate, ΔK is the stress intensity factor range, while A, B, and C are fitting parameters. The relationship between ΔK and a defect radius 'a' can be described as

$$\Delta K = \Delta\sigma Y\sqrt{\pi a}, \quad (2)$$

where $\Delta\sigma$ is the stress range which is corrected according to a stress concentration factor K_t [21], and Y is a geometry factor. By substituting (2) in (1) and solving for N_f accumulatively for the whole crack lifetime, the final fatigue lifetime of a crack can be calculated according to

$$N_f = \sum_{i=1}^n \int_{a_{i-1}}^{a_i} \gamma_i(a) da, \quad (3)$$

where $\gamma_i(a)$ is the relationship between defect size and stress intensity factor range. The calculated fatigue lifetime is calibrated using a weakest-link model based on Weibull probability density function

$$f(x; \alpha, \beta) = \begin{cases} \alpha \beta x^{\beta-1} e^{-\alpha x^\beta}, & x > 0 \\ 0, & \text{elsewhere} \end{cases}, \quad (4)$$

where α is Weibull scale parameter, β is Weibull shape parameter x is a random variable. Details for the derivation of α and β by the maximum likelihood method is found in [19]. The probability of failure resulting from every defect is calculated based on the cumulative probability density function of Weibull. The highest probability of failure presents the failure event of the specimen according to the weakest-link theory. Furthermore, an estimate of the central tendency of the resulting density function can estimate the mean of the fatigue lifetime

$$\mu = \alpha^{\frac{-1}{\beta}} \cdot \Gamma\left(1 + \frac{1}{\beta}\right), \quad (5)$$

where Γ stands for the gamma function. The scatter of fatigue strength can be estimated by the variance of Weibull probability density function

$$\sigma^2 = \alpha^{\frac{-2}{\beta}} \cdot \left\{ \Gamma\left(1 + \frac{2}{\beta}\right) - \left[\Gamma\left(1 + \frac{1}{\beta}\right) \right]^2 \right\}, \quad (6)$$

where the gamma function Γ is given by definition as

$$\Gamma(\alpha) = \int_0^\infty N_f^{\alpha-1} \cdot e^{-N_f} dN_f, \quad (7)$$

where N_f is the random variable of interest as fatigue lifetime in cycles. Figure 6 shows a schematic illustration of the modeling procedure. It illustrates how the defect stress

concentration factors based on the μ -CT analysis are being calculated. Numerical integration of fatigue lifetime is preceded by curve fitting of da/dN test. Constant amplitude fatigue testing provides input for establishing Weibull density function based on the maximum likelihood method. The function is used to conclude the fatigue lifetime with the highest probability of failure.

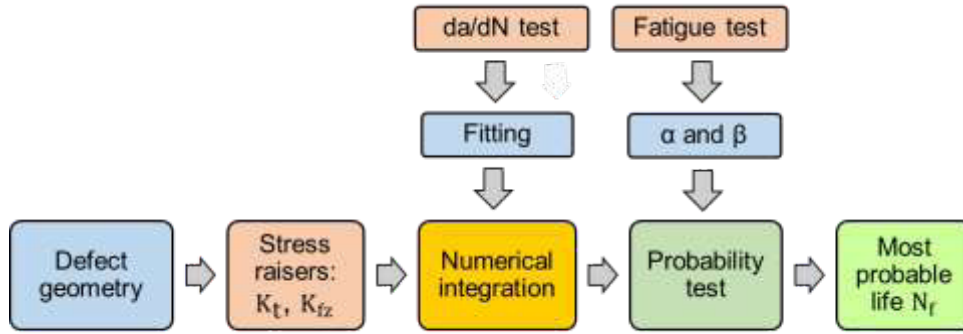


Figure 6: Schematic illustration of the procedure of fatigue lifetime calculation based on defect analysis and crack propagation approaches.

While cyclic plasticity parameters in the load increase test (LIT), were derived to simulate one stable cycle of fatigue loading at a given stress amplitude [22]. The simulation was carried on an FE-model built by the μ -CT analysis. And the field parameter displacement (u) is represented based on Fourier series. The latter representation is more effective than Lagrangian polynomials in expressing the complex variation of displacement under cyclic loading. The aim is to calculate real stress and damage state of a specimen at a point where the specimen response stabilizes. Element-wise stress-based damage is presented according to Dang-Van HCF criterion

$$\sigma_{DV} = \tau_{\max} + \varphi P_{\max}, \quad (8)$$

where σ_{DV} is Dang-Van stress, τ_{\max} is the maximum shear stress, φ is the sensitivity factor, P_{\max} is the maximum hydrostatic pressure. Numerical transformation of element-wise stresses is carried out by

$$x'_i = b + \frac{x_i - x_{\min}}{x_{\max} - x_{\min}} (a - b), \quad (9)$$

where x'_i is a transformed random variable, 'a' and 'b' are the limits of transformation interval, such that valid expressions of Eq. (4) is possible using the maximum likelihood method. Iterative selection of the boundaries of the transformation interval goes on until the first possible fatigue failure is detected, which represents the lower bound of fatigue life. Fatigue lifetime is calculated accordingly

$$N_f^P = \left(\frac{b_n \sigma_a}{P_r K} \right)^{1/b_m}, \quad (10)$$

where N_f^P is a probabilistic fatigue life, b_n is Monte-Carlo quadrature, P_r is probability correction factor, K is the fatigue strength coefficient, b_m is the fatigue strength exponent.

Random selection of elements for fatigue failure detection by Monte-Carlo simulation continues until failure probability is no longer valid.

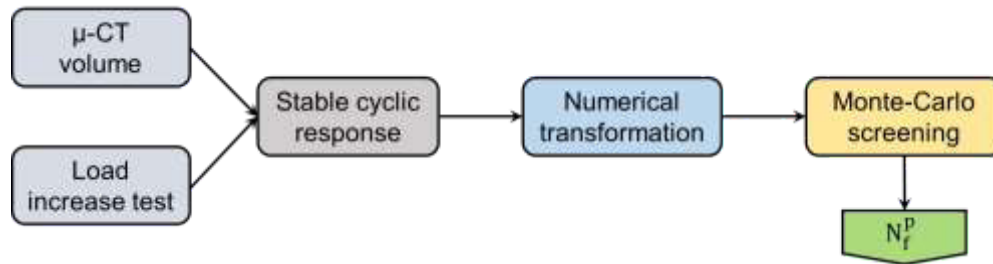


Figure 7: Schematic illustration of the procedure of fatigue lifetime calculation based on plastic damage and material reaction in a continuous load increase test.

3 RESULTS AND DISCUSSION

Through this section, the experimental and modeling results will be discussed to show the difference between them. Figure 8a shows the quasi-static flow behavior of two batches A and B. It is observed that batch A has higher tensile and yield strength than of batch B. However, batch B (PH) showed higher total fracture strain by 20% than of batch A. This is probably because of lower cooling rates leading to microstructural coarsening.

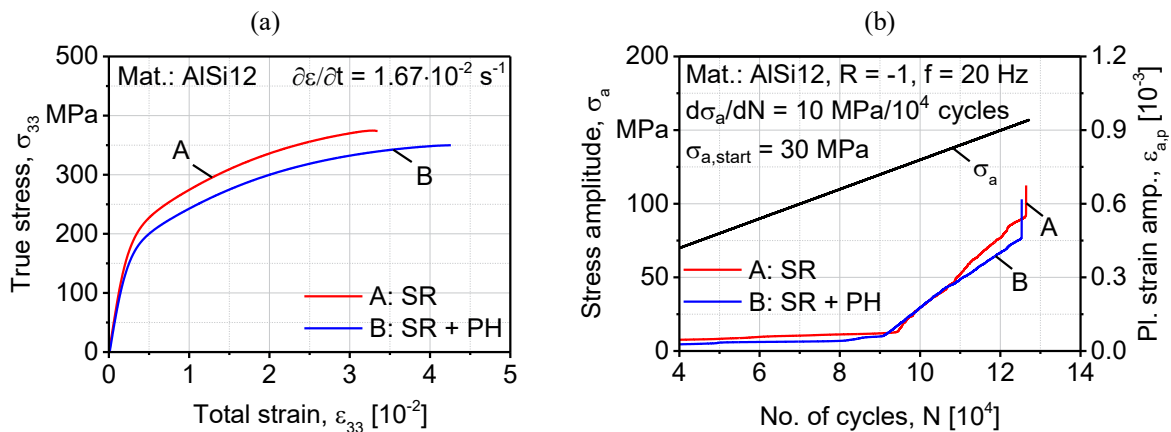


Figure 8: Flow properties of AlSi12 in batches A (SR) and B (SR + PH): (a) quasi-static loading; (b) cyclic deformation and plastic strain material reaction in continuous load increase test.

While Figure 8b illustrates the cyclic deformation and plastic strain material reaction in continuous load increase test (LIT). It shows no significant difference in the resulting fracture stress. Batch B also shows lower plastic strain and accordingly damage in the range of 30 to 110 MPa, this means higher fatigue resistance into this stress range (HCF and VHCF). At ~110 MPa onwards, the resistance to cyclic loading regarding plastic strain is higher for batch A that translates to higher fatigue resistance into LCF.

Furthermore, Figure 9a presents the crack propagation curves for batches A and B, and it is shown that there is no difference in crack propagation resistance. However, batch B has a slightly higher threshold stress intensity factor range (ΔK_{th}). In region (2), there is no difference

in the crack propagation rate between the two batches. While in the region (3), batch B has higher fracture toughness. In Figure 9b, the S-N curves of VHCF regime of the two batches are presented. It shows a superior VHCF strength of batch B rather than batch A, as the fatigue strength at 1E9 cycles was higher by ~33% in batch B. This leads to the assumption that although internal porosity acts as fatigue failure initiation sites [21], microstructural features induced in-process play a more dominant role in the lifetime of a specimen until a crack is initiated.

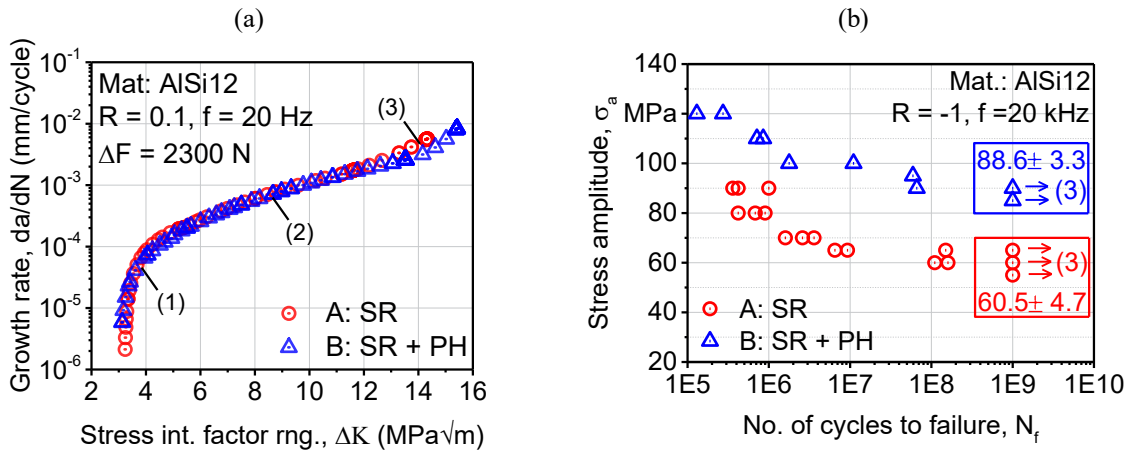


Figure 9: Fatigue strength characterization of batches A (SR) and B (SR + PH): (a) crack propagation curves based on stress intensity factor range (ΔK); (b) VHCF Woehler curve.

Moreover, Figure 10a presented a comparison between experimental and calculated fatigue lifetime. It shows that the calculation is well precise at 120 MPa. Otherwise, it is much less accurate for batch A at 110 MPa and batch B at 140 MPa. In Figure 10b, the scatter of fatigue strength by Eq. (5,6) is illustrated. Batch A shows consistently higher scatter along with the entire range of applied stresses as it has significantly more remnant porosity, means more probable crack initiation sites.

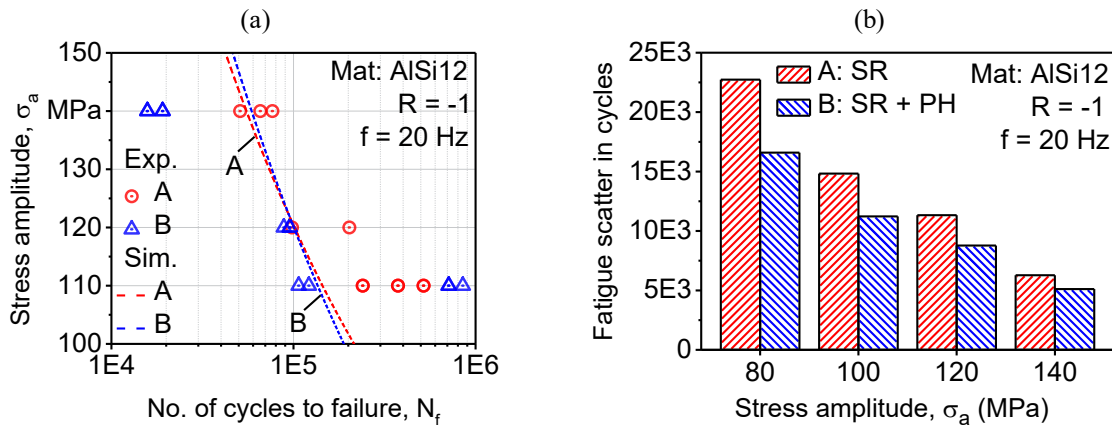


Figure 10: Comparison between simulated and experimental fatigue lifetimes according to the defect-based approach: (a) Woehler curves; (b) fatigue scatter according to Weibull functions.

The effect of the defect size on the fatigue lifetime is also studied, and Figure 11a shows the fatigue lifetime as a function of pore diameter for three stress levels. It is observed that the difference between the maximum and minimum fatigue lifetime is increasing at lower stress amplitudes. This concludes that the fatigue scatter will increase at VHCF stress amplitudes. It also concluded that the defect proximity to the surface has a detrimental effect on a specimen fatigue lifetime. Figure 11b is presenting the relation between the failure probability against pore characterization, which is the ratio between pore size and shortest distance to the surface. The point of highest probability of failure represents the fatigue lifetime for the whole specimen according to the weakest-link theory. The relation is inversely proportional with Figure 11a.

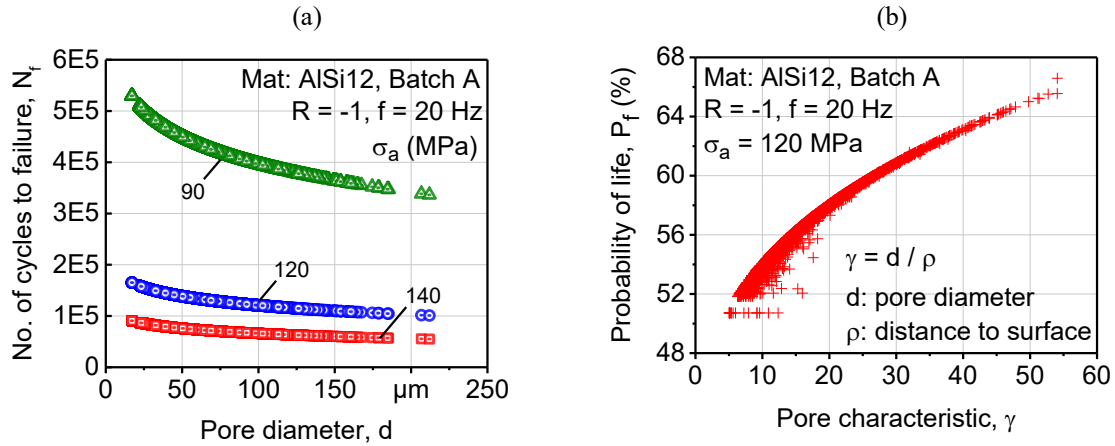


Figure 11: Effect of porosity, pore size, and location on fatigue strength: (a) fatigue lifetime as a function of pore diameter; (b) effect of pore characteristic on the probability of failure.

Figure 12 shows a comparison between the experimental fatigue lifetime and Monte-Carlo simulation prediction for both batches.

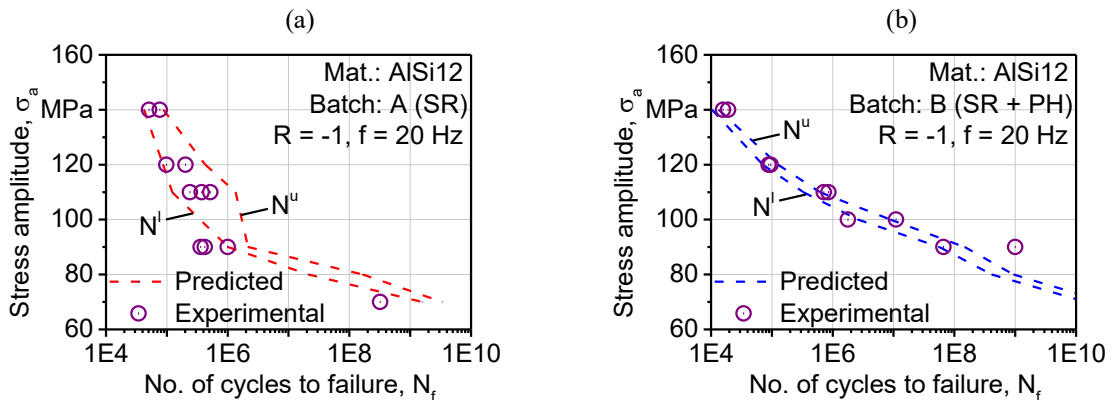


Figure 12: Comparison of predicted and experimental fatigue lifetimes as a result of the damage-based approach and Monte-Carlo simulation for batches: (a) A (SR); (b) B (SR + PH).

For batch A, the agreement along the range of stresses was following the same behavior except for the prediction of fatigue scatter between 90 and 60 MPa. However, it was better regarding the mean value and its variance at values above 90 MPa. On another side, the agreement for batch B was good from both aspects in LCF to VHCF range.

4 CONCLUSIONS AND OUTLOOK

Through this study, two fatigue lifetime prediction approaches were presented for two batches of SLM AlSi12. Batch A was manufactured without platform heated (No PH) while batch B was manufactured with platform heated (PH) to decrease the cooling rate during the manufacturing process. The results showed microstructural coarsening and a reduction in quasi-static strength, improvement of ductility, and enhancing the fatigue strength by ~33% in VHCF range.

The first-lifetime prediction approach was based on defect tolerance and crack propagation curves as well as the weakest-link theory. While the derivation of statistical parameters followed concepts of the maximum likelihood method and the calculation was fairly accurate within the same range at which crack propagation test was carried out. The qualitative representation of scattering of fatigue strength in batch B, following this approach was consistent.

The second approach, which was a plastic damage-based one, by using the continuous load increase test. Its results showed more coherent results in LCF to VHCF range with respect to the mean of fatigue strength and its variance. The approach integrated an FE-modeling of the stable cyclic response as well as a Monte-Carlo simulation. The results concluded that the damage-based approach is better regarding mechanical testing efficiency and quality of the results.

This concept is open for further utilization for the investigation of damage mechanisms in SLM AlSi12 on the microstructural scale. The developed scheme will be applied to the new concept of functionally graded materials in additive manufacturing.

Acknowledgments: The authors would like to thank the German Research Foundation (DFG, Deutsche Forschungsgemeinschaft) for its financial support to the conduct of this research work “Mechanism-based understanding of functional grading focused on fatigue behavior of additively processed Ti-6Al-4V and Al-12Si alloys.” (WA 1672/25-1; EM 95/2-1).

5 REFERENCES

- [1] Palmgren, A.: Durability of ball bearings. *Journal of German Society of Engineers* (1924) 14: 339-341.
- [2] Miner, M.: Cumulative damage in fatigue. *Journal of Applied Mechanics* (1945) 67: A159.
- [3] Cui, W.: A state-of-the-art review on fatigue life prediction methods for metal structures. *Journal of Marine Science and Technology* (2002) 7:43-56
- [4] Santecchia, E.; Hamouda, A.; Musharavati, F.; Zalnezhad, E.; Cabibbo, M.; El Mehtedi, M.; Spigarelli, S.: A review on fatigue life prediction methods for metals. *Advances in Materials Science and Engineering* (2016) Article ID 9573524, 26 pages.
- [5] Fatemi, A.; Yang, L.: Cumulative fatigue damage and life prediction theories: A survey of the state of the art for homogeneous materials. *International Journal of Fatigue* (1998) 20:9-34.
- [6] Basquin, O.: The exponential law of endurance tests. *Materials* (1910) 10: 625-630.
- [7] Gough, H.; Pollard, V.: The strength of metals under combined alternating stress. *Institute of Mechanical Engineers* (1935) 131: 3-18.

- [8] Gough, H.; Pollard, V.: Properties of some materials for cast crankshafts, with special reference to combined alternating stresses. *Institute of Automobile Engineering* (1937) 31: 821-93.
- [9] Lee, S.: A criterion for fully reversed out-of-phase torsion and bending. *American Society for Testing and Materials* (1985) 553-68.
- [10] Coffin, L.: Design aspects of high-temperature fatigue with particular reference to thermal stresses. *Transactions of the American Society of Mechanical Engineers* (1956) 78: 527-532.
- [11] Baldwin, E.; Sokol, G.; Coffin, L.: Cyclic strain fatigue studies on AISI 347 stainless steel. *American Society for Testing and Materials* (1957) 57: 567-586.
- [12] Manson, S.; Hirschberg M.: *Fatigue: An interdisciplinary approach*. Syracuse University Press, Syracuse (1964).
- [13] Coffin, L.; Tavernelli, J.: The cyclic straining and fatigue of metals. *Transactions of Metallurgical Society* (1959) 215:794.
- [14] Paris, P.; Gomez, M.; Anderson, W.: A rational analytical theory of fatigue. *Trends in Engineering* (1961) 13: 9-14.
- [15] Cain, V.; Thijs, L.; van Humbeeck, J.; van Hooreweder, B.; Knutsen, R.: Crack propagation and fracture toughness of Ti-6Al-4V alloy produced by selective laser melting. *Additive Manufacturing* (2015) 5: 68-76.
- [16] Brandl, E.; Heckenberger, U.; Holzinger, V.; Buchbinder, D.: Additive manufactured AlSi10Mg samples using selective laser melting (SLM): Microstructure, high cycle fatigue, and fracture behavior. *Materials and Design* (2012) 34: 159-169.
- [17] Edwards, P.; Ramulu, M.: Fatigue performance evaluation of selective laser melted Ti-6Al-4V. *Materials Science and Engineering: A* (2014) 598: 327-337.
- [18] Siddique, S.; Imran, M.; Wycisk, E.; Emmelmann, C.; Walther, F.: Influence of process-induced microstructure and imperfections on mechanical properties of AlSi12 processed by selective laser melting. *Journal of Materials Processing Technology* (2015) 221: 205-213.
- [19] Siddique, S.; Awd, M.; Tenkamp, J.; Walther, F.: Development of a stochastic approach for fatigue life prediction of AlSi12 alloy processed by selective laser melting. *Engineering Failure Analysis* (2017) 79: 34-50.
- [20] Siddique, S.; Imran, M.; Walther, F.: Very high cycle fatigue and fatigue crack propagation behavior of selective laser melted AlSi12 alloy. *International Journal of Fatigue* (2017) 94, 2: 246-254.
- [21] Siddique, S.; Imran, M.; Rauer, M.; Kaloudis, M.; Wycisk, E.; Emmelmann, C.; Walther F.: Computed tomography for characterization of fatigue performance of selective laser melted parts. *Materials and Design* (2015) 83: 661-669.
- [22] Awd, M.; Tenkamp, J.; Hirtler, M.; Siddique, S.; Bambach, M.; Walther, F.: Comparison of microstructure and mechanical properties of Scalmetalloy® produced by selective laser melting and laser metal deposition. *Materials* (2018) 11, 1: 1-17.

A MESOSCOPIC APPROACH FOR MODELLING LASER BEAM MELTING (LBM)

YAASIN A. MAYI^{1,3}, MORGAN DAL¹, PATRICE PEYRE¹, MICHEL BELLET²,
CHARLOTTE METTON³, CLARA MORICONI³, RÉMY FABBRO¹

¹ Laboratoire PIMM, Arts et Métiers, CNRS, Cnam, HESAM Université
151 Bd de l'hôpital 75013 Paris, France
e-mail: yaasin.mayi@protonmail.com, web page: <https://pimm.artsetmetiers.fr>

² CEMEF, UR 7635 PSL Research University MINES ParisTech
06904 Sophia Antipolis, France
web page: <http://www.cemef.mines-paristech.fr>

³ Safran Additive Manufacturing, a technology platform of Safran Tech
Rue des Jeunes Bois, Châteaufort, 78114 Magny-Les-Hameaux, France
web page: <https://www.safran-group.com>

Key words: Laser Beam Melting (LBM), Powder Bed Fusion (PBF), Selective Laser Melting (SLM), additive manufacturing, laser-matter interaction, Arbitrary Lagrangian Eulerian (ALE).

Summary: *Laser Beam Melting (LBM) is currently garnering industrial attention and many numerical researches have been carried out in order to understand the physics behind the process. However, due to the gap between the grain scale (micrometres) and the bead scale (millimetres), current state-of-the-art multi-physical models are computationally expensive as each powder grain is individually represented. Hence, simulating more than a single LBM track in a reasonable computational time is a challenging task. To overcome this limitation, a new mesoscopic approach is proposed, which intends to bridge the fine thermo-hydrodynamic representation and the macroscopic thermal models. The powder bed is represented by a homogeneous medium with both equivalent thermal and fluid properties. A bulk heat source is considered when the laser heats the powder bed whereas a surface heat flux is imposed on the melted powder bed surface. Apparent viscosity and surface tension are attributed to the homogenized medium so that modelling powder densification, melting and spheroidization of the melt pool is made possible by solving compressible Navier-Stokes equations. In addition, thermocapillary effects as well as vaporisation-induced recoil pressure are implemented, so that realistic thermo-hydrodynamic phenomena are successfully taken into account.*

1 INTRODUCTION

Laser Beam Melting (LBM) is an additive manufacturing process where successive layers of metallic powder are selectively melted by a laser beam, following a computer-programmed strategy. This technology is garnering an important industrial attention, especially in the aerospace sector, as it gives design flexibility that brings the opportunity to think differently the shape and the functionalities of manufactured components. The interaction between the laser beam and the powder bed gives rise to complex physical phenomena (energy absorption by the powder, melting, melt pool convection, metal vaporisation, rapid solidification and so on)

which must be understood to control the process at the industrial scale. In this regard, multi-physical simulation of laser-material interaction becomes an essential research tool to complete experimental diagnostics, to help understanding the origin of some defects such as porosities or cracks and to predict solidification conditions.

However, due to the gap between the grain scale (micrometres) and the bead scale (millimetres), numerical simulation of LBM leads to the use of important computational resources. Generally, to bypass this limitation, two simulation strategies are encountered [1,2]. Firstly, at the micro/mesoscale, the models are focused on the laser-matter interaction and on the thermo-hydrodynamic phenomena involved at the vicinity of the melt pool. Current state-of-the-art multi-physical models are still computationally expensive as each powder grain is individually represented [3,4]. Hence, simulating more than a single LBM track in a reasonable computational time is a challenging task. Secondly, at the macroscale, the models are interested in the thermomechanical behaviour of the component during the process. At this scale, thermal problem is generally reduced to a simple conduction problem where the laser input is represented by an equivalent moving heat source [5,6]. As the energy input is approximated, the predicted mechanical behaviour is sometimes far from reality.

Consequently, in order to make the bridge between these two scales, a new mesoscopic approach is proposed, based on the pioneering works of Dal et al. (2016) [7] and Chen et al. (2017) [8]. This intermediate methodology intends to bridge the gap between the fine thermo-hydrodynamic models and the purely thermal macroscopic models. The present proof of concept is performed in a static laser configuration, using the commercial software COMSOL Multiphysics[®]. The powder bed is represented by a homogeneous absorbing medium with both homogenized thermal and fluid properties. A bulk heat source is considered when the laser heats the powder bed whereas a surface heat flux is imposed on the surface of the liquid pool. Apparent viscosity and surface tension are attributed to the equivalent medium so that modelling powder densification (due to powder coalescence), melting and spheroidization of the melt pool is made possible by solving compressible Navier-Stokes equations. In addition, thermocapillary effects as well as vaporisation-induced recoil pressure are implemented and experimentally validated, so that realistic thermo-hydrodynamic phenomena are successfully taken into account. This makes the present approach a promising alternative to current multi-physical models, which will be easily transposed into a 3D geometry, in single and multiple LBM tracks configurations.

2 PHYSICAL MODEL

2.1 Principles of the mesoscopic approach

The method treats the powder bed, which is a granular medium, as a homogenized continuous material with a given initial porosity and homogenized thermal and fluid properties (Figure 1a). When the equivalent medium is heated, powder irreversible transformation is handled with a densification function ϕ (Figure 1b), which gives the fraction of powder phase as a function of temperature. The medium properties ψ are then expressed as a function of ϕ , to ensure transition from powder to condensed phase properties:

$$\psi = \phi\psi_{\text{powder}} + (1 - \phi)\psi_{\text{condensed}} \quad (1)$$

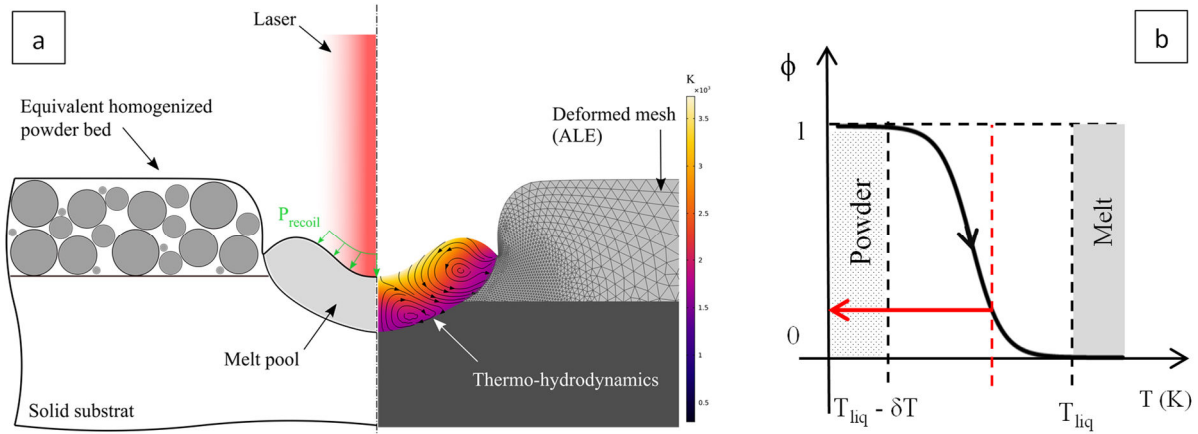


Figure 1: (a) Schematic of the new mesoscopic approach in static laser configuration. (b) Fraction of powder versus temperature. Material transformation is made irreversible, using a hysteresis function (red arrow).

2.2 Governing equations

▪ Thermal problem

Thermal field is computed by solving the energy conservation law in transient condition:

$$\rho c_p^{eq} \frac{\partial T}{\partial t} + \rho c_p (\vec{u} \cdot \vec{\nabla} T) = \vec{\nabla} \cdot (k \vec{\nabla} T) + \phi Q \quad (2)$$

where c_p , ρ , and k are respectively the specific heat, the density and the conductivity of the different phases and Q is the laser heat source. Latent heat of melting L_m is introduced thanks to an equivalent specific heat [9]:

$$c_p^{eq} = c_p + \frac{L_m}{\sqrt{\pi} \Delta T^2} \exp \left[-\frac{(T - T_m)^2}{\Delta T^2} \right] \quad (3)$$

where $T_m = 0.5(T_{liq} + T_{sol})$ is the ‘‘melting’’ temperature and $2\Delta T = (T_{liq} - T_{sol})$ is the melting/solidification interval. Regarding the laser source, two cases should be considered, whether the equivalent medium is in powder form or in condensed state. Nevertheless, in both cases, a Gaussian heat flux is imposed on the domain upper boundary [EC] (Figure 2):

$$I_{laser} = A \cos(\theta) \frac{P}{\pi R_0^2} \exp \left(-\frac{2r^2}{R_0^2} \right) g(t) \quad (4)$$

where A is the material absorptivity, θ is the laser incident angle relative to the material/vapour interface; P and R_0 are the laser power and radius respectively. In addition, $g(t) = 1 - \exp(-t/\tau)$ is the temporal profile of the laser pulse, with a characteristic rise time $\tau = 150 \mu s$.

In the first case, when the irradiated material is in powder state, Gusarov et al. (2009) [10] demonstrated that the powder bed could be approximated to a homogeneous absorbing-scattering medium. Actually, when the laser beam interacts with loose powder, the incident beam penetrates in the bulk medium as it is reflected several times by the powder grains. More recently, Dayal et al. (2017) [11] confirmed this behaviour by means of ray-tracing simulations. Consequently, laser input should be modelled as a bulk heat source, which penetrates in the

powder layer depth. Gusarov et al. proposed an analytical law, which expresses Q as a function of the powder average diameter, the bed porosity and the bed depth. Here, the authors used instead the Beer-Lambert law, which is easier to implement in a finite element code and which gives similar results:

$$Q = \frac{\partial I}{\partial z} = \alpha I \quad (5)$$

where α is the extinction coefficient and I is the heat flux which decays exponentially with the bed depth. Notice that in equation (2), the laser bulk heat source term Q is weighted by the function ϕ , to ensure it only applies in the powder.

In the second case, when the powder is melted, the bulk heat source is not applied anymore ($\phi = 0$) and the laser input reduces to a heat flux on boundary [EC] (Figure 2):

$$k\vec{\nabla}T \cdot (-\vec{n}) = (1 - \phi)I_{laser} - \varphi_{losses} \quad (6)$$

where φ_{losses} contains the heat lost by vaporization, radiation and convection.

Here, the authors should make a remark regarding the chosen heat source model. In practice, it is observed that the laser beam interacts mostly with the melt pool during the process in the steady state regime [12]. The powder bed melts almost instantaneously ($\approx 10 \mu s$) at the very first interaction with the laser beam and then the surrounding powder is melted by contact with the melt pool. So one could argue that, as the melting time is negligible compared to the dwell time ($\approx 100 \mu s$), it is not necessary to include the first heating stage with the bulk heat source – especially in a moving laser source configuration. This objection would be physically founded. However numerically speaking, our equivalent powder medium has a relatively small thermal diffusivity. Hence, imposing a high heat flux prior to densification would require smaller elements and time steps (and thus longer computational times) to avoid numerical thermal undershoot. Therefore, this approach is also a convenient way to ensure numerical stability.

In addition, heat lost by vaporization equals to the product of the latent heat of vaporisation L_V and the evaporation mass flux. The latter is commonly expressed thanks to the Hertz-Langmuir equation [13]:

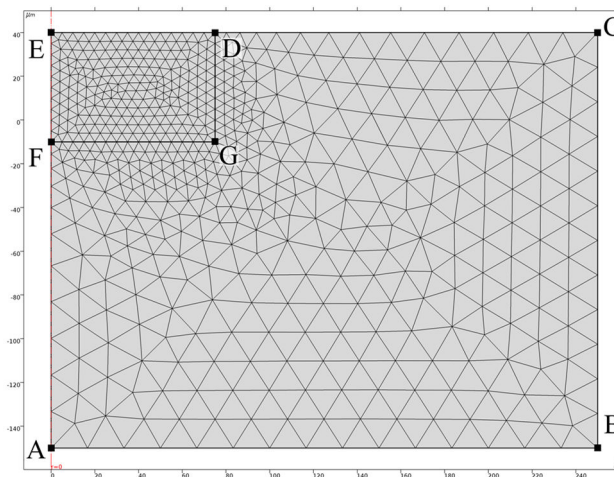


Figure 2: Initial geometry and mesh. Notice that here the mesh has voluntarily been coarsened to lighten the figure. Mesh is refined down to $1 \mu m$ in the subdomain [DEFG].

$$\dot{m} = (1 - \beta_R) \sqrt{\frac{M}{2\pi RT}} P_{sat}(T) \quad (7)$$

where β_R is the retro-diffusion coefficient (i.e. the fraction of vaporized particles which re-condensates when they interact with the surrounding particles), M is the molar mass of the vaporised species and P_{sat} is the saturated vapour pressure. P_{sat} is calculated thanks to the Clausius-Clapeyron law:

$$P_{sat}(T) = P_{atm} \exp\left[\frac{ML_v}{RT_v} \left(1 - \frac{T_v}{T}\right)\right] \quad (8)$$

where P_{atm} is the atmospheric pressure and T_v is the boiling point at atmospheric pressure.

In previous works [14,15], we have explained that equation (7) could not be consistently used as it is, because the Hertz-Langmuir law is valid only in vacuum or at temperature much greater than the boiling point, when vaporization is strong enough to expel the surrounding ambient gas. In these cases, β_R tends toward 0.18 [16,17]. Pang et al. (2015) [18] and later Girardot et al. (2017) [19] generalized equation (7) to account for the ambient pressure effects in the whole temperature range. The authors actually followed their recommendations. For conciseness purpose, we will not provide more details here, please report to the cited papers.

Finally, the external boundaries [AB] and [BC] are sufficiently far from the heat source to be set as adiabatic.

▪ *Fluid flow problem*

At the laser intensities involved in LBM ($I \gtrsim 1 \text{ MW/cm}^2$), similar to laser welding, Semak and Matsunawa (1997) [20] clearly demonstrated that such a process is thermally limited (at steady state) by melt pool convection driven by vaporization-induced recoil pressure. Thanks to their so-called ‘‘piston’’ model, they have estimated that at this intensity order of magnitude, 70% to 90% of the laser energy is exchanged by convection [20]. It is thus of a major importance to compute fluid flow with maximum fidelity.

Fluid flow problem is thus established by solving mass and momentum conservation laws in compressible form to allow powder densification:

$$\frac{\partial \rho}{\partial t} + \vec{\nabla} \cdot (\rho \vec{u}) = 0 \quad (9)$$

$$\rho \frac{\partial \vec{u}}{\partial t} + \rho (\vec{u} \cdot \vec{\nabla}) \vec{u} = \vec{\nabla} \cdot \left\{ -pI + \mu \left[\vec{\nabla} \vec{u} + (\vec{\nabla} \vec{u})^T \right] - \frac{2}{3} (\vec{\nabla} \cdot \vec{u}) I \right\} + K \vec{u} + \rho \vec{g} \quad (10)$$

where μ is the dynamic viscosity and K is a Darcy penalization term, which allows computing the solid/liquid transition in the substrate [21]:

$$K = C_1 \frac{(1 - f_{liq})^2}{f_{liq}^3 + C_2} \quad (11)$$

where f_{liq} is the liquid fraction, C_1 and C_2 are numerical constants tailored to penalize velocity in the solid. In the powder bed, the powder/liquid transition is handled with the ϕ -dependant dynamic viscosity [8].

The melt pool hydrodynamics is driven by different forces applied to the liquid/vapour interface, namely the recoil pressure, surface tension and thermocapillary shear stress:

$$\left(-pI + \mu \left[\vec{\nabla}\vec{u} + (\vec{\nabla}\vec{u})^T\right] - \frac{2}{3}(\vec{\nabla} \cdot \vec{u})I\right) \cdot \vec{n} = -P_{recoil} \cdot \vec{n} + \sigma\kappa\vec{n} + \frac{\partial\sigma}{\partial T}\vec{\nabla}_s T \quad (12)$$

where the recoil pressure is commonly expressed by [13]:

$$P_{recoil}(T) = \frac{1}{2}(1 + \beta_R)P_{sat}(T) \quad (13)$$

As for the vaporization mass flux, we use Pang's recommendations to account for the ambient pressure effects on the recoil pressure [18].

Finally, no slip boundary condition is applied on boundaries [AB] and [BC].

- *Arbitrary Lagrangian Eulerian Method*

The evolution of the domain free boundary [EC] is tracked using the Arbitrary Lagrangian Eulerian (ALE) method, pre-implemented in COMSOL Multiphysics[®]. With this method, the interface vertices follow the fluid movement through equation (14):

$$V_I = \vec{u}_L \cdot \vec{n} \quad (14)$$

where V_I is the interface velocity and $\vec{u}_L \cdot \vec{n}$ is the fluid velocity projected to the normal of the interface. Interface displacement is then propagated throughout the domain, following the so-called Yeoh smoothing method, which looks at minimising mesh deformation energy [22].

3 MATERIALS PROPERTIES

In the present paper, we present two cases of static laser-matter interaction, with and without powder bed. Except for the thermal conductivity, the initial powder bed properties are calculated as the weighted average of the powder grain properties (Inconel 625[®]) and the interstitial gas properties (argon):

$$\psi_{powder} = \varepsilon\psi_{argon} + (1 - \varepsilon)\psi_{IN625} \quad (16)$$

where ε is the powder bed porosity. Thermal conductivity is estimated as one hundredth of the conductivity of the powder grains [23,24]. All the thermophysical properties used during the simulation are summarized in Table 1 and Table 2.

Table 1: Properties of the powder bed.

Properties (unit)	Value
A Absorptivity powder/liquid	0.6/0.3
ep Thickness (μm)	40
k Thermal conductivity ($\text{Wm}^{-1}\text{K}^{-1}$)	0.27
α Extinction coefficient (m^{-1})	1/ep
δT Densification interval (K)	300
ε Porosity	0.5
μ Dynamic viscosity (Pa.s)	15
σ Surface tension (N.m^{-1})	0.01

Table 2: Thermophysical properties and parameters used in the simulation [25,26].

Properties (unit)		IN625	Argon
c_p	Specific heat ($\text{J.kg}^{-1}.\text{K}^{-1}$)	680	520
k	Thermal conductivity ($\text{W.m}^{-1}.\text{K}^{-1}$)	26.9	1.7E-2
L_m	Latent heat of melting (kJ.kg^{-1})	270	
L_v	Latent heat of vaporization (kJ.kg^{-1})	6294	
M	Molar mass (g.mol^{-1})	59.47	
T_{sol}	Solidus temperature (K)	1533	
T_{liq}	Solidus temperature (K)	1609	
T_v	Boiling temperature (K)	3190	
$\gamma = \partial\sigma/\partial T$	Thermocapillary coefficient ($\text{mN.m}^{-1}.\text{K}^{-1}$)	0.11	
μ	Dynamic viscosity (Pa.s)	2E-3	
ρ	Density (kg.m^{-3})	7886	1.6
σ	Surface tension (N.m^{-1})	1.842	

4 APPLICATION CASES

Prior to modelling the case of powder bed fusion, we should check if our physical model is able to describe correctly the melt pool thermo-hydrodynamics, independently to the powder bed aspect. A preliminary study is thus the case of laser spot welding (i.e. static shooting on plates).

The computational domain with the mesh is shown in Figure 2. To optimize mesh deformation via the ALE method, we have defined a single computational domain where the transition from the substrate to the powder bed is smoothly set, thanks to a Heaviside function. With a two-domain strategy (Figure 3a), the deformed mesh volume would be restrained to the powder layer. With the single-domain strategy (Figure 3b), mesh deforms across the materials domains and elements distortion is propagated throughout the whole volume.

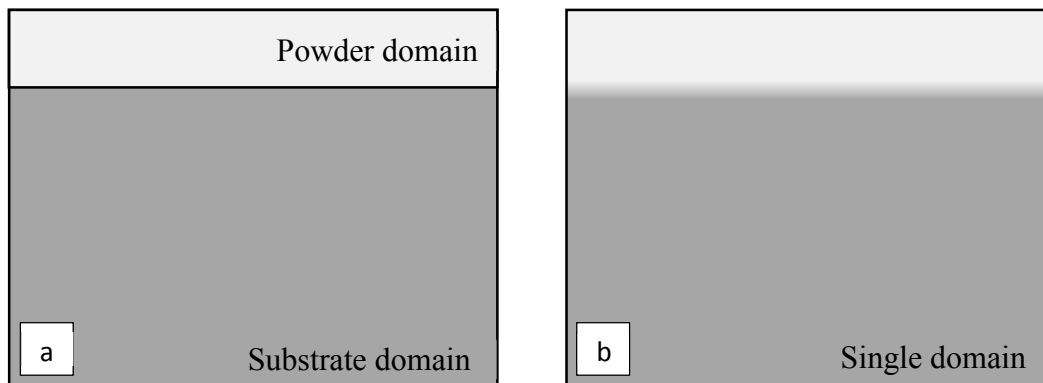


Figure 3: Configuration of the computational domain. (a) Each material (powder/substrate) has its own geometrical domain. (b) There is only one geometrical domain with a smooth transition between the powder layer and the substrate.

Mesh is locally refined, down to $1\ \mu\text{m}$, around the laser-material interaction zone, where a fine discretization is needed to compute thermal gradient and fluid flow accurately, and where most mesh distortion is expected. With such a mesh, approximately 100,000 degrees of freedom have to be solved. The time step is fixed to $10^{-6}\ \text{s}$, using a Backward Euler temporal scheme (BDF, order 1). The problem is solved using the direct PARDISO solver.

Finally, computation took about 3h to simulate 0.1 ms of laser shot with powder, using 8 cores of a Dell® workstation (CPU: Intel® Xeon® @3.2 GHz, RAM: 128 Go).

5 RESULTS

5.1 Case without powder

Below are presented the results of a series of laser spot welding simulations and experiments. We compare on Figure 4a, the macrograph of a fused zone obtained with a 3 ms-long static shot performed on an Inconel 625® plate with a Yb-YAG laser. The focal spot is set to $205\ \mu\text{m}$ and the incident power is 700 W. The shape of the melt pool predicted by finite element method agrees well with the final shape of the fused zone. The temperature of the melt pool free surface, on a width equivalent to the laser spot diameter, is around 3500 K, which is superior to the boiling point at atmospheric pressure ($T_v = 3190\ \text{K}$). Consequently, the pressure difference between the centre ($\approx P_{\text{atm}} + P_{\text{recoil}}$) and the sides (P_{atm}) of the melt pool, induces a depression zone (keyhole) which controls the depth of the fused zone. As highlighted by the white streamlines, the melt pool is fed by the solid from the bottom and liquid metal is driven by the recoil pressure, from the centre of the interaction zone to the rim of the melt pool. A small melt volume in the bottom centre of the interaction zone is thus sheared by this ejected melt, generating a small recirculation zone. A second recirculation zone is created at the vicinity of the liquid/solid transition, due to thermocapillary shear stress. This local vortex increases the melt penetration in the solid, hence increasing the local melt pool width.

In addition Figure 4b compares, for different laser incident intensities, the fused zone width and depth predicted by our model and obtained experimentally. Within this intensity range, our model predicts the dimensions of the fused zone with an average error inferior than 10% (5 % for the width and 7% for the depth), which is very satisfying.

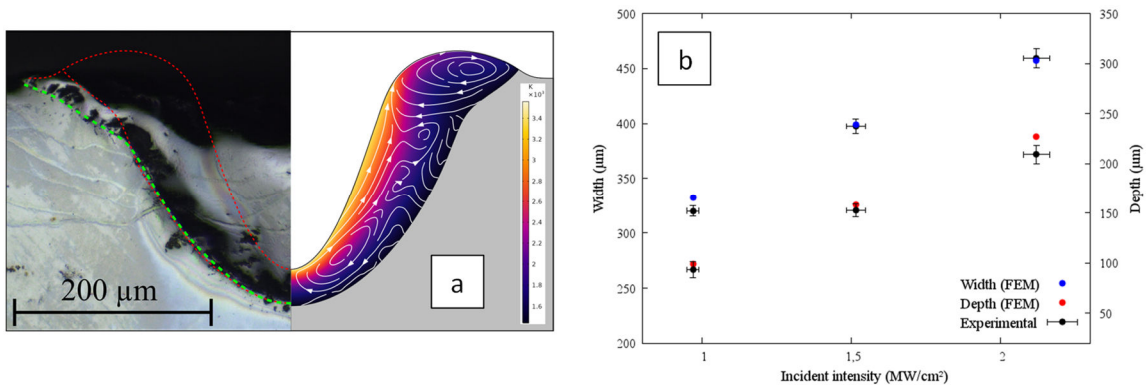


Figure 4: (a) Numerical melt pool compared to the macrograph of the fused zone obtained in the same conditions ($P = 700\ \text{W}$, $R_0 = 102.5\ \mu\text{m}$, $t = 3\ \text{ms}$). (b) Comparison of the dimensions of the experimental fused zones and the numerical melt pool for different incident intensities.

5.2 Case with powder

Our model presents a good ability to take into account the role of recoil pressure on melt pool hydrodynamics and to predict the shape and the dimensions of the fused zone. Now the study should be focused on the equivalent powder bed.

Figure 5 gives the dynamics of powder bed melting, obtained with a 0.1 ms-long static laser shot, with a focal spot set to 50 μm (typical to LBM) and an incident powder of 250 W. The melting sequence can be decomposed in three steps.

Firstly, during the first tens of microseconds, the equivalent powder bed densifies and melts. The powder volume under the laser spot hence collapses (Figure 5a). Physically speaking, powder densification is due to the melting of individual powder grains which coalesce. A good illustration is given by Körner's simulations [27]. Here, this mechanism is handled with a variation of the equivalent powder bed density with temperature, via the function ϕ . Note that for numerical stability reasons, we have used an artificial densification interval $\delta T = 300$ K, which is larger than the melting interval $2\Delta T = 76$ K. Hence, in our model, densification starts before melting, which is not physical – here, regarding the melting time scale, we do not expect for solid sintering to occur. Nevertheless, this numerical artifice should not have a significant impact at the scale of the LBM bead as it is restrained to short time and length scales.

Secondly, the melt pool created gets its spherical shape due to surface tension (Figure 5b). With our equivalent approach, this is possible because we attribute to the powder, a sufficiently low surface tension (one hundredth of the liquid surface tension), so that powder has no mechanical effect on the melt pool. The melt pool is free to spheroidize. Physically speaking, shaping of the fusion zone is governed by the balance between the melted grain inertia and surface tension. The time scale for the melt pool shaping is given by the Rayleigh time $t_{\text{ray}} = (\rho D^3 / \sigma)^{1/2}$, which is of the order of 10^{-5} - 10^{-4} s for metals [27].

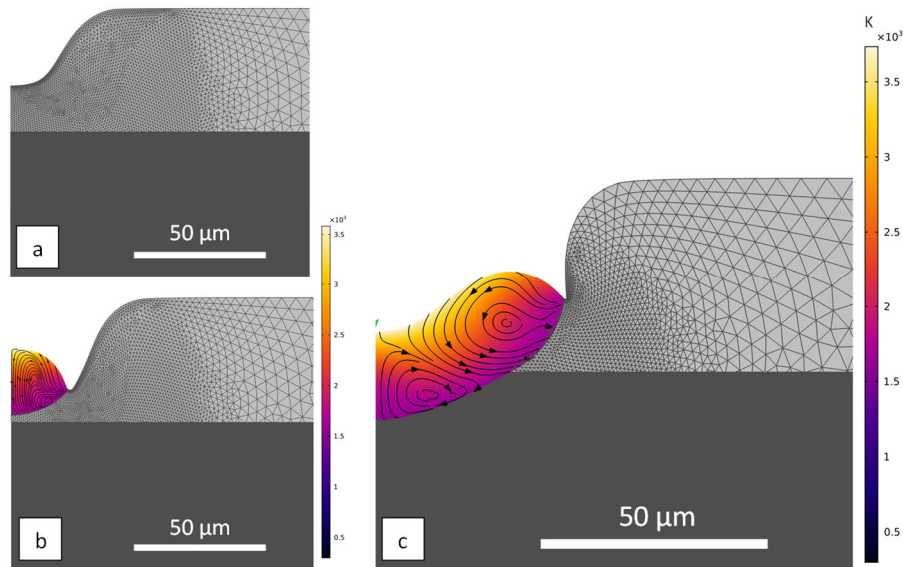


Figure 5: (a) Densification of the powder bed ($t \approx 50 \mu\text{s}$). (b) Spheroidization of the melt pool, prior to vaporisation ($t \approx 65 \mu\text{s}$). (c) Vaporisation: the melt pool is deflected by the recoil pressure ($t \approx 80 \mu\text{s}$).

Finally, the melt surface temperature rapidly reaches the boiling point, after about 65 μ s. The spherical melt pool is deformed by the recoil pressure, which favours its penetration in the substrate underneath (Figure 5c).

6 CONCLUSION AND PERSPECTIVES

An original mesoscopic method has been proposed to simulate laser-material interaction during LBM. This new methodology, which treats the powder bed as an equivalent homogeneous medium, has proven to be efficient in modelling hydrodynamics phenomena associated to powder bed fusion – densification, melting and vaporisation – without resorting to the granular description. It is believed that this method is a good alternative to current state-of-the-art multi-physical models as it reduces computational effort associated to meshing granular media. Without powder, the model reduces to the case of laser spot welding, which was successfully validated with experiments.

The next step will be to transpose the current model into a 3D geometry, to simulate a single LBM pass. The shape and dimensions of the obtained bead will be confronted to experiments and to numerical results provided by an alternative level-set approach developed at Mines ParisTech [28], in a context of a collaborative study.

REFERENCES

- [1] Dal M and Fabbro R 2016 [INVITED] An overview of the state of art in laser welding simulation *Opt. Laser Technol.* **78** 2–14
- [2] Francois M M, Sun A, King W E, Henson N J, Tourret D, Bronkhorst C A, Carlson N N, Newman C K, Haut T, Bakosi J, Gibbs J W, Livescu V, Vander Wiel S A, Clarke A J, Schraad M W, Blacker T, Lim H, Rodgers T, Owen S, Abdeljawad F, Madison J, Anderson A T, Fattebert J L, Ferencz R M, Hodge N E, Khairallah S A and Walton O 2017 Modeling of additive manufacturing processes for metals: Challenges and opportunities *Curr. Opin. Solid State Mater. Sci.* **21** 198–206
- [3] Khairallah S A, Anderson A T, Rubenchik A and King W E 2016 Laser powder-bed fusion additive manufacturing: Physics of complex melt flow and formation mechanisms of pores, spatter, and denudation zones *Acta Mater.* **108** 36–45
- [4] Tang M, Pistorius P C and Beuth J L 2017 Prediction of lack-of-fusion porosity for powder bed fusion *Addit. Manuf.* **14** 39–48
- [5] Papadakis L, Loizou A, Risse J and Schrage J 2014 Numerical computation of component shape distortion manufactured by Selective Laser Melting *Procedia CIRP* **18** 90–5
- [6] B Y Z and Guillemot G 2017 Macroscopic Finite Element Thermal Modelling of Selective Laser Melting for IN718 Real Part Geometries Yancheng *Ind. Addit. Manuf. - Proc. Addit. Manuf. Prod. Appl. - AMPA2017*
- [7] Dal M, Peyre P, Gunenthiram V and Schneider M 2016 A New Equivalent Approach For Additive Layer Manufacturing (ALM) Numerical Modelling *ICALEO Proceedings*
- [8] Chen Q, Guillemot G, Gandin C-A and Bellet M 2017 Three-dimensional finite element thermomechanical modeling of additive manufacturing by selective laser melting for ceramic materials *Addit. Manuf.* **16** 124–37
- [9] Bonacina C, Comini G, Fasano A and Primicerio M 1973 Numerical solution of

- phase-change problems *Int. J. Heat Mass Transf.* **16** 1825–32
- [10] Gusarov A V., Yadroitsev I, Bertrand P and Smurov I 2009 Model of Radiation and Heat Transfer in Laser-Powder Interaction Zone at Selective Laser Melting *J. Heat Transfer* **131** 072101
- [11] Dayal R and Gambaryan-Roisman T 2017 Heat transfer in granular medium for application to selective laser melting: A numerical study *Int. J. Therm. Sci.* **113** 38–50
- [12] Scipioni Bertoli U, Wolfer A J, Matthews M J, Delplanque J P R and Schoenung J M 2017 On the limitations of Volumetric Energy Density as a design parameter for Selective Laser Melting *Mater. Des.* **113** 331–40
- [13] Samokhin A A 1990 *Effect of Laser Radiation on Absorbing Condensed Matter* ed V B Fedorov (Nova Science Publishers)
- [14] Mayi Y A, Dal M, Peyre P, Bellet M, Metton C, Moriconi C and Fabbro R 2018 Two-Phase Flow Modelling of Metal Vaporisation under Static Laser Shot using a Double Domain ALE Method – A Feasibility Study *Proceedings of the 2018 COMSOL Conference* (Lausanne)
- [15] Mayi Y A, Dal M, Peyre P, Bellet M, Metton C, Moriconi C and Fabbro R 2019 Effets de la Nature du Gaz Ambiant sur les Ecoulements Induits lors de la Vaporisation d’un Alliage Métallique sous Faisceau Laser
- [16] Anisimov S I 1968 Vaporization of metal absorbing laser radiation *Sov. Phys. JETP* **27** 182–3
- [17] Knight C J 1979 Theoretical Modeling of Rapid Surface Vaporization with Back Pressure *AIAA J.* **17** 519–23
- [18] Pang S, Hirano K, Fabbro R and Jiang T 2015 Explanation of penetration depth variation during laser welding under variable ambient pressure *J. Laser Appl.* **27** 022007
- [19] Girardot J, Lorong P, Illoul L, Ranc N, Schneider M and Favier V 2017 Modeling laser drilling in percussion regime using constraint natural element method *Int. J. Mater. Form.* **10** 205–19
- [20] Semak V and Matsunawa A 1997 The role of recoil pressure in energy balance during laser materials processing *J. Phys. D. Appl. Phys.* **30** 2541–52
- [21] Voller V R and Prakash C 1987 A fixed grid numerical modelling methodology for convection-diffusion mushy region phase-change problems *Int. J. Heat Mass Transf.* **30** 1709–19
- [22] Comsol Mutliphysics User’s Guide 2018 Comsol Multiphysics User’s Guide
- [23] Zehner P and U Schlünder E 1970 Thermal conductivity of granular materials at moderate temperatures *Chem Ing-Tech* **42** 933–41
- [24] Rombouts M, Froyen L, Gusarov A V., Bentefour E H and Glorieux C 2005 Photopyroelectric measurement of thermal conductivity of metallic powders *J. Appl. Phys.* **97**
- [25] Mills K C 2002 *Recommended values of thermophysical properties for selected commercial alloys* (Cambridge: Woodhead Publishing Limited)
- [26] Anon Gas Encyclopedia Air Liquide | Air Liquide
- [27] Körner C, Bauereiß A and Attar E 2013 Fundamental consolidation mechanisms during selective beam melting of powders *Model. Simul. Mater. Sci. Eng.* **21**
- [28] Queva A, Mayi Y, Bellet M, Guillemot G, Peyre P, Dal M, Moriconi C and Metton C

2019 Thermo-mechanical simulation of track development in the Laser Beam Melting process - Effect of laser-metal interaction *IOP Conf. Ser. Mater. Sci. Eng.* **529** 012005

A NUMERICAL MODEL FOR THE SIMULATION OF SHALLOW LASER SURFACE MELTING

Alexandre Caboussat^{*,a}, Julien Hess^{a,b}, Alexandre Masserey^b and Marco Picasso^c

^a Geneva School of Business Administration
University of Applied Sciences and Arts Western Switzerland (HES-SO)
Rue de la Tambourine 17, 1227 Carouge, Switzerland
e-mail: {alexandre.caboussat/julien.hess}@hesge.ch - web page: <http://campus.hesge.ch/caboussat>

^b Ycoor Systems SA, Technopôle 10, 3960 Sierre, Switzerland
e-mail: {masserey/hess}@ycoorsystems.com - web page: <http://www.ycoorsystems.com>

^c Institute of Mathematics, Ecole Polytechnique Fédérale de Lausanne (EPFL)
Station 8, 1015 Lausanne, Switzerland
e-mail: marco.picasso@epfl.ch - web page: <https://people.epfl.ch/marco.picasso>

Key words: Computational methods, Coupled problems, Marangoni effects, Operator splitting, Laser surface melting

Abstract. We present a multi-physics model for the approximation of the coupled system formed by the temperature-dependent Navier-Stokes equations with free surfaces. The main application is the industrial process of shallow laser surface melting (SLSM), for laser polishing of metal surfaces. We consider incompressible flow equations with solidification, and we model the laser source through physically-consistent boundary conditions. We incorporate Marangoni effects in the surface tension model to drive internal motion in the liquid metal. The numerical method relies on an operator splitting strategy and a two-grid approach. A proof of concept of the numerical model is achieved through a static laser melting process.

1 INTRODUCTION

Laser polishing is a widespread process in various industries [2, 14, 15], consisting in re-melting the surface of a metal in order to reduce surface roughness when re-solidifying. Its effectiveness relies on the strong dependency between the fluid flow properties of the metal (or alloy), and the heat effect [1]. The underlying multi-physics model for such a system is composed by the temperature-dependent Navier-Stokes equations, coupled with the heat equation for solidification processes, and with a free surfaces model for the simulation of the surface of the re-melting metal. Although no substrate is incorporated into the mixture here, the goal of this study is to simulate the internal motion of the melting pool, and accurately model the free surfaces that arise in laser polishing processes. In particular, we model the complex relationship between internal currents in the liquid metal, the temperature and the free surface evolution through Marangoni effects [5, 13]. The objective of this work is thus to highlight the internal fluid motion induced by Marangoni effects in laser surface melting processes.

We consider incompressible flow equations with solidification, by using a Navier-Stokes model with an additional Carman-Kozeny term [9]. We add thermal effects with an enthalpy-based convection-diffusion heat equation, and we model the laser source by applying a heat flux boundary condition on the free surface. We incorporate Marangoni effects in the surface tension model to drive internal motion in the liquid metal. The numerical method relies on an operator splitting strategy and a two-grid approach, which has been tested in other situations (without solidification effects) in [3, 4, 6]. The operator splitting allows to decouple the various physical phenomena, in particular advection and diffusion processes. The two-grid approach allows to have an accurate description of the free surfaces.

A proof of concept of the numerical approach is achieved through an example of static laser melting, to show how laser polishing processes can induce convective currents in the melting regions, through Marangoni effects, and affect surface roughness.

2 MODELING

Let us consider a bounded domain $\Lambda \subset \mathbb{R}^3$, and let $t_{max} > 0$ be a given final time. For any time $t \in (0, t_{max})$, let $\Omega_t \subset \Lambda$ be the domain occupied by the metal (solidified or not) and $\Gamma_t := \partial\Omega_t \setminus \partial\Lambda$ be the free surface between the metal and the ambient air, namely the boundary of the metal domain that is not in contact with the boundary of the whole cavity. The air is considered as vacuum. Typically, we consider the laser polishing of a metal plate Ω_t , as illustrated in Figure 1 in two space dimensions.

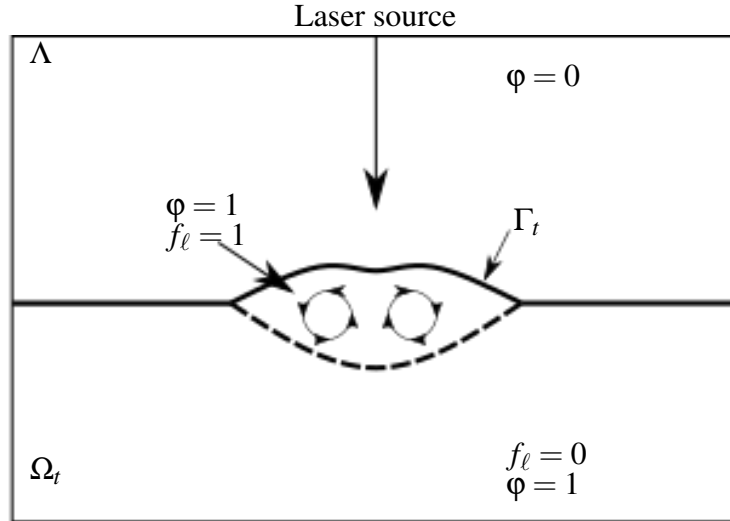


Figure 1: Laser melting of a metal plate (2D sketch). The cavity Λ contains metal and air. At each time $t \in (0, t_{max})$, the metal domain Ω_t (solid and liquid) is separated from the ambient air by the metal-air interface Γ_t . A vertical laser source is applied in the middle of the domain and melts the central region of the metal. A vorticity flow develops in the liquid region. The metal domain is described by its volume fraction of metal φ , while the temperature T determines the liquid and solid regions.

Let Q be the space-time domain containing the metal:

$$Q = \{(\mathbf{x}, t) \in \Lambda \times (0, t_{max}) : \mathbf{x} \in \Omega_t, 0 < t < t_{max}\}.$$

The velocity field $\mathbf{v} : Q \rightarrow \mathbb{R}^3$ and the pressure field $p : Q \rightarrow \mathbb{R}$ are assumed to satisfy incompressible, time-dependent Navier-Stokes equations in Q . The Navier-Stokes equations include an additional Darcy-like reaction term to model the solidification process, penalizing the velocity in the solid region. The enthalpy $H : Q \rightarrow \mathbb{R}$ is assumed to satisfy the classical enthalpy formulation of the heat conservation equation, which can be derived by simplifying the general energy conservation equation with Fourier's law (see [9] for details). The complete set of equations in Q thus reads:

$$\rho \frac{\partial \mathbf{v}}{\partial t} + \rho(\mathbf{v} \cdot \nabla) \mathbf{v} - 2\nabla \cdot (\mu \mathbf{D}(\mathbf{v})) + \alpha(T) \mathbf{v} + \nabla p = \rho \mathbf{g}, \quad (2.1)$$

$$\nabla \cdot \mathbf{v} = 0, \quad (2.2)$$

$$\frac{\partial H}{\partial t} + \mathbf{v} \cdot \nabla H - \nabla \cdot (k \nabla \beta(H)) = 0. \quad (2.3)$$

Here $\mathbf{D}(\mathbf{v}) = 1/2(\nabla \mathbf{v} + \nabla \mathbf{v}^T)$ is the symmetric deformation tensor, ρ , μ and k are respectively the density, the viscosity and the thermal conductivity of the metal, and $\rho \mathbf{g}$ is the gravity force. The function $T = \beta(H)$ describes the relationship between the enthalpy H and the temperature T , and is determined by the phase transition and properties of the material.

In order to model the solidification process with a diffuse model (mushy zone), the velocity is penalized with the Carman-Kozeny empirical law, which represents the coupling with a Darcy flow in porous media [9]. The reaction coefficient in (2.1) is given by:

$$\alpha(T) = \bar{\alpha} \frac{\mu(1 - f_\ell(T))^2}{(f_\ell(T) + \varepsilon)^3}, \quad (2.4)$$

where $\bar{\alpha}$ is a constant to be calibrated and f_ℓ is the liquid fraction, which equals one in the liquid region (above the temperature of fusion) and zero in the solid region. Note that $0 < \varepsilon \ll 1$ is a numerical parameter to avoid a division by zero.

Let $\varphi : \Lambda \times (0, t_{max}) \rightarrow \{0, 1\}$ be the volume fraction of metal, which equals one if the metal is present (solid or liquid) and zero if it is not (also known as the characteristic function of the metal domain), and thus the space-time metal domain can be defined as:

$$Q = \{(\mathbf{x}, t) \in \Lambda \times (0, t_{max}) : \varphi(\mathbf{x}, t) = 1\}.$$

In order to describe the kinematics of the free surface, the volume fraction of metal φ must satisfy (in a weak sense) the transport equation:

$$\frac{\partial \varphi}{\partial t} + \mathbf{v} \cdot \nabla \varphi = 0 \quad \text{in } \Lambda \times (0, t_{max}), \quad (2.5)$$

The model is completed with initial and boundary conditions. The volume fraction of metal $\varphi(\cdot, 0)$ is given at initial time, which is equivalent to defining the initial metal region $\Omega_0 = \{\mathbf{x} \in \Lambda : \varphi(\mathbf{x}, 0) = 1\}$. The initial enthalpy (or equivalently temperature), and velocity fields are then prescribed in Ω_0 . Boundary conditions for φ are applied, if necessary, on the inlet part of $\partial\Omega_t$ for (2.5). The Navier-Stokes equations (2.1)-(2.2) are completed with slip or no-slip boundary conditions imposed on the boundary of the metal domain $\partial\Omega_t$ that is in contact with the boundary of the cavity $\partial\Lambda$.

Surface tension and Marangoni effects on the liquid metal-air interface are taken into account via a force term on the free surface [13]. The ambient air is assumed to have no influence on the metal, and is treated as vacuum. The boundary conditions on the metal-air interface are thus given by:

$$-p\mathbf{I} + 2\mu\mathbf{D}(\mathbf{v}) = \gamma\kappa\mathbf{n}_{\Gamma_t} + \nabla_{\Gamma_t}\gamma, \quad \text{on } \Gamma_t = \partial\Omega_t \setminus \partial\Lambda, \quad (2.6)$$

where \mathbf{n}_{Γ_t} is the external unit normal vector to Γ_t towards the vacuum, κ is the curvature of Γ_t , and γ is the surface tension coefficient. In the sequel, we'll assume that $\gamma = \gamma(T)$ only depends on the temperature. In this case, the term $\nabla_{\Gamma_t}\gamma$ is defined as $\nabla_{\Gamma_t}\gamma = \gamma'(T)\nabla T \cdot \mathbf{t}_1 + \gamma'(T)\nabla T \cdot \mathbf{t}_2$, where \mathbf{t}_i , $i = 1, 2$, are two linearly independent vectors in the plane tangent to Γ_t , and perpendicular to \mathbf{n}_{Γ_t} .¹

The boundary conditions for the heat equation (2.3) are as follows: the laser source is modeled via a given heat flux on the boundary Γ_t of the metal domain, while adiabatic boundary conditions are applied on the rest of the boundary.

The coupled multiphysics problem thus consists in finding the time evolution of the position of the volume fraction of metal φ in the cavity Λ , together with the enthalpy H , the velocity \mathbf{v} and the pressure p in the metal domain only.

3 NUMERICAL METHODS

The numerical method is inspired from [3, 4, 6], where it has been validated in various situations. It is adapted here to the coupled multi-physics problem arising when considering temperature-related effects. It relies on *operator splitting* and a *two-grid* method: the splitting algorithm decouples advection and diffusion phenomena, while the two-grid algorithm allows to increase the accuracy of the approximation of the free surface by considering finer grids for the approximation of advection problems.

3.1 Time splitting algorithm

Let $N \in \mathbb{N}$, and $\tau = t_{max}/N$ a constant time step. A subdivision of the time interval $[0, t_{max}]$ is given by $t^n = n\tau$, $n = 0, \dots, N$. Assume that φ^n is an approximation of φ available at time t^n , which defines the metal domain $\Omega^n = \{\mathbf{x} \in \Lambda : \varphi^n(\mathbf{x}) = 1\}$, and that $\mathbf{v}^n, p^n, T^n, H^n$ are known approximations of \mathbf{v}, p, T, H respectively on Ω^n at time t^n . Then the approximations φ^{n+1} ,

¹Note that if γ is a function of $\mathbf{x} \in \mathbb{R}^3$, the operator ∇_{Γ} is the surface gradient for the surface Γ , and is defined by $\nabla_{\Gamma}\gamma := \nabla\gamma - \mathbf{n}_{\Gamma}(\mathbf{n}_{\Gamma} \cdot \nabla\gamma)$.

$\Omega^{n+1}, \mathbf{v}^{n+1}, p^{n+1}, T^{n+1}, H^{n+1}$ at time t^{n+1} are computed by means of a splitting algorithm as illustrated in Figure 2.

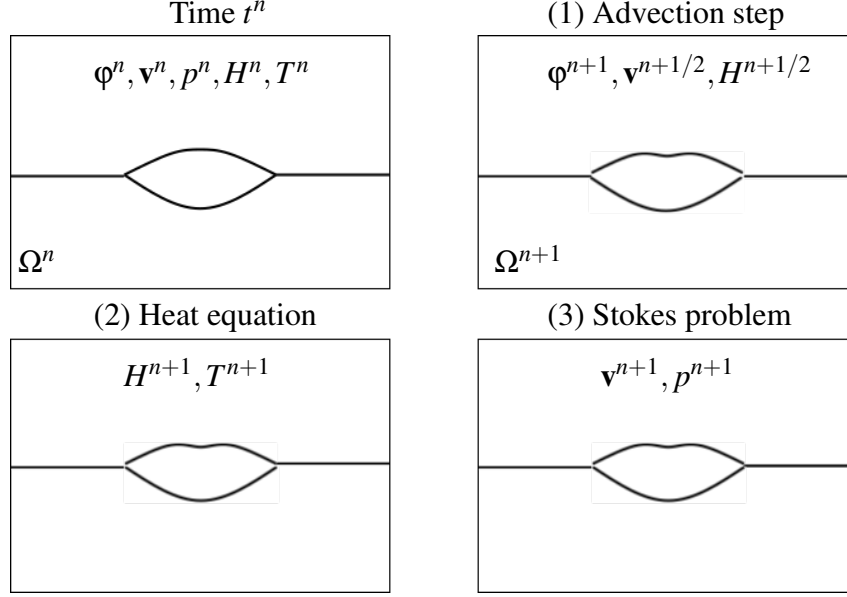


Figure 2: Operator splitting algorithm (from left to right, top to bottom). We solve successively (1) Three advection problems in order to obtain $\varphi^{n+1}, \mathbf{v}^{n+1/2}, H^{n+1/2}$ and thus Ω^{n+1} . (2) The heat diffusion equation (without convection) to determine H^{n+1} (and thus T^{n+1}). (3) A generalized Stokes problem in order to obtain \mathbf{v}^{n+1} and p^{n+1} .

3.1.1 Advection equations

First, three advection problems are solved in order to obtain the new volume fraction of metal φ^{n+1} (and thus the new metal domain Ω^{n+1}), the predicted velocity $\mathbf{v}^{n+1/2}$ and the predicted enthalpy $H^{n+1/2}$. In order to do so, the advection operators in (2.1), (2.3) and (2.5) are solved in Λ between t^n and t^{n+1} :

$$\frac{\partial \varphi}{\partial t} + \mathbf{v} \cdot \nabla \varphi = 0, \quad \frac{\partial H}{\partial t} + \mathbf{v} \cdot \nabla H = 0, \quad \frac{\partial \mathbf{v}}{\partial t} + (\mathbf{v} \cdot \nabla) \mathbf{v} = \mathbf{0}, \quad (3.1)$$

with initial conditions provided by φ^n, H^n and \mathbf{v}^n respectively. This system of hyperbolic equations is linearized and solved with a forward characteristics method [6], which reads:

$$\varphi^{n+1}(\mathbf{x} + \tau \mathbf{v}^n(\mathbf{x})) = \varphi^n(\mathbf{x}), \quad H^{n+1/2}(\mathbf{x} + \tau \mathbf{v}^n(\mathbf{x})) = H^n(\mathbf{x}), \quad \mathbf{v}^{n+1/2}(\mathbf{x} + \tau \mathbf{v}^n(\mathbf{x})) = \mathbf{v}^n(\mathbf{x}),$$

for all $\mathbf{x} \in \Lambda$. The new metal domain is then defined as $\Omega^{n+1} = \{\mathbf{x} \in \Lambda : \varphi^{n+1}(\mathbf{x}) = 1\}$.

3.1.2 Heat equation

Then the heat equation (without convection term) allows to determine the corrected enthalpy H^{n+1} in the new metal domain Ω^{n+1} by solving:

$$\frac{\partial H}{\partial t} - \nabla \cdot (k \nabla \beta(H)) = 0, \quad (3.2)$$

with initial conditions provided by $H^{n+1/2}$. We use an implicit Euler scheme with appropriate boundary conditions, together with the implicit enthalpy-temperature relation $T^{n+1} = \beta(H^{n+1})$ for the determination of the new temperature T^{n+1} . This time-discretized system of equations is solved with the so called Chernoff numerical scheme [10].

3.1.3 Stokes equations

Finally, a generalized Stokes problem is solved in order to obtain the corrected velocity \mathbf{v}^{n+1} and pressure p^{n+1} in the new metal domain Ω^{n+1} , by solving:

$$\rho \frac{\partial \mathbf{v}}{\partial t} - 2 \nabla \cdot (\mu \mathbf{D}(\mathbf{v})) + \alpha(T^{n+1}) \mathbf{v} + \nabla p = \rho \mathbf{g}, \quad (3.3)$$

$$\nabla \cdot \mathbf{v} = 0. \quad (3.4)$$

An implicit Euler scheme is used for the time discretization of this Stokes system in Ω^{n+1} , together with the natural force condition on the metal-air interface:

$$-p \mathbf{I} + 2\mu \mathbf{D}(\mathbf{v}) = \gamma(T^{n+1}) \kappa \mathbf{n}_{\Gamma^{n+1}} + \nabla_{\Gamma^{n+1}} \gamma(T^{n+1}), \quad \text{on } \Gamma^{n+1}. \quad (3.5)$$

3.2 Space Discretization

In order to solve this multi-physics problem, a two-grid method is used, following [3, 4, 6]. As illustrated in Figure 3 (in two dimensions of space), a regular grid of small structured cells (with typical cell size h_{cells}) is used to solve the advection problems (3.1), while the solutions of the heat problem (3.2) and of the Stokes problem (3.3)-(3.5) are obtained via a finite element approximation on a coarser unstructured tetrahedral finite element mesh (with typical mesh size h_{fe}).

The initial goal of introducing a two-grid method is to increase the accuracy of the approximation of the free surface (by decreasing the numerical diffusion of the approximation φ^{n+1} in (3.1)), while keeping reasonable the computational cost of solving parabolic problems (incl. the Stokes problem) implicitly. Following [6], we typically advocate $h_{fe} \simeq 3h_{cells}$ for a reasonable trade-off between accuracy and computational efficiency.

More precisely, (3.1) is solved with a *forward characteristics method* on the grid of small cells, together with a SLIC interface reconstruction algorithm for the approximation of φ^{n+1} [7],

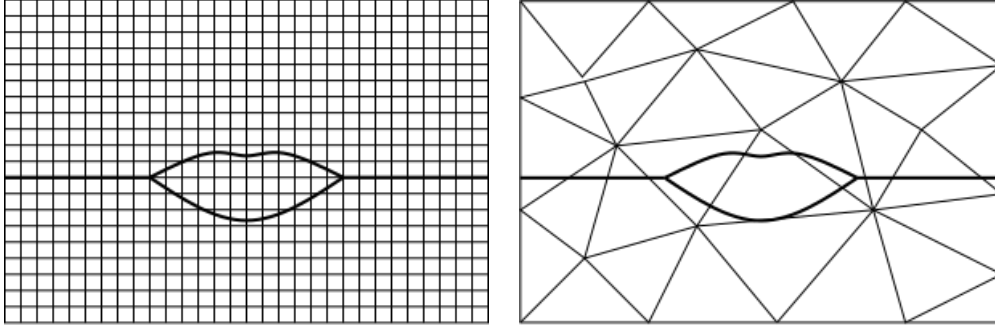


Figure 3: Two-grid method (2D sketch). The advection problems are solved on a structured grid of small cubic cells of typical size h_{cells} (left), and the diffusion problems are solved on an unstructured finite element mesh of typical size h_{fe} (right).

and post-processing heuristics to avoid artificial compression. Although the forward characteristics method does not have to satisfy a CFL condition theoretically, the time step τ is chosen in order to control the CFL number (to be typically between 1 and 5).

Stabilized finite elements, based on continuous piecewise linear finite elements, are used to approximate the Stokes problem (3.3)-(3.5), while classical continuous piecewise linear finite elements are used for the approximation of the heat equation (3.2).

4 NUMERICAL RESULTS

In order to illustrate the efficiency of our method, we present one numerical experiment that consists of a single static laser source melting a piece of metal. This experiment was also treated in [12], and first reported in [8]. We consider the Böhler S705 steel, whose physical properties are listed in Table 1. The variation of active elements, typically sulphur concentration in the material, affects the surface tension gradient with respect to the temperature, and as a consequence the direction and strength of the Marangoni convective flow and eventually the melting pool shape.

In addition to the physical properties in Table 1, the enthalpy-temperature relation $T = \beta(H)$ is constructed from ρ , C_{p_s} , C_{p_l} , T_f and L , as in [10]. The surface tension coefficient is constructed as $\gamma(T) = 1.943 + \gamma'(T)T$ [N/m], where the surface tension derivative $\gamma'(T)$ is given in Figure 4 for two sulphur contents (see [11] for more details). The numerical results presented here are obtained with the curve corresponding to 150 ppm.

The static laser source is considered as a beam of radius $R = 1.4$ [mm] with a power of $P = 5200$ [W]. The absorptivity of the surface to the laser is $\eta = 0.13$ [-]. We simulate the process during $t_{max} = 1$ [s].

We setup a pseudo-2D geometry as illustrated in Figure 5. The computational domain is $\Lambda = D_1 \cup D_2 \cup D_3$, with the initial metal domain $\Omega_0 = D_1 \cup D_2$. The bounding box of the whole domain is $(0, 14) \times (0, 0.05) \times (0, 7.25)$ [mm]. The finite-element mesh in regions D_2 and D_3 is very fine to capture fluid motions in the melting pool, while D_1 is coarser. This allows

Properties	Values	Units
Density (ρ)	8100	[kg/m ³]
Temperature of fusion (T_f)	1620	[K]
Dynamic viscosity (μ)	0.006	[kg/(m.s)]
Thermal conductivity of solid (k_s)	22.9	[J/(m.s.K)]
Thermal conductivity of liquid (k_l)	22.9	[J/(m.s.K)]
Enhancement factor for viscosity and liquid thermal conductivity	7.0	[-]
Specific heat of solid (C_{p_s})	627	[J/(kg.K)]
Specific heat of liquid (C_{p_l})	723.14	[J/(kg.K)]
Latent heat of fusion (L)	2.508e+5	[J/kg]

Table 1: Material properties for Böhler S705 steel.

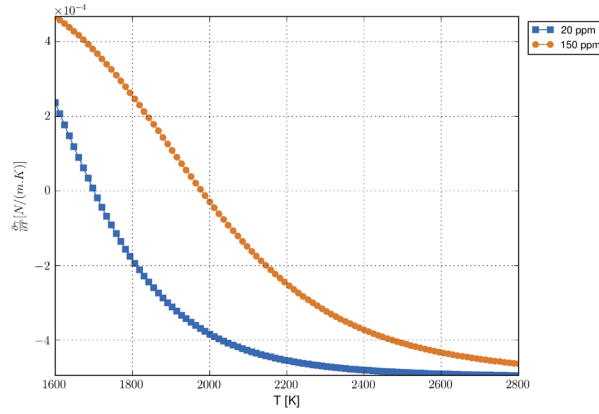


Figure 4: Surface tension derivative $\gamma'(T)$ as a function of temperature.

to decrease the computational time while keeping a good precision in the liquid metal. The discretization parameters are $\tau = 5 \cdot 10^{-5}$ [s], $h_{fe} = 5 \cdot 10^{-2}$ [mm], and $h_{cells} = 1.5 \cdot 10^{-2}$ [mm].

The laser source is modeled by a heat flux boundary condition (where heat loss is neglected). We assume that the flux distribution depends only on the distance r to the central point, and has the following profile:

$$k \frac{\partial T}{\partial n} = \begin{cases} \frac{C\eta P}{\pi R^2} & r \leq R \\ 0 & r > R \end{cases} \quad \text{on } \Gamma_t,$$

where $C = 0.2$ is a constant to account for the pseudo-2D approximation, η is the metal absorptivity, P is the laser power and R is the laser beam radius. Adiabatic boundary conditions are imposed on the rest of the boundary. The initial condition for the heat problem is the ambient temperature (no liquid region), and $f_\ell \equiv 0$ in Ω_0 .

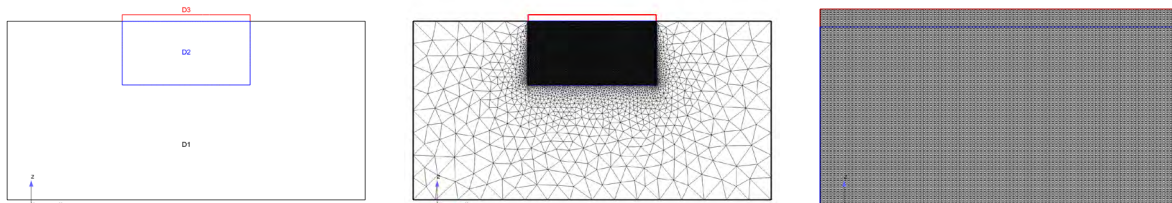


Figure 5: Static laser melting (2D sketch). Computational domains (left), finite element mesh (middle) and structured grid of small cells (right).

For the Stokes problem, we consider the gravity forces with \mathbf{g} aligned with \mathbf{e}_z . The coefficients in the Carman-Kozeny term are given by $\bar{\alpha} = 100$ and $\varepsilon = 10^{-3}$. We apply slip boundary conditions in the xz -plane (pseudo-2D), no slip boundary conditions on $\partial\Lambda$ and the natural force conditions on the free surface Γ_t . The initial condition for the velocity is the zero velocity.

The laser source induces a heating effect that creates a liquid metal zone in the center of the metal domain. Marangoni effects generate a horizontal force at the liquid metal interface and set the fluid in motion. The internal currents induce a deformation of the free surface between the liquid metal and the ambient air.

Figure 6 illustrates the solution after $t = 1$ [s], namely the liquid fraction, the velocity field, the temperature and the shape of the free surface. Numerical experiments show a strong coupling between the thermal aspects and the deformation of the free surface.

5 CONCLUSIONS AND PERSPECTIVES

A set of equations has been presented to model melting metal with a free surface as it appears in laser surface melting processes. It allows to couple incompressible fluid flow equations with the heat equation and a free surface. A numerical model combining an operator splitting algorithm and a two-grid method has been used to test the model. Preliminary results have illustrated the coupling between the different physical phenomena (Marangoni effects, free surface evolution, melting zone). In particular, results have emphasized the strong effect of the varying temperature, due to laser processing, on the free surface and metal roughness.

6 ACKNOWLEDGMENTS

The authors thank B. Meylan, K. Wassmer, P. Hoffman (EMPA), E. Boillat (EPFL), I. Calderon and J.-C. Prélaz (Unitechnologies SA) for fruitful discussions. All the computations were performed using the software `cfsFlow++` developed by EPFL and Ycoor Systems SA.

REFERENCES

- [1] E. Boillat, S. Kolossov, and R. Glardon. *Three dimensional FEM-simulation of the selective laser sintering process with locally renewed meshes and non-constant thermal con-*

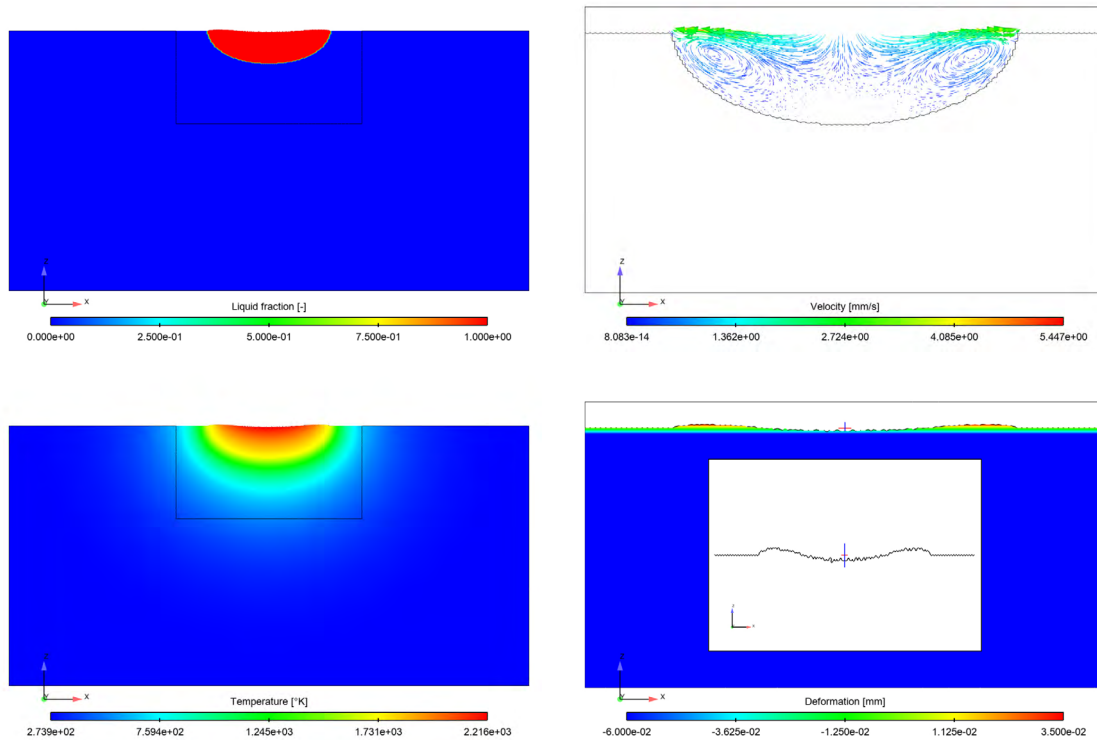


Figure 6: Static laser melting. Snapshots at time $t = 1$ [s], of the numerical approximation of: the liquid fraction f_l (top left); the velocity field \mathbf{v} (top right); the temperature T (bottom left); the deformation of the free surface Γ_f defined by the transport of φ (bottom right).

ductivity, pages 357–367. Proceedings of the 8th Solid Freeform Fabrication Symposium. 2002.

- [2] E. V. Bordatchev, A. M. K. Hafiz, and O. R. Tutunea-Fatan. Performance of laser polishing in finishing of metallic surfaces. *Int. J. Adv. Manuf. Technol.*, 73(1-4):35–52, 2014.
- [3] A. Caboussat. A numerical method for the simulation of free surface flows with surface tension. *Computers and Fluids*, 35(10):1205–1216, 2006.
- [4] A. Caboussat, M. Picasso, and J. Rappaz. Numerical simulation of free surface incompressible liquid flows surrounded by compressible gas. *J. Comput. Phys.*, 203(2):626–649, 2005.
- [5] D. Kothe, M. M. Francois, and J. M. Sicilian. Modeling of thermocapillary forces within a volume tracking algorithm. *Modeling of Casting, Welding and Advanced Solidification Processes - XI*, 2:935–942, 2006.
- [6] V. Maronnier, M. Picasso, and J. Rappaz. Numerical simulation of three dimensional free surface flows. *Int. J. Num. Meth. Fluids*, 42(7):697–716, 2003.

- [7] W. F. Noh and P. Woodward. SLIC (simple line interface calculation). *Proceedings of the Fifth International Conference on Numerical Methods in Fluid Dynamics*, 59:330–340, 1976.
- [8] W. Pitscheneder, T. Debroy, K. Mundra, and R. Ebner. Role of sulfur and processing variables on the temporal evolution of weld pool geometry during multikilowatt laser beam welding of steels. *Welding research*, 75:71–80, 03 1996.
- [9] M. Rappaz, M. Bellet, and M. Deville. *Modeling in Materials Science and Engineering*. Springer Series in Computational Mathematics. Springer Verlag, Berlin Heidelberg, 2003.
- [10] Y. Safa, M. Flueck, and J. Rappaz. Numerical simulation of thermal problems coupled with magnetohydrodynamic effects in aluminium cell. *Applied Mathematical Modelling*, 33(3):1479 – 1492, 2009.
- [11] P. Sahoo, T. Debroy, and M. J. McNallan. Surface tension of binary metal - surface active solute systems under conditions relevant to welding metallurgy. *Metallurgical Transactions B*, 19(3):483–491, 1988.
- [12] Z. S. Saldi. *Marangoni driven free surface flows in liquid weld pools*. PhD thesis, Department of MultiScale Physics, Faculty of Applied Sciences, Delft University of Technology, Delft, The Netherlands., 2012.
- [13] G. P. Sasmal and J. I. Hochstein. Marangoni convection with a curved and deforming free surface in a cavity. *Journal of Fluids Engineering*, 116(3):577–582, 1994.
- [14] A. Temmler, E. Willenborg, and K. Wissenbach. Design surfaces by laser remelting. *Physics Procedia*, 12:419–430, 2011.
- [15] A. Temmler, E. Willenborg, and K. Wissenbach. Laser polishing. *Proceedings of SPIE - The International Society for Optical Engineering*, 8243:19–, 02 2012.

FINDING OPTIMAL PARAMETER RANGES FOR LASER POWDER BED FUSION WITH PREDICTIVE MODELING AT MESOSCALE

DMITRY S. NAKAPKIN^{*,‡}, ANDREY V. ZAKIROV^{*}, SERGEI A. BELOUSOV^{*},
MARIA V. BOGDANOVA^{*}, BORIS A. KORNEEV^{*}, ANDREY E. STEPANOV^{*},
ANASTASIA Yu. PEREPELKINA^{*}, VADIM D. LEVCHENKO^{*}, BORIS V.
POTAPKIN^{*}, AND ANDREY MESHKOV[†]

^{*}Kintech Lab Ltd, 3rd Khoroshevskaya St. 12, Moscow, 123298, Russia
e-mail: info@kintechlab.com, Web page: <http://www.kintechlab.com/>

[‡] Moscow Institute of Physics and Technology, 9 Institutskiy per., Dolgoprudny, Moscow Region,
141701, Russia e-mail: info@mipt.ru - Web page: <http://mipt.ru/english>

[†] General Electric Global Research Center, 1 Research Circle, Niskayuna, New York 12309, USA
e-mail: meshkov@research.ge.com - Web page: <https://www.ge.com/research/>

Key words: Additive Manufacturing, Selective Laser Melting, 3D Mesoscale Modelling, Lattice Boltzmann Method, High-performance computing, Process Map

Abstract. We present the results of a 3D modeling of the laser powder bed fusion process on the mesoscale level with an advanced multiphysical numerical tool. High-performance simulation allowed to conduct a vast parametric study. Thus, the model has been extensively verified against experimental results in a large parameter range, and, further, it has been used to construct detailed process maps in the range not covered by the available experimental data.

The analysis of the results that were obtained in the model along with the data in the published research allowed to propose the quantitative criteria for determining the behavior of the track formation. The key phenomena that affect this behavior have been studied. We conclude that the productivity limit that arises with the proportional increase in scanning speed and laser beam power is caused by the spatter ejection. The sensitivity analysis shows that the transition to the spattering regime is caused by the overheating of the melt pool surface layer, and, consequently, the development of the surface instability. The instability development is assumed to be due to the fact that the recoil pressure becomes much higher in comparison with the surface tension.

1 INTRODUCTION

Despite the fact that the Additive Manufacturing (AM) with Laser Powder Bed Fusion (LPBF) is a widely spread and well-established practice, its further acceptance is limited by a number of issues, that have to be overcome in the nearest future. First, the speed of manufacturing is currently quite low, and the search for the methods to increase it is a relevant task in contemporary research. This increase leads to an increase in productivity, and, as a

consequence, to the decrease in cost and broadening of the applicability range. Second, manufacturing of parts with high quality, that is, with low porosity, high surface quality, durability, and a desired material structure, is still an issue as well. The quality of the parts manufactured by the LPBF process is determined by many factors, including the scanning strategy, laser beam parameters (power, spot shape, intensity distribution), and powder properties. Many of these parameters may be varied during the manufacturing process to adapt to the change of the melting conditions.

In light of the above, the trial and error approach to the increase of productivity while maintaining high product quality is a complex and costly task. That is why the predictive modelling at the finest possible level can be applied to both help with the experiments and to understand the phenomena that affect the manufacturing process to guide the experts in the design of the AM machines.

1.1 Product quality

The LPBF process is complex as it includes many physical phenomena, such as absorption and scattering of the laser beam, heat conduction, phase transitions, material evaporation, the flow of the liquid metal, recoil pressure on the melt pool surface, Marangoni convection, etc. The melt pool which appears as a result of the laser pulse interaction with the powder particles is highly unstable. In the mutual interaction of all these physical processes, some undesirable outcomes are possible, for instance, keyhole formation and balling effect.

As a result, the final part could contain defects. The search for the optimal parameters that grant a high quality of the material should take into account the whole system of the interconnected physical phenomena. At the same time, since the manufactured objects consist of many layers, which, in turn, are a series of tracks, achieving a high quality of one track is the foremost task.

Process maps, that is, 2D graphs which show the quality of the track depending on two control parameters, such as the laser beam power and scanning speed, are widely used to define the optimal parameter range for a given environment and material.

The search for optimal scanning parameters is a popular topic in contemporary research. The methods rely both on experimental data and simulation models. Since the experimental measuring technology is limited, a computer simulation may give more insight into the process of track formation and help to clarify the influence of various aspects.

In [1], the numerical investigation has proven the importance of the recoil pressure under the laser beam and its influence on the keyhole formation. In [2], the 2D numerical model based on the Lattice Boltzmann Method (LBM) is presented. The model helped to investigate the influence of the powder position [3], transition to the balling regime [2]. Further, a 3D model allowed to find optimal parameter region in terms of line energy and scanning speed [4].

The published research contains abundant experimental studies, where the optimal parameters have been found for different materials [5].

1.2 Productivity increase

The productivity of LPBF manufacturing is proportional to the layer thickness (h), scanning speed (V), and hatch spacing (d) [5].

It may be evaluated as

$$\text{Productivity} = V \times h \times d \text{ [mm}^3\text{/s]} \quad (1)$$

Multiple methods can be applied to improve the productivity. One of them is the increase in the number of lasers in the machine, which leads to a considerable cost escalation. Another method is an increase in the laser spot size. This method has been studied in [5]. However, since optimal scanning speed has decreased with the growth of the track width, the productivity did not increase in the result.

The increase of the powder layer thickness is also treated as one of the ways to a higher productivity. Indeed, the idea has been proven in experiments, where the productivity was reported to increase significantly, when the authors used higher powder layer thickness [6, 7, 8, 9].

However, under these conditions, two major defects may be formed: large lack of fusion regions, and small spherical micropores. The former may be caused by the inadequate track overlap, and the unstable scanning strategies. The scanning strategy should be adapted during the manufacturing process. At the same time, the micropore formation appears to be unavoidable. Furthermore, larger powder layer thickness affects the roughness of the manufactured part surface.

The aim of the current study is to make a contribution to the search of the optimal parameter range for the highest possible productivity. With the use of a rigorous numerical model implemented in a high-performance code, we conduct a large number of experiments, find several thresholds of the track quality transitions, and try to explain them with the theoretical study of several specific cases.

2 SIMULATION CODE DESCRIPTION

2.1 Numerical model

The numerical model is based on the extension of the lattice Boltzmann Method and includes phase transitions, thermal conductivity, volume heat generation, liquid dynamics of molten metal, evaporation of metal and recoil pressure, surface tension, Marangoni convection, wettability of a surface with melt, and movement of powder particles under the surface tension and vapor flux forces [2, 10]. The powder particle finite size is taken into account, and any random distribution in size is possible. The distribution is generated by the YADE software [11] so as to imitate the real powder size distribution and particle placement. The propagation of laser radiation with full ray tracing model includes multiple reflections.

2.2 Implementation

The model is implemented in a high-performance code `FASTLAB` for General Purpose Graphical Processing Units (GPGPUs). We have developed a novel data structure for storage of the

data and a streaming algorithm that provide highly coalesced memory transactions for the majority of streaming operations. A memory manager has been introduced to store only the fluid data in the device memory. This allows efficient storage of sparse fluid domain on GPU. The 'computational window' approach is developed so that the simulation domain tracks the melt pool region. Outside the computational window the computationally cheap procedure of heat transfer takes place. The resulting program performance rate on a typical run is about 10^8 lattice cell updates per second on a single GPU GTX1080.

3 PROBLEM STATEMENT

3.1 LPBF parameters

3.1.1 Material

The powder that was used for the numerical simulation consists of spherical particles with the properties of the stainless steel 17-4PH (17-4PH SS). The size distribution covers the sizes from 20 to 100 μm . 10th, 50th and 90th percentiles of the equivalent diameters are $D_{10} = 30.5\mu\text{m}$, $D_{50} = 40.3\mu\text{m}$, and $D_{90} = 64.1\mu\text{m}$ correspondingly. The substrate material is the same.

The material properties are summarized in Tab. 1

Table 1: Substrate material properties

Viscosity	$7.3 \cdot 10^{-7} \text{ m}^2/\text{s}$
Surface tension coefficient	1.642 N/m
Eötvös coefficient	$-2 \cdot 10^{-4} \text{ N}/(\text{m} \cdot \text{K})$
Volume heat capacity of the solid metal	$5.27 \cdot 10^6 \text{ J}/(\text{m}^3 \cdot \text{K})$
Volume heat capacity of the liquid metal	$5.27 \cdot 10^6 \text{ J}/(\text{m}^3 \cdot \text{K})$
Solidus temperature T_s	1673 K
Liquidus temperature T_l	1713 K
Temperature-dependent thermal diffusivity $\alpha(T) = \alpha_s + \alpha_T(T - T_s)$, α_s is thermal diffusivity at T_s	$7.9 \cdot 10^{-6} \text{ m}^2/\text{s}$
Linear coefficient of the temperature-dependent thermal diffusivity α_T	$3 \cdot 10^{-9} \text{ m}^2/(\text{s} \cdot \text{K})$
Wetting angle	10 degrees
Absorption coefficient for the solid metal	0.3
Absorption coefficient for the liquid metal	0.3
Recoil pressure $p(T) = 10^{(A-B/T)}$ given by Nesmeyanov model [12]	$(A, B) =$ (9.6811, 20733)

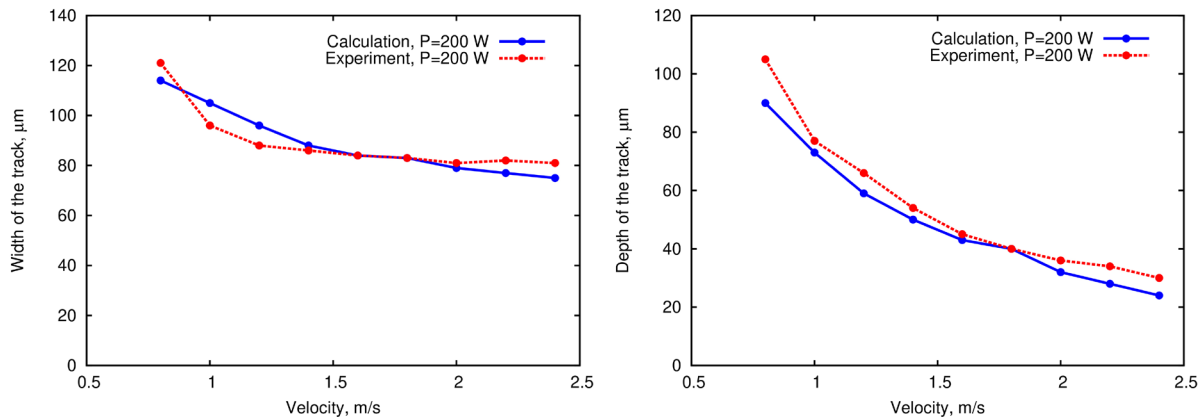


Figure 1: The track width (left) and depth (right) is shown depending on the scanning speed with fixed power $P = 200\text{W}$ and powder layer thickness of $50\mu\text{m}$

3.1.2 Simulation scan parameters

The laser beam power has been varied in the $25 \div 1000\text{ W}$ range. The scanning speed has been varied in the $60 \div 20000\text{ mm/s}$ range.

3.2 Validation

For the model validation the results from the experiments [5] were reproduced in the simulation. The material parameters were chosen based on the survey of the published data (Tab. 1). The laser power in the numerical experiment is 200 W , powder layer thickness is $50\mu\text{m}$. The results comparison is shown in Fig. 1. A good agreement has been observed. Simulations with several other input parameters have also shown good agreement.

3.3 Classification of the melting regimes

There are known quality criteria [13], which may be obtained from a single track:

- The scan track must be continuous.
- The scan track must lightly penetrate the previous layer, to accomplish a good connection of the layers.
- The scan track must be sufficiently high to build up the part.

The loss of continuity of the track is mainly described by the *the balling effect*. For some conditions, the melt pool gets sufficiently long that it breaks apart into several liquid regions, which gather into drops due to the surface tension. The drops solidify, and thus the track shape is highly irregular.

The proper remelting of the track can be prevented due to the keyholing or lack of fusion effects. If the laser power is too high and the speed is too slow, the *keyhole formation* is observed. In this regime, the laser intensively melts the material, and the material reaches the temperature

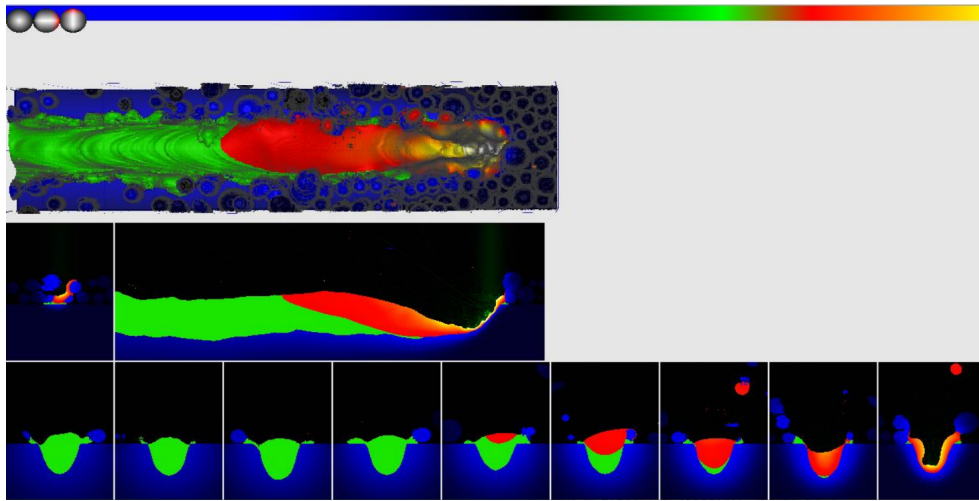


Figure 2: The visualization of the track formation during the simulation. The solid material is shown in blue, where the lighter shade shows higher temperature. The region that has been melted and solidified is shown in green. The shades of red, yellow and white show the temperature of the liquid region (melt pool)

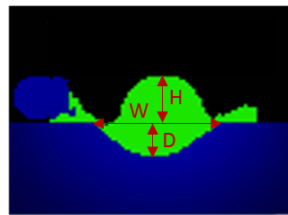


Figure 3: The track height, depth and width as extracted from the computation results.

range of rapid evaporation. The recoil pressure forms the depression in the melt pool, leading to multiple reflections of the laser beam and gives rise to a strong instability. This leads to the rapid increase in the melting depth, and the formation of pores is possible.

At some scanning parameters the *spattering* may be observed. The spatter ejection may lead to the loss of material, resulting in relatively low track height, compared with the one expected from the original powder volume, and the building of the part becomes difficult.

The simulation results include the visualization of the melt pool dynamics in 3D and in several transverse and longitudinal 2D slices (Fig. 2). After post-processing of the simulation results, we can discern such quantifiable characteristics as the height of the track H , its width W at the substrate level, and depth D (Fig. 3) at different positions of the track.

We propose to use the track parameters from the simulation to express the criteria of a good track quantitatively, as well as the criteria for *balling*, *keyholing*, *spattering* and *lack of fusion*.

First of all, for every measured track parameter X , we calculate the mean \bar{X} and the deviation

σ_X as

$$\bar{X} = \frac{\sum_{i=1}^N X_i}{N}, \quad \sigma_X = \sqrt{\frac{\sum_{i=1}^N (X_i - \bar{X})^2}{N-1}}.$$

The **balling** or scan track discontinuity is manifested in the track height H variability along the scanning direction. Numerically it can be formulated by the following expression

$$\frac{\sigma_H}{\bar{H} + \bar{D}} > \mathcal{E}_B, \quad (2)$$

where $\bar{H} + \bar{D}$ is the average total vertical size of the track, and \mathcal{E}_B is the parameter of allowed irregularity.

The **keyholing** is detected if the melt is excessively deep. We propose the condition:

$$\frac{\bar{D}}{T \cdot ff} > \mathcal{E}_K, \quad (3)$$

where T is the powder layer thickness, ff is the powder filling factor (powder tap density) and $T \cdot ff$ is the estimated molten layer thickness that is closely related to the build platform step. \mathcal{E}_K is the parameter of allowed melting.

The **spattering** is characterized by a decreased height of the track with respect to the layer thickness. We suggest to use the measure

$$\frac{\bar{H}}{T \cdot ff} < \varepsilon_S, \quad (4)$$

where ε_S is the parameter of minimum track growth ratio.

Lack of fusion indicator uses the same ratio as (3), but is formulated in terms of the minimum track depth required for proper fusion and fully dense part.

$$\frac{\bar{D}}{T \cdot ff} < \varepsilon_L. \quad (5)$$

The parameters \mathcal{E}_B , \mathcal{E}_K , ε_S , ε_L were chosen manually from an initial set of the numerical data. Then, using these values and expressions (2)–(5), we calculate a complete process map that shows how the track quality depends on a range of values of the laser power and the scanning speed.

4 SIMULATION RESULTS

4.1 Process map generation

To generate the process map, simulations with the same powder and material properties were performed on a set of experimental parameters covering wide range of laser powers and velocities. The following numerical parameters were used in all simulations: time step 12ns, mesh cell size 2 μ m. The average track length was \sim 4mm. The simulation region is a moving

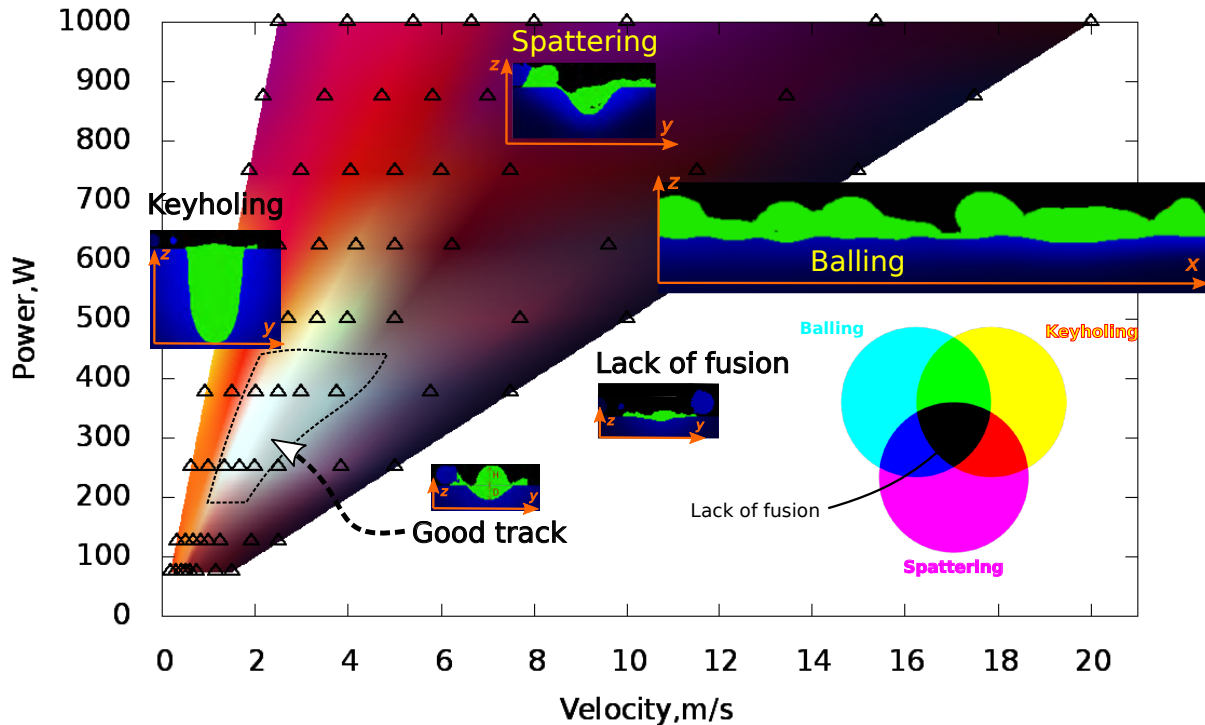


Figure 4: The process map for the 17-4 PH SS material obtained in the computer simulation. The powder layer thickness is 50 μ m. The shapes of obtained tracks are shown in the inserts, the longitudinal cross-sections were used in the track height and the related balling analysis. The color map show how the considered effects are captured by the numerical criteria (2)–(5) developed in section 3.3

window along the track, so that it covers only the region of currently liquid metal. The total number of cells in the simulation region is greater than 15 million.

We have conducted more than 100 numerical experiments (Fig. 4). One NVidia Tesla K80 GPU was used per simulation. A typical run takes about 1 day. The computations for different parameters were run in parallel on many nodes of the supercomputer at the federal collective usage center Complex for Simulation and Data Processing for Mega-science Facilities at NRC Kurchatov Institute.

The results are divided into series with a constant power to speed ratio P/V . The resulting tracks are classified according to the parameters in section 3.3. We can see that the simulation correctly predicts the optimal parameter range, and, moreover, reproduces the regimes that lead to the defect formation. Another series of calculations was carried out for the powder layer thickness of 100 μ m. Comparison of the optimal parameter ranges for the two series (Fig. 5) shows that the process parameters can be selected for the thicker powder layer such that the track quality remains high. This is consistent with the previously reported increase in the productivity

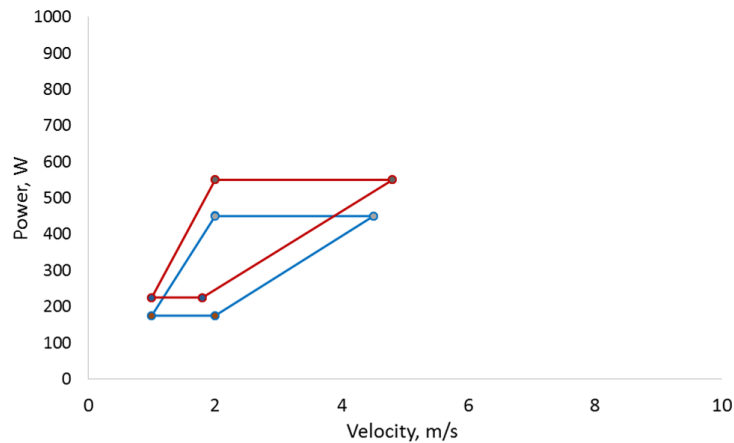


Figure 5: Optimal parameter ranges for good melting regime for two values of the powder layer thickness: 50µm (blue) and 100µm (red)

for thicker layers.

4.2 Analysis of the productivity limit

As can be seen from the simulation results, the proportional increase in P and V leads to the transition to the spatter ejection regime. Thus, we may conclude that this transition limits the productivity, which makes study of the physical effects that lead to this transition highly relevant.

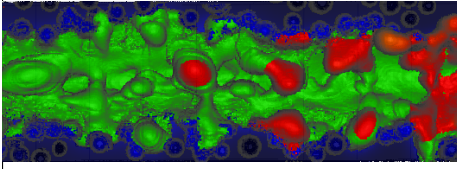
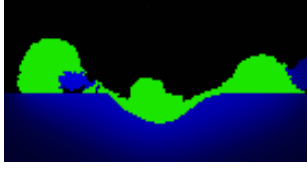
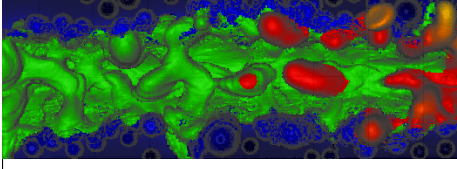
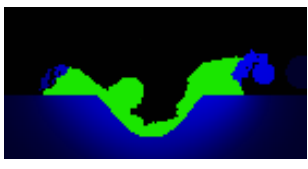
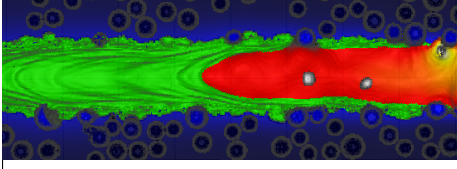
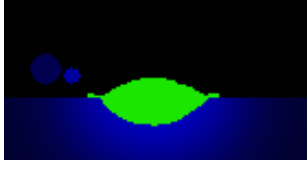
In the spattering process, the laser melts the material, which, in turn, reaches the temperatures of rapid evaporation and causes the flux of vapor near the surface. When the liquid metal elongates, it thins out and breaks up into small droplets due to surface tension. The pressure of the vapor leads to ejection of these liquid metal droplets [10].

To find the causes of the spatter ejection, the simulation model was modified to investigate the contribution of different phenomena.

For this purpose, we have chosen the calculation with $P = 750$ W, $V = 6000$ mm/s (Tab. 2). For the same parameters, we have conducted the computation after switching off the surface tension in the model, and one more simulation with the recoil pressure switched off. The analysis of the results of these numerical experiments allows pinpointing the phenomena with the strongest influence on the transition to the spattering regime. For the chosen parameter set, when the surface tension is turned off, the change in the quality of the track is negligible. When the recoil pressure is turned off in the same situation, the spattering is not observed. The obtained results demonstrate that the recoil pressure reinforces the outward spread of the melt pool and spattering of the liquid metal droplets over the sides of the scan track.

A qualitative analysis of the onset of the spattering phenomenon can be made by introducing the following two time scales [14, 3]. The characteristic time scale of the laser beam contact with the powder layer is $t_{contact} = D/V$. The characteristic time of thermal diffusion, i.e., the time required for the heat to diffuse by a distance $d = T \cdot ff$ in a material with heat conductivity k , may be estimated as $t_{diff} = d^2/k$. As the scan velocity is increased

Table 2: Calculation with modification of the model. Laser power $P = 750\text{W}$, scan speed $V = 6000\text{m/s}$.

	Top view	Cross section
Recoil pressure + Surface tension		
No surface tension		
No recoil pressure		

at a fixed P/V value, $t_{contact}$ becomes less than t_{diff} . In this regime, the heat transfer away from the laser spot is limited by diffusion. Consequently, the surface overheats and a strong evaporation takes place, which, as is shown above, is a necessary prerequisite for the spattering phenomenon.

5 CONCLUSION

In this work, we have used a numerical model to study optimal parameter ranges in the LPBF process. The model has been implemented in high-performance code for General Purpose Graphical Processing Units (GPGPUs) with special attention to minimize the overhead on memory transactions. Owing to the high performance of the code, a large number of code runs is possible to conduct extensive verification tests, study the sensitivity to the model parameters, and, most importantly, cover the large parameter ranges to predict the track quality dependence on the input parameters of the LPBF process.

The current study focused on 17-4PH stainless steel powder fusion.

We have validated the model for several sets of parameters, and the calculation results show adequate correspondence with the experimental results taken from references. A good agreement is demonstrated both for the track parameters (depth and width) and for the transitions between the track formation regimes.

We have proposed the quantitative criteria, which may be extracted by post-processing of a large number of results. With the use of these parameters, several track formation regimes have been classified, such as the optimal regime, keyhole formation, lack of fusion, balling effect, spattering. Quantitative criteria definition allows for the automatic construction of the process maps.

The dependency of the maximal productivity on the powder layer thickness have been stud-

ied. The obtained results suggest that a thicker powder layer can be used to increase the productivity, which agrees with the published research.

The mechanism of the regime transition from optimal range to the spatter ejection, which occurs with a proportional increase in laser power and the scanning speed, has been studied. The sensitivity study leads to a conclusion that the transition is observed due to the overheating of the melt pool surface and the development of the surface instability. The dominance of the recoil pressure effect over the surface tension causes this instability.

The study, described in this paper, proves the advantages of the developed simulation code for the advancement of the AM technology. The model describes the process at the mesoscopic level and captures many relevant physical phenomena. At the same time, it has been implemented for GPU with special considerations for memory and performance efficiency. Thus, multiple simulation runs are possible both on the personal workstation and on many-node supercomputers. In the latter case, the exhaustive parameter study is possible in a reasonable time frame. The details of the equations and implementation methods in the FaSTLaB code will be reported elsewhere.

ACKNOWLEDGEMENT

The computation has been carried out using computing resources of the federal collective usage center Complex for Simulation and Data Processing for Mega-science Facilities at NRC Kurchatov Institute, <http://ckp.nrcki.ru/>.

References

- [1] Saad A Khairallah and Andy Anderson. “Mesoscopic simulation model of selective laser melting of stainless steel powder”. In: *Journal of Materials Processing Technology* 214.11 (2014), pp. 2627–2636.
- [2] Carolin Körner, Elham Attar, and Peter Heinl. “Mesoscopic simulation of selective beam melting processes”. In: *Journal of Materials Processing Technology* 211.6 (2011), pp. 978–987.
- [3] Carolin Körner, Andreas Bauereiß, and Elham Attar. “Fundamental consolidation mechanisms during selective beam melting of powders”. In: *Modelling and Simulation in Materials Science and Engineering* 21.8 (2013), p. 085011.
- [4] Matthias Markl et al. “Numerical investigations on hatching process strategies for powder-bed-based additive manufacturing using an electron beam”. In: *The International Journal of Advanced Manufacturing Technology* 78.1-4 (2015), pp. 239–247.
- [5] Nkutwane Makoana et al. “Characterization of 17-4PH single tracks produced at different parametric conditions towards increased productivity of LPBF systems — the effect of laser power and spot size upscaling”. In: *Metals* 8.7 (2018), p. 475.
- [6] Xuezhi Shi et al. “Performance of high layer thickness in selective laser melting of Ti6Al4V”. In: *Materials* 9.12 (2016), p. 975.
- [7] Shuo Wang et al. “Research on high layer thickness fabricated of 316L by selective laser melting”. In: *Materials* 10.9 (2017), p. 1055.

- [8] Mingming Ma et al. “Layer thickness dependence of performance in high-power selective laser melting of 1Cr18Ni9Ti stainless steel”. In: *Journal of Materials Processing Technology* 215 (2015), pp. 142–150.
- [9] Sebastian Bremen, Wilhelm Meiners, and Andrei Diatlov. “Selective laser melting: a manufacturing technology for the future?” In: *Laser Technik Journal* 9.2 (2012), pp. 33–38.
- [10] Saad A Khairallah et al. “Laser powder-bed fusion additive manufacturing: Physics of complex melt flow and formation mechanisms of pores, spatter, and denudation zones”. In: *Acta Materialia* 108 (2016), pp. 36–45.
- [11] V. Šmilauer and B. Chareyre. “DEM formulation”. In: *Yade Documentation 2nd ed.* <http://yade-dem.org/doc/>. The Yade Project, 2015. DOI: 10.5281/zenodo.34044.
- [12] A. N. Nescmeyerov. *Vapour pressure of the elements*. USSR Academy of Sciences, 1963.
- [13] K Kempen et al. “Process optimization and microstructural analysis for selective laser melting of AlSi10Mg”. In: *Solid Freeform Fabrication Symposium*. Vol. 22. 2011, pp. 484–495.
- [14] Alexander M Rubenchik, Wayne E King, and Sheldon S Wu. “Scaling laws for the additive manufacturing”. In: *Journal of Materials Processing Technology* 257 (2018), pp. 234–243.

PARTICLE SCALE NUMERICAL MODELLING OF HEAT TRANSFER AND MELT POOL DYNAMICS IN SELECTIVE LASER MELTING

ERLEI LI, RUIPING ZOU, AIBING YU, ZONGYAN ZHOU*

ARC Research Hub for Computational Particle Technology, Department of Chemical Engineering,
Monash University, Clayton, VIC 3800, Australia
email: zongyan.zhou@monash.edu, www.monash.edu/comparticletech

Key words: Selective Laser Melting, Additive Manufacturing, Powder Scale Modelling, Thermal Multiphase Flow and Solidification, Fresnel Reflection

Abstract. Selective laser melting (SLM), with the advantages in producing complex geometry, is becoming one of the most promising additive manufacturing (AM) technologies [1]. In order to understand the multiple physical phenomena which is crucial for successful manufacturing during SLM process, different computational models that are less expensive but challenging compared with experiments and real-time monitor technologies have been developed in the past years. In order to investigate particle scale thermal-physical phenomena in SLM process, a three-dimensional model considering Fresnel reflection is developed to and the volume of fluid approach is used to track melting and solidification phenomena. Numerical results show that the melt track is broken into several regions to minimize surface energy because of surface tension. The molten liquid tends to flow outwards from the laser spot caused by Marangoni effects. The solidified surface of multiple particle diameter powders is much rougher compared with powder bed with layer thickness of one particle diameter. The developed model provides a comprehensive understanding about physical phenomena during SLM process.

1 INTRODUCTION

As an advanced additive manufacturing (AM) technology, selective laser melting (SLM) is becoming more and more attractive in recent years. During SLM processing, a laser beam energy is absorbed at the surface of powders which is deposited as one layer before laser scanning and deep penetration occurs due to multiple reflections. The adsorbed energy is further distributed into the powder bed because of thermal conduction. After melting and consideration of the material, the temperature decreases and material solidifies. Once the laser scanning is completed, a new powder layer is applied and the process restarts until acquiring desired components [1]. SLM can manufacture complex geometry and reduce production process time and costs, which has been adopted in various industries such as aerospace, biomedical and automotive [2-4]. However, SLM technology is faced with complex process which involves numerous input parameters, such as powder bed layer thickness, particles distribution, laser power, scanning method and so on, and quality issues including defects, such as porosity, low surface finish quality and high residual stresses [5-7]. Experiments and numerical simulations on SLM process have been carried by many researchers to improve manufacturing quality. Conducting experiments to investigate input parameters on SLM process can be time-consuming and expensive, and it is difficult to get real-time information, such as porosity generation, melting process and melt pool flow behaviour. Therefore, computational models have been developed in the past years. Tan et al. [8] studied effects of laser power and scanning speed on melt pool characteristics and found that laser power has a dominant influence on melt pool size. Saad A. et al. [9] established a powder-scale model and studied the porosity generation mechanism. They explained how three kinds of pore defects were generated and discussed how to avoid defects. However, energy reflection effect on the

keyhole surface during SLM process is rarely mentioned, which will result in an increase of laser beam energy absorption portion and a deeper penetration in powder bed [10]. It works like that laser beam energy coming from the gas to the solid will be reflected back to the gas and transmitted on to the solid when the keyhole surface is generated, and the adsorbed energy portion of laser beam will increase dramatically due to multiple reflections.

In this paper, a three-dimensional model is developed to investigate particle scale heat transfer and melt pool dynamics during SLM process. The volume of fluid approach is used to track melting and solidification phenomena when laser interacts with powders. The Fresnel reflection and transmission model are implemented to trace the laser ray. Powder bed with thickness of one and multiple particle diameter are simulated. This current study provides a comprehensive understanding about thermal-physical phenomena during SLM process.

2 MODELLING METHOD

In order to simulate multiphase thermal flow during SLM process, the volume of fluid (VOF) approach is employed in this paper, which is based on an open source code OpenFOAM[®]. In the simulation, physical properties of stainless steels type 316L, such as density, specific heat capacity, dynamic viscosity and thermal conductivity, are weighted by volume fraction of different phases.

For powder bed with thickness of one particle diameter, the 3D computation domain is $300 \times 140 \times 150 \mu\text{m}^3$, which consists of a $70\text{-}\mu\text{m}$ tall substrate, a $20\text{-}\mu\text{m}$ tall powder bed, a $60\text{-}\mu\text{m}$ tall gas region. For powder bed with thickness of multiple particle diameter, the analytical computation domain is $300 \times 140 \times 320 \mu\text{m}^3$, which consists of a $70\text{-}\mu\text{m}$ tall substrate, a $60\text{-}\mu\text{m}$ tall powder bed, a $190\text{-}\mu\text{m}$ tall gas region, as shown in Figure 1. The simulation domain meshed with a size of $2 \times 2 \times 2 \mu\text{m}^3$ and the grid size is $2 \times 2 \times 1 \mu\text{m}^3$ for powder bed region which provide convergent computational results. The time step is 10^{-8} s to satisfy the CFL condition. Thermophysical properties of material 316L [11] and laser beam parameters in simulation are listed in Table 1.

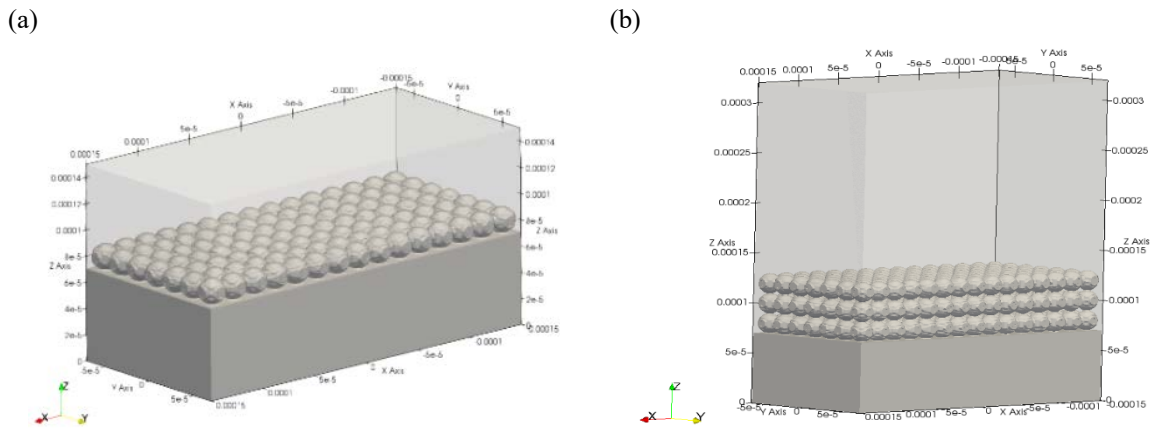


Figure 1: Computational domain: (a) powder bed with layer thickness of one particle diameter, and (b) powder bed with layer thickness of multiple particle diameter

2.1 Volume of fluid equation

The VOF equation is written as

$$\frac{\partial \alpha}{\partial t} + \nabla \cdot (\alpha \mathbf{U}) = 0 \quad (1)$$

where α ($0 \leq \alpha \leq 1$) represents volume fraction, t is time, \mathbf{U} is the velocity.

2.2 Continuity equation

The fluid flow in the simulation is assumed to be incompressible and therefore the continuity equation is expressed as

$$\nabla \cdot \mathbf{U} = 0 \quad (2)$$

Table 1: Parameters used in simulation

Parameters	Values
Density of solid	8084 kg m ⁻³
Density of liquid	7433 kg m ⁻³
Specific heat capacity of solid	462 J kg ⁻¹ K ⁻¹
Specific heat capacity of liquid	775 J kg ⁻¹ K ⁻¹
Thermal conductivity of solid	9.25 W m ⁻¹ K ⁻¹
Thermal conductivity of liquid	12.41 W m ⁻¹ K ⁻¹
Dynamic viscosity	0.0015 kg m ⁻¹ s ⁻¹
Latent heat	2.7×10 ⁶ J kg ⁻¹
Liquidus temperature	1658 K
Solidus temperature	1723 K
Surface tension coefficient	1.6 kg s ⁻²
Temperature coefficient of surface tension	8×10 ⁻⁴ kg s ⁻² K ⁻¹
Convective heat transfer coefficient	80 W m ⁻² K ⁻¹
Laser radius	1×10 ⁻⁵ m
Laser power	100 W
Laser scanning velocity	1.0 m s ⁻¹
Laser absorptivity	0.3

2.3 Momentum equation

Source term associated with liquid friction for meshy zone, surface tension and Marangoni force are considered in the following momentum conservation

$$\frac{\partial(\rho\mathbf{U})}{\partial t} + \nabla \cdot (\rho\mathbf{U}\mathbf{U}) = -\nabla p + \rho\mathbf{g} + \nabla \cdot (\mu(\nabla\mathbf{U} + \nabla\mathbf{U}^T)) \quad (3)$$

$$+ C \frac{(1-\lambda)^2}{\lambda^3 + a} \mathbf{U} + \sigma\kappa\nabla\alpha + \frac{d\sigma}{dT} (\nabla T - \mathbf{n}(\mathbf{n} \cdot \nabla T))\nabla\alpha$$

where ρ is density, p is pressure, \mathbf{g} is the gravity acceleration, μ is dynamic viscosity, C is a constant permeability coefficient, λ is liquid friction, a is a small value to avoid division by zero, σ is the surface tension coefficient, $\kappa = -\nabla \cdot \mathbf{n}$ is curvature at the metal and gas interface, $\mathbf{n} = \nabla\alpha/|\nabla\alpha|$ is the interface unit normal vector. The last source term in Eq. (3) is Marangoni convection, where $d\sigma/dT$, T and ∇T represent temperature coefficient of surface tension, temperature and temperature gradient respectively.

2.4 Energy equation

For the conservation of energy, the following equation in which latent heat of fusion, input energy from laser, convective heat transfer and radiative heat transfer are taken into consideration is given by

$$\frac{\partial(\rho C_p T)}{\partial t} + \nabla \cdot (\rho C_p T \mathbf{U}) = \nabla \cdot (k \nabla T) - L \left(\frac{\partial(\rho \lambda)}{\partial t} + \nabla \cdot (\rho \lambda \mathbf{U}) \right) \quad (4)$$

$$+ |\nabla \alpha| \left(F_q - h_c (T - T_{ref}) - \sigma_{sb} \varepsilon (T^4 - T_{ref}^4) \right)$$

Where C_p represents specific heat capacity, k denotes thermal conductivity, L is the latent heat of fusion, F_q is laser beam energy considering the Fresnel reflection, h_c is the convective heat transfer coefficient, T_{ref} is the reference temperature, σ_{sb} is the Stefan-Boltzmann constant, ε is emissivity.

A Gaussian distribution laser energy is employed

$$q = \frac{2\eta P}{\pi r^2} \exp\left(\frac{-2(x - vt - x_0)^2 + (y - y_0)^2}{r^2}\right) \quad (5)$$

where η is adsorption coefficient, P is the laser power, r is laser beam radius, x and y are coordinates of laser beam centre, v is laser beam scanning velocity, (x_0, y_0) is the beginning coordinate of the laser.

For the Fresnel reflection and transmission, the reflectance R [10] at the molten material surface is given as follows

$$R = \frac{1}{2} \left(\frac{1 + (1 - \varepsilon \cos \theta)^2}{1 + (1 + \varepsilon \cos \theta)^2} + \frac{\varepsilon^2 - 2\varepsilon \cos \theta + 2 \cos^2 \theta}{\varepsilon^2 + 2\varepsilon \cos \theta + 2 \cos^2 \theta} \right) \quad (6)$$

and the transmittance T will be $1-R$, where ε is related to the electrical conductance per unit depth of metal and its value is 0.25 in this paper, θ is the angle that the incident rays makes to the normal of the interface.

3 RESULTS AND DISCUSSION

3.1 Powders modelling with layer thickness of one particle diameter

To understand particle scale interaction between laser and powders, melt pool dynamics and melting and consideration phenomena during SLM process, single-track on layer thickness of one particle diameter simulation has been carried out.

As shown in Fig. 2, the laser scanning direction is along negative x axis and a continues track is generated. Fig. 2(a) displays the melt pool region where powders are melted due to heat energy from laser beam. Once laser beam moves forwards, temperature shown in Fig. 2(b) decreases and the rear melted liquid solidifies with a volume shrinkage. It can be seen from Fig. 2(a) and Fig. 2(b) that the melt track is broken into different regions to minimize surface energy because of surface tension, which is reminiscent of the Plateau-Rayleigh instability that explains why and how fluid breaks up into smaller packets. Similar results were observed in SLM experiments [12]. It can be noticed that the keyhole is created where Fresnel reflection and transmission occurs and a depression zone is shown in Fig. 2(c) and Fig. 2(d).

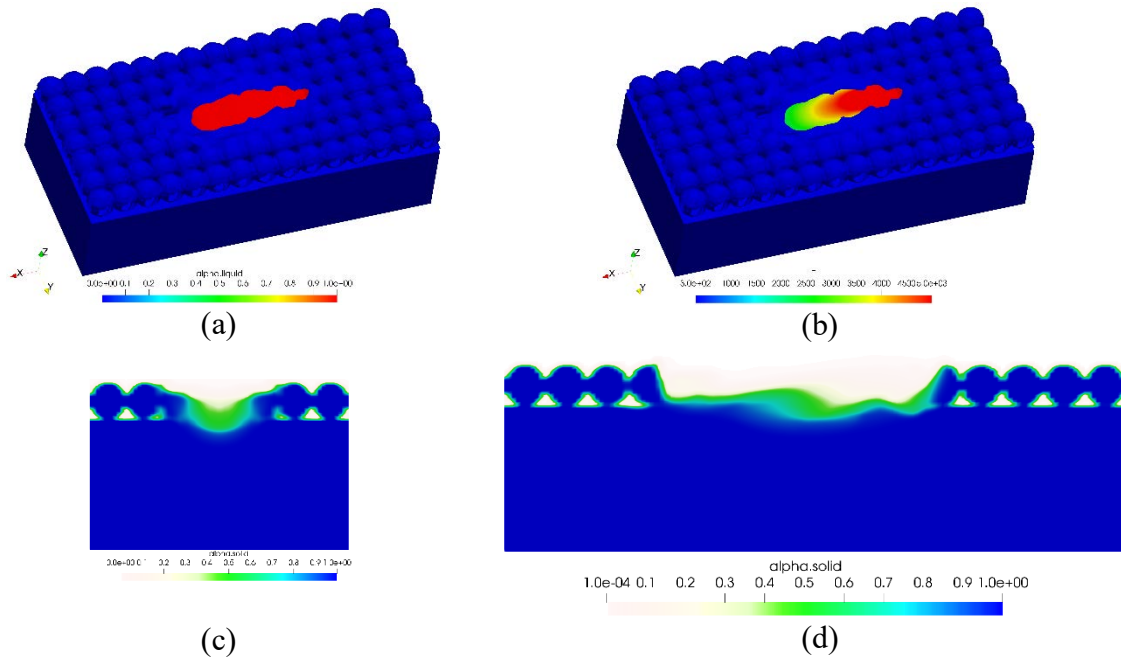


Figure 2: Simulation of single-track at 120 μs : (a) melt pool region, (b) temperature distribution, (c) 2D slice along the YZ plane ($x=0 \mu\text{m}$) and (d) 2D slice along the XZ plane ($y=0 \mu\text{m}$)

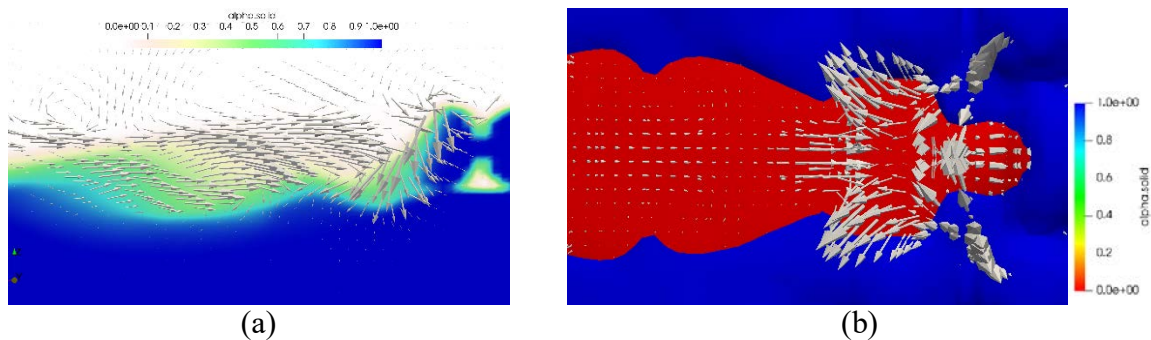


Figure 3: Melt pool dynamics at 120 μs : (a) partial 2D slice along the XZ plane ($y=0 \mu\text{m}$), (b) top view of partial melt pool

Fig. 3 shows the melt pool dynamics, and it can be seen that molten track tends to flow outwards from the laser spot, which is because larger temperature gradient is formed around the laser centre, thus Marangoni force drives the molten material to flow away from the laser spot. As laser beam moves forwards, the velocity vector of molten metal near the laser spot is downward along the interface between gas and metal and molten metal liquid flows to the depression region. Such simulation results correspond well with Wu et al.'s work [13].

3.2 Powders modelling with layer thickness of multiple particle diameter

Single-track on layer thickness of multiple particle diameter is simulated to understand physical phenomena in SLM process so as to be more practical.

Similar to one particle diameter simulation results, as shown in Fig. 4, melting occurs when heat energy is added to the system, and molten material solidifies once laser beam spot moves forwards to another position. Also, different regions of melt pool are generated due to surface tension. While the solidified track surface is rougher compared with small thickness seen from Fig. 4(a), which is due to limited laser power and some powders are not fully molten. Similar conclusions can be drawn from Qiu et al.'s experiments [14]. It can be seen from Fig. 4(b) that molten material located in the front of molten pool region has a down velocity and it flows to

collapsed zone, which raises heat and mass transport. Deep penetration occurs due to multiple reflections and thermal conduction; thus, a deeper keyhole is formed shown in Fig. 4(c) and Fig. 4(d). In order to provide the high surface quality for next packing process, effect of laser power, laser scanning speed and laser radius on one-layer and multi-layers powders should to be investigated in the future.

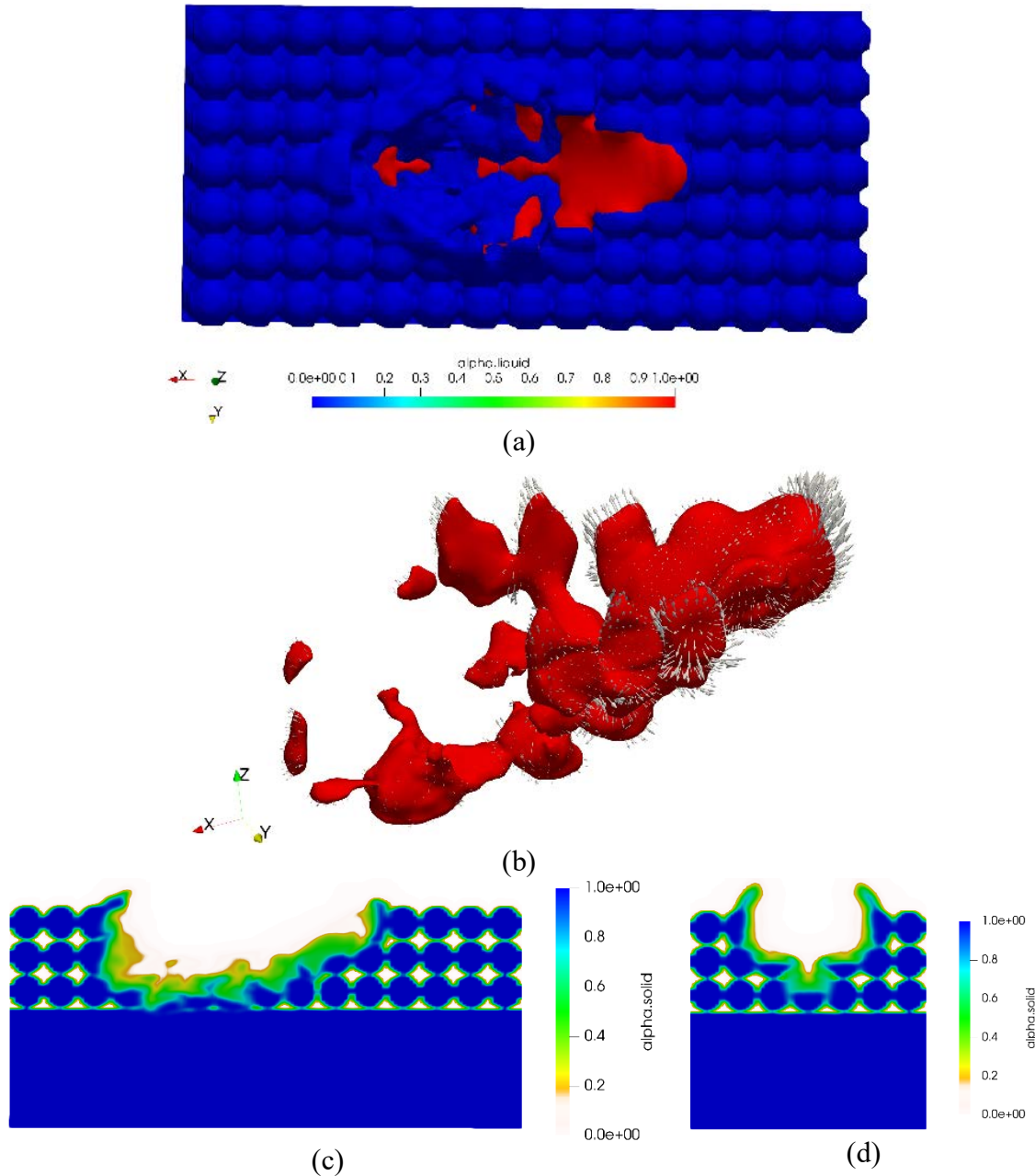


Figure 4: Simulation of single-track at 120 μ s: (a) top view with melt region, (b) melt pool region with velocity distribution (c) 2D slice along the XZ plane ($y=0 \mu\text{m}$) with velocity vectors and (d) 2D slice along the YZ plane ($x=0 \mu\text{m}$)

4 CONCLUSIONS

In this paper, a computational model is developed using OpenFOAM open source codes to investigate multiphase thermal flow in the SLM process. Powder bed with thickness of one and multiple particle diameter simulations have been undertaken. During SLM process, the material melts and forms a melt pool. Once laser beam moves forwards, the temperature decreases and

rear melted material solidifies. It can be concluded that different regions of melt pool are generated due to surface tension. Marangoni force caused by larger temperature gradient drives the molten liquid to flow away from the laser spot. For the larger thickness of multiple particle diameter powders bed, the rougher solidified surface is formed due to limited laser energy and partly melted metal.

REFERENCES

- [1] Markl, M. and Körner, C., 2016. Multiscale modeling of powder bed-based additive manufacturing. *Annual Review of Materials Research*, 46, pp.93-123.
- [2] Antonysamy, A. A. (2012). Microstructure, texture and mechanical property evolution during additive manufacturing of Ti6Al4V alloy for aerospace applications (Doctoral dissertation, The University of Manchester (United Kingdom)).
- [3] Gowers, S.A., Curto, V.F., Seneci, C.A., Wang, C., Anastasova, S., Vadgama, P., Yang, G.Z. and Boutelle, M.G., 2015. 3D printed microfluidic device with integrated biosensors for online analysis of subcutaneous human microdialysate. *Analytical chemistry*, 87(15), pp.7763-7770.
- [4] Lim, C.W.J., Le, K.Q., Lu, Q. and Wong, C.H., 2016. An overview of 3-D printing in manufacturing, aerospace, and automotive industries. *IEEE Potentials*, 35(4), pp.18-22.
- [5] Liu, Y.J., Li, S.J., Wang, H.L., Hou, W.T., Hao, Y.L., Yang, R., Sercombe, T.B. and Zhang, L.C., 2016. Microstructure, defects and mechanical behavior of beta-type titanium porous structures manufactured by electron beam melting and selective laser melting. *Acta Materialia*, 113, pp.56-67.
- [6] Fatemi, S.A., Ashany, J.Z., Aghchai, A.J. and Abolghasemi, A., 2017. Experimental investigation of process parameters on layer thickness and density in direct metal laser sintering: a response surface methodology approach. *Virtual and Physical Prototyping*, 12(2), pp.133-140.
- [7] AlMangour, B., Grzesiak, D., Borkar, T. and Yang, J.M., 2018. Densification behavior, microstructural evolution, and mechanical properties of TiC/316L stainless steel nanocomposites fabricated by selective laser melting. *Materials & Design*, 138, pp.119-128.
- [8] Tan, J.L., Tang, C. and Wong, C.H., 2018. Study and modeling of melt pool evolution in selective laser melting process of SS316L. *MRS Communications*, 8(3), pp.1178-1183.
- [9] Khairallah, S.A., Anderson, A.T., Rubenchik, A. and King, W.E., 2016. Laser powder-bed fusion additive manufacturing: Physics of complex melt flow and formation mechanisms of pores, spatter, and denudation zones. *Acta Materialia*, 108, pp.36-45.
- [10] Cho, J.H. and Na, S.J., 2006. Implementation of real-time multiple reflection and Fresnel absorption of laser beam in keyhole. *Journal of Physics D: Applied Physics*, 39(24), p.5372.
- [11] Kim, C.S., 1975. Thermophysical properties of stainless steels (No. ANL-75-55). Argonne National Lab., III (USA).
- [12] Yadroitsev, I., Gusarov, A., Yadroitsava, I. and Smurov, I., 2010. Single track formation in selective laser melting of metal powders. *Journal of Materials Processing Technology*, 210(12), pp.1624-1631.
- [13] Wu, D., Hua, X., Li, F. and Huang, L., 2017. Understanding of spatter formation in fiber laser welding of 5083 aluminum alloy. *International Journal of Heat and Mass Transfer*, 113, pp.730-740.
- [14] Qiu, C., Panwisawas, C., Ward, M., Basoalto, H.C., Brooks, J.W. and Attallah, M.M., 2015. On the role of melt flow into the surface structure and porosity development during selective laser melting. *Acta Materialia*, 96, pp.72-79.

PARTICLE-BASED SIMULATIONS AND DIMENSIONAL ANALYSIS OF SELECTIVE LASER SINTERING OF PA12 POWDER

Sim-AM 2019

CLAAS BIERWISCH^{*}, SHOYA MOHSENI-MOFIDI^{*}, BASTIEN DIETEMANN^{*},
JOHANNES RUDLOFF[†], STÉPHANIE BAUMANN[†], KEVIN POPP[†]
AND MARIELOUISE LANG[†]

^{*} Fraunhofer IWM
Wöhlerstr. 11, 79108 Freiburg, Germany
e-mail: claas.bierwisch@iwm.fraunhofer.de, www.simpartix.com

[†] SKZ – German Plastics Center
Friedrich-Bergius-Ring 22, 97076 Würzburg, Germany
e-mail: j.rudloff@skz.de, www.skz.de

Key words: Melt track, grain scale, mesh free simulation, smoothed particle hydrodynamics, experimental validation, dimensionless numbers

Abstract. A numerical model based on the Smoothed Particle Hydrodynamics (SPH) method is developed for 2D and 3D simulations of the laser sintering process of polyamide 12 (PA12) powder on the grain scale. Melt track simulations yield detailed insights in the visco-thermal dynamics of the process including the porosity evolution. The simulations are validated by measurements of the transient surface temperature. A dimensional analysis of the process allows for quantification of the importance of all involved physical mechanisms and predicts the magnitudes of the observable physical quantities with good accuracy.

1 INTRODUCTION

Early sintering models are provided by Frenkel [1] and Mackenzie & Shuttleworth [2] describing the behavior of metal particles. In both models the material properties particle diameter, viscosity and surface tension are used to quantify differences in the sintering behavior. The model of Frenkel is later used for the rotation sintering process and modified for the inclusion of viscoelastic effects [3]. The early models are modified and used by Schultz to describe the laser sintering (LS) process of polycarbonate and polyethylene-oxide [4]. Schultz validates his models with a self-built LS machine and found a basic agreement between calculated and measured part densities. Riedlbauer et al. model the heat transfer in laser sintering of PA12 using a homogenized finite element analysis [5]. They predict the width and depth of a melt track and find good agreement with experimental measurements. Wohlgemuth & Alig study the physical modelling of the additive sintering processes for polymer materials including viscoelasticity [6]. All models taking viscoelastic effects into account incorporate a relaxation time which can be measured in a rheometer. Osmanlic et al. develop a ray tracing model for the laser beam absorption in the powder bed [7]. They find that the effective laser penetration depth in the powder can be lower than in bulk material.

Mokrane et al. provide homogenized simulations of the temperature field of a series of melt tracks [8]. They also predict spatial distributions of the porosity and of the degree of crystallization, however, without experimental validation. Balemans et al. model the laser sintering of two particles with high spatial resolution in 2D [9]. They also carry out a dimensional analysis of the system and vary several process parameters such as, e.g., laser power or ambient temperature to study the influence on the sintering behavior.

In summary within our brief survey, several works [3], [4], [6] show that the models by Frenkel or Mackenzie & Shuttleworth can be used to describe the influence of some relevant material parameters on the sintering process. But to use the models for accelerated material development, further work including more sophisticated material models is necessary. Especially, including process parameters [5], [9], considering the granular nature of the powder bed [7] and linking the model predictions to part quality [8] is required.

The present work introduces a mess-free simulation method to model the laser sintering process of PA12 on the length scale of the melt track while representing each powder particle individually. The simulations are validated by measurements of the surface temperature. A dimensional analysis sheds light on the fundamental hierarchy of time scales inherent to the laser sintering process of polymers.

2 NUMERICAL METHODS

A cornerstone for the numerical simulations within this study is laid by implementing an implicit solver for the time integration of the highly viscous liquid polymers. The solver is based on the scheme presented in [10] and is now fully integrated in our simulation code. This enables transient simulations of several seconds real time flow of polymers with a viscosity in the order of several kPa s. The required computational time is of the order of hours to days. However, without the new solver technique the computational time would have been of the order of months to years.

The present work focuses on the coupled visco-thermal melt pool dynamics which is simulated using the SPH method [11]. To do so, the continuity equation,

$$\frac{D\rho}{Dt} = -\rho \nabla \cdot \mathbf{u}, \quad (1)$$

as well as the Navier-Stokes momentum equation,

$$\rho \frac{D\mathbf{u}}{Dt} = -\nabla p + \mu \nabla^2 \mathbf{u} + \mathbf{f}_\Sigma + \rho \mathbf{g}, \quad (2)$$

are solved. Here, \mathbf{u} is the velocity, ρ is the mass density, p is the hydrostatic pressure, μ is the dynamic viscosity, \mathbf{f}_Σ is the volumetric surface tension force and $\mathbf{g} = -g\hat{\mathbf{z}}$ is the acceleration due to gravity. Bold face symbols denote vector quantities.

The hydrostatic pressure is given by an equation of state,

$$p = \rho_0 s^2 \left[\frac{1}{\gamma} \left[\left(\frac{\rho}{\rho_0} \right)^\gamma - 1 \right] + d \beta (T - T_0) \right], \quad (3)$$

where ρ_0 is the equilibrium bulk density, s is the speed of sound, γ is the isentropic exponent, d is the number of spatial dimensions, and β is the linear thermal expansion coefficient, T is the temperature and T_0 is the ambient temperature.

The melt rheology is modeled by means of a temperature-dependent viscosity. The viscosity changes depending on the state of matter of the material. Here, we differentiate three states: fully solid (S) below the solidus temperature T_S , fully liquid (L) above the liquidus temperature T_L and an intermediate state in between,

$$\mu(T) = \begin{cases} \mu_L \exp\left[\frac{E_a}{R}\left(\frac{1}{T} - \frac{1}{T_L}\right)\right], & T \geq T_L, \\ \mu_S + (\mu_L - \mu_S) \frac{T - T_S}{T_L - T_S}, & T_S < T < T_L, \\ \infty, & T \leq T_S. \end{cases} \quad (4)$$

Above the liquidus temperature the viscosity is modeled by an Arrhenius law using the activation energy E_a and the universal gas constant R . Below the solidus temperature the material is spatially fixed. The asymmetry between heating and cooling of PA12 is considered by applying an offset temperature θ to T_S and T_L if the material is cooling down,

$$T_S^{\text{cool}} = T_S - \theta, \quad T_L^{\text{cool}} = T_L - \theta. \quad (5)$$

The surface tension force,

$$\mathbf{f}_\Sigma = (-\sigma_N \kappa \mathbf{n} + \sigma_T \nabla_\Sigma T) \delta_\Sigma, \quad (6)$$

is composed of a contribution normal to and a contribution tangential to the local surface. Here, σ_N is the surface tension, κ the surface curvature and \mathbf{n} the surface unit normal vector. σ_T is the Marangoni coefficient describing the variation of surface tension with temperature and $\nabla_\Sigma T$ is the gradient of the surface temperature field. δ_Σ is a delta function marking the location of the surface in space. Details of the SPH surface tension model are given in [12].

The balance equation for the thermal energy per unit mass e ,

$$\rho \frac{De}{Dt} = k \nabla^2 T + 2 \mu \underline{E} : \underline{E} - \varepsilon \sigma_B (T^4 - T_0^4) \delta_\Sigma + \frac{dI}{dz} \quad (7)$$

is composed of contributions from heat conduction, viscous heating, Stefan-Boltzmann radiation and absorbed laser radiation. Here, k is the thermal conductivity, \underline{E} is the strain rate tensor, ε is the emissivity, σ_B is the Stefan-Boltzmann constant and I is the local intensity of the laser radiation.

The strain rate tensor is defined as

$$\underline{E} = \frac{1}{2} [\nabla \mathbf{u} + (\nabla \mathbf{u})^T] \quad (8)$$

where the superscript $()^T$ denotes the transposed tensor.

The absorption of the laser radiation along the vertical coordinate z is described by the Lambert-Beer law with an attenuation coefficient a ,

$$\frac{dI}{dz} = a I. \quad (9)$$

The relation between temperature T and thermal energy per unit mass e is given by the following expression which takes into account the specific heat capacity c and the latent heat of melting H ,

$$T(e) = \begin{cases} T_L + \frac{e - e_L}{c}, & e \geq e_L, \\ T_S + \frac{e - e_S}{c + \frac{H}{T_L - T_S}}, & e_S < e < e_L, \\ \frac{e}{c}, & e \leq e_S. \end{cases} \quad (10)$$

Here, $e_S = c T_S$ is the solidus thermal energy per unit mass and $e_L = c T_L + H$ is the liquidus thermal energy per unit mass.

The laser radiation is described by a Gaussian intensity profile in 2D,

$$I(x) = \frac{P}{\sqrt{2\pi} 3 w^2} \exp\left[-\frac{(x - x_0)^2}{2w^2}\right], \quad (11)$$

or in 3D,

$$I(x, y) = \frac{P}{2\pi w^2} \exp\left[-\frac{(x - x_0)^2 + (y - y_0)^2}{2w^2}\right], \quad (12)$$

with the power P , the characteristic width w and the laser spot center coordinates x_0 and y_0 .

3 RESULTS

First, laser-induced sintering simulations of two spherical particles in 3D are investigated. Second, melt track simulations of either a regular or a random particle arrangement in 2D are presented. Finally, a dimensional analysis of the process is carried out and its results are compared with the data obtained from the numerical simulations. The parameters of the simulations are summarized in Table 1.

3.1 Three-dimensional simulations of two particles

As an initial case we take a look at the laser sintering behavior of two stacked particles with a diameter of 50 μm upon a plane substrate. The simulation volume is periodic in both lateral dimensions and, thus, effectively represents two layers of particles placed on a simple cubic lattice. The laser irradiates the system from above for the duration of 50 μs and is switched off afterwards representing a scan speed in the order of a meter per second. The system has an initial temperature equal to the ambient temperature of 169 $^\circ\text{C}$ and the lower surface of the substrate is kept constantly at this value acting as a heat sink.

Figure 1 depicts the system at six distinct times which allows for following the course of the sintering process. Initially, the upper particle is rather hot with a temperature above 350 $^\circ\text{C}$ while the lower particle is roughly 80 $^\circ\text{C}$ cooler. Accordingly, the polymer viscosity of the upper particles is lower and its strain rate and velocity are higher compared to the particle below. During the first 100 ms the temperature gradient becomes smaller due to thermal diffusion while the maximum strain rate drops from about 10/s to 1/s and the maximum velocity from about 300 $\mu\text{m/s}$ to 50 $\mu\text{m/s}$. At the same time the sintering necks between the particles grow. After roughly 300 ms the vertical temperature gradient has vanished and the viscosity is around 5 kPa s throughout the system. With a strain rate of the order of 0.3/s the particles slowly continue to sinter until they form a dense volume after about 2 s.

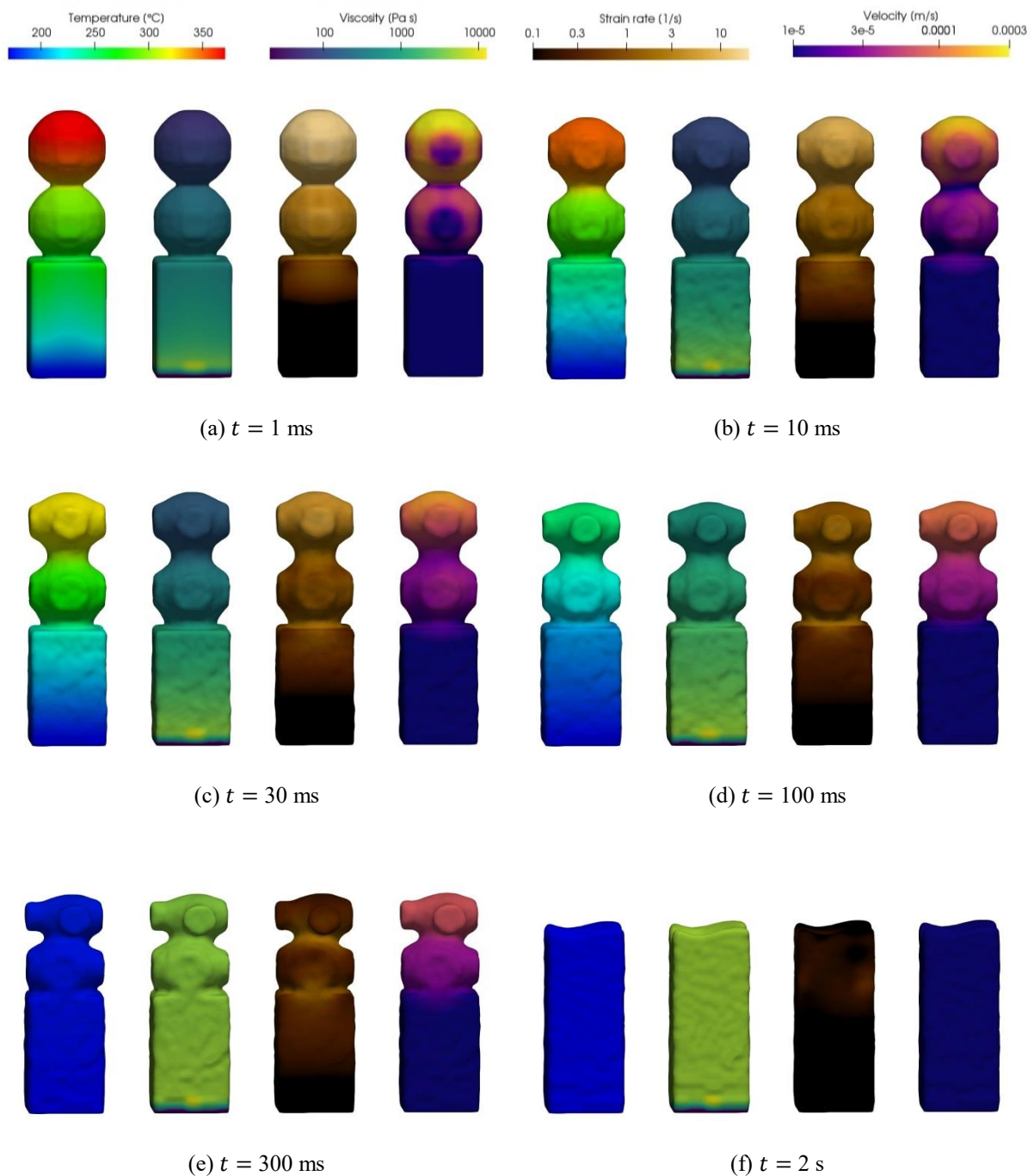


Figure 1: 3D simulation of the laser sintering of two PA12 particles on a substrate with periodic boundary conditions in both lateral directions. The subfigures (a) to (f) show the system at different times after the initial laser irradiation for $50 \mu\text{s}$. The columns in each subfigure show color-coded fields of temperature, viscosity, strain rate and velocity magnitude (from left to right).

Table 1: Simulation parameters.

Quantity	Symbol	Value
Particle radius	r	25 μm
Bulk density	ρ_0	1020 kg/m^3
Speed of sound	s	1 m/s
Isentropic exponent	γ	7
Heat capacity	c	2.7 $\text{kJ}/(\text{kg K})$
Thermal conductivity	k	0.24 $\text{W}/(\text{m K})$
Thermal expansion	β	$1.71 \cdot 10^{-4} / \text{K}$
Latent heat	H	50 kJ/kg
Attenuation coefficient	a	$1.3 \cdot 10^4 / \text{m}$
Emissivity	ε	0.5
Liquidus temperature	T_L	190 $^\circ\text{C}$
Solidus temperature	T_S	170 $^\circ\text{C}$
Offset temperature	θ	40 $^\circ\text{C}$
Activation energy	E_a	50 kJ/mol
Liquidus viscosity	μ_L	9.1 kPa s
Solidus viscosity	μ_S	15 kPa s
Surface tension	σ_N	35 mN/m
Marangoni coefficient	σ_T	$-1.2 \cdot 10^{-4} \text{N}/(\text{m K})$
Laser power	P	25 W
Laser spot diameter	$4w$	240 μm
Laser scan speed	v	3 m/s (2D)
Ambient temperature	T_0	169 $^\circ\text{C}$
Stefan-Boltzmann constant	σ_B	$5.67 \cdot 10^{-8} \text{W}/(\text{m}^2 \text{K}^4)$
Universal gas constant	R	8.31 $\text{J}/(\text{mol K})$
Gravitational acceleration	g	9.81 m/s^2
Number of dimensions	d	3 (3D); 2 (2D)
Spatial resolution	Δx	2.5 μm (3D); 5 μm (2D)
Temporal resolution	Δt	0.4 μs (3D); 0.5 μs (2D)

3.2 Two-dimensional simulations of a melt track

As a compromise between computational effort and a more realistic process scenario, the following melt track simulations are carried out using a 2D setup.

Figure 2 shows snapshots from the simulation using a 25 W laser source moving along a regular lattice of eight layers of PA12 particles with scan speed of 3 m/s. The ambient temperature is again 169 $^\circ\text{C}$. While the laser traverses the particles only marginal thermal diffusion occurs. Then, the temperature field becomes more and more homogeneous in combination with cooling from the substrate. On the largest time scale densification due to sintering of the particles takes place. Despite omitting the third dimension, all observations from the previously discussed 3D simulation still hold qualitatively and are even quantitatively rather close.

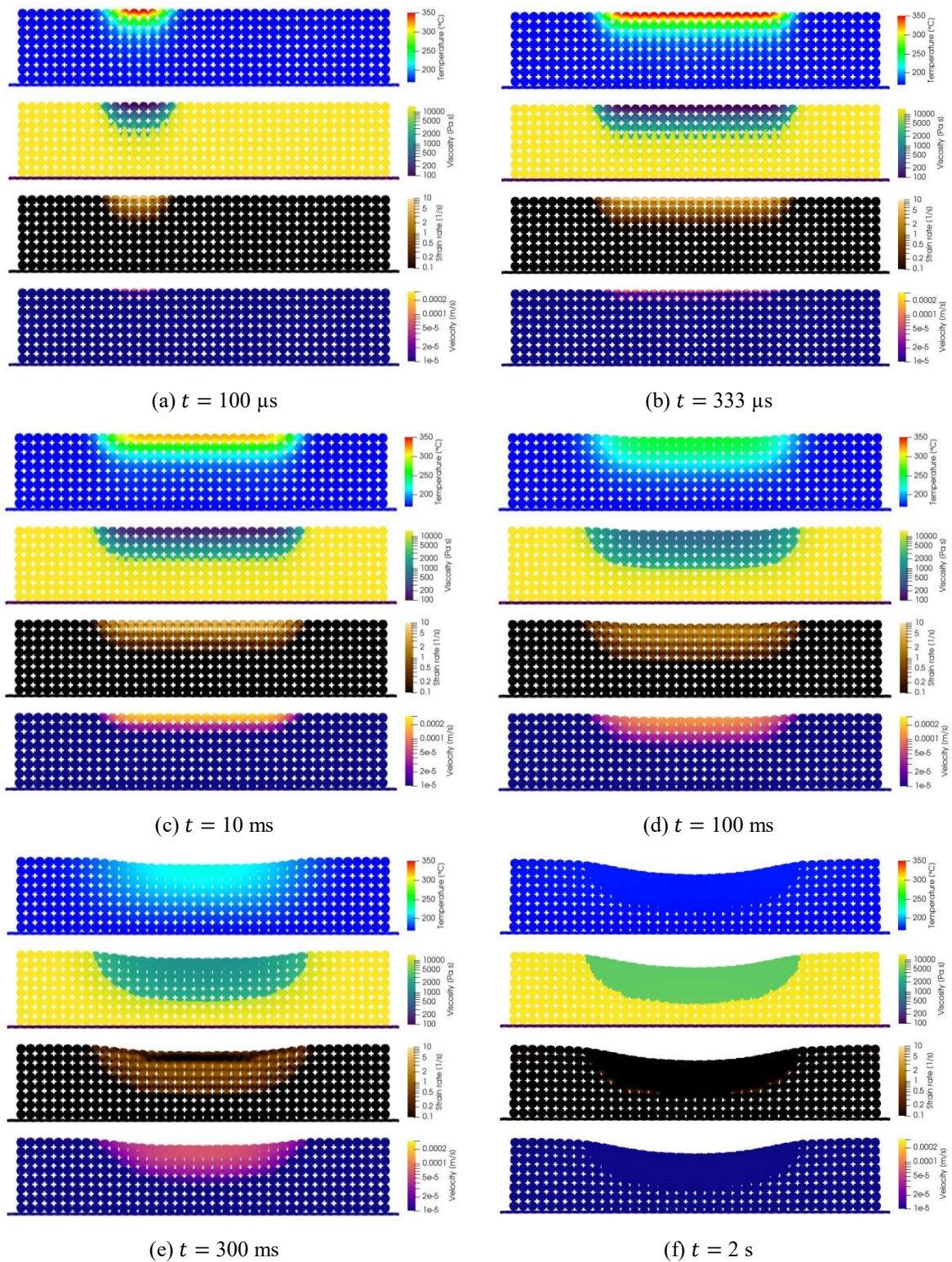


Figure 2: 2D simulations of the laser sintering of PA12 particle layers on a lattice. The subfigures (a) to (f) show the system at different times. The laser moves during the initial 333 μs and is then turned off. The rows in each subfigure show color-coded fields of temperature, viscosity, strain rate and velocity magnitude (top to bottom).

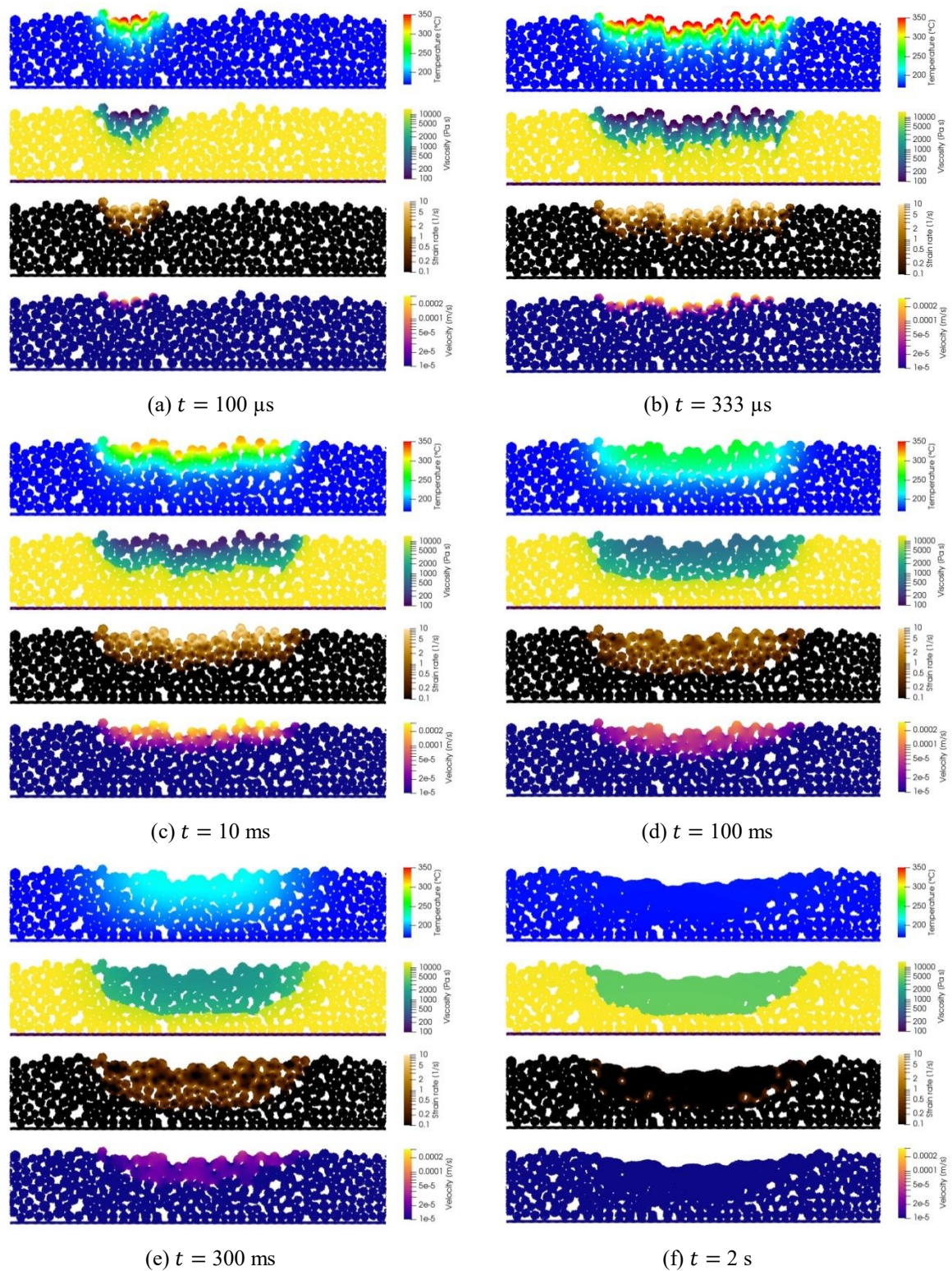


Figure 3: Like Figure 2 but for a random arrangement of PA12 particles.

In order to assess the influence of the simplified lattice structure, the 2D simulation is repeated using a random particle arrangement. Figure 3 shows the results. All of the analyzed quantities take very similar values as a function of both space and time when compared to the lattice arrangement. However, the most striking difference is the pronounced surface roughness at the final stage which can be related to the initial particle positions. Furthermore, initially large pores between the particles do not completely vanish for the random arrangement.

From the simulations it can be deduced that the process includes three time scales. First, a laser irradiation time scale of the order of tens of microseconds. Next, a thermal diffusion time scale of the order of tens of millisecond. And finally, a viscous flow time scale of the order of seconds.

3.3 Dimensional analysis

A dimensional analysis based on the material properties and process parameters listed in Table 1 is carried out to gain insights into the relative importance of the considered physical mechanisms and to obtain typical orders of magnitude of the observable physical quantities.

As a starting point, the laser absorption depth is calculated as

$$D = \frac{2}{a} \approx 150 \mu\text{m}, \quad (13)$$

yielding $D \approx 6r$ in our case which is in reasonably good agreement with the depth of increased temperature during the initial phase of the simulations.

Next, the temperature in the melt zone is estimated as

$$T_{\text{Melt}} = T_0 + \Delta T = T_0 + \frac{P}{4\rho_0 c v w D} - \frac{H}{c} \approx T_0 + 63 \text{ }^\circ\text{C} \approx 232 \text{ }^\circ\text{C} \quad (14)$$

inspired by the expression used in [9], however, also including the influence of the attenuation coefficient and the latent heat of melting.

The temperature difference ΔT allows for the definition of a typical temperature gradient,

$$\text{grad } T = \frac{\Delta T}{D} \approx 4 \cdot 10^5 \text{ K/m}. \quad (15)$$

It is now possible to identify a series of stress scales representing the different mechanisms driving the melt flow in the process. In particular, these are the surface tension stress,

$$\Sigma_N = \sigma_N \kappa = \frac{\sigma_N}{r} \approx 1400 \text{ Pa}, \quad (16)$$

the Marangoni stress,

$$\Sigma_T = -\sigma_T \text{ grad } T \approx 50 \text{ Pa}, \quad (17)$$

the thermal expansion stress,

$$\Sigma_E = \rho_0 s^2 d \beta \Delta T \approx 20 \text{ Pa}, \quad (18)$$

and the gravity stress,

$$\Sigma_G = \rho_0 g r \approx 0.3 \text{ Pa}. \quad (19)$$

A comparison of the stress scales indicates that surface tension is the main mechanism causing the flow of the molten polymer.

Furthermore, a series of time scales are relevant in the process. The laser spot traverses a particle at a time scale

$$t_{\text{Laser}} = \frac{r}{v} \approx 8 \mu\text{s}. \quad (20)$$

Heat diffuses through a particle at a time scale

$$t_{\text{Heat}} = \frac{r^2 \rho_0 c}{k} \approx 7 \text{ ms}. \quad (21)$$

Surface tension driven flow counteracted by viscosity ($\mu_{\text{Melt}} = \mu(T_{\text{Melt}}) \approx 3 \text{ kPa s}$) would occur at a time scale

$$t_{\text{Frenkel}} = \frac{\mu_{\text{Melt}}}{\sigma_N \kappa} = \frac{\mu_{\text{Melt}} r}{\sigma_N} \approx 2 \text{ s}, \quad (22)$$

while surface tension driven flow counteracted by inertia would occur at a time scale

$$t_{\text{Rayleigh}} = r \sqrt{\frac{\rho_0}{\sigma_N \kappa}} = \sqrt{\frac{\rho_0 r^3}{\sigma_N}} \approx 20 \mu\text{s}. \quad (23)$$

By dividing both surface tension time scales the Ohnesorge number is obtained,

$$\text{Oh} = \frac{t_{\text{Frenkel}}}{t_{\text{Rayleigh}}} = \frac{\mu_{\text{Melt}}}{\sqrt{\rho_0 \sigma_N} r} \approx 10^5, \quad (24)$$

which reveals that the influence of viscosity is by far stronger than the influence of inertia and, thus, the melt flow takes place at the Frenkel time scale. It is finally possible to derive a series of dimensionless scales for time, temperature, viscosity, strain rate and velocity ($u_{\text{Melt}} = r/t_{\text{Frenkel}} = \sigma_N/\mu_{\text{Melt}} \approx 10 \mu\text{m/s}$) for the thermo-viscous melt flow,

$$t^* = \frac{t}{t_{\text{Frenkel}}}, \quad (25)$$

$$T^* = \frac{T - T_0}{\Delta T}, \quad (26)$$

$$\mu^* = \frac{\mu}{\mu_{\text{Melt}}}, \quad (27)$$

$$E^* = E t_{\text{Frenkel}}, \quad (28)$$

$$u^* = \frac{u}{u_{\text{Melt}}}. \quad (29)$$

The data obtained from the 2D melt track simulations is shown in Figure 4 using both SI units and the scales derived from the dimensional analysis. It is evident that the derived scales give very good estimates for the quantities observed in the simulations.

A final validation for the accuracy of the simulations is done by comparing the temperature evolution with data obtained from an infrared camera. In the experiment a 10 mm x 10 mm monolayer is sintered while the measurement spot of the camera has a size of 0.8 mm x 0.8 mm. Although there are some differences in the curvature of the temperature transients, the agreement between simulation and experiment is quantitatively very good.

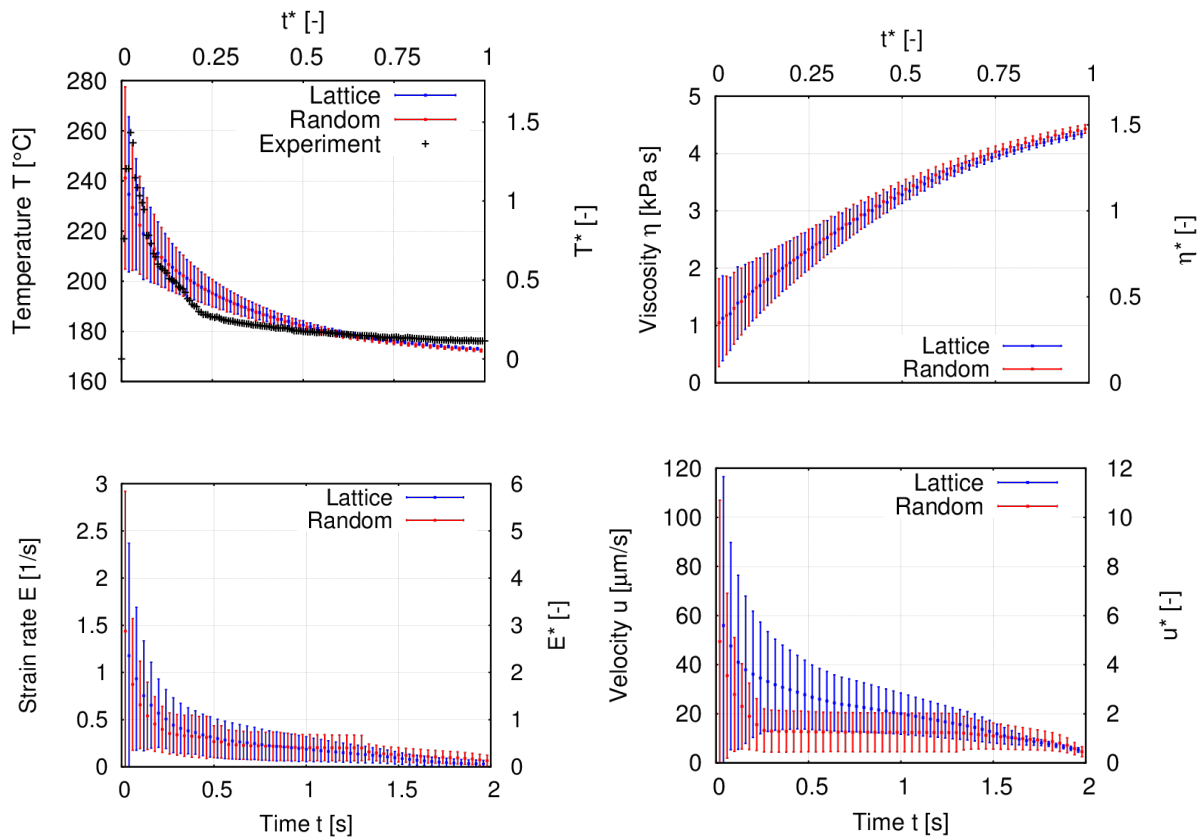


Figure 4: Transient behavior of temperature, viscosity, strain rate and velocity magnitude for the molten polymer in the 2D laser sintering simulations with particles positioned either on a lattice or in a random arrangement. Displayed for each time are the spatial mean value and one standard deviation as error bar. For the temperature transient, experimental data measured by an infrared camera is also shown.

4 CONCLUSIONS

- Particle-based 2D melt track simulations are an efficient tool to analyze the spatial and temporal evolution of all relevant physical quantities.
- For analyses of the porosity and the surface roughness it is important to include the randomness of particle positions within a powder bed.
- The laser sintering process can be divided into three temporal regimes: (1) laser motion, (2) thermal diffusion and (3) viscous flow driven by surface tension.
- A dimensional analysis yields the correct magnitudes of all physical quantities.

5 ACKNOWLEDGEMENTS

Financial support by the Deutsche Forschungsgemeinschaft (DFG) under grants number BI 1859/2-1 and LA 4328/1-1 within the priority program 2122 *Materials for Additive Manufacturing* is greatly acknowledged. All simulations are carried out using the SimPARTIX® software developed by Fraunhofer IWM [13].

REFERENCES

- [1] Frenkel, J. Viscous flow of crystalline bodies under the action of surface tension. *J. Phys.* (1945) **9**(5):385–391.
- [2] Mackenzie, J.K. and Shuttleworth, R. A Phenomenological Theory of Sintering. *Proc. Phys. Soc. B* (1949) **62**(12):833–852.
- [3] Bellehumeur, C.T., Kontopoulou, M. and Vlachopoulos, J. The role of viscoelasticity in polymer sintering. *Rheol. Acta* (1998) **37**(3):270–278.
- [4] Schultz, J.P. Modeling Heat Transfer and Densification during Laser Sintering of Viscoelastic Polymers. PhD Thesis, Virginia Polytechnic Institute and State University (2003).
- [5] Riedlbauer, D., Drexler, M., Drummer, D., Steinmann, P. and Mergheim, J. Modelling, simulation and experimental validation of heat transfer in selective laser melting of the polymeric material PA12. *Comput. Mater. Sci.* (2014) **93**:239–248.
- [6] Wohlgemuth, F. and Alig, I. Physikalische Modellbildung für das Additive Sintern von Kunststoffmaterialien. In: *Additive Fertigung von Bauteilen und Strukturen*. Richard, H.A. (Ed.). Springer Fachmedien, Wiesbaden, Germany (2017) 121–136.
- [7] Osmanlic, F., Wudy, K., Laumer, T., Schmidt, M., Drummer, D. and Körner, C. Modeling of Laser Beam Absorption in a Polymer Powder Bed. *Polymers* (2018) **10**:784.
- [8] Mokrane, A., Boutaous, M. and Xin, S. Process of selective laser sintering of polymer powders: Modeling, simulation, and validation. *C. R. Mecanique* (2018) **346**:1087–1103.
- [9] Balemans, C., Jaensson, N.O., Hulsen, M.A. and Anderson, P.D. Temperature-dependent sintering of two viscous particles. *Additive Manufacturing* (2018) **24**:528–542.
- [10] Fan, X.-J., Tanner, R.I. and Zhang, R. Smoothed particle hydrodynamics simulation of non-Newtonian moulding flow. *J. Non-Newtonian Fluid Mech.* (2010) **165**(5–6):219–226.
- [11] Gingold, R.A. and Monaghan, J.J. Smoothed Particle Hydrodynamics: Theory and Application to Non-Spherical Stars. *Mon. Not. R. Astron. Soc.* (1977) **181**:375–389.
- [12] Bierwisch, C. A surface tension and wetting model for the δ^+ -SPH scheme. In: *Proceedings of the 13th SPHERIC International Workshop 2018*. Quinlan, N.J., Tong, M., Moghimi, M.H. and McLoone, M. (Eds.). National University of Ireland, Galway, Ireland (2018) 95–102.
- [13] <http://www.simpartix.com>

SIMULATION OF HEAT TRANSFER AND METAL FLOW IN WIRE-BASED ELECTRO BEAM ADDITIVE MANUFACTURING

**ALEXEY V. SHCHERBAKOV, DARIA A. GAPONOVA, REGINA V. RODYAKINA,
ALEXANDER V. GUDENKO, ANDREY P. SLIVA, VIKTOR P. RUBTSOV AND
VIKTOR K. DRAGUNOV**

National Research University "Moscow Power Engineering Institute (MPEI)"
Krasnokazarmennaya 14, 111250 Moscow, Russia
e-mail: ShcherbakovAV@mpei.ru, web page: <http://mpei.ru>

Key words: Metal Wire Deposition, Electron Beam Melting, Navier-Stokes Equations, Metal Flow, Finite Difference Method, Surface Tension, Electron Beam Sweep

Abstract. The urgency of mathematical model development for wire-based electron-beam additive manufacturing process analysis is shown. The procedure of solving heat equation for metal in the solid phase and the Navier-Stokes equations in the liquid phase, based on the use of the finite-difference method and the predictor-corrector procedure is described. An algorithm for numerical approximation of free melt surface motion, using the concept of the volume of fluid (VOF), is described as well. A numerical algorithm for surface tension force calculating is proposed. The model described above was realized as a program in the Microsoft Visual Studio environment. Series of computational experiments were carried out to calculate metal flow during deposition with the use of 316L steel wire. The results of experiments are compared with experimental data.

1 INTRODUCTION

Wire-based electron-beam additive manufacturing (also known as electron beam freeform fabrication, EBF³ [1]) meets the requirements for structure and quality of formed metal layer, since the whole process is realized in vacuum ($10^{-3} \dots 10^{-5}$ Torr), and size and shape of heat source can be varied by the use of magnetic deflection coils. Usually, wire with a diameter of 0.8 to 2.4 mm is used, and the wire feed rate is 3-5 times higher than the deposition rate. The minimum width of deposit layer for this process is 6-8 mm, what determines the spatial resolution of this technology. Typical for the technology process performance for large-sized products with dimensions of 500 mm and more can vary from 3 to 12 kilograms of metal per hour [2]. Today, it is too early to talk about the wide industrial use of the technology. Control of metal transfer mode, which is influenced by many factors, remains an unsolved problem, and is primarily associated with inconstancy of heat transfer conditions. Experimental methods such as high-speed imaging in visible or infrared optical range can be used to control the mode of metal flow. These methods provide indirect information, such as temperature distribution over the observed surface or bead shape in the deposition process. Moreover, these methods require expensive equipment and many series of experiments. Therefore, predicting the results of surfacing using experimental studies will be a time-consuming process. To obtain information about velocity distribution and pressure, as well as temperature distribution over the depth of weld pool, it is necessary to use methods of mathematical modelling.

2 MODEL DESCRIPTION

A graphical representation of the model is shown in Fig. 1. Wire is fed with the rate of v_{wire} to the area in which electron beam is applied. Metal melts and flows onto the substrate, forming a bead. Electron gun moves with wire feeder at a given speed. Heat and mass transfer in the system “electron beam – wire – substrate” should be described in a formulation that takes into account the flow of metal under the action of pressure field, gravity, and forces due to viscosity and surface tension. For this, it is necessary to use the Navier-Stokes equations, which describe the flow of a viscous incompressible fluid, and include, firstly, the continuity equation

$$\frac{\partial v_x}{\partial x} + \frac{\partial v_y}{\partial y} + \frac{\partial v_z}{\partial z} = 0, \quad (1)$$

where v_x , v_y and v_z are the projections of velocity vector on the x , y and z axes.

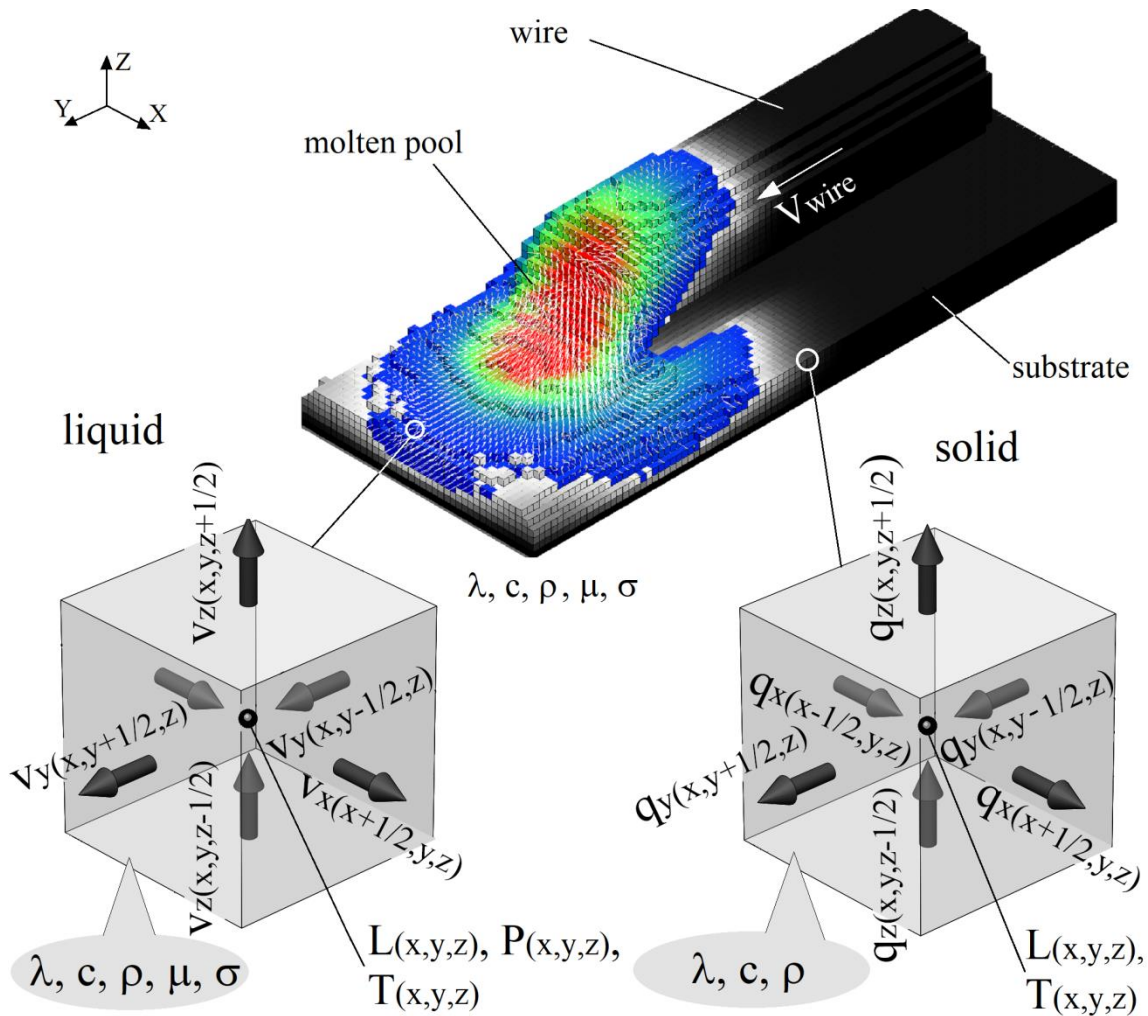


Figure 1: Surfacing process presented in accordance with the concept of cubic control volumes

Secondly, the system includes the momentum equation, which written in projection form

$$\begin{aligned} \frac{\partial v_x}{\partial t} + v_x \frac{\partial v_x}{\partial x} + v_y \frac{\partial v_x}{\partial y} + v_z \frac{\partial v_x}{\partial z} &= -\frac{1}{\rho} \frac{\partial P}{\partial x} + \mu \left(\frac{\partial^2 v_x}{\partial x^2} + \frac{\partial^2 v_x}{\partial y^2} + \frac{\partial^2 v_x}{\partial z^2} \right) + \frac{1}{\rho} \sigma \kappa \frac{dL}{dx}; \\ \frac{\partial v_y}{\partial t} + v_x \frac{\partial v_y}{\partial x} + v_y \frac{\partial v_y}{\partial y} + v_z \frac{\partial v_y}{\partial z} &= -\frac{1}{\rho} \frac{\partial P}{\partial y} + \mu \left(\frac{\partial^2 v_y}{\partial x^2} + \frac{\partial^2 v_y}{\partial y^2} + \frac{\partial^2 v_y}{\partial z^2} \right) + \frac{1}{\rho} \sigma \kappa \frac{dL}{dy}; \\ \frac{\partial v_z}{\partial t} + v_x \frac{\partial v_z}{\partial x} + v_y \frac{\partial v_z}{\partial y} + v_z \frac{\partial v_z}{\partial z} &= -\frac{1}{\rho} \frac{\partial P}{\partial z} + \mu \left(\frac{\partial^2 v_z}{\partial x^2} + \frac{\partial^2 v_z}{\partial y^2} + \frac{\partial^2 v_z}{\partial z^2} \right) + \frac{1}{\rho} \sigma \kappa \frac{dL}{dz} - g, \end{aligned} \quad (2)$$

where P is pressure, Pa; μ is kinematic viscosity, m^2/s , t is time, s; g is gravity acceleration, m/s^2 , ρ is density, kg/m^3 , σ is surface tension coefficient, J/m^2 , κ is curvature index, $1/m$, L is dimensionless function of filling the control volume with fluid, $0 < L < 1$. At $L = 1$, the control volume is filled with fluid, and at $L = 0$ it is empty. This method is known as the Volume of Fluid (VOF) method, and it has proven itself for solving hydrodynamic problems [3, 4]. The VOF concept used in the model is illustrated by Figure 2.

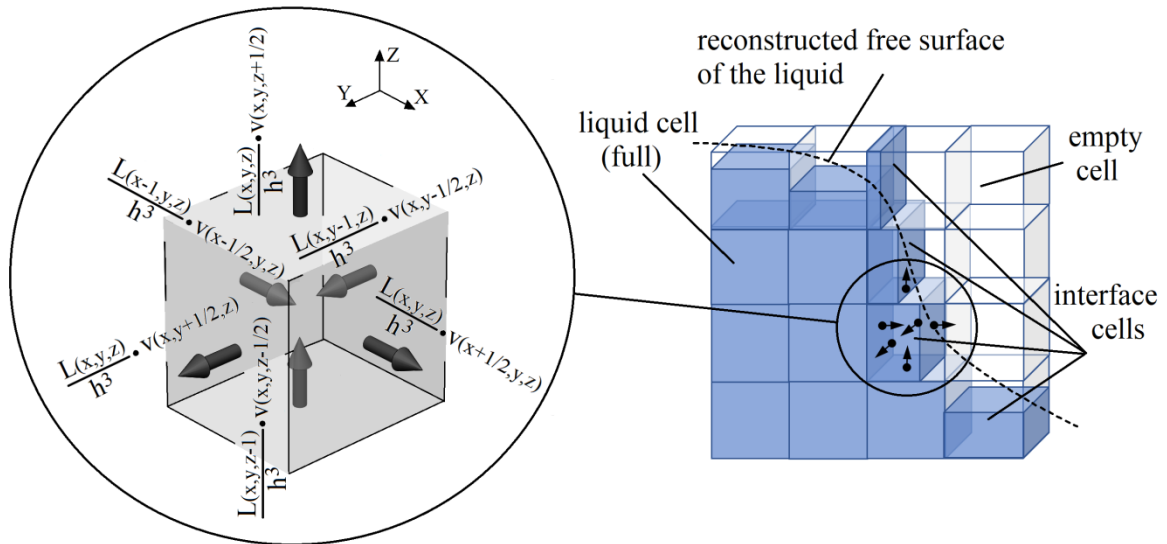


Figure 2: VOF concept used in the proposed model: h^3 is the volume of full liquid cell (sides of a cubic cell had a size h)

In accordance with this method, the flow of fluid between the control volumes is described by means of equation

$$\frac{\partial L}{\partial t} + v_x \frac{\partial L}{\partial x} + v_y \frac{\partial L}{\partial y} + v_z \frac{\partial L}{\partial z} = 0. \quad (3)$$

In cells with $\nabla L \neq 0$, surface tension forces (see eq. 2) acts to prevent the free surface from stretching. These forces depend on temperature and free surface curvature.

Heat transfer in a liquid pool is carried out due to convection and heat conduction and it is described by the energy equation

$$\frac{\partial T}{\partial t} + v_x \frac{\partial T}{\partial x} + v_y \frac{\partial T}{\partial y} + v_z \frac{\partial T}{\partial z} = \frac{\lambda}{c_p} \left(\frac{\partial^2 T}{\partial x^2} + \frac{\partial^2 T}{\partial y^2} + \frac{\partial^2 T}{\partial z^2} \right) + \frac{Q_v}{c_p}. \quad (4)$$

In the last equation, T is temperature, K, c is specific heat capacity, J/(kg·K), Q_v is volume representation of electron beam energy released in the control volume as a heat, W/m³. Heat transfer in the solid phase is described by the equation of heat conductivity (the projections of heat flux vectors between cubic cells are shown in Fig. 1 as q_x , q_y and q_z)

$$\frac{\partial T}{\partial t} = \frac{\lambda}{c_p} \left(\frac{\partial^2 T}{\partial x^2} + \frac{\partial^2 T}{\partial y^2} + \frac{\partial^2 T}{\partial z^2} \right) + \frac{Q_v}{c_p} - H_m \cdot \rho \frac{\partial \psi_m}{\partial t}, \quad (5)$$

where H_m is latent heat of fusion of metal, J/kg; $\psi_m(T)$ is relative amount of fluid in the control volume, calculated with using equation

$$\psi_m(T) = \begin{cases} 0, & T < T_S \\ \frac{T - T_S}{T_L - T_S}, & T_S < T < T_L \\ 1, & T > T_L \end{cases} \quad (6)$$

In the equation (6) T_S and T_L are, respectively, solidus and liquidus temperatures of the material being remelted, K.

Now it is necessary to describe the boundary conditions. Stefan-Boltzmann condition is set on surfaces facing vacuum

$$q_{\perp} = -\varepsilon \cdot k \cdot (T_{surface}^4 - T_{chamber}^4), \quad (7)$$

where ε is the total emissivity for the radiating surface, $k = 5.67 \cdot 10^{-8}$ W/(m²K⁴) is the Stefan-Boltzmann constant, $T_{surface}$ is the surface temperature and $T_{chamber}$ is vacuum chamber temperature, which is assumed to be 25°C. A heat transfer condition by heat conduction into the fixture was proposed for the substrate bottom surface

$$q_{\perp} = -\lambda_{fix} \frac{T_{surface} - T_{chamber}}{S_{fix}}, \quad (8)$$

where $\lambda_{fix} = 400$ W/(m·K) is the thermal conductivity of a copper fixture and S_{fix} is the fixture thickness, which is assumed to be 0.02 meters. Heat source was represented by volumetric function Q_v , which depends on z according to the equation

$$Q_v = \begin{cases} 0, & z < z_{surface} \\ \frac{1}{\pi \cdot r_{eff}^2} I_b U_a \exp\left(-\frac{\left((x - x_{pos}(t))^2 + (y - y_{pos}(t))^2\right)}{r_{eff}^2}\right) \frac{1}{dz}, & z = z_{surface} \\ 0, & z > z_{surface} \end{cases} \quad (9)$$

In the equation (9) $z_{surface}$ is z -coordinate of control volume in which electrons energy is converted into heat; I_b is beam's current, A; U_a is accelerating voltage, V; x_{pos} , y_{pos} are the current values of electron beam center coordinates (depends on time t), m; r_{eff} is beam effective radius (assumed to be 0.2-0.5 mm), m; dz is z -size of the control volume in which

electron beam heating is effected, m.

The most complex boundary conditions for the momentum equation are given on the free surfaces of liquid metal. The acceleration due to the action of surface tension forces is described in the momentum equation (2) and appears only when a gradient of the function L exists. The vapor recoil pressure (Pa) can be described by the Antoine equation as

$$P_{recoil} = 133 \cdot 10^{8.8-18700/T_{surface}} \quad (10)$$

and the acceleration due to this pressure, m/s^2

$$a_{recoil} = P_{recoil} \frac{\nabla L}{L|\nabla L| \rho h} \quad (11)$$

where ∇L is the gradient of function L , which appears on the surfaces. The pressure outside the metal (in the empty cells with $L=0$) is assumed to be equal to the vacuum chamber pressure (in these experiments the chamber pressure was 0.1 Pa)

$$P_{(L=0)} = P_{chamber} \quad (12)$$

On the boundary between liquid and solid metal there is the condition

$$v_L = v_S, \quad (13)$$

where index L refers to the liquid phase, and index S refers to the solid phase. For example, if the wire moves at a speed v_{wire} , then metal's velocity flow at the wire's melting boundary will also be equal to v_{wire} .

The physical properties of metal are temperature dependent. To account for data dependencies for steel 316L were collected literature data [5, 6, 7, 8]. Figure 3 shows the dependencies used in the development of heat and mass transfer model.

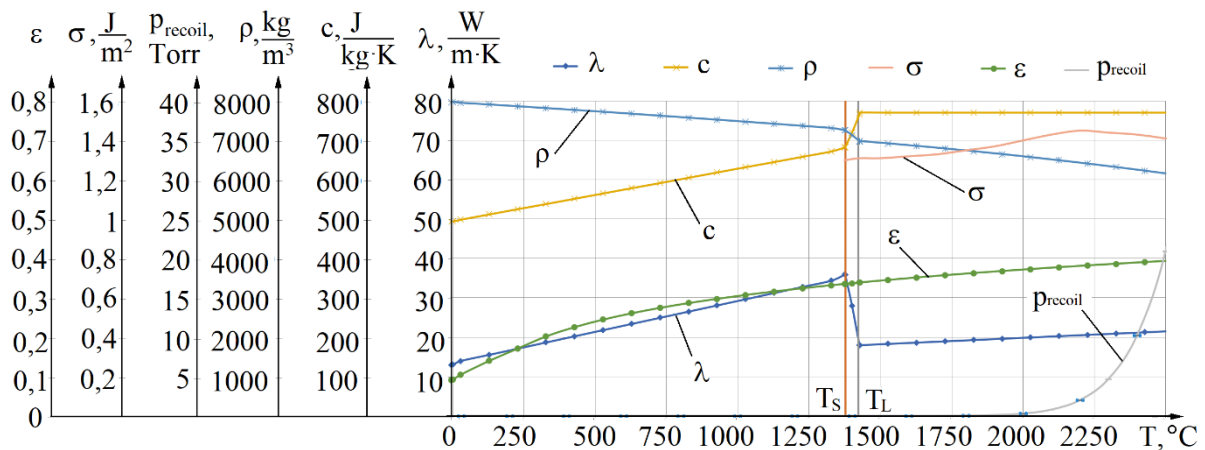


Figure 3: Physical properties of steel 316L vs temperature

3 NUMERICAL MODEL IMPLEMENTATION AND SOME ALGORITHMS

To solve the system of equations (1)–(13), the finite difference method and a fixed grid with cubic cells were used. This grid has “staggered” structure [9]. In such a grid, the nodes, in which velocities are calculated, are displaced along all three axes by half the coordinate

step relative to the nodes in which there are calculated pressure P , function of cell's filling L and fluid temperature T (Fig. 1). The grid spacing was taken to be $h = 0.05 \dots 0.1$ mm, and the time interval was $5 \cdot 10^{-6} \dots 1,25 \cdot 10^{-5}$ s. At the current stage of research, an explicit difference scheme was used with fixed coordinate and time steps.

At the beginning of heating process, melting does not occur, so it is necessary to solve the equation (5). For example, to calculate the temperature in the current coordinate node at time moment $t + 1$, we used the following finite-difference approximation of equation (5):

$$T_{(x,y,z)}^{t+1} = T_{(x,y,z)}^t + \Delta t \left(\frac{\lambda}{c\rho} \left(\frac{T_{(x+1,y,z)}^t - 2T_{(x,y,z)}^t + T_{(x-1,y,z)}^t}{h^2} + \frac{T_{(x,y+1,z)}^t - 2T_{(x,y,z)}^t + T_{(x,y-1,z)}^t}{h^2} + \frac{T_{(x,y,z+1)}^t - 2T_{(x,y,z)}^t + T_{(x,y,z-1)}^t}{h^2} \right) + \frac{Q_v}{c\rho} \right) \quad (14)$$

After reaching the temperature T_L in the control volume metal was considered to be molten and the system of equations (1)–(4) must be solved. For the numerical calculation of pressure and velocity fields (equations 1 and 2), a method proposed by S. Patankar [9] was used. At the first time step, velocity field is assumed known (all velocities are zero). Velocity increments were calculated by equation (2) without taking into account values of pressure (predictor step). For example, the x -projection of velocity was calculated according to the equation

$$\begin{aligned} v_{x(x,y,z)}^{t(t+1)_{predictor}} &= v_{x(x,y,z)}^t + \Delta t \times \\ &\times \left(-v_{x(x,y,z)}^t \cdot \frac{v_{x(x+1,y,z)}^t - v_{x(x-1,y,z)}^t}{2h} - v_{y(x,y,z)}^t \cdot \frac{v_{x(x,y+1,z)}^t - v_{x(x,y-1,z)}^t}{2h} - v_{z(x,y,z)}^t \cdot \frac{v_{x(x,y,z+1)}^t - v_{x(x,y,z-1)}^t}{2h} + \right. \\ &+ \mu \left(\frac{v_{x(x+1,y,z)}^t - 2v_{x(x,y,z)}^t + v_{x(x-1,y,z)}^t}{h^2} + \frac{v_{y(x,y+1,z)}^t - 2v_{y(x,y,z)}^t + v_{y(x,y-1,z)}^t}{h^2} + \frac{v_{z(x,y,z+1)}^t - 2v_{z(x,y,z)}^t + v_{z(x,y,z-1)}^t}{h^2} \right) + \\ &\left. + \frac{1}{\rho} (\sigma\kappa + p_{recoil}) \frac{L_{(x+1,y,z)}^t - L_{(x-1,y,z)}^t}{2h} \right). \end{aligned} \quad (15)$$

Then, the scalar pressure field in the liquid metal (step-corrector) was calculated using the method described in [9,10,11]. The pressure was calculated by the Poisson equation, which satisfies the continuity equation (1)

$$\frac{\partial^2 P}{\partial x^2} + \frac{\partial^2 P}{\partial y^2} + \frac{\partial^2 P}{\partial z^2} = \frac{\rho}{\Delta t} \cdot \left(\frac{\partial v_x}{\partial x} + \frac{\partial v_y}{\partial y} + \frac{\partial v_z}{\partial z} \right). \quad (16)$$

The resulting pressure field is necessary to adjust the velocity field. All values on the right side of the equation are constants for the considered time step (the velocities are calculated at the predictor step). Equation (16) was solved with using simple iteration method by expressing the pressure in the (x,y,z) node (in the center of cell) through the pressures in the surrounding cells and the derivatives of velocities calculated in displaced grid nodes

$$\begin{aligned} P_{(x,y,z)} &= \frac{1}{6} (P_{(x+1,y,z)} + P_{(x-1,y,z)} + P_{(x,y+1,z)} + P_{(x,y-1,z)} + P_{(x,y,z+1)} + P_{(x,y,z-1)} + \\ &- \frac{h^2 \rho}{6\Delta t} \left(\frac{v_{x(x+\frac{1}{2},y,z)} - v_{x(x-\frac{1}{2},y,z)}}{h} + \frac{v_{y(x,y+\frac{1}{2},z)} - v_{y(x,y-\frac{1}{2},z)}}{h} + \frac{v_{z(x,y,z+\frac{1}{2})} - v_{z(x,y,z-\frac{1}{2})}}{h} \right). \end{aligned} \quad (17)$$

After pressure field finding, the acceleration projections due to its action were calculated and the velocity field was corrected. For example, for velocity projection on the x -axis we have the following equation:

$$v_{x(x,y,z)}^{(t+1)corrector} = v_{x(x,y,z)}^{(t+1)predictor} + \left(-\frac{1}{\rho} \frac{P(x+1,y,z) - P(x-1,y,z)}{2h} \right) \Delta t. \quad (18)$$

In the liquid phase, thermal conductivity and convection will be simultaneously present, and the numerical form of heat transfer equation will be written as follows

$$\begin{aligned} T_{(x,y,z)}^{t+1} &= T_{(x,y,z)}^t + \Delta t \times \\ \times \left(\frac{\lambda}{c\rho} \left(\frac{T_{(x+1,y,z)}^t - 2T_{(x,y,z)}^t + T_{(x-1,y,z)}^t}{h^2} + \frac{T_{(x,y+1,z)}^t - 2T_{(x,y,z)}^t + T_{(x,y-1,z)}^t}{h^2} + \frac{T_{(x,y,z+1)}^t - 2T_{(x,y,z)}^t + T_{(x,y,z-1)}^t}{h^2} \right) - \right. \\ &\left. -v_{x(x,y,z)}^t \cdot \frac{T_{(x+\frac{1}{2},y,z)}^t - T_{(x-\frac{1}{2},y,z)}^t}{h} - v_y^t(x,y,z) \cdot \frac{T_{(x,y+\frac{1}{2},z)}^t - T_{(x,y-\frac{1}{2},z)}^t}{h} - v_z^t(x,y,z) \cdot \frac{T_{(x,y,z+\frac{1}{2})}^t - T_{(x,y,z-\frac{1}{2})}^t}{h} + \frac{Q_v}{c\rho} \right). \end{aligned} \quad (19)$$

After that, it is necessary to simulate the motion of free surface, and also to determine the fields of surface tension force. The finite difference approximation of equation (3) for the case, if no additional conditions are specified, should have the following form

$$\begin{aligned} L_{(x,y,z)}^{t+1} &= L_{(x,y,z)}^t + \Delta t \times \left(\frac{L_{(x+\frac{1}{2},y,z)}^t v_{x(x+\frac{1}{2},y,z)}^t - L_{(x-\frac{1}{2},y,z)}^t v_{x(x-\frac{1}{2},y,z)}^t}{h} + \right. \\ &\left. + \frac{L_{(x,y+\frac{1}{2},z)}^t v_{y(x,y+\frac{1}{2},z)}^t - L_{(x,y-\frac{1}{2},z)}^t v_{y(x,y-\frac{1}{2},z)}^t}{h} + \frac{L_{(x,y,z+\frac{1}{2})}^t v_{z(x,y,z+\frac{1}{2})}^t - L_{(x,y,z-\frac{1}{2})}^t v_{z(x,y,z-\frac{1}{2})}^t}{h} \right) = \\ &= L_{(x,y,z)}^t + \Delta t \cdot \Omega. \end{aligned} \quad (20)$$

However, a direct numerical solution of such a system can lead to the appearance of anomalous results, since this approach does not take into account that function L in each control volume should always take values in the range from 0 to 1. This circumstance led to the creation of various methods for solving equation (3), described in the literature [3, 10,11,12]. In this work, the sign of velocity and magnitude of flux flowing into the control volume, or, on the contrary, flowing from it, was tracked. In the case of control volume overflow, or, on the contrary, its emptying, a proportional decrease in the stream was made to prevent function L value output out of the interval $[0...1]$.

In addition to the above conditions introduced into the algorithm for solving equation (20), the calculation of the function L distribution was carried out iteratively with fragmentation of time step. The maximum fractional step Δt_{frac} was selected from the condition

$$\Delta t_{frac} \cdot \max \Omega \leq 0.1. \quad (21)$$

The next step was the calculation of surface tension forces. The normal to the free surface was calculated as function gradient L direction, and the sign and magnitude of the force were

calculated from the surface curvature κ (see eq. 2 and eq. 15). The curvature index was determined as follows. In the computational grid, a spherical region with a center at the point under consideration (x,y,z) lying on the free surface was distinguished (Fig. 4).

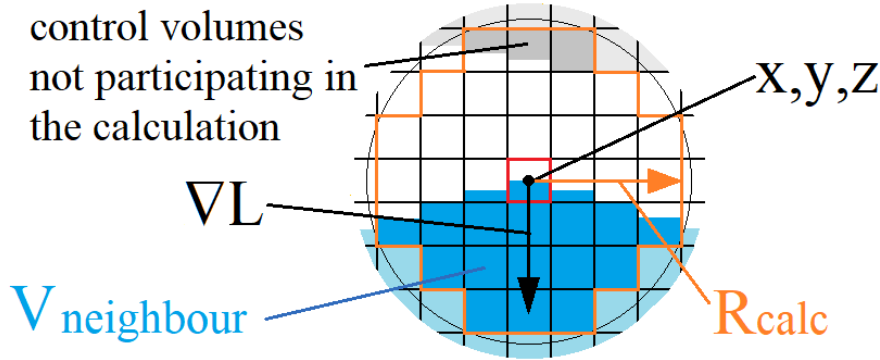


Figure 4: To the calculation of curvature index of the surface

The region has radius R_{calc} (this value determines the accuracy of calculation, we took 4-6 grid points). Then, by summing the volumes inside the sphere ($V_{neighbour}$ shown in Fig. 2) we calculated the curvature index from geometric considerations by means of equation

$$\kappa = - \frac{12V_{neighbour} - 8\pi R_{calc}^3}{3\pi R_{calc}^4} \quad (22)$$

This algorithm was implemented only for cells in which $\nabla L \neq 0$, the direction of ∇L is similar with the direction of surface tension force, and the force sign depends on the surface curvature sign. Since the surface tension force contains the derivative of function L , this allows to provide the “compression” of free surface and eliminates its “blurring”, which is typical for the VOF-algorithms described by equation (3).

4 TEST PROBLEMS AND VERIFICATION

At the first stage, melting of a fixed wire with beam power of 800 W oscillating at a frequency of 400 Hz around a circular trajectory with the radius of 0.8 mm and moving along the wire at a speed of 20 mm/s was simulated. The effective beam radius was assumed to be 0.8 mm. The simulation results are graphically shown in Fig. 5.

Caption *a,b...e* in Fig. 5 corresponds to different time points: *a* – 2.75 ms; *b* – 31.25 ms; *c* – 93.75 ms; *d* – 125 ms and *e* – 375 ms. Beam position at these points is shown by dashed line (marked by number 1). For the entire period electron beam moves at a distance of 7.5 mm, making 150 oscillations along a circular path with a radius of 0.8 mm (sweep radius).

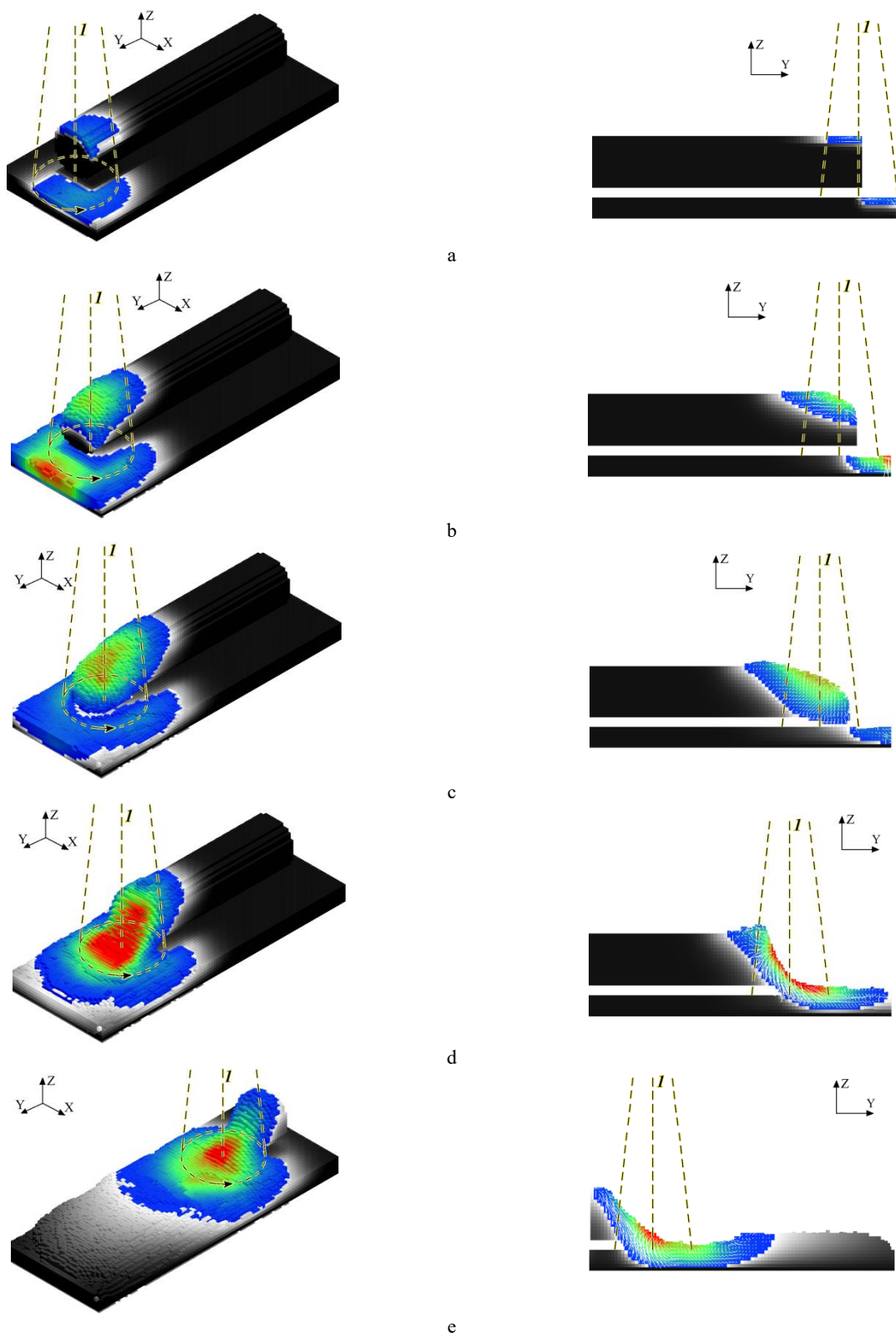


Figure 5: Simulation results at a different time moments

The flow is almost laminar: metal flows mainly due to gravity, and turbulence is observed only in the tail part of liquid pool, and it is caused by interaction of the flow with a solid bead wall. The maximum flow velocity calculated during the transition to stationary mode of transfer was recorded in the central part of metal jet and amounted to 0.68 m/s. The bead shape (ratio of height to width) corresponds to published literature data [13]. It is reasonable to assume that an increase in the rate of metal flow due to an increase in the wire feed rate (and, correspondingly, beam power) may lead to an intensification of the process of forcing the fluid to the top.

It is also obvious that reducing beam sweep radius will reduce width of molten area on the substrate, which in turn should lead to the formation of a narrower and higher bead. Fig. 6 shows the use of a narrow beam sweep, in which virtually all power is released in an area not exceeding the wire itself. In this example, the wire diameter is 0.8 mm, the sweep radius is 0.15 mm and the beam radius is 0.2 mm. The wire moves at a speed of 7.5 mm/s relative to the substrate, and the oscillating beam moves in the opposite direction at a speed of 5 mm/s (deposition rate is 5 mm/s and equivalent wire feed rate is 12,5 mm/s). The frequency of beam oscillations was 600 Hz and electron beam power was 1 kW.

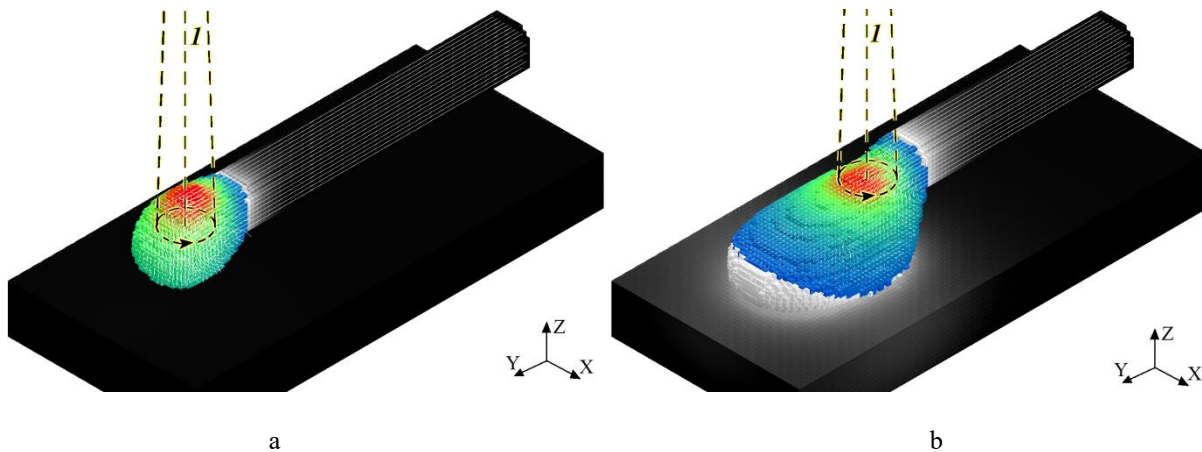


Figure 6: Simulation results for the case of narrow beam oscillations

To verify the process, a mode was chosen that is implemented in the laboratory on the ELA-15I installation. The deposition rate was 5.6 mm/s, and the wire feed rate was 30 mm/s. The wire diameter was 1.2 mm, and the beam sweep radius was 0.6 mm (a wider scan was used than in the previous case). The beam power was 1.5 kW. Figure 7 shows the additive manufacturing modeling results with the single bead deposited with the above parameters. Fig. 7, a, shows velocity field and temperature field during depositing in stationary mode. It is seen that material feed rate has a significant impact on metal transfer in the molten pool. There are vortex flows in the upper and lower parts of the bead. As a result of metal displacement to the top, the pool height increases, and periodical nature of transfer leads to the appearance of ripples. Metal transfer in the lower part of the pool leads to the slope of molten pool. This example shows the differences in the nature of metal transfer when the wire feed rate exceeds the deposition rate. Fig. 7, b, shows a comparison of shape and size of weld bead obtained as a result of experiments (left) and modeling (right). It is seen that the forms

are similar to each other, there are slight differences in the height and shape of the upper part of the bead. The differences seem to be related to the discrete representation of computational domain and methods used for calculation. These data show that the model can be used to analyze the processes of wire-based additive manufacturing.

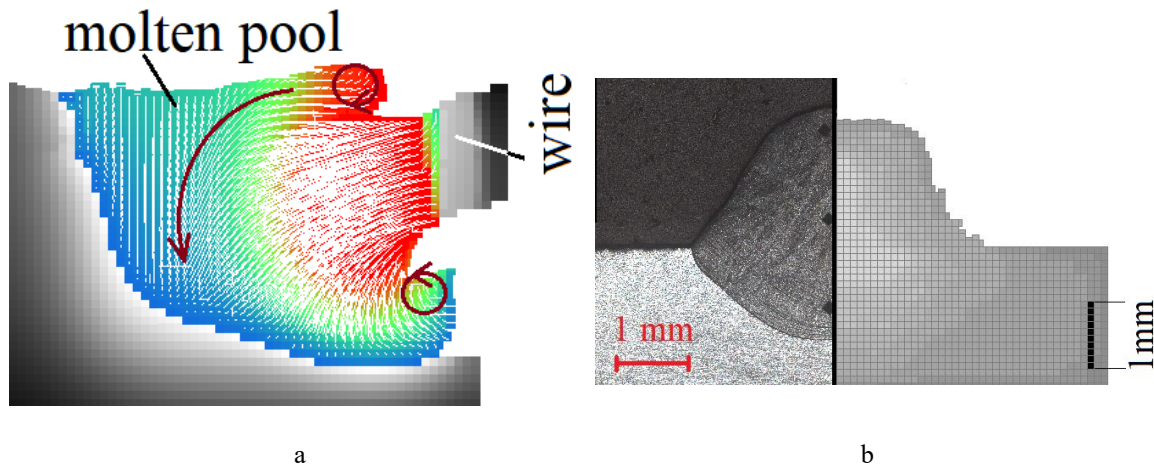


Figure 7: Verification of results: velocity and temperature fields (a) and comparison of bead cross-section with experiment result (b)

5 CONCLUSIONS

- A model based on the use of a fixed offset grid and the VOF method, which allow to realize the simulation of wire-based additive manufacturing, has been proposed. It is shown that the model is distinguished by the possibility of taking into account temperature dependences of materials physical properties, surface tension forces and vapor recoil pressure, as well as the possibility of simulating heating by oscillating electron beam.
- It is shown that in the absence of wire movement (when beam moves relative to the wire), or at wire feed rate close to the deposition rate, the nature of metal transfer will be laminar, vortex flows may appear only near crystallization front, and their velocities are small. The maximum speed will be observed in the area of metal jet, and this speed was within 0.4-0.8 m/s.
- According to the results of simulation experiments, the effect of electron beam circular oscillation size on bead parameters was studied. It is shown that reducing the oscillation to values less than wire diameter allows to form a higher and narrow beads on the substrate.
- Verification of the process at a wire feed rate 5.6 times greater than deposition rate was carried out. A satisfactory coincidence of bead shape with experimental data was reached. With the help of the model, a significant change in metal transfer in the pool due to the formation of vortex flows in the upper and lower parts of the pool is shown.

6 ACKNOWLEDGMENTS

This work was carried out in National Research University «Moscow Power Engineering Institute»; it was supported by grant from the Russian Science Foundation (Project 17-79-20015).

REFERENCES

- [1] K.M.B. Taminger, R.A. Hafley. Electron beam freeform fabrication: a rapid metal deposition process // Proceedings of third annual automotive composites conference. Society of Plastic Engineers, Troy, Michigan, USA; 2003. P. 9–10.
- [2] I. Gibson, D. Rosen, B. Stucker. Additive Manufacturing technologies. 3D Printing, Rapid Prototyping, and Direct Digital Manufacturing/New York: Springer Science+Business Media, 2015, 498 p.
- [3] C.W. Hirt, B.D. Nichols. Volume of fluid (VOF) method for the dynamics of free boundaries // Journal of Computational Physics, Volume 39, Issue 1, January 1981, Pages 201-225
- [4] Noh, W.F.; Woodward, P. (1976). "SLIC (Simple Line Interface Calculation). In proceedings of 5th International Conference of Fluid Dynamics, edited by A. I. van de Vooren & P.J. Zandbergen". Lecture Notes in Physics. 59: 330–340.
- [5] Choong S. Kim. Thermophysical Properties of Stainless Steels. Argonne National Laboratory, 1975.
- [6] Tristan S. Hunnewell, Kyle L. Walton, Sangita Sharma, Tushar K. Ghosh, Robert V. Tompson, Dabir S. Viswanath & Sudarshan K. Loyalka. Total Hemispherical Emissivity of SS 316L with Simulated Very High Temperature Reactor Surface Conditions//Nuclear Technology, Volume 198, 2017, Issue 3, pp. 293-305. DOI: 10.13182/NT10-6
- [7] Y. Wang, Q. Shi, and H.L. Tsai. Modeling of the Effects of Surface-Active Elements on Flow Patterns and Weld Penetration // Metallurgical and materials transactions B, volume 32B, February 2006, pp. 145-161
- [8] T. DebRoy, H.L. Wei, J.S. Zuback, T. Mukherjee, J.W. Elmer, J.O. Milewski, A.M. Beese, A. Wilson-Heid, A. De, W. Zhang. Additive manufacturing of metallic components – Process, structure and properties // Progress in Materials Science 92 (2018) 112–224
- [9] S.V. Patankar. Numerical Heat transfer and fluid flow. Series in computational methods in mechanics and thermal sciences, 1980
- [10] Nikolaos A. Kampanis, John A. Ekaterinaris. A staggered grid, high-order accurate method for the incompressible Navier–Stokes equations // Journal of Computational Physics, Volume 215, Issue 2, 1 July 2006, Pages 589-613
- [11] H.K. Versteeg, W. Malalasekera. An introduction to computational fluid dynamics: The finite volume method. Longman Scientific & Technical, 1995, 257 pp.
- [12] Vinay R. Gopala, Berend G.M. van Wachem. Volume of fluid methods for immiscible-fluid and free-surface flows //Chemical Engineering Journal, Volume 141, Issues 1–3, 15 July 2008, Pages 204-221
- [13] L. Wang. Microstructure and Mechanical Properties of Electron Beam Deposits of AISI 316L Stainless steel. ASME 2011 International Mechanical Engineering Congress & Exposition IMECE2011. November 11-17, 2011, Denver, Colorado, USA.

FORECASTING THE RESIDUAL STRESSES IN A POLYMER LAYER MANUFACTURED ADDITIVELY BY THE TECHNOLOGY OF CENTRIFUGAL MATERIAL APPLICATION

DMITRY A. PARSHIN^{*†}

^{*} Ishlinsky Institute for Problems in Mechanics of the Russian Academy of Sciences (IPMech RAS)
Vernadskogo Ave. 101 Bldg 1, 119526 Moscow, Russia
e-mail: parshin@ipmnet.ru, www.ipmnet.ru

[†] Bauman Moscow State Technical University (BMSTU)
2nd Baumanskaya Str. 5 Bldg 1, 105005 Moscow, Russia
e-mail: parshin_da@bmstu.ru, www.bmstu.ru

Key words: Additive Manufacturing, Centrifugal Application, Polymer Layer, Technological Stress, Residual Stress, Contact Pressure

Abstract. With the help of current approaches in the mechanics of additively manufactured deformable solids, a non-classical mathematical model is developed to predict the stress-strain state of polymer layers gradually formed on a rotating substrate in an arbitrary number of continuous stages of centrifugal material application. On the basis of numerous calculations performed, the qualitative and quantitative features of the residual technological stresses distributions in the finished cylindrical product for different variants of its release from the mechanical loading and the kinematic bonds acting during the manufacturing process are analyzed in detail. Previously unknown mechanical effects are found. The appropriate recommendations of a practical nature are given.

1 INTRODUCTION

Additive manufacturing processes accompanied with increase of solids in size by means of adding new material layers to their surface are characterized by the fact that the solids do not exist in their final configurations before the start of deforming, versus classical solid mechanics, as all additively manufactured solids keep being formed in course of the deformation. The mechanical analysis of additive processes has to take into account external loads actual in the simulated technological process, including those acting on the additional material, simultaneously with mechanical peculiarities of gradual attaching the material to the solid surface. Such account cannot be correctly carried out within the framework of classical solid mechanics, even if the traditional equations and boundary conditions are formulated for a time variable spatial domain. This is due to absence of any unstressed configuration for the entire additive-manufactured solid. Thus, the problems on mechanical modeling for additive-manufactured solids constitute a special class of problems in solid mechanics and possess a number of non-classical features. Approaches to statement and solution of such problems are being successfully developed nowadays by Russian scientific school in mechanics of additive processes founded by Professor A.V. Manzhurov (see, e.g., works [1–6]).

External mechanical loads arise due to specific features of an additive process under

consideration. One can observe that bulk forces often act as mechanical loads in different additive processes. In particular, those include the forces of inertia of the motion of the being formed solid as a rigid whole. Thus, the centrifugal forces of inertia can not be ignored in the analysis of centrifugal material application technologies used for manufacturing or strengthening various axisymmetric products, as well as for applying layers of coatings onto such products. The presented research is devoted to the modeling of such technologies from the point of view of mechanics of deformable solids.

2 SCOPE OF THE STUDY

The loads acting on any additive manufactured solid will obviously cause the appearance and further development of stress and strain fields throughout this solid. The corresponding technological stress-strain state (SSS) of the resulting solid can be characterized by very significant quantitative values. Technological stresses and deformations can, on the one hand, cause significant distortions of the geometry of the formed product or even its destruction, perhaps, already in the manufacturing process. On the other hand successfully distributed, in a certain sense, residual technological stresses and deformations caused by the loads acting on the solid during its manufacture and remaining in the finished product at the end of this process, can to some extent compensate for stresses or deformations from various negative effects on the product during its further operation. The latter circumstance will certainly contribute to an increase in strength, stiffness, stability, bearing capacity or durability of the resulting product or to a certain expansion of its functionality. It is clear that the purposeful provision of favorable distributions of characteristics of technological SSS of manufactured products can be possible only with a detailed understanding of the mechanisms of its formation in the particular technological process. In order to effectively manage these processes for obtaining SSS with pre-prescribed properties, it is also necessary to have an adequate quantitative description of these mechanisms. The latter, obviously, can be achieved only by mathematical modeling the manufacture processes from the standpoint of mechanics.

The present work is devoted to the study of mechanical problems associated with the gradual centrifugal application on the inner surface of the axisymmetric cylindrical substrate of a layer of polymer material uniform in thickness. The angular velocity ω of rotation of the substrate around its axis in the simulated additive process can change arbitrarily over the time t . It is however considered that the derivative $\omega'(t)$ of the given function $\omega(t)$ has not too high values, that is $|\omega'(t)| \ll \omega^2(t)$. This corresponds to a fairly slow variation in the speed of rotation of the substrate during the application of the material onto it. The specified condition on the angular velocity rate imposed in the considered problem allows to neglect tangential forces of inertia of rotation of the formed layer of material together with a substrate in comparison with the corresponding centrifugal forces. It is also assumed that the instantaneous interaction of the applied additional material with the surface of the already formed layer is carried out in such a way that the potentially possible dynamic effects of this interaction are not significant. Therefore, it is possible to neglect the forces of inertia of the deformation of the formed layer in comparison with the centrifugal forces of inertia of its rotation together with the substrate and to consider the corresponding problem of mechanics in a quasi-static formulation.

In the considered process of multilayer applying the additional material onto a rotating

substrate, the thickness of each additional elementary layer formed on the surface of a growing axisymmetric solid in one revolution around its axis is considered to be very small compared to the radius of this layer. This, firstly, means that the rate of inflow of additional material to the formed solid in the circumferential direction is much higher than the rate of its inflow in the radial direction, which makes it possible to simulate the process of centrifugal application of the material by axisymmetric additive process of replenishment of the formed solid with a new material simultaneously over the whole inner side surface. Secondly, this assumption makes it possible to simulate this process as a continuous one, in which an infinitely thin layer of additional material is attached to the formed solid each infinitesimal period of time. Thus, the variable inner radius $R_{\text{int}}(t)$ of the formed layer will be a continuous function of time t . The outer radius R_{ext} of the formed layer throughout the process coincides with the radius of the working surface of the substrate used. Neglecting the flexibility of the latter in comparison with the flexibility of the layer formed on it, we consider the outer radius of the layer unchanged in time, i.e. $R_{\text{ext}} = \text{const}$.

It should be noted that the assumption of constancy of the formed layer outer radius is not essential in the model proposed in this paper. On the one hand, this assumption is adopted to simplify the analysis of all the relations obtained. On the other hand, the absence, in the used model, of the deformation response of the substrate to the pressure exerted on it by the applied material seeking to expand under the action of centrifugal forces allows us to give a refined demonstration of the mechanical effects that occur when the layer-by-layer formation of the solid with the simultaneous action of the field of bulk forces on it (in our problem, this is the forces of inertia of the rotational motion) regardless of the influence of deformation processes occurring in that part of the solid in question which existed before the organization of the influx of additional material to it. This must be considered as a very significant special case of deforming an additively manufactured solid, because of the fact that if a layer of additional material is attached to the surface of any solid that is already in the process of deformation under the influence of any external impacts, then the joined layer will be inevitably also involved in the deformation process.

The objectives of the presented study are:

- to build a mechanical model of the above described additive process of manufacturing a layer of polymer material on a cylindrical substrate by centrifugal method;
- to predict the evolution of the SSS of the being formed layer under the action of centrifugal forces of inertia of its rotational motion together with the substrate;
- to identify quantitative and qualitative characteristics of this evolution and to explain the mechanical effects observed in the simulated process;
- to formulate practical recommendations that should be taken into account in the design and organization of additive processes of centrifugal application of the material.

3 DESCRIPTION OF THE MECHANICAL BEHAVIOR OF THE MATERIAL

As it is known (see, for example, [7]), polymeric materials exhibit pronounced rheological properties. Their deformation response to the applied loads has an aftereffect (deformation delay), and in addition, as a rule, their mechanical characteristics change significantly with age, regardless of actual stresses. The last effect, called aging, is manifested in a decrease in

the material compliance with time, that is, in the weakening of its deformation response, both instantaneous and developing over time.

Additive processes in which solids are formed from materials with similar behavior are very difficult to model. This is explained by the continuous interaction of the deformation reaction of the formed solid to the loads acting on it, on the one hand, with the arising redistribution of stresses throughout the solid due to its replenishment with new material elements, on the other hand. Despite this, the study of this kind of additive processes is very important for a variety of technological applications.

This paper uses a model of the mechanical behavior of a polymer material described in the framework of the linear hereditary theory of viscoelasticity of aging isotropic media [8]. The relationship between the stress tensor \mathbf{T} and the small strain tensor \mathbf{E} for such a medium has the following form:

$$H_{\tau_0} \mathbf{T} = 2\mathbf{E} + (\kappa - 1) \mathbf{1} I_1[\mathbf{E}], \quad \kappa = (1 - 2\nu)^{-1}, \quad (1)$$

where $\mathbf{1}$ is the rank 2 unit tensor, I_1 is the linear invariant of the tensor, ν is the constant Poisson's ratio both for instantaneous elastic strain and creep strain developing over time. Relationship (1) contains the Volterra integral operator over time:

$$H_{\tau_0} f(t) = \frac{f(t)}{G(t)} - \int_{\tau_0}^t \frac{f(\tau)}{G(\tau)} K(t, \tau) d\tau \quad (2)$$

where $G(t)$ is the elastic shear modulus of the material at the age t , and $K(t, \tau)$ is the creep kernel. The latter can be expressed through various characteristics of the material which describe its behavior in different elementary stress state. For example, using the characteristics for pure shear we have

$$K(t, \tau) = G(\tau) \frac{\partial}{\partial \tau} \left[\frac{1}{G(\tau)} + c_{\text{shear}}(t, \tau) \right] \quad (3)$$

where $c_{\text{shear}}(t, \tau)$ is the creep measure in pure shear, $c_{\text{shear}}(\tau, \tau) \equiv 0$. Remark that the given by the expression in square brackets in (3) function of variables t and τ is usually referred to as the function of the specific strain in pure shear. It describes the development over time t of the shear strain caused by the stress state of the pure shear occurring in a specimen at a time τ and not changing further, related to the magnitude of the acting shear stress. The parameter τ_0 of operator (2) has a sense of the time of occurrence of the stress state in the neighbourhood of the given point of the solid.

One can find typical experimental creep curves representing the development over time of specific deformation of samples made of materials with the above mentioned deformation properties for different ages at which the load was applied to them, for example, in [9].

4 DISCUSSION OF THE FEATURES OF THE PROBLEM UNDER STUDY

Since in the simulated processes the deformable solid does not exist in its final composition before the application of loads but is replenished with new material elements already in the course of deformation caused by their action, the moment τ_0 of appearance of

stresses at the points of such a solid will change from point to point, so will not be a constant.

Thus, the lower limit of integration in (2) in the simulated processes should be set by some function $\tau_0 = \tau_0(\mathbf{r})$ of the radius-vector \mathbf{r} of the solid points. The specific type of this function will be determined by the program of solid formation implemented in the concrete additive process. In our case, due to the axial symmetry of the additive process, it is obvious that $\tau_0(\mathbf{r}) = \tau_0(\rho)$ where ρ is the distance from the given point \mathbf{r} of the material layer being manufactured on the substrate to the axis of symmetry being simultaneously its rotation axis. So, the function $\tau_0(\rho)$ for $R_{\text{int}}^{\text{fin}} < \rho < R_{\text{ext}}$, where $R_{\text{int}}^{\text{fin}}$ is the final (achieved by the end of the manufacturing process) value of the layer inner radius, should be determined from the condition $R_{\text{int}}(\tau_0(\rho)) \equiv \rho$ which means that non-zero stresses in the neighbourhood of the considered point of the formed material layer arise directly at the time of inclusion of this point in its composition.

Elements of additional material attached to the solid in question in the process of its gradual formation may by virtue of certain mechanical, physical or chemical features of this process acquire at the time of joining some non-trivial stress state. Taking into account the initial stresses in the elements of any solid formed in the additive process should be part and parcel of the formulation of correct boundary conditions on that part of its surface to which the new material flows. This part of the boundary surface of an additively formed solid is usually called the surface of its growth. In this paper we consider the case when by applying additional material onto the surface of the growth of the produced layer, i.e. its inner surface $\rho = R_{\text{int}}(t)$, this surface does not experience the action of any external loads. In other words, the initial stresses at the points of the formed layer, set at these points at the time when the growth surface passes through them, are consistent with the zero load on this surface:

$$\mathbf{e}_\rho \cdot \mathbf{T}|_{t=\tau_0(\rho)} = \mathbf{0}, \quad \mathbf{e}_\rho = \frac{\partial \mathbf{r}}{\partial \rho} \bigg/ \left| \frac{\partial \mathbf{r}}{\partial \rho} \right|, \quad (4)$$

where $\mathbf{e}_\rho = \mathbf{e}_\rho(\mathbf{r})$ is the unit vector that specifies the radial direction in the cross-sectional plane of the cylindrical layer being produced.

The problem of deformation of the produced cylindrical layer is solved in the presented study in the approximation of plane strain state. The case of small strain is considered. In view of the latter circumstance, it does not make sense to take into account the deformation component in the time-dependence of the formed layer internal radius R_{int} which is decreasing in time due to the influx of additional material to the layer. So this dependence can be considered as given by virtue of the implemented program of material application. Thus, the function $R_{\text{int}}(t)$ is a known function, strictly decreasing at those time intervals in which the application of the material is carried out, and constant at those time intervals, in which the inflow of additional material to the formed layer is temporarily or permanently terminated, that is, in pauses between the individual stages of continuous application of the material and after the final completion of the layer additive formation.

In the context of the problem under study in this paper, it is necessary to pay attention to the following circumstances. If we were talking about the additive formation of a purely

elastic solid, the rate of change of its SSS at each point would be determined only by the instantaneous characteristics of the processes of its loading and replenishment with new material, and after the termination of the formation, fixation or removal of loads and kinematic bonds, the state of the solid would no longer change. The situation is different in the case of using the material which is viscoelastic and aging in their mechanical properties. Here, the nature of the development of the SSS of the whole formed solid at each time instant depends on the full history of the formation and loading of the solid, that is, on the duration of staying of the various material elements in its composition, on the age of their entry into this composition, and on the laws of change of the loads applied to the solid in all previous moments of time. Along with this, in the pauses between the stages of continuous inflow of new material to the solid, as well as after the completion of the solid manufacturing, its SSS will continue to change over time, striving for some final characteristics.

5 THE TAKEN APPROACH

Statements of initial boundary value mechanical problems at all stages of continuous application of the additional material, in the pauses between these stages and after the final termination of the additive process are non-classical in solid mechanics. They are formulated in the present study in terms of the rates of change of the SSS characteristics of the being formed solid in the variable in time region occupied by this solid at the current time instant. The set initial and boundary conditions take into account the kinematic and force specifics of the interaction of the additionally attached material with the already formed part of the solid over the entire instantaneous surface of its growth. A significant mathematical difficulty in solving the initial boundary value problems stated is the dependence of the moment of the beginning of stresses development in the material on the point of the formed solid due to the non-simultaneous inclusion of various material elements in the process of deformation. The mathematical apparatus developed in the framework of the established by Professor A.V. Manzhurov Russian scientific school in mechanics of additive processes allows to overcome the announced difficulty. According to this apparatus, the procedure of solving the stated non-classical problems can be reduced to solving a series of boundary problems having a mathematical form of classical problems of solid mechanics, followed by the treatment of certain integral equations in time for each point of the finally formed solid. In the presented work, the solutions of the corresponding classical problems are constructed analytically in a closed form containing quadratures depending in a complex way on different parameters of the simulated additive process and on rheological properties of the material used for manufacturing. Calculation of these quadratures and further inversion of integral equations are carried out by numerical methods.

6 THE OBTAINED RESULTS AND PRACTICAL FINDINGS

Numerous numerical calculations were performed using the developed mathematical model. In the calculations, a variant of centrifugal application of the material is considered, in which the features of its entry into the composition of the formed solid do not lead to the appearance in the latter of initial stresses other than zero near the surface of its growth.

The stress distributions in a polymer layer additively formed on a substrate are compared with the corresponding classical distributions in a similar layer coupled with the same

substrate and rotating with it around its axis but completely made in advance without any residual stresses before the start of rotation. The latter distributions are found from the solution of the corresponding classical solid mechanics problem which does not take into account the process of solid formation and assumes the application of all loads to it already in its final composition. The principal qualitative and quantitative differences of the above distributions are demonstrated: they differ in the character of monotony, positions and values of extreme values, have different intervals of sign-constancy. It is extremely important to point out that the revealed differences are due not to the rheological manifestations in the deformation response of the material used, but to the mechanical features of the additive process itself of layer-by-layer formation of a solid at the same time with the loads acting on it. It can be shown (see, for example, [1]) that in the absence of rheological manifestations — in the case of using a purely elastic material — the demonstrated differences would be even more pronounced, whereas the creep process in the solid during its gradual formation affords slurring over these differences.

The evolution of the technological stress state of the formed polymer layer during its manufacture is analyzed. It is shown that the intensity of shear stresses, which is an important stress characteristic of the product in terms of assessing its strength, reaches a maximum in the immediate vicinity of the substrate. This fact can not be found on the basis of the solution of the classical mechanical problem on deformation under the action of centrifugal forces of a material layer coupled with the rotating substrate, not taking into account the mechanical features of the manufacturing process of this layer. Indeed, from such solution it would follow that the maximum of the intensity of shear stresses should be achieved at the free surface of the layer, the most distant from the substrate, which directly contradicts the results obtained taking into account the specifics of the additive technological process.

In the presented work it is demonstrated that the technological stresses in the polymer layer arising in the process of its manufacture depend in a decisive way on the speed and nature of the whole process. Thus, the presence of pauses in the process of applying the material leads to a qualitative and very significant quantitative change in the pattern of the technological stress state of the finished layer compared to that obtained in a continuous process.

The very specificity of the simulated technological processes dictates the appearance of residual technological stresses in the resulting products. The final distributions of residual stresses, which are eventually settled in the finally formed polymer layer, are found in various situations: after the rotation stops at the completion of the layer formation, as well as after the rotation stops and the finished layer is detached from the substrate (if the latter is provided by the simulated technological process). It could be expected that the stresses arising under the action of centrifugal forces in the layer during its fabrication, together with the stop of rotation and therefore the disappearance of these forces should essentially reduce their values. However, as the calculations show, this does not happen: for example, the maximum values of compressive circumferential stress and the intensity of shear stresses may even increase significantly after the termination of the rotational motion. The reduction of all residual stresses is observed only after the finished layer is detached from the substrate, but the corresponding stresses can still not be neglected compared to those that have acted during the centrifugal application of the material.

If the finished layer remains bonded to the substrate after the termination of the centrifugal application of the material, then, despite the absence of inertial effects on the non-rotating

material layer, the normal contact stresses at the interface of this layer and the substrate will remain compressive indefinitely. This circumstance, obviously, prevents spontaneous detachment of the finished layer from the substrate, which is especially important in cases where it is supposed to be further used as an entity together with the substrate on which it was manufactured. If the substrate was used in the simulated process only as a tooling and is disconnected from the finished layer after the material application process, then the corresponding residual radial stresses will be compressive throughout the thickness of the layer, and the residual circumferential stresses will be stretching in the part that was adjacent to the substrate, and compressing in another part.

7 CONCLUSIONS

In the present study the additive technological processes of layer-by-layer manufacturing polymer pieces on the inner surface of a rotating cylindrical substrate are investigated. Polymer materials exhibit rheological mechanical properties. Their behavior is described in the study in the framework of the linear hereditary theory of viscoelasticity of aging media. A non-classical mechanical model of the processes in question is proposed. The model is based on considerations of the current theory of additively formed deformable solids. The corresponding initial boundary value problems for description of the deformation process of the being formed polymer layers under the simultaneous action of centrifugal forces are formulated. The numerical-analytical solutions are obtained. Numerous calculation are performed. The evolution of the stress state of a polymer layer during and after its manufacturing is described. It is demonstrated that the found distributions of technological stresses in the produced layer depend in a decisive way on the realized manufacturing regime and essentially differ from the classical stress distributions in a similar rotating polymer layer that has not undergone any external impacts during the process of manufacturing. The mentioned difference is explained by fundamental mechanical features of the additive process itself and causes the inevitable occurrence of residual stresses in the finished layer after stopping its rotation and, if it is necessary, after its detaching from the substrate. The distributions of these residual stresses are found and analyzed in detail in the present study.

ACKNOWLEDGEMENT

The study was supported by the Russian Science Foundation under grant No. 17-19-01257.

REFERENCES

- [1] Manzhirov, A.V. and Parshin, D.A. Influence of the erection regime on the stress state of a viscoelastic arched structure erected by an additive technology under the force of gravity. *Mech. Solids* (2015) **50** (6): 657-675.
- [2] Manzhirov, A.V. and Parshin, D.A. Application of prestressed structural elements in the erection of heavy viscoelastic arched structures with the use of an additive technology. *Mech. Solids* (2016) **51** (6): 692-700.
- [3] Parshin, D.A. Analytic solution of the problem of additive formation of an inhomogeneous elastic spherical solid in an arbitrary nonstationary central force field. *Mech. Solids* (2017) **52** (5): 530-540.

- [4] Parshin, D.A. The technological stresses in a vaulted structure built up on a falsework. *Advanced Structured Materials* (2017) **46**: 377-386.
- [5] Manzhirov, A.V. and Parshin, D.A. Analytical solution of the mechanical problem on additive thickening of aging viscoelastic tapers under nonstationary longitudinal end forces. *Engng Letters* (2018) **26** (2): 267-275.
- [6] Parshin, D.A. Solving a problem of theory of viscoelasticity for continuously accreted solids with the satisfaction of static boundary conditions in the integral sense. *J. Phys.: Conf. Ser.* (2019) **1203**: 012006.
- [7] Askadsky, A. A. *Deformation of polymers*. Chemistry, Moscow (1973) [in Russian].
- [8] Arutyunyan, N.Kh. and Manzhirov, A.V. *Contact problems of the theory of creep*. Izdat. Inst. Mekhaniki NAN RA, Erevan (1999) [in Russian].
- [9] Struik, L.C.E. *Physical aging in amorphous polymers and other materials*. Elsevier, Amsterdam (1978).

NUMERICAL ANALYSIS OF SUPPORT STRUCTURES' REMOVAL FROM ADDITIVELY MANUFACTURED COMPONENTS

LOUCAS PAPADAKIS*

* Department of Mechanical Engineering, Frederick University
Y. Frederickou Str. 7, CY-1036 Nicosia, Cyprus
e-mail: l.papadakis@frederick.ac.cy, www.frederick.ac.cy

Keywords: Selective Laser Melting, Finite Element Analysis, Simulation of Stresses, Simulation of Shape Distortion, Post-processing Cutting Operations, Elastic Recovery, Shape Distortion Compensation

Abstract. The finite element analysis (FEA) of components' build-up has recently proved to be a valuable tool for accompanying the product and process development during additive manufacturing (AM). In this numerical method a first key aspect is the heat input modelling of laser scanning for building-up AM products of industrial relevance, as close to reality as possible, by applying equivalent heat source models. Based on these reduction models the stress distribution in a successive thermo-mechanical simulation is calculated approximating the sum of thermal, elastic and plastic stresses during processing and the remaining elastic and plastic stresses after cooling. A further key aspect is, thereupon, to predict the final shape of the additively manufactured component by means of the FEA after its removal from the substrate or the support structures. This work aims to analyze the development of stresses in components during their additive laser processing and cooling to ambient temperature as well as after post-processing cutting operations. Moreover, the associated stress development simulated final part shape is evaluated with the aid of 3d measurements on an additively manufactured twin cantilever of industrial relevance. Finally, based on the rendered simulation results a compensation of the undesired shape distortions is proposed based on reverse engineering approach.

1 INTRODUCTION

Modeling and simulation methods have recently proved high potential in accompanying additive manufacturing process and product development. In the frame of the AMable Project [1] these potentials have been identified and captured in form of potential services which can be adopted by innovative technology carriers and industrial manufacturers operating in additive manufacturing related business. The increasing knowledge and apparent benefits as well as the flexibility of modeling and simulation methods and tools allows their utilization not only in large-scale enterprises but also in small and middle-sized companies (SMEs). The major reasons motivating companies to apply modeling and simulation raise from the increasing demands and challenges during product development when using additive manufacturing techniques, e.g. application of new powders, manufacture of novel and complex shapes or functionalities, new machines etc. Additionally, the increasing required product quality and the need for reducing processing times are further reasons which

encourage companies to use modeling and simulation solutions.

The main key aspects which are identified in which modeling and simulation can provide useful support for developing products with additive manufacturing processes are following:

- weld pool shape prediction by means of analytical high performance models, i.e. quasi real time, in order to assist process control [3-5],
- thermo-mechanical models with reduced equivalent heat sources for shape distortion and residual stress computation [6],
- facilitation of pre-deformed geometry shapes to limit shape inaccuracies by applying reverse engineering strategies [7],
- path planning optimization to reduce processing times and unnecessary heat input [3,8],
- modeling of post-processing operations, i.e. cutting and support structures' removal with comparison of the simulated component shape with the 3d geometry of real additively manufactured components [9,10],
- thermodynamical and kinetical models for alloy, microstructure and powder tailoring and design, such as phase field changes [11,12],
- determination of mechanical material properties based on crystal plasticity and micromechanical evaluation of resistance to fatigue, i.e. fatigue performance indicators [13], and
- further specific modeling and simulation aspects under the umbrella of integrated computational materials engineering (ICME).

However, occasional lack of specific knowledge for certain complex modeling aspects or the need for specific software or high performance computing (HPC) recourses increase the necessity for regular update, training and know-how exchange among the modeling and simulation experts [1]. Besides providing an overlook of the potential use of modeling and simulation in the additive manufacturing business, this paper focuses specifically on the finite element analysis (FEA) of post-processing operations, i.e. support structures' removal, after components' manufacture by means of selective laser melting (SLM).

2 THERMAL MODEL WITH REDUCED EQUIVALENT HEAT SOURCE

In literature several numerical approaches exist which account for the heat effects occurring during additive manufacturing processes, especially SLM [3-9]. In author's previous work a systematic modeling approach was introduced for the realization of a simulation solution with reasonable time durations for practical industrial applications based on a reduction heat input during the build-up process with metallic powders [6]. Hereby, a transient temperature profile is applied on whole model layers or multi layers, representing the total heat load per volume, based on powders melting point and the SLM process parameters (processing time, scan speed, hatch distance, laser powder etc.) for industrial relevant examples [2]. In this paper a twin-cantilever geometry is used to demonstrate the heat effects and thermo-mechanical modeling as well as the structural results, i.e. stress and deformation development, after the component creation and its cut-off from the support structures. Figure 1 illustrates the main dimensions of the twin-cantilever geometry with the support structures and the heat losses to substrate and surrounding powder due to conduction as well as the convection and radiation on the upper, currently processed layer.

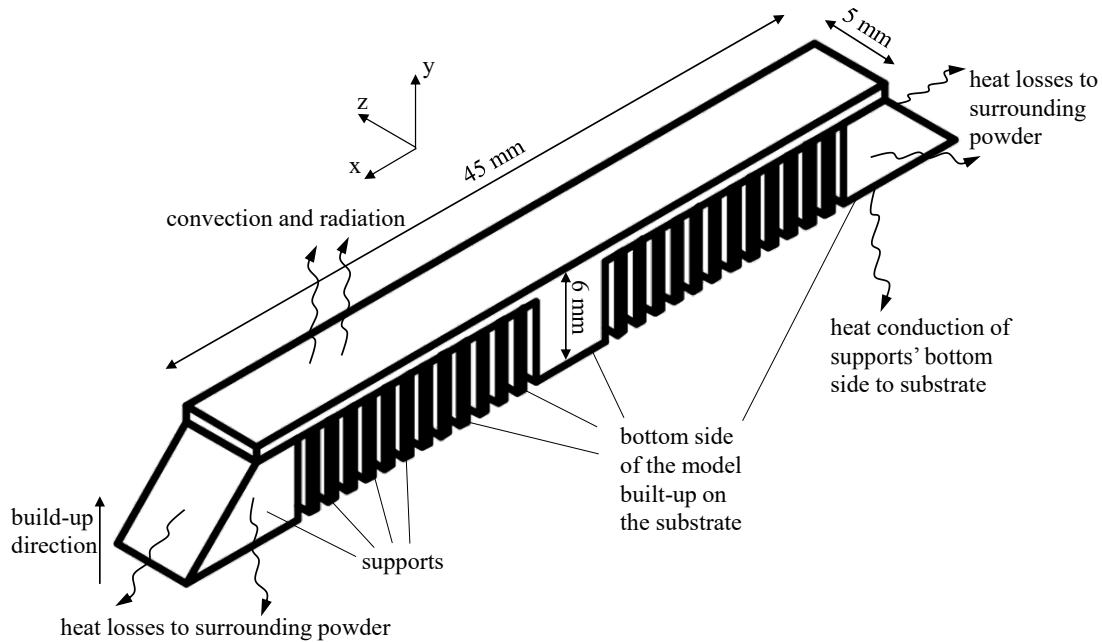


Figure 1: Twin-cantilever geometry with support structures with defined heat losses as considered in the transient thermal finite element model approximating the build-up process during SLM

The equivalent heat load within the transient thermal simulation of the twin-cantilever was adjusted accordingly in each volume layer of elements in the form of temperature-time function as illustrated in Figure 2. In the FE mesh of the twin-cantilever each element layer has a thickness of $90\ \mu\text{m}$ corresponding to the threefold of the powder layer thickness of the real SLM process. This trade-off was made in order to reduce time-consuming simulation duration and enormous amount of data storage. Between each process layer the real process sequences were considered, i.e. approximately 10 s for the powder layer deposition prior to the processing of the subsequent overlying layer. Table 1 summarizes the SLM process parameters used by Fraunhofer ILT on SLM@280 HL machine with IN718 powder for the manufacture of the twin-cantilever [2]. The laser scanning was performed longitudinally to the twin-cantilever with no hatch angle increment.

Table 1: SLM process parameters in IN718 powder for the manufacture of the twin-cantilever [2]

Process parameters	Value	Units
Laser power	300	W
Scan speed	1600	mm/s
Laser beam diameter	90	μm
Layer thickness	30	μm
Hatch distance	80	μm
Hatch angle increment	0	$^{\circ}$ degrees
Time interval for powder deposition	10	s

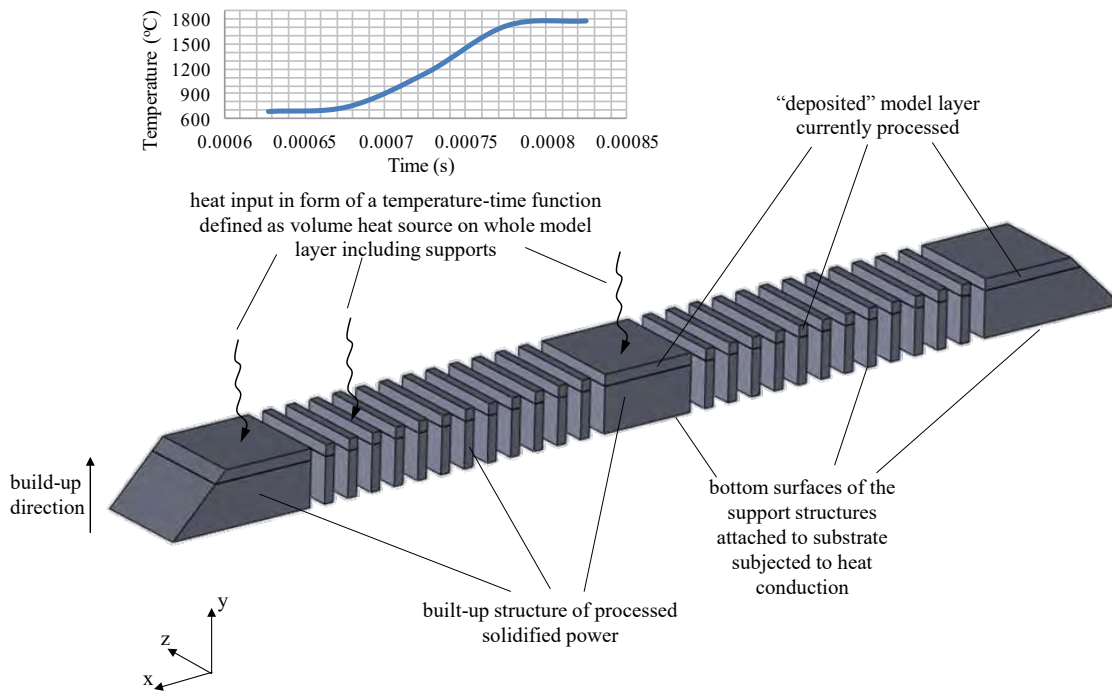


Figure 2: Twin-cantilever geometry with support structures with heat losses as defined in the transient thermal finite element model approximating the built-up process during SLM

During the “build-up process” of the twin-cantilever within the transient thermal and the successive thermo-mechanical numerical analysis, overlying, i.e. not yet deposited, elements in the FE mesh were assigned with negligible thermal and mechanical properties, i.e. were deactivated. They were assigned with the powder material properties, i.e. activated, once the layer they represented was to be processed. During processing, i.e. heating, and after reaching the melting point the powder material was assigned with the material properties of the solid IN718 with the aid of a phase transformation model implemented within the thermal analysis [11,12]. The thermal and mechanical material properties used for IN718 were temperature and phase dependant and were taken from the literature [2]. The thermal material properties for IN718 powder were induced according to the work of Biceroglu et al. [14]. The model layers were processed one after the other until the whole twin-cantilever was built. In order to ensure the “binding” of the processed model layer to underlying solid material, a partial re-melting of the underlying element layer was undertaken, similar to the real SLM process. After each layer build-up, i.e. the phase change from powder to liquid and finally to solid, and the cooling to ambient temperature, the model attained its final thermal and mechanical equilibrium.

The results of the temperature field during the model layerwise “build-up process” is shown in Figure 3 for exemplary model layers. The whole simulation time including the cooling time intervals for a new powder layer deposition and the final cooling of the complete twin-cantilever to ambient temperature equals to 850 s. The calculated transient temperature field of each model layer including the change of phase from powder to liquid and finally to solid was used as a load for a sequential thermo-mechanical numerical analysis.

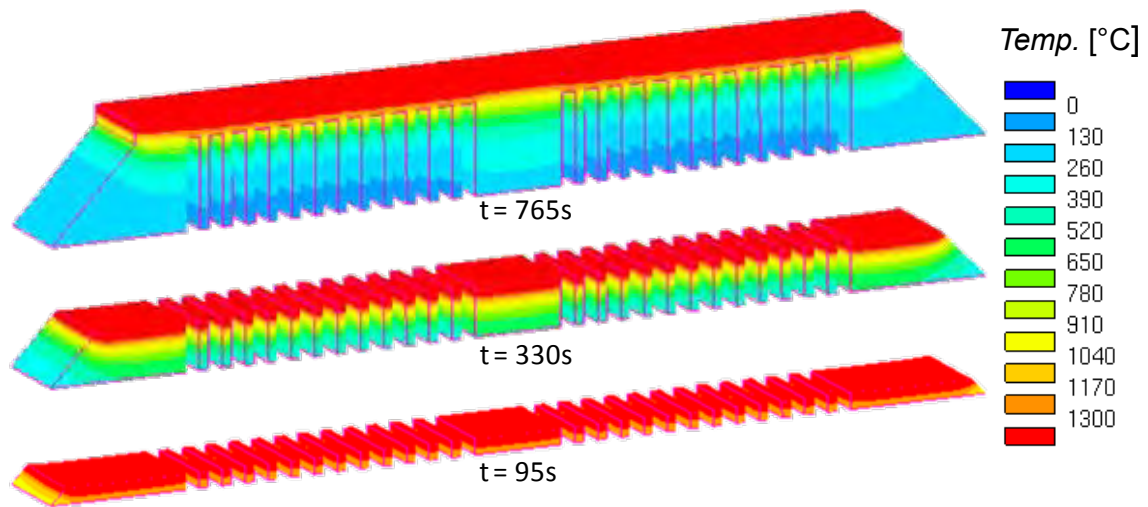


Figure 3: Temperature field results of exemplary successive element layers during the model “build-up process”

3 RESIDUAL STRESS AND DEFORMATION COMPUTATIONAL RESULTS

The thermal analysis presented in the previous section, based on a reduced heat source model replicating the real SLM process of the twin-cantilever, provided the transient temperature field of successive processed model layers as result. This transient temperature field was thereafter applied as a thermal load in an uncoupled thermo-mechanical analysis. For this numerical calculation, an isotropic elastic–plastic material definition with temperature dependant mechanical values for the Young’s modulus, yield stresses and strain hardening was employed. Additionally the change of phase from powder to melt and finally to solidified material was considered in the earlier transient thermal analysis by applying a phase change model in the finite element program SYSWELD carrying temperature and phase dependant mechanical properties of the nickel based steel alloy IN718 [2,12].

First the shape deformation and residual stresses of the twin-cantilever while still attached on the substrate and support structures (i.e. prior to cut-off operation) were computed. After cutting-off the twin-cantilever support structures in the experiment by means of electrical discharge machining (EDM) as illustrated in Figure 4, a spring-back, i.e. elastic recovery, is observed with a maximum measured deformation of approximately 0.8 mm on the edges.

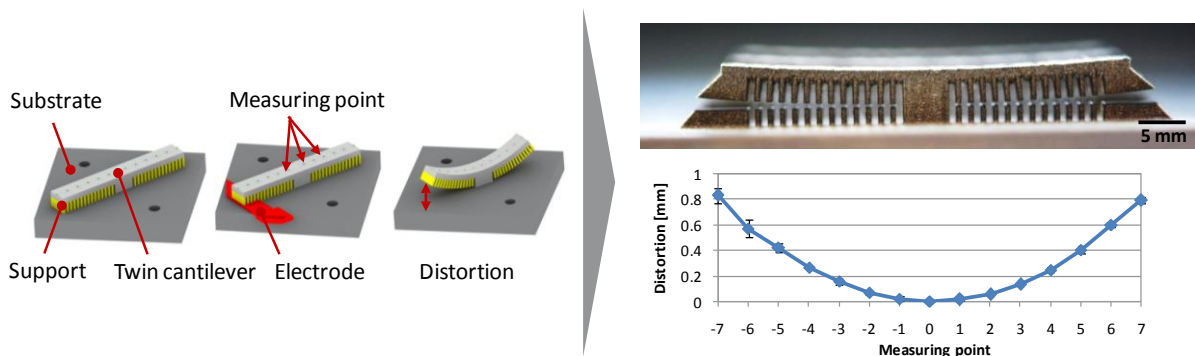


Figure 4: Support structures’ cut-off process and final deformation of the twin-cantilever geometry

Due to the nature of the SLM process in conjunction with the twin-cantilever geometry, the component was manufactured with support structures which were cut-off after manufacturing and cooling to ambient temperature. It was significant to include this process step in the simulation chain, in order to replicate the spring-back, i.e. geometrical changes and final stress state equilibrium of the component's structure after elastic recovery. In order to calculate the component's final shape after the material removal the final state of equilibrium, i.e. elastic recovery, was considered. After the thermo-mechanical simulation of the main build-up process and the cooling to ambient temperature, the elements in cutting area were removed in the FE model, whilst the stress state and final temperature at the end of the thermo-mechanical simulation were maintained with the component still attached to the support structures. At a subsequent step the simulation was restarted and the mentioned solid element removal in the support structures forced the component to its final shape providing an elastic recovery and, thus, a relaxation of the total stresses and a final state of equilibrium. The final distortion in the vertical build-up direction as calculated after the spring-back by the numerical model is demonstrated in Figure 5 providing a visual comparison with the experimental result of the real twin-cantilever geometry. The defined mechanical boundary conditions, i.e. constraints, did not allow any displacement on the bottom of the substrate, i.e. the substrate was mounted on the working bench.

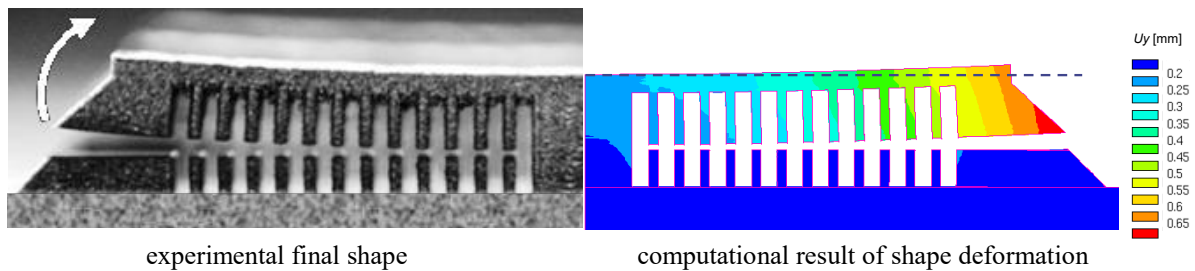


Figure 5: Experimental (left) and computational final shape (right) of the twin-cantilever in the build-up direction after the support structures' removal

The computed residual stresses variation before (left) and after cut-off (right) are presented in Figure 6. A significant relaxation, i.e. reduction, of the von-Mises residual stresses after the material removal is observed. The residual stresses' decrease is more perceivable in the upper area of the twin-cantilever and in the support structures.

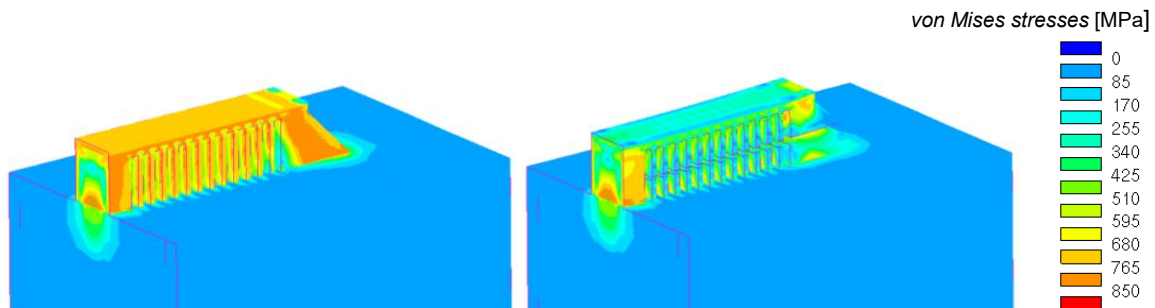


Figure 5: Residual stresses variation before (left) and after support structures' removal (right)

Not only are the computer capacity requirements and computational times of significance but also the reliability of the introduced method, which can essentially be applied in the design phase of SLM products for future industrial applications. The reliability of the applied numerical method was appraised with a model validation using deformation measurements on the manufactured twin-cantilever. The vertical displacements were measured on a path at the top of the twin-cantilever with a step of 2.5 mm, from the symmetry plane to the right side of the component as illustrated in Figure 7. As observed there is a 26% maximum discrepancy in the results on the far right edge of the component. This is acceptable, since it is related to the modeling reduction approach, and the fact that three powder layers are being “fabricated” simultaneously in the numerical model.

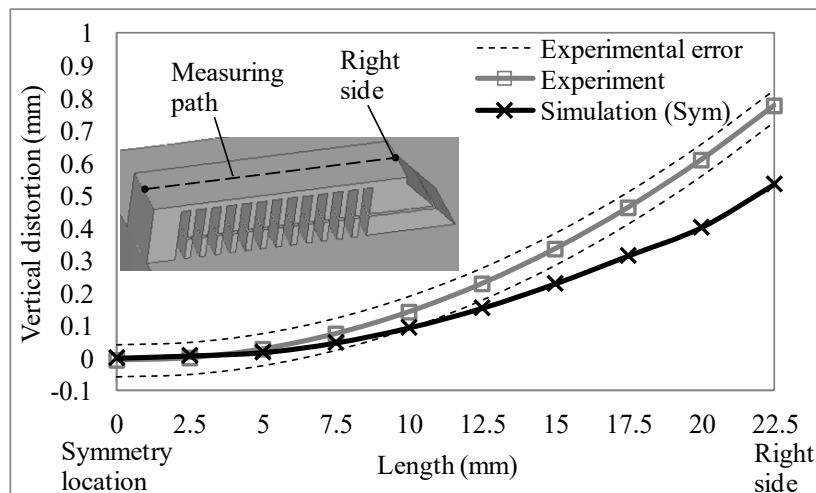


Figure 7: Comparison of experimental and numerical deformation results of the twin-cantilever after cut-off

In addition, a parameter study on the twin-cantilever component was performed in order to investigate the sensibility of the proposed modeling method. This was done by running simulations of thicker horizontal part thicknesses of the twin-cantilever geometry. The supplementary simulations included thicknesses of 1.5 mm, 2.0 mm and 3.0 mm. This has added a +0.5 mm, +1.0 mm and +2.0 mm respectively to the reference model of the 1.0 mm thickness. The computed deformation behavior for increasing component thickness was verified with the measurements on real SLM manufactured components with the corresponding thicknesses by Fraunhofer ILT [2]. The provided measurements indicate a shape distortion decrease for higher component thicknesses. Figure 8 presents the comparison of the distortion results between simulation and measurements on real components. It is observed that the model managed to provide reliable results with an accuracy improvement for increasing component thickness. This is associated with the used mesh discretization of 90 μm per layer of elements, which appears to be more sufficient for increasing component thicknesses. An attempt to lower the model thickness proved to be quite sensitive in terms of the computed deformations, i.e. unstable deformation trend was observed, due to insufficient FE mesh degree of discretization through the reduced twin-cantilever thickness resulting to even less number of element layers along the build-up direction.

The improved accuracy of simulation results for models with increasing component thickness compared to measurements along the twin-cantilever upper area is exhibited in Figure 8. Particularly for a sufficient increase of the component thickness to 2.0 mm and 3.0 mm an adequate correlation with only marginal deviations has been achieved with the use of the introduced modeling method. This proves the reliability of the developed modeling approach especially for components with sufficient thicknesses for the adopted FE discretization.

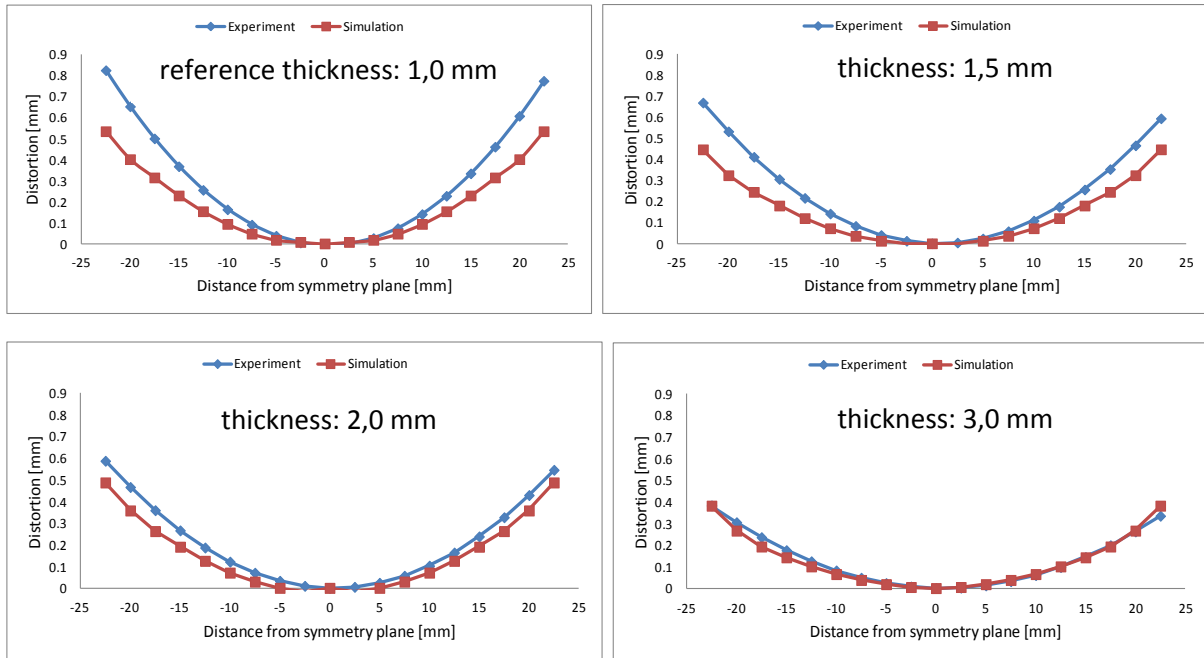


Figure 8: Improved simulation result accuracy compared to experimental measurements on real manufactured components with increasing twin-cantilever thickness

4. SHAPE DISTORTION COMPANSATION BY MEANS OF “PRE-BENT” MODEL

A further aim of this paper is to demonstrate a potential compensation of the twin-cantilever’s shape deformations after its SLM manufacture. To compensate shape distortions and counteract the resulting final deformations after the support structures removal’, a “pre-bent” twin-cantilever model with “negative geometry” was facilitated considering the already simulated deformation results, as presented in Figure. The “pre-bent” model was prepared based on the distortion results of the twin-cantilever geometry with the reference thickness of 1.0 mm. Hereby, the calculated distortions along the measuring path on the top area of the twin-cantilever (cp. Figure 5 and Figure 7) were applied in the opposite, i.e. negative, direction. Based on this deformed shape the “pre-bent” twin-cantilever geometry is remodeled with a curvature in the negative direction of the initial spring-back as demonstrated in Figure 9. The “pre-distorted” twin-cantilever is illustrated compared to the target geometry, i.e. the horizontal plane, which should be targeted after the cut-off operation.

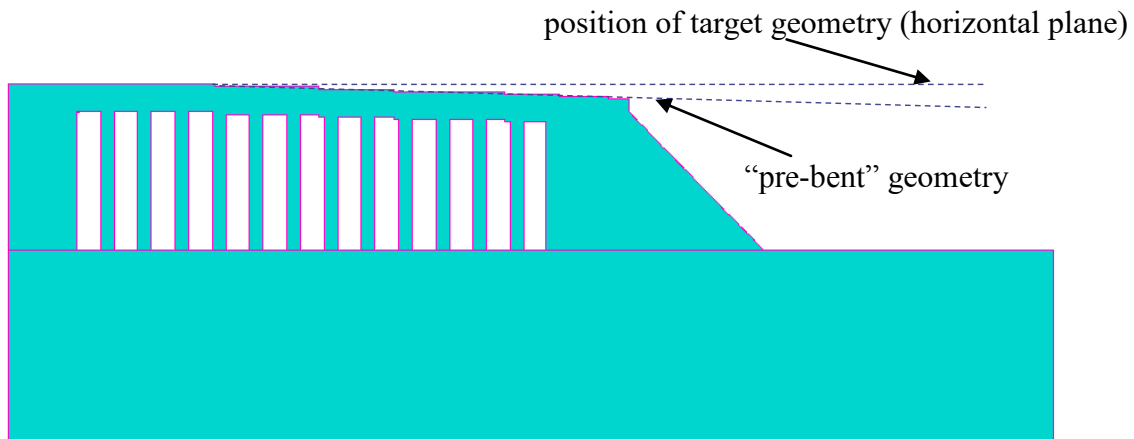


Figure 9: “Pre-bent” twin-cantilever geometry based on the original model deformation results compared to the horizontal target geometry

The overall distortion of the “pre-bent” model after the numerical analyses proved to be only slightly higher compared to the original model with approximately solely 0.1 mm of maximum discrepancy on the tip of the twin-cantilever. The final distortion of the “pre-bent” model appears to provide a sufficient improvement compared to the initial reference model approaching the horizontal plane in a very good manner as shown in Figure 10.

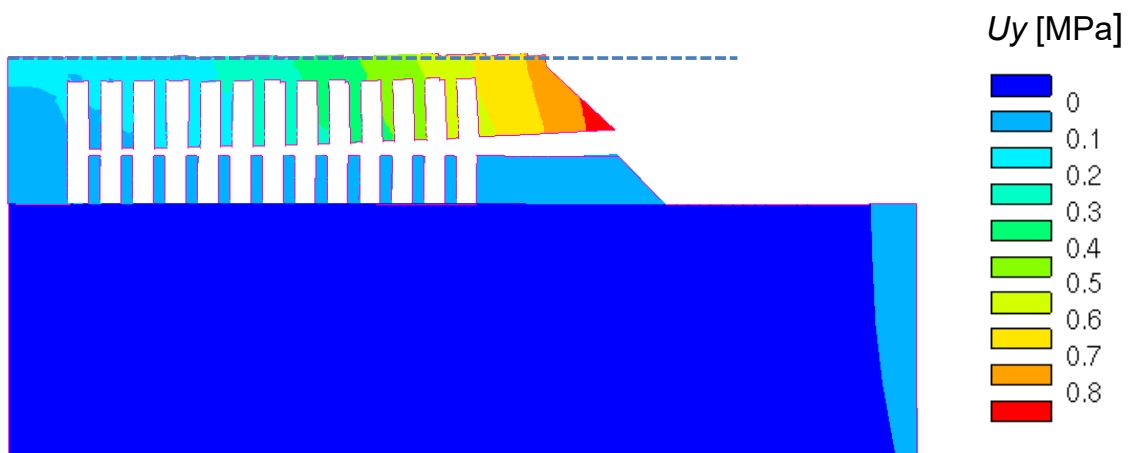


Figure 10: Final distortion of the “pre-bent” twin cantilever model compared to the target horizontal plane

To compare the original and “pre-bent” model’s final shape distortion, the distance of the horizontal part to the target geometry horizontal plane was taken into account. As observed in Figure 11, the pre-distorted model has provided improvements on the final component shape accuracy with a limitation of the discrepancies to only 0.1 mm on the right edge of the twin-cantilever.

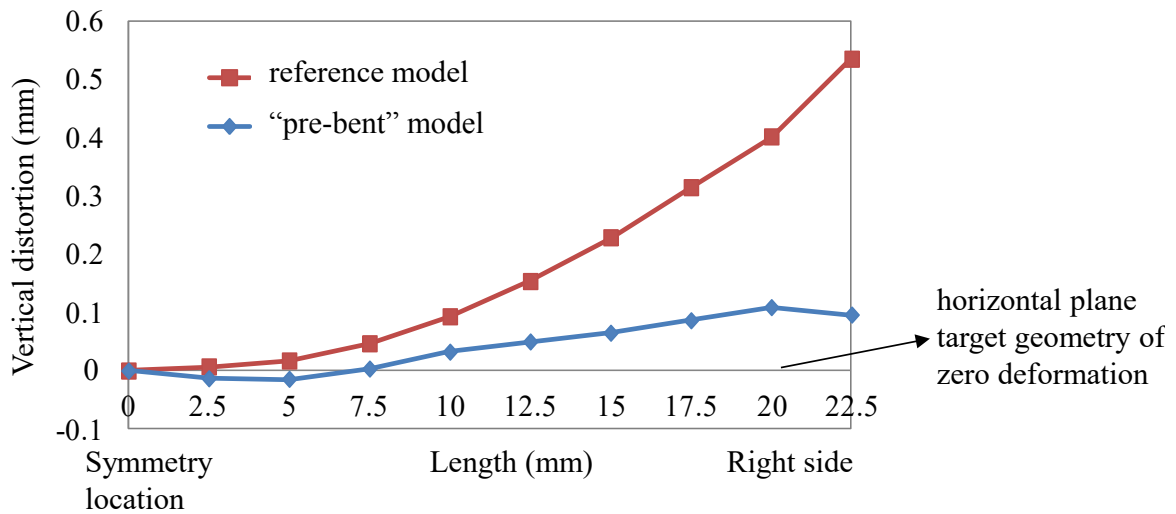


Figure 11: Improvement of the final shape accuracy for the “pre-bent” model compared to the reference model

Figure 12 shows the residual stress distribution of the pre-distorted twin-cantilever model after the build-up process (left) and after support structures’ removal (right) indicating a very similar trend to the reference model in Figure 5. This was expected as there are not any significant changes in the geometry and the build-up process apart from the trimming on the twin-cantilever’s upper area in order to approximate the negative shape distortion of the reference model after the cut-off operation.

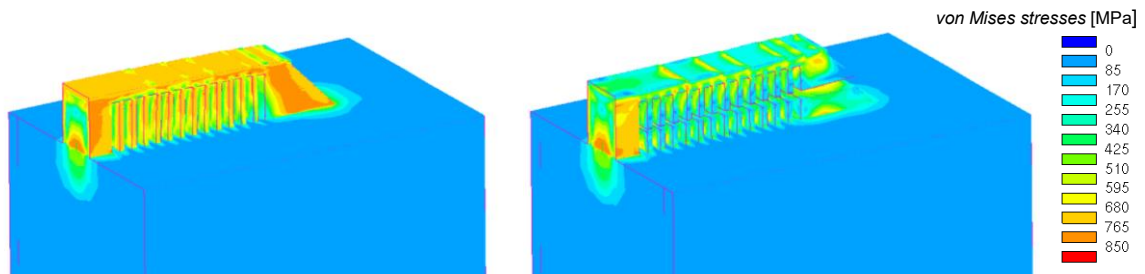


Figure 12: Residual stresses variation of the “pre-bent” model before (left) and after support structures’ removal (right) with a similar trend as the reference model.

5 CONCLUSIONS

In this paper the structural behavior of a twin-cantilever manufactured by means of SLM including the post-processing operation of support structures’ removal is presented. The thermo-mechanical effects during the build-up process as well as the “spring-back” of the created twin-cantilever after support structures’ removal were replicated by means of a numerical analysis. Based on a reduced equivalent heat source model the SLM process was approximated on a FE mesh discretized to a certain degree. Thereupon, the component’s residual stresses and deformations were computed once the component was manufactured and

cooled to ambient temperature and subsequently after it was detached from the support structures. In order to draw conclusions on the reliability of the proposed computation chain, including the build-up process and the supports' removal operation, experimental measurements of the shape deformation on real twin-cantilever geometries were conducted and compared with the simulation results. The rendered results have led to following conclusions:

- After the build-up process of the twin-cantilever and its cooling to ambient temperature no significant shape deviation were observed, i.e. <0.1 mm, compared to the initial target CAD geometry, in both experiments and simulation.
- The reference experiment utilized for evaluating the numerical model demonstrated a maximum deviation between numerical and experimental results of 26% at the edge of the twin-cantilever after the cutting operation. This error was linked with the heat source reduction approach and the degree of mesh discretization which led to a less accurate computation of stress distribution in the component. However, these approximation were inevitable in order to demonstrate the structural results on a practical component with reasonable computational times and storage capacity.
- The conducted parameter study proved that the coarse mesh discretization in the build-up direction in the numerical models becomes less significant with increasing twin-cantilever thickness, since deviations to experimental deformation proved to diminish.
- The relaxation of residual stresses after the support structures' removal are closely associated with the induced deformations. This is the reason why the comparison of the twin-cantilever final shape between simulation and experiment allowed us to conclude on the quality of the computed residual stresses.
- The computed or measured shape distortions caused after support structures' removal can be used to manufacture components with negative geometries, i.e. pre-bent, so that they can compensate the induced deformations and approximate more accurately the target, i.e. ideal, final component shape after the cut-off operation.

To summarize, by applying appropriate approximation methods and simplifications along the introduced simulation chain, it was possible to compute the residual stresses and deformation behavior of components of industrial relevance after support structures' removal. The potential to reach a higher agreement with measurements increases when applying the appropriate model refinements. In this way simulation methods can assist in making the right design decisions during the development of products created by additive manufacturing processes.

ACKNOWLEDGEMENT

The experimental and simulation results presented in this paper were accomplished in the framework of the MERLIN Project which received funding from the European Commission's 7th Framework Programme FP7 2007–2013 under the Grant agreement 266271. Project website: <http://www.merlin-project.eu>. Further work presented in this paper was partially performed in the framework of the AMable Project which has received funding from the European Union Horizon 2020 research and innovation program under the Grant agreement 768775. Project website: <http://www.amable.eu>.

REFERENCES

- [1] AMable Project AdditiveManufacturABLE: Enabling SME and Mid-Cap Uptake of Additive Manufacturing by Bridging Gaps in the Digital Process Chain (2017-2021), Horizon 2020. Available online: <http://www.amable.eu> (accessed on 10 June 2019).
- [2] MERLIN Project: Development of Aero Engine Component Manufacture Using Laser Additive Manufacturing (2007-2013), 7th Framework Program FP7. Available online: <http://www.merlin-project.eu> (accessed on 15 April 2019).
- [3] Letenneur, M.; Kreitchberg, A. and Brailovski, V. Optimization of Laser Powder Bed Fusion Processing Using a Combination of Melt Pool Modeling and Design of Experiment Approaches: Density Control. *J Manuf Mater Process* (2019); **3**.
- [4] Fyrillas, M.M. and Papadakis, L. Transient Powder Melting in SLM Using an Analytical Model with Phase Change and Spherical Symmetry in a Semi-Infinite Medium. *J. Manuf. Mater. Process.* (2019); **3**.
- [5] Kruth, J.P.; Duou, J.; Mercelis, P.; Van Vaerenbergh, J.; Craeghs, T. and De Kuester, J. On-line monitoring and process control in selective laser melting and laser cutting. In Proceedings of the 5th Lane Conference, Laser Assisted Net Shape Engineering, Erlangen, Germany, (2007): 23–37.
- [6] Papadakis, L.; Loizou, A.; Risse, J. Bremen, S. and Schrage, J. A computational reduction model for appraising structural effects in selective laser melting manufacturing: a methodical model reduction proposed for time-efficient finite element analysis of larger components in Selective Laser Melting. *Virt. and Phys. Protot.* (2014); **9**:17-25.
- [7] Afazov, S.; Denmark, W.A.D.; Toralles, B.L.; Holloway A. and Yaghi, A. Distortion prediction and compensation in selective laser melting. *Addit. Manuf.* (2017) **17**:15-22.
- [8] Xing, W.; Ouyang, D.; Li, N. and Liu, L. Estimation of Residual Stress in Selective Laser Melting of a Zr-Based Amorphous Alloy. *Materials* (2018); **11**:1480.
- [9] Yaghi, A.; Ayvar-Soberanis, S.; Moturu, S.; Bilkhu, R. and Afazov, S. Design against distortion for additive manufacturing. *Addit. Manuf.* (2019); **27**:224-35.
- [10] Papadakis, L. and Hauser, C. Experimental and computational appraisal of the shape accuracy of a thin-walled virole aero-engine casing manufactured by means of laser metal deposition. *Prod. Eng.* (2017); **11**:389-399.
- [11] Leblond, J.B. A new kinetic model for anisothermal metallurgical transformations in steels including effect of austenite grain size. *Acta Metall.* (1984); **32**:137-146.
- [12] SYSWELD. Sysweld user's manual. ESI Group, (2006).
- [13] Dallago, M.; Zanini, F.; Carmignato, S.; Pasini, D. and Benedetti, M. Effect of the geometrical defectiveness on the mechanical properties of SLM biomedical Ti6Al4V lattices. *Proc. Struct. Integr.* (2018); **13**:161-167.
- [14] Biceroglu, O.; Mujumdar, A.S.; van Heiningen; A.R.P. and Douglas, W.J.M. Thermal conductivity of sintered metal powders at room temperature. *Lett. Heat Mass Transf.* (1976); **3**:183-192.

3D FINITE ELEMENT SIMULATION OF POLYMER EXTRUDATE IN FDM 3D PRINTERS

Sim-AM 2019

ONUR HIRA* AND ATAKAN ALTINKAYNAK*

* Mechanical Engineering Department
Istanbul Technical University
Gumussuyu Campus, 34437 Istanbul, Turkey
e-mail: altinkayna@itu.edu.tr, web page: <http://akademi.itu.edu.tr/altinkayna/>

Key words: Fused Deposition Modelling (FDM), Polymer Extrudate Shape, Finite Element Method, Level Set Method

Abstract. 3D finite element simulation of a FDM printer nozzle region was performed using COMSOL Multiphysics software. The polymer exiting the nozzle of the FDM printer was also included in the simulation in order to capture the dimensional behavior of the polymer. The domain of the simulation consisted of a nozzle, printer table, and the surrounding air. In the simulation, mass and momentum equations were solved to determine the non-Newtonian flow characteristics of the polymer. The interface between the polymer and ambient air was modelled using the level set method. Experiments were conducted to validate the numerical results. One experimental specimen with 30 strips was printed using a 3D printer. In the CAD model of the specimen, each strip had the same width as the nozzle diameter. While printing, it was ensured that the nozzle had only one continuous vertical movement to print each strip. The printed strips were measured with a caliper at five different locations. The difference between the numerical and experimental results of strip width were less than 10%. The developed model provided information about the transient shape of the polymer extrudate and can be used to predict the dimensional accuracy of the FDM-printed parts.

1 INTRODUCTION

Additive manufacturing methods, also known as 3D printing, have the advantage of manufacturing complex geometries [1]. Out of various types of additive manufacturing techniques, Fused Deposition Modelling (FDM) is perhaps the most popular when low-cost is important [2]. In FDM, a structure is built layer by layer by discharging a stream of material from a nozzle. Even though thermoplastics have been commonly used for FDM process [3], other materials such as fiber-reinforced polymers [4], bio-degradable materials [5], ceramic [6], and concrete [7] are also available.

FDM is a rapidly progressing branch of additive manufacturing. Researchers have conducted several experimental studies to improve the process of FDM and part quality [8]. The investigated parameters have generally been layer thickness and orientation, infill type and rate, extrusion angle, and nozzle diameter [9]. The quality of FDM parts also depends on extrusion temperature and feed rate [10]. These parameters have an effect on residual stresses, shrinkage and bonding quality [11-13]. Due to the vast number of process parameters, many studies have been focused on finding optimal settings for manufacturing time, surface quality,

dimensional tolerances, and mechanical strength [1, 14-16].

In recent years, researchers have paid more attention to the numerical simulations of FDM process. Initial attempts were focused on the thermomechanical simulations of the final part in order to determine the characteristics of shrinkage, warpage, residual stresses, and potential crack initiation locations [17-19]. Current numerical studies are based on three dimensional CFD simulations. Non-isothermal and non-Newtonian flow, cooling, and solidification of polymer were simulated in a FDM process [20, 21]. Viscoelastic stresses were included in the model later [22]. An isothermal and Newtonian model was developed to simulate the deposition of polymer on a moving plane [23] and the model was validated with experiments [24]. It was found that the shape of extrudate changed from circle to rectangle as the gap height to velocity ratio decreased. Successive deposition of extrudate layer simulations showed that the layer thickness and distance between extrudates influenced the previous extrudate shape and pore formation [25]. In these numerical models, polymer was assumed to be discharged from a cylindrical volume.

In this work, the nozzle region of a FDM printer was simulated using finite element method. The simulations included the nozzle with a flow channel, printer table, and the air surrounding the nozzle region. Level set method was used to predict the shape of the polymer discharged from the nozzle. The polymer/printer table contact was also considered in the simulations. Non-Newtonian characteristics of the polymer was taken into account for predictions. An experimental sample was printed to validate the numerical simulations.

2 EXPERIMENTAL METHOD

ABS filament was used to perform experiments at nozzle temperature of 220°C and feed rate of 40 mm/s. Two rows and 15 columns of strips with dimensions of 0.4 mm width and height were printed on a 0.1 mm thick base. The dimensions of the printed sample are shown in Fig. 1.

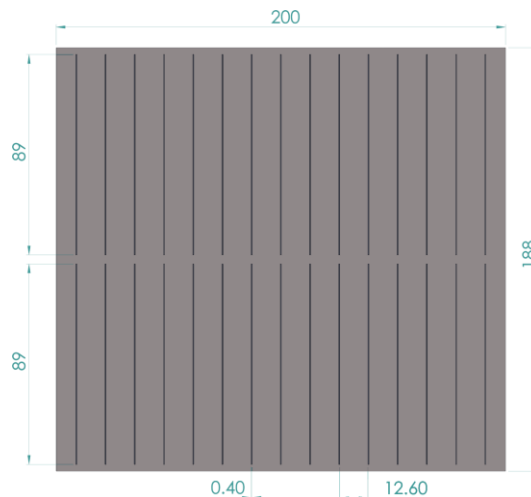


Figure 1: A schematic of the sample with dimensions

The diameter of the nozzle was 0.4 mm which was the same as the strip width on CAD data supplied to the slicer software. One continuous vertical movement of the nozzle was

enforced to print each strip. Experiment was performed at a printer temperature of 80°C. Each strip was measured at five positions to compare the experimental data with the numerical results.

3 NUMERICAL METHOD

The discharge and the deposition of ABS polymer on printer table were simulated using COMSOL Multiphysics 5.4 software. The cross-section of the 3D domain is shown in Fig. 2. The domain included the flow channel, nozzle, printer table, and the surrounding air. The molten polymer entered the flow channel from the inlet. The nozzle tip was located 0.2 mm above the printer table. This value was the same as the layer thickness in the experiment. The flow was defined as fully developed at the inlet, and the average velocity was calculated based on the experimental feed rate of 40 mm/s. The average velocity at the entrance was increased from zero to steady-state in one second. The printer table velocity in the vicinity of polymer deposition was set to feed rate speed in order to convey the extruded polymer towards the outlet. No slip condition was enforced on the nozzle/polymer boundaries. The simulation was performed for a period of time taken to print one strip.

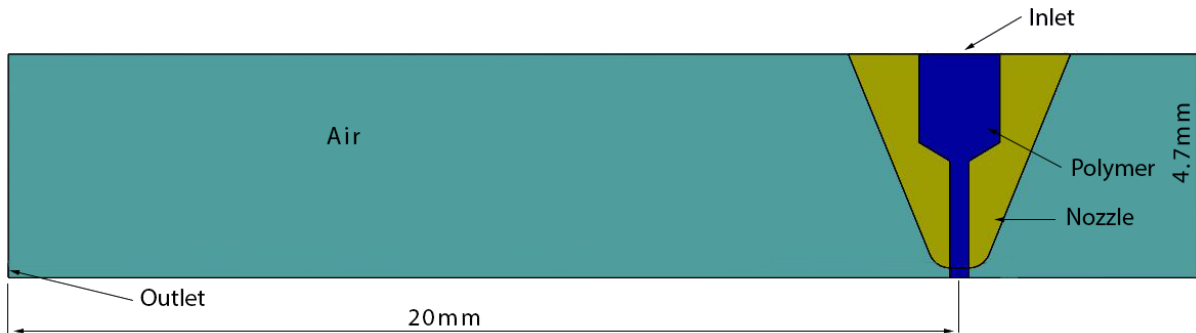


Figure 2: The cross-section of the 3D domain

The continuity and momentum equations were solved to simulate the polymer flow and deposition. The effect of temperature was not taken into account in this study. The shear rate dependence of polymer shear viscosity was modelled using Cross [26] model (Eq. 1).

$$\eta_s = \frac{\eta_0}{1 + \left(\frac{\eta_0 \dot{\gamma}}{\tau^*} \right)^{1-n}} \quad (1)$$

where η_0 is the zero-shear viscosity, $\dot{\gamma}$ is the shear rate, and τ^* and n are material-dependent constants. These material constants and material properties such as density, heat capacity, and thermal conductivity were obtained from the literature [27] and are presented in Table 1.

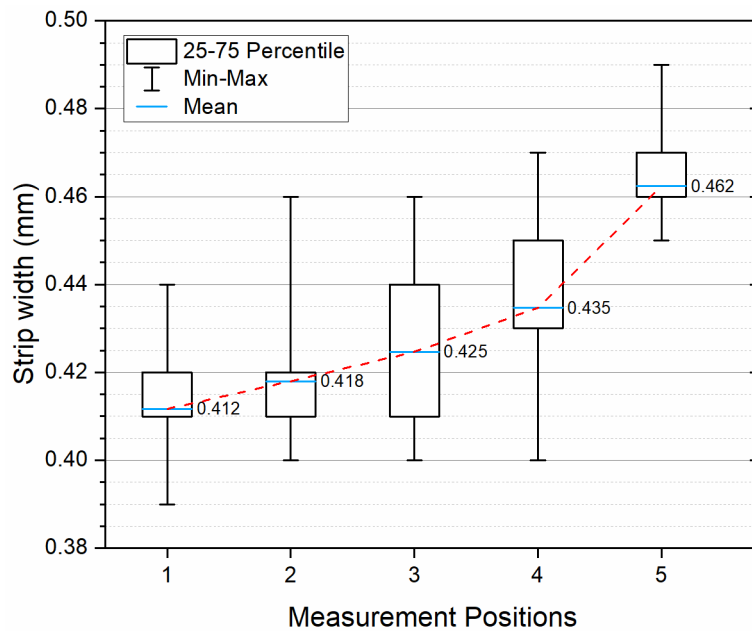
Besides solving the continuity and momentum equations, one transport equation was also solved to determine the interface between the polymer and ambient air using level set method. In level set method, level set function (ϕ) represents the interface between two domains. The value of ϕ varies from zero to one indicating the transition from one domain to the other. In this study, $\phi = 0.5$ was used to define the polymer/air interface.

Table 1: Material parameters used in the numerical simulation

	Density (gr/cm ³)	Heat Capacity (J/(kg K))	Thermal Conductivity (W/(m K))	τ^* (Pa)	n
ABS	1040	2345	0.18	2.90×10^4	0.33

4 RESULTS AND DISCUSSIONS

The experimental measurements obtained from the ABS sample printed at 40 mm/s are shown in Fig. 3. The average of measured strip width at five locations varied between 0.41 and 0.46 mm. The overall average of strip width was calculated as 0.430 mm indicating a difference of 7.5% compared to the nominal width of 0.4 mm. Figure 3 shows that the measured width had the tendency to increase along the printing direction. This characteristic may be due to the control algorithm of the nozzle and feed rate. Prior to printing, the polymer and the nozzle are generally at rest. While the nozzle accelerates to the steady state velocity, the filament is also pushed into the nozzle to supply the required material. The control of these two parameters will affect the amount of material discharged from the nozzle per unit time.

**Figure 3:** Measured strip width of ABS sample at five separate positions along the strip

The simulation result of polymer flow and deposition on printer table at 40 mm/s is presented in Fig. 4. The deposited ABS was conveyed along the z -axis. The extrudate shape away from the nozzle exit was dome-like. However, a barrel-like shape was observed near the nozzle exit. Previous experimental and numerical study suggested a barrel-like cross-section when the layer height is relatively small [24]. It is also evident that some of the polymer escalated on the nozzle surface facing towards the deposited material. The amount of polymer elevation is shown in Fig. 5 ($z=0.5$). The cross-section of polymer/air interface started as a

rectangular shape at the discharge and converted into a dome shape right after. The height of the strip increased above 0.3 mm and then decreased as low as 0.1 mm. The linear decrease of strip height beyond $z=2$ mm was expected and it was due to the transient increase of feed rate during the first 1 s.

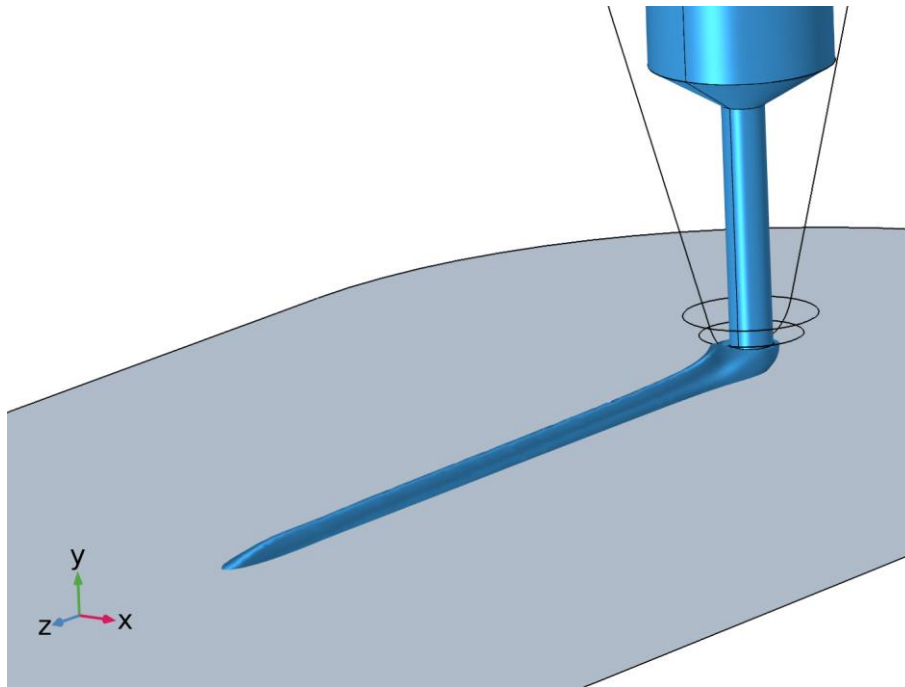


Figure 4: Predicted ABS deposition on printer table at 40 mm/s during 0.7 s.

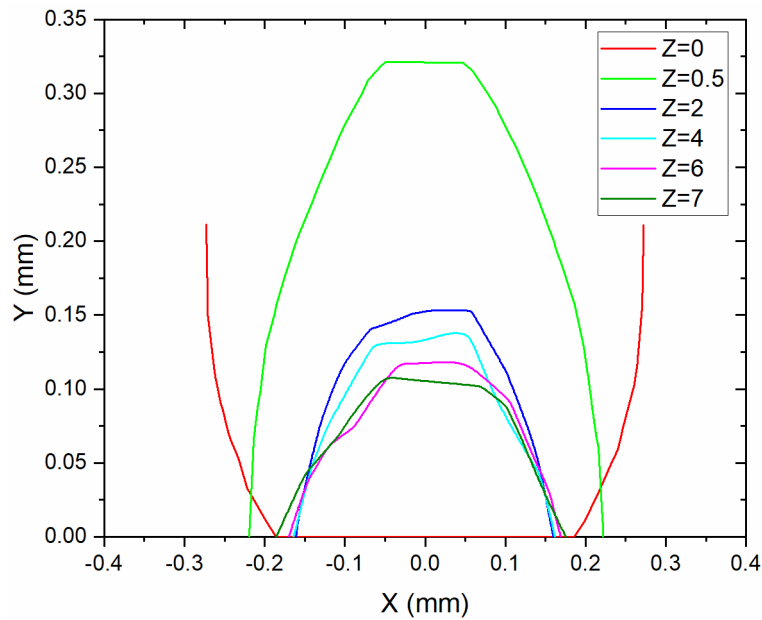


Figure 5: The cross-section of polymer/air interface along the printing direction at 0.7 s.

The mean strip width from the numerical simulations was 0.371 mm which was moderately lower than the experimental result of 0.430 mm. Once the steady state was reached after a period of 1 s, the strip width was essentially the same at measurement locations. Even though 0.441 mm strip width was obtained at a distance of $z=0.5$ mm, both the strip width and height were instantly decreased to lower values at $z=2$ mm. The reason for this shape change may be due to the lack of temperature dependency of shear viscosity. Shear viscosity of polymers decreases drastically with temperature especially when the temperature is below the glass transition temperature. The experimental printer temperature was 80°C which was lower than the glass transition temperature of ABS. Once the non-isothermal simulations are performed, the polymer touching the printer table is expected to have much higher shear viscosity which will limit the deformation of the polymer.

5 CONCLUSIONS

- Three-dimensional finite element simulations of polymer flow and deposition on printer table were performed. The simulations included the non-Newtonian characteristics of the polymer shear viscosity. The polymer/air interface was determined using the level set method. Experimental sample was printed to validate the numerical model.
- The shape of the strip changed from rectangular shape to dome shape right after the nozzle tip. The numerical result was 13.7% lower than that of the experimental result. Non-isothermal effects were not included in the model. Particularly, updating the model with temperature dependency of the shear viscosity is expected to improve the predictions.
- The developed numerical model can be used to understand the relationship between process parameters and the dimensional accuracy of FDM-printed parts. Further improvements can be implemented to reduce the discrepancies between the experimental and numerical results.

6 ACKNOWLEDGMENTS

This work was supported by TÜBİTAK Project No: 217M687.

REFERENCES

- [1] Turner, B.N. and S.A. Gold, *A review of melt extrusion additive manufacturing processes: II. Materials, dimensional accuracy, and surface roughness*. Rapid Prototyping Journal, 2015. **21**(3): 250-261.
- [2] N. Turner, B., R. Strong, and S. A. Gold, *A review of melt extrusion additive manufacturing processes: I. Process design and modeling*. Rapid Prototyping Journal, 2014. **20**(3): 192-204.
- [3] Cicek, O.Y., A. Altinkaynak, and E.C. Balta. *Numerical and experimental analysis of infill rate on the mechanical properties of fused deposition modelling polylactic acid parts*. in *Proceedings of the SPE ANTEC®*. 2017. Anaheim, CA, USA: 75-81.
- [4] Zhong, W., F. Li, Z. Zhang, L. Song, and Z. Li, *Short fiber reinforced composites for fused deposition modeling*. Materials Science and Engineering: A, 2001. **301**(2): 125-130.

- [5] Zein, I., D.W. Hutmacher, K.C. Tan, and S.H. Teoh, *Fused deposition modeling of novel scaffold architectures for tissue engineering applications*. *Biomaterials*, 2002. **23**(4): 1169-1185.
- [6] Bellini, A., *Fused deposition of ceramics: a comprehensive experimental, analytical and computational study of material behavior, fabrication process and equipment design*. 2002, Drexel University, Ann Arbor, MI.
- [7] Gosselin, C., R. Duballet, P. Roux, N. Gaudillière, J. Dirrenberger, and P. Morel, *Large-scale 3D printing of ultra-high performance concrete—a new processing route for architects and builders*. *Materials & Design*, 2016. **100**: 102-109.
- [8] Ngo, T.D., A. Kashani, G. Imbalzano, K.T. Nguyen, and D. Hui, *Additive manufacturing (3D printing): A review of materials, methods, applications and challenges*. *Composites Part B: Engineering*, 2018. **143**: 172-196.
- [9] Domingo-Espin, M., J.M. Puigoriol-Forcada, A.-A. Garcia-Granada, J. Llumà, S. Borros, and G. Reyes, *Mechanical property characterization and simulation of fused deposition modeling Polycarbonate parts*. *Materials & Design*, 2015. **83**: 670-677.
- [10] Kaveh, M., M. Badrossamay, E. Foroozmehr, and A.H. Etefagh, *Optimization of the printing parameters affecting dimensional accuracy and internal cavity for HIPS material used in fused deposition modeling processes*. *Journal of Materials processing technology*, 2015. **226**: 280-286.
- [11] Alhubail, M., *Statistical-based optimization of process parameters of fused deposition modelling for improved quality*. 2012, University of Portsmouth.
- [12] Monzón, M.D., I. Gibson, A.N. Benítez, L. Lorenzo, P.M. Hernandez, and M.D. Marrero, *Process and material behavior modeling for a new design of micro-additive fused deposition*. *The International Journal of Advanced Manufacturing Technology*, 2013. **67**(9-12): 2717-2726.
- [13] Costa, S., F. Duarte, and J. Covas, *Estimation of filament temperature and adhesion development in fused deposition techniques*. *Journal of Materials Processing Technology*, 2017. **245**: 167-179.
- [14] Mohan, N., P. Senthil, S. Vinodh, and N. Jayanth, *A review on composite materials and process parameters optimisation for the fused deposition modelling process*. *Virtual and Physical Prototyping*, 2017. **12**(1): 47-59.
- [15] Mohamed, O.A., S.H. Masood, and J.L. Bhowmik, *Optimization of fused deposition modeling process parameters: a review of current research and future prospects*. *Advances in Manufacturing*, 2015. **3**(1): 42-53.
- [16] Li, H., T. Wang, and Z. Yu, *The quantitative research of interaction between key parameters and the effects on mechanical property in FDM*. *Advances in Materials Science and Engineering*, 2017. **2017**.
- [17] Brenken, B., E. Barocio, A. Favaloro, and R.B. Pipes, *Simulation of semi-crystalline composites in the extrusion deposition additive manufacturing process*. *Science in the Age of Experience*, 2017: 90-102.
- [18] Talagani, M., S. DorMohammadi, R. Dutton, C. Godines, H. Baid, F. Abdi, V. Kunc, B. Compton, S. Simunovic, and C. Duty, *Numerical simulation of big area additive manufacturing (3D printing) of a full size car*. *SAMPE Journal*, 2015. **51**(4): 27-36.

- [19] Bikas, H., P. Stavropoulos, and G. Chryssolouris, *Additive manufacturing methods and modelling approaches: a critical review*. The International Journal of Advanced Manufacturing Technology, 2016. **83**(1-4): 389-405.
- [20] Xia, H., J. Lu, S. Dabiri, and G. Tryggvason, *Fully resolved numerical simulations of fused deposition modeling. Part I: fluid flow*. Rapid Prototyping Journal, 2018. **24**(2): 463-476.
- [21] Xia, H., J. Lu, and G. Tryggvason, *Fully resolved numerical simulations of fused deposition modeling. Part II—solidification, residual stresses and modeling of the nozzle*. Rapid Prototyping Journal, 2018. **24**(6): 973-987.
- [22] Xia, H., J. Lu, and G. Tryggvason, *A numerical study of the effect of viscoelastic stresses in fused filament fabrication*. Computer Methods in Applied Mechanics and Engineering, 2019. **346**: 242-259.
- [23] Comminal, R., M.P. Serdeczny, D.B. Pedersen, and J. Spangenberg, *Numerical modeling of the strand deposition flow in extrusion-based additive manufacturing*. Additive Manufacturing, 2018. **20**: 68-76.
- [24] Serdeczny, M.P., R. Comminal, D.B. Pedersen, and J. Spangenberg, *Experimental validation of a numerical model for the strand shape in material extrusion additive manufacturing*. Additive Manufacturing, 2018. **24**: 145-153.
- [25] Serdeczny, M.P., R. Comminal, D.B. Pedersen, and J. Spangenberg, *Numerical simulations of the mesostructure formation in material extrusion additive manufacturing*. Additive Manufacturing, 2019.
- [26] Cross, M.M., *Relation between viscoelasticity and shear-thinning behaviour in liquids*. Rheologica Acta, 1979. **18**(5): 609-614.
- [27] Altinkaynak, A., M. Gupta, M.A. Spalding, and S.L. Crabtree, *Melting in a Single Screw Extruder: Experiments and 3D Finite Element Simulations*. International Polymer Processing, 2011. **26**(2): 182-196.

COMPUTATIONAL AND EXPERIMENTAL INVESTIGATION OF VIBRATION CHARACTERISTICS OF VARIABLE UNIT-CELL GYROID STRUCTURES

Sim-AM 2019

U. SIMSEK*, C. GAYIR¹, B. KAVAS² and P. SENDUR³

* Özyeğin University
Nişantepe Mahallesi, Orman Sk., 34794 İstanbul, Turkey
Email: ugur.simsek.16339@ozu.edu.tr

¹ UT High School
The University of Texas at Austin, 2901 North IH-35, 78722 Texas, USA
Email: cemal.efegayir@gmail.com

² General Electric Marmara Technology Center
Barış Mahallesi, 41400 İstanbul, Kocaeli
Email: baris.kavas@ge.com

³ Özyeğin University
Nişantepe Mahallesi, Orman Sk., 34794 İstanbul, Turkey
Email: polat.sendur@ozyegin.edu.tr

Key words: Triply periodic minimal surfaces, double gyroid, finite element method, compression test, modal analysis, modal testing

ABSTRACT

Triply periodic minimal surface (TPMS) based geometries exhibit extraordinary mechanical, thermal, electrical and acoustic properties thanks to their unique topologies. There are various types of structures in the TPMS family. One of the most well-known TPMS structures is the gyroid structure. This paper focuses on the vibrational behavior of a novel sandwiched gyroid structure in terms of their natural frequencies and mode shapes with three different feasible unit sizes at same volume ratio. Powder bed fusion technology is employed to fabricate gyroid porous specimens made of HS188 material. Modal testing is performed to deduce the vibration characteristics of aforementioned cellular structures. Besides the experimental study, the dynamic performance of the considered structures is investigated computationally by performing modal analysis using Finite Element (FE) models. A key challenge facing FE modelling of large scale gyroid structure is computation time and accuracy. For that reason, small size of gyroid lattices are utilized for compression tests in order to extract elastic properties. Then sandwiched gyroid plate is modelled as solid body with calculated elastic properties instead of complex gyroid topology and analyzed. Finally correlation level between experimental and FE results are presented.

1 INTRODUCTION

Additive manufacturing (AM) is a type of a manufacturing process, where material is added layer-by-layer in contrast to the traditional methods in order to create the end product. AM has gained great attention from industry since it reduces the design restrictions associated with the conventional manufacturing methods. This method allows the manufacturing of complex free-form geometries providing high mechanical properties with lower weight and superior functional characteristics. The essence of all AM processes is the generation of each layer by slicing the Computer Aided Design (CAD) data. The AM system utilizes the aforementioned data to create the end product layer-by-layer with suitable techniques according to the selected material. For metals, there are many modalities used in the industry and many more are still under development. The selection of the correct modality plays a critical role in achieving the desired characteristics of the final products [1, 2].

Powder bed fusion systems, also as known as selective laser sintering (SLS), selective laser melting (SLM) or direct metal laser melting (DMLM), are the most widely researched AM modalities. In particular, DMLM has opened up new possibilities for creating various meta-materials. These materials possess favorable properties regardless of the chemical contents, manufacturing methods used and enhancing post-processes applied. Therefore, such materials gained the attention of aerospace, personal protective equipment and transportation industries.

In applications where the weight is critical, it is important to meet the durability requirements of the structure using minimum amount of material under operational loads. Components in such applications are, in general, subject to combined loading due to torsion, tension, and bending loadings. This requires that such design is carefully engineered in order to achieve material properties much better than that of the bulk material. To achieve this, cellular structures have long been used in many engineering applications because of their highly configurable mechanical properties together with light weights. A cellular structure is considered as the building block of the whole structure. Each of these units is called unit cells and the properties of each unit cell along with the stacking method define the mechanical properties of the whole structure [3].

A type of cellular structures, lattices, is composed of network of trusses and beams varying in size and arrangement. A study on lattices can be conducted treating them as either a complex network of trusses, beams and connections by traditional means or as meta-materials [4]. As much as lattices have their advantages, manufacturing of such structures is costly using traditional methods. With the recent advances in additive manufacturing, lattices have started to gain significant consideration. A variety of different unit cell designs have been recently investigated to further understand their mechanical properties [5, 6].

Another great enhancement that AM brings in manufacturing of lattices is the capability of changing the unit cell design parameters relative to the loading conditions and structural requirements. Due to their tunable stiffness and different truss diameters, lattice structures are also proposed and proven to have supportive functionality in additive manufacturing [7]. Effect of design parameters of lattice structures on their mechanical properties should be well understood for their further utilization in the aforementioned industries. The current state of the art in unit cell design is yet to reach its limit for efficiency. By numerical proofs, computational models and bio-mimics, there is a huge potential for inventing and implementing novel advanced unit cell designs.

Among the promising unit cell designs, periodic structure model of minimal surfaces have captured researcher's attention. Mathematical advances especially in group theories are essentially significant for explaining and analytically modeling the repetitive occurrences observed in nature. One of the well-known periodic surface models is triply periodic minimal surface (TPMS). There are many surfaces belonging to the TPMS family in the literature. Such surfaces include Schwarz crossed layers of parallels (CLP), Diamond, Neovius, Schoen I graph and wrapped package-graph (IWP) and Fischer-Koch S models. These TPMS were characterized using different methods in the previous studies [8-10]. Utilizing additive manufacturing, TPMS models can now be manufactured in addition to their computational analysis.

As the studies on lattice structures have shifted towards surface models that can provide better properties than truss lattices, many reported using additive manufacturing for printing TPMS models and testing [11, 12]. Being a member of the large TPMS family, double gyroid (DG), which is a subtype of gyroid form, has shown to express high stiffness and low Von Misses stress compared to many other surfaces in the literature [13]. Same study also revealed that double gyroid structures also possess similar stiffness in both axes, which can be utilized in applications where direction of the stress is unknown. Another research suggests that DG lattices are a promising candidate for usage in lightweight energy absorbing applications [14]. In another study, vibration characteristics of TPMS based geometries including gyroid form were analyzed and effect of wall thickness was investigated computationally [15].

In the aforementioned studies from the literature, the mechanical characteristics of various type of TPMS forms were investigated in terms of compressive and energy absorption behaviors experimentally and numerically. In this paper, it is aimed to reveal dynamic characteristics of a novel double gyroid sandwich structure with three different unit cell sizes. Unlike finite element modelling approaches using 3D elements in the literature, in this study, a computationally efficient simulation methodology via representative models is proposed for double gyroid structure. For that purpose, small scales of gyroid samples with different unit cell sizes at same volume ratio are subjected to compression test in order to identify elastic material properties. Thereafter, calculated young modulus values are assigned to sandwiched gyroid structures in which gyroid unit cells are not modelled explicitly but as solid geometry. Finally, numerical studies are validated by experimentally for one additively manufactured gyroid sandwich structure using modal testing equipment.

The paper is organized as follows. First, we extract the elastic constants of the gyroid lattice by performing compressive tests for various unit cell sizes. Next, a static analysis performed for a cube, which directly represents gyroid test samples, in order to find correct young moduli. Verified young modulus is used to finite element modelling of a sandwiched gyroid structures. The dynamic response of considered geometry is then investigated in terms of natural frequencies and mode shapes.

2 EXPERIMENTAL METHODS

2.1 Design and Manufacturing of the Gyroid Cellular Structure for Compression Test

Computer-Aided Design (CAD) files can be designed using different approaches. For the aforementioned periodic cellular structures, instead of direct CAD modelling, unit cells are

modelled by using a mathematical formula given in Eq. (1) as:

$$\left(\cos\left(\frac{2\pi}{a}x\right)\sin\left(\frac{2\pi}{a}y\right) + \cos\left(\frac{2\pi}{a}y\right)\sin\left(\frac{2\pi}{a}z\right) + \cos\left(\frac{2\pi}{a}z\right)\sin\left(\frac{2\pi}{a}x\right) \right)^2 = t^2 \quad (1)$$

where a is unit cell size and t is the thickness of DG's model.

The function is utilized for generating surface of DG structures in MATLAB platform. This approach enables the generation of continuous modelling of specimens in a computationally efficient way for the subsequent operations performed in Unigraphics (UG) 12. Once the surface representation is completed in MATLAB as shown Figure 1, geometry is exported in facet body format. Wall thickness of complex DG unit cells is then assigned in UG using solid modeling options. In this study, we used three different unit cell sizes of 6, 8, 12 mm to create 24x24x24 mm test samples at same volume ratio for compression tests. Theoretical properties of three test specimens are given in Table 1.

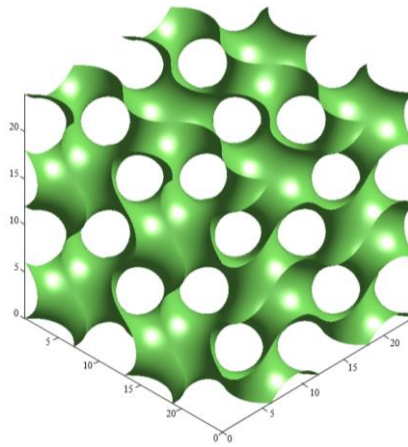


Figure 1: Surface representation in Matlab.

Table 1: Theoretical properties of the specimen

Unit cell size (mm)	thickness (mm)	Volume (mm ³)	Cell count	Volume fraction	Surface area (mm ²)
6	0.4	2829	96	0.20	14648
8	0.533	2830	27	0.20	10496
12	0.8	2830	8	0.20	7596

The finalized geometry files should be sliced prior to the printing process. Selected software generates the path that the laser will scan through during the process. Hence, sliced file mainly contains the laser scan path for each layer and layer thickness. In this study, specimens are additively manufactured in Concept Laser M2 Cusing, which is a direct metal laser melting machine containing 2 x 400 W fiber laser systems. Among the additive manufacturing modalities and hardware available, powder bed fusion is the most advanced technology. Ability to manufacture small part features with high precision, resulting solid material integrity and reduced lead times make this modality very convenient for manufacturing micro, mezzo and macro scale lattice structures. Considering the advantages of

manufacturing specimens of interest as well as the powder and machine availability, direct metal laser melting system is used in the study.

Material selection is another crucial factor, which plays an important role for additive manufacturing process and directly determines the mechanical characteristics of specimens. The DG test samples are fabricated with HS188 powder with spherical morphology is used. HS188 is widely preferred as super-alloy due to its high oxidation resistance up to 1095°C and creep strength. This property enables the structure to be utilized as part of gas turbine engines operating at elevated temperatures. Main disadvantage of high temperature super alloys is related to their weight. Therefore, utilizing the high strength to weight ratio of structural lattices with a high temperature super alloy shows considerable amount of potential especially for lightweight and performance requiring high temperature applications. Essential material properties of HS188 are illustrated in Table 2. However, in AM perspective, specialized HS188 powder for powder bed additive manufacturing systems are not widespread and parameter sets for processing this material is found not to be commercially available. Acceptable powder size distribution of the Concept Laser M2 is recommended to be in the interval of 10-70 μm .

Table 2: Material properties of HS188 [16]

Density (g/cm ³)	Poison's Ratio (-)	Young's Modulus (GPa)
8.98	0.3	232

Three DG specimens including 6, 8, and 12 mm unit cell sizes are manufactured as 24x24x24 mm cubes at same volume ratio. Fabricated test samples are illustrated in Figure 2. After completion of manufacturing process, specimens are welded to a steel plate and the entire process chamber is completely filled with powder. This powder is required to be evacuated from the chamber and the parts must be cleaned of powder residues. Once cleaning phase is done, samples are ready for compression test in order to identify elastic material properties.

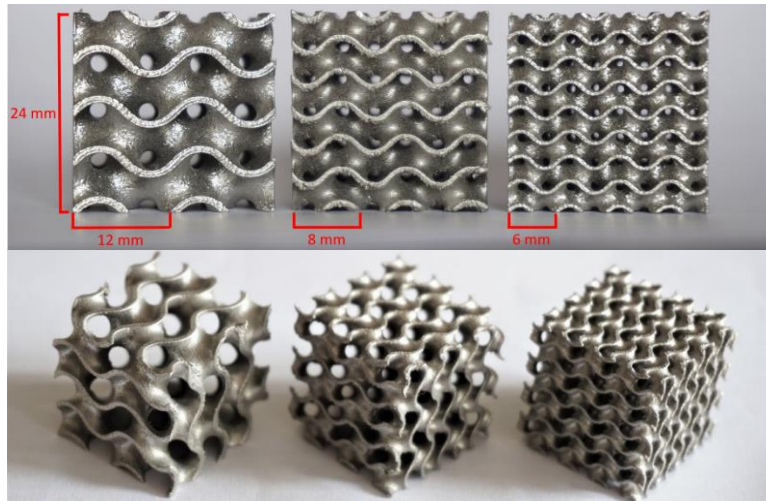


Figure 2: HS188 DG samples from left to right with 12, 8 and 6 mm unitcell sizes respectively

2.3 Compression Tests and Results

Lattice structures have recently been extensively studied to understand their mechanical properties under certain loading conditions. Aforementioned design parameters of lattices such as unit cell types and geometrical aspects are found to have significant effect on the failure mechanisms of lattices. Fundamental mechanical properties for critical design solutions such as yield stress, ultimate stress and energy absorption prior to densification and elasticity modulus of lattice structures are required to be documented for design assessments. To characterize the mechanical properties of double gyroid structure to research its potential in aforementioned application areas, the compression characteristics is of great consideration. The rate of compression in the compression testing is set to 1 mm per minute since it is the lowest strain rate available. Each specimen is placed on the compression fixture in the build direction in order to avoid the effect of anisotropy.

Representative force-displacement and stress-strain curves from compressive testing of three different DG lattices at same volume ratio presented in Figure 3. Each stress-strain curve exhibits four distinct regions: linear region, beginning of non-linear regime which reaches to maximum stress point, then plateau phase and finally pure densification regime. However, it is aimed to investigate linear response of DG structure as part of the proposed methodology enabling computational efficient modeling of large scale cellular structures. Stress-strain and force-displacement graphs cover linear region and early non-linear region results.

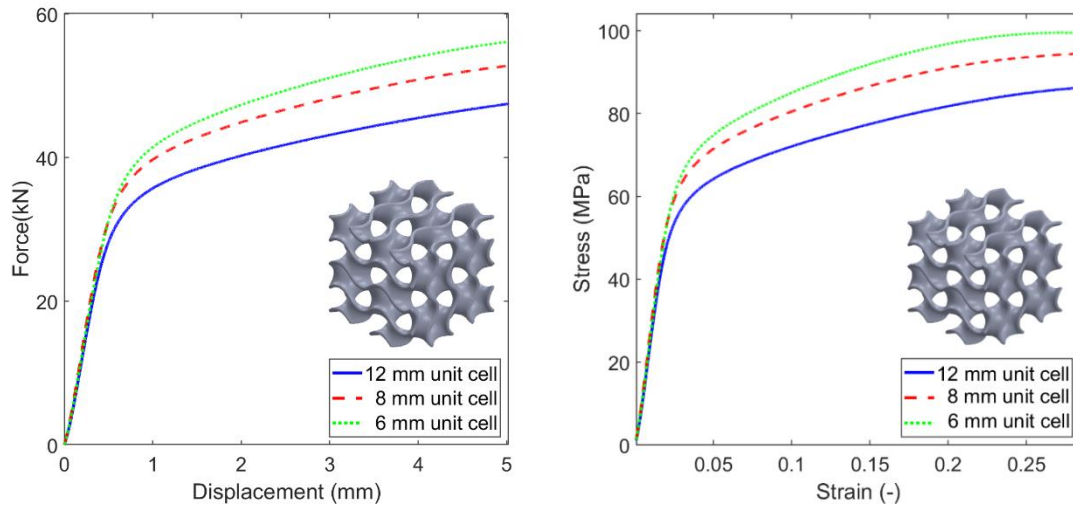


Figure 3: Compression test results for each unit cell

The elastic modulus extracted from the linear elastic regions, where the slope of linear curve represents the elastic modulus, for all three different gyroid specimens with different unit sizes are given in Table 3. These results show that average elastic moduli of individual unit cells are quite similar. These mechanical properties are utilized to validate numeric methods and to simplify complex gyroid structure to bulk geometry.

Table 3: Yield stress and elastic modulus for each unit cell size specimen

Unit cell size (mm)	Yield stress (MPa)	Elastic modulus (GPa)
6	67.3	2.7
8	60.1	2.8
12	51.4	2.5

3 FINITE ELEMENT METHOD AND MODAL TESTING

It is common in literature to model the gyroid lattice structures explicitly as hexagonal solid finite elements or ten-node tetrahedral elements. In addition, it is observed that the previous studies are limited to relatively small unit cells in order to avoid high CPU times [17, 18]. Our objective, in this study, is to investigate the dynamic performance of a 192x192x25.6 mm sandwiched gyroid structures using finite element method. Therefore, it is not appropriate to model gyroid unit cells explicitly using hexagonal or tetrahedral elements due to geometric complexity of the structure and the computational efficiency. Therefore, an alternative approach is proposed in this paper, which makes use of the experimental data. The details of the proposed methodology are explained in this section.

3.1 Modal Analysis of Sandwiched Gyroid Structure

Undamped natural frequencies and mode shapes depend on the overall system stiffness and mass. Hence the accurate estimation of elastic modulus and overall mass of the structure is critical for the accuracy of the modal analysis. Elastic moduli of test samples with different unit cell sizes were determined from compression test as explained in Section 2.3. These mechanical properties are used to analyze a novel structure consisting of 64 unit cells sandwiched between two plates. This structure, shown in Figure 4, is additively fabricated. The properties of the specimen are given in Table 4.

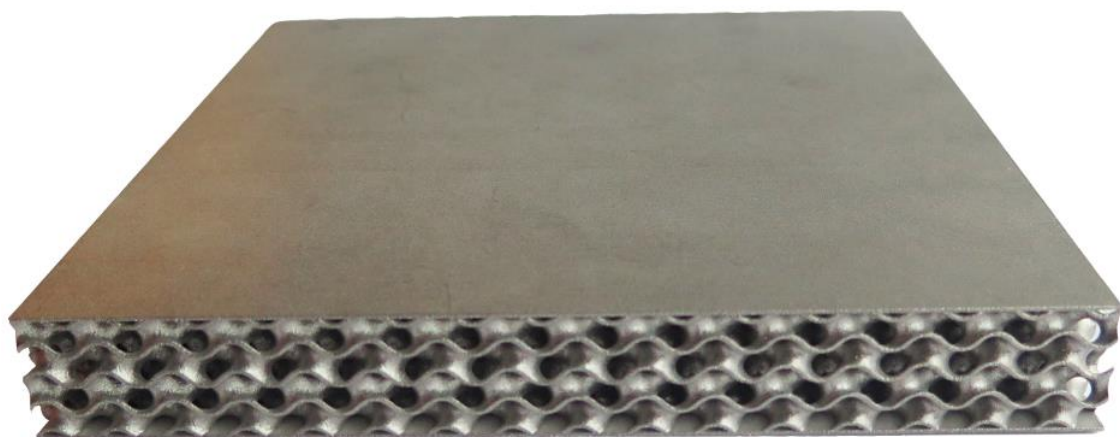
**Figure 4:** Sandwiched gyroid structure of 192x192x25.6 mm

Table 4: Properties of different test specimens

Unit cell size (mm)	Thickness (mm)	Volume (mm ³)	Cell count	Volume fraction
6	0.4	181120	6144	0.20
8	0.533	181120	1728	0.20
12	0.8	181120	512	0.20

The proposed methodology for modelling complex gyroid structure for an efficient FE analysis is presented in Figure 5. The first step is to determine the elastic modulus of the test specimen from stress-strain curves obtained from compression test. These curves do not refer local stress and strain on the gyroid walls, but capture stress and strain characteristics of entire structure, derived by dividing the applied force by the specimen area of 576 mm². The elastic modulus of gyroid test specimens, given in Table 3, is simply calculated from Eq. 2 as:

$$E_{gyroid} = \frac{F \times L}{A_c \times d} \quad (2)$$

where, E_{gyroid} is the elastic modulus of test samples extracted from stress-strain curve, A_c is cross-sectional area of gyroid domain (576 mm² for our case), F is the from the magnitude of the force applied during compression test, L is the height of gyroid and d is the displacement of the top surface in the loading direction.

Once elastic modulus is determined, a preliminary FE analysis is performed on a 24x24x24 mm solid cube as part of the complex gyroid topology. For this purpose elastic modulus value, E_{gyroid} , from Step 1 is assigned to the finite element model of representative cube and an iterative static analysis is performed. During the static analysis, the loadings are applied to the FE model replicating the compression test slope from compression test. Once experimental and representative models exhibit same mechanical characteristic, tuned elastic modulus is set as, E_{cube} , which is considered as the equivalent elastic modulus of cube.

In Eq. 2 projection area of gyroid structure is used in accordance with common practice of cellular structure. However, the effective cross-sectional area of gyroid structure is not equal to full projection area and it depends on design parameters of gyroid such as unit cell size and wall thickness. Additionally, cross-sectional area of gyroid slightly varies along the height of gyroid structure and therefore determination of this quantity is more difficult. On the other hand, it is known that volume ratio (VR) directly depends on the cross-sectional area of gyroid structure. Therefore, in this study, we assumed that effective elastic modulus of gyroid form, E_{eff} , can be expressed as in Eq. 3:

$$E_{eff} = E_{cube}/VR \quad (3)$$

The elastic modulus from Eq. 3 can be used as the material properties of the complex geometry. In this study, we fabricated only one sandwiched gyroid structure with 12 mm unit cell size additively for experimental validation.

Gyroid sandwich structure is modelled using 8-noded hexagonal elements. The experimentally calculated elastic modulus is assigned to gyroid portion of the structure. The two plates have thickness of 0.8 mm. Conventional HS188 material properties from Table 2 are used as part of the material model of the plates. FE model of novel sandwich structure is shown in Figure 6. We performed a modal analysis in free-free condition up to 5000 Hz and

compared the modes and mode shapes from modal testing. For this purpose, we used Dewesoft hardware/software in modal testing.

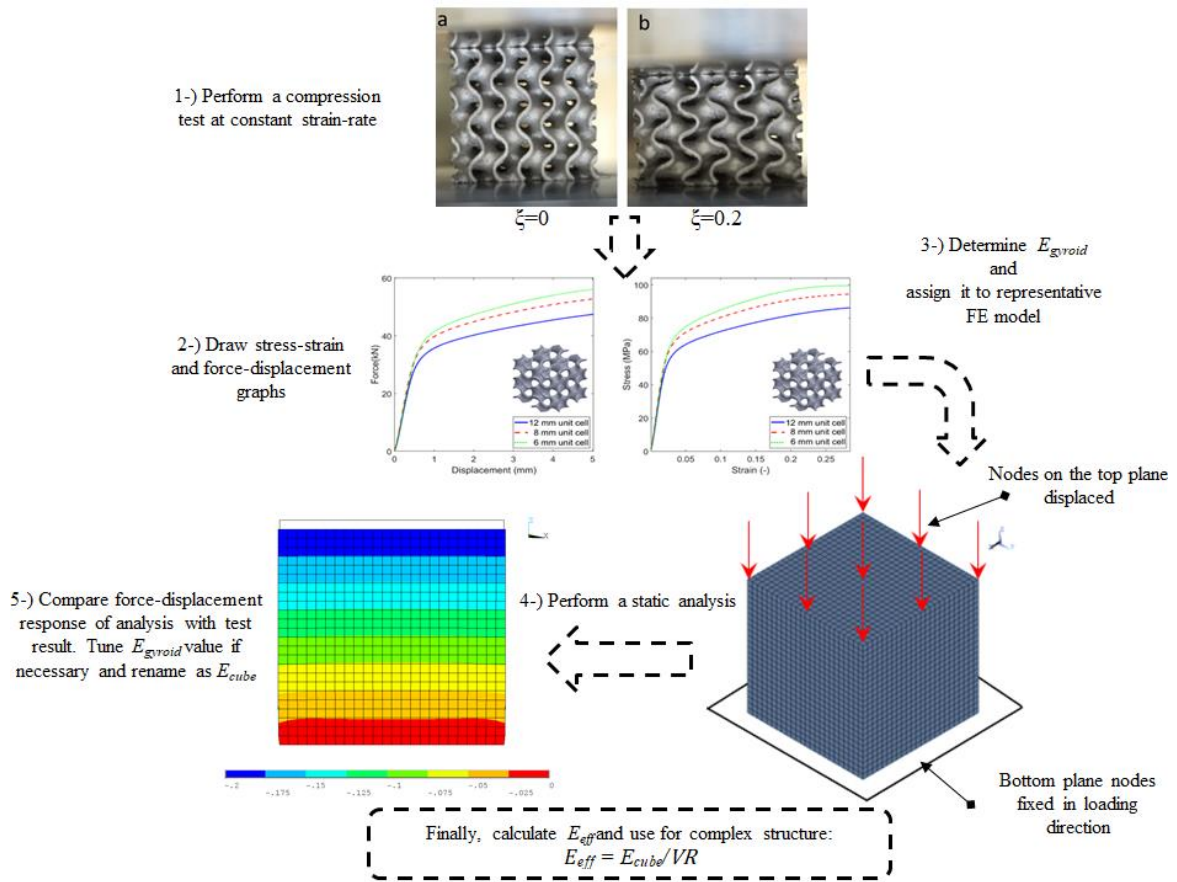


Figure 5: Methodology schematic

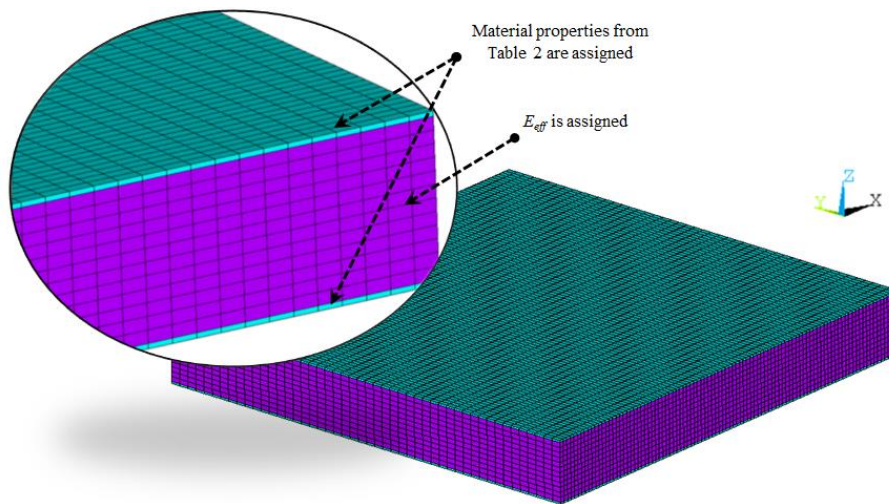


Figure 6: FE model of sandwiched gyroid structure

3.1 FE Analysis and Modal Testing Results

Comparison of natural frequencies and mode shapes of gyroid structure for the aforementioned 12 mm unit cells from modal analysis and modal testing are presented in Figure 7. The results indicate a high level correlation between modal analysis and testing. More specifically the relative error on the first 4 modes between modal analysis and testing are 3%, 6%, 4% and 1%, respectively. Also, the computational study is repeated for 6 and 8 mm unit cell sizes using Elastic Modulus from Table 3. The simulations yield the same natural frequencies as in Figure 7. The results from this study show that the modes are directly dependent on elastic modulus. It can also be concluded that the natural frequencies do not change with respect to the size of the unit cell.

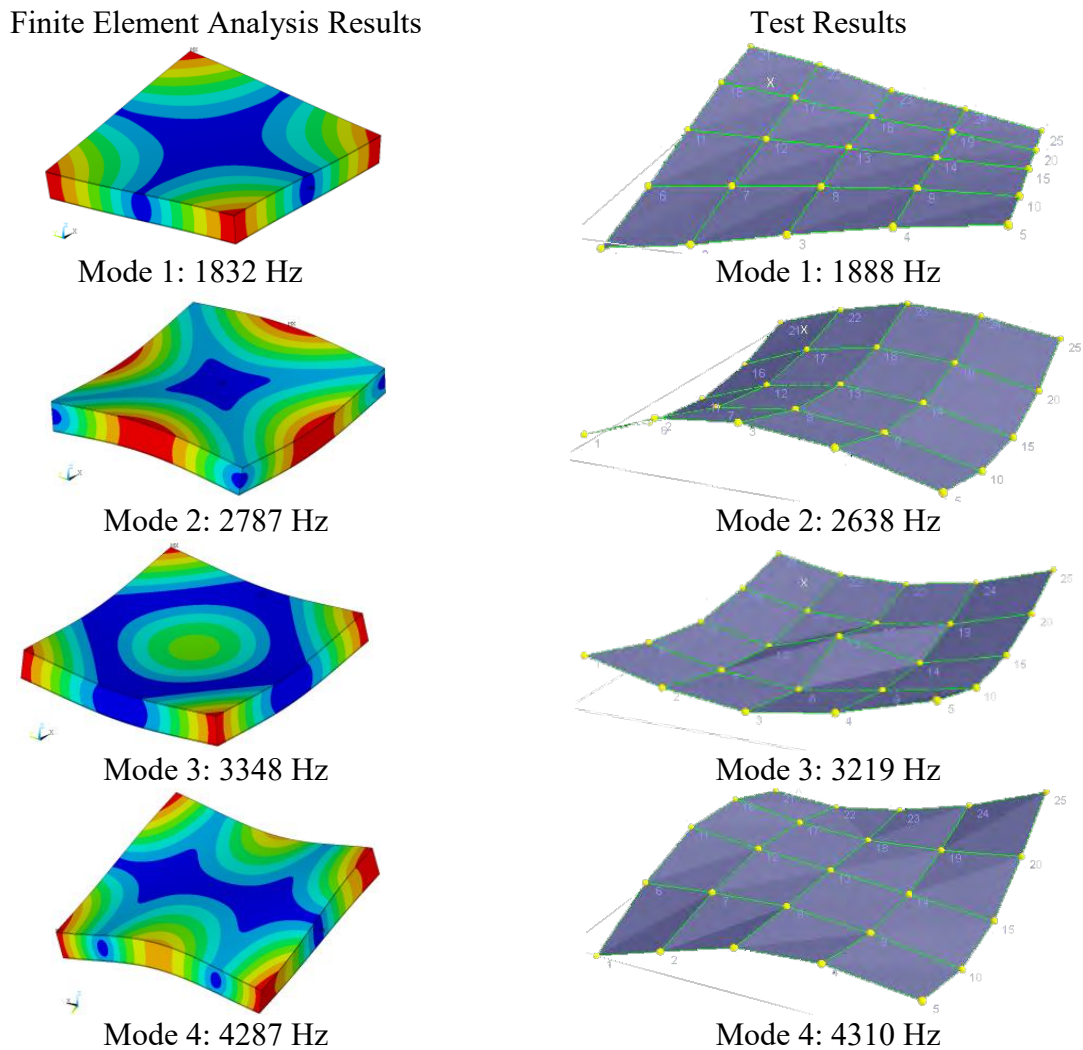


Figure 7: Comparison of modal analysis and modal testing results

Table 5: Properties of different test specimens

Unit Cell Size (mm)	Method	Mode 1 (Hz)	Mode 2 (Hz)	Mode 3 (Hz)	Mode 4 (Hz)
6	Simulation	1855	2820	3393	4358
8	Simulation	1866	2835	3415	4389
12	Simulation	1832	2787	3348	4287
	Experiment	1888	2638	3219	4310
	Relative Error	56 (%3)	149 (%6)	129 (%4)	23 (%1)

4 CONCLUSIONS

An efficient finite element modeling approach is presented in this paper as an alternative to the conventional solid mesh models of gyroid lattice structures. The proposed methodology makes use of the Young's Modulus of the unit cell test specimen, which is determined from compression test. A subsequent static analysis with the Young Modulus from the compression test is performed to derive the equivalent Young Modulus of the full gyroid structure. The proposed methodology is demonstrated on a gyroid structure with dimension of 192x192x2 5.6mm. The results from modal analysis and modal testing show that the proposed methodology can predict the first 4 modes of the structure with a maximum relative error of 6%. The results indicate that the proposed methodology has a potential to develop computational efficient yet accurate models of predicting the dynamic characteristics of gyroid structures. Authors acknowledge the assessment of the correlation of the proposed methodology for forced response of gyroid structures as a future work.

Acknowledgement

This study was carried out using TUBITAK Technology and Innovation Support Program.

REFERENCES

- [1] Frazier, W. E. Metal Additive Manufacturing : A Review (2014), 23(June), 1917–1928.
- [2] Jasiuk, I., Abueidda, D. W., Kozuch, C., Pang, S., Su, F. Y., & Mckittrick J. An Overview on Additive Manufacturing of Polymers. *JOM* (2018).
- [3] Gibson, L. J., Ashby, M. F. *Cellular Solids Structure and Properties* (Second Edi). Cambridge Solid State Science Series (1997).
- [4] Bauer, J., Meza, L. R., Schaedler, T. A., Schwaiger, R., Zheng, X., & Valdevit, L. Nanolattices : An Emerging Class of Mechanical Metamaterials (2017)., *1701850*, 1–26
- [5] Delpero, T., Bergamini, A., Ermanni, P., & Kochmann, D. M. 3D Auxetic Microlattices with Independently Controllable Acoustic Band Gaps and Quasi-Static Elastic Moduli (2014), (4), 357–363.
- [6] Ullah, I., Elambasseril, J., Brandt, M., & Feih, S. Performance of bio-inspired Kagome truss core structures under compression and shear loading. *COMPOSITE STRUCTURE*

- (2014), *118*, 294–302.
- [7] Hanzl, P., Zetková, I., & Daňa, M. Advanced lattice support structures for metal additive manufacturing. *Manufacturing Technology* (2017), *17*(6), 853–857.
- [8] Abueidda, D. W., Jasiuk, I., & Sobh, N. A. Acoustic band gaps and elastic stiffness of PMMA cellular solids based on triply periodic minimal surfaces. *Materials & Design* (2018).
- [9] Lee, D., Khan, K. A., & Jasiuk, I. Effective conductivities and elastic moduli of novel foams with triply periodic minimal surfaces. *Mechanics of Materials* (2016).
- [10] Lee, W., Kang, D., Song, J., Moon, J. H., & Kim, D. Controlled Unusual Stiffness of Mechanical Metamaterials. *Nature Publishing Group* (2016), (December 2015), 1–7.
- [11] Li, D., Liao, W., Dai, N., Dong, G., Tang, Y., & Xie, Y. M. Optimal design and modeling of gyroid-based functionally graded cellular structures for additive manufacturing. *Computer-Aided Design* (2018).
- [12] Vaezi, M., Seitz, H., & Yang, S. A review on 3D micro-additive manufacturing technologies (2013), 1721–1754.
- [13] Aremu, A., Maskery, I., Tuck, C., Ashcroft, I., Wildman, R., & Hague, R. A comparative finite element study of cubic unit cells for selective laser melting. In *Solid Freeform Fabrication Symposium* (2014).
- [14] Maskery, I., Aboulkhair, N., Aremu, A., Tuck, C., Ashcroft, I. Compressive failure modes and energy absorption in additively manufactured double gyroid lattices. *Additive Manufacturing* (2017), *16*, 24–29.
- [15] Altintas, G. Vibration properties of TPMS based Structures. *International Journal of Scientific and Technological Research* (2018).
- [16] Matweb 2019, Haynes 188 alloy, 0% cold reduction, 3.2 mm thick sheet, <http://www.matweb.com/search/DataSheet.aspx?MatGUID=8681846d59904d1086ce346298a79347> (Date accessed 20 April 2019)
- [17] Maskery, I., Sturm, L., Aremu, A. O., Panesar, A., Williams, C. B., Tuck, C. J., Hague, R. J. M. Insights into the mechanical properties of several triply periodic minimal surface lattice structures made by polymer additive manufacturing. *Polymer (United Kingdom)* (2017).
- [18] Yáñez, A., Cuadrado, A., Martel, O., Afonso, H., Monopoli, D. Gyroid porous titanium structures: A versatile solution to be used as scaffolds in bone defect reconstruction. *Materials and Design* (2018).

DESIGNING ADDITIVELY MANUFACTURED PARTS VIA TOPOLOGY OPTIMIZATION - A SPACE INDUSTRY CASE STUDY

B. Barroqueiro^{1,2,*}, A. Andrade-Campos¹ and R.A.F. Valente¹

¹ Department of Mechanical Engineering, Centre for Mechanical Technology & Automation, University of Aveiro, 3810-193 Aveiro, Portugal.

² Active Space Technologies, Actividades Aeroespaciais S.A., Parque Industrial de Taveiro, Lote12, 3045-508 Coimbra, Portugal.

* Corresponding Author: B. Barroqueiro (bjfb@ua.pt)

Key words: Topology Optimization; Additive Manufacturing; Case Study; Space Industry;

Abstract. Additive Manufacturing (AM) allows unprecedented design freedom, which can be explored by the Topology Optimization (TO) algorithm. Their interplay allows a new engineering cycle with the potential to design and manufacture disruptive concepts. Thus, a systematic methodology for designing AM parts is presented, being the main goal of this study. The methodology is subdivided into several phases, each phase contains several tasks. Moreover, the data flow between phases is considered and solutions are provided. Finally, the methodology is applied to a space case study and preliminary results of the AM engineering cycle (TO, part design and structural analysis) are depicted.

1 INTRODUCTION

“Additive Manufacturing (AM) is a process of joining bulk raw materials to make parts from 3D model data, usually layer upon layer, as opposed to subtractive manufacturing and formative methodologies. It is an inherent part of the parts development or production process. It is used to manufacture prototypes and production parts” [1]. Moreover, this process provides great geometrical freedom and the tools to explore the referred freedom are needed. The search-optimal material layout can be performed by Topology Optimization (TO) and its interplay with AM has proven to be advantageous [2]. In the space industry, there are successful examples, where the interplay of TO and AM allow the reduction of the number of parts, assembling operations, mass and, therefore, cost (*e.g.* [3, 4]). Beyond that, the new technology opens a new dimension of design solutions by overcoming the restrictions of conventional manufacturing processes. The adopted engineering cycle consists in topology optimization (*e.g.* MSC Nastran[®] tool for an initial design), manual CAD¹ construction (*e.g.* CATIA V5[®]), structural analysis and production (process preparation and manufacturing). However, manual CAD reconstruction is ineffective. In the one hand, TO commonly produces complex geometries that are labour intensive to reproduce in CAD software. On the other hand, the TO design can be simplified in

¹Computer Aided Design

order to allow a rapid CAD model construction with a performance cost. Thus, in this work, the presented methodology proposes an alternative methodology to the manual CAD model construction, which allows for a quicker engineering cycle. Moreover, this paper proposes a systematic methodology of a complete engineering cycle for space AM part. Furthermore, a space case study is presented, where the topology optimization, part design and structural analysis are presented and discussed. Finally, the main goal of this article is the methodology systematization for designing AM parts. Therefore, this work can provide valuable guidance for new engineers working in this field.

2 Methodologies

The complete engineering cycle of AM structures involves numerous steps. Figure 1 depicts the whole process of designing structures within framework subsystems structures of the space industry. For the sake of clarity, the process is illustrated as a linear flow, but iterative work between steps is expected to originate a non-linear flow.

2.1 Topology optimization

Topology optimization is a type of structural optimization that seeks the optimum material layout [5]. Within the scope of this work, solver 200 from MSC Software [6] was used to perform the Topology Optimization (TO) analysis, considering compliance minimization with a volume constraint. The referred solver uses the well known Solid Isotropic Material with Penalization (SIMP) method and the process starts with initial domain definition [6, 7]. Within the scope of this work, the domain is meshed using isoparametric `HEX8` elements. The mesher is available on a Patran utility named *Regular Cube Mesher 2*. After application of the boundary conditions, objective, constraint and design/non-design domains definition, the optimization cycle can start. After convergence, the resultant material distribution would ideally be a binary distribution (void or solid material) across the design domain. However, the SIMP model uses a continuous function and some intermediate densities may remain after convergence. These intermediate densities have to become either void (zero) or solid (one) and, thus, the user has to define the threshold. At the end, all solid elements become the optimized topology. Using the referred topology, the skin elements are extracted using the utility named *Skin Solid Elements*. Then, the resultant `QUAD` elements are broken into `TRIA` elements and the surface STL mesh is exported using the export STL utility.

2.2 Smoothing and Part Edition

The smoothing operation can be done within Patran[®] with limited options. Within the scope of this work, the Netfabb[®] from Autodesk[®] is used to perform all the smoothing, remeshing and repair operations. The translation between the surface STL mesh to a volume `TET` mesh is not possible in Netfabb neither in Patran. The free software named GMSH [8], is used to make the referred translation, being a straightforward procedure². A Nastran input file is a GMSH output, which can be imported in Patran.

²GMSH list of instructions: File>Merge>*.STL; Geometry>Add>Volume; Mesh>3D; File>Export>*.bdf

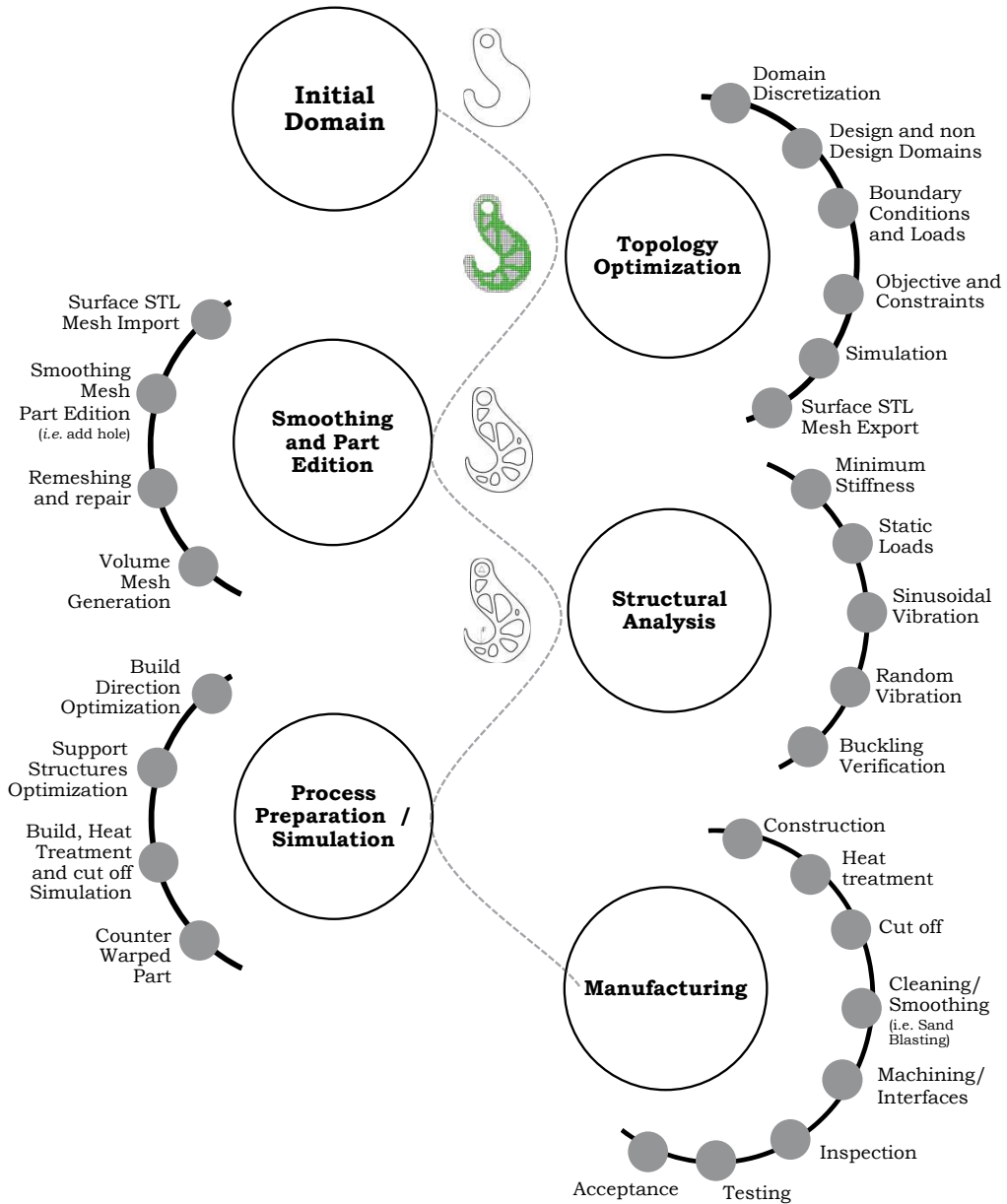


Figure 1: Engineering cycle of AM structures for the space industry.

2.3 Structural Analysis

In the space industry, the structural analysis involves at least static loads, minimum stiffness and sinusoidal/random vibration loads. Due to the typical slenderness of the designs, buckling verification is also performed. The static loads are analysed with MSC Nastran solver 101 using inertial loads [9]. The minimum stiffness requirement is verified using the MSC Nastran

solver 103 (normal modes analysis) [10], where the first eigenvalue should be above a defined limit. The sinusoidal vibration analysis is verified using the MSC Nastran modal solver 111 (Lanczos solver: frequency response) [10], considering modal damping. The random vibration is a two-step analysis. First, the frequency response analysis is performed for sinusoidal loading conditions at a sequence of frequencies. Typically, these loads are chosen to be unit loads. Thus, the output response works as a transfer function. The second step uses the referred function in order to compute the amplified random response. A quality factor of 400, a 3σ analysis and a log-log integration are considered. Additionally, the load levels are quantified in terms of Power Spectral Densities (G^2/Hz) [10]. Finally, the buckling verification is performed with MSC Nastran solver 105 using equivalent inertial loads derived the most severe load case [9].

2.4 Process Preparation and Simulation

The process preparation can be performed with some software such as Netfabb[®]. The first step is the optimization of the build direction, where several orientations are considered and classified in terms of different criteria (*e.g.* ratio between area and volume of support structures and/or height and volume of the build). The second step is the support structures generation, which can be generated by different available algorithms. Finally, the simulation of the build layer by layer can be also simulated in order to predict residual stress, distortions and some defects such as support structures failure or recoater interference or hot/cold spots. For instance, the Simulation Utility for Netfabb can be allegedly used to make such predictions [11]. Moreover, the software also performs the stress relief (viscoplastic analysis) and part response to the cut-off from the base. This integrated procedure allows the prediction of the part total distortion and excessive distortion on the part may lead to failure of dimensional tolerances. Thus, the process simulation can be used to apply a negative distortion on the part in order to minimize distortions and overbuild.

2.5 Manufacturing

The manufacturing stage shall start with the slicing operation of the prepared part and the G-Code generation, which can be performed in Netfabb, for example. After construction, the part shall be stress relieved, in order to decrease residual stress. Then, the part can be cut off from the baseplate and the cleaning/smoothing process (*e.g.* sandblasting) can be performed. The interfaces with tight tolerances are typically machined. Regarding quality control, the non-destructive inspection campaign can take advantage of methods such as computed tomography, eddy current testing, infrared thermography, neutron diffraction and ultrasonic testing [12]. Finally, the testing campaign involves static, sinusoidal and random testing, where the structure shall survive without deterioration. The deterioration detection can be performed with a low-intensity sinusoidal vibration sweep before and after each vibration test. If the response curve of the low-intensity sine sweeps (before and after each vibration test) are identical, no major structural deterioration will occur. The success criteria can be defined by a maximum shift of 5% and 20% for frequency and amplitude, respectively [13].

3 Case Study

The structure responsible for supporting the lens for a space instrument is analysed, named as Large Lens Mount (LLM). Titanium alloy (Ti6Al4V) shall be its manufacturing material and I/F to its supporting structure is composed of six bolted connections. This use case was derived from a use case of OHB Systems at Oberpfaffenhofen.

3.1 Topology Optimization and Smoothing

The design domain was discretised with linear isoparametric `HEX8` elements and the transition between the solid elements and the bolted connection centre point is modelled with rigid connection (RBE2). The connection between the lens (reduced to a point element) and the solid elements are modelled with RBE3, where the master nodes of volume mesh connects to a slave node on the lens's CoG location (see Sub-figure 2(a)). The RBE2 element was not used, because it adds stiffness to the model. In fact, the interface region of the lens would become rigid and the TO algorithm would take advantage of the referred fact, leaving the interface poorly reinforced or the user would add to include it in the non-design domain (defeating the propose of the TO algorithm). Regarding loading conditions, the acceleration levels were replaced by an equivalent force on the lens's node. Finally, the TO was performed and its objective function consists in the compliance minimization of the LLM structure, when loaded in directions X, Y and Z (weighted sum of three static load cases).

Sub-figures 2(b), 2(d), 2(f) and 2(h) describe the TO results for the volume constraints of 40%, 20%, 10% and 5%, respectively. Sub-figures 2(c), 2(e), 2(g) and 2(i) show the resultant smooth surface mesh after smoothing in Netfabb. Preliminary analysis on the designs of Sub-figures 2(c) and 2(e) revealed a design overestimation for the considered loading conditions. On the other hand, a visual inspection of the design of the Sub-figure 2(i) indicates high level of risk from the manufacturing point of view. For instance, the removal of referred support structures could lead to fracture of the thin members of the referred part. Therefore, the design of the Sub-figure 2(g) was selected and it weights 0.628 kg, which is compliant with the mass requirement. In order to facilitate the previous assessment, the model of the Sub-figures 2(g) and 2(i) were prototyped in PLA for part visualization proposes only. The Figure 3 illustrates the referred prototypes.

3.2 Structural Analysis

The design domain, Sub-figure 2(g), was discretised with isoparametric `TET10` quadratic elements [9] and the transition between the solid elements and the bolted connection center point is modelled with a rigid connection (RBE2). The connection between the lens and the volume mesh is modelled as RBE2 and the lens is modelled as a lumped mass (see Sub-figure 4(a)). In contrast with the TO analysis, the structural analysis uses RBE2, since the lens adds some stiffness and the main goal is a correct distribution of stress maps.

Table 1 lists the first ten eigenvalues of the LLM with its modal effective mass fraction for the translation (TX, TY, TZ) and rotational (RX, RY, RZ) degrees of freedom. . Within the scope of this work, only the first three modes are in excitation range and, thus, only these are

considered in analysis of the LLM. It should be noted the relevant level of coupling between the first three modes, meaning that an excitation in a given axis is likely to activate all modes in excitation range. The sine vibration excitation range (up to 100 Hz with 47 G in plane and 36 G out of plane) are far from the first eigenvalue (1461.9 Hz) and, thus, the sinusoidal vibrational analysis should be approximated to a static analysis since no relevant dynamic amplification is foreseen. The random vibration is likely to activate the first three modes and, thus, their dynamic amplification should be estimated. The direct responses for the X, Y and Z directions are shown in Sub-figures 5(a) and 5(b), considering the lens node as the monitoring point and quality factor of 400. As expected, all three modes appear in the excitation directions and their magnitude is directly related to their modal effective mass fraction.

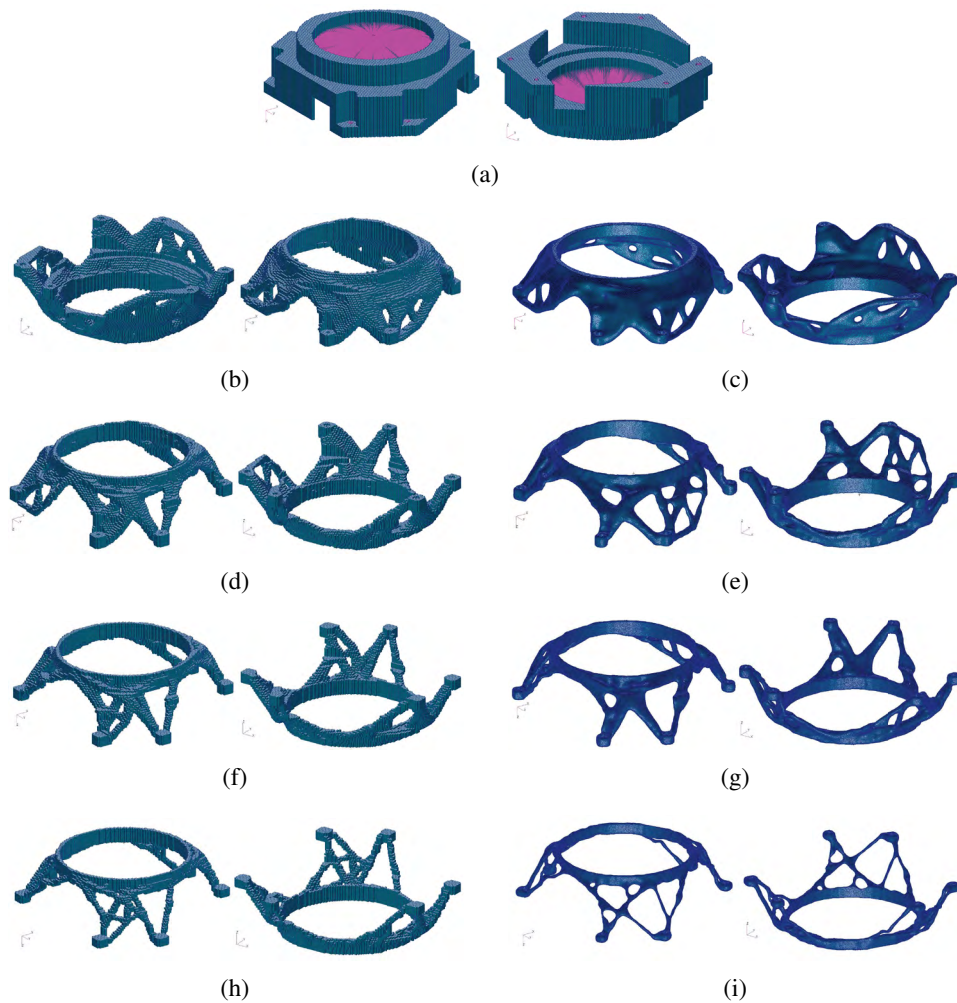


Figure 2: Discretisation of design domain in Sub-figure (a). Sub-figures (b), (d), (f) and (h) are topology optimisation results for 40%, 20%, 10% and 5% of volume fractions, respectively. Sub-figures (c), (e), (g) and (i) depicts the smooth surface meshes of the respective volume fractions.

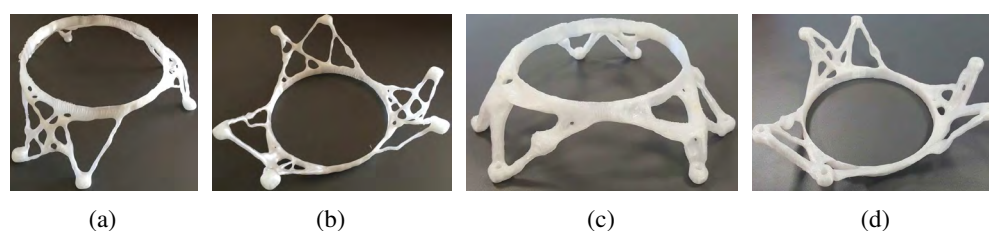


Figure 3: The LLM physical model printed in a dummy material (PLA). Sub-figures (a) and (b) are the design resultant from 5% of volume constraint, while Sub-figures (c) and (d) are the design resultant from 10% of volume constraint.

Table 1: List of the first ten eigenvalues of the LLM with its modal effective mass fraction for the translation.

Mode	Frequency (Hz)	TX	TY	TZ	RX	RY	RZ
1	1461.9	0.134	0.762	0.034	0.036	0.038	0.615
2	1580.0	0.757	0.152	0.014	0.014	0.009	0.178
3	1913.3	0.039	0.018	0.731	0.640	0.650	0.045
4	3142.8	0.003	0.003	0.018	0.036	0.010	0.001
5	3303.0	0.008	0.005	0.000	0.000	0.013	0.013
6	3447.1	0.000	0.006	0.003	0.000	0.001	0.001
7	3920.5	0.003	0.000	0.006	0.016	0.008	0.000
8	4173.8	0.002	0.001	0.002	0.030	0.000	0.001
9	4401.5	0.000	0.000	0.003	0.001	0.001	0.059
10	4641.9	0.001	0.001	0.039	0.002	0.009	0.008

Sub-figures 4(b), 4(d) and 4(f) depicts modal shapes of the first three eigenvalues values of the LLM. While, Sub-figures 4(c), 4(e) and 4(g) describe the static stress levels (von Mises) from the sinusoidal vibration loads and Sub-figures 4(h), 4(j) and 4(l) depict the Root Mean Square (RMS) of the stress levels (von Mises) from the random vibration loads. Due to the slenderness of the structure, buckling analysis are also presented and its inputs loads were derived from random vibration analysis. Each load case of the random vibration analysis originates a buckling load case, where the indirect and direct responses are used to compute equivalent quasi-static accelerations. The buckling stability factor is presented in Sub-figures 4(i), 4(k) and 4(m).

The minimum stiffness requirement is reached with the first eigenvalue at 1461.9 Hz when compared with 400 Hz requirement. The geometrical stability (buckling) has a relevant positive margin. The stability factor (MSC Nastran result output) should be superior to one, otherwise, the solver is predicting failure. The current design of LLM has a stability factor of 2560.9 ⁽³⁾.

Regarding strength margins, the yield stress of the Ti6Al4V should be at least 825 MPa [14] and the maximum stress levels expected from the analysis is 40 MPa, leaving the margin for further optimization (in theory). However, due to manufacturing risk, the compliance minimization with a lower volume fraction constraint (see Sub-figure 2(i)) is not used.

³If the factor was dangerously closer to one, a knock-down factor analysis needed to be performed due to analysis uncertainty.

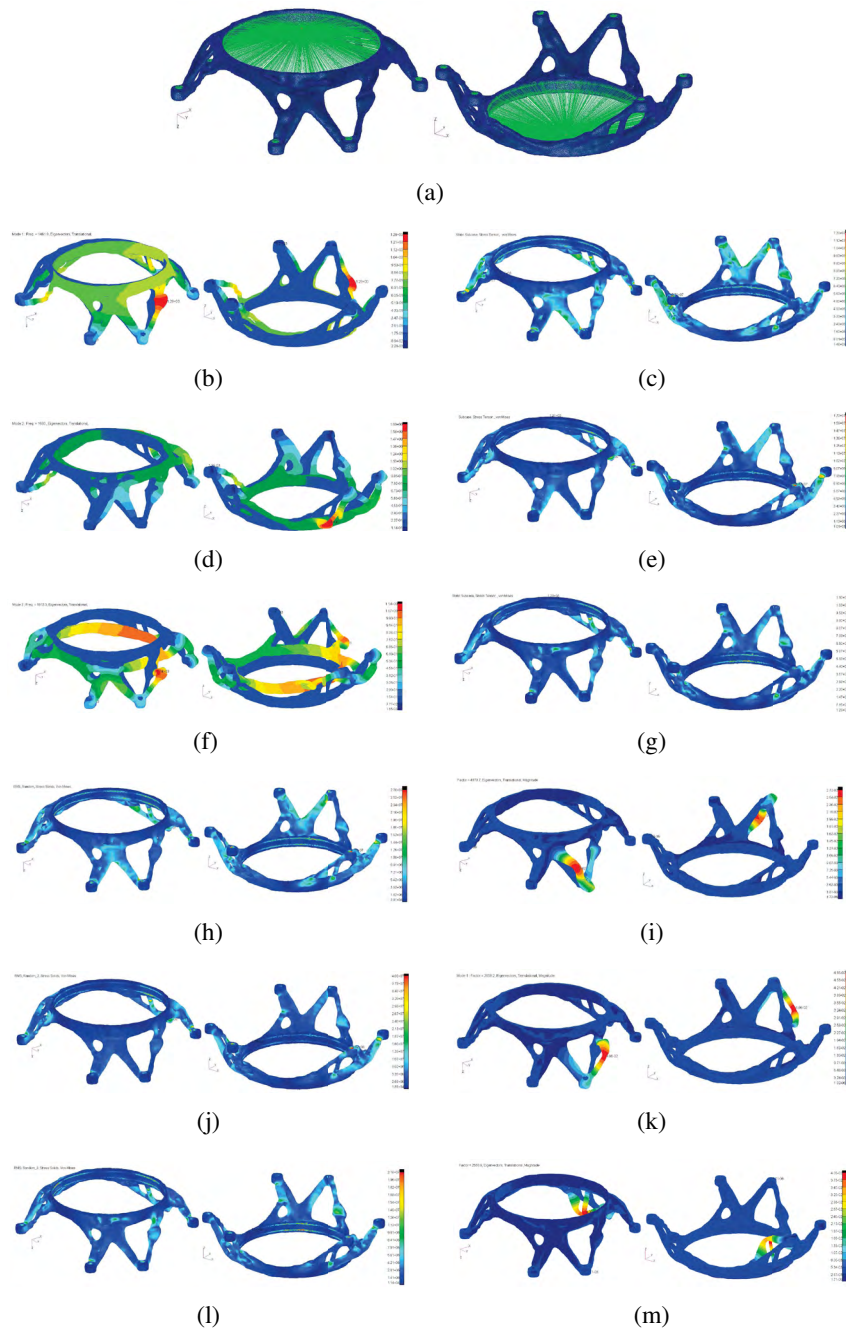


Figure 4: (a) FE modal analysis of the optimized LLM. Sub-figures (b), (d) and (f) are the modal shapes of first three eigenvalues. (c), (e) and (g) are the static von Mises stress maps when loaded in direction X, Y and Z, respectively. Sub-figures (h), (j) and (l) are the von Mises RMS values of the random vibration when excited in X, Y and Z directions, respectively. Sub-figures (i), (k) and (m) are the first buckling mode when loaded in directions X, Y and Z, respectively. All stress maps are in Pa.

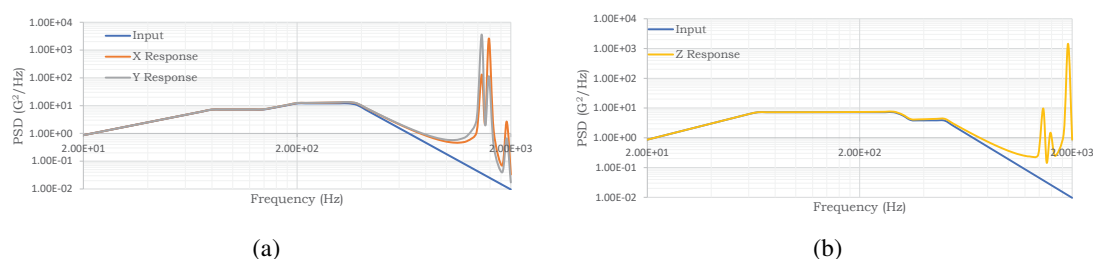


Figure 5: Random vibration responses. Sub-figures (a) and (b) are the in plane response and out of plane response, respectively.

4 Concluding remarks

A systematic methodology for designing AM parts is conceptually presented in a step-by-step manner. Issues of communication between different softwares were considered and a solution was provided. Finally, the presented methodology is applied to a case study and some encouraging preliminary results of the topology optimization, part design (smoothing and part edition) and structural analysis stages are shown. The resultant design, compliant with the mass constraint, shows good behaviour in terms of stress and stiffness considering structural requirements only.

5 Future Work

In the short term, the engineering cycle of the LLM needs to be concluded. At this point, the engineering cycle of LLM considered structural requirements only. However, the work environment of an optomechanical part requires additional load cases and requirements. For instance, mechanical loading due to I/F tolerances and thermo-elastic loading due to the mismatch of thermal expansion coefficients. Finally, the process preparation and manufacturing campaign stages need to be also concluded. Moreover, the presented methodology is still in development and some key aspects are still missing. For instance, Ti6Al4V constitutive data (anisotropy, porosity and strength data) is missing, which shall be obtained from the ongoing experimental testing campaign. Additionally, fatigue testing campaign will be also performed in order to evaluate the probability of failure during launch. Finally, AM manufacturing constraints need to be added to the TO algorithm, namely the overhang constraints.

Acknowledgements

The authors gratefully acknowledge the financial support of the Portuguese Foundation for Science and Technology (FCT) under the projects CENTRO-01-0145-FEDER-029713 by UE/FEDER through the programs CENTRO 2020 and COMPETE 2020, and UID/EMS/ 00481/2013-FCT under CENTRO-01-0145-FEDER-022083. Financial support of program CENTRO 2020 and UE/FEDER is acknowledged through the project CENTRO-01-0247-FEDER-024039, designated as ADVANSS. B. Barroqueiro also acknowledges the financial support by the FCT through the scholarship SFRH/BD/120779/2016. The authors also acknowledge all the technical recommendations and revision cycles from OHB Systems at Oberpfaffenhofen.

References

- [1] ISO International Standard. Additive manufacturing General principles Part 3: Main characteristics and corresponding test methods, 2014.
- [2] Anders Clausen. *Topology Optimization for Additive Manufacturing*. PhD thesis, DTU Mechanical Engineering, Technical University of Denmark, 2016.
- [3] Sebastian Kébreau, Dr. Patricia Cambrésy, André Dröse, Vincent Gröne, Kai Schimanski, and Freerk Syassen. Maturation of additive manufacturing for implementation into ariane secondary structures: Overview and status of “alm iscar”. In *14th European Conference on Spacecraft Structures, Materials And Environmental Testing*.
- [4] Gilles Pommatau, Florence Montredon, Antoine Carlino, Marion Salvi, Emmanuel Kot, Florence Clement, and Stephane Abed. Engineering design cycle for an additive layer manufactured secondary structure, from concept to final validation. In *Thales Alenia Space Communication*.
- [5] Aremu A, Ashcroft I, Hague R, Wildman R, and Tuck C. Suitability of SIMP and BESO Topology Optimization Algorithms for Additive Manufacture. *Wolfson School of Mechanical and Manufacturing Engineering*, 2010.
- [6] MSC Software. MSC Nastran 2017.1: Design Sensitivity and Optimization User Guide, .
- [7] M. P. Bendsøe. Optimal shape design as a material distribution problem. *Structural Optimization*, 1(4):193–202, dec 1989.
- [8] C. Geuzaine and J.-F. Remacle. Gmsh: a three-dimensional finite element mesh generator with built-in pre- and post-processing facilities. *International Journal for Numerical Methods in Engineering*, 79(11):1309–1331, 2009.
- [9] MSC Software. MSC Nastran 2017.1: Linear Static Analysis User Guide, .
- [10] MSC Software. MSC Nastran 2017.1: Dynamic Analysis User Guide, .
- [11] Michael Gouge and Pan Michaleris, editors. *Thermo-Mechanical Modeling of Additive Manufacturing*. Elsevier, 2018.
- [12] ASTM International, West Conshohocken. ASTM WK47031: New Guide for Nondestructive Testing of Additive Manufactured Metal Parts Used in Aerospace Applications, 2014.
- [13] ECSS E ST 10 03C. Space engineering: Testing, 2012.
- [14] ASTM International, West Conshohocken. ASTM F3001-14, Standard Specification for Additive Manufacturing Titanium-6 Aluminum-4 Vanadium ELI (Extra Low Interstitial) with Powder Bed Fusion, 2014.

DUOADD[§]: A SOFTWARE TO DETECT AND EXPORT DAMAGES OF 3D SCANNED OBJECTS

MATTEO PERINI^{*}, PAOLO BOSETTI[†]

University of Trento
Department of Industrial Engineering
^{*} e-mail: matteo.perini@unitn.it
[†] e-mail: paolo.bosetti@unitn.it
web page: <https://www.promfacility.eu/>

Key words: Direct Laser Deposition, Object Repair, Octree, Hybrid Manufacturing

Abstract.

The recent appearance of hybrid CNC machines – which can both add and remove material to an object – has facilitated a new type of approach to the problem of repairing damaged components. Up to now, repair operations have been carried out manually and for this reason they are errors prone, costly and time consuming. The use of precise and repeatable CNC machines in this field is therefore very attractive for the sake of reliability and repeatability. One of the biggest obstacles on the automation of the repairing process is that the CAM software requires a solid CAD model to create the toolpaths needed to perform additive operations. The present work proposes the use of octrees to detect the damaged spot starting from the 3D scan of the damaged object. A software named DUOADD has been developed to convert these informations into a CAD model suitable to be used by the CAM software. The new workflow designed to perform a complete repair operation is here described. DUOADD allows to approach the repairing problem from a new point of view opening the doors to save both time and money. The successful application of the entire process to repair a damaged die injection mold is also here reported.

[§] DUOADD = DUOADD Uses Octrees As Damage Detector

1 INTRODUCTION

Direct laser deposition (DLD)[1, 2, 3] is an additive manufacturing (AM) technique[4, 5] that allows metal material to be deposited using a process similar to FDM (Fusion Deposition Modeling) 3D printing. The main difference between the two is that the raw material is powder rather than wire. The metal powder is sprayed by a nozzle with a flow of inert gas and is melted by a laser beam. The powder ends up in a pool of molten material and becomes part of the object, adding thickness to the working surface. By adding material layer by layer, it is possible to create three-dimensional objects.

One of the very interesting aspects of this technology is that the printhead can be mounted on various machines such as industrial robots or 5-axis CNC machines. This allows the deposition of material even on free form surfaces and/or to create very complex objects. In the present

work the Authors used a hybrid manufacturing machine: the DMG MORI Lasertec 65 3D. Hybrid manufacturing in this case means that the 5-axis CNC machine has the ability both to add material and to remove it through a milling process.

The ability to add new material to an existing object and remove any excess material makes this 3D printing technique particularly suitable for repairing damaged objects[6, 7, 8]. Nowadays it often happens that critical components are replaced in their entirety after suffering minor damages that affect the part functionality. This results in a huge waste of material, energy and money. Being able to refurbish these objects becomes very important both from an economic point of view and from that of environmental sustainability[9]. Extending the life of objects becomes crucial if, as the European Commission has recently pointed out¹, companies are invited to develop production techniques that are increasingly geared towards reduced environmental impact and the circular economy. Until now, the repair of mechanical components is carried out manually by highly skilled workers through welding and finishing operations. This makes repair operations very expensive and prone to errors due to the non-repeatability of the process.

The idea of using the precise and repeatable DLD technology to repair and finish components by milling is therefore very attractive[10, 11], with the added advantage of using only one machines during the entire process. One of the main problems to face in using this technology for repair damaged object is the difficulty in detecting the volume where the material needs to be deposited. In fact, CAM software use three-dimensional solid models, not meshes, to create the toolpaths that guide the CNC machine through additive operations. In this work the Authors present a software and a procedure that allow the identification of the damage, its digitalization and finally the creation of a digital model in a format that can be used by the CAM.

The process consists of 5 main steps:

1. 3D scanning of the damaged component;
2. alignment of the scan with the original solid model;
3. discretization via octree[12, 13] of both models;
4. boolean comparison between the two discretized objects
5. conversion of the damage representation into a solid model.

This paper will describe in detail these steps with particular emphasis on the software part. Finally, the results obtained on a case study showing the effectiveness of the process developed in the repair of real objects will be reported and discussed.

2 3D SCAN AND ALIGNMENT

The process of identifying a damage on a component requires a couple of three-dimensional models, the first obtained by 3D scanning of the damaged object, and the second representing the theoretical solid model of the original geometry. To obtain the model of the damage,

¹http://europa.eu/rapid/press-release_IP-15-6203_en.htm

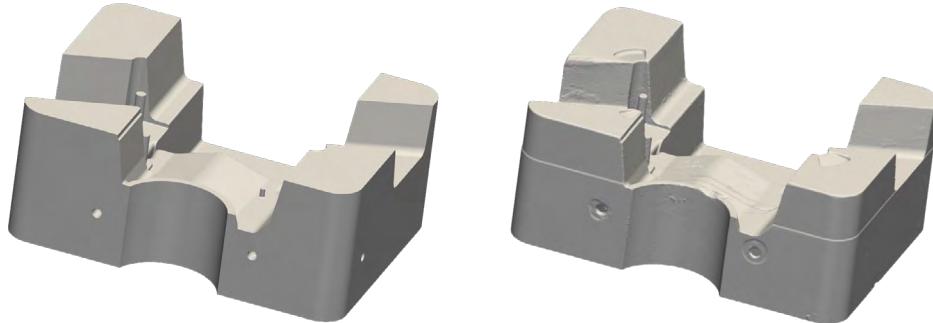


Figure 1: Left: The original solid model. Right: The mesh of the 3D scan.

these two models must be compared by means of a Boolean operation, see Figure 1. When boolean operations are performed by working with surfaces represented as triangulated meshes – typically obtained by 3D scans – it is very easy to incur in broken geometries or a multitude of micro-volumes that have no practical value[14]. For this reason, after several attempts to directly compare two mesh models, it was decided to change approach and discretize both geometries using octrees. This technique will be explained in detail in section 3.1.

There are various techniques that allow to digitize the geometry of the damaged component[15, 16] but for this work it was decided to use a structured light 3D scanner: the Metrascan 3D CMM by Creaform. This scanner has a resolution of 0.03 mm and an overall accuracy of 0.12 mm. This precision is more than sufficient for repair operations as it is about an order of magnitude smaller than the voxel resolution of the DLD machine.

One of the most advantages of this type of 3D scan is that the entire geometry of the object can be reconstructed at once. In fact, the Metrascan is equipped with a scanning head that can be manually moved and therefore allows to reconstruct the object from many points of view during the same scanning session. The scanner software processes all the information received from the cameras and returns a triangulated mesh. It also allows an adaptive sampling that increases the number of triangles in detail-rich areas leaving less important areas – e.g. flat areas – with fewer triangles. In this way it is possible to obtain a mesh with a good resolution while keeping the number of triangles limited, with the consequence that it will decrease the computational calculation of the following octree creation.

The second model – that represents the nominal geometry – is transformed from a solid CAD model into a mesh by software. This allows one to have absolute control on the maximum deviation error of the mesh from the theoretical model.

The resulting meshes should be checked to ensure that they are watertight and coherently

oriented.

The next step consists in the alignment of the two models and their positioning in space relative to a known coordinate system. While alignment is essential for the comparing operation of the two models, positioning the models is optional but greatly facilitates dealing with the models inside the CAM software.

The procedure that gave the best results places the theoretical model in a convenient position for the identification of a local coordinate system. Subsequently, the 3D model obtained by three-dimensional scanning of the damaged object is aligned with the theoretical model using one of the following software: Creaform VX Elements², Cloud Compare³ or Meshlab [17]⁴.

All the software mentioned use least square algorithms for minimizing alignment errors and gave good results. These software have differences that could sometimes make the alignment process easier. For example, VX Elements allows one to perform alignment by giving more importance to some areas of the mesh than others – i.e. the undamaged areas. Consequently, the choice of the alignment software often depends on the availability of software and on the skill/knowledge of the operator.

The alignment operation results in two meshes that have the same position and orientation in space, these can be used for the next operations.

3 DUOADD

At the time being, there are only few CAM software that can handle DLD processes in 5-axis CNC machines and none of them can use meshes to define where the material has to be added. It is therefore necessary to have a solid model of the volume to be created/added. The purpose of DUOADD is precisely to convert the information from the 3D scan of the damaged component into a model that can be easily used within the CAM. DMG MORI – the company making the Lasertec 65 3D – uses Siemens NX CAD/CAM to prepare part programs for hybrid processes. The process that DUOADD uses to arrive at the STEP [18] file representing the solid damage model is divided into several steps:

1. octree-based discretization of both meshes, the one resulted by the 3D scan and the one obtained from the original solid model;
2. complete the data structure filling the void space inside the shell of the octrees;
3. boolean comparison between the octrees by NOR operation;
4. filter the obtained results by removing isolated nodes;
5. conversion of the octree structure into a solid STEP/IGES model;
6. export of results.

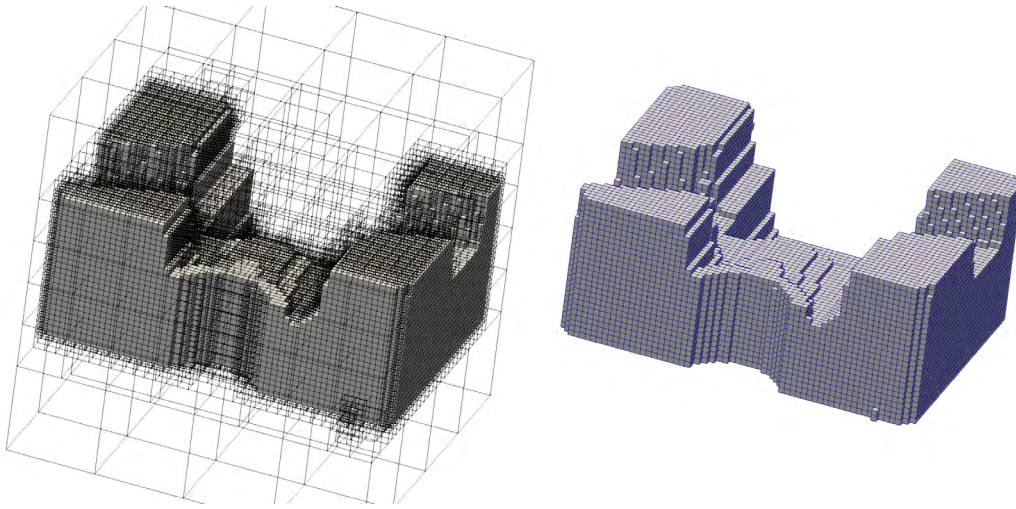


Figure 2: Left: The structure of the octree. Right: The leaves representing the mesh.

3.1 Octree-based discretization

This section describes in detail the process of discretization by octree of a mesh. The octree-based data structure was chosen by the Authors because of its robustness and effectiveness. An octree is a recursive tree-based structure that develops from an initial volume – called root – in the shape of a cube, built around the mesh you want to discretize. Octrees have only a single root which is divided into eight octants – called children – all identical to each other. During the recursive discretization process each child that contains or intersects at least one triangle of the mesh is again subdivided into 8 identical children. This process continues until the desired spatial resolution is reached or when an octant – also called node – is completely empty. The resolution can be controlled by setting the maximum number of iterations that corresponds to a certain depth level. For example, starting from a root of 100 mm side, after $n = 10$ iterations the size of the edge of each leaf will be: $L = 100/2^{10} = 0.0976$ mm. It is evident that, thanks to this power law, the level of discretization is improving quickly with n . However, it is also important to consider that the number of nodes increases exponentially in relation to the level of depth. It can be shown that the theoretical maximum number of nodes is $N = \sum_{i=1}^n 8^{n-1}$. Octrees therefore allow to obtain a denser data structure only where necessary, leaving the rest of the structure lighter. All nodes that are at the end of a branch – i.e. they have no children of their own – are called leaves. The set of all the leaves belonging to the last level of the tree represent the actual discretization of the mesh surface with the added value of including the description of the bulk. Figure 2 shows the octree structure on the left side and the set of leaves – obtained with seven iterations – on the right.

The construction of the octree starts with the calculation of the center of the root and its

²<https://www.creaform3d.com/>

³<http://www.danielgm.net/cc/>

⁴<http://www.meshlab.net/>

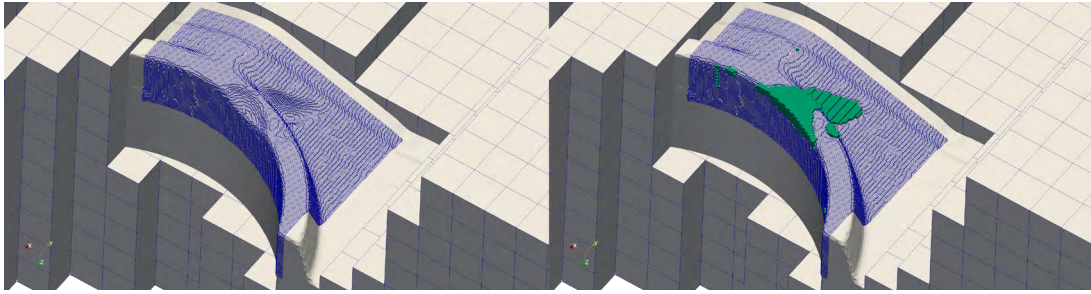


Figure 3: An example of higher resolution where is needed (left). The volume of the detected damage in green (right).

dimensions. In order to obtain two comparable octrees, position and dimensions of both octrees must match so that all the vertices of both meshes are taken into consideration.

Each vertex has coordinates – i.e. X_v, Y_v, Z_v – that will define its position in space. By checking the coordinates of all vertices it is possible to detect the maximum and minimum extension of the models along the three main axes $(X_{v,max}, X_{v,min}, Y_{v,max}, Y_{v,min}, Z_{v,max}, Z_{v,min})$. The center of the root node is calculated as $\mathbf{R}_c = \left\{ \frac{X_{v,max} + X_{v,min}}{2}, \frac{Y_{v,max} + Y_{v,min}}{2}, \frac{Z_{v,max} + Z_{v,min}}{2} \right\}$ while the size of the root side will be: $l = \max\{X_{v,max} - X_{v,min}; Y_{v,max} - Y_{v,min}; Z_{v,max} - Z_{v,min}\}$.

The construction of the octree proceeds with the division of the root node into 8 octants. Each triangle of the mesh that intersects even partially the volume of a child node is assigned to that node. In this way, each child node will have its own list of triangles which, at the next iteration, will be distributed among the new children. Note that the same triangle may belong to several octants of the same level. To check if a triangle belongs to an octant or not, it is sufficient to check if at least one vertex of the triangle is inside the volume of the node. DUOADD also checks if there are empty nodes and, in that case, they are not subdivided any further, thus keeping the data structure light.

A recursive routine continues in the subdivision of the nodes until the maximum level of recursion is reached. This level is defined by the user according to the sought resolution. This function assigns to each node newly created its position, size and a name programmatically created, according to the place occupied by the node in the octree data structure. In fact, one of the advantages of using a rigorous tree structure like the octree is that the position within the data structure is uniquely correlated to the geometric properties of the node itself – i.e. position and size of the node.

One of the disadvantages of octrees is that the number of nodes increases exponentially as the number of levels increases. To prevent the octree from reaching unmanageable size, a procedure has been used that allows the level reached by the octree to be increased only in a certain area – e.g. the damage area. This allows the resolution to be higher only where it is really needed. Figure 3 shows a localized higher resolution that casts the focus of the analysis only on the damaged area.

The nodes that are present in the last level of recursion and that contain triangles of the mesh are marked as “object” and are the nodes that represent the triangulated surface.

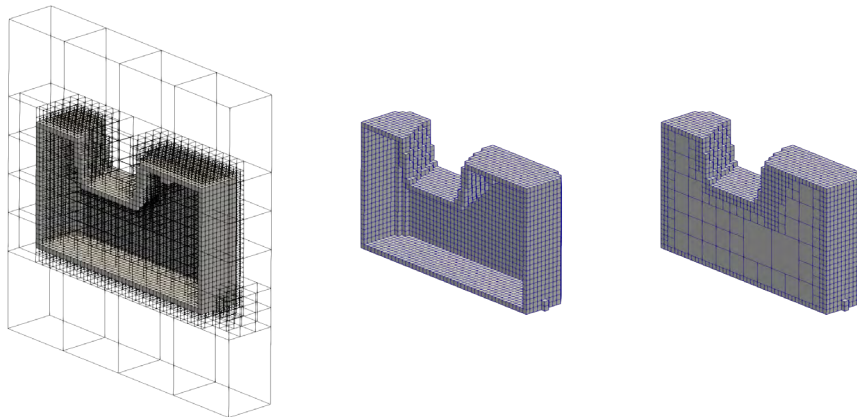


Figure 4: Empty structure (left and center). Filled octree (right).

3.2 Octree filling

The result of the previous phase is a complete octree where all the leaves completely inside or outside of the mesh are not marked as “object” because they do not intersect any triangle. To perform the Boolean operation between the two octrees, it is necessary to have the entire volume inside the triangulated surface to be marked as “object”, leaving only the external nodes marked “void”. The filling operation[19] is performed using a ray-triangle intersection algorithm[20]. This algorithm traces a ray from a point belonging to the root node to a point outside and counts the number of intersections of this segment with the triangulated surface of the mesh. If the number of intersections is odd it means that the starting point lays inside the mesh volume, otherwise the point is external. The routine repeats this procedure for all nodes not already marked as “object” using the center of the node itself as the starting point of the ray. Figure 4 shows the result of the filling operation. This filling operation could be computationally heavy because for each node one has to theoretically look for the intersections with each triangle of the mesh. To attenuate this problem a possible improvement is to point the ray along the vertical axis so that it is possible to select a priori the set of triangles that might have intersections, excluding all others from the analysis.

3.3 Boolean comparison

At this point the octree represents the actual volume enclosed by the mesh. The last problem to be solved before comparing the 3D scan octree with the octree of the original solid model is that the two data structures may be locally inconsistent due to the geometric differences of the starting meshes. In order to compare the two structures a recursive procedure has been written that, iterating simultaneously on both octrees, checks the presence of structure inconsistencies – i.e. different number of leaves or depth reached by each branch of the octrees – and corrects them creating two coherent structures.

Normally this operation does not involve a considerable weight increase of the octrees as the two models usually differ from each other only in the volume of the damage.

Once the two data structures have been made uniform, it is possible to carry out the comparison. This happens with another recursive routine that compares each node having the same position in both octrees and saves the result of the comparison in a new octree that has exactly the same data structure. During the comparison procedure only nodes that are not marked both “inside” or both “outside” are marked as “damage” and kept in the new octree. It is therefore a XOR boolean operation.

DUOADD performs this operation on both octrees at the same time, covering the entire data structure only once. The result of this operation is an octree in which only the nodes that actually represent the volume of the damage remain active.

A problem resulting from the boolean XOR operation is that, in addition to the volume of damage, other disconnected nodes – unnecessary for the purpose of this work – are created. In fact, in some cases even very small differences between the STL models lead to differences in the octrees created. Disconnected and scattered knots are not useful for repair purpose and for this reason must be removed. Duoadd implements some algorithms for filtering and deleting those unnecessary nodes, discussed hereafter.

3.4 Filtering

Several methods of filtering the result have been implemented and tested but the two that gave the best results are:

- (a) filtering based on the number of neighbours of a node;
- (b) filtering based on the connection with other nodes along the main directions – i.e. not along the diagonals.

In both cases an algorithm has been written that finds the neighbours of a node[21] and controls their position and quantity. This routine is performed on each node marked as “damage” and, if it is not sufficiently connected with the other nodes, the node itself is deleted from the resulting volume. The first algorithm erodes the component especially in conditions of very scattered results. The second method is more conservative and in some cases does not remove all disconnected components. On the other hand, however, the second method returns a geometry more representative of the real damage and for this reason is the one that is used by default. The fact that few disconnected parts remain in the resulting octree does not represent a big issue because in the next steps they can be easily removed.

3.5 Octree representation

The data structure of the octree must be translated into a solid model to be used by Siemens NX. Each node is represented starting from its position inside the tree. Three different methods for exporting the octree have been implemented. The first uses the Visualization Toolkit (VTK) library[22] and outputs a set of cubes consisting of vertices, edges, faces and finally volumes. This type of representation is very efficient and allows a quick inspection of the results. The output obtained with this technique is not useful for the conversion of the octree into a solid CAD model but is therefore only used for debugging purposes. The second and third methods

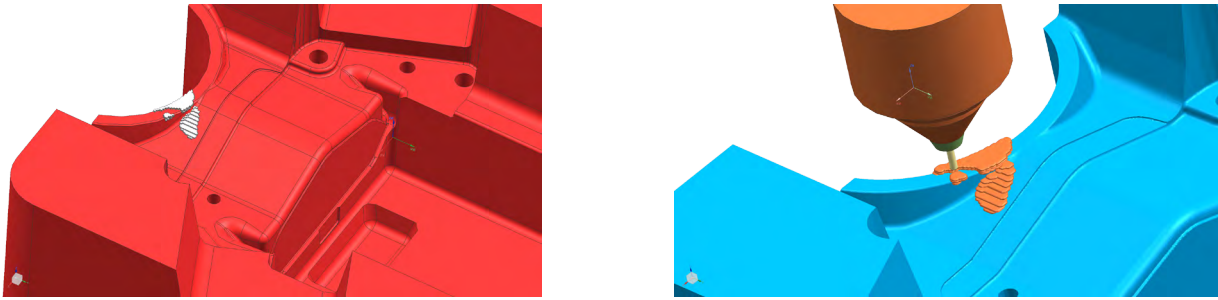


Figure 5: In red the original solid model while the white model represents the damage (left). Simulation of the additive operation (right).

use the OpenCascade (OCC) library[23] with which each node, representing the damage, is transformed into a cube object. The set of all the generated cubes can now be exported as a three-dimensional STEP [18] or IGES [24] model. The file thus obtained is the exact translation of the octree into a CAD model. The resulting solid will be a set of cubes disconnected from each other. These should be merged to use the total volume within the CAM software. To do that, the user can merge all cubes into one or more solids directly via any CAM software. However, it has been observed that this can take a long time if the number of cubes is high – i.e. tens of thousands of individual cubes can take hours to join. One of the reasons why this happens is that the union of many objects greatly increases the complexity of the resulting solid. Tests have shown that the joining operation remains very rapid until the solids to be joined are about one hundred. To overcome this problem, a routine has been written that combines 100 cubes at a time and puts the result in a new list of solids. The volumes resulting from the above operation are then joined together and will form a single solid. This STEP (or IGES) model is much lighter than the set of cubes of which it was composed in the beginning and is much more manageable within CAD/CAM software. With this routine, the time required for the joining operation has been drastically reduced.

4 CAM OPERATIONS AND MACHINING

The solid STEP file obtained in the previous step can be used in CAM to create the toolpaths necessary for the deposition of the new material on the damaged component and, subsequently, for finishing operations. The solid created by DUOADD is already located in space according with the same coordinate system as the original solid model. This is very important because it would be difficult to place a solid model without having precise references. Figure 5 shows the CAD model of the damage automatically placed in the exact position into workspace and the simulation of the additive operation. Thanks to DUOADD instead we can move both solids and position them simultaneously in the workspace avoiding misalignments. As with the normal NX workflow, the solid to be added to the component must be expanded to ensure that sufficient material is brought in. Then it is possible to proceed with the creation of toolpaths for both deposition and finishing operations.

The CAM-generated part program is then used by the hybrid CNC machine – i.e. the DMG MORI Lasertec 65 3D – to add the missing material and remove the excess material. The



Figure 6: The new material added to fill the damage (left). The worn area after the finishing operation (right).

DLD process can deposit material with a deposition rate of 10-25 g/min, which means that, in a few minutes, the material required for filling the damage is deposited. Subsequent milling operations return the component to its original shape, restoring its functionality. Figure 6 shows the actual additive operation on the left, and the removal of the surplus material on the right.

5 CONCLUSIONS

In this work, the problem of repairing damaged objects has been addressed using an effective and innovative approach. The workflow designed and implemented within DUOADD has proven to be repeatable and robust.

With just a few steps, DUOADD allows to detect the volume of the damage in a quick and easy way. It returns the solid model of the damage ready to be used in the CAM software. The speed of the software is strongly dependent on the level of resolution that the user wants to obtain and on the number of triangles of which the meshes are composed, but usually the whole process takes a few tens of seconds. Currently the only two possible alternatives to DUOADD are to manually build the solid model to be used in CAM with a CAD software and then use the DLD machine, or to manually add the material through welding, but these procedures take much longer and are not repeatable.

Authors successfully use DUOADD to repair a die for injection molding but there are many other applications that could benefit from the use of this software – e.g propeller/turbine blades restoration or the refurbishment of artistic/historic artifacts.

Many improvements are expected in the near future such as the binary encoding of the octree structure and the smoothing of the shape of the exported solid body.

ACKNOWLEDGMENT

The authors would like to thank the ProM facility laboratory⁵ for strongly supporting this work.

⁵<https://www.promfacility.eu/>

REFERENCES

- [1] M. Labudovic, D. Hu, and R. Kovacevic, “A three dimensional model for direct laser metal powder deposition and rapid prototyping,” *Journal of Materials Science*, vol. 38, no. 1, pp. 35–49, 2003. [Online]. Available: <http://dx.doi.org/10.1023/A:1021153513925>
- [2] G. Lewis, J. Milewski, D. Thoma, and R. Nemec, “Properties of near-net shape metallic components made by the directed light fabrication process,” in *Proceedings to the Solid Freeform Fabrication Symposium, Univ. of Texas at Austin*. Citeseer, 1997.
- [3] J. Mazumder, J. Choi, K. Nagarathnam, J. Koch, and D. Hetzner, “The direct metal deposition of H13 tool steel for 3-D components,” *JOM*, vol. 49, no. 5, pp. 55–60, 1997. [Online]. Available: <http://dx.doi.org/10.1007/BF02914687>
- [4] B. S. a. Ian Gibson, David Rosen, *Additive Manufacturing Technologies: 3D Printing, Rapid Prototyping, and Direct Digital Manufacturing*, 2nd ed. Springer-Verlag New York, 2015.
- [5] N. Hopkinson, R. Hague, and P. Dickens, *Rapid manufacturing: an industrial revolution for the digital age*. John Wiley & Sons, 2006.
- [6] A. Pinkerton, W. Wang, and L. Li, “Component repair using laser direct metal deposition,” *Proceedings of the Institution of Mechanical Engineers, Part B: Journal of Engineering Manufacture*, vol. 222, no. 7, pp. 827–836, 2008.
- [7] J. H. Jang, B. D. Joo, S. M. Mun, M. Y. Sung, and Y. H. Moon, “Application of direct laser melting to restore damaged steel dies,” *Metals and Materials International*, vol. 17, no. 1, pp. 167–174, 2011.
- [8] L. Han, K. M. Phatak, and F. W. Liou, “Modeling of laser deposition and repair process,” *Journal of Laser Applications*, vol. 17, no. 2, pp. 89–99, 2005.
- [9] J. M. Wilson, C. Piya, Y. C. Shin, F. Zhao, and K. Ramani, “Remanufacturing of turbine blades by laser direct deposition with its energy and environmental impact analysis,” *Journal of Cleaner Production*, vol. 80, pp. 170–178, 2014.
- [10] J.-Y. Hascoët, S. Touzé, and M. Rauch, “Automated identification of defect geometry for metallic part repair by an additive manufacturing process,” *Welding in the World*, vol. 62, no. 2, pp. 229–241, 2018.
- [11] J. L. Rickli, A. K. Dasgupta, and G. P. Dinda, “A descriptive framework for additive remanufacturing systems,” *International Journal of Rapid Manufacturing*, vol. 4, no. 2-4, pp. 199–218, 2014.
- [12] E. Dyllong and C. Grimm, “A Reliable Extended Octree Representation of CSG Objects with an Adaptive Subdivision Depth,” in *Proceedings of the 7th*

- International Conference on Parallel Processing and Applied Mathematics*, ser. PPAM'07. Berlin, Heidelberg: Springer-Verlag, 2008, pp. 1341–1350. [Online]. Available: <http://dl.acm.org/citation.cfm?id=1786194.1786353>
- [13] H. Samet, “An Overview of Quadtrees, Octrees, and Related Hierarchical Data Structures,” in *Theoretical Foundations of Computer Graphics and CAD*, R. A. Earnshaw, Ed. Berlin, Heidelberg: Springer Berlin Heidelberg, 1988, pp. 51–68.
- [14] Y. Zhang, Z. Yang, G. He, Y. Qin, and H.-c. Zhang, “Remanufacturing oriented geometric modelling for the damaged region of components,” *Procedia CIRP*, vol. 29, pp. 798–803, 2015.
- [15] E. Bagci, “Reverse engineering applications for recovery of broken or worn parts and re-manufacturing: Three case studies,” *Advances in Engineering Software*, vol. 40, no. 6, pp. 407–418, 2009.
- [16] R. Liu, Z. Wang, T. Sparks, F. Liou, and C. Nedic, “Stereo vision-based repair of metallic components,” *Rapid Prototyping Journal*, vol. 23, no. 1, pp. 65–73, 2017.
- [17] P. Cignoni. MeshLab. [Online]. Available: <http://meshlab.sourceforge.net/>
- [18] I. 110303-21:2016, *STEP-file, ISO 10303-21 – Industrial automation systems and integration – Product data representation and exchange – Part 21: Implementation methods: Clear text encoding of the exchange structure*. ISO, Geneva, Switzerland, March 2013. [Online]. Available: <https://www.iso.org/standard/63141.html>
- [19] S.-N. Yang and T.-W. Lin, “A new linear octree construction by filling algorithms,” in *[1991 Proceedings] Tenth Annual International Phoenix Conference on Computers and Communications*, Mar 1991, pp. 740–746.
- [20] T. Akenine-Möllser, “Fast 3D triangle-box overlap testing,” *Journal of graphics tools*, vol. 6, no. 1, pp. 29–33, 2001.
- [21] G. Schrack, “Finding neighbors of equal size in linear quadtrees and octrees in constant time,” *CVGIP: Image Understanding*, vol. 55, no. 3, pp. 221 – 230, 1992. [Online]. Available: <http://www.sciencedirect.com/science/article/pii/104996609290022U>
- [22] W. M. Schroeder, K. Martin, and B. Lorensen, “The Visualization Toolkit: An Object Oriented Approach to 3D Graphics 3rd Edition, Kitware,” *Inc. Publisher*, 2003.
- [23] J. Russell and R. Cohn, *Open Cascade Technology*. Book on Demand, 2012. [Online]. Available: <https://books.google.ro/books?id=thWNMQEACAAJ>
- [24] M. Kahrs, “The Heart of IGES,” *Softw. Pract. Exper.*, vol. 25, no. 8, pp. 935–946, Aug. 1995. [Online]. Available: <http://dx.doi.org/10.1002/spe.4380250806>

EARLY STUDENT ENGAGEMENT IN THE DEVELOPMENT OF PROCESS MONITORING TOOLS FOR ADDITIVE MANUFACTURING

Sim-AM 2019

MICHAEL J. MOECKEL

University of Applied Sciences Aschaffenburg, Faculty for Engineering,
Wuerzburger Str. 45, 63743 Aschaffenburg, Germany
e-mail: Michael.Moeckel@th-ab.de, web page: <http://www.th-ab.de>

Key words: Additive Manufacturing, Selective Laser Melting, Process Monitoring, Data Analysis, Software Engineering, Education

Abstract. Project work accompanying an undergraduate course on software engineering has been re-designed to provide early student exposure to data analysis for process monitoring in additive manufacturing. For original data from a local research group active in selective laser melting (SLM) process development, i.e. for sensor measurements and control flags, a set of established mathematical and statistical routines were made conveniently available by developing scientific software tools. Standardized procedures for software engineering were taught and applied. Students experienced challenges and professional approaches involved in collaborative software development, implemented project management ideas and delivered a working software tool together with proper documentation. Gain in domain knowledge on process monitoring for additive manufacturing supported the activity as a motivating factor.

1 INTRODUCTION

The development of advanced physics-based simulations techniques and data-driven process monitoring tools is required to improve process control in additive manufacturing, in particular for 3D printing of metals, alloys and oxides. For this purpose, a substantial number of qualified experts will be required both in industry and academic research groups. To allow prospective PhD students to quickly enter productive research, early training of students on mathematical techniques as well as familiarity with real experimental data is highly desirable. For this purpose, exposure to current research activities in additive manufacturing has been provided for undergraduate students (4th semester) by re-defining project work accompanying a taught course on software engineering in the programme “Electrical Engineering and Information Technologies” at the University of Applied Sciences Aschaffenburg, Germany.

While the university already offers a well-established research group on experimental additive manufacturing techniques and process development led by Prof Ralf Hellmann [1], questions related to simulation and process monitoring will gain additional relevance in the near future [2,3]. Such approaches require competences in mathematical algorithm development as well as software implementation. Therefore, a specific concept addressing these needs has been

developed by combining elements of a mathematical seminar on statistical data analysis for additive manufacturing with project work required for software engineering. The programme is part of training on professional scientific and technical software development.

2 GOALS

The following objectives had been defined:

- Familiarity of students with the basic usage of mathematical concepts for process monitoring, e.g. descriptive statistics, sliding averages, Fourier transform and filtering, principle component analysis (PCA)
- Developing critical thinking for testing, assessment and integration of existing libraries containing mathematical routines
- Working with real data, including pre-processing steps and understanding the basic aspects of data acquisition during a selective laser melting (SLM) process
- Systematic approach towards software development based on: setting up software requirement specifications, choosing a suitable analysis model, defining software design specifications, implementing those following a project management plan and, finally, a clear documentation of all functionalities in a user guide.
- Stimulating a collaborative team effort to develop and test a problem-specific software tool using an integrated development environment (IDE, e.g. MS Visual Studio or Eclipse) and source control manager (GIT archive provided).
- Producing a configurable software tool which allows for a straightforward and convenient visualization and first inspection of process data collected from a SLM process.

3 SETUP

3.1 Educational environment

The course was organized as a lecture on models, methods and standards in Software Engineering (90 min per week) and an accompanying team project. The team project was supervised weekly for twelve weeks. Students were free to develop their own approaches within the set tasks. External resources had to be tested and cited before inclusion in the project. Python was used as programming language. A working software tool and a use case scenario had to be presented as part of an oral examination.

To illustrate project management techniques, intermediate deliverables had been defined as milestones of the project: A presentation of the software architecture and interfaces was expected four weeks after starting the project, a first working prototype of the software with reduced functionalities had to be presented after eight weeks. While full functioning was not expected, awareness for inconsistent definitions and outstanding contributions was raised. Moreover, the need to contribute to the project continuously was stressed. Three working days

before the examination the final result had to be submitted by upload.

3.2 Data

Sensor and image data from real selective laser melting building processes performed on a DMG MORI Lasertech 30 printing machine was kindly provided by Prof Ralf Hellmann's group. The data consisted of more than 70 data outputs which were collected continuously during previous building processes. Sensor measurements included, for instance, temperatures taken at various points, oxygen concentration, Ar gas pressure and flow in the building chamber, some laser characteristics (laser power, backreflection, etc.) and powder properties. A number of control and action variables, first of all the platform position and the powder level, as well as error flags were recorded. Thus, a high dimensional data set was available. Some data pre-processing was needed to ensure data consistency.

Moreover, photographic images of the powder bed were taken each 50 μm . Images are greyscale, consist of 1280 x 960 pixels at 24 bit and picture the building chamber as well as the surrounding box. Their size is roughly 1 MB each. The resolution is suitable to detect the built objects and to observe macroscopic inhomogeneity in the powder distribution like stripes or holes. It is not sufficient for an inspection of finer details directly.

Data sets were taken from correctly terminated as well as from early abandoned building processes. In the later cases, problems in the powder preparation caused fatal outcomes.

3.3 Student teams

Two student teams were formed consisting of five members each. Each team member was assigned responsibility for a particular mathematical routine, its software implementation, and a document describing some aspect of the software engineering process. Responsibility for the software architecture, the definition of interfaces and the final integration of subroutines as well as systematic testing was shared among all team members.

While one student team (team A) focussed on the time series analysis of physical sensor data (temperatures, etc.), the other team (team B) was involved in image processing. Two independent solutions have been developed and presented.

One of the teams (team A) quickly started productive activities and a well-balanced collaborative working habit and continued until the software tool had been developed. However, the other team (team B) struggled to organize itself already in the beginning. Despite of regular supervisions, early student disengagement could not be avoided: Three students continued to form a hard working core of the team, one student cancelled his participation early, still trying to minimize damage to the team, while another student continuously reduced involvement and, despite ongoing encouragement, did not contribute to the project outcome. This required some late stage interventions to ensure that a working software tool with reduced functionalities could be presented by the remaining team members. Reasons for this outcome cannot be clearly specified. They are not primarily linked to the abilities of the students since all tasks were designed to work on various levels of engagement and ability. For instance, a graphic user interface (GUI) could be built in a very elementary form by essentially copying textbook examples or including specific features and advanced

design. Dropout was, in particular, not linked to the kind of -and the challenges of- the mathematical routine chosen.

4 RESULTS & OBSERVATIONS

4.1 Selective Laser Melting Process and Data Analysis Methods

Participating students got in contact with current research activities in the field of additive manufacturing. They learned about the basic aspects of the selective laser melting process and are able to link relevant sensor parameters to steps and particular features of the process. They reviewed previous knowledge on signal processing, e.g. based on Fourier transforms, and extended their mathematical knowledge slightly beyond eigenvalue problems by making the principal component analysis available for the given data set. Working with real data generated at their home university and contributing at least a tiny step to research activities was for many a motivating experience.

4.2 Scientific software development

The main focus, however, was the development of a software tool for scientific purpose. As a result, two independent programmes were specifically designed for first inspection of data sets from a particular selective laser melting process performed by a research group. Simple time series analysis of historic data can be rather conveniently performed with the tool. Data visualization was performed wherever appropriate to support the growth of data and process intuition.

Team A developed a user-friendly graphical user interface (GUI) suitable for a quick search for dominant correlations between various data traces. Team B suffered an unexpected shortage of manpower and designed a command line control approach as a backup solution. Both teams developed concepts to make observations reproducible by logging configuration and input parameters and, partly, storing intermediate results.

Documentation reached a satisfactory standard to allow future thesis students to use this tool for a first analysis of similar data and to add own contributions, e.g. additional mathematical routines, within the given framework. A bit of further software development would be needed to integrate both programmes into a joint tool.

Performance analytics was conducted by both groups as part of the final testing to benchmark the programme developed. It clearly shows room for further improvements.

4.3 Perspectives

The chosen approach motivates the development of new and specific educational programmes at the intersection of mathematics, software engineering and process analytics. While traditional mathematical seminars constrain themselves to purely theoretical analysis, practical software engineering projects often approach problems based on advanced high-level frameworks; those may completely disguise mathematical content. Scientific software

development requires the ability to combine both, using efficient numerical core routines while making slight adaptations to overall mathematical implementations where needed.

Further work could involve the combination of a seminar on higher machine learning techniques with a direct development of code aimed at addressing specific research tasks. Natural candidates are tools for error detection or state prognostics.

5 ACKNOWLEDGEMENTS

The data used for the student projects had been collected independently by Prof Ralf Hellmann and his group. It was provided free of charge for educational purposes. In particular, the author thanks Jakob Feldmann for supporting the project by annotating and explaining some of the sensor data labels.

The lecturer of the course *Software Engineering*, Prof Konrad Doll, provided the opportunity to complement existing software engineering projects by reaching out to joint data analysis and software development for additive manufacturing.

Furthermore, the author gratefully acknowledges funding provided by the State Government of Bavaria under the project PromoAdd^{3D}.

REFERENCES

- [1] Hellmann, R. <http://www.alp-aschaffenburg.de> (downloaded 11th of July 2019)
- [2] Tapia, G. and Elwany, A. *A Review on Process Monitoring and Control in Metal-Based Additive Manufacturing*, J of Manufac Science and Engineering (2014) **136**:060801.
- [3] *Measurement Science Roadmap for Metal-Based Additive Manufacturing*, NIST (2013)

NUMERICAL AND EXPERIMENTAL CRUSHING BEHAVIOUR INVESTIGATION OF EBM PRINTED AUXETIC CHIRAL LATTICES

**Kadir Gunaydin^{†‡*}, Francesco G. Gallina^{†¶}, Alessandro Airoidi[†], Giuseppe Sala[†] and
Antonio M. Grande[†]**

[†] Department of Aerospace Science and Technology
Politecnico di Milano
Via La Masa 34, 20156 Milano, Italy
e-mail: kadir.gunaydin@polimi.it, web page: <https://www.aero.polimi.it/>

[‡] Aeronautics and Astronautics Faculty
Istanbul Technical University
Maslak, 80626, Istanbul, Turkey
Web page: <http://www.uubf.itu.edu.tr/>

[¶] Department of Mechanical Engineering
Politecnico di Milano
Via La Masa 1, 20156 Milano, Italy
Web page: <https://www.mecc.polimi.it/>

Key words: Chiral, Auxetic, EBM, Crushing

Abstract. In this study, Electron Beam Melting (EBM) is used to produce chiral auxetic lattices, and the compression of chiral auxetic lattice is investigated experimentally and numerically in the edgewise direction, where auxeticity can be experienced. Titanium Alloy (Ti6Al4V) metallic powder is used in this study. To understand mechanical behaviour and to characterize EBM printed parts, tensile tests are conducted. According to the tensile test results, a constitutive equation is selected, calibrated and adopted to represent the behaviour of the material. Furthermore, a chiral unit cell is manufactured and tested with a compressive load profile to investigate its displacement limit by applying large displacements without experiencing permanent deformations, degradation or failures. The same scenarios explored in the experiments are then analyzed by means of non-linear computational models using a commercial finite element code to validate a numerical approach for optimal design and performance prediction.

1 INTRODUCTION

In aeronautics, aerospace, automotive and military applications, lightweight structures such as sandwich structures have an important role considering crush resistance during impact and blast situations. For crashworthy structures, different types of sandwich structures have been proposed with different cores such as foams, lattices and trusses. The lattice cores have come forward regarding crashworthiness, and one of the most promising lattice structures are auxetic cellular solid structures [1]. Auxetic lattice structures are special structures experiencing negative Poisson's ratio so that they behave differently from conventional materials which shrinks

under a compressive load and expands under a tensile load. Amongst them chiral structures are one of the prominent auxetic structures that show -1 Poisson's ratio [2].

Chiral auxetic cellular solid was originally proposed by Prall and Lakes, and in their study -1 Poisson's ratio was proved theoretically [2]. Chiral cellular solids show anisotropic behaviour due to its asymmetric topology, and auxeticity emerges on the edgewise (in-plane) direction, thus, studies in the literature can be divided into two groups which are edgewise and flatwise (out-of-plane) studies. A certain number of edgewise studies were performed, and one of these studies includes a numerical model using dynamic shape functions to describe dynamic behaviour over a wide frequency range. A validation study was conducted to propose chiral network concept for aerodynamic applications by Spadoni et al. [3]. Chiral structures show auxeticity under small deformation however, when they are subjected to large elastoplastic deformation, they lose their auxeticity. Zhu et al. [4] used wavy ligaments to increase two mechanical properties, and as a result, the new structure showed higher energy absorption capacity. Additionally, chiral solid cellulars are proposed as a filling material for morphing structures due to their ability of undergoing large overall displacement [5, 6, 7].

In this study, EBM technology is used to produce tensile specimens and chiral unit lattice cells. In addition, EBM is used for understanding the effect of production method on mechanical properties. Specimens were produced in two different directions which are perpendicular (90°) and parallel (0°) to the powder deposition direction. Chiral lattice unit cells are produced where their flatwise surface is parallel to powder deposition direction to have higher mechanical performance and prevent additional inner support structure usage. As a result, a compression load profile is applied to the chiral unit cells, and a validation study is conducted using ABAQUS Standard.

2 METHODS

2.1 Material and Processing

Poisson's ratio of the chiral cellular solids is independent from its constituent material, however, besides the topology of the cellular solids, the constituent material is important for determining the mechanical performance for crush applications. Therefore, manufacturing method is implicitly playing a significant role in the cost, production challenges, and performance. Commercially offered metal based honeycomb structures are continuously produced from an aluminium sheet by the help of cutting and bending metal rolls [8]. The development of the additive manufacturing (AM) processes in recent years provide an opportunity to produce arbitrary topologies with less limitation comparing to conventional production methods. One of the promising AM technique is EBM additive manufacturing process that uses an electron beam to melt metallic powders [9]. Arcam A2 EBM metallic 3D printer and ARCAM Ti6Al4V ELI metallic powder have been used in this study. Titanium alloy is used due to its outstanding mechanical properties of high specific strength, high corrosion resistance, excellent biocompatibility, thus titanium alloys are prominent material for aerospace and bio-engineering fields. ARCAM Ti6Al4V ELI is a gas atomized prealloyed powder in a size range of $45\text{-}100\ \mu\text{m}$ [10], the chemical specification and mechanical performance of the powder material can be seen in

Table 1 and 2.

Table 1: Chemical specifications of Arcam Ti6Al4V ELI

Aluminium	Vanadium	Carbon	Iron	Oxygen	Nitrogen	Hydrogen	Titanium
6.0 %	4.0 %	0.03 %	0.10%	0.10%	0.01%	< 0.003%	Balance

The metal powder under vacuum is melted with electron beam gun which accelerates electrons to a velocity range of 0.1-0.4 times the speed of light using heated tungsten filament by a high voltage of 60kV [11]. Consequently, electrons hit the metal powders and transfer the kinetic energy mostly as thermal energy to the metal powder, and with this energy particles melt and merge according to the energy of electron beam and layer thickness. The company suggested default building parameters with a layer thickness of 50 μm is used in this study.

Table 2: Mechanical specifications of Arcam Ti6Al4V ELI

Yield Strength	Ultimate Tensile Strength	Rockwell Hardness	Elongation	Area Reduction	Elastic Modulus
930 MPa	970 MPa	32 HRC	16%	50%	120 GPa

2.2 Chiral cellular structures

The unit cell and topology parameters of chiral hexagonal structure is shown in Figure 1 consists of equal sized nodes or cylinders joined by the ligaments, or ribs, or walls of equal length L . The outer radius of nodes are denoted by r , and the auxeticity is provided by the wrapping of the ligaments around the nodes. The extrusion length of the chiral cell is denoted by e . In the study of Prall and Lakes, nodes were considered rigid structures when obtaining negative Poisson's ratio [2]. The ligaments are connected to the nodes tangentially. However, in this design 0.5 mm fillets, f are used in the tangential constraints to prevent stress concentration. The angle of β and θ are the topology parameters, can be calculated using Equation 1, which describes the configuration of assembly and orientation of ligaments respects to the line between the center of nodes [2, 5]. Chiral geometry is significantly dominated by $\cos \beta$, and according to the studies of Spadoni et al. [12] about chiral structure filled truss-core aerofoils, the mechanical performance of the chiral structure is affected by L/R .

$$\sin \beta = \frac{2r}{R}, \tan \beta = \frac{2r}{L}, \sin \theta = \frac{R/2}{R}, \cos \beta = \frac{L}{R} \quad (1)$$

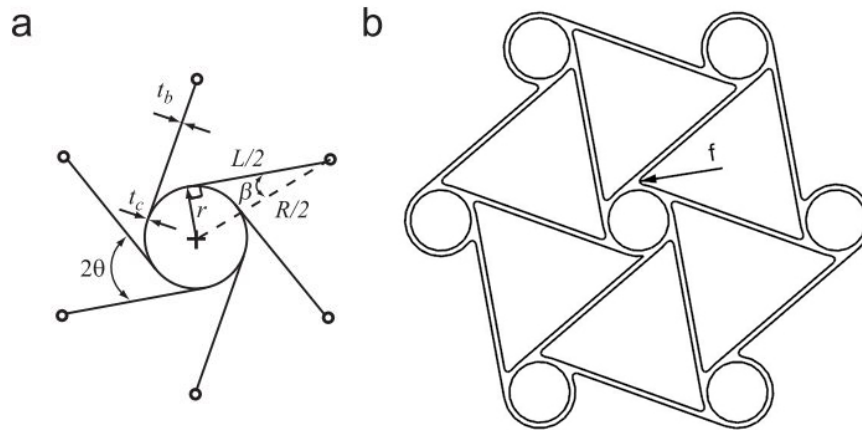


Figure 1: Geometry of a hexagonal chiral lattice: (a) topology parameters and (b) unit cell

Dimensions of the chiral unit cell are given in Table 3. It is also seen from Figure 1 that there are two thickness parameters, t_c denotes the thickness of the nodes, and t_b defines the ligament thickness. The main reason of this difference is the production method because commercially offered metal based honeycomb structures are continuously produced from an aluminium sheet by the help of cutting and bending metal rolls, and adhesion or welding of the spare plates [8]. However, the same thicknesses of nodes and ligaments can be obtained using additive manufacturing.

Table 3: Dimensions of the unit chiral cell.

R	L	r	t_b	t_c	f	e
28.77 mm	26.81 mm	5.22 mm	0.8 mm	0.8 mm	0.5 mm	16 mm

2.3 Mechanical Characterization

To understand the mechanical behaviour and characterize EBM printed parts tensile tests are conducted according to ASTM E8 with a velocity of 0.45 mm/min. Each test specimens are produced in two different directions, 0° and 90° due to characteristic anisotropic behaviour of EBM printed parts. Chiral lattice cells are produced laterally on the flatwise direction to prevent the difficulty of supports removal process and obtain higher mechanical performance in the edgewise direction. In all tests, MTS 810 Material Test System (250 max payload) is used with MTS 647 Hydraulic Wedge Grip, and MTS 634.31F-24 extensometer is used in the tensile tests. Moreover, an additional fixture is designed and produced for the chiral lattices compression tests. For the exhibition of auxeticity two upper and lower nodes supported with two cylindrical pins and bearings to free the movement of the unit chiral cell upper and lower nodes on the lateral direction and rotation on the edgewise direction.

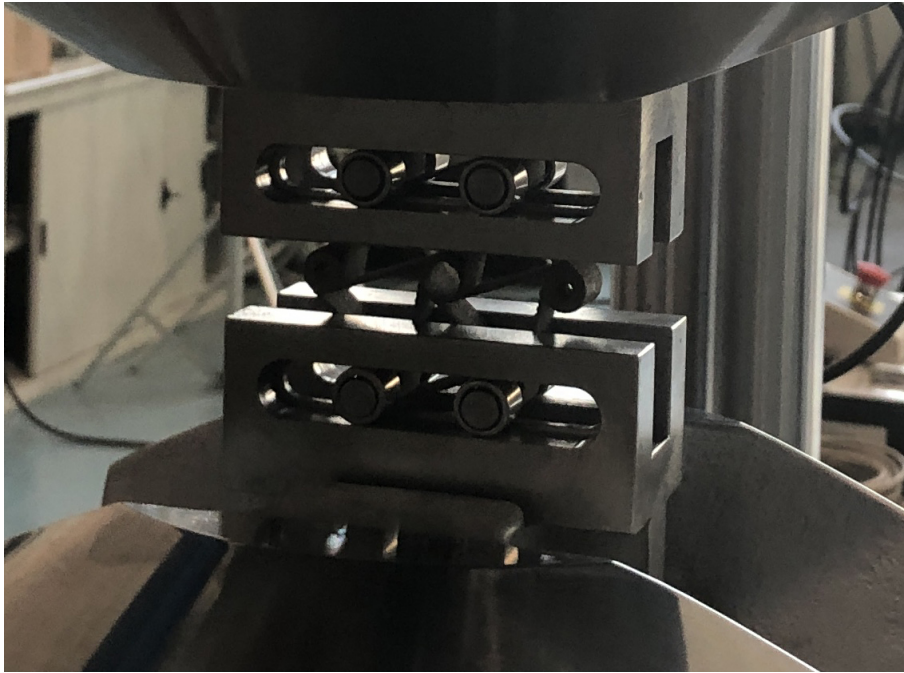


Figure 2: Fixture for chiral lattice compression

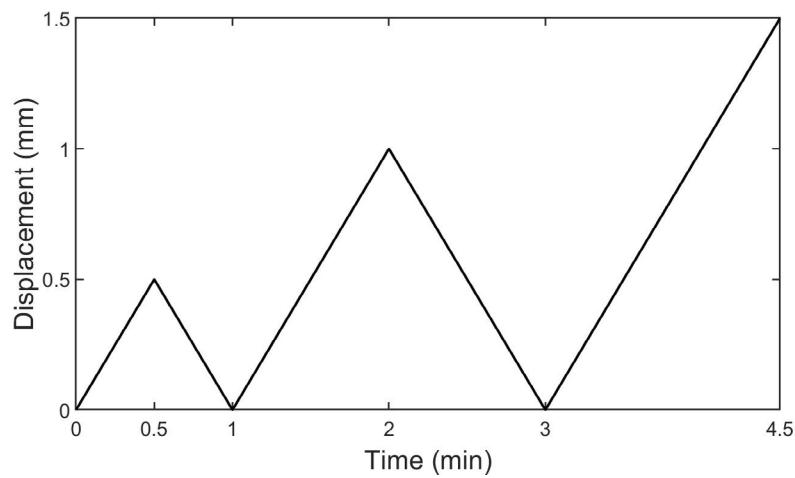


Figure 3: Compressive load profile for chiral lattices

2.4 Numerical Analysis

A three steps compressive load profile analysis of the chiral hexagonal unit cell is carried out by implicit finite element models developed using the commercial code ABAQUS 2018. The elements used for the numeric analysis are C3D20R, quadratic brick element, with reduced integration (2x2x2 integration points). The model consists of 47628 elements with an average aspect ratio of 1.70. The finite element simulation is conducted on a computer with 16 cores

and 24 GB of RAM, and the wall clock time for the simulation is 22 hours. The deformation of chiral structures are estimated using a linear material by a geometric stiffening and finite strain elements including non-linear analysis. The equilibrium is computed by the implicit Newton-Raphson method, with a fixed step of $1.661e-3$. The constituent material is considered linearly elastic, and onset of the plastic deformation is specified with the onset of the yields stress of EBM printed Ti6Al4V. Continuum distributing couplings are used in two upper and lower nodes to provide simulation of the rigid pin and bearing mechanism. The inner surface of the upper and lower nodes become rigid surface and connected to the single nodes in the middle of the centre line of the node where boundary conditions are applied. Additionally, one node is created to measure displacement and load which is connected to the upper nodes with equation constraint. For the boundary conditions, every upper and lower nodes of unit chiral lattice can rotate on the edgewise direction, one of the upper nodes freed on Y and X directions, and the other is freed on the only X direction as it seen in Figure 4. Additionally, for the lower nodes, one of them is fixed and other can move only in the lateral direction.

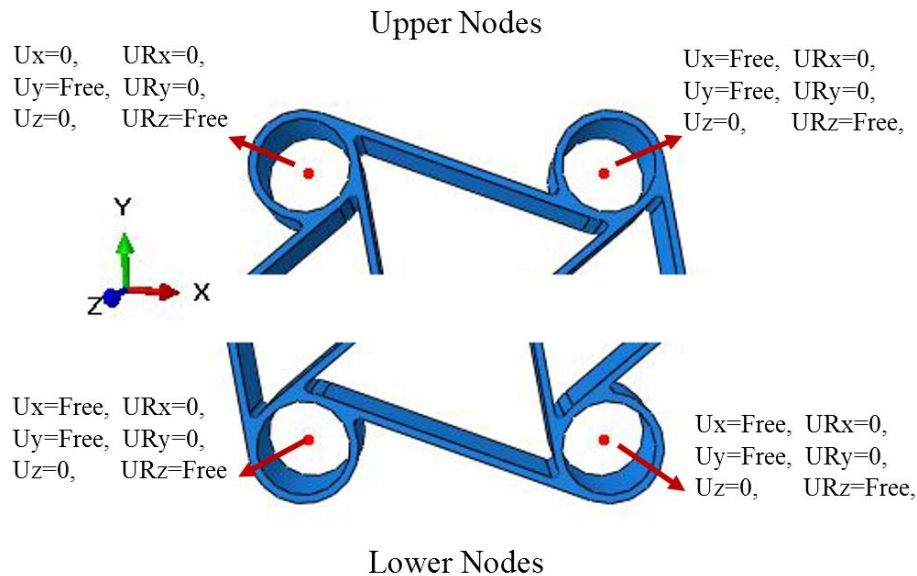


Figure 4: Boundary conditions for chiral unit lattice cell

3 RESULTS

Tensile specimens were produced in the vertical and horizontal direction with Ti6Al4V. The tests were conducted according to ASTM E8. For each direction, five specimens were tested in the as-built conditions. Before the testings, sandblasting was applied to all the specimens to reduce the surface roughness. The average Ra value of the 0-degree and 90-degree specimens $6.74 \mu\text{m}$ and $14.12 \mu\text{m}$, respectively.

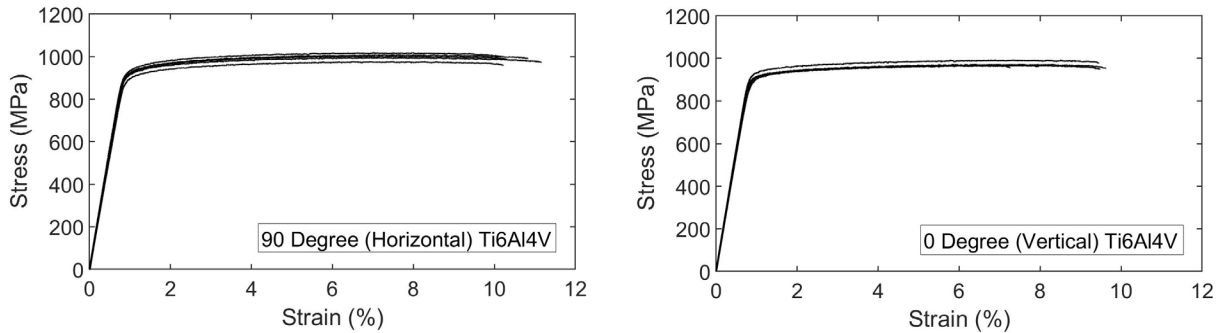


Figure 5: Stress-strain graphs for 0 and 90-degree orientations build specimens

The resulting engineering stress-strain data can be seen in Figure 5. As a result of the investigation the tensile results, Young's moduli that measured have no significant difference according to angular orientation with a value of 110 GPa. The yield stress and ultimate tensile strength values are $922 \pm 2\%$ and $1001 \pm 2.3\%$ for 0-degree orientation production, and $917 \pm 1.9\%$ and $974.7 \pm 1.8\%$ for 90-degree orientation builds, respectively. It is obviously seen from the results the build direction is not a dominating factor for Young's modulus, yields stress and ultimate tensile strength, however considering breaking strain, 0° build exhibits $10.65 \pm 0.58\%$ as the highest value compared to the 90 degree of $8.83 \pm 1.65\%$. As it seen from Table 2, proposed mechanical properties are better than the experimental results. This situation can be explained by the lack of fusion problems caused by EBM production method and material inhomogeneity. As a result of the tensile study, it is understood that Ti4Al6V productions with EBM technology show isotropic elasticity but anisotropic plasticity. In addition, according to variations, 0° build shows consistent mechanical performance comparing the other production degree, this is also the reason of chiral cells were produced where their flatwise direction is parallel to the building plate. Consequently, as a result of experimental studies, inputs for the constitutive equation is obtained, calibrated and imported to FEM codes to represent the behaviour of the material. In the FEM analysis, isotropic elasticity and plasticity were deployed to measure the deformation limit of chiral unit cell without experiencing permanent deformations, degradation or failures. Different boundary condition studies have been conducted, and the change in the boundary conditions increased divergence from the experimental results. As a result of the chiral compressive load tests and FEM analysis, Figure 6 is obtained. In the first two cycles which have 0.5 and 1 mm displacement limits, no permanent deformations were observed. However, in the last cycle having a displacement limit of 1.5 mm, plastic deformation was observed under the compressive load of 1790 N and 1.312 mm displacement.

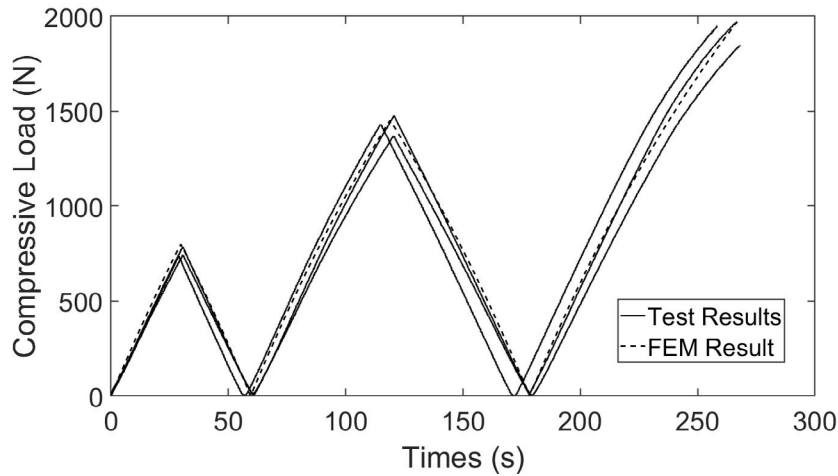


Figure 6: Compressive load profile experimental and FEM results for chiral unit cells

4 CONCLUSIONS

The result of the material characterization of EBM printed Ti6Al4V can be summarized as isotropic elasticity and anisotropic plasticity. In 0° and 90° building orientation, 0° build showed the consistent and better results with the average 10.65% breaking strain value, and 90° showed lower breaking strain which is not preferable for compression applications. Furthermore, chiral lattice cells showed similar reactions under compressive load profile with slight differences which was caused by the displacement control of the testing machine. As a result of compressive load profile, the unit chiral lattice cells have permanent failures under the compressive loads greater than 1790 N in the last cycle of load profile with a displacement of 1.312 mm. In addition, the FEM model including isotropic elasticity and plasticity were validated with the experimental results.

REFERENCES

- [1] Evans, K. E. and Nkansah, I. J. and Hutchinson, I. J. and Rogers, S. C. Molecular network design. *Nature* (1991) **353(6340)**:124–124.
- [2] Prall, D. and Lakes, R. S. Properties of a chiral honeycomb with a Poisson's ratio of $\tilde{\nu} \approx 1$. *International Journal of Mechanical Sciences* (1997) **39(3)**:305–314.
- [3] Spadoni, A. and Ruzzene, M. and Scarpa, F. Dynamic Response of Chiral Truss-core Assemblies. *Journal of Intelligent Material Systems and Structures* (2006) **17(11)**:941–952.
- [4] Zhu, Y., Wang, Z. and Poh, L. H. Auxetic hexachiral structures with wavy ligaments for large elasto-plastic deformation. *Smart Materials and Structures* (2018) **27(5)**:0555001.

- [5] Spadoni, A. and Ruzzene, M. and Scarpa, F. Global and local linear buckling behavior of a chiral cellular structure. *Physica status solidi (b)* (2005) **242(3)**:695–709.
- [6] Bettini, P., Airoidi, A., Sala, G., Landro, L. D., Ruzzene, ., and Spadoni, A. Composite chiral structures for morphing airfoils: Numerical analyses and development of a manufacturing process. *Composites Part B: Engineering* (2010) **41(2)**:133–147.
- [7] Airoidi, A., Crespi, M., Quaranti, G. and Sala, G. Design of a Morphing Airfoil with Composite Chiral Structure. *Journal of Aircraft* (2012) **49(4)**:1008–1019.
- [8] Gibson, L. J. and Ashby, M. F. Cellular Solids: Structure and Properties. (*Cambridge Solid State Science Series*) (1997) **2nd ed.**
- [9] Heinl, P. and Rottmair, A. and Körner, C. and Singer, R. F. Cellular titanium by selective electron beam melting. *Material a Design* (2007) **9(5)**:360–364.
- [10] Arcam AB, (n.d.). Arcam Ti6Al4V Titanium Alloy [Brochure] MÅlndal, Sweden. Retrieved from <http://www.arcam.com/wp-content/uploads/Arcam-Ti6Al4V-Titanium-Alloy.pdf> (Last access 25/06/2019).
- [11] Heinl, P., Rottmair, A., Korner, C. and Singer, R. F. Cellular Titanium by Selective Electron Beam Melting. *Advanced Engineering Materials* (2007) **9(5)**:360–364.
- [12] Spadoni, A. and Ruzzene, M. Numerical and experimental analysis of the static compliance of chiral truss-core airfoils. *Mechanics of Materials and Structures* (2007) **5(2)**:965–981.

PARAMETRIC STUDY IN CO-EXTRUSION-BASED ADDITIVE MANUFACTURING OF CONTINUOUS FIBER-REINFORCED PLASTIC COMPOSITES

Sim-AM 2019

HANNY ALBRECHT¹, CHETHAN SAVANDAIAH^{*,2}, ALEXANDER LEPSCHI²,
BERNHARD LÖW-BASELLI¹, AND ANDREAS HAIDER²

¹Institute of Polymer Extrusion and Compounding
Johannes Kepler University
Altenberger Strasse 69, 4040 Linz, Austria
e-mail: hanny.albrecht@jku.at, web page: <https://www.jku.at/ipeec>

^{*, 2}Wood K Plus GmbH
Biobased Composites & Processes
Altenberger Strasse 69, 4040 Linz, Austria
e-mail: c.savandaiah@wood-kplus.at, web page: <https://www.wood-kplus.at>

Keywords: Additive manufacturing, Continuous carbon fiber, Numerical simulation, Composite co-extrusion

Abstract

The main objective of this research is to investigate the newly designed geometry and process parameters in a dual matrix composite filament co-extrusion technology (CFC), a co-extrusion of continuous carbon fiber pre-impregnated with thermoset (1.5K) also known as composite carbon fiber (CCF) filament with a special binder thermoplastic filament. Accordingly, non-isothermal fluid flow and particle tracking analysis were employed in order to examine the melt flow dynamics. In addition, critical parameters like pressure drop, velocity, shear stress, residence time, and swelling/shrinkage ratio were evaluated. In particular, the computational fluid dynamics (CFD) simulations indicates distress in the conventional die design, recirculation and stagnation of melt flow in the dead zones causing longer melt residence leading to the thermal degradation of thermoplastic material. Furthermore, a new print head was designed to expedite the solution for the possible flow instabilities that may lead to a disparity in the material and mechanical properties, a side-fed mandrel die was used as a melt distributor. Consequently, the side-fed mandrel die ensured a homogeneous melt distribution inside the CFC print head, particularly at the die exit.

1 INTRODUCTION

The advancement in Additive manufacturing (AM) has catered the need of the lightweight design industries like automotive and aerospace, where a high strength to weight ratio is a crucial aspect, as an alternative manufacturing method to produce high-performance composite materials [1]. Specifically, in the field of fused filament fabrication (FFF), the different processing methods have evolved into the industrial-grade application such as big area additive

manufacturing, composite FFF and the newly developed CFC.

The advanced CFC method involves the inclusion of endless carbon fiber reinforcement into the molten thermoplastic polymer; the synergy of high strength to weight ratio of endless carbon fiber and the ease of processing of thermoplastic is accomplished, which is an essential property of high-performance lightweight materials. Furthermore, with design optimization, the properties of the final printed part can be improved, whereby the modulus and strength of the material may be improved up to 4 to 6 times [1]. Moreover, in order to elevate the need for high strength to weight ratio and defect free printed composite part, a new print head design based on the 1st generation CFC print head is being considered. This is achieved by identifying the critical issues associated with the current design and addressing them in newly designed side-fed mandrel print head. Furthermore, the side-fed mandrel die is being used in the extrusion industry for decades as a melt distributor is also beneficial for the CFC print head, the die can distribute the polymer melt uniformly through the melting chamber and eliminate recirculation flow problem observed in the 1st generation CFC.

Furthermore, Bellini et al., Ramanath et al., and Turner et al., [2-4] had discussed about several models used for calculating pressure and temperature distribution of neat filament without fiber inclusion in the conventional print head.

In the present work, authors performed CFD simulation on both, 1st generation and the newly designed CFC print head, and investigated the critical parameters such as pressure drop, velocity shear stress, residence time, and swelling/shrinkage ratio, to mitigate the understanding of the CFC printing process.

2 PRINTING PROCESS

A straight extrusion flow model combined with heat transfer is assumed due to the first-stage process of the CFC resembles conventional extrusion-based additive manufacturing. Furthermore, the melt flow process with CCF filament is analogous to coating process in a pressure-type die. The 1st generation CFC and modified CFC print head are illustrated in figure 1 (a) and (b), respectively.

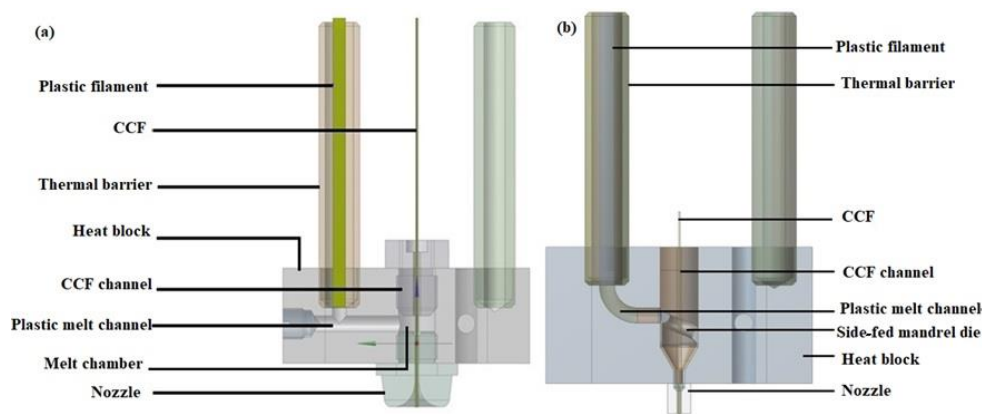


Figure 1: Schematics of the print heads, (a) 1st generation CFC print head, (b) Modified CFC print head with side-fed mandrel die

In Figure 1 (a) and Figure 1 (b), a thermoplastic filament with 1.75 mm diameter is fed through the lateral channel covered by a thermal barrier, which restricts the high gradient thermal variation in the plastic filament to ensure the solid state before entering the melting channel. In the melting channel, the filament is being heated into a semi-viscous state. Meanwhile, CCF filament is being fed through the CCF channel and goes through the inner bore of the fiber inlet. Herein, as the CCF enters the inner zone of the melt chamber it is coated with the molten thermoplastic polymer and subsequently, the dual matrix composite is extruded through nozzle outlet and is deposited on a print bed.

3 MATERIAL AND METHODOLOGY

3.1 Material

In this study, the most common printing material Polylactide (PLA) polymer was used, PLA grade REVODE190 was purchased from Zhejiang Hisun Biomaterials Co., Ltd. The rheological characterization of the PLA was performed in Anton Paar MCR-502; a plate-plate methodology was used to determine the viscosity, storage- and loss modulus. The experiments were performed at two temperatures, 190 °C and 210 °C. The measurement data with its fitting are plotted in Figure 2 (a) and Figure 2 (b), and the model parameters are listed in Table 1 and Table 2. The CCF is a 1.5k grade carbon-fiber tow pre-impregnated with a thermoset resin, has an effective diameter of 0.37 mm.

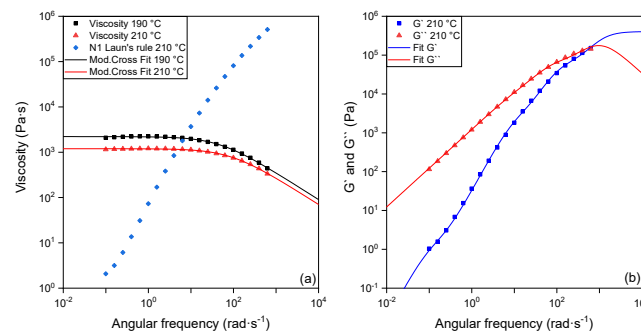


Figure 2: (a) Shear viscosity of PLA at 190 °C and 210 °C fitted with the modified Cross model, first normal stress difference N_1 is calculated with Laun's rule [5]; (b) Experimental G' and G'' of PLA sample obtained at 210°C.

Table 1: K-BKZ model parameters for PLA at $T = 210^\circ\text{C}$ ($\alpha = 8.78$, $\beta = 0.74$, $\theta = 0$, $\bar{\lambda} = 1.94$ s) and Arrhenius approximation law parameter ($\alpha = 0.03$, $T_0 = 483.15$)

k	λ_k [s]	a_k [Pa]
1	0.001	3.44E+05
2	0.01	6.07E+04
3	0.1	2.27E+03
4	1	1.15E+01
5	10	1.12E-04
6	100	2.31E-01

Table 2: Modified Cross model parameters for PLA at $T = 210^\circ\text{C}$ and other material constants

Parameter	Unit	Value
η_0	Pa.s	1194.31
λ	s	0.011
m	-	0.597
α	K^{-1}	0.031
T_0	K	483.15
ρ_m	kg/m^3	1096.51
κ	$\text{W}/\text{m K}$	0.13
C_p	$\text{J}/(\text{kg K})$	2237

3.2 Governing equations

Steady, creeping, incompressible non-isothermal flow of polymer melts inside the heat block is considered for the purpose of computational fluid dynamic simulations. In this study, two different constitutive equations for defining the extra stress tensor τ are proposed. The inelastic viscous stress component τ_s , in which the shear-rate dependence viscosity is represented by a modified Cross model:

$$\eta(\dot{\gamma}) = \frac{\eta_0}{(1 + \lambda\dot{\gamma})^m} \quad (1)$$

Where η_0 is the zero shear viscosity (Pa.s), λ is a natural time (s), $\dot{\gamma}$ is the shear rate which is a second invariant of the rate deformation tensor (s^{-1}), m is the Cross-law index. In addition, the Kaye – Bernstein Kearsley Zapas (K-BKZ) [6] is applied for the viscoelastic extra-stress τ_p and the given equation as follows:

$$\tau_p = \frac{1}{1-\theta} \int_{-\infty}^t \sum_{k=1}^N \frac{a_k}{\lambda_k} \exp\left(-\frac{t-t'}{\lambda_k}\right) \left(\frac{\alpha}{(\alpha-3) + \beta I_{C^{-1}} + (1-\beta)I_C} \right) [C_t^{-1}(t') + \theta C_t(t')] dt' \quad (2)$$

where a_k and λ_k are the relaxation modulus and relaxation time for mode k , t is the current time, N is the number of relaxation modes, α and β are non-linear material constants, θ is a scalar parameter that controls the ratio of the normal stress differences, I_c and I_c^{-1} are the first invariants of the Cauchy-Green strain tensor C_t and its inverse C_t^{-1} , the Finger strain tensor.

The temperature shift factor examined in this study is given by the approximate Arrhenius law:

$$a_T = \exp(-\alpha(T - T_0)) \quad (3)$$

Where α is the material coefficient (K^{-1}), T_0 is the reference temperature (K). The shear thinning behavior and melt temperature observed in thermoplastic material used in 3D-printing has a direct influence on the pressure drop across the system [4]. Furthermore, the melt temperature is one of the critical parameters for the process, since it increases due to viscous dissipation caused by the shearing effect at the nozzle [3]. The viscosity of the melt changes not only with the shear rate but also with temperature, which leads to the alteration of the shape of the dual

matrix extrudate. Moreover, to impede the material degradation due to high temperature rise and cause decline in mechanical properties, herein, numerical simulation is being applied to optimize the CFC processing conditions.

4 CFD SIMULATION

Numerical simulations were carried out using ANSYS Polyflow and Fluent software. A three-dimensional generalized Newtonian fluid flow analysis was conducted, firstly, the entire extruder geometry was considered, and then only on nozzle domain. A simplification was applied in nozzle geometry; an axisymmetric two-dimensional analysis was performed. Moreover, all analyses are a coupled problem of melt flow and heat transfer.

4.1 Boundary conditions and processing parameters

During the extrusion of the thermoplastic filament, plug flow is assumed at the entrance of the melting chamber due to the solid state of the filament at that region. In order to avoid clogging of the material, it should be taken into consideration that the plastic filament has a slower feed rate than the reinforcing fiber. In this analysis, plastic feed rate varies between 6 – 8% of reinforcing fiber feed that varies from 60 mm/min up to 1500 mm/min. The entry temperature at the melting chamber is calculated from steady thermal analysis, where only the energy equation is being solved. As for the two-dimensional nozzle model, a fully developed velocity profile corresponding to a given flow rate along the inflow boundary and a uniform polymer temperature as in the nozzle wall is being imposed. Since the reinforced composite fiber is continuous and rather stiff, hence it is assumed that it acts like a moving solid, where the tangential velocity is imposed with the value of fiber feed rate. Non-slip boundary condition with all velocity components being set to zero and fixed temperature are imposed along the wall. At the nozzle exit region a constant pressure outlet boundary conditions are applied. The air temperature at the entrance and exit was assumed to be the same as ambient temperature, 297.15 K. As for the extrudate swell analysis, the computational domain is extended with a free surface region, which has zero stresses and convective cooling boundary condition.

5 RESULTS AND DISCUSSIONS

5.1 Effect of design geometry

Prior to the CFD simulation with modified CFC print head, simulation in 1st generation CFC print head was performed in order to evaluate the flow pattern, pressure drop and melt residence time inside the print head. In Figure 3, the flow of polymer melt through the melt chamber in both, 1st generation CFC print head and modified side-fed CFC print head are illustrated. Evidently, in Figure 3 (a) some stagnation and recirculation of the melt flow in the 1st generation CFC print head were observed, which may result in longer residence time causing material disparities. Moreover, strong recirculation flow forming a secondary vortex was found in the left zone from the primary flow direction. In addition, another recirculation flow region was observed as the melt encountered the drag flow of composite fiber. Furthermore, several simulations were performed for varied fiber feed rates, $U = 60$ mm/min (Low), 900 mm/min (Moderate), and 1500 mm/min (High) in order to investigate the melt flow behavior in the modified CFC print head. As for the plastic filament feed rate, the set-up with 7% of fiber feed

rate was chosen based on the extrudate swell calculation, see section 5.2. In Figure 3 (b), Figure 3(c) and Figure 3(d) show the streamlines of velocity magnitude in the flow domain. The modified CFC print head delivers a flow enhancement, thus the polymer melt conveys smoothly from the melting chamber entrance to the nozzle exit without any appearance of stagnation and recirculation flow. Furthermore, Figure 4 illustrates that the largest gradient of pressure-drop occurred especially in the nozzle part. With the utilization of the new design, a significant reduction of pressure drop is achieved, so that better print resolution can be obtained.

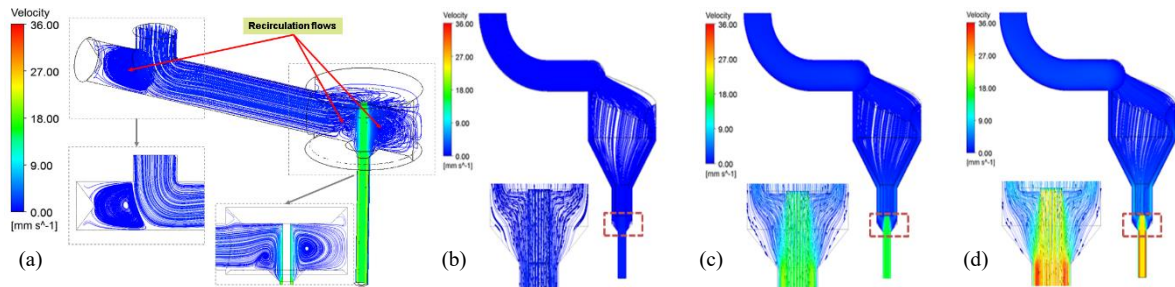


Figure 3: Streamlines of the 1st generation CFC print head and modified side- fed CFC print head; 1st generation, (a) U = 900 mm/min; modified side- fed CFC print head, (b) L/D=5, U = 60 mm/min (c) L/D=5, U = 900 mm/min (d) L/D=5, U = 1500 mm/min

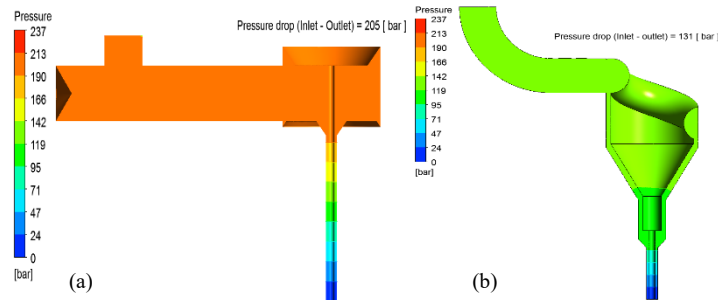


Figure 4: Pressure distribution for extrusion of the PLA at T = 200°C (U = 900 mm/min) (a) 1st generation CFC print head (b) modified side- fed CFC print head

The effect of the flow residence time is directly related to the velocity and local shear rate. Residence time becomes very large along the zone, where the velocity vanishes and has low wall shear rate. A very low residence time could indicate that some amount of the polymer may not have enough time to melt completely and high residence time implies the stagnation of the molten polymer in low local shear rate region. Since residence time distribution inside the geometry is one of the essential matters for quality of the extrudate, particle tracking simulations were conducted by using the mixing module and statistical functions of ANSYS Polystat. In order to investigate the residence time inside the geometry, 5000 particles were released from the inlet section and tracked until the nozzle exit.

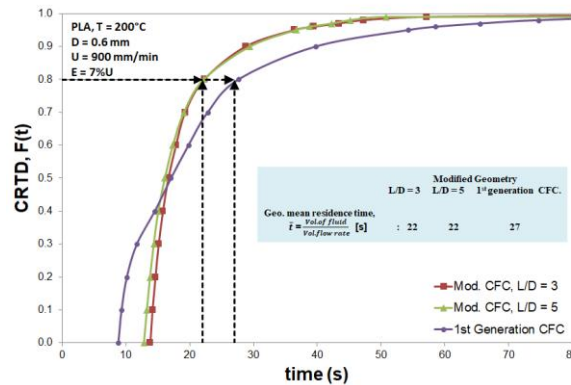


Figure 5: Cumulative residence time distribution function, $F(t)$ of PLA at $T = 200^\circ\text{C}$

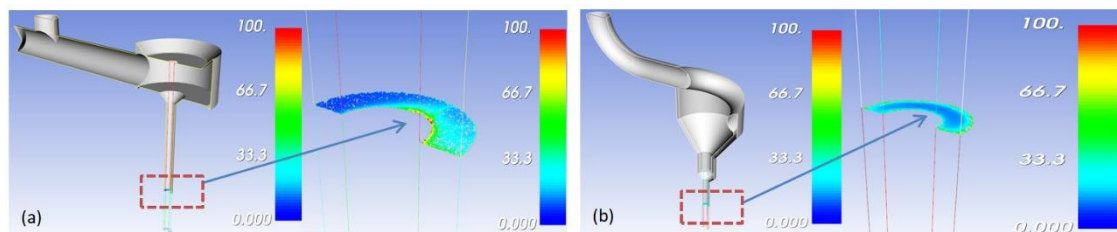


Figure 6: Particle tracking results of PLA at $T = 200^\circ\text{C}$ (fiber feed rate = 900 mm/min) (a) 1st generation CFC print head and (b) modified side-fed CFC print head with $L/D = 5$.

Figure 5, shows the result of the cumulative resident time distribution (CRTD) at the nozzle exit section for modified CFC print head and 1st generation print head. The majority of the particles exits the nozzle for both, modified CFC and 1st generation CFC print head, is relatively short, approximately 80% of the particles exit the nozzle in around 22 s and 27 s, which are analogous to the analytical calculation of geometrical mean residence time. Moreover, for a given feed rate, the average residence time is reduced by 18% for the modified CFC print head. Furthermore, in Figure 6 (a), 1st generation CFC print head, Non-uniform residence time distribution (highlighted) was detected in the exit section due to the unbalanced flow field. In addition, a small fraction of the particles in the core region (between CCF filament and plastic melt) have even longer residence time leading to uneven material coating of the extruded dual matrix composite. Furthermore, the particle tracking simulation infers that the optimization via modified print head yielded better and uniform residence time distribution along the nozzle, thus optimal utilization of the print head was achieved.

5.2 Pressure Drop and Extrudate Shape Prediction

In order to predict and determine the effect of viscoelasticity on the dual matrix extrusion process, besides the viscous model, the viscoelastic numerical simulations using multimode integral K-BKZ are considered. Furthermore, the current work comprising of all parametric studies concerning extrudate swell/shrinkage were performed using nozzles with the same diameter, 0.6 mm and various length to diameter ($L/D = 3$ and 5) ratios. Herein, by solving the model parametrically, a gradually increase in plastic- and fibers feed rates can be achieved, and simultaneously investigate its influence on the quality of extruded dual matrix composite.

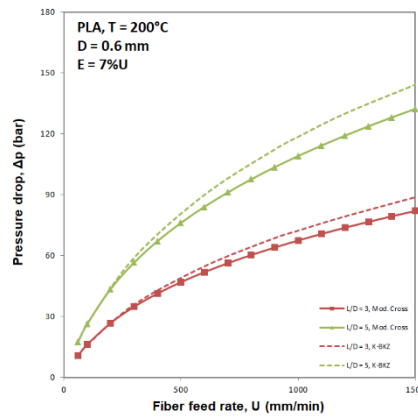


Figure 7: Predicted pressure drop as a function of the fiber feed rate along the nozzle using viscous- (solid symbol lines) and viscoelastic models (dashed lines) for PLA at $T = 200^\circ\text{C}$

The pressure drops shown in Figure 7 were obtained from the resulting nozzle inlet and outlet melt pressure differential for the selected thermoplastic material. As expected, the use of long nozzle influenced in highest pressure drop in both viscous- and viscoelastic model, the predicted pressure drop from viscoelastic model tends to be higher than viscous model due to the extra-stress addition from the elastic part. Furthermore, pressure drop prediction using viscous- and viscoelastic models for the PLA matrix are identical up to fiber feed rate of 300 mm/min, with increase in feed rate difference between the two rheological models becomes significant. In order to have a consistent layer width during the printing and to avoid CCF filament buckling due to excess compression, the melt pressure should not exceed the critical value (Euler's buckling analysis) [7] and needs to be kept to a minimum. Hence the optimal feed rate for both, plastic and fiber, must be carefully selected so that excessive extrusion pressure can be avoided. Since the print resolution is also affected by the ovality of the of dual matrix extrudate, predictions of extrudate swell based on different plastic feed rates were performed. Firstly, the results obtained by modified Cross model shown in Figure 8 (a) infers that the predicted plastic feed rate, $E = 7\%$ configuration seems to be the optimized processing parameter in comparison to $E = 6\%$, shows a shrinkage behavior, whereas, $E = 8\%$ shows more swell ratio.

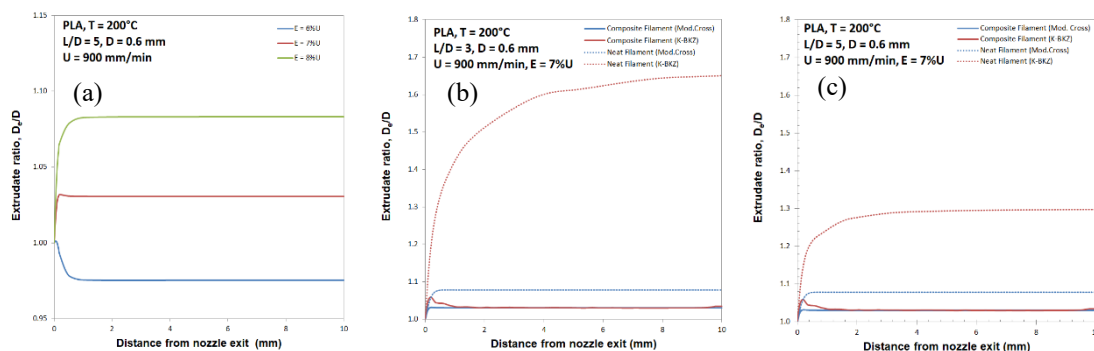


Figure 8: Predicted extrudate profiles, (a) viscous model for dual matrix composite, (b) viscous and viscoelastic models for dual matrix composite and neat filament with $L/D = 3$, (c) viscous and viscoelastic models for dual matrix composite and neat filament with $L/D = 5$

In order to check the effect of nozzle length on extrudate swell for composite and neat filament, simulations with and without the presence of reinforced fiber were conducted. Figure 8 (b) and Figure 8 (c) depicts the effect of rheology on extrudate profiles and their shape variation for two different L/D ratios. Furthermore, simulations show that the size of the extrudate was found to be larger right after exiting nozzle, due to the memory effects. Swelling behavior is well captured in viscoelastic model than the viscous model. Notably, in case of neat filament, the predicted extrudate swell by viscoelastic model is 53% (Nozzle L/D = 3) and 20% (Nozzle L/D = 5) higher than the value predicated by viscous model. Furthermore, with the longer nozzle land lengths, the memory effects declines, thus, promoting flow stability and reducing extrudate swell by 21%, especially for extruding neat filament. In case of composite filament, the extrudate swell predicted by viscoelastic model reaches its maximum value shortly after the nozzle exit, indicating that the memory effects fade away fast, and then flatten due to the drag of the reinforced fiber that restricts the mobility of the matrix. Generally, swell ratio decreases with increasing L/D ratio, but higher melt pressures and wall shear rate must be taken into consideration.

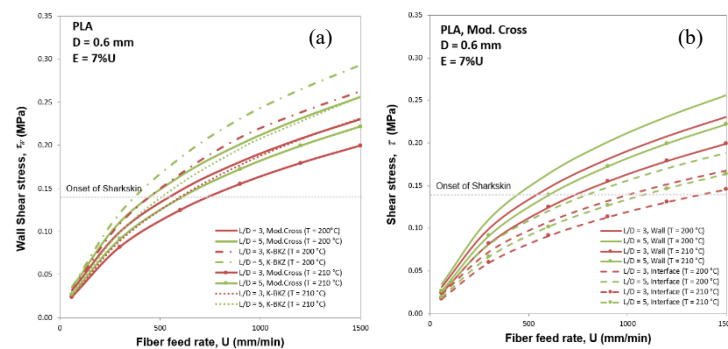


Figure 9: Predicted shear stress at two different temperatures for modified CFC print head with two different L/D ratios, a) predicted shear stress by viscous and viscoelastic model along the nozzle wall, (b) predicted shear stress by viscous model along the nozzle wall and melt-fiber interface

Since it is known that melt instability (Surface roughness and melt fracture) can occur at high shear stress and it may hinder the optical and mechanical properties of the final extruded part. Thus, a proper process parameter setting e.g. feed rate, temperature, are important aspects in limiting the resultant of the high shear stress.

Figure 9 (a) shows the predictions of shear stress for different L/D ratios by viscous and viscoelastic model along the nozzle wall at various fiber feed rates. As can be seen, the effect of rheology and processing condition are significant that extrusion instabilities during part printing could possibly occur, if the shear stress exceeds the critical value. One of the initial extrusion instabilities that may occur due to increasing feed rate is a “sharkskin effect”, a phenomenon where the extrudate loss its surface gloss [8]. According to Kanev et al. and Vlachopoulos et al., the onset of sharkskin for most common polymers occurs at 0.14 to 0.18 MPa, beyond this value melt fracture is observed [9,10]. These critical values may be used as benchmark for regulating the print speed during printing. However, the increase in printing speed may aggravate the probability of occurrence of the extrudate distortion. Furthermore, the predicted shear stress by viscous model, for example, with L/D = 3 nozzle at 200 °C, feed rate up to 550 mm/min in modified CFC print head is a secure range, beyond which the probability

of onset of sharkskin increases. However, if the process demands faster print rate then increasing temperature can be a quick solution in order to minimize shear stress as shown in Figure 9 (b), since the viscosity of molten polymer will become lower.

6 CONCLUSIONS

In the present work, the CFD simulation investigated with straight extrusion flow model with a heat transfer is an accurate characterization for CFC printing process which provides comprehensive data analytics and understanding related to design limitations. Analysis of the CFD simulation results revealed the design flaws in the 1st generation CFC print head, such as longer residence time, high pressure- drop, stagnated and recirculating melt regions. These bottlenecks were addressed in the newly designed, modified CFC print head where a side-fed mandrel is used to iron out the impeding issues, not only reduced the melt residence time, overall pressure drop but also helped in realizing the uniform melt distribution inside the melt chamber and the complete elimination of stagnation and recirculation of fully developed melt. The overall pressure- drop investigated in the modified CFC print head nozzles with different L/D ratios are in sync with the tolerance for the optimal print condition predicated on extrudate swell ratio and shear stress. The optimal printing setting for PLA in the modified CFC print head with nozzle of L/D = 5 is found to be in the range of 600 mm/min to 900 mm/min at 200 °C to 210 °C, respectively. In future, for the further references, the CFD modelling presented in the current research work may be considered as a benchmark for any given thermoplastic materials i.e., neat polymers or filled polymers.

7 ACKNOWLEDGEMENT

The work for the project “3D-CFRP” was supported by the EU funded network M-Era.Net, the BMVIT (Austrian Ministry for Transport, Innovation and Technology), the FFG (Austrian Research Promotion Agency), as well as the RCL (Research Council of Lithuania) and FASIE (Foundation for Assistance to Small Innovative Enterprises, Russia).

REFERENCES

- [1] R. Matsuzaki, M. Ueda, M. Namiki, T.K. Jeong, H. Asahara, K. Horiguchi, T. Nakamura, A. Todoroki, Y. Hirano, *Three-dimensional printing of continuous-fiber composites by in-nozzle impregnation*, Scientific Reports (2016)
- [2] A. Bellini, S. Güçeri, M. Bertoldi, *Liquefier dynamics in fused deposition*, *Journal of Manufacturing Science and Engineering*, Transactions of the ASME (2004) 126:237-246
- [3] H. S. Ramanath, C. K. Chua, K. F. Leong, K. D. Shah, *Melt flow behaviour of poly-ε-caprolactone in fused deposition modelling*, *J Mater Sci: Mater Med* (2008) 19:2541–2550
- [4] B. N. Turner, R. Strong, S. A. Gold, *A review of melt extrusion additive manufacturing processes: I. Process design and modeling*, *Rapid Prototyping Journal* (2014) 20-3:192-204
- [5] H.M. Laun, *Prediction of Elastic Strains of Polymer Melts in Shear and Elongation*, *Journal of Rheology* (1986) 30: 459
- [6] E. Mitsoulis, *50 Years of the K-BKZ Constitutive Relation for Polymers*, ISRN Polymer

- Science (2013): 22
- [7] M. A. Yardimci, S.I. Guceri, *Numerical modeling of fused deposition processing*, Proceedings of the ASME Materials Division IMECE (1995) 69-2:1225-1235
 - [8] J. Molenaar, R.J. Koopmans, C.F.J. Doelder, den, *Onset of the sharkskin phenomenon in polymer extrusion*, Physical Review E (1998) 58-4: 4683-4691
 - [9] D. Kanev, E. Takacs, and J. Vlachopoulos, *Rheological Evaluation and Observations of Extrusion Instabilities of Biodegradable Polyesters*, International Polymer Processing (2007) 22-5: 395-401
 - [10] J. Vlachopoulos J, D. Strutt, *The Role of Rheology in Polymer Extrusion*. New Technology for Extrusion Conference. Italy, Milan (2003): 20-21

PARTICLE FINITE ELEMENT SIMULATION OF EXTRUSION PROCESSES OF FRESH CONCRETE DURING 3D-CONCRETE-PRINTING

J. Reinold*, V.N. Nerella[†], V. Mechtcherine[†], G. Meschke*

* Institute for Structural Mechanics
Ruhr University Bochum (RUB)
Universitätsstraße 150, 44801 Bochum, Germany
Email: janis.reinold@rub.de, web page: <http://www.sd.ruhr-uni-bochum.de>

[†] Institute of Construction Materials
Technische Universität Dresden
Georg-Schumann-Straße 7, 01187 Dresden, Germany
Email: venkatesh_naidu.nerella@tu-dresden.de, web page:
<https://tu-dresden.de/bu/bauingenieurwesen/ifb>

Key words: Particle Finite Element Method, Additive Manufacturing, Concrete Rheology, Fluid Dynamics, Bingham Model, Perzyna Formulation

Abstract. In this work, a numerical model based on the Particle Finite Element Method (PFEM) for the simulation of extrusion-based additive manufacturing of fresh concrete is presented. The balance of momentum and mass are solved with a mixed velocity-pressure formulation in an updated Lagrangian framework. The constitutive law is based on a Bingham model, that is approximated by a Perzyna formulation in order to account for the elastic regime before yielding, which is relevant for the analysis of printed material at rest. The channel flow test, a numerical benchmark for the flow of fresh concrete, is used to validate the model. Finally, 2D examples of extrusion-based additive manufacturing processes of fresh concrete are discussed.

1 INTRODUCTION

The trend of additive manufacturing, initiating in mechanical engineering and related industry sectors, has recently also found rapidly growing interest in the construction industry [1, 2, 3, 4, 5, 6, 7]. Different techniques with high-performance concretes and mortars are under development, that allow for accurate and automated construction of complex concrete structures and components. Most of these manufacturing techniques can be broadly categorized into selective-binding and more common extrusion techniques [8]. 3D-printing with concrete requires precise setting and control of time dependent rheological properties of concrete. At the same time the machine and process parameters must be dynamically adjusted depending on the material and surrounding changes. As a result properties of 3D-printed concrete structures are much more dependent on the manufacturing process as compared to conventional casted structures. There is an ongoing scientific discussion about the mechanical characterization of

printable cement-based materials [3, 9, 10]; which is challenging due to the fact their early age rheological properties often increase multiple orders in few tens of minutes requiring novel test setups. Numerical models can assist to understand the complex interactions between the printing process and the evolution of material and structural properties during the fabrication processes. However, as a matter of the complexity of these processes, their widely varying technical setups, little work has been done in terms of numerical modeling so far. In [11] a time-dependent Mohr-Coulomb failure criterion and linear stress-strain behavior was used to model the early age behavior of fresh concrete in a finite element software in a quasi-static framework. This work was extended in [12] by mechanical modeling of elastic buckling and plastic collapse of additively manufactured wall structures. Nevertheless, to the best of the authors' knowledge, the dynamic effects of the extrusion process with respect to the structural response of already printed material has not been adequately addressed yet.

Accordingly, a numerical framework for the extrusion process in layered extrusion-based additive manufacturing of cementitious materials is presented. As the numerical model needs to account for large deformations and accurate tracking of the free surface, the governing equations including balance of momentum and mass, are solved via the Particle Finite Element Method (PFEM) [13, 14]. In the PFEM the underlying equations are discretized by standard finite elements in an updated Lagrangian formulation, so that nodal positions are updated in each time step. In order to deal with large deformations and element distortions, the domain is frequently re-meshed. Therefore, robust and fast re-meshing using triangular and tetrahedral elements in two and three dimensions, respectively, is fundamental. Due to its reliability and robustness, PFEM is applied in various disciplines, for example, in fluid-structure interaction [15, 16], multiphase flow problems [17, 18], ground excavation [19] or flow of fresh cement suspensions [20].

The established approach for describing the flow of homogenized fresh concrete, which is a non-Newtonian fluid, is based on the Bingham model [21]. In special cases, when complex shear and flow histories with shear thickening and thinning must be analyzed, more advanced constitutive laws such as the Herschel-Bulkley model can be used. All of the fresh concrete rheological models have a certain yield stress, that must be exceeded to initiate viscous flow. The common approach for modeling this behavior is based on regularized models [22], where the regime below the yield stress is approximated with a large viscosity. These models have the advantage that no internal variables must be stored. A drawback of these methods, however, is, that the material never really comes to rest and that stresses of material "at rest" are always viscous. Alternatively, in this work a classical elasto-viscoplastic model is used to approximate the material behavior of fresh concrete. While the stresses below the yield stress are elastic, the stresses during yielding are approximated with an overstress function [23]. Hence, when the material is at rest, stresses can be assessed more accurately, which is important for analyzing initial stress states of 3D-printed concrete structures. Furthermore, in extrusion-based additive manufacturing processes of concrete, the concrete mix is designed, so that the printed material inherits adequate shape-stability properties. Therefore, once the material is extruded, the mechanical behavior is governed by the material response before yielding. Perzyna based flow models have already been successfully applied in flow simulations of geomaterials [24].

The constitutive law followed in this paper is based on an elasto-viscoplastic Perzyna formulation and the underlying governing equations and weak forms in an updated Lagrangian description; see Section 2. Furthermore, in Section 3 the numerical framework with the basics of the Particle Finite Element Method and the discretized set of equations are given. Finally, in Section 4 a numerical benchmark of the channel flow problem and numerical analyses of extrusion processes of additive manufacturing of fresh concrete are discussed.

2 THEORETICAL FRAMEWORK

2.1 Constitutive law

An elastoplastic material model formulated in rate form is employed. Even though hypoelastic models do not necessarily conserve energy in a closed deformation cycle, when the elastic strains are assumed small in comparison to plastic deformations, these models give an adequate approximation of the elastic behavior [26]. Therefore, the deformation rate tensor \mathbf{d} is additively split into elastic and plastic parts as

$$\mathbf{d} = \mathbf{d}_e + \mathbf{d}_p \quad (1)$$

with the subscript e and p denoting the elastic and plastic parts, respectively. The elastic deformation rate is related to the stress rate via

$$\boldsymbol{\tau}^{\nabla J} = \mathbf{C} : (\mathbf{d} - \mathbf{d}_e) \quad (2)$$

with the objective Jaumann stress rate of the Kirchhoff stresses $\boldsymbol{\tau}^{\nabla J}$ and the elasticity tensor \mathbf{C} defined as

$$\mathbf{C} = \kappa \mathbf{I} \otimes \mathbf{I} + 2\mu \left(\mathbf{I} - \frac{1}{3} \mathbf{I} \otimes \mathbf{I} \right) \quad (3)$$

where κ denotes the bulk modulus, μ the shear modulus, $I_{ij} = \delta_{ij}$ the second order identity tensor and $\mathbf{I}_{ijkl} = (\delta_{ik}\delta_{jl} + \delta_{il}\delta_{kj})/2$ the fourth order symmetric identity tensor.

The material is assumed to satisfy a von Mises yield function as

$$\Phi(\boldsymbol{\tau}) = q(\boldsymbol{\tau}) - \sigma_0 \quad (4)$$

in which $q(\boldsymbol{\tau}) = \sqrt{\frac{3}{2} \text{dev}[\boldsymbol{\tau}] : \text{dev}[\boldsymbol{\tau}]}$ is the equivalent stress and σ_0 the yield stress. Furthermore, the plastic flow rule [25] is given by

$$\mathbf{d}_p = \dot{\gamma} \frac{\partial \Phi}{\partial \boldsymbol{\tau}} \quad (5)$$

with the plastic multiplier $\dot{\gamma}$, that must obey the standard Kuhn-Tucker loading/unloading conditions along with the consistency condition, defined for classical rate-independent plasticity as

$$\Phi(\boldsymbol{\tau}) \leq 0, \quad \dot{\gamma} \geq 0, \quad \Phi(\boldsymbol{\tau})\dot{\gamma} = 0 \quad (6)$$

and the consistency condition

$$\dot{\gamma} \dot{\Phi}(\boldsymbol{\tau}) = 0. \quad (7)$$

The Perzyna formulation [23] of the plastic multiplier is given by the introduction of an overstress function by

$$\dot{\gamma} = \frac{\langle f(\boldsymbol{\tau}) \rangle}{\eta} \quad (8)$$

where η is a viscosity parameter, f is the overstress function and " $\langle . \rangle$ " are the McCauley brackets defined as

$$\langle f(\boldsymbol{\tau}) \rangle = \begin{cases} f(\boldsymbol{\tau}) & \text{if } f(\boldsymbol{\tau}) \geq 0, \\ 0 & \text{if } f(\boldsymbol{\tau}) < 0. \end{cases} \quad (9)$$

When the overstress function f is chosen equal to the yield function Φ , a Bingham-like response is gained. Hence, the viscosity parameter η can be related to the fluid viscosity μ by $\eta = 3\mu$.

2.2 Governing equations

When fresh concrete, containing water, cement, aggregates and other admixtures, is considered as a homogenized material, the local form of the balance of momentum, covering the domain Ω in the time interval $(0, T)$, becomes

$$\rho \frac{D\mathbf{v}}{Dt} = \nabla \cdot \boldsymbol{\sigma} + \mathbf{b} \quad \text{in } \Omega \times (0, T) \quad (10)$$

with the density ρ , the velocity \mathbf{v} , the Cauchy stress tensor $\boldsymbol{\sigma}$ and the body forces \mathbf{b} . The boundary conditions on the Neumann $\partial\Omega_N$ and Dirichlet boundary $\partial\Omega_D$ are

$$\boldsymbol{\sigma}(\mathbf{x}, t)\mathbf{n} = \mathbf{t}^p(\mathbf{x}, t) \quad \text{on } \partial\Omega_N \times (0, T), \quad (11)$$

$$\mathbf{v}(\mathbf{x}, t) = \mathbf{v}^p(\mathbf{x}, t) \quad \text{on } \partial\Omega_D \times (0, T) \quad (12)$$

with the normal vector \mathbf{n} and the prescribed tractions $\mathbf{t}^p(\mathbf{x}, t)$ and velocities $\mathbf{v}^p(\mathbf{x}, t)$ on the Neumann and Dirichlet boundary, respectively. Due to incompressibility, that may arise from material behavior in plastic deformation, locking phenomena might occur with a pure velocity formulation. Therefore, the hydrostatic components are separated from the stress field and discretized over an additional equilibrium equation, which is called the balance of mass. The balance of mass is given for nearly incompressible materials by

$$\nabla \cdot \mathbf{v} = \frac{1}{\kappa} \frac{Dp}{Dt} \quad \text{in } \Omega \times (0, T) \quad (13)$$

where p denotes the pressure, assumed as negative in compression, and κ denotes the bulk modulus, which can be interpreted as a penalty parameter of this mixed formulation. By separating the compressibility κ from the elasticity tensor (3), objective stress integration is just performed on the deviatoric parts of the stress tensor.

2.3 Weak form

Integration of equation (10) over the domain Ω in the updated configuration and multiplication with the arbitrary weight function $\delta\mathbf{v}$ belonging to the velocity field leads to the weak form

of the momentum balance equation as

$$\int_{\Omega} \delta \mathbf{v} \left(\rho \frac{D\mathbf{v}}{Dt} - \nabla \cdot \boldsymbol{\sigma} - \mathbf{b} \right) d\Omega = 0. \quad (14)$$

By integration by parts and using the Neumann boundary condition (11) the momentum balance equation is rewritten as

$$\int_{\Omega} \delta \mathbf{v} \rho \frac{D\mathbf{v}}{Dt} d\Omega + \int_{\Omega} \nabla \delta \mathbf{v} : \boldsymbol{\sigma} d\Omega - \int_{\Omega} \delta \mathbf{v} \mathbf{b} d\Omega - \int_{\partial\Omega_N} \delta \mathbf{v} \mathbf{t}^p d\partial\Omega = 0. \quad (15)$$

Similar to the weak form of the balance of momentum, the weak form of the balance of mass is derived as

$$\int_{\Omega} \delta p \nabla \mathbf{v} d\Omega - \int_{\Omega} \delta p \frac{1}{\kappa} \frac{Dp}{Dt} d\Omega = 0 \quad (16)$$

with the weight function δp belonging to the pressure field.

3 NUMERICAL FRAMEWORK

3.1 The particle finite element method

The Particle Finite Element Method (PFEM) is a numerical method for solving partial differential equations in a Lagrangian framework by means of a finite element discretization. In order to deal with large deformations, updated Lagrangian schemes are utilized in combination with remeshing of the finite element mesh [13, 14]. Remeshing is typically performed after a certain number of time steps or when the mesh quality, due to too distorted or poorly shaped elements, becomes too bad. Hence, fast remeshing is essential and can only be guaranteed by using triangular and tetrahedral elements in two or three dimensions, respectively. The remeshing algorithm is based on the so called α -shape method. First, a Delaunay triangulation of a point cloud is formed and second, elements with a circumcircle or circumsphere larger than a threshold value α are removed from the mesh.

3.2 Discretized set of equations

As pointed out in the previous section, in PFEM the underlying weak form of the problem is approximated by means of finite elements. Consequently, the pressure and velocity fields are discretized by standard linear shape functions as

$$\mathbf{v} = \mathbf{N}_v \bar{\mathbf{v}} \quad \mathbf{p} = \mathbf{N}_p \bar{\mathbf{p}} \quad (17)$$

with $\bar{\mathbf{v}}$ and $\bar{\mathbf{p}}$ denoting the nodal values for the velocity and pressure. The shape functions are defined as $\mathbf{N}_v = [N_1 \mathbf{I}, N_2 \mathbf{I}, \dots, N_{\mathcal{N}} \mathbf{I}]$ and $\mathbf{N}_p = [N_1, N_2, \dots, N_{\mathcal{N}}]$ with \mathcal{N} number of nodes per element and the identity matrix \mathbf{I} . By choosing a Galerkin formulation, substitution of the previous approximations into the weak forms Eqs. (14) and (15) and elimination of the nodal values of the weight functions, the discretized form of the system of equations is obtained as

$$\mathbf{r}_v = \mathbf{M}_{vv} \cdot \dot{\bar{\mathbf{v}}} + \mathbf{f}_{int} - \mathbf{f}_{ext} = \mathbf{0}, \quad (18)$$

$$\mathbf{r}_p = \mathbf{G}_{vp}^T \cdot \bar{\mathbf{v}} - \mathbf{K}_{pp} \cdot \dot{\bar{\mathbf{p}}} = \mathbf{0} \quad (19)$$

with

$$\mathbf{f}_{ext} = \int_{\partial\Omega_{n+1}} \mathbf{N}_v^T \mathbf{t}_{n+1}^p d\partial\Omega_{n+1} + \int_{\Omega_{n+1}} \mathbf{N}_v^T \mathbf{b}_{n+1} d\Omega_{n+1}, \quad (20)$$

$$\mathbf{f}_{int} = \int_{\Omega_{n+1}} \mathbf{B}_v^T \boldsymbol{\sigma}_{n+1} d\Omega_{n+1}, \quad \mathbf{M}_{vv} = \int_{\Omega_{n+1}} \mathbf{N}_v^T \rho \mathbf{N}_v d\Omega_{n+1}, \quad (21)$$

$$\mathbf{G}_{vp} = \int_{\Omega_{n+1}} \mathbf{B}_v^T \mathbf{m} \mathbf{N}_p d\Omega_{n+1}, \quad \mathbf{K}_{pp} = \int_{\Omega_{n+1}} \mathbf{N}_p^T 1/\kappa \mathbf{N}_p d\Omega_{n+1} \quad (22)$$

where $\mathbf{m} = [1, 1, 0]^T$ for 2D elements and \mathbf{B}_v denotes the discretized differential operator, that is compatible with the velocity field. The tangent stiffness matrices are derived from linearization of the internal nodal forces Eq. (21) as [16, 26]

$$\mathbf{K}_{mat,vv} = \int_{\Omega_{n+1}} \mathbf{B}_v^T \Delta t \mathbf{C}_{n+1}^{\sigma,T} \mathbf{B}_v d\Omega_{n+1}, \quad (23)$$

$$\mathbf{K}_{geo,vv} = \int_{\Omega_{n+1}} \mathbf{G}_v^T \Delta t [\boldsymbol{\sigma}_{n+1}] \mathbf{G}_v d\Omega_{n+1} \quad (24)$$

with the incremental size of a time step Δt and the tangent constitutive operator $\mathbf{C}_{n+1}^{\sigma,T}$ in terms of the Truesdell rate expressed in the updated configuration. The Truesdell tangent modulus of the Cauchy stresses is related to the Jaumann tangent modulus of the Kirchhoff stresses as $\mathbf{C}_{n+1}^{\sigma,T} = J^{-1} \mathbf{C}_{n+1}^{\tau,J} - \mathbf{C}'$ with the determinant of the deformation gradient J and $C'_{ijkl} = \frac{1}{2}(\delta_{ik}\sigma_{jl} + \delta_{il}\sigma_{jk} + \delta_{jk}\sigma_{il} + \delta_{jl}\sigma_{ik})$ [26]. However, approximating the tangent constitutive operator only by the tangent constitutive operator of the Jaumann rate of the Kirchhoff stresses was found to be sufficient for rapid convergence in all studied examples. The discretized set of equations (18) and (19) can be solved by the introduction of proper time integration schemes. In this study the implicit α -Bossak [28] time integration scheme is used for the velocity field and the backward Euler for the pressure field. Furthermore, as the mixed formulation is discretized by equal order finite elements, the Ladyzhenskaya-Babuska-Brezzi (LBB) condition is violated and a proper stabilization technique must be introduced. To this end, a direct pressure stabilization technique based on the polynomial pressure projection (PPP) is chosen and applied to the balance of mass [27].

4 NUMERICAL APPLICATION

4.1 Benchmark: Channel flow

The channel flow test is a practical test to assess the yield stress of self compacting concrete (SCC). In [29] the experimental procedure is explained as follows: From a bucket 6 l of fresh concrete is slowly poured (over 30 s) at one extreme end of a rectangular channel ($l = 1.2$ m, $w = 0.2$ m, $h = 0.15$ m). After waiting for the stoppage of the fluid (max. 120 s) the final shape of the material can be analyzed and related to the yield stress τ_0 of the material. A numerical benchmark comparison of the channel flow test with a virtual concrete ($\mu = 50$ Pa·s, $\tau_0 = 50$ Pa and $\rho = 2300$ kg/m³) was performed in [30]. The same virtual concrete as in [30] is used

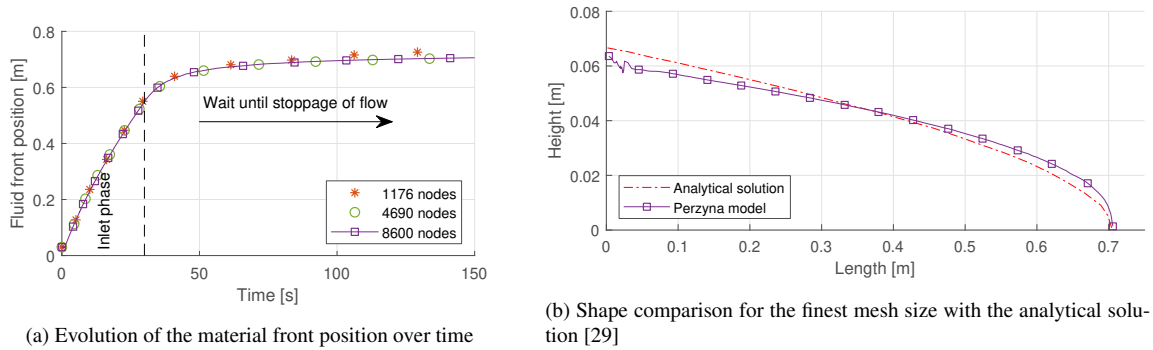


Figure 1: Results for the channel flow test

for benchmark analysis of the proposed numerical model. The simulations were performed in 2D with three different mesh sizes, in order to assess convergence of the numerical model. Moreover, the pouring process of the concrete is modeled by a velocity inlet flow: new nodes (elements) are pushed by a row of fixed nodes into the domain and after a certain number of time steps the fixed nodes are placed to their initial position in height direction and the process restarts with a new set of nodes. This will approximately result in initial element sizes of 0.005, 0.0023 and 0.0016 and 1176, 4690 and 8600 number of nodes when the inlet phase is finished. At all boundary nodes no slip boundary condition are considered.

The results are given in Figure 1a) and b). The flow process stops at around 100 s, as can be observed from the material front over time diagram, see Figure 1a). Furthermore, the final shape of the material is in a good agreement with the analytical solution [29] and the final length varies by 1.01 % from the average value found by different numerical methods in [30]. Differences between the analytical solution and numerical results at the left end of the channel can be explained by simplified stress states in the analytical solution.

4.2 Additive manufacturing of concrete

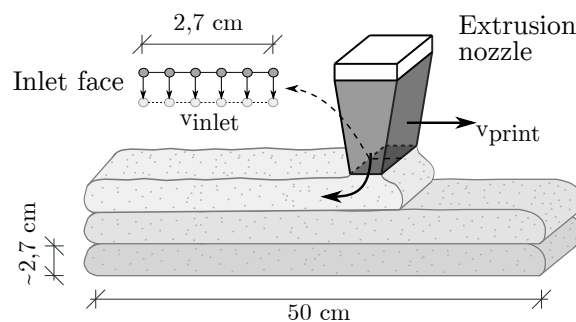


Figure 2: Extrusion-based additive manufacturing of fresh concrete - geometry

In the following, the capability of the proposed numerical model is analyzed by test case scenarios of extrusion-based additive manufacturing of fresh concrete, where three layers of 50 cm length and 2.7 cm height are numerically printed, see Figure 2. The problem is studied in a

2D plain strain framework. The selected results presented in this paper focus on the geometry of the concrete immediately after leaving the nozzle outlet and vertical loads on extruded layers, below the nozzle, due to pressure exerted by vertical concrete extrusion. The concrete flow rate at the nozzle outlet is assumed to be constant. In other words, dynamic variation in the concrete flowrate due to potential pulsations of screw extruder are not considered. Furthermore, the time dependent behavior (structural build-up) of concrete is not considered as the time for extruding three layers is few seconds. All the printing process parameters including nozzle dimensions are obtained from a large-scale 3D-printer developed at the TU Dresden. The inlet flow is approximated with a velocity inlet, see Figure 2. The simulation is performed with three different element sizes 0.27, 0.135 and 0.09 cm with three different sets of material parameters, to reflect different states of structuration of the printed material. The material and simulation parameters are plastic viscosity $\mu = 10, 15, 20 \text{ Pa}\cdot\text{s}$, dynamic yield stress $\tau_0 = 0.5, 0.75, 1 \text{ kPa}$, fresh density $\rho = 2000 \text{ kg/m}^3$, $E = 0.1 \text{ MPa}$, Poisson's ratio $\nu = 0.3$, printing velocity $v_{print} = 0.1 \text{ m/s}$, material flow rate $v_{inlet} = 0.09744 \text{ m/s}$, nozzle-separation distance $\Delta z_{nozzle} = 2.7 \text{ cm}$, $\Delta t = 10^{-4} \text{ s}$ and $t_{max} = 15 \text{ s}$. Furthermore, the yield stress of already printed layers is set to a value of 1 kPa, which serves as material yield stress after extrusion i.e. at rest (static yield stress) and is responsible to prevent the collapse of already printed layers in the simulation process. Note that rheological measurements conducted at TU Dresden with rotational rheometer by following stress growth tests confirm similar static yield stress for printable concretes.

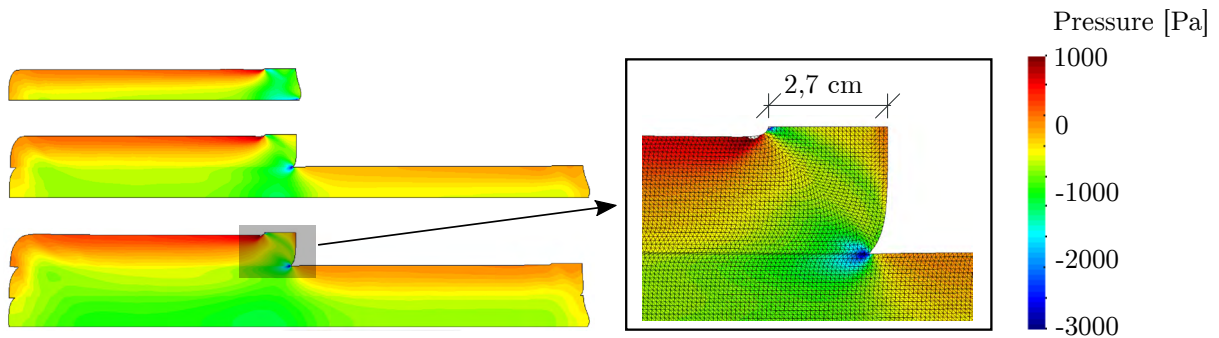
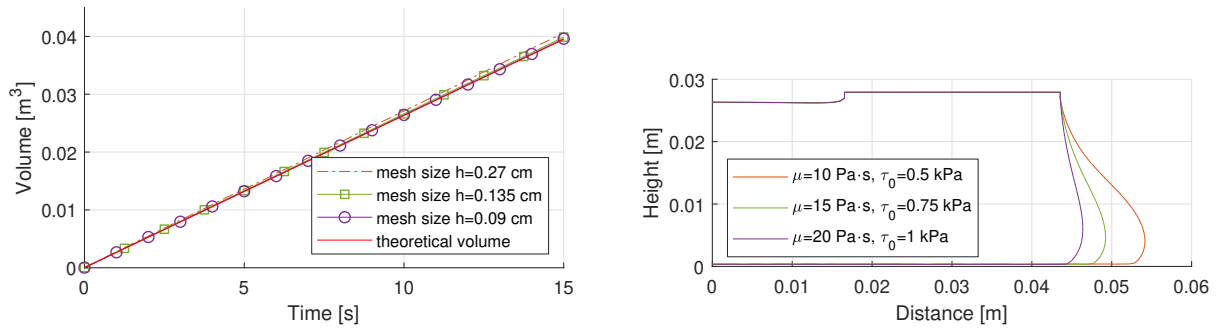


Figure 3: Shape of the printed material with the pressure contours [Pa] for the time instances $t = 2.5, 7.5, 12.5 \text{ s}$ with $\mu = 15 \text{ Pa}\cdot\text{s}$ and $\tau_0 = 0.75 \text{ kPa}$

The printed layers with $\mu = 15 \text{ Pa}\cdot\text{s}$ and $\tau_0 = 0.75 \text{ kPa}$ along with the contour plot of the pressure for the finest mesh size and the time instances $t = 2.5, 7.5, 12.5 \text{ s}$ are given in Figure 3. As can be observed, lower layers are under compression from the simulation inlet (in reality nozzle outlet) flow, while a small region behind the extrusion nozzle is subjected to tension. From the generation of contact or boundary elements, when two bodies get into contact, a certain volume gain is caused by the remeshing procedure in PFEM simulations. Furthermore, due to the numerical formulation, assuming slight compressibility, newly printed material will get compressed, which on the other hand causes a certain volume loss. For analyzing the interaction between these two processes, the evolution of the total volume over time is given in Figure 4a). The final relative volume gain in relation to the theoretical volume evolution is given for all 3



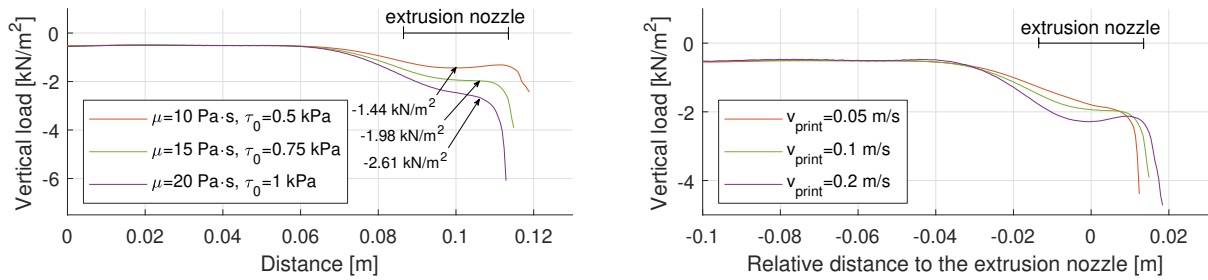
(a) Total evolution of the volume over time for $\mu = 15 \text{ Pa} \cdot \text{s}$ and $\tau_0 = 0.75 \text{ kPa}$

(b) Shape of the printed material for the finest mesh size at the extrusion nozzle for $t = 5 \text{ s}$ (end of the first layer)

Figure 4: Results for the additive manufacturing of concrete study

mesh sizes, starting from the coarsest element size, as 2.78 %, 0.95 % and 0.29 %. Hence, the volume gain caused by contact elements prevails the effect of volume loss from compressibility. This volume gain is particularly critical for the printing simulation of the first layers, because additional volume is simply accumulated in front of the extrusion nozzle, see Figure 4b). As can be concluded from Figure 4b) this effect also increases for materials with lower viscosity and yield stresses, as the resulting layer height is slightly lower for these materials. In this study, the volume gain is less important for upper layers, as the effectively printed layer height is slightly less than 2.7 cm and the extrusion nozzle, however, is lifted up by the total distance of $\Delta z = 2.7 \text{ cm}$, when a new layer is started to be printed. Hence, the distance between the extrusion nozzle and the printing surface increases for upper layers and there is more space for the printed material to flow to.

To study the dynamic impact of the inlet flow, the vertical reaction forces at the boundary nodes are evaluated while printing the first layer. In a post-process these reaction forces are averaged and converted to a distributed load. The results are depicted in Figures 5a) and b), along with the relative distance to the extrusion nozzle. The results can be separated into a purely static (distance $< 0.06 \text{ m}$) and an inlet flow regime (distance $> 0.06 \text{ m}$). For the purely static regime, the vertical load is constant and for all materials almost the same ($\approx 0.51 \text{ kN/m}^2$), which is plausible, since all materials share the same density and body loads. For the inlet flow regime, however, the behavior is more complex. First, right below the extrusion nozzle an increased loading is observed and second a concentrated force at the front of the printed material is found. Regarding the region right below the extrusion nozzle, peak values of 1.44, 1.98 and 2.61 kN/m^2 are observed, see Figure 5a). Therefore, lower layers would need to bear an impact load, that is approximately $1.48/0.51 \approx 3$ - $2.61/0.51 \approx 5$ times larger, depending on the printed material, than the pure static load. The concentrated load at the front of the printed material is caused by a sharp edge and a stress concentration. Additional studies with varying printing speeds v_{print} show, that with larger printing speeds this impact also increases, due to the increased inlet flow rates, see Figure 5b). Hence, it can be concluded, that the printed material should not only bear its self weight, but also temporarily the impact loads from the printing process of upper layers.



(a) Vertical load below the extrusion nozzle for different material parameters (reflecting different states of structuration of the fresh concrete) along the relative distance to the extrusion nozzle

(b) Vertical load below the extrusion nozzle for different printing speeds v_{print} along the relative distance to the extrusion nozzle for a material with $\mu = 15$ Pa·s and $\tau_0 = 0.75$ kPa

Figure 5: Vertical load below the extrusion nozzle along the relative distance to the extrusion nozzle

5 CONCLUSIONS

A numerical model based on the Particle Finite Element Model for the simulation of extrusion processes of additive manufacturing of fresh concrete is presented. The material model is based on a Bingham model and is approximated with an elasto-viscoplastic Perzyna formulation in a hypoelastic rate form. In order to overcome issues arising from the incompressible plastic flow, inherited from the underlying J2 plasticity, a mixed velocity-pressure formulation is chosen for the approximation of the problem. Furthermore, as equal order finite element approximations are used for the discretization of the velocity and pressure fields, the formulation is stabilized by a direct pressure stabilization to treat the LBB condition. Results show, that extrusion processes of additive manufacturing of fresh concrete can effectively be simulated. Volume gain that appears from the remeshing procedure in PFEM is found to be a crucial aspect in the simulation procedure. Furthermore, studies on the reaction forces on the boundary show, that a dynamic impact by the inlet flow appears and that already printed layers need to bear this impact load. The peak value of the impact load depends on the material properties of the printed material and is 3-5 times larger than the pure static load for the studied examples. This analysis also highlights the complex interactions between process and material parameters with the structural response in extrusion-based additive manufacturing processes of concrete. The proposed numerical model indicates, that the whole additive manufacturing process, consisting of extrusion of the fresh concrete as a fluid and ageing like a solid can be performed in a unified way, as the numerical model can easily be extended by an adequate modeling of structural build-up (increase of yield stress and elastic parameters).

REFERENCES

- [1] Khoshnevis, B. Automated construction by contour crafting-related robotics and information technologies. *Autom. Constr.* (2004) **13**:5–19.
- [2] Lim, S., Buswell, R.A., Le, T.T., Austin, S.A., Gibb A.G.F. and Thorpe T. Developments in construction-scale additive manufacturing processes. *Autom. Constr.* (2012) **21**:262–268.
- [3] Bos, F.P., Wolfs, R.J.M., Ahmed, Z.Y. and Salet, T.A.M. Additive manufacturing of con-

- crete in construction: potentials and challenges of 3d concrete printing. *Virtual Phys. Prototyp.* (2016) **11**(3):209–225.
- [4] Wu, P., Wang, J. and Wang X. A critical review of the use of 3-D printing in the construction industry. *Autom. Constr.* (2016) **68**:21–31.
- [5] Wangler, T., Lloret, E., Reiter, L., Hack, N., Gramazio, F., Kohler, M., Bernhard, M., Dillenburger, B., Buchli, J., Roussel, N., and Flatt, R. Digital Concrete: Opportunities and Challenges. *RILEM Tech. Lett.* (2016) **1**:67–75.
- [6] De Schutter, G., Lesage, K., Mechtcherine, V., Nerella, V.N., Habert, G. and Agusti-Juan, I. Vision of 3D printing with concrete — Technical, economic and environmental potentials. *Cem. Concr. Res.* (2018) **112**:25–36.
- [7] Buswell, R.A., Leal de Silva W.R., Jones S.Z. and Dirrenberger J. 3D printing using concrete extrusion: A roadmap for research. *Cem. Concr. Res.* (2018) **112**:37–49.
- [8] Nerella, V.N., Hempel, S. and Mechtcherine, V. Effects of layer-interface properties on mechanical performance of concrete elements produced by extrusion-based 3D-printing. *Constr. Build. Mater.* (2019) **205**:586–601.
- [9] Roussel, N. Rheological requirements for printable concretes. *Cem. Concr. Res.* (2018) **112**:76–85.
- [10] Nerella, V.N., Beigh, M.A.B., Fataei, S. and Mechtcherine V. Strain-based approach for measuring structural build-up of cement pastes in the context of digital construction. *Cem. Concr. Res.* (2019) **115**:530–544.
- [11] Wolfs, R.J.M., Bos F.P., Salet, T.A.M. Early age mechanical behaviour of 3D printed concrete: Numerical modeling and experimental testing. *Cem. Concr. Res.* (2018) **106**:103–116.
- [12] Wolfs, R.J.M. and Suiker, A. Structural failure during extrusion-based 3D printing processes. *Int. J. Adv. Manuf. Technol.* (2019) 1–20.
- [13] Oñate, E., Idelsohn, S.R., Del Pin, F. and Aubray, R. The particle finite element method. An overview *Int. J. Comput. Methods* (2004) **1**(2):267–307.
- [14] Idelsohn, S.R., Oñate, E. and Del Pin, F. The particle finite element method: a powerful tool to solve incompressible flows with free-surfaces and breaking waves *Int. J. Numer. Methods Eng.* (2004) **61**(7):964–989.
- [15] Idelsohn S.R., Marti J., Limache A. and Oñate E. Unified Lagrangian formulation for elastic solids and incompressible fluids: Application to fluid-structure interaction problems via the PFEM. *Comput. Methods Appl. Mech. Eng.* (2008) **197**33:1762–1776.

- [16] Franci A., Oñate E. and Carbonell J.M. Unified Lagrangian formulation for solid and fluid mechanics and FSI problems. *Comput. Methods Appl. Mech. Eng.* (2016) **298**:520–547.
- [17] Idelsohn S.R., Mier-Torrecilla M. and Oñate E. Multi-fluid flows with the Particle Finite Element Method. *Comput. Methods Appl. Mech. Eng.* (2014) **198**:2750–2767.
- [18] Dang, T.S. and Meschke, G. An ALE-PFEM method for the numerical simulation of two-phase mixture flow. *Comput. Methods Appl. Mech. Eng.* (2014) **278**:599–620.
- [19] Carbonell, J.M., Oñate, E. and Suarez, B. Modeling of Ground Excavation with the Particle Finite-Element Method. *J. Eng. Mech.* (2010) **136**(4):455–463.
- [20] Cremonesi M., Ferrara L., Frangi A. and Perego U. Simulation of the flow of fresh cement suspensions by a Lagrangian finite element approach. *J. Non-Newtonian Fluid Mech.* (2010) **165**(23):1555–1563.
- [21] Roussel N. A thixotropy model for fresh fluid concretes: Theory, validation and applications. *Cem. Concr. Res.* (2006) **36**(10):1797–1806.
- [22] Papanastasiou, T.C. Flows of materials with yield *J. Rheol.* (1987) **31**(5):385–404.
- [23] Perzyna, P. Fundamental problems in viscoplasticity *Adv. Appl. Mech.* (1966) **9**:243–377.
- [24] Pastor, M., Stickle, M., Dutto, P. Mira, P., Fernandez-Merodo, J.A., Blanc, T., Sancho Hernando, S. and Benítez A. A viscoplastic approach to the behaviour of fluidized geomaterials with application to fast landslides. *Continuum Mech. Thermodyn.* (2013) **27**(1-2):21–47.
- [25] Simo, J.C. and Hughes T.J.R. *Computational inelasticity*. Springer, (1998)
- [26] Belytschko, T., Liu W.K., Moran, B. and Elkhodadry, K.I. *Nonlinear finite elements for continua and structures. Second edition*. John Wiley & Sons, (2014).
- [27] Dohrmann, C.R. and Bochev, P. A stabilized finite element method for the Stokes problem based on polynomial pressure projections. *Int. J. Numer. Methods Fluids* (2004) **46**:183–201.
- [28] Wood, W. L., Bossak, M. and Zienkiewicz, O. C. An alpha modification of Newmark’s method. *Int. J. Numer. Methods Eng.* (1980) **15**(10):1562–1566.
- [29] Roussel, N. The LCPC BOX: A cheap and simple technique for yield stress measurements of SCC. *Mater. Struct.* (2007) **40**:889–896.
- [30] Roussel N., Gram A., Cremonesi M., Ferrara L., Krenzer K., Mechtcherine V., Shyshko S., Skocec J., Spangenberg J., Svec O., Thrane L.N. and Vasilic K. Numerical simulations of concrete flow: A benchmark comparison. *Cem. Concr. Res.* (2016) **79**:265–271.

POEAM – a method for the Part Orientation Evaluation for Additive Manufacturing

Simon JUNG^{1*}, Sebastian PEETZ², Michael KOCH³

Abstract—In the industrial application of additive manufacturing processes, a significant amount of time and resources is dedicated to the orientation and pre-print setup of the geometry. Steps such as the generation of support structures and the process simulation are among the most time-consuming. For the thorough assessment of an orientation of a given geometry, even more criteria, like print time or surface quality, need to be considered. POEAM proposes a method for an efficient assessment of a set of orientations, by means of well formulated criteria and an early elimination of insufficient orientations. The goal is to narrow the search field, so costly preparation steps will only be performed on orientations that promise a superior end result. Furthermore, POEAM is an automated process, which means it can be performed with minimal human interaction, resulting in an optimum regarding cost-efficiency and evaluation time. The method was applied to a representative geometry and has shown results that confirm the above mentioned advantages.

I. INTRODUCTION

During the Additive Manufacturing (AM) process - especially during the SLM (Selective Laser Melting) process - extensive user experience is required, particularly in preprocessing. As AM becomes more widespread, however, users with a lower level of experience are being addressed in increasing numbers. The lack of detailed process knowledge and experience on the part of the user often leads to incorrect alignment of the components in the machine's building chamber and to incorrectly arranged support structures in the event of overhangs. As a result, AM components cannot be built up to the aspired geometrical precision in the first build process, or the process cannot even be successfully completed. This leads to delays in the process and additional costs when using AM technology. The aim of the described method is to automate the pre-print preparation of a CAD design so that minimal human interaction is required. This will free

the engineer of tedious tasks that can be performed by a machine faster and more efficiently.

POEAM was developed with the manufacturing process of SLM in mind, but the method is not limited to that. With only small adaptations, it can be used for various forms of AM.

In order to take advantage of the proposed method, four user inputs need to be given:

1. The geometry of the part.
2. A search field of orientations.
3. A set of criteria to evaluate the part on.
4. The properties of the printer.

The first point defines the geometric shape of the component. The second point determines the angle of rotation within which the alignment of the component is to be varied in three axes. The third point defines criteria according to which the orientations found are evaluated. The fourth point specifies the AM machine's properties for the process simulation.

As a result, the POEAM method yields the optimal orientation of the produced part in the building chamber of the AM machine, taking into account the specified parameters.

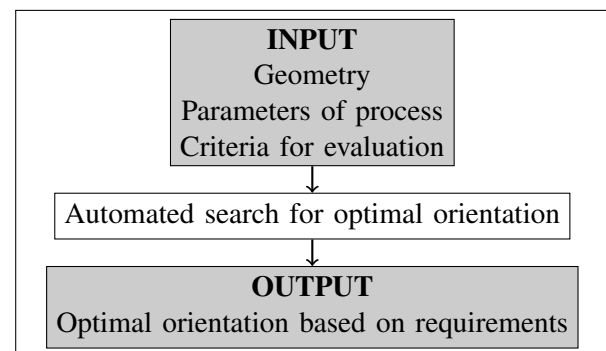


Fig. 1. Workflow Overview

II. SEARCH FIELD DEFINITION

The user-defined search field specifies the range within which the geometry can be rotated to find the optimal orientation. This includes upper/lower angles and rotation increments for the specified rotation axis. Before the actual evaluation of the criteria, this search field can be narrowed by identifying symmetries and equivalent orientations.

¹S. Jung (jung.simon@gmx.net) is with inuTech GmbH, Fürther Straße 212, 90429 Nuremberg, Germany

²S. Peetz (sebastian.peetz@inutech.de) is with inuTech GmbH, Fürther Straße 212, 90429 Nuremberg, Germany

³M. Koch (michael.koch@th-nuernberg.de) is with Faculty of Mechanical Engineering and Building Services Engineering, Nuremberg Tech, Keßlerplatz 12, 90408 Nuremberg, Germany

A. Symmetries

If two orientations show mirror symmetry in a plane perpendicular to the baseplate, only one of the two symmetrical orientations needs to be evaluated. From the AM point-of-view, these two orientations are identical, because a rotation of the part around the z-axis is of no consequence to the printing process.

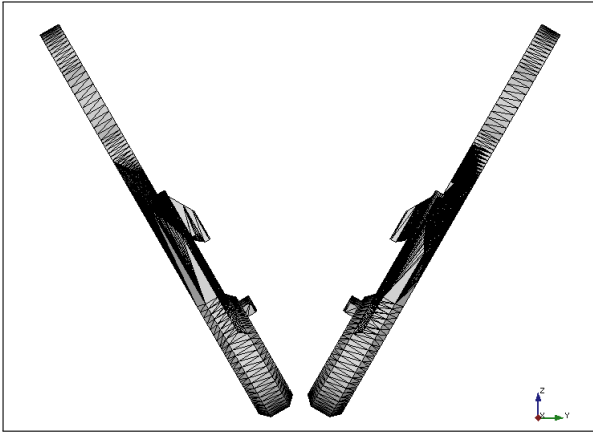


Fig. 2. Two orientations showing symmetry

B. Equivalent Orientations

Two orientations may be equivalent, as in the case of symmetry (see II-A). Another cause for equivalence can be the rotation process itself. Depending on the used method to rotate the initial geometry, two sets of rotations (e.g. around the global x- and y-axes) may result in an identical orientation of the part. This needs to be detected and equivalent orientations need to be excluded from the analysis.

III. CRITERIA DEFINITION

The results generated by variation are evaluated on the basis of a list of criteria. To check the fulfillment of a single criterion, a numerical boundary is required. For each criterion a threshold value range is defined within which a result value is permissible. The fulfillment of a criterion is expressed as a percentage within the defined range. All values below this range are regarded as insufficient (0%) and will be excluded from further analysis. Values above the defined range are accepted as sufficient (100%). Values within the boundaries are scored in relation to their distance from the boundaries edges, with values between 0 and 100%.

This scoring scheme allows for the easy recognition of insufficient orientations (score of 0%) and the rating of sufficient orientations by means of their relative fulfillment.

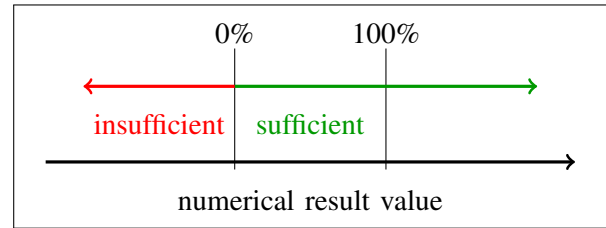


Fig. 3. The scoring scheme

A. List of Criteria

The user needs to define a list of criteria, upon which the orientations can be evaluated. To illustrate the process, the following exemplary criteria are defined:

- The interface area between part and support structure.
- The height of the oriented part.
- The time required to build the component in this orientation.

The list is by no means exhaustive and needs to be extended for a productive application.

B. Weighted Total Score

For each criterion, the orientation is given a partial score between 0 and 100%. Those partial scores are summed up into one numerical value. The partial scores are weighted by the user, giving certain criteria priority over others. This "Weighted Total Score" is used to determine the orientations that have the highest overall fulfillment of the required characteristics. Visualizing the orientations with a high weighted total score in a heatmap shows the formation of clusters.

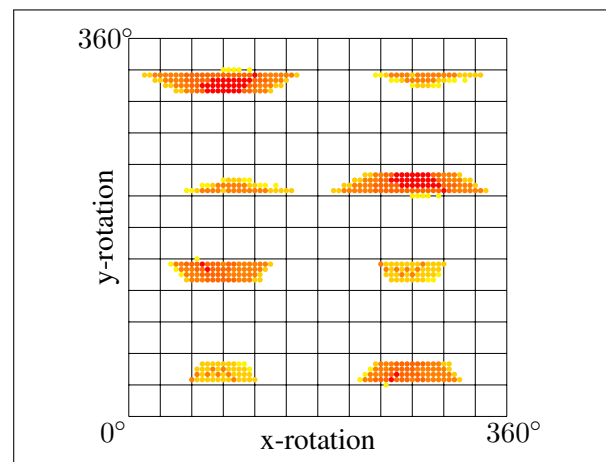


Fig. 4. Heat map of weighted total scores

This indicates regions of orientations with a high criteria fulfillment. Inside those regions a refined search may be advantageous. This is very useful if the results are not yet accurate enough or if the search is carried out in several steps with increasing accuracy.

IV. CRITERIA CHECKING ORDER

A critical step in the procedure is the checking order of the criteria, since the goal is the early exclusion of insufficient orientations. This means, if an orientation can not fulfill a criterion it will be excluded from further analysis. This non-fulfillment needs to be detected early in the analysis, so no resources are wasted on an orientation that will eventually fail to satisfy the requirements. To achieve this, two approaches will be illustrated.

A. Sort by Runtime

The criteria may be sorted by the individual runtime needed to calculate and check a criterion. This results in criteria that are quick to calculate being checked first, whereas time-consuming criteria are checked last.

B. Sort by Previous Exclusion

In contrast to the static order of criteria being sorted by runtime, sorting by previous exclusion changes the order dynamically during the analysis. If an orientation is excluded due to non-fulfillment of a criterion, that criterion will be the one checked first on the next orientation. This is based on the assumption, that orientations that are similarly oriented will yield similar results and are therefore likely to (not) fulfill criteria to a similar degree.

Both approaches rank criteria that may lead to an exclusion higher, than obligatory criteria that are of interest, but can not lead to an exclusion. Such an obligatory criterion may be the volume of the support structure, which the user wants to consider in the weighted total score, but should not result in an exclusion.

Certain criteria are dependent on the results of another criterion, e.g. for the calculation of the time to print the orientation, the build height has to be calculated first. Dependencies like this have to be considered during the generation of the checking order, so the necessary input values for a criterion are available upon calculation.

V. THE PROCEDURE

The workflow starts with the user defining:

- the geometry
- the search field
- the criteria including their boundaries and weights
- the printer parameters

Knowing the geometry of the part, equivalent orientations can be discarded. By evaluating the criteria that were set, the criteria are sorted by runtime. After setting the criteria checking order, the analysis is started. During the analysis the checking order is changed dynamically, depending on previous exclusions.

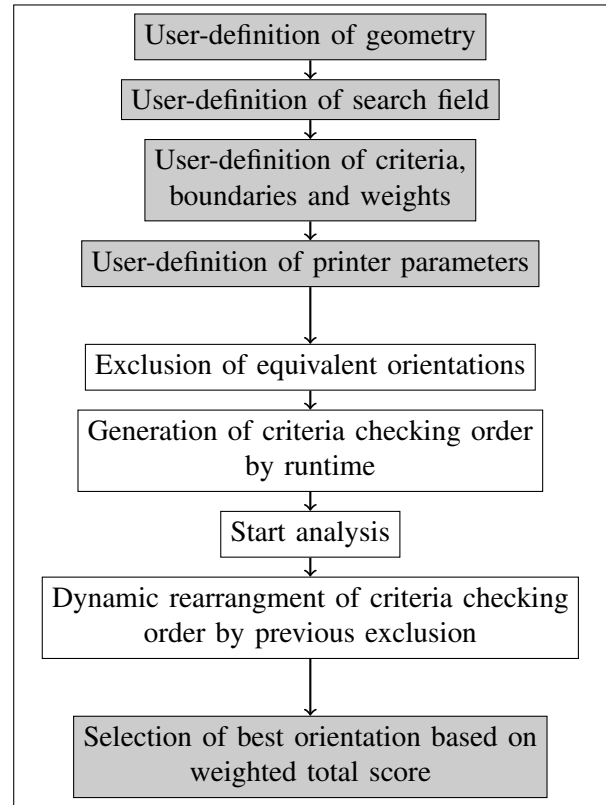


Fig. 5. The workflow

The last step of the analysis is the selection of the best orientation, based on the highest weighted total score.

VI. DEMO

The following section is an exemplary orientation, using the method described above. The orientation was performed by a prototype, which implements key features, but has not yet all the functionalities described in the previous sections. The program shows nevertheless, the efficiency of the process and its potential to improve the current print preparation. To include the critical steps of support structure generation and process simulation, the tool "Amphyon" (Amphyon Trial Version; Source: Additive Works GmbH Germany) was used.

A. Input and Criteria Definition

The first step consists of the user providing the CAD geometry of the part. The geometry in this demo had the following characteristics:

Points:	33,854
Edges:	101,598
Faces:	67,732

The relevant criteria for the analysis were:

- Evaluate all possible orientations in 3D space, with a rotation increment of 10° . Refine the search around promising orientations to an increment of 5° .

- The critical overhang for part surfaces is 35° .
- No support on running surface, located at center of the geometry.
- Low print time.
- Small support interface (area on the part which needs support).
- Low stresses and distortions in the final part.
- Material: Steel 1.4404

For the simulation parameters the properties of a “Concept Laser M2” laser cusing machine were set.

B. Results

As shown in figure 3, a score of 0% is considered insufficient and results in the exclusion of the orientation.

Figure 4 shows the results of the refined search, where dark red indicates a high criteria fulfillment. The graph shows the formation of clusters around promising orientations. An interesting feature is the half-oval form of the clusters (e.g. at a y-rotation of 150°), which result from the exclusion process. This shows that an exclusion of insufficient orientations can save calculation time, but also makes the analysis less intuitive and requires some kind of automation.

After the first sweep, before the support generation and the process simulation, the first exclusion was conducted. The exclusion rate was at 92%, which means only 8% of the orientations analyzed met the criteria. Only those remaining orientations were considered in the following support generation and process simulation.

Assuming that each cluster centers around a local maximum, one orientation from each cluster was run through the support generation and process simulation, resulting in 8 orientations checked. After this step only 3 orientations (0.2%) remained, which fulfilled all the criteria. From this list the best candidate was chosen by finding the one with the highest total weighted score.

The value of an estimate for the time saved by automating the process is limited, since such a process would not be performed manually in an industrial application. Therefore, the time savings will be illustrated indirectly, with the following result values:

- 92% of all orientations could be excluded after the first sweep and before the support generation and process simulation.
- Less than 1% of all orientations fulfilled all the requirements.

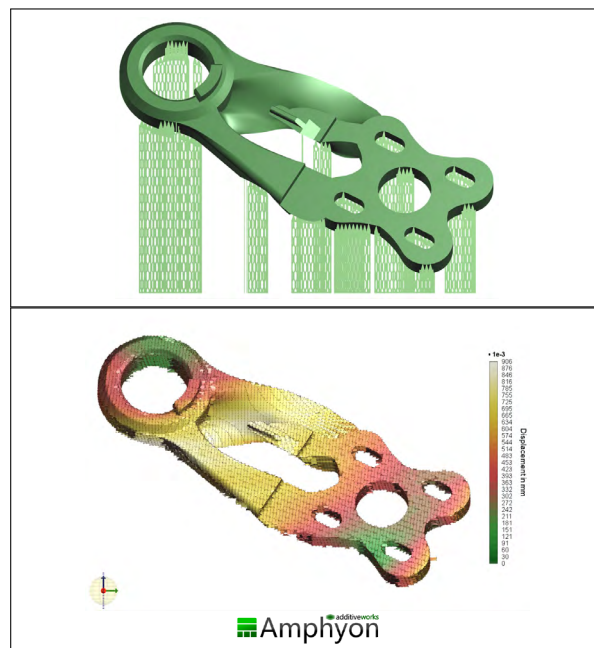


Fig. 6. Exemplary results of process simulation in Amphyon

In order to give some estimate of the analysis duration, the following list shows the computing time of the demo on a “HP EliteBook 8740w”:

Time for orientation and checks:	3 min
Time for support generation and simulation (using Amphyon):	~ 24 h
Total time:	~ 24 h

Comparing the time needed for the orientation and checking of the criteria, to the total time needed for the whole analysis, it stands out that this step has only a marginal impact on the analysis time. The main portion of the computational resources is consumed by the support generation and the process simulation. This fact emphasizes the importance of limiting the number of orientations on which these costly operations are performed.

VII. CONCLUSIONS

The potential of the proposed method lies in the simplification of the print preparation process. As the exemplary demo has shown, POEAM enables the unexperienced user of AM technology to prepare a geometry to be manufactured accurately and in compliance with required properties. In addition, POEAM also offers the benefit of saving time during the print preparation, by automating the process and therefore making the use of AM more efficient. This makes the method also attractive for expert users, who want to maximize the quality of their work.

ACKNOWLEDGMENT

We want to thank Fabian Müller at Nuremberg Tech, for providing the geometry used in the Demo section.

PROBABILISTIC FINITE ELEMENT ANALYSIS OF BESPOKE TITANIUM VETERINARY IMPLANTS

Akash Gupta^{*}, Huw Millward¹, Ffion O' Malley² and Alan Lewis³

^{*}Wales Centre for Advanced Batch Manufacture (CBM),
University of Wales, Ethos Building,
King Road, Swansea, SA1 8AS, U.K.
e-mail^{*}: akash.gupta@cbmwales.co.uk
e-mail¹: huw.millward@cbmwales.co.uk
e-mail²: ffion.omalley@cbmwales.co.uk
e-mail³: ProfAlan.Lewis@wales.ac.uk
Web page: <http://www.cbmwales.co.uk/about/>

Key words: Additive Manufacturing, Finite Element Analysis, Probability of Failure

Abstract. This study analyses canine limb-sparing implants with an integrated lattice structure, manufactured in Ti-6Al-4V ELI alloy using Electron Beam Melting (EBM) technology. The research aim is to determine the technical risk associated with the implant through probabilistic numerical analysis. A series of boundary conditions are employed on the implants in order to investigate the robustness of the design. The output stress and strain values are then employed to further examine fatigue life parameters under cyclic loading of the implants. The probabilistic numerical analysis has successfully identified the location of a key failure mode (yield stress limit) and the modelling correlated to veterinary case-study observations. In regard to the lattice structure, it is shown that the structure does provide mechanical integrity to the implant assembly, but the geometry requires significant simplification while modelling. This is primarily due to: (a) the limitations of CAD tools in generating NURB surfaces from point cloud data, and (b) the node and element count associated with these small structures makes the model computationally expensive.

1 INTRODUCTION

The introduction of additive manufacturing (AM) technology has facilitated the fabrication of patient-specific implant design which accommodates variabilities better than their off-the-shelf counterparts. AM solutions not only reduces surgery time but also provides the patient the with a better fit and ease in mobility. With no restriction in design constraints, bone mimicking lattice structures can be integrated within the implant to provide enhanced osseointegration [1]. Despite numerous advantages offered by bespoke AM solutions, a major concern is evaluating failure modes associated with these devices. This is because failures are seldom reported in real world scenarios and scarcity of data with regards to patient-specific complications makes risk evaluation a key challenge.

The Wales Centre for Advanced Batch Manufacture (CBM) employs the ARCAM Q10 Electron Beam Melting (EBM) AM technique for the fabrication of bespoke medical implants. CBM uses a range of inhouse tools to generate anatomical models from patient specific computer tomography (CT) scans that are employed to design a range of spinal, maxillofacial and orthopaedic solutions. This study employs a retrospective CBM case study of a bespoke limb-sparing canine implant (I-2a) with an integrated lattice structure, and implant (I-2b) that was manufactured for revision surgery. The boundary conditions associated with the two aforementioned implants are unknown, and simulation of lattice structures can require extensive computational resources [2]. Therefore, this study aims to find synergy in simulating complex implant design with minimal computational resources through probabilistic numerical analysis. This was conducted by subjecting the implant I-2a through multiple loading regimes in order to investigate the cause of failure. Identical boundary conditions were then be employed on implant I-2b to inspect the robustness of the new design. Apart from boundary conditions, there are several other intrinsic and extrinsic uncertainties that are integral to veterinary (and medical) devices. Hence, this study scrutinises the majority of these parameters through statistical measures. It is believed that this research can be an initiator in determining the vital parameters that are integral to weight-bearing bespoke implants and acknowledge challenges associated with simulation of additively manufactured geometries.

2 MATERIAL AND METHODS

The retrospective case employed in this study is a nine-year-old 45kg mixed canine breed, presenting a complaint of a distal radius osteosarcoma in left forelimb. The surgeon prescribed a limb-sparing surgery thereby requesting an implant with integrated lattice structure in the cut away section, and screw holes with a diameter(s) of 3.5 mm in upper and radial carpal and 2.7 mm in metacarpals. Additionally, they also requested a polished section around the screw holes and truss structure to hold the lattice together. Based on these requirements, a preliminary implant I-2a was designed for the surgery. Three months after operation, the surgeon reported that the dog had been presented to the referral centre lame, and on CT-scan it was found that the implant had fractured. Hence, the surgeon requested a new implant I-2b with full solid bar and with alternate screw positions to that of the fracture. Figure 1 depicts the initial design I-2a, CT-scan indicating region of fracture and implant I-2b designed for revision surgery.

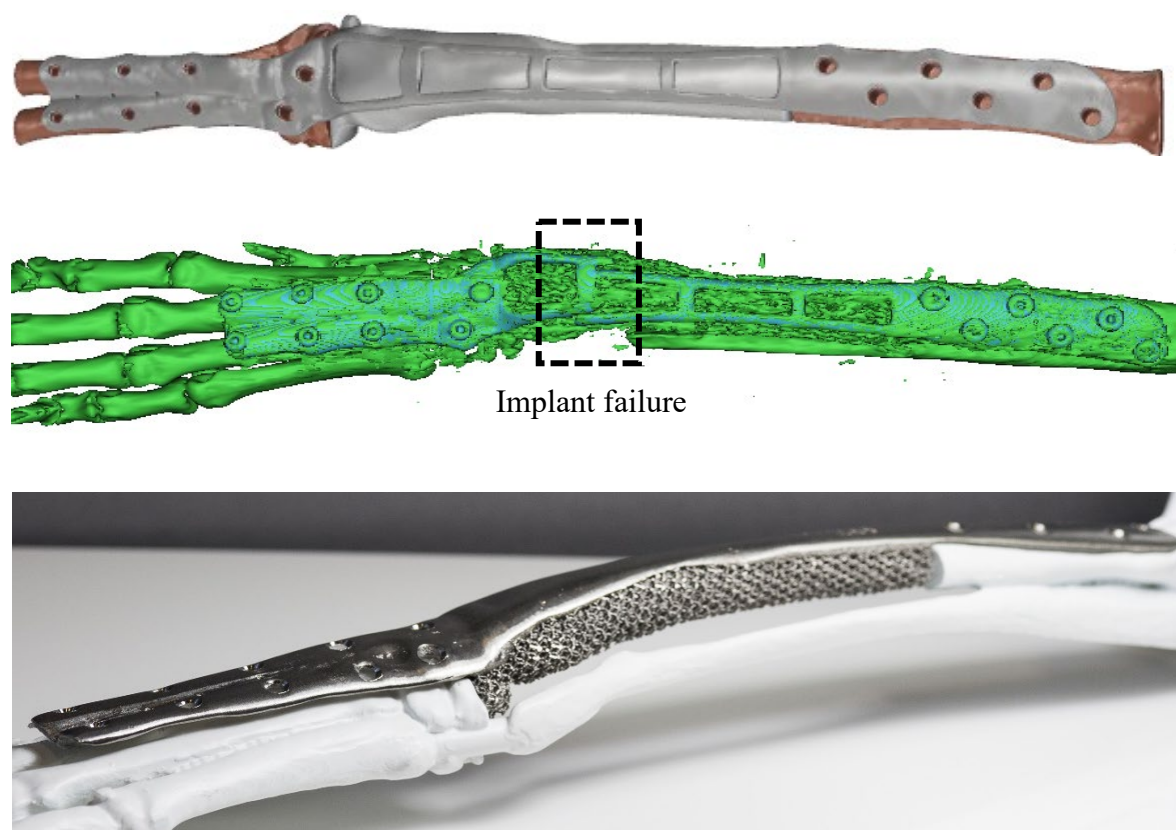


Figure 1: (Top) Implant assembly I-2a with simplified lattice structure and cropped bone represented in brown, (Middle) CT-Scan of left-limb depicting region of implant failure and (Bottom) 3D printed anatomical bone model and implant I-2b with representative lattice structure manufactured for revision surgery

2.1 Design

Patient specific computer tomography (CT) scan were imported in Materialise Mimics to extract the anatomical model for reconstruction. The bone model for implant design was extracted by employing a scale of 226 – 3071 Hounsfield Unit during segmentation. This segmented bone was then imported in Geomagic Freeform to design surgical guides and implants.

2.2 Manufacturing

In order to validate the design and fitting of the implant, the anatomical bone model was 3D printed in polymer (Somos Watershed XC11122) and implant in Titanium Ti-6Al-4V ELI alloy through EBM. The mechanical integrity of parts fabricated from EBM manufacturing process depend on various pre/post processing parameters [3]. Hence, to determine the mechanical properties of parts fabricated from the inhouse ARCAM Q10 machine, a small batch of (n=6) specimen were fabricated for tensile testing. Monotonic testing gave Young's modulus of 107 GPa, yield strength (σ_{ys}) of 822 MPa and ultimate tensile strength (σ_{uts}) of 926 MPa for the manufactured parts.

2.3 Finite Element Analysis

The data obtained from tensile testing was employed to update the material library in Ansys v.19.1 for Finite Element Analysis (FEA) of the implant. The actual lattice structure as shown in Figure 1 possessed a non-stochastic dodecahedron structure with a strut size of 2.8mm. Meshing such fine lattice structures for numerical analysis could prove computationally expensive, therefore as shown in Figure 2, the lattice was simplified into a planer structure and allocated a Young's modulus of 0.55 GPa [4]. Furthermore, the bone was allocated an isotropic elasticity of 10.5 GPa [5] and friction coefficient of 0.001 was allocated between bone-lattice and bone-implant [6]. Finally, the screws were modelled as fixed beam joints with material properties similar to that of the implant and analysed by enabling 'Large Deflection' to capture any non-linear effects.

A comprehensive study in the sagittal plane on 327 dogs from 32 breed suggests that underlying motion for all dogs is identical [7]. However, modelling and simulation of canine implants is not so straightforward due to variability in boundary conditions intrinsic to individual dogs. Additionally, old and impaired dogs show significantly low levels of activity compared to healthy dogs [8]. According to the surgeon, the front limbs sustains 60% and hind limbs bears 40% of the total weight of the dog. However, this ratio constantly changes depending on the locomotion performed by the dog.

Based on these aforementioned findings, preliminary FEA analysis for both implants was conducted by fixing the distal end of the implant assembly and applying a resultant force (F_R) at an angle (θ) on the proximal end. As shown in Figure 2, F_R was further discretised into normal and perpendicular component based on the relationship given in Eq. 1-3. The reference value allocated to all input parameters for preliminary FEA are briefly described in Table 1. The implant assembly was meshed using patch independent quadratic tetrahedron elements ranging from 0.1 – 0.9 mm allocated after conducting a mesh sensitivity analysis.

$$F_z = F_R \times \cos(\theta) \quad (1)$$

$$F_y = F_R \times \sin(\theta) \quad (2)$$

$$M_x = F_y \times (\text{Perpendicular distance of } F_y \text{ from fixed end}) \quad (3)$$

2.4 Fatigue Analysis

As demonstrated earlier for mechanical properties, fatigue properties also depend on several post-processing factors [9]. Additionally, cyclic fatigue properties obtained from experimentation are generally computed from completely reversed, constant amplitude tests. However, actual components seldom experience such pure loading, suggesting presence of some mean stress. Additionally, for a typical EBM manufactured geometry a fatigue stress limit ≤ 600 MPa corresponded to maximum life [9,10]. These findings were employed to update the fatigue stress and strain life parameters for Ti-6Al-4V ELI alloy in Ansys. The analysis was conducted using Soderberg mean correction theory and loading ratio of 0.1 to compute fatigue life performance of the implants.

2.5 Probabilistic analysis

In order to identify input parameters crucial to the produced stress and strain, sensitivity analysis was conducted in optiSLang 7.1 (extension for Ansys). To reduce computational time, sensitivity analysis was conducted external to Ansys workbench module by allocating a range to the reference values of input parameters employed in preliminary FEA. As shown in Table 1, these ranges were employed to generate 100 design points using LHS (Latin Hypercube Sampling) technique to generate metamodel of optimized prognosis [11]; this metamodel was then employed to generate CoP (Coefficient of Optimised Prognosis) matrix which gave correlation between vital input parameters and the stress and strain generated in the implant.

The vital parameters identified from sensitivity analysis were then employed for robustness analysis in optiSLang. A mean (μ) and standard deviation (σ) was allocated to these parameters to further generate 100 design points to compute mean stress, mean fatigue life and standard deviation(s) associated with the implant. The value of mean and standard deviation obtained from robustness analysis for the implant were employed in Eq. 4 to compute respective Z score. This Z score in conjunction with Z score table enabled in determining the probability of failure associated with the implant. Figure 3 provides a complete schematic of methodology overview employed in this study.

$$Z \text{ score} = |\text{Reference value} - \text{Mean value}| / \text{Standard deviation} \quad (4)$$

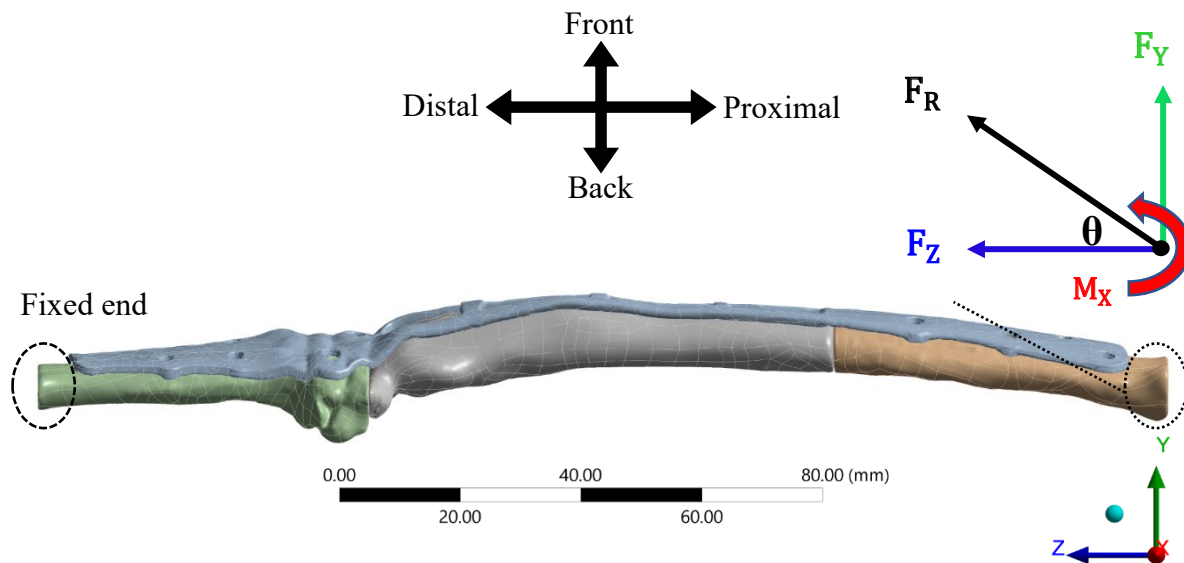


Figure 2: Boundary conditions associated with the implant assembly for Finite Element Analysis

Input parameters	Parameter type	Reference value	Range	
Friction Bone-Lattice	Optimised	0.001	0.001 - 0.2	
Friction Implant-Bone	Optimised	0.001	0.001 - 0.2	
Young's Modulus for lattice (GPa)	Optimised	0.55	0.20 - 3.49	
			Mean (μ)	Standard deviation (σ)
Resultant Force (N)	Stochastic	90.00	135.00	20.25
Angle (degree)	Stochastic	5.00	7.00	0.02
Force_Z (N)	Dependent	Eq. 1	Derived	
Moment_X (Nmm)	Dependent	Eq. 3	Derived	

Table 1: Reference value associated with preliminary FEA and range allocated for sensitivity and robustness analysis

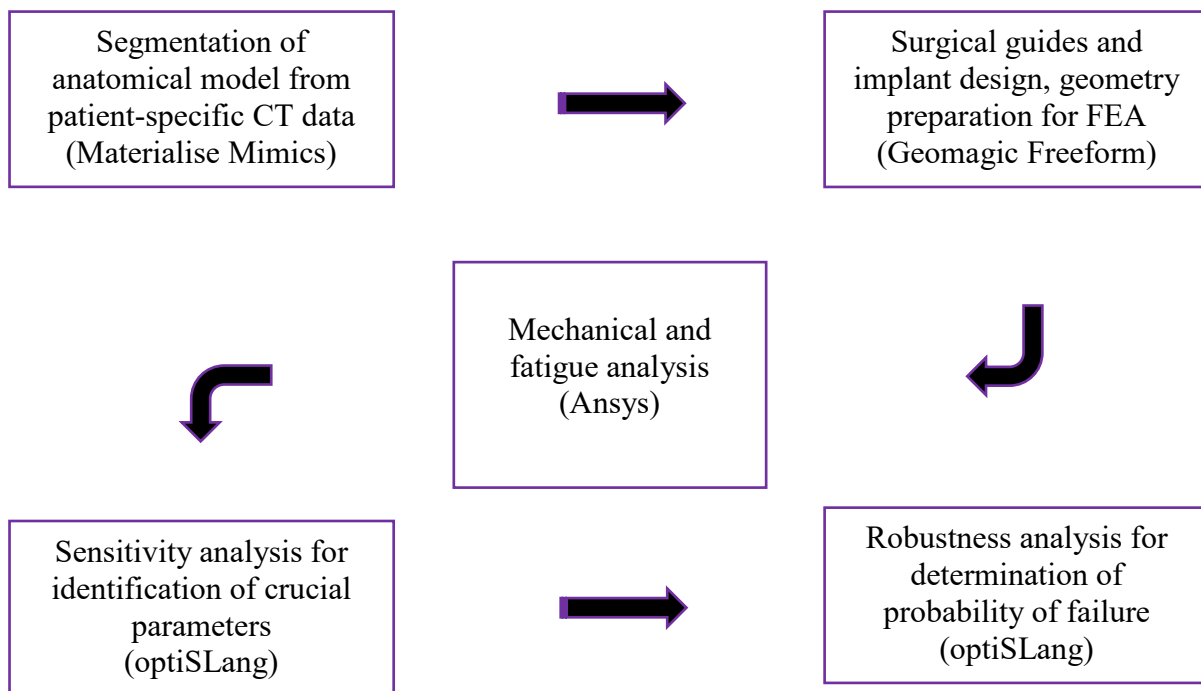


Figure 3: Methodology overview

3 RESULTS AND DISCUSSION

The preliminary FEA was conducted on I-2a design with lattice structure as shown in Figure 2. The analysis gave a maximum equivalent von-Mises stress (σ_{vm}) and strain (ϵ_{vm}) of 387.3 MPa [Fig. 4] and 3.62×10^{-3} in the implant and 11.54 MPa [Fig. 5] and 0.02 in lattice structure. Front view of Figure 4 demonstrates that high stress concentration in I-2a was simulated near the proximal and distal end of the implant. However, magnified front view of fracture region depicts absence of any critical stress hotspots. With regard to stress in the lattice, it was observed that the maximum stress bore a spatialised pattern and was localised in the distal end of the lattice. Although it is noteworthy from the front and back view of Figure 5 that a majority of lattice geometry remains unstressed, which can be regarded as stability offered by the screws.

Implant stress

Type: Equivalent (von-Mises) Stress

Unit: MPa

Time: 1

Custom

Max: 387.3

Min: 0.01938

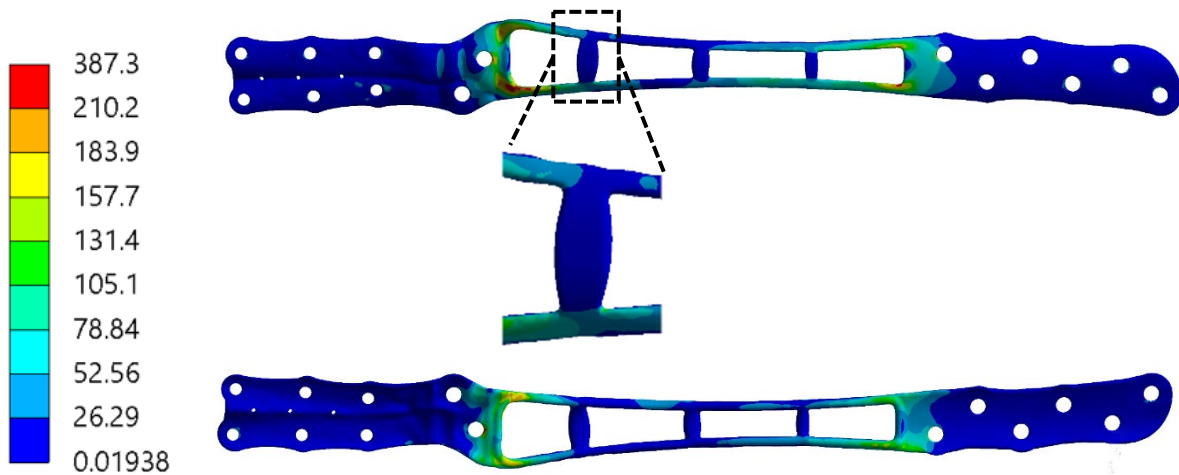


Figure 4: Preliminary FEA stress results for implant I-2a simulated with lattice structure representing front view on top and back view in bottom



Figure 5: Preliminary FEA stress results for simplified lattice structure representing front view on left and back view on right

A major geometrical limitation in the previous FEA of I-2a design is lattice simplification. Contrary to the realistic lattice structure in the implant, FEA of I-2a considered both 100% dense lattice structure and pure bonding with the implant. Realistically, it is only the circular strut diameter of the dodecahedron lattice that bonds with the implant. Hence, a secondary FEA of I-2a was conducted by disregarding the lattice structure. The simulation gave a maximum stress and strain of 396 MPa [Fig. 6] and 3.70×10^{-3} associated with the implant. It is evident from the magnified view of Figure 6 that ignoring the lattice structure simulated stress hotspots within the fracture region. However, back view of I-2a in Figure 6 also shows that ignoring lattice structure simulates stress hotspots in the distal end of the implant.

Since simulation of I-2a without lattice structure gave more realistic stress hotspots identical boundary conditions were employed to simulate I-2b implant assembly without lattice. As shown in Figure 7, preliminary FEA of I-2b gave a maximum σ_{vm} of 167.70 MPa and ϵ_{vm} of 1.56×10^{-3} associated with the implant. The preliminary FEA was followed by additional fatigue analysis for both I-2a and I-2b design for sensitivity analysis.

Implant stress

Type: Equivalent (von-Mises) Stress

Unit: MPa

Time: 1

Custom

Max: 396

Min: 0.01953

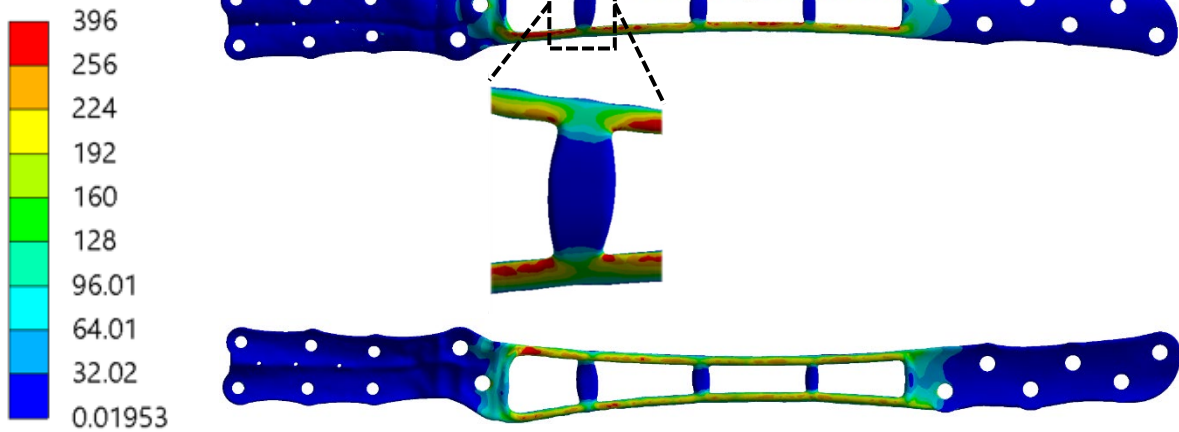


Figure 6: Preliminary FEA stress results for implant I-2a simulated without lattice structure representing front view on top and back view in bottom

Implant stress

Type: Equivalent (von-Mises) Stress

Unit: MPa

Time: 1

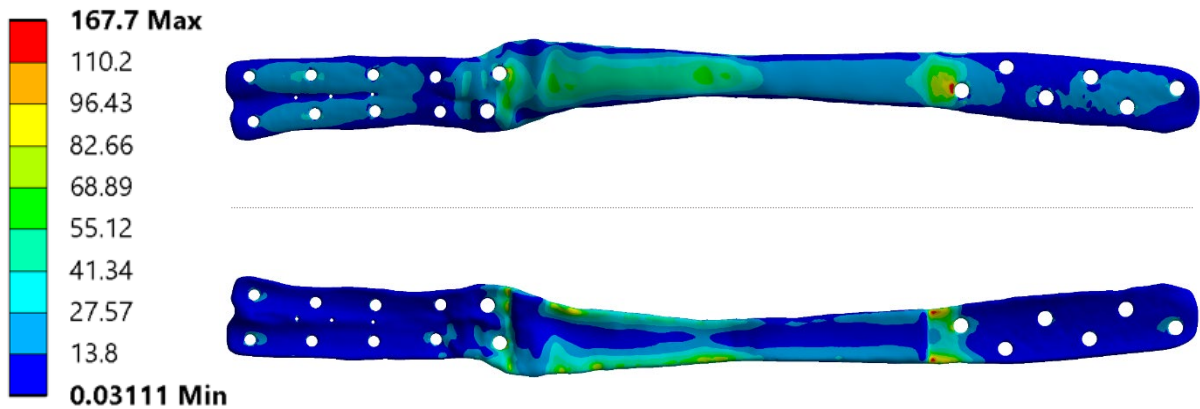


Figure 7: Preliminary FEA stress results for implant I-2b simulated without lattice structure representing front view on top and back view in bottom

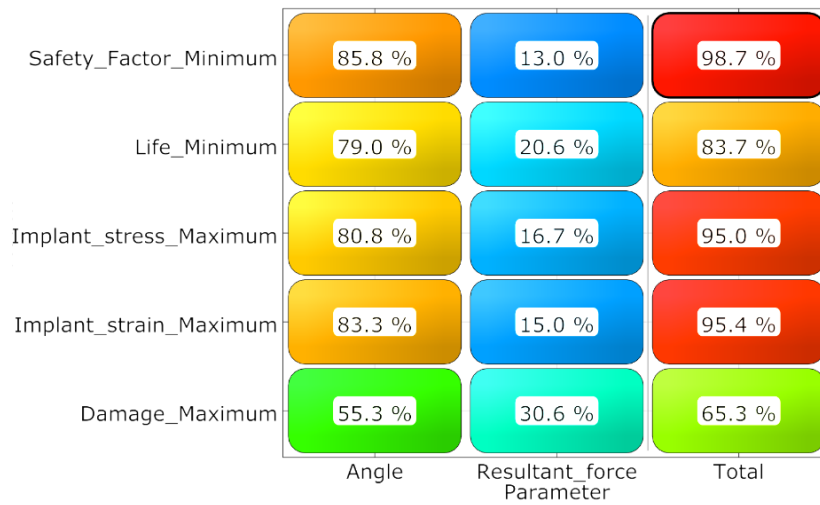


Figure 8: CoP matrix obtained from sensitivity analysis

Since simulation of implant I-2a and I-2b without lattice simulated more realistic hotspots. Therefore, output value of maximum σ_{vm} and ϵ_{vm} for I-2a along with fatigue life, damage and safety factor were parameterised for sensitivity analysis. As shown in Figure 8, sensitivity analysis simulated F_R and θ as two most vital parameters responsible for more than 95% of stress and strain produced in the implant. This suggests that modelling of alternate values for friction coefficient and Young's modulus are redundant for further analysis.

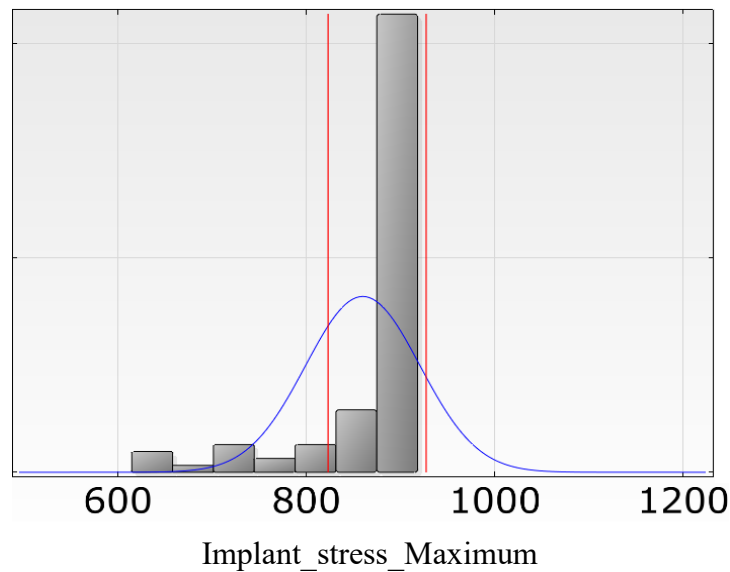


Figure 9: Histogram obtained from robustness analysis of I-2a design without lattice structure, fitted with a normal distribution represented in blue and lower and upper bound of failure limit in red

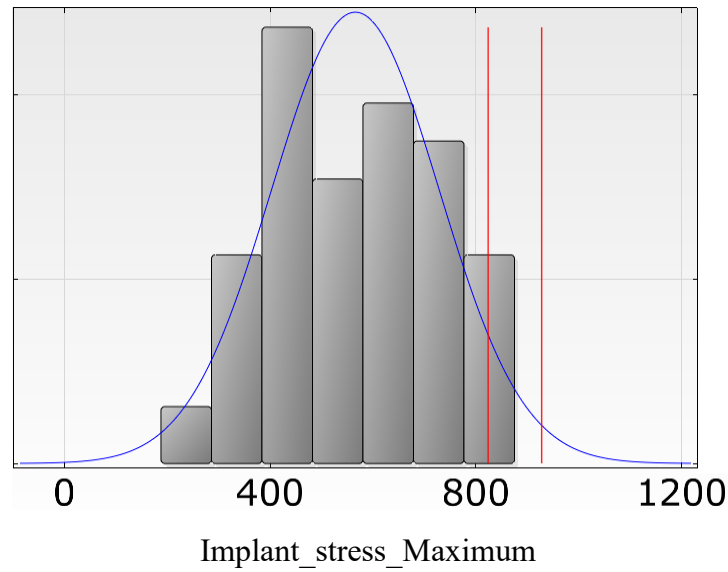


Figure 10: Histogram obtained from robustness analysis of I-2b design without lattice structure, fitted with a normal distribution represented in blue and lower and upper bound of failure limit in red

Therefore, these additional parameters were kept constant. Robustness analysis on I-2a and I-2b was conducted by employing μ and σ for F_R and θ as described in Table 1. Robustness analysis produced a histogram, which was fitted with a normal distribution to compute the mean maximum stress and standard deviation associated with both implant I-2a and I-2b. Figure 9 and Figure 10 clearly demonstrates that the stress distribution associated with I-2a is significantly higher than the stress distribution associated with I-2b. Additionally, employing σ_{ys} and σ_{uts} as reference value for lower and upper limit for failure. The analysis gave a 72.50% probability of reaching σ_{ys} for I-2a and 5.65% probability for I-2b. The corresponding values obtained from robustness analysis for both I-2a and I-2b are described in Table 2. It is noteworthy that the implant I-2b has been under operation for past eleven months with no complaints so far.

Implant	Mean (σ_{vm})	Standard deviation (σ_{vm})	Probability of reaching (%)	
			σ_{ys}	σ_{uts}
I-2a	858.47 MPa	61.03	72.5	13.42
I-2b	563.91 MPa	162.89	5.65	1.31

Table 2: Results from robustness analysis of implants

4 CONCLUSIONS

Probabilistic FEA of bespoke implants in this study successfully highlighted the cause of failure of implant I-2a and robustness (continued successful working life) of implant I-2b. Simulation results demonstrate that a high mean stress associated with I-2a gave a low fatigue life

associated with the implant. However, replacing the truss structure with a solid bar in the new I-2b design enabled the reduction in mean stress, thus providing a higher fatigue life and much lower risk of failing. The veterinary observations from two implants have helped to validate the overall probabilistic methodology employed in this study.

The use of AM technology enables the fabrication of complex lattice structures; however, the analysis of these geometries can be quite challenging. Modelling the whole lattice is computationally expensive due to the limitations of CAD tools in handling dense point-cloud data. This study has shown that removing the lattice structure from the simulation produces acceptable errors, and this simplified analysis can still identify the crucial regions in order to successfully predict implant failure.

REFERENCES

- [1] G. Campoli, M. S. Borleffs, S. Amin Yavari, R. Wauthle, H. Weinans, and A. A. Zadpoor, 'Mechanical properties of open-cell metallic biomaterials manufactured using additive manufacturing', *Mater. Des.*, (2013).
- [2] A. Alberich-Bayarri, M. Sánchez, M. Pérez, and D. Moratal, 'Microfinite Element Modelling for Evaluating Polymer Scaffolds Architecture and their Mechanical Properties from', in *Finite Element Analysis*, Sciyo, (2010).
- [3] H. Galarraga, R. J. Warren, D. A. Lados, R. R. Dehoff, M. M. Kirka, and P. Nandwana, 'Effects of heat treatments on microstructure and properties of Ti-6Al-4V ELI alloy fabricated by electron beam melting (EBM)', *Mater. Sci. Eng. A*, (2017).
- [4] X.-Y. Zhang, G. Fang, and J. Zhou, 'Additively Manufactured Scaffolds for Bone Tissue Engineering and the Prediction of their Mechanical Behavior: A Review', *Materials (Basel)*, (2017).
- [5] I. N. and H. W. Thomas Pressel, Anas Bouguecha, Ute Vogt, Andrea Meyer-Lindenberg, Bernd-Arno Behrens, 'Mechanical properties of femoral trabecular bone in dogs', *BioMedical Engineering OnLine*, vol. 4, no. 1, BioMed Central, (2005).
- [6] A. Doi, H. Takahashi, B. Syuto, M. Katayama, H. Nagashima, and M. Okumura, 'Tailor-made plate design and manufacturing system for treating bone fractures in small animals', *J. Adv. Comput. Intell. Informatics*, (2013).
- [7] K. E. Fischer, Martin S and Lilje, *Dogs in Motion*, Second. The Pet Book Publishing Company Ltd, (2014).
- [8] C. T. Siwak *et al.*, 'Locomotor activity rhythms in dogs vary with age and cognitive status', *Behav. Neurosci.*, (2003).
- [9] A. H. Chern *et al.*, 'A review on the fatigue behavior of Ti-6Al-4V fabricated by electron beam melting additive manufacturing', *Int. J. Fatigue*, (2019).
- [10] P. E. Carrion, N. Shamsaei, S. R. Daniewicz, and R. D. Moser, 'Fatigue behavior of Ti-6Al-4V ELI including mean stress effects', *Int. J. Fatigue*, (2017).
- [11] A. Ptchelintsev, G. Grewolls, J. Will, and M. Theman, 'Applying Sensitivity Analysis and Robustness Evaluation in Virtual Prototyping on Product Level using optiSLang', *Proceeding Simulia Cust. Conf.*, (2010).

VARIATION OF OPTIMAL GAS-SUPPLY CONDITION ALONG WITH DEPOSITION HEIGHT IN DIRECTED ENERGY DEPOSITION

SHIHO TAKEMURA^{*}, RYO KOIKE^{*}, YASUHIRO KAKINUMA^{*}
AND YOHEI ODA[†]

^{*} Department of System Design Engineering, Keio University,
3-14-1 Hiyoshi, Kohoku-ku, Yokohama, Kanagawa 223-8522, Japan
e-mail: takemura@ams.sd.keio.ac.jp

[†]DMG MORI CO., LTD,
2-35-16 Meieki, Nakamura-ku, Nagoya, Aichi 450-0002, Japan
e-mail: yo-oda@dmgmori.co.jp

Key words: Directed Energy Deposition, Computational Fluid Dynamics, Inconel 625, Multiphase-flow Simulation

Summary. Directed energy deposition (DED), which is one of additive manufacturing applicable to metals, laminates the material on a baseplate by melting and solidifying with a high-power heat source. In terms of powder-based DED, the material waste tends to be large because powder flow is difficult to converge on the melt pool precisely. This study evaluates the variation in powder distribution when the deposition height is changed in order to obtain the optimal gas-flow rate and powder-nozzle shape. The powder flow is estimated with a computational fluid dynamics simulation based on Euler-Lagrange approach. The simulation results indicate that the proposed nozzles can achieve the high powder convergence stably even if the total amount of gas supply is reduced.

1 INTRODUCTION

Directed energy deposition (DED), which is one of additive manufacturing applicable to metals, attracts various kinds of industries such as aerospace, automotive, and medical products [1]. However, powder-based DED unnecessarily wastes the material because the powder flow is difficult to direct to the melt pool precisely. The powder supply efficiency needs to be stable for the process stability [2] so that the powder flow control is an important issue to enhance the DED's potential for industrial use. In order to improve the powder supply efficiency, it is necessary to analyse the powder distribution under various parameters such as gas-flow rate, powder-nozzle shape and deposit geometry. Therefore, many researchers have been investigating the powder supply process with theoretical and experimental approaches. For example, Pan et al. analysed the gravity-driven metal powder flow in a coaxial nozzle with various gas-flow rates and nozzle geometries [3]. A fluid-dynamics simulation would be helpful

to estimate the powder behavior under the powder nozzle. Although Zhu et al. dealt with the influence of deposition height on the powder distribution with a 2D-axisymmetric model of coaxial nozzle [4], the conventional researches conducted the simulations assuming that the powder flow is free jet, otherwise injected on a flat baseplate [5,6,7]. However, from the practical viewpoint, a detail investigation needs to be conducted considering the variation in the powder flow according to the geometry around the deposition point.

In this study, the powder distribution during the deposition on various heights is numerically evaluated by a computational fluid dynamics (CFD) simulation. To stabilize the powder supply, 3D models including the deposit with various heights are designed, and the influence of carrier gas-flow rate is investigated by analysing the powder-flow around the deposition point. Moreover, the powder-nozzle shape is also discussed along with the CFD simulation results.

2 METHODOLOGY

2.1 Directed energy deposition

In directed energy deposition (DED), the material is laminated on a baseplate by melting and solidifying with a high-power heat source as shown in Fig. 1. In this study, a coaxial powder nozzle initiating a conical powder flow is employed. The powder is supplied to the melt pool by the carrier gas through the outer path of the nozzle. In addition, the shield gas is supplied through the inner path of the nozzle to protect the heat source module. Inert gas like Argon is generally used for carrier and shield gases to prevent the oxidation of deposit. The deposition process can be conducted in all horizontal directions because the coaxial nozzle ensures stable powder supply even when the feed direction is changed [8].

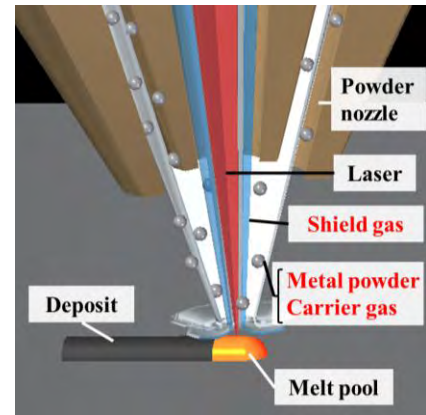


Figure 1: Schematic of DED

2.2 Computational fluid dynamics (CFD) simulation

A gas-solid multiphase-flow simulation is conducted based on the Euler-Lagrange approach.

The gas phase is treated as a turbulent flow and described by a continuity equation and Navier-Stokes equation based on the Reynolds-averaging. The Reynolds-averaged governing equations are given by Eqs. (1) and (2).

$$\frac{\partial \bar{u}_i}{\partial x_i} = 0 \quad (1)$$

$$\frac{\partial \bar{u}_i}{\partial t} + \bar{u}_j \frac{\partial \bar{u}_i}{\partial x_j} = -\frac{1}{\rho} \frac{\partial \bar{p}}{\partial x_i} + \nu \frac{\partial^2 \bar{u}_i}{\partial x_j^2} - \frac{\partial \overline{u_i' u_j'}}{\partial x_j} \quad (2)$$

where u_i [m/s] is the flow velocity, x_i [m] is the Cartesian coordinate, t [s] is the time, ρ [kg/m³] is the density, p [kg/m·s²] is the pressure, ν [m²/s] is the kinematic viscosity, and bar denotes the time-averaged value. In Eq. (2), the first and second terms on the left side represent the time term and the convection term, respectively, and the terms on the right side represent

the pressure term, viscosity term, and turbulent diffusion term in order. To complete the equation, modeling of the Reynolds stress $-\rho\overline{u_i' u_j'}$ is necessary. The Reynolds stress is expressed by using the turbulent viscosity and given as

$$-\rho\overline{u_i' u_j'} = \mu_t \left(\frac{\partial \bar{u}_i}{\partial x_j} + \frac{\partial \bar{u}_j}{\partial x_i} \right) - \frac{2}{3} \rho k \delta_{ij} \quad (3)$$

where μ_t [kg/(m·s)] is the turbulent viscosity, k [m²/s²] is the turbulent kinetic energy and $\delta_{ij} = 1$ for $i = j$, otherwise $\delta_{ij} = 0$. In this study, a k - ε turbulent model, developed by Launder and Spalding [9], is applied to solve the equations. In this model, the turbulent viscosity μ_t is given as Eq. (4).

$$\mu_t = C_\mu \rho \frac{k^2}{\varepsilon} \quad (4)$$

where C_μ is the model constant, ε [m²/s³] is the dissipation of kinetic energy of the turbulence. The conservation of the turbulent kinetic energy is expressed as

$$\frac{\partial(\rho k)}{\partial t} + \frac{\partial(\rho k u_i)}{\partial x_i} = \frac{\partial}{\partial x_j} \left\{ \left(\mu + \frac{\mu_t}{\sigma_k} \right) \frac{\partial k}{\partial x_j} \right\} + \overline{\rho u_i' u_j'} \frac{\partial \bar{u}_i}{\partial x_j} - \rho \varepsilon \quad (5)$$

The conservation of the dissipation of kinetic energy of the turbulence is expressed as

$$\frac{\partial(\rho \varepsilon)}{\partial t} + \frac{\partial(\rho \varepsilon u_i)}{\partial x_i} = \frac{\partial}{\partial x_j} \left\{ \left(\mu + \frac{\mu_t}{\sigma_\varepsilon} \right) \frac{\partial \varepsilon}{\partial x_j} \right\} + \left(C_{\varepsilon 1} \overline{\rho u_i' u_j'} \frac{\partial \bar{u}_i}{\partial x_j} - C_{\varepsilon 2} \rho \varepsilon \right) \frac{\varepsilon}{k} \quad (6)$$

where, $C_\mu = 0.09$, $\sigma_k = 1.0$, $\sigma_\varepsilon = 1.3$, $C_{\varepsilon 1} = 1.44$, and $C_{\varepsilon 2} = 1.92$ are the empirical constants.

In the Euler-Lagrange approach, the discrete phase is computed by solving a motion equation for each particle. The motion equation is given by Eq. (7).

$$\frac{du_p}{dt} = \frac{u - u_p}{\tau_r} + g \frac{\rho_p - \rho}{\rho_p} \quad (7)$$

where u_p [m/s] is the particle velocity, u [m/s] is the fluid velocity, ρ_p [kg/m³] is the particle density, ρ [kg/m³] is the fluid density, τ_r [s] is the particle relaxation time, and g [m/s²] is the gravitational acceleration. The first and second terms on the left side represent the drag force and the gravitational force respectively. Since the fluid density is much smaller than the particle density ($\rho/\rho_p \ll 1$), the drag force and the gravitational force dominantly work on the particles. Then, the particle relaxation time τ_r is given by

$$\tau_r = \frac{\rho_p d_p^2}{18\mu C_d Re_p} \frac{24}{Re_p} \quad (8)$$

where d_p [m] is the particle diameter, μ [kg/(m·s)] is the fluid viscosity. Re_p is the particle Reynolds number and defined as

$$Re_p = \frac{\rho d_p |u_p - u|}{\mu} \quad (9)$$

By solving the Eq. (7), the particle velocity can be obtained. In addition, the particle trajectory can be represented by following Eq. (10).

$$\frac{dx_p}{dt} = u_p \quad (10)$$

where x_p is the position of particle.

3 SIMULATION ASSUMPTIONS AND SETUP

3.1 Simulation assumptions

The CFD simulation in this study is conducted by using ANSYS Fluent (ANSYS, Inc.), and following assumptions are taken into the simulation;

- (1) A steady-state gas flow is considered.
- (2) Collisions among particles are not considered.
- (3) Particle is assumed to be spherical.
- (4) Particle size is assumed to follow a Rosin-Rammler distribution.
- (5) Any thermal effect like an interaction between particles and the laser is not considered.
- (6) At the outlet, the gauge pressure is set to be zero.
- (7) At the wall, a no-slip condition is applied.

3.2 Simulation model and setup

The 3D CAD models are created for the CFD simulation as shown in Fig. 2. In order to evaluate the variation in powder distribution along with the deposition height, the CAD models including the deposit are created as shown in (a). In addition, the CAD model only with a baseplate, assuming the first-layer deposition, is also created for comparison as presented in (b). The powder-nozzle shape is based on a five-axial combined machining center (LASERTEC 65 3D, DMG MORI CO., LTD.). As for (a), the geometry of deposit is decided according to the results in preliminary experiments; therefore, the top of deposit is rounded. Figure 3 shows the cross-section of CAD model. In this study, the powder convergence distance L , defined as the height between the nozzle exit and the convergence point of conical powder stream, is 13 mm. The standoff distance S , which is the distance from the nozzle exit to the baseplate, is also set to be 13 mm. Figure 4 shows the boundary conditions for the discrete phase. Particles are escaped from the outlet and trapped at the bottom of the processing area or the top surface of deposit.

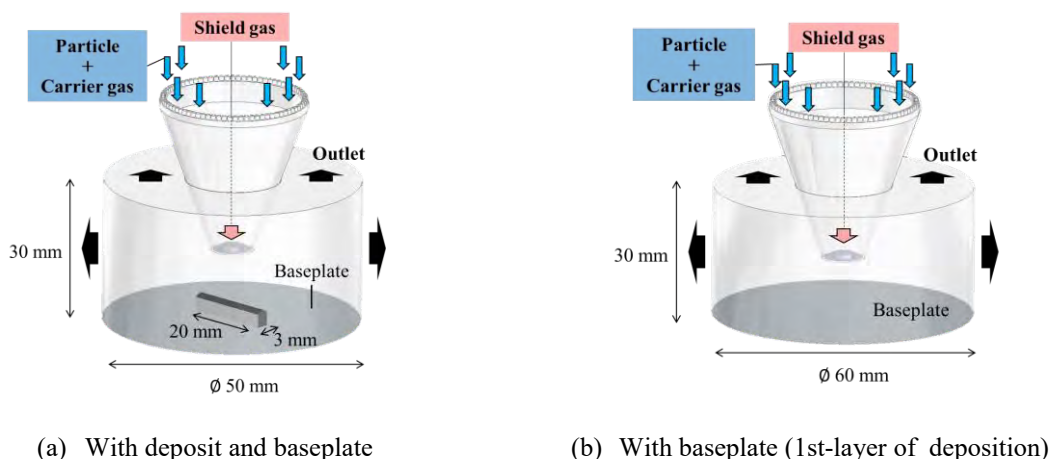


Figure 2: CAD model

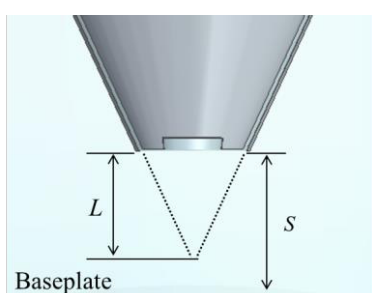
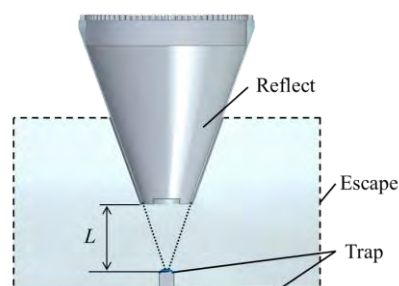
Figure 3: Definition of powder convergence distance (L) and standoff distance (S)

Figure 4: Boundary conditions

In this study, the simulations are conducted with 4 types of carrier gas-flow rate. The CAD models are created with 3 types of deposition height, on a baseplate, 9-layer and 49-layer deposits, i.e., models are assuming the 1st-layer, 10th-layer and 50th-layer depositions, respectively. Other simulation conditions are summarized in Table 1. Physical properties of argon are applied to decide the fluid density and viscosity, and the particle density refers to the density of Inconel 625 alloy.

Table 1: Simulation conditions

Carrier gas-flow rate	L/min	3, 4, 6, 8
Shield gas-flow rate	L/min	4
Powder feed rate	kg/min	18×10^{-3}
Fluid density	kg/m ³	1.784
Fluid viscosity	kg/(m·s)	2.22×10^{-5}
Particle density	kg/m ³	8440
Particle size	μm	53 – 105

4 PARTICLE DISTRIBUTION ON TOP SURFACE OF DEPOSIT AND BASEPLATE

As a result of the simulation, the particle trajectory is obtained as shown in Fig. 5. To clarify the powder convergence, the distribution of trapped particles is mapped corresponding to the XY coordinate. Figure 6 shows the particle distribution viewed from the powder nozzle, when the carrier gas-flow rate is 4 L/min. This result indicates that the particle distribution slightly spreads at the higher layer. Furthermore, the particles are not supplied at the center of the processing point. In order to compare the particle distribution quantitatively, Fig. 7 shows the probability distribution of particles for every 0.1 mm radius from the center of melt pool.

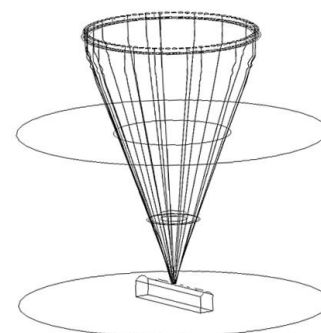


Figure 5: Particle trajectory

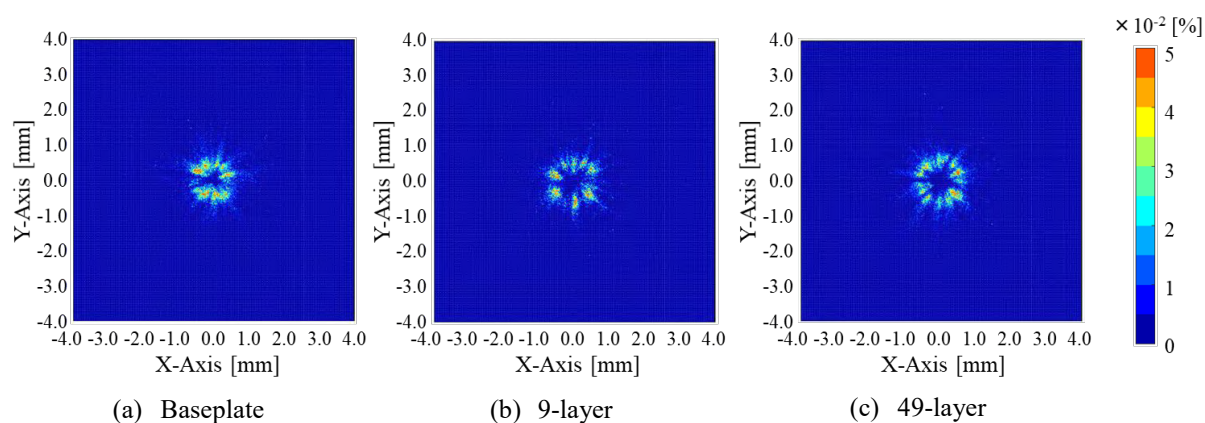


Figure 6 Particle distribution on top surface of deposit and baseplate (Carrier gas-flow rate : 4 L/min)

Comparing the distributions in Fig. 7 regarding deposition height, more particles distribute at the distant position from the center of melt pool when the deposit is higher, excepting the carrier gas-flow rate of 3 L/min. The variation in gas flow between the nozzle exit and baseplate would influence on the spread of particle distribution. Figure 8 shows the velocity distribution of gas flow at the cross-section of processing area. In (b), the flow spreads on the baseplate below the deposition point. On the other hand, the flow goes to downward along the side surface of deposit in (c). Figures 9 are the enlarged pictures of the nozzle exit in Figs. 8(b), (c). In case of 49-layer shown in Fig. 9(b), the flow near the nozzle exit is slightly goes to downward by comparison with the flow of 9-layer deposition as (a). Figure 10 shows the pressure distribution at the cross-section of processing area, and indicates that the stagnation area gets small when the deposit becomes high. In other words, the flow direction hardly changes around the processing point in 49-layer deposition.

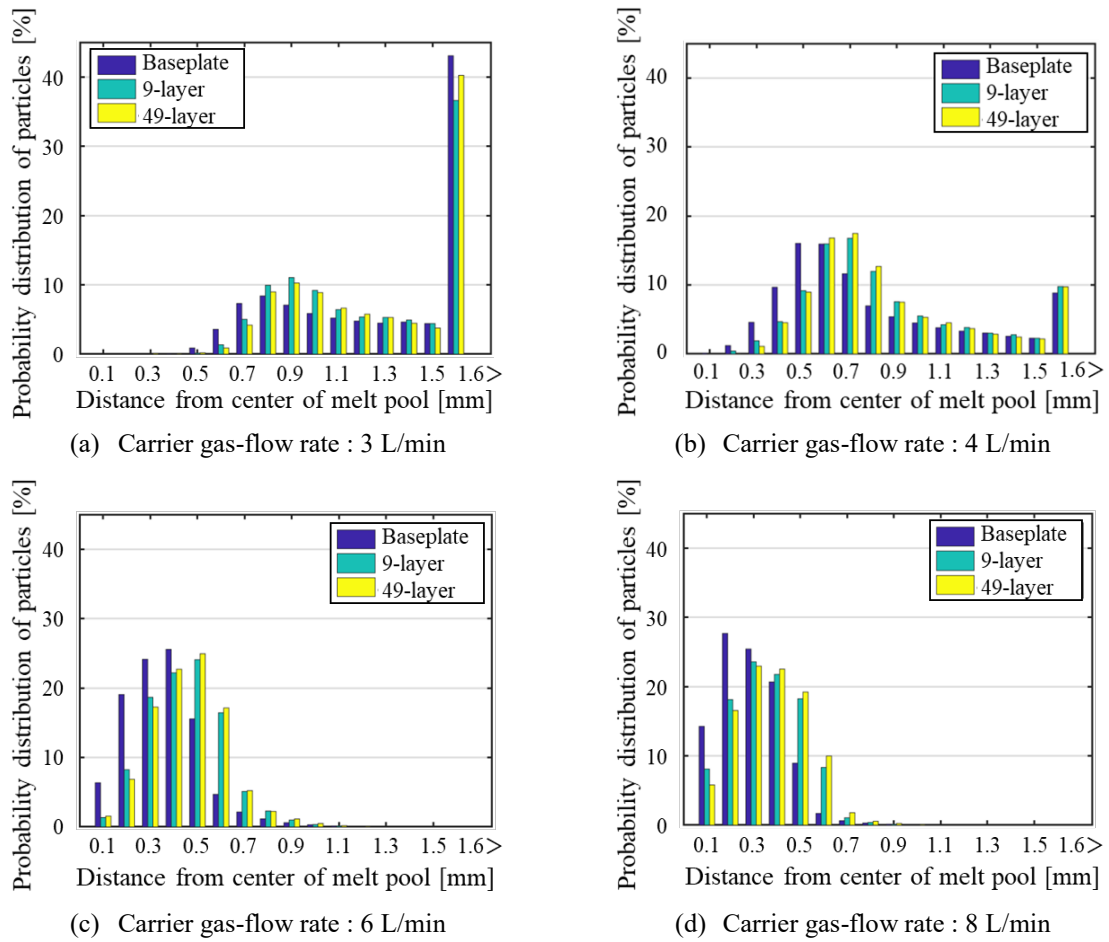


Figure 7: Probability distribution of particles

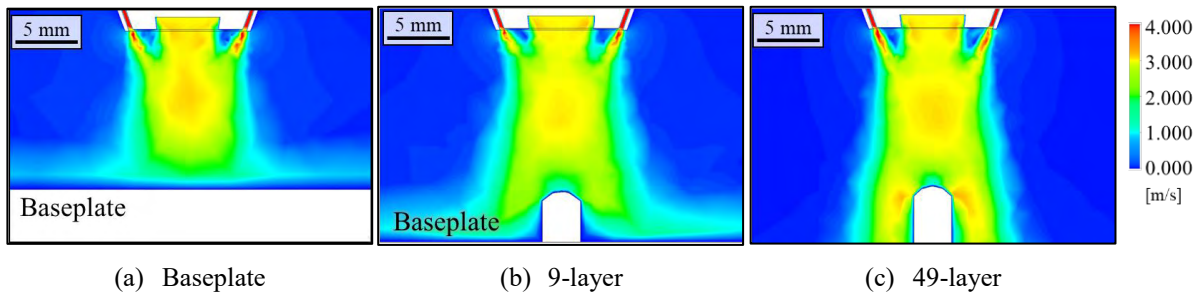


Figure 8: Flow velocity distribution (Carrier gas-flow rate : 4 L/min)

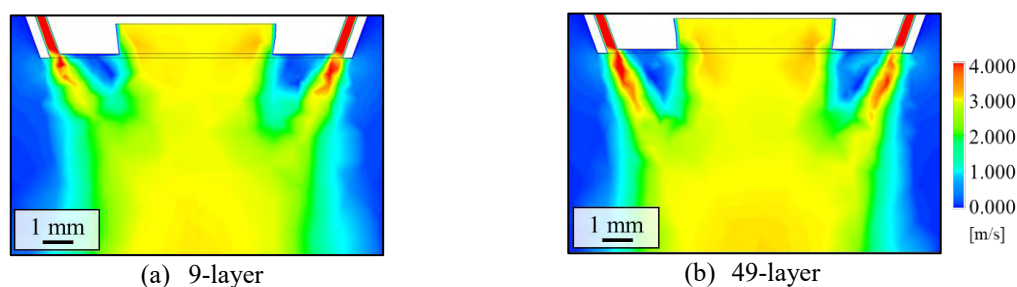


Figure 9: Flow velocity distribution around nozzle exit

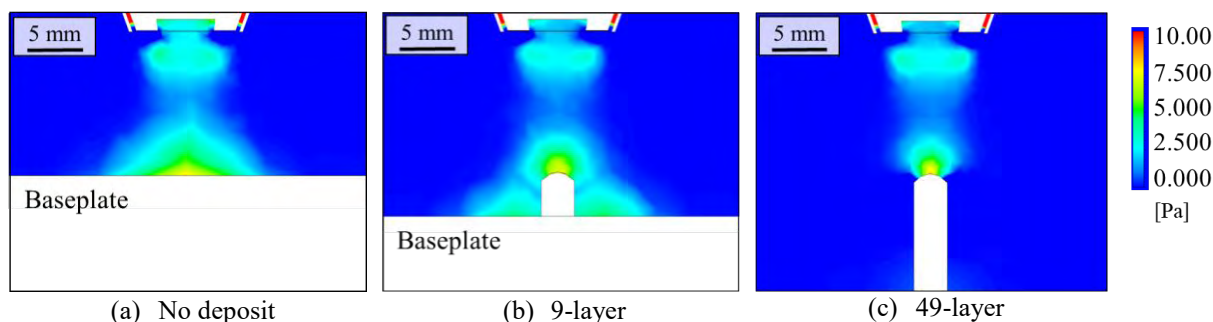


Figure 10: Pressure distribution (Carrier gas-flow rate : 4 L/min)

The velocity and pressure distributions represent that the distance from the top surface of deposit and the baseplate would affect the particle trajectory under the nozzle. Considering that the gas flow becomes downward in 49-layer deposition, some particles may reach at an off-center region. From these results, the gas-flow condition needs to be modified according to the deposition height for enhancing the stability of powder supply.

In addition, comparing the particle distribution shown in Fig. 7 regarding the carrier gas-flow rate, the particle convergence is more enhanced with larger carrier gas-flow rate regardless the deposition height. The average ratio of particles distributing within 1.5 mm from the center of melt pool in 3-type deposition heights ($= \bar{p}_{1.5}$) are 99.9% in the carrier gas-flow rate of 6 and 8 L/min, whereas the $\bar{p}_{1.5}$ are 60.0% and 90.5% in the carrier gas-flow rate of 3 and 4 L/min, respectively. As a result, the carrier gas-flow rate should be at least 6 L/min or more for high powder convergence with this powder nozzle when the deposition height changes.

5 MODIFICATION OF POWDER NOZZLE

The modification of the powder-nozzle shape is also considered. Although particles can be supplied to the melt pool when the carrier gas-flow rate is high as 6 L/min according to the simulation results, the higher carrier gas-flow rate drastically generates sputter. Moreover, in terms of cost and resource saving, a reduction of gas consumption is beneficial for DED. From the view point of the powder supply efficiency, which is a percentage of material actually used for the deposit, the powder convergence should be improved even with the low carrier gas-flow rate.

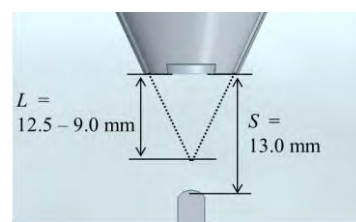


Figure 11: Cross-section of modified powder nozzle

The powder convergence distance L is changed in the coaxial powder nozzle in this simulation. Considering that the particles are hardly supplied into the center of melt pool in Fig. 6, the actual converged height would be below the designed height represented with the convergence distance L . From this reason, the convergence distance L is shorter than the standoff distance S in the new powder nozzle. Concretely, L is designed to be 9.0 – 12.5 mm at 0.5 mm intervals (Fig. 11), and the simulation conditions are same as Table 1, excepting the carrier gas-flow rate is set to be 4 L/min.

Figures 12 and 13 show the simulation results of the particle distribution on the XY coordinates when $L = 10.5$ and 11.0 mm, respectively. Comparing with Fig. 6, particles are supplied to the center of melt pool and the powder convergence would be improved with the new nozzles.

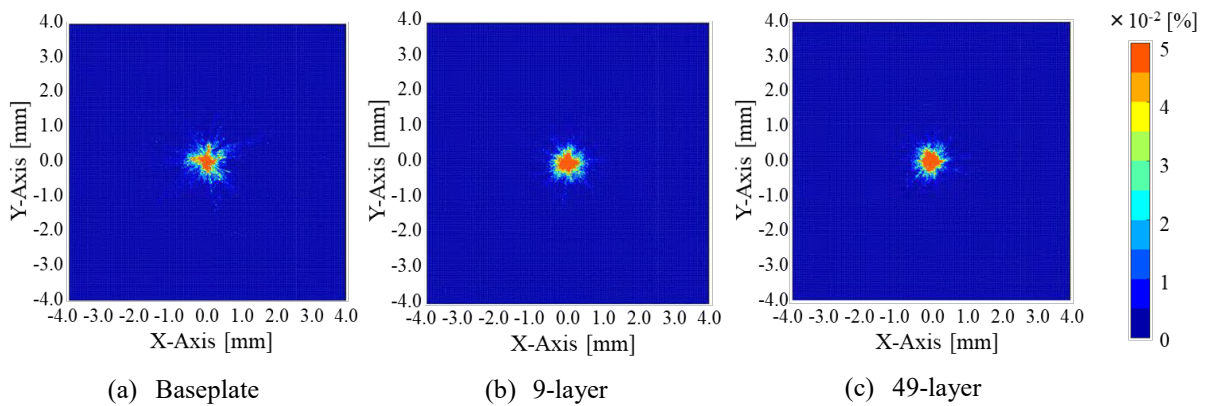


Figure 12 Particle distribution on top surface of deposit and baseplate (Convergence distance : 10.5 mm)

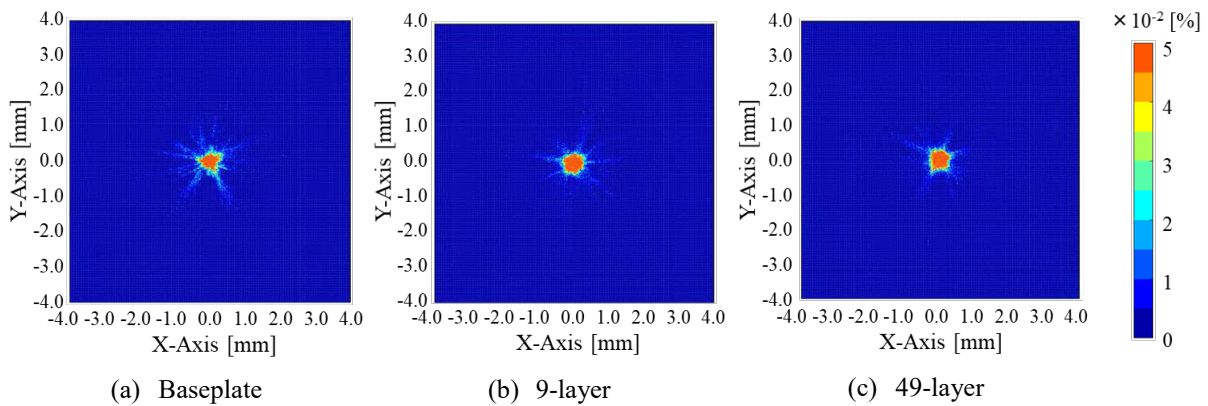


Figure 13 Particle distribution on top surface of deposit and baseplate (Convergence distance : 11.0 mm)

Furthermore, Fig. 14 shows the probability distribution of particles when $L = 10.5$ and 11.0 mm. Comparing with Fig. 7(b), the powder distribution gets close to the center of melt pool, and $\bar{p}_{1.5}$ is improved to 94.8% and 93.3% respectively. Moreover, the expected distance between the center of melt pool and arrival point of particle ($=E$) is calculated. In the results of $L = 10.5$ mm, the expected distance E becomes 0.66, 0.46 and 0.43 mm on the baseplate, 9-

layer and 49-layer deposit respectively. In the results of $L = 11.0$ mm, the E becomes 0.70, 0.48 and 0.46 mm on the baseplate, 9-layer and 49-layer deposit respectively. The conventional nozzle with carrier gas-flow rate of 6 L/min (Fig. 7(c)) showed that the E was 0.36, 0.45 and 0.46 mm. From these results, the high particle convergence is achieved even with low carrier gas-flow rate in 9- and 49-layer deposit. On the other hand, the particle convergence on the baseplate is not improved enough when the carrier gas supply is small as 4 L/min.

In practical usage, an adjustment of the carrier gas-flow rate would be effective to achieve the stable powder convergence. The simulation is also conducted by using the new nozzle model ($L = 10.5, 11.0$ mm) with 6 L/min of carrier gas-flow rate, and the probability distribution of particle is obtain as shown in Fig. 15. In the both results with new nozzles, $p_{1.5}$ on the baseplate reaches 99.9 %. Therefore, the new nozzles can achieve the high particle convergence stably by supplying carrier gas of 6 L/min only for the deposition on a baseplate. Furthermore, the particle convergence is kept in high even with small carrier gas supply as 4 L/min during the deposition on higher layer. As a future work, experimental investigation needs to be conducted with the suggested nozzle design and carrier gas-flow rate corresponding to the vilification of simulation.

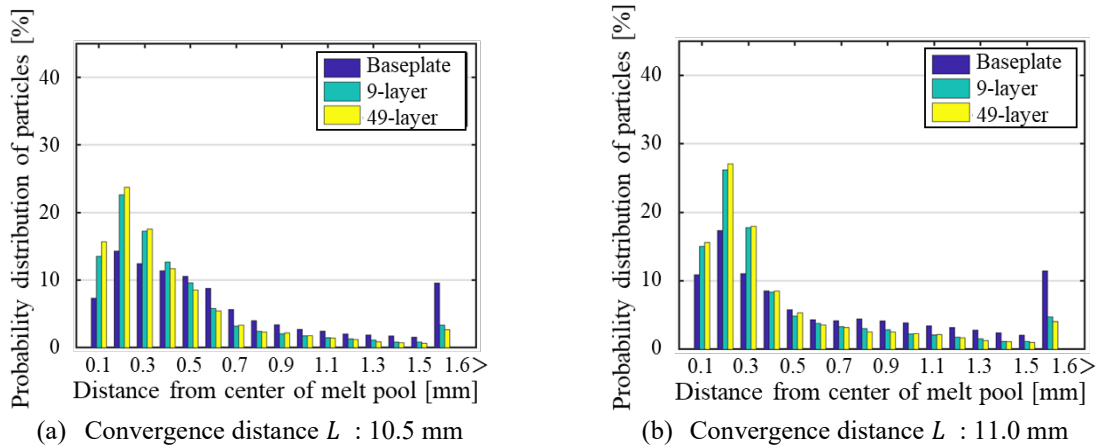


Figure 14: Probability distribution of particles (Convergence distance : 10.5, 11.0 mm)

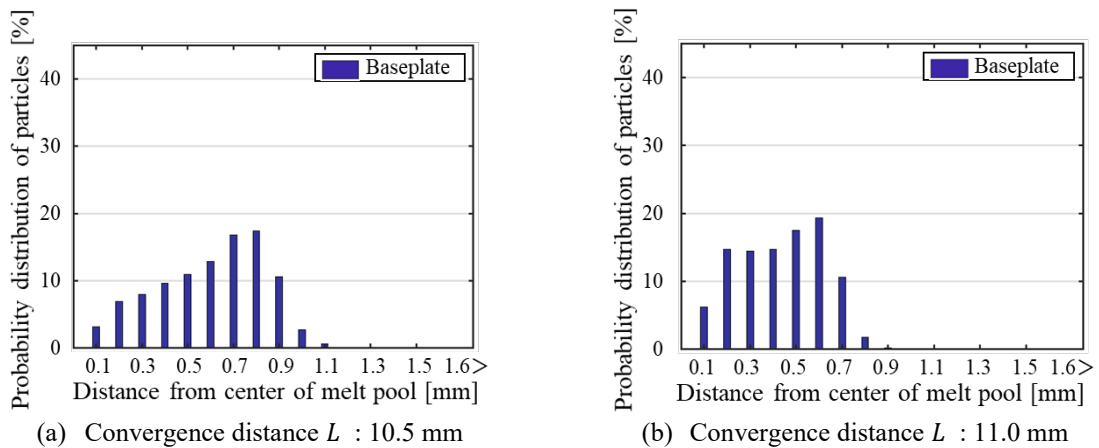


Figure 15: Probability distribution of particles (Carrier gas-flow rate : 6 L/min)

6 CONCLUSIONS

An influence of carrier gas-flow rate and the deposition height on the particle distribution is investigated by conducting the computational fluid dynamics simulation. Furthermore, the design of powder-nozzle shape is discussed and evaluated numerically. The obtained results are summarized as follows:

- According to the simulation considering the deposit with various heights, the particle distribution slightly spreads when the deposit is higher. The analysis of the flow velocity and pressure distribution indicates that the distance from the top surface of deposit and baseplate affects the particle trajectory under the nozzle.
- In order to enhance the powder convergence even with low carrier gas supply, the powder-nozzle shape is changed by shortening the convergence distance L than the standoff distance S . In the results of $L = 10.5$ and 11.0 mm, $\bar{p}_{1.5}$ is improved to 94.8% and 93.3% respectively from the result in conventional nozzle of 90.5%.
- The powder convergence on the baseplate is still low. The simulation results indicate that the new nozzles can achieve the high convergence stably and reduce total amount of gas supply by increasing the carrier gas-flow rate only on the baseplate.

REFERENCES

- [1] Michael, S. and Marion, M. et al. Laser based additive manufacturing in industry and academia, *CIRP Annals - Manufacturing Technology* (2017) **66**:561-583.
- [2] James, C. H. and Baolong, Z. et al. Working distance passive stability in laser directed energy deposition, *Materials and Design* (2019) **161**:86-94.
- [3] Heng, P. and Todd, S. et al. The Investigation of Gravity-Driven Metal Powder Flow in Coaxial Nozzle for Laser-Aided Direct Metal Deposition Process, *Journal of Manufacturing Science and Engineering* (2006) **128**:541–553.
- [4] Gangxian, Z. and Dichen, L. et al. Numerical simulation of metallic powder flow in a coaxial nozzle in laser direct metal deposition, *Optics & Laser Technology* (2011) **43**:106–113.
- [5] Arrizubieta, J. L. and Tabernero, I. et al. Continuous coaxial nozzle design for LMD based on numerical simulation, *Physics Procedia* (2014) **56**:429-438.
- [6] Christopher, K. and Weixiao, S. et al. Modeling Particle Spray and Capture Efficiency for Direct Laser Deposition Using a Four Nozzle Powder Injection System, *Journal of Manufacturing Science and Engineering* (2018) **140**:041014.
- [7] Zhang, B. and Coddet, C. Numerical study on the effect of pressure and nozzle dimension on particle distribution and velocity in laser cladding under vacuum base on CFD, *Journal of Manufacturing Processes* (2016) **23**:54-60.
- [8] Uazir, D.O. and Vaclav, O. Analysis of coaxial laser cladding processing conditions, *Surface and Coatings Technology* (2005) **197**:127-136.
- [9] B.E. Launder, Spalding DB. *Lectures in mathematical models of turbulence*. Academic Press, (1972).

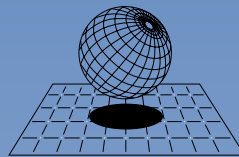
AUTHORS INDEX

Airoidi, A. A.	408	Gudenko, A.	328
Akarçay, E.	154	Gumenyuk, A.	246
Alaimo, G.	162	Gunaydin, K.	408
Albrecht, H.	417	Gupta, A.	444
Altinkaynak, A.	361	Gümüő, Ö. F.	154
Altenburg, S. J.	246	Hira, O.	361
Andrade-Campos, A.	381	Haider, A.	417
Auricchio, F.	162	Hassila, C-J	51
Awd, M.	262	Hess, J.	286
Aydın, İ.	154	Hochberg, U.	142
Barroqueiro, B.	381	Johlitz, M.	256
Bassani, P.	72	Jung, S.	440
Baumann, S.	316	Junk, S.	142
Bellet, M.	274	Kakinuma, Y.	456
Belousov, S.	297	Kato, J.	205
Biancolini, M. E.	19	Kavas, B.	369
Bierwisch, C.	316	Kiener, L.	237
Biffi, C. A.	72	Klerch, B.	142
Bogdanova, M.	297	Koch, M.	440
Bosetti, P.	391	Koike, R.	456
Caboussat, A.	286	Koike, Y.	205
Capelli, C.	31	Komini, L.	237
Carraturo, M.	162	Korneev, B.	297
Castelli, K.	120	Kruis, J.	237
Cavallo, A.	19	Lammers, S.	174
Celi, S.	19, 31	Landini, L.	31
Cella, U.	19	Lang, M.	316
Chinesta, F.	215	Lepschi, A.	417
Cosandier, F.	237	Levchenko, V.	297
Costa, E.	19	Lewis, A.	444
Dal, M.	274	Li, E.L.	309
Davididi, D.	91	Lindwall, J.	51
Dietemann, B.	316	Lion, A.	256
Dragunov, V.	328	Loew-Baselli, B.	417
El Rai, K.	215	Lorenz, U.	193
Engin, C.B.	154	Losi, P.	19
Fabbro, R.	274	Lutey, A.	83
Fanni, B.M.	31	Lyroni, N.	225
Fiocchi, J.	72	López, C.	186
Fornaci, A.	91	Maierhofer, C.	246
Gallina, F. G.	408	Marattukalam, J J	51
Gaponova, D.	328	Masserey, A.	286
Gasparotti, E.	19, 31	Mayi, Y.A.	274
Gayir, C.	369	Mechtcherine, V.	428
Ghnatios, C.	215	Meschke, G.	428
Giberti, H.	111, 120	Meshkov, A.	297
Grande, A. M.	408	Metton, C.	274

Millward, H	444	Saudan, H.	237
Moeckel, M.	403	Sauvage, E.	31
Mohseni-Mofidi, S.	316	Savandaiah, C.	417
Moriconi, C.	274	Scheuschner, N.	246
Nakapkin, D.	297	Schievano, S.	31
Nerella, V.N.	428	Sendur, P.	369
Nicoletto, G.	83, 91	Shcherbakov, A.	328
Ntintakis, I.	225	Silvestri, M.	111
Oda, Y.	456	Simsek, U.	369
Özcan, Ş.	154	Sliva, A.	328
Papadakis, L.	349	Soldani, G.	19
Papadopoli, S.	40	Stavroulakis, G. E.	225
Parshin, D.A.	340	Stepanov, A.	297
Peetz, S.	440	Strada, R.	99
Perepelkina, A.	297	Straße, A.	246
Perini, M.	391	Stroobants, J.	186
Perruchoud, G.	237	Strömberg, N.	130
Peyre, P.	274	Takemura, S.	456
Picasso, M.	286	Tinelli, G.	83
Plakia, N.	225	Tominski, J.	174
Popp, K.	316	Tuissi, A.	72
Positano, V.	31	Ushijima, K.	205
Potapkin, B.	297	Valente, F.	40
Reali, A.	162	Valente, R.A.F.	381
Rehbein, T.	256	Vignali, E.	19, 31
Reinold, J.	428	Walther, F.	262
Reintjes, C.	193	Weisz-Patrault, D.	60
Righettini, P.	99	Yelek, H.	154
Rocca, E.	162	Yu, A.B.	309
Rodyakina, R.	328	Zakirov, A.	297
Romoli, L.	83	Zhou, Z.Y.	309
Rubtsov, V.	328	Zimmer, D.	174
Rudloff, J.	316	Zou, R.P.	309
Sala, G.	408		



UNIVERSITÀ
DI PAVIA



CIMNE

International Center
for Numerical Methods in Engineering

www.cimne.com